

# **Rational design of multi-component functionalized supramolecular assemblies**

This dissertation is submitted for the degree of  
“Doctor rerum naturalium” in chemistry

TU Dortmund

Fakultät für Chemie und Chemische Biologie



Clever Lab

Qianqian Yan

From Hebei, China

Dortmund, September 2022

This work has been prepared from October 2018 to September 2022 at the Faculty of Chemistry and Chemical Biology at TU Dortmund University under supervision of Prof. Dr. Guido H. Clever.

**Principal advisor:**           **Prof. Dr. Guido H. Clever**  
Faculty of Chemistry and Chemical Biology,  
TU Dortmund University

**Coexaminer:**               **Prof. Dr. Sebastian Henke**  
Faculty of Chemistry and Chemical Biology,  
TU Dortmund University

**Submission Date:**       19.09.2022

## Eidesstattliche Versicherung (Affidavit)

\_\_\_\_\_  
Name, Vorname  
(Surname, first name)

\_\_\_\_\_  
Matrikel-Nr.  
(Enrolment number)

**Belehrung:**

Wer vorsätzlich gegen eine die Täuschung über Prüfungsleistungen betreffende Regelung einer Hochschulprüfungsordnung verstößt, handelt ordnungswidrig. Die Ordnungswidrigkeit kann mit einer Geldbuße von bis zu 50.000,00 € geahndet werden. Zuständige Verwaltungsbehörde für die Verfolgung und Ahndung von Ordnungswidrigkeiten ist der Kanzler/die Kanzlerin der Technischen Universität Dortmund. Im Falle eines mehrfachen oder sonstigen schwerwiegenden Täuschungsversuches kann der Prüfling zudem exmatrikuliert werden, § 63 Abs. 5 Hochschulgesetz NRW.

Die Abgabe einer falschen Versicherung an Eides statt ist strafbar.

Wer vorsätzlich eine falsche Versicherung an Eides statt abgibt, kann mit einer Freiheitsstrafe bis zu drei Jahren oder mit Geldstrafe bestraft werden, § 156 StGB. Die fahrlässige Abgabe einer falschen Versicherung an Eides statt kann mit einer Freiheitsstrafe bis zu einem Jahr oder Geldstrafe bestraft werden, § 161 StGB.

Die oben stehende Belehrung habe ich zur Kenntnis genommen:

**Official notification:**

Any person who intentionally breaches any regulation of university examination regulations relating to deception in examination performance is acting improperly. This offence can be punished with a fine of up to EUR 50,000.00. The competent administrative authority for the pursuit and prosecution of offences of this type is the chancellor of the TU Dortmund University. In the case of multiple or other serious attempts at deception, the candidate can also be unenrolled, Section 63, paragraph 5 of the Universities Act of North Rhine-Westphalia.

The submission of a false affidavit is punishable.

Any person who intentionally submits a false affidavit can be punished with a prison sentence of up to three years or a fine, Section 156 of the Criminal Code. The negligent submission of a false affidavit can be punished with a prison sentence of up to one year or a fine, Section 161 of the Criminal Code.

I have taken note of the above official notification.

\_\_\_\_\_  
Ort, Datum  
(Place, date)

\_\_\_\_\_  
Unterschrift  
(Signature)

\_\_\_\_\_  
Titel der Dissertation:  
(Title of the thesis):

\_\_\_\_\_  
\_\_\_\_\_  
\_\_\_\_\_

Ich versichere hiermit an Eides statt, dass ich die vorliegende Dissertation mit dem Titel selbstständig und ohne unzulässige fremde Hilfe angefertigt habe. Ich habe keine anderen als die angegebenen Quellen und Hilfsmittel benutzt sowie wörtliche und sinngemäße Zitate kenntlich gemacht.

Die Arbeit hat in gegenwärtiger oder in einer anderen Fassung weder der TU Dortmund noch einer anderen Hochschule im Zusammenhang mit einer staatlichen oder akademischen Prüfung vorgelegen.

I hereby swear that I have completed the present dissertation independently and without inadmissible external support. I have not used any sources or tools other than those indicated and have identified literal and analogous quotations.

The thesis in its current version or another version has not been presented to the TU Dortmund University or another university in connection with a state or academic examination.\*

\*Please be aware that solely the German version of the affidavit ("Eidesstattliche Versicherung") for the PhD thesis is the official and legally binding version.

\_\_\_\_\_  
Ort, Datum  
(Place, date)

\_\_\_\_\_  
Unterschrift  
(Signature)



## List of publication and conference contributions

### Publications

1. "Self-Assembly of a Tetraphenylethylene-Based Capsule Showing Both Aggregation- and Encapsulation-Induced Emission Properties"

T. Zhang, G.-L. Zhang, **Q.-Q. Yan**, L. -P. Zhou, L. -X. Cai, X. -Q. Guo, Q. -F. Sun, *Inorg. Chem.* **2018**, *57*, 3596.

2. "Coordination-Enhanced Luminescence on Tetraphenylethylene-Based Supramolecular Assemblies"

**Q. -Q. Yan**, S. -J. Hu, G. -L. Zhang, T.-Zhang, L. -P. Zhou, Q. -F. Sun, *Molecules* **2018**, *23*, 363.

3. "Metallopolymers cross-linked with self-assembled Ln<sub>4</sub>L<sub>4</sub> cages"

**Q. -Q. Yan**, L. -P. Zhou, H.-Y. Zhou, Z. Wang, L. -X. Cai, X. -Q. Guo, X. -Q. Sun, Q. -F. Sun, *Dalton Trans.* **2019**, *48*, 7080.

4. "Dinuclear helicate or mononuclear pincer lanthanide complexes from one ligand: stereo-controlled assembly and catalysis"

R. Chen, **Q. -Q. Yan**, S. -J. Hu, X. -Q. Guo, L. -X. Cai, D. -N. Yan, L. -P. Zhou, Q. -F. Sun, *Org. Chem. Front.* **2021**, *8*, 2576.

5. "Endohedrally Functionalized Heteroleptic Coordination Cages for Phosphate Ester Binding"

A. Platzek, S. Juber, C. Yurtseven, S. Hasegawa, L. Schneider, C. Drechsler, K. E. Ebbert, R. Rudolf, **Q.-Q. Yan**, J. J. Holstein, L. V. Schäfer, G. H. Clever, *Angew. Chem. In. Ed.* **2022**, *61*, e202209305.

6. "AIE-active metallamacrocycles with reversal of circularly polarized luminescence"

**Q. -Q. Yan**, J. Tessarolo, Y. -Ting Chen, J. J. Holstein, G. H. Clever. *In preparation*.

### Conference Contributions

1. Poster, SupraChem 2022, Mainz, Germany.
2. Poster, The 14<sup>th</sup> International Symposium on Macrocyclic and Supramolecular Chemistry (ISMSC), 2019, Lecce, Italy.
3. Poster, The 14<sup>th</sup> International Symposium on Macrocyclic and Supramolecular Chemistry (ISMSC), 2019, Lecce, Italy.
4. Poster, SupraChem 2019, Würzburg, Germany.



## Abstract

In the past few decades, a plethora of metalla-supramolecular architectures, obtained by rational design approaches, were successfully explored. In recent years, the focus of the field has progressively expanded from the purely structural studies, towards the implementation of functions such as catalysis and sensing. In this work, a series of salen- (or salphen-) based macrocyclic architectures is obtained through the condensation of functionalized bis-salicylaldehyde derivative ligands, with diamine derivatives, followed by metal complexation with transition metal ions. The self-assembled metallacycles' properties have been tuned by modification of the building blocks, to explore: *i*) chiroptical properties and assembly into nanomaterials, *ii*) photoredox catalysis, and *iii*) formation of mechanically interlocked molecules (MIMs).

Circularly polarized luminescence (CPL) with high luminescence dissymmetry factor ( $g_{lum}$ ) are highly desirable for promising applications in 3D displays, molecular recognition, etc. Here, inspired by benefits of supramolecular chemistry and aggregation-induced emission (AIE) materials, a new class of binuclear CPL-active metallamacrocycles **Zn<sub>2</sub>R** based on tetraphenylethylene (TPE) was designed. The structural and chiroptical properties of the assemblies were fully characterized with a wide range of techniques. Combination of luminescence and chirality was successfully endowed in **Zn<sub>2</sub>R**, deriving from the single building blocks in a modular fashion, resulting in a new class of materials with AIE, CD, and CPL properties. Furthermore, **Zn<sub>2</sub>R** assemble in helical filaments upon aggregation, resulting in a change of sign and increase of the CPL signals.

Metal salen Schiff base complexes are widely used for catalytic transformations. Here, a phenoxazine-based metal salen macrocycle **Zn<sub>2</sub>R<sup>PZ</sup>**, designed for photoredox catalysis, is reported. The structural and photophysical properties of ligand **L**, macrocycles **R<sup>PZ</sup>** and **Zn<sub>2</sub>R<sup>PZ</sup>** were investigated. The obtained macrocycles show strong visible-light absorption, low oxidation potential and reversible redox properties, thus the photoredox-catalyzed pinacol coupling of aldehydes was investigated, obtaining high conversion yields under visible light irradiation.

The reported metallacycles can also be used as macrocyclic units to form (pseudo-)rotaxane structures, where an additional ligand can coordinate to the metal centers, acting as a stopper, while its backbone substituents constitute the thread. Based on this design, two carbazole-based bis-bidentate pyridine ligands with different functional substituents on the backbone were synthesized. Both ligand  $L^R$  having a flexible substituent and ligand  $L^{NH_2}$  with a rigid substituent can self-assemble with a binuclear Co(III) macrocycle  $Co(III)_2R^{ACR}$  to form a bow-shape architectures with the substituent located inside the cycle cavity. The possible connection of two bowls to form [3]rotaxane was explored by reacting functional groups on the substituents of the ligands. Furthermore, the combination of two ligands with geometric shape-complementary, endowed with catalytic active sites, were assembled with  $Co(III)_2R^{ACR}$ , leading to the formation of an heteroleptic cage with potential applications in supramolecular catalysis.



## Zusammenfassung

In den letzten Jahrzehnten wurde eine Vielzahl von metalla-supramolekularen Architekturen, welche durch rationale Designansätze erhalten wurden, erfolgreich erforscht. Der Schwerpunkt des Forschungsfelds hat sich in den letzten Jahren zunehmend von der bloßen Untersuchung der Strukturen auf die Einführung von Funktionalitäten, beispielsweise für die Katalyse oder die Sensorik, erweitert. In dieser Arbeit wurde eine Reihe von makrozyklischen Architekturen auf Salen- (oder Salphen-) Basis durch die Kondensation von funktionalisierten Bis-Salicylaldehyd-Derivat-Liganden mit Diaminen und anschließender Komplexierung mit Übergangsmetallionen erhalten. Durch Modifizierung der Bausteine wurden die Eigenschaften der selbstassemblierten Metallamakrozyklen eingestellt, um i) chiroptische Eigenschaften und die Assemblierung zu Nanomaterialien, ii) Photo-Redox-Katalyse und iii) die Bildung mechanisch verzahnter Moleküle (*mechanically interlocked molecules*, MIMs) zu erforschen.

Zirkular polarisierte Lumineszenz (*Circularly polarized luminescence*, CPL) mit hohem Lumineszenz-Dissymmetriefaktor ( $g_{lum}$ ) ist für vielversprechende Anwendungen, beispielsweise in der 3D Displays Technologie und der molekularen Erkennung, äußerst wünschenswert. Inspiriert von den Vorteilen der supramolekularen Chemie und von Materialien mit aggregationsinduzierter Emission (AIE) wurde hier eine neue Klasse von dinuklearen CPL-aktiven Metallamakrozyklen **Zn<sub>2</sub>R** auf der Basis von Tetraphenylethylen (TPE) entwickelt. Die strukturellen und chiroptischen Eigenschaften der Assemblierungen wurden mit einer Vielzahl von Techniken vollständig charakterisiert. In den Metallamakrozyklen **Zn<sub>2</sub>R**, welche in einer modularen Weise aus den einzelnen Bausteinen gebildet werden, wurden Lumineszenz und Chiralität erfolgreich kombiniert. Die Metallamakrozyklen stellen somit eine neue Klasse von Materialien mit AIE-, CD- und CPL-Eigenschaften dar. Bei Aggregation assemblieren **Zn<sub>2</sub>R** Bausteine zu spiralförmigen Filamenten, was zu einer Änderung des Vorzeichens und einer Steigerung der CPL-Eigenschaften führt.

Metall-Salen-Schiff'sche-Base-Komplexe werden häufig für katalytische Umwandlungen verwendet. Hier wird über einen auf Phenoxazin basierenden Metall-Salen-Makrozyklus **Zn<sub>2</sub>R<sup>PZ</sup>** berichtet, welcher für die Photo-Redox-Katalyse

entwickelt wurde. Die strukturellen und photophysikalischen Eigenschaften des Liganden **L** sowie der Makrozyklen **R<sup>PZ</sup>** und **Zn<sub>2</sub>R<sup>PZ</sup>** wurden untersucht. Die erhaltenen Makrozyklen zeigen eine starke Absorption von sichtbarem Licht, ein niedriges Oxidationspotenzial und reversible Redox Eigenschaften. Daher wurde die photo-redox-katalysierte Pinakol-Kupplung von Aldehyden untersucht, bei der unter Bestrahlung mit sichtbarem Licht hohe Umsätze erzielt wurden.

Die Metallazyklen, über welche hier berichtet wird, können als makrozyklische Einheiten zur Bildung von (Pseudo-)Rotaxanen verwendet werden. Dabei koordiniert ein zusätzlicher Ligand an die Metallzentren und fungiert so als Stopper, während die Substituenten am Rückgrat des Liganden die Achse bilden. Auf der Grundlage dieses Konzepts wurden zwei bis-bidentate Pyridin-Liganden auf Carbazol-Basis mit unterschiedlichen funktionellen Substituenten am Rückgrat synthetisiert. Sowohl der Ligand **L<sup>R</sup>** mit einem flexiblen Substituenten als auch der Ligand **L<sup>NH2</sup>** mit einem starren Substituenten können mit einem zweikernigen Co(III)-Makrozyklus **Co(III)<sub>2</sub>R<sup>ACR</sup>** assemblieren, um eine schalenförmige Architektur zu bilden, bei der sich der Substituent im Inneren der Kavität des Zyklus befindet. Die mögliche Verbindung von zwei Schalen zur Bildung von [3]Rotaxanen wurde durch Reaktion der funktionellen Gruppen am Ligandensubstituenten untersucht. Darüber hinaus wurden zwei Liganden, welche geometrisch komplementäre Formen aufweisen und mit katalytisch aktiven Stellen ausgestattet sind, mit **Co(III)<sub>2</sub>R<sup>ACR</sup>** assembliert, was zur Bildung eines heteroleptischen Käfigs mit potenziellen Anwendungen in der supramolekularen Katalyse führte.

## Table of contents

ABSTRACT .....	I
ZUSAMMENFASSUNG .....	III
1 GENERAL INTRODUCTION.....	1
1.1 Supramolecular self-assembly.....	1
1.2 Supramolecular macrocycles.....	6
1.3 Metal salen supramolecular complexes.....	8
1.4 References.....	13
2 SCOPE OF THIS THESIS.....	19
3 TETRAPHENYLETHYLENE-BASED MACROCYCLES WITH ADJUSTABLE CPL.....	21
3.1 Introduction .....	23
3.2 Synthesis of TPE-based ligands and macrocycles .....	34
3.3 Self-assembly of metal salen macrocycles .....	36
3.4 Chiroptical properties study in solution .....	42
3.5 The investigation of AIE properties .....	44
3.6 Conclusion and outlook.....	49
3.7 Experimental part.....	51
3.8 References.....	82
4 PHENOXAZINE-BASED MACROCYCLES FOR PHOTO-REDOX CATALYSIS.....	85
4.1 Introduction .....	87
4.2 Design of phenoxazine-based ligand macrocycles.....	93
4.3 Photophysical properties of $Zn_2R^{PZ}$ .....	98
4.4 Photoredox catalysis.....	103
4.5 Conclusion .....	107
4.6 Experimental part.....	108
4.7 References.....	161
5 COORDINATION-DRIVEN CONSTRUCTION OF [3]ROTAXANE BASED ON HIERARCHICAL ASSEMBLY .....	163
5.1 Introduction .....	165
5.2 Ligand design and synthesis.....	167
5.3 Formation of the bowl .....	171

5.4 Formation of an axle .....	179
5.5 Formation of rotaxanes .....	181
5.6 Formation of a heteroleptic cage.....	183
5.7 Conclusion .....	189
5.8 Experiment Part .....	189
5.9 References .....	234
6 CONCLUSION AND PERSPECTIVES .....	237
ABBREVIATIONS.....	239
ACKNOWLEDGEMENTS.....	241

# 1 General introduction

## 1.1 Supramolecular self-assembly

Supramolecules are defined in IUPAC as following: “A system of two or more molecular entities held together and organized by means of intermolecular (noncovalent) binding interactions”.<sup>[1]</sup> Intermolecular connections which are often seen in supramolecules are electrostatic interactions (i.e. hydrogen bond), hydrophobic interactions, and van der Waals forces. For example, double stranded DNA can be classified as a supramolecule held together chemoselectively via hydrogen bonds between appropriate base-pairs. One of the biggest differences between supramolecules and single molecules is the dynamicity inherited from such weak yet dynamic interactions. As it can be seen in the crucial role of DNA in living organisms to store and inhere genetic information, the dynamicity of the bonds endows supramolecules with functions which single molecules cannot do.

Supramolecular chemistry has attracted attention due to the potential of supramolecules in material development,<sup>[2]</sup> biological applications,<sup>[3]</sup> catalysis<sup>[4]</sup> and so forth. Further, introduction of the concept of coordination-driven self-assembly, allowing dynamicity through largely covalent but labile metal-ligand interactions, by Lehn and other pioneers have broadened the diversity of structural motifs in supramolecular chemistry.<sup>[5]</sup> In the past few decades, Fujita<sup>[6]</sup>, Stang,<sup>[7]</sup> Mirkin,<sup>[8]</sup> Raymond,<sup>[9]</sup> Nitschke,<sup>[10]</sup> and others have pioneered the coordination-driven self-assembly, which has been proven to be one of the most powerful methods to provide a wide variety of discrete two- and three- dimensional structures with well-defined shapes and precisely controlled sizes.<sup>[11,12]</sup> Most reported self-assembly processes of metal-organic complexes proceed under thermodynamic control, with an “error correction” process, affording the thermodynamically most stable product. In coordination-driven self-assembly, the shape, size and topology of the resulting compounds is defined by the coordination fashion of the metal nodes (acceptors) and bent angle of ligand (donors) (Figure 1.1).

## 1. General introduction

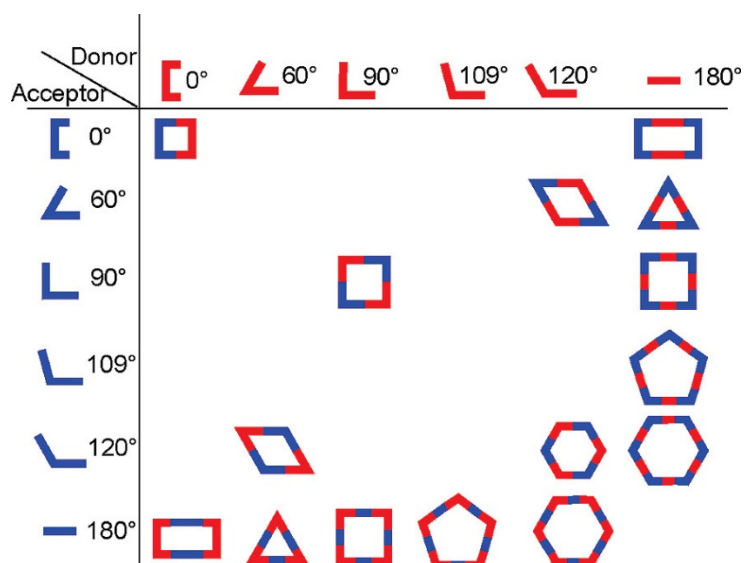


Figure 1.1: Schematic illustration of building blocks to generate 2D architectures via self-assembly.<sup>[13]</sup> Copyright © 2012 American Chemical Society.

For instance, Fujita and co-workers have reported the quantitative formation of a macrocyclic coordination compound by coordination-driven self-assembly of linear 4,4'-bipyridine and *cis*-protected Pd(II) in the early 1990s (Figure 1.2).<sup>[14]</sup> The square is defined by the coordination number and manner of Pd(II) centers forming a square planar coordination environment. Design principle and synthesis of such metal-organic macrocyclic compounds are well summarized in *Metallamacrocycles* by Hai-Bo Yang published by The Royal Society of Chemistry,<sup>[15]</sup> as well as in some reviews by Stang<sup>[16–18]</sup> and so on.

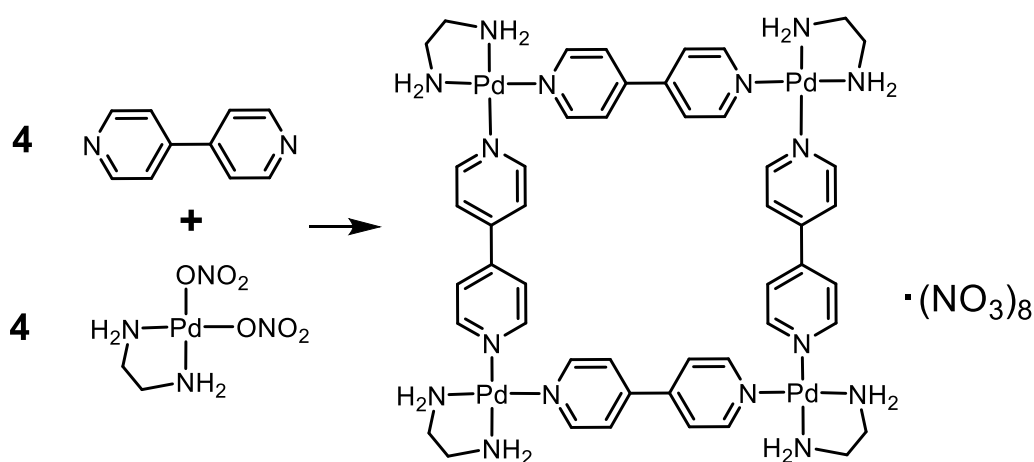


Figure 1.2: Self-assembly of square complex from 4,4'-bipyridine and *cis*-protected Pd(II).

Taking advantage of the rational design approach based on the ligand geometry and metal coordination geometry, the field of metallasupramolecular self-assembly has emerged as a promising area for the development of intricate architectures with increasing complexity and functionality.<sup>[19–29]</sup>

### 1.1.1 Functionalized metal-organic assemblies

To date, a wide range of metal-organic assemblies with well-defined geometries and sizes have been reported.<sup>[30–33]</sup> The rationally designed structures also allow the incorporation of functionalities. Recently, efforts have shifted from syntheses of aesthetic architectures to generating functional systems and exploiting their properties.

In general, the functionalities can be incorporated into the coordination assemblies through the following methods (Figure 1.3), which have been successfully explored. (i) Using the building blocks with functional moieties (edge or corner functionalization);<sup>[34,35]</sup> (ii) Covalent attachment of functional units to the inside (*endo*-functionalization)<sup>[36–38]</sup> or outside (*exo*-functionalization)<sup>[39]</sup> of the building block, which can lead to the formation of assemblies with functional moieties positioned within the interior and on the periphery of the structures, respectively.

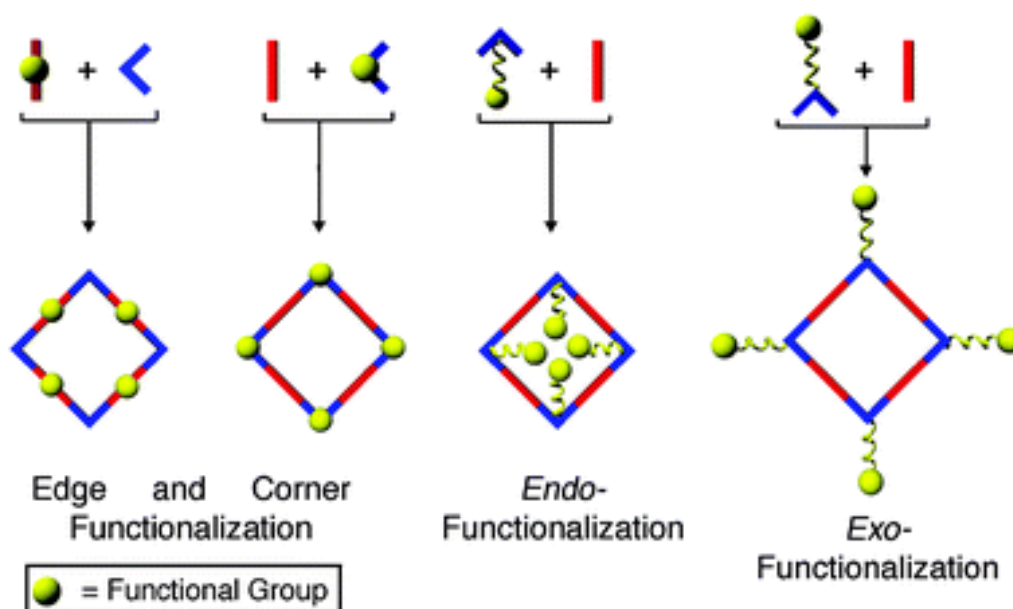


Figure 1.3: The approaches to incorporating functional moieties into metal-organic assemblies through the use of functionalized building blocks or *endo*-/*exo*-functionalization.<sup>[40]</sup> Copyright ©The Royal Society of Chemistry 2008.

## 1. General introduction

### 1.1.2 Chiral assemblies

Chiral molecules are ubiquitous and indispensable components existing in biological systems.<sup>[41]</sup> Recently, chiral self-assembly at supramolecular levels has attracted considerable attention.<sup>[42–45]</sup> The incorporation of chirality into metalla-assemblies provides them unique potentials in recognition,<sup>[46]</sup> asymmetric catalysis,<sup>[47]</sup> and nonlinear optical materials.<sup>[48]</sup> Various artificial chiral metalla-supramolecular architectures have been constructed via coordination driven self-assembly.<sup>[49–51]</sup>

In general, the chirality can be introduced within metal-organic assemblies in two different ways (Figure 1.4).<sup>[52]</sup> (i) “Hard” approach. The enantiopure structure is produced from the optically pure chiral building blocks, either chiral organic ligand<sup>[53]</sup> or metal center with auxiliary groups attached.<sup>[54,55]</sup> (ii) “soft” approach. Chirality of assemblies is produced by achiral building blocks, arising from the spatial arrangement of coordinating ligands around the metal center<sup>[56]</sup> or results from twisting of the ligand arrangement.<sup>[57]</sup>

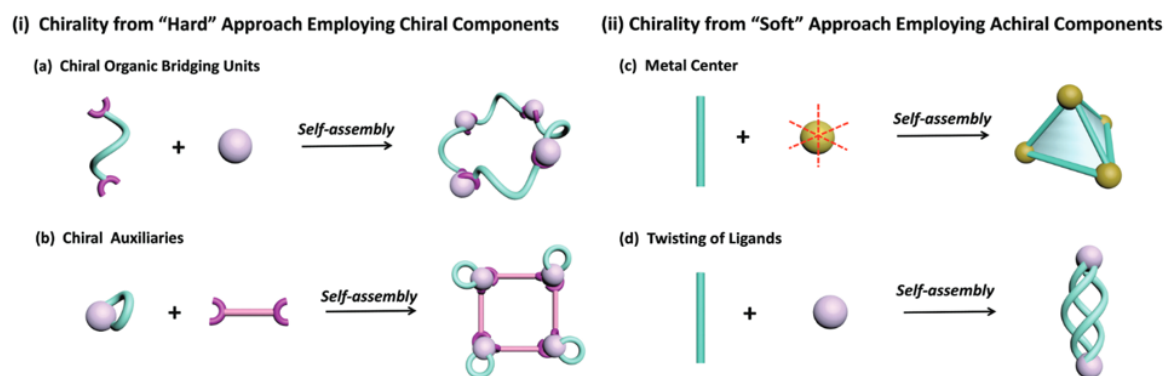


Figure 1.4: Possible approaches for the construction of chiral coordination assemblies<sup>[52]</sup>. Copyright © The Royal Society of Chemistry 2017.

Chirality transfer from a chiral guest to achiral assemblies was also investigated in host-guest systems.<sup>[58,59]</sup> The rational design of assemblies to achieve chiral retention, enhancement, switch, and transfer of preset chiral units is still a challenge and drawing increasing attention for the potential application in stereoselective recognition, and as asymmetric reaction container.



### 1.1.3 Photoluminescent assemblies

The optical properties of metal-organic complexes are of considerable interest for their application in sensing and bioimaging. Some emissive assemblies have been prepared by using ligands comprised of well-known fluorophores, such as anthracene, BODIPY, and porphyrin, etc (Figure 1.5) or certain metal ions.<sup>[60]</sup>

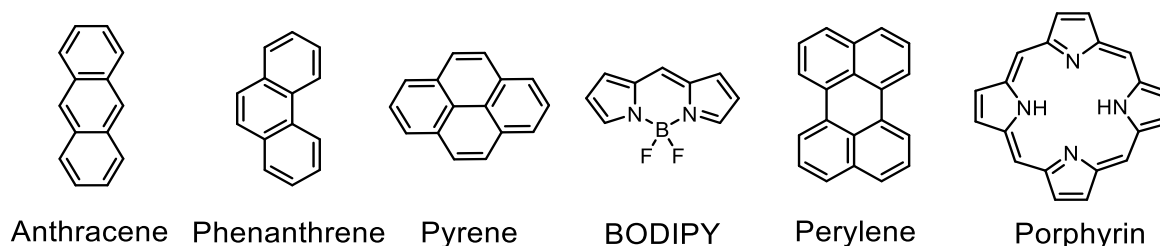


Figure 1.5: Chemical structures of luminophores

Most aromatic hydrocarbons are commonly known to show aggregation-caused quenching (ACQ) effect, a phenomenon where the luminescence of molecules is quenched at high concentrations due to strong  $\pi$ - $\pi$  stacking interactions of the aromatic rings (Figure 1.6 a). This has been a great obstacle to the development of luminescent materials.

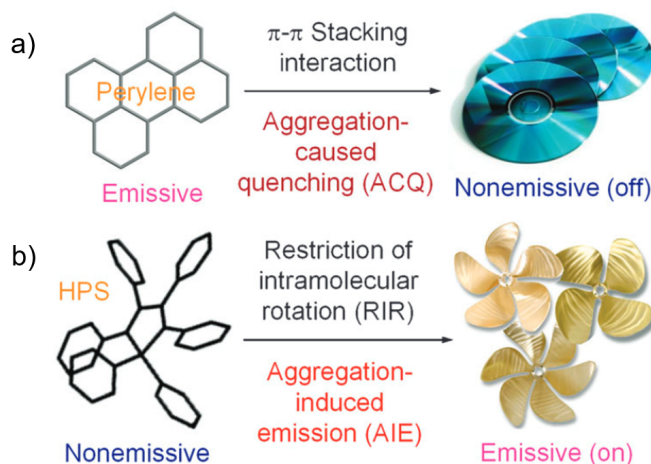


Figure 1.6: Illustration of the aggregation of a) planar luminophoric molecules such as perylene tending to aggregate as discs piled up and b) non-planar luminogenic molecules such as hexaphenylsilole (HPS)<sup>[61]</sup>. Copyright © The Royal Society of Chemistry 2011.

In 2001, Tang and co-workers reported an aggregation-induced emission (AIE) phenomenon where the molecules show low emission in solution but strong emission in the aggregated state. The proposed mechanism of restriction of intramolecular rotation (RIR) has been widely investigated. The AIE chromophores,

## 1. General introduction

so-called AIEgens, have a propeller-like structure. As a consequence, AIE molecules cannot pack through  $\pi$ - $\pi$  stacking in the aggregated state (Figure 1.6 b). Simultaneously, the restriction of intramolecular rotation blocks the non-radiative pathway and thus turns on the emission. Recently, AIE chromophores have been used as building blocks for the construction of emissive coordination assemblies (See chapter 3.1).<sup>[62]</sup>

### 1.2 Supramolecular macrocycles

Macrocyclic molecules represented by crown ethers, cryptands, cyclodextrins, cucurbiturils, calixarenes, pillar[ $n$ ]arenes, and metal-organic coordination macrocycles are well known to show a good host-guest capability owing to the well-defined space inside and the ability to induce multiple weak interactions thanks to the structures.<sup>[63]</sup>

Unlike three dimensional macrocyclic molecules, planar macrocyclic molecules can stack on top of each other forming higher-order supramolecular assemblies.<sup>[64]</sup> When, for example, a macrocycle assembles into a highly ordered nanostructure such as columnar assembly driven by  $\pi$ - $\pi$  interactions or hydrogen bonds, the hollow inner space in the ordered structure stemming from the macrocyclic structure has highly potential applications.<sup>[65]</sup> For example, the self-assembly of a cyclic peptide forms organic nanotubes with an well-defined diameter via hydrogen bonds upon acidification.<sup>[66]</sup> A highly directional aggregation of aromatic oligoamide macrocycles was reported by Gong and co-workers.<sup>[67]</sup> The formed tubular assembly shows a high ion-conductivity.<sup>[68]</sup> In addition to those fully organic macrocyclic compounds, metal-organic macrocycles have been utilized as building blocks to form supramolecular assemblies. One of the peculiarities of the supramolecular assembly of metal-organic macrocycles is the versatility of them originating from the concept of coordination-driven self-assembly. Chemical modification of ligands may change the whole structural, chemical, and physical properties of the resulting assemblies.

A majority of research on hierarchical assembly of metal-organic macrocycles are based on Pt(II)-containing metallacycles.<sup>[69]</sup> The thermal stability of ligand-Pt(II) bonds endows the metallacycles with stability during the assembly process under

various conditions. A common strategy to realize hierarchical self-assembly of metallacycles is to implement chemical groups to stimulate the self-assembly via weak interactions.

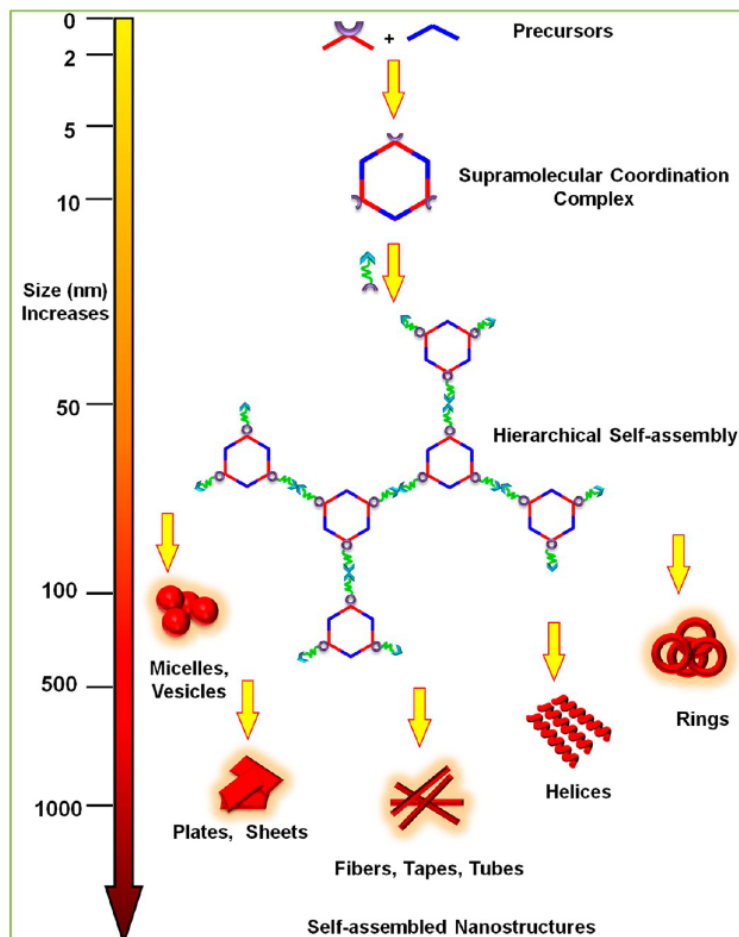


Figure 1.7: schematic representation of a hexagonal supramolecular coordination complexes assembled from suitable precursors and its hierarchical self-assembly into nanostructures.<sup>[70]</sup> Copyright © 2018 American Chemical Society.

Metal-organic macrocycles are a good platform to control assembly and to manipulate physical properties of supramolecular materials. To further explore the potential of metal-organic macrocycles in various applications, it is important to expand the diversity.

## 1. General introduction

### 1.3 Metal salen supramolecular complexes

Schiff base, formed by the condensation between an aldehyde and an amine derivative, was first reported by Hugo Schiff in 1864.<sup>[71]</sup> Salen or salphen ligands are one of the most studied Schiff base ligands (Figure 1.8).<sup>[72,73]</sup> Salen ligands are generally synthesized by condensation reaction between diamine and salicylaldehyde derivative. In numerous cases, diamines and salicylaldehydes are commercially available. Therefore, a wide variety of salen-type ligands have been intensively studied.<sup>[74]</sup> Salen-type ligands can coordinate various metals with different oxidation states via  $N_2O_2$  motif. Salen-type metal complexes are well known to catalyze many kinds of reactions. Furthermore, the facile synthetic procedure and the simple structure are advantageous for diversifying their structures and functions, and thus, applications of salen-complexes are not limited to catalysis. Material development using compounds bearing a salen-complex motif, have been attracted attention in recent years.<sup>[75]</sup>

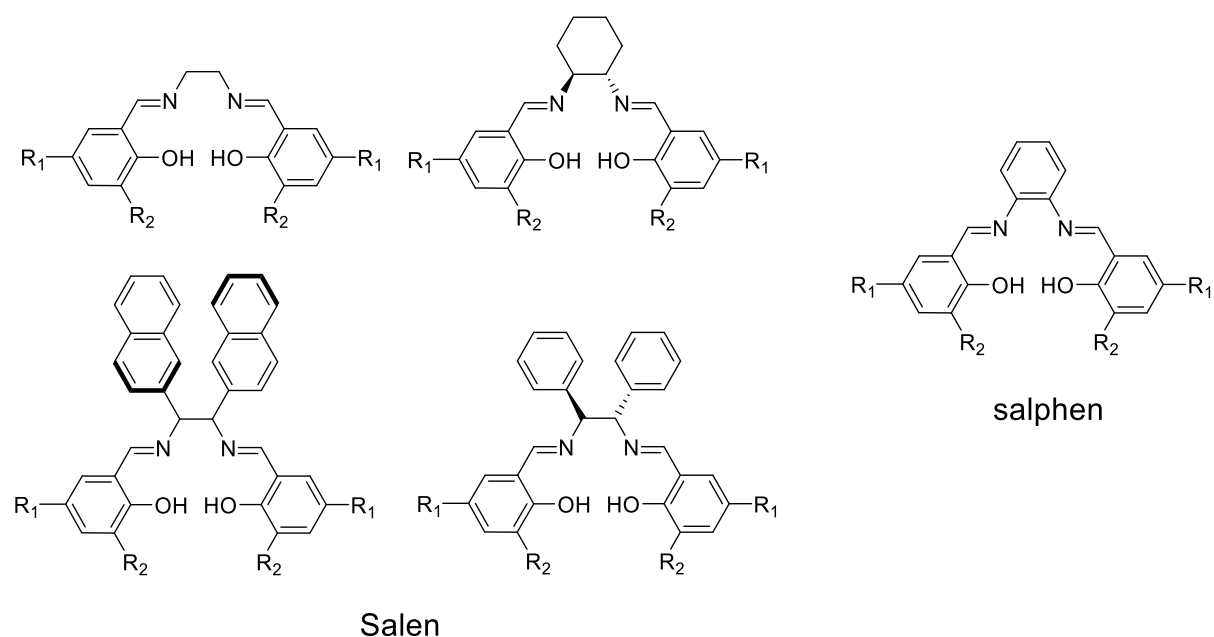


Figure 1.8: Structures of the most commonly used salen and salphen compounds.

One of the most peculiar features of such salen-complexes is the vacant coordination sites of the metal centers.<sup>[76]</sup> The vacant coordination sites play a significant role in most of the catalytic reactions using salen-complexes. Fine engineering of the vacant coordination sites can improve catalytic activity of salen-complexes.<sup>[77]</sup> The metal salen complexes have emerged as versatile building

blocks for functional supramolecular architectures, such as macrocycles,<sup>[78–80]</sup> and coordination cages.<sup>[81,82]</sup>

Macrocycles comprised of multiple salen-moieties show a unique binding capability towards metal ions as well.<sup>[83]</sup> For instance, macrocyclic trimers of salphen show multiple transition metals binding.<sup>[84]</sup> Depending on the transition metals, the macrocycle even forms a cluster of transition metals on the ring. The inner cavity of the macrocycle can be compared to a crown-ethers like structure. Thanks to the oxygen atoms surrounding the void in an ordered manner, supramolecular assembly by addition of alkali metal cations has been also reported.<sup>[85,86]</sup> A larger macrocycle, hexamer of salphen, has even been reported.<sup>[79]</sup> Although not macrocyclic structure, supramolecular assembly of Zn(II) salen complexes has been showcased as well. The salen-motif has even been applied in DNA-engineering. Clever, Carell and co-workers demonstrated stabilization of a DNA duplex by cross-linking via a salen-complex motif.<sup>[87]</sup> Depending on the bound metals on the  $N_2O_2$  binding site, the stabilization effect on the DNA duplex can differ. As shown and evidenced by these examples, salen/salphen based metal-organic macrocycles are an intriguing and attractive motif to be further investigated.

In 2003, Hupp and co-worker have reported Zn salen based ligands to construct supramolecular box assemblies with similar photophysical behavior than (porphyrin)Zn complexes (Figure 1.9).<sup>[88]</sup> The box consists of Zn(II) salen ligands as edges and Rhenium(I) complexes as corners.

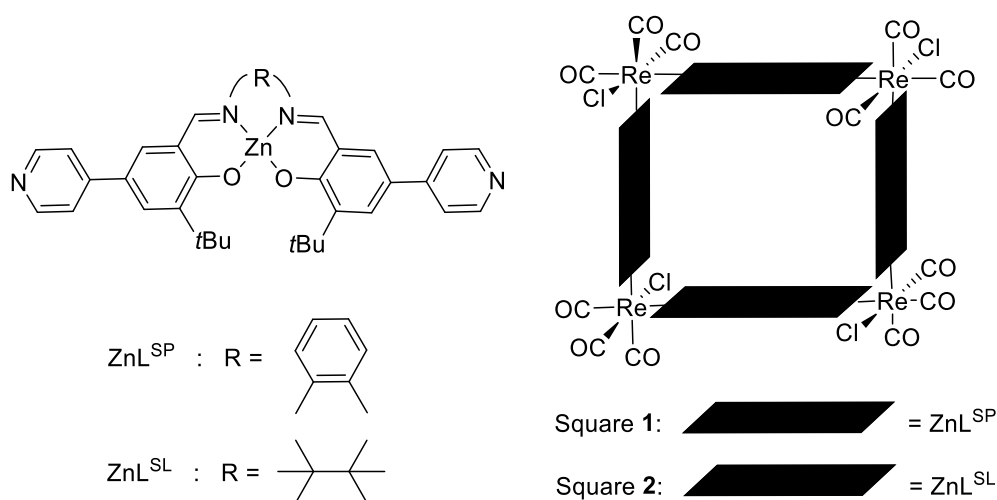


Figure 1.9: The structures of Zn salen ligand and supramolecular box structure.

## 1. General introduction

Reek and co-workers have demonstrated a synthesis of porous materials by bridging bis-Zn(II) salphen with ditopic ligands as pillars (Figure 1.10).<sup>[89,90]</sup> While addition of a short pillar results in supramolecular polymerization intermediated via Zn-N coordination bonds, addition of longer ligands yields a box-shaped discrete molecule with pores showing ordered alignment in the solid state.<sup>[91]</sup>

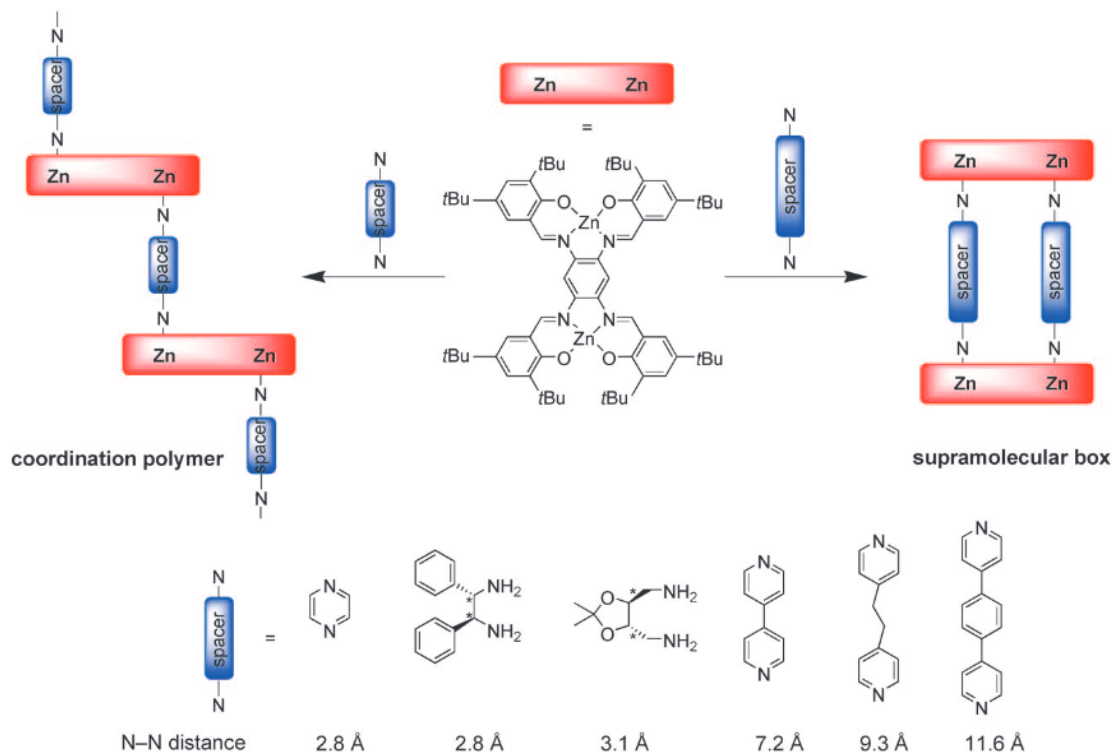
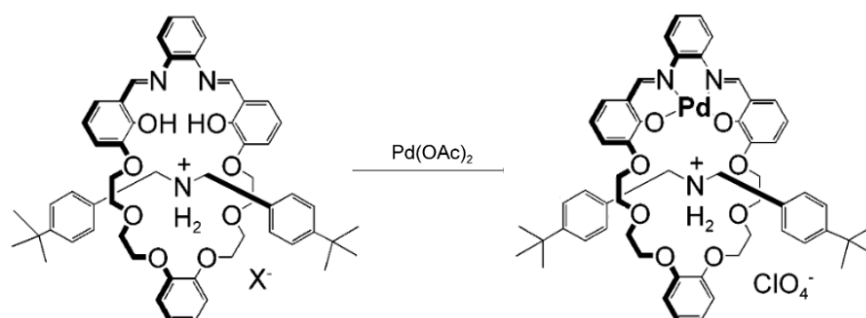
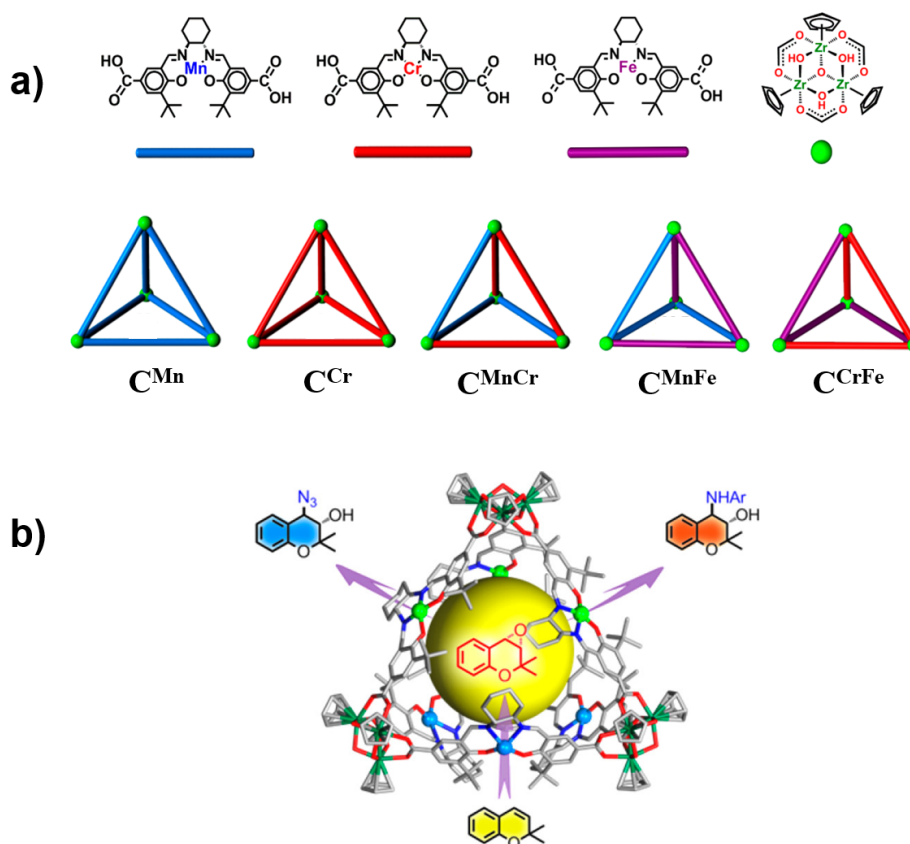


Figure 1.10: Schematic representation of the formation of a coordination polymer or supramolecular box by self-assembly of bis-Zn(II) salphen with ditopic ligands with different lengths.<sup>[91]</sup> Copyright © 2009 Wiley-VCH Verlag GmbH & Co. KGaA, Weinheim.

A similar approach to synthesize a coordination cage for specific guest encapsulation has been also reported by Tanaka and co-workers.<sup>[92]</sup> Further, a macrocyclic salphen derivative has been applied to develop a coordination-responsive rotaxane by Asakawa and co-workers (Figure 1.11).<sup>[93]</sup> A salphen-based crown ether forms a pseudo-rotaxane with a secondary alkylammonium salt. Upon coordination to Pd(II) via the N<sub>2</sub>O<sub>2</sub> coordination site, shrinkage of the macrocycle occurs, leading to the formation of a stable rotaxane. Such hybrids of salen and crown ether have been studied for recognition of multiple metals.

Figure 1.11: Synthesis of a Pd(II)-salphen based [2]rotaxane<sup>[93]</sup>

Salen ligands have been exploited for a variety of challenging asymmetric reactions as a privileged catalyst. Cui and co-workers reported a series of chiral tetrahedral cages for asymmetric catalysis, constructed from the self-assembly of enantiopure metalla-salen based ligands  $M(\text{salen})$  ( $M = \text{Mn}(\text{II}), \text{Fe}(\text{II}), \text{Cr}(\text{II})$ ) and  $\text{Cp}_3\text{Zr}_3$  clusters (Figure 1.12).<sup>[94]</sup> The coordination cages feature a nanoscale hydrophobic cavity and multiple catalytically active sites. Comparing with the single-linker cage, the stereoselectivity and reactivity of mixed-linker cages were demonstrated.

Figure 1.12: Schematic representation of structure of a) ligand, trimetallic cluster and cage, b) asymmetric sequential reactions in the cavity of cage.<sup>[94]</sup> Copyright © 2018 American Chemical Society.

## 1. General introduction

In our previous work, a series of homo- and heteroleptic cages was constructed. The combination of salphen macrocycles, formed by condensation of salicylaldehyde ligands and diamine, with  $\text{Co}(\text{OAc})_2$  in the presence of air, afforded a binuclear  $\text{Co}(\text{III})$  macrocycle. Two shape-complementary ligands were installed on the axial positions of the octahedral coordination center (Figure 1.13).<sup>[95]</sup> It provides a new approach to produce heteroleptic cages with increasing complexity. The functionality of assemblies can be further investigated by the incorporation of functional moieties on the backbone of ligands.

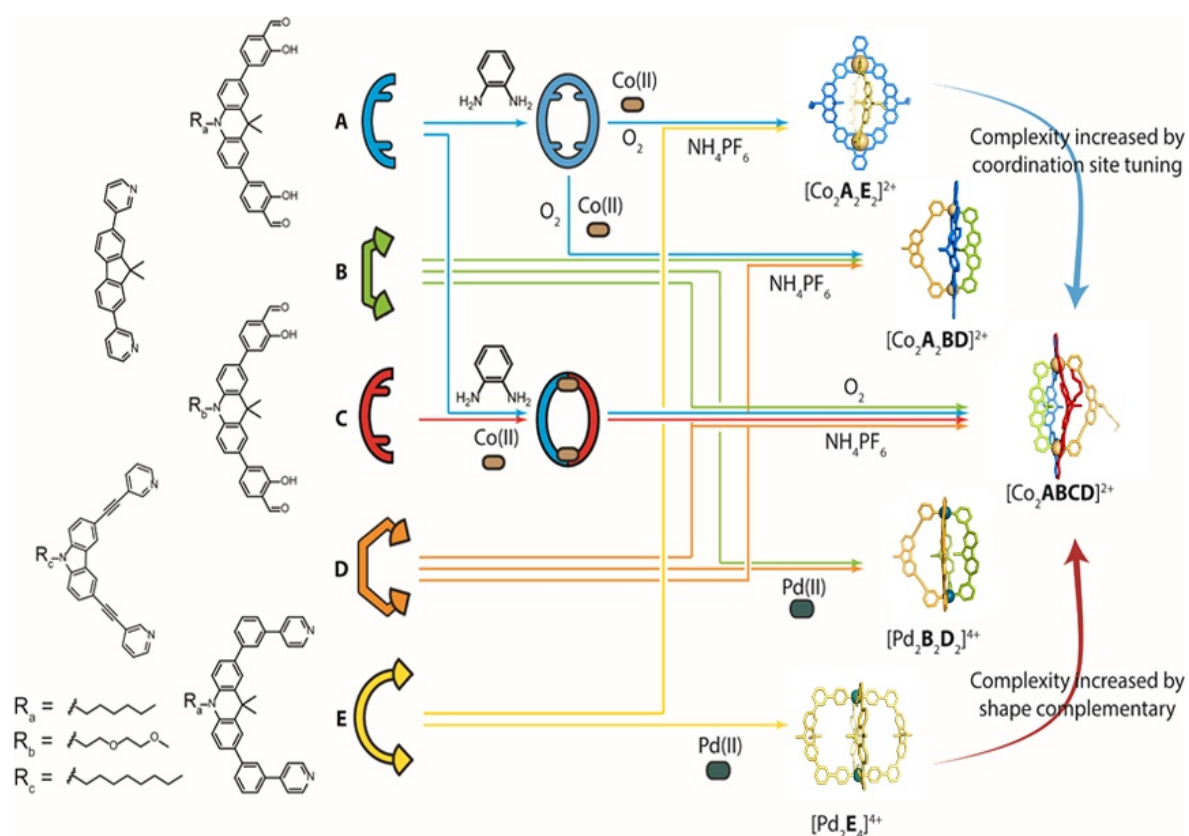


Figure 1.13: Evolution of coordination cages with increasing complexity based on shape complementary approach.<sup>[95]</sup>



## 1.4 References

- [1] V. I. Minkin, *Pure. Appl. Chem.* **1999**, *71*, 1919–1981.
- [2] T. Aida, E. W. Meijer, S. I. Stupp, *Science*. **2012**, *335*, 813–817.
- [3] M. J. Webber, E. A. Appel, E. W. Meijer, R. Langer, *Nat. Mater.* **2016**, *15*, 13–26.
- [4] U. H. Brinker, J. Mieusset, *Molecular Encapsulations: Organic Reactions in Constrained Systems*, John Wiley & Sons, Ltd, West Sussex, UK, **2010**.
- [5] J. M. Lehn, A. Rigault, J. Siegel, J. Harrowfield, B. Chevrier, D. Moras, *Proc. National. Acad. Sci.* **1987**, *84*, 2565–2569.
- [6] M. Fujita, *Chem. Soc. Rev.* **1998**, *27*, 417–425.
- [7] T. R. Cook, P. J. Stang. *Chem. Rev.* **2015**, *115*, 7001–45.
- [8] C. G. Oliveri, P. A. Ulmann, M. J. Wiester, C. A. Mirkin, *Acc. Chem. Res.* **2008**, *41*, 1618–1629.
- [9] C. J. Brown, F. D. Toste, R. G. Bergman, K. N. Raymond, *Chem. Rev.* **2015**, *115*, 3012–3035.
- [10] A. J. McConnell, C. S. Wood, P. P. Neelakandan, J. R. Nitschke, *Chem. Rev.* **2015**, *115*, 7729–7793.
- [11] H. Li, Z.-J. Yao, D. Liu, G.-X. Jin, *Coord. Chem. Rev.* **2015**, *293*, 139–157.
- [12] S. Pullen, G. H. Clever, *Acc. Chem. Res.* **2018**, *51*, 3052–3064.
- [13] T. R. Cook, Y.-R. Zheng, P. J. Stang, *Chem. Rev.* **2013**, *113*, 734–777.
- [14] M. Fujita, M. Tominaga, A. Hori, B. Therrien, *Acc. Chem. Res.* **2005**, *38*, 369–378.
- [15] B. Jiang, B. Ou, H.-B. Yang, *Monogr, Supra. Chem.* **2019**, 20–46.
- [16] Y. Sun, C. Chen, J. Liu, P. J. Stang, *Chem. Soc. Rev.* **2020**, *49*, 3889–3919.
- [17] S. Leininger, B. Olenyuk, P. J. Stang, *Chem. Rev.* **2000**, *100*, 853–908.
- [18] R. Chakrabarty, P. S. Mukherjee, P. J. Stang, *Chem. Rev.* **2011**, *111*, 6810–6918.
- [19] S. Zarra, D. M. Wood, D. A. Roberts, J. R. Nitschke, *Chem. Soc. Rev.* **2014**, *44*, 419–432.
- [20] R. Zhu, I. Regeni, J. J. Holstein, B. Dittrich, M. Simon, S. Prévost, M. Gradzielski, G. H. Clever, *Angew. Chem. Int. Ed.* **2018**, *57*, 13652–13656.
- [21] B. Chen, J. J. Holstein, A. Platzek, L. Schneider, K. Wu, G. H. Clever, *Chem. Sci.* **2022**, *13*, 1829–1834.
- [22] R. Zhu, W. M. Bloch, J. J. Holstein, S. Mandal, L. V. Schäfer, G. H. Clever, *Chem. Eur. J.* **2018**, *24*, 12976–12982.

## 1. General introduction

- [23] W. M. Bloch, J. J. Holstein, B. Dittrich, W. Hiller, G. H. Clever, *Angew. Chem. Int. Ed.* **2018**, *57*, 5534–5538.
- [24] J. Tessarolo, H. Lee, E. Sakuda, K. Umakoshi, G. H. Clever, *J. Am. Chem. Soc.* **2021**, *143*, 6339–6344.
- [25] S. Hasegawa, S. L. Meichsner, J. J. Holstein, A. Baksi, M. Kasanmascheff, G. H. Clever, *J. Am. Chem. Soc.* **2021**, *143*, 9718–9723.
- [26] R.-J. Li, J. J. Holstein, W. G. Hiller, J. Andréasson, G. H. Clever, *J. Am. Chem. Soc.* **2019**, *141*, 2097–2103.
- [27] D. Preston, J. E. M. Lewis, J. D. Crowley, *J. Am. Chem. Soc.* **2017**, *139*, 2379–2386.
- [28] Y.-Y. Zhang, W.-X. Gao, L. Lin, G.-X. Jin, *Coord. Chem. Rev.* **2017**, *344*, 323–344.
- [29] S. De, K. Mahata, M. Schmittl, *Chem. Soc. Rev.* **2010**, *39*, 1555–1575.
- [30] D. P. August, G. S. Nichol, P. J. Lusby, *Angew. Chem. Int. Ed.* **2016**, *55*, 15022–15026.
- [31] L.-X. Cai, S.-C. Li, D.-N. Yan, L.-P. Zhou, F. Guo, Q.-F. Sun, *J. Am. Chem. Soc.* **2018**, *140*, 4869–4876.
- [32] R. W. Saalfrank, H. Maid, A. Scheurer, *Angew. Chem. Int. Ed.* **2008**, *47*, 8794–8824.
- [33] C. Colombari, V. Martin-Diaconescu, T. Parella, S. Goeb, C. García-Simón, J. Lloret-Fillol, M. Costas, X. Ribas, *Inorg. Chem.* **2018**, *57*, 3529–3539.
- [34] K. Matsumoto, S. Kusaba, Y. Tanaka, Y. Sei, M. Akita, K. Aritani, M. Haga, M. Yoshizawa, *Angew. Chem. Int. Ed.* **2019**, *58*, 8463–8467.
- [35] S. Pullen, J. Tessarolo, G. H. Clever, *Chem. Sci.* **2021**, *12*, 7269–7293.
- [36] L. R. Holloway, P. M. Bogie, Y. Lyon, C. Ngai, T. F. Miller, R. R. Julian, R. J. Hooley, *J. Am. Chem. Soc.* **2018**, *140*, 8078–8081.
- [37] Q.-Q. Wang, S. Gonell, S. H. A. M. Leenders, M. Dürr, I. Ivanović-Burmazović, J. N. H. Reek, *Nat. Chem.* **2016**, *8*, 225–230.
- [38] M. Krick, J. Holstein, C. Würtele, G. H. Clever, *Chem. Commun.* **2016**, *52*, 10411–10414.
- [39] K. Harris, D. Fujita, M. Fujita, *Chem. Commun.* **2013**, *49*, 6703–6712.
- [40] B. H. Northrop, H.-B. Yang, P. J. Stang, *Chem. Commun.* **2008**, *0*, 5896–5908.
- [41] D. Philp, J. F. Stoddart, *Angew. Chem. Int. Ed.* **1996**, *35*, 1154–1196.
- [42] L.-L. Yan, C.-H. Tan, G.-L. Zhang, L.-P. Zhou, J.-C. Bünzli, Q.-F. Sun, *J. Am. Chem. Soc.* **2015**, *137*, 8550–8555.
- [43] T. R. Schulte, J. J. Holstein, G. H. Clever, *Angew. Chem. Int. Ed.* **2019**, *58*, 5562–5566.
- [44] H.-Y. Wong, W.-S. Lo, K.-H. Yim, G.-L. Law, *Chem.* **2019**, *5*, 3058–3095.

- [45] N. Ousaka, S. Grunder, A. M. Castilla, A. C. Whalley, J. F. Stoddart, J. R. Nitschke, *J. Am. Chem. Soc.* **2012**, *134*, 15528–15537.
- [46] M. A. Mateos-Timoneda, M. Crego-Calama, D. N. Reinhoudt, *Chem. Soc. Rev.* **2004**, *33*, 363–372.
- [47] G. A. Hembury, V. V. Borovkov, Y. Inoue, *Chem. Rev.* **2008**, *10*, 1–73.
- [48] M. Pan, K. Wu, J.-H. Zhang, C.-Y. Su, *Coord. Chem. Rev.* **2017**, *378*, 333–349.
- [49] K. Wu, K. Li, Y.-J. Hou, M. Pan, L.-Y. Zhang, L. Chen, C.-Y. Su, *Nat. Commun.* **2016**, *7*, 10487.
- [50] C. Zhao, Q.-F. Sun, W. M. Hart-Cooper, A. G. DiPasquale, F. D. Toste, R. G. Bergman, K. N. Raymond, *J. Am. Chem. Soc.* **2013**, *135*, 18802–18805.
- [51] C. Tan, J. Jiao, Z. Li, Y. Liu, X. Han, Y. Cui, *Angew. Chem. Int. Ed.* **2018**, *57*, 2085–2090.
- [52] L.-J. Chen, H.-B. Yang, M. Shionoya, *Chem. Soc. Rev.* **2017**, *46*, 2555–2576.
- [53] C. Klein, C. Gütz, M. Bogner, F. Topić, K. Rissanen, A. Lützen, *Angew. Chem. Int. Ed.* **2014**, *53*, 3739–3742.
- [54] Y. Kubota, K. Biradha, M. Fujita, S. Sakamoto, K. Yamaguchi, *B. Chem. Soc. Jpn.* **2002**, *75*, 559–565.
- [55] Q.-Y. Zhu, L.-P. Zhou, L.-X. Cai, X.-Z. Li, J. Zhou, Q.-F. Sun, *Chem. Commun.* **2020**, *56*, 2861–2864.
- [56] A. V. Davis, D. Fiedler, M. Ziegler, A. Terpin, K. N. Raymond, *J. Am. Chem. Soc.* **2007**, *129*, 15354–15363.
- [57] P. Howlader, P. S. Mukherjee, *Chem. Sci.* **2016**, *7*, 5893–5899.
- [58] L. Cheng, K. Liu, Y. Duan, H. Duan, Y. Li, M. Gao, L. Cao, *Ccs. Chem.* **2021**, *3*, 2749–2763.
- [59] I. Regeni, B. Chen, M. Frank, A. Baksi, J. J. Holstein, G. H. Clever, *Angew. Chem. Int. Ed.* **2020**, *60*, 5673–5678.
- [60] Y. Sun, P. J. Stang, *Aggreg.* **2021**, *2*, e94.
- [61] Y. Hong, J. W. Y. Lam, B. Z. Tang, *Chem. Soc. Rev.* **2011**, *40*, 5361–5388.
- [62] H.-T. Feng, Y.-X. Yuan, J.-B. Xiong, Y.-S. Zheng, B. Z. Tang, *Chem. Soc. Rev.* **2018**, *47*, 7452–7476.
- [63] Z. Liu, S. K. M. Nalluri, J. F. Stoddart, *Chem. Soc. Rev.* **2017**, *46*, 2459–2478.
- [64] L. F. Lindoy, K.-M. Park, S. S. Lee, *Chem. Soc. Rev.* **2012**, *42*, 1713–1727.
- [65] Y. Itoh, S. Chen, R. Hirahara, T. Konda, T. Aoki, T. Ueda, I. Shimada, J. J. Cannon, C. Shao, J. Shiomi, K. V. Tabata, H. Noji, K. Sato, T. Aida, *Science* **2022**, *376*, 738–743.

## 1. General introduction

- [66] M. R. Ghadiri, J. R. Granja, R. A. Milligan, D. E. McRee, N. Khazanovich, *Nature* **1993**, *366*, 324–327.
- [67] Y. Yang, W. Feng, J. Hu, S. Zou, R. Gao, K. Yamato, M. Kline, Z. Cai, Y. Gao, Y. Wang, Y. Li, Y. Yang, L. Yuan, X. C. Zeng, B. Gong, *J. Am. Chem. Soc.* **2011**, *133*, 18590–18593.
- [68] A. J. Helsel, A. L. Brown, K. Yamato, W. Feng, L. Yuan, A. J. Clements, S. V. Harding, G. Szabo, Z. Shao, B. Gong, *J. Am. Chem. Soc.* **2008**, *130*, 15784–15785.
- [69] L.-J. Chen, J.-L. Zhu, H.-B. Yang, *Monogr Supramol Chem* **2019**, 195–225.
- [70] S. Datta, M. L. Saha, P. J. Stang, *Acc. Chem. Res.* **2018**, *51*, 2047–2063.
- [71] H. Schiff, *Liebigs. Ann. Chem.* **1864**, *131*, 118–119.
- [72] C. J. Whiteoak, G. Salassa, A. W. Kleij, *Chem. Soc. Rev.* **2011**, *41*, 622–631.
- [73] P. G. Cozzi, *Chem. Soc. Rev.* **2004**, *33*, 410–421.
- [74] S. Shaw, J. D. White, *Chem. Rev.* **2019**, *119*, 9381–9426.
- [75] S. J. Wezenberg, A. W. Kleij, *Angew. Chem. Int. Ed.* **2008**, *47*, 2354–2364.
- [76] J. K. -H. Hui, Z. Yu, M. J. MacLachlan, *Angew. Chem. Int. Ed.* **2007**, *46*, 7980–7983.
- [77] A. D. Cort, P. D. Bernardin, G. Forte, F. Y. Mihan, *Chem. Soc. Rev.* **2010**, *39*, 3863–3874.
- [78] N. E. Borisova, M. D. Reshetova, Y. A. Ustynyuk, *Chem. Rev.* **2007**, *107*, 46–79.
- [79] J. K.-H. Hui, M. J. MacLachlan, *Chem. Commun.* **2006**, *0*, 2480–2482.
- [80] P. D. Frischmann, S. H. M. Mehr, B. O. Patrick, F. Lejl, M. J. MacLachlan, *Inorg Chem* **2012**, *51*, 3443–3453.
- [81] S. Akine, M. Miyashita, T. Nabeshima, *J. Am. Chem. Soc.* **2017**, *139*, 4631–4634.
- [82] S. Akine, M. Miyashita, T. Nabeshima, *Chem. Eur. J.* **2019**, *25*, 1432–1435.
- [83] M. T. Chaudhry, S. Akine, M. J. MacLachlan, *Chem. Soc. Rev.* **2021**, *50*, 10713–10732.
- [84] T. Nabeshima, H. Miyazaki, A. Iwasaki, S. Akine, T. Saiki, C. Ikeda, *Tetrahedron.* **2007**, *63*, 3328–3333.
- [85] A. J. Gallant, M. J. MacLachlan, *Angew. Chem. Int. Ed.* **2003**, *42*, 5307–5310.
- [86] S. Akine, F. Utsuno, S. Piao, H. Orita, S. Tsuzuki, T. Nabeshima, *Inorg. Chem.* **2016**, *55*, 810–821.
- [87] G. H. Clever, K. Polborn, T. Carell, *Angew. Chem. Int. Ed.* **2005**, *44*, 7204–7208.
- [88] K. E. Splan, A. M. Massari, G. A. Morris, S. Sun, E. Reina, S. T. Nguyen, J. T. Hupp, *Eur. J. Inorg. Chem.* **2003**, *2003*, 2348–2351.

- [89] T. Gadzikwa, R. Bellini, H. L. Dekker, J. N. H. Reek, *J. Am. Chem. Soc.* **2012**, *134*, 2860–2863.
- [90] A. W. Kleij, M. Kuil, D. M. Tooke, M. Lutz, A. L. Spek, J. N. H. Reek, *Chem. Eur. J.* **2005**, *11*, 4743–4750.
- [91] M. Kuil, I. M. Puijk, A. W. Kleij, D. M. Tooke, A. L. Spek, J. N. H. Reek, *Chem. Asian. J.* **2008**, *4*, 50–7.
- [92] S. Kawano, T. Fukushima, K. Tanaka, *Angew. Chem. Int. Ed.* **2018**, *57*, 14827–14831.
- [93] I. Yoon, M. Narita, T. Shimizu, M. Asakawa, *J. Am. Chem. Soc.* **2004**, *126*, 16740–16741.
- [94] J. Jiao, C. Tan, Z. Li, Y. Liu, X. Han, Y. Cui, *J. Am. Chem. Soc.* **2018**, *140*, 2251–2259.
- [95] B. Zhang, Design and Synthesis of Novel Self Assembled Supramolecular Coordination Cages. Doctoral dissertation, TU Dortmund, **2020**.



## 2 Scope of this thesis

Macrocycles in supramolecular chemistry have rapidly developed over the past few decades due to their structural features and easy accessibility. A variety of macrocycles, such as crown ethers, pillar[n]arenes, and metal–organic coordination macrocycles, have been synthesized. The possibility to introduce diverse functionality led to intriguing applications in the fields of molecular recognition, catalysis, molecular machines and many more. Among several building blocks, salen/salphen ligands, which can be easily prepared by the condensation of salicylaldehydes and imines, are intriguing for the assembly of supramolecular architecture due to their versatility and access to a modular approach where functional groups can be easily inserted or modified. To this aim, this work reports the design, synthesis and characterization of a series of metal salen/salphen-based metallamacrocycle architectures, based on three building blocks: ligand, diamine and metal-center. The modularity and versatility of the reported approach allows to achieve self-assembled compounds towards luminescent materials, catalysis application and formation of MIMs.

In chapter 3, an AIE active metallamacrocycle with adjustable CPL properties is reported. A TPE based salicylaldehyde ligand **L** was designed and synthesized. The condensation of **L** with an enantiopure diamine derivative affords a chiral macrocycle **R**. Next, a new class of luminescent binuclear metallamacrocycles **Zn<sub>2</sub>R** was obtained by self-assembly of **R** with Zn(II). The formation of **Zn<sub>2</sub>R** was characterized by NMR, X-ray diffraction and FT-IR techniques. The AIE properties and chiroptical properties of **L**, **R**, and **Zn<sub>2</sub>R** were studied with UV-Vis absorption, CD spectroscopy, fluorescence spectroscopy, CPL, SEM, and DLS techniques.

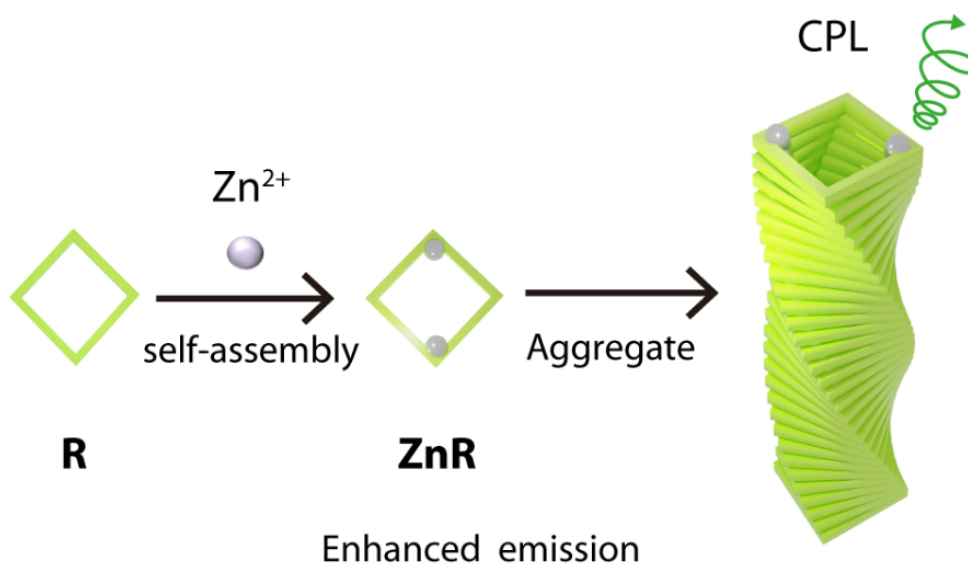
In chapter 4, a phenoxazine-based salicylaldehyde ligand **L<sup>PZ</sup>**, a macrocycle **R<sup>PZ</sup>** and a metallamacrocycle **Zn<sub>2</sub>R<sup>PZ</sup>** were designed and synthesized specifically for performing photoredox catalysis. The structural and photophysical properties of compounds were studied by NMR, ESI-MS, FT-IR, UV-Vis, fluorescence, cyclic voltammetry analysis. The photoredox catalysis properties of the macrocycles were investigated studying a pinacol coupling reaction with a scope of aldehyde substrates.

## 2. Scope of this Thesis

In chapter 5, a new approach for the construction of a [3]rotaxane was introduced. Two carbazole-based ligands were designed and self-assembled with a binuclear Co(III) macrocycle. The coordination geometry of Co(III) and the ligand binding angles allow only the formation of bowl-shaped structures. Two bowls are then connected by reacting proper substituents at the carbazole ligands backbones. The bowl structures were characterized by NMR, ESI-MS and X-ray diffraction. The formation of the [3]rotaxane was confirmed by ESI-MS. Finally, two different ligands endowed with catalytic groups, were combined with the Co(III) macrocycle, thus forming an heteroleptic cage to be explored for further supramolecular catalysis applications.



### 3 Tetraphenylethylene-based macrocycles with adjustable CPL





### 3.1 Introduction

#### 3.1.1 TPE

Since Tang's group firstly reported the aggregation-induced emission (AIE) phenomenon in 2001, great advances have been made in this field.<sup>[1]</sup> Lots of AIEgens were recently developed showing potential application in luminescent materials, such as hexaphenylsilole (HPS) and tetraphenylethylene (TPE). Those molecules bear a propeller-like conformation, which is the key feature for AIE property. Among those AIEgens, TPE is an archetypal and the most studied AIE chromophore.<sup>[2,3]</sup> On the one hand, it is readily accessible and has four positions, which could be easily modified with functional groups, going from mono- to tetra-topic molecules, forming interesting building blocks for construction of luminescent micro-/nanostructures (Figure 3.1).<sup>[4]</sup> On the other hand, the repulsion of four crowded phenyl substituents brings them to a propeller-like arrangement. It then gains a stable AIE property in which the restriction of phenyl-ring rotation and the ethylenic C=C bond twist can activate the emission.<sup>[5]</sup> TPE is also a popular building block to construct supramolecular assemblies. In recent decades, TPE-based macrocycles, triangular prisms, and cages have been explored.<sup>[6–9]</sup>

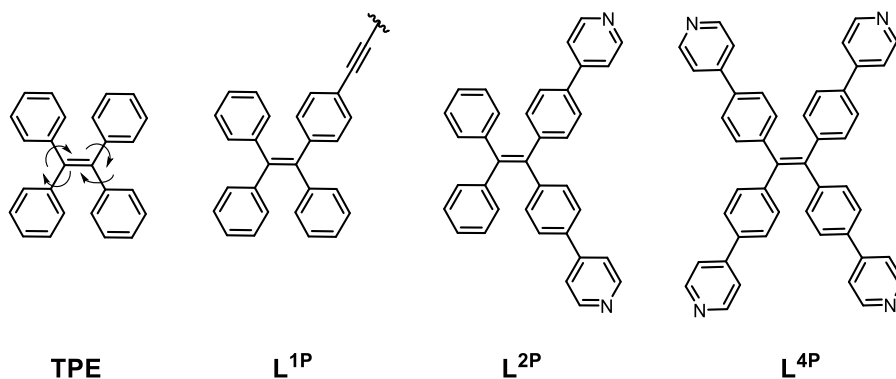


Figure 3.1: The structure of TPE and the examples of TPE based ligands.

#### 3.1.2 TPE-based macrocycles and cages

According to the RIR mechanism (See chapter 1.2.2), the AIE effect of the TPE unit is enhanced after the formation of a cycle, which restricts the intramolecular rotations. Recent studies showed that the aggregation is not the only way to turn on the emission of TPE. A similar phenomenon can also be found if the RIR is achieved by other strategies. Restriction of phenyl ring rotation to turn on the emission has

### 3. Tetraphenylethylene-based macrocycles with adjustable CPL

been achieved through covalent modification, host-guest chemistry, and embedding into MOFs.<sup>[10,11]</sup> Numerous of TPE macrocycles with AIE effect have appeared in the literature (Figure 3.2). Those TPE-based macrocycles are formed by covalent bond connections. The modifications on different positions of the TPE units to restrict phenyl-ring rotation or the C=C bond twist activate the emission of those macrocycles.

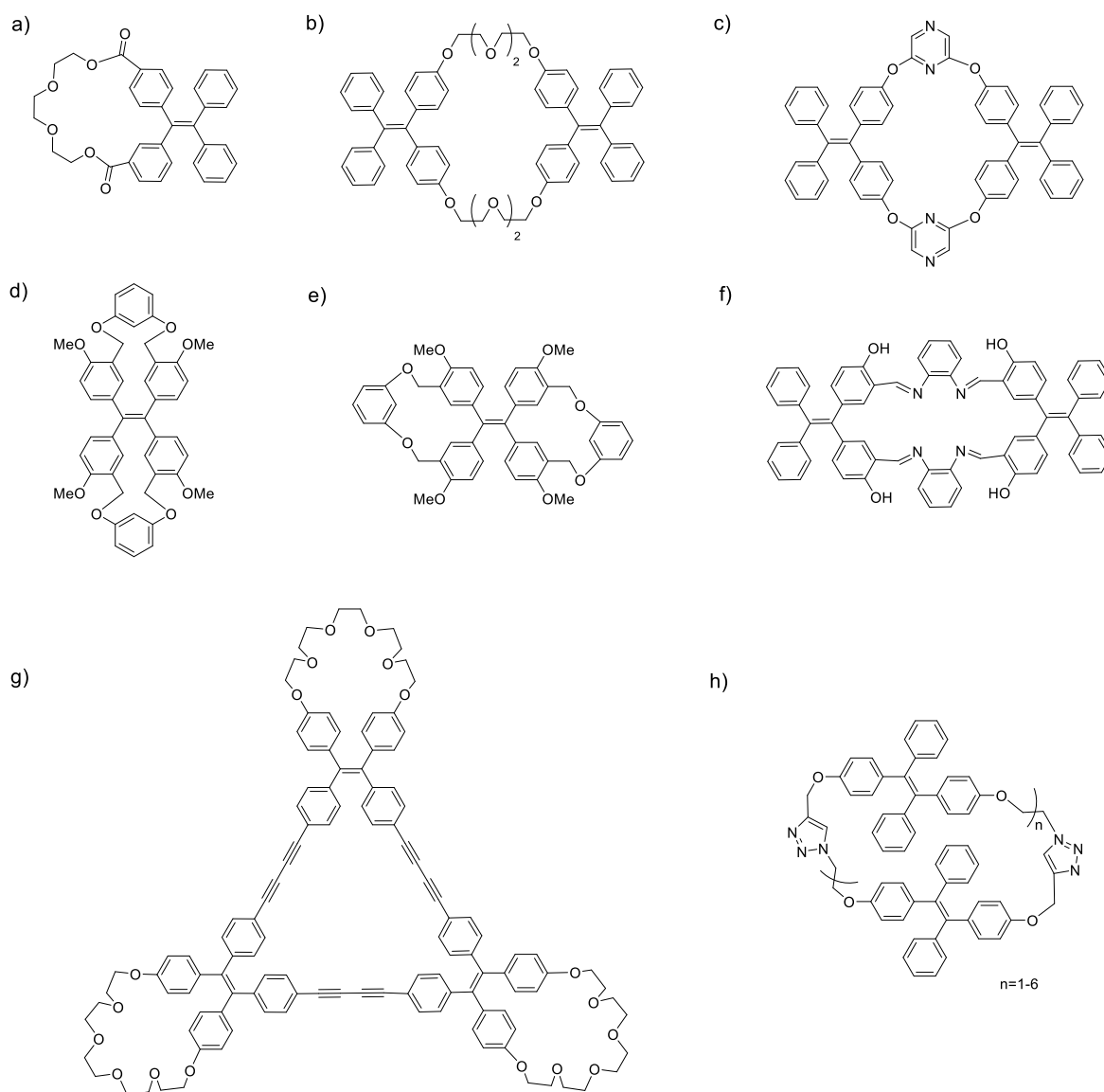


Figure 3.2: Chemical structures of selected TPE-based macrocycles. a) TPE-crown macrocycle synthesized by etherification.<sup>[12]</sup> b) Macrocycle that can self-assemble into hollow spheres with intrinsic and extrinsic porous channels.<sup>[13]</sup> c) TPE-based expanded oxalixarene. Different supramolecular grid structures in the solid state can be adjusted by the encapsulated guests.<sup>[14]</sup> d) *cis*-TPE dicycle connected by rigid short tethers at *cis*-position with the free rotation restriction of double bond. e) *gem*-TPE dicycle connected by rigid short tethers at *gem*-positions.<sup>[15]</sup> f) TPE-macrocycle based on Schiff bases. It can

### 3. Tetraphenylethylene-based macrocycles with adjustable CPL

aggregate into nanofibers and shows potential for the visual detection of copper(II) ions in water.<sup>[16]</sup> g) TPE trimeric macrocycle bearing crown ether rings bridged at the *cis*-phenyl rings of the TPE unit. It exhibits CD and CPL signals induced by chiral acids. h) TPE cyclic oligomers bearing up to seven TPE segments in the main chain by a stepwise chain growth strategy.<sup>[17]</sup>

Three-dimensional shape-persistent cages also have attracted considerable attention because of their fascinating structures and potential application in gas storage, host-guest chemistry, catalysis, and separation. TPE units as an ideal building blocks for constructing supramolecular cages have been explored.

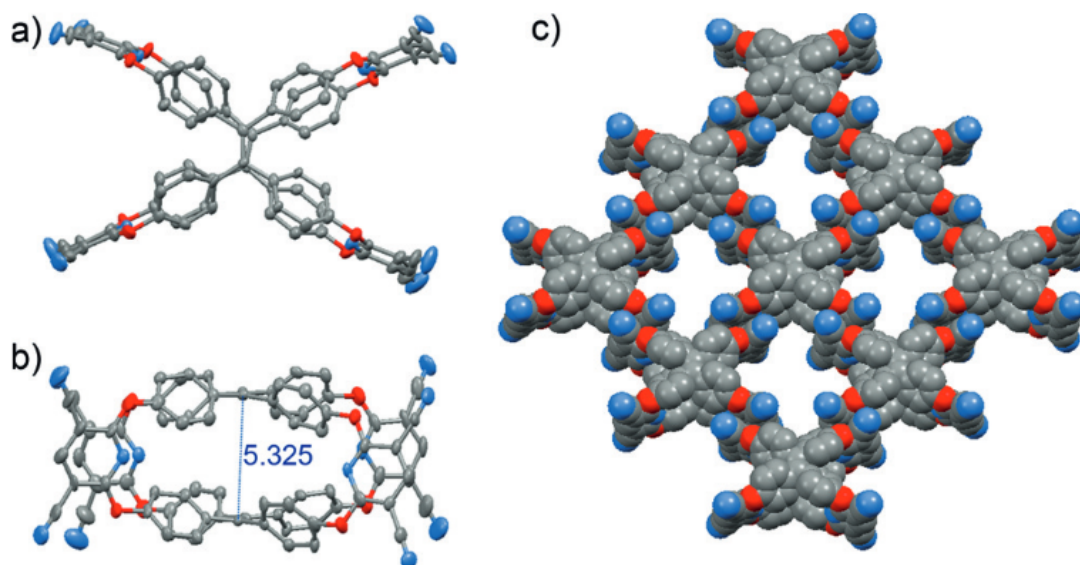


Figure 3.3: a) Top view and b) side view of the X-ray crystal structure of tricyclooxacalixarene cage. c) Grid-like porous structure from the crystal packing of cage shown in space-filling mode.<sup>[18]</sup> Copyright © 2015 Wiley-VCH Verlag GmbH & Co. KGaA, Weinheim.

A porous prismatic tricyclooxacalixarene cage based on TPE was reported by Zheng and co-workers (Figure 3.3). Two TPE units were connected by four pyridine rings through one-pot condensation reactions, which suppress the motion of phenyl rings and turn on the emission in solution. The cage assembled into a grid-like structure with external pores and displayed high adsorption capacity for CO<sub>2</sub>.

### 3. Tetraphenylethylene-based macrocycles with adjustable CPL

#### **3.1.3 Coordination-enhanced emission of AIE-active metallamacrocycles and metallacages**

Coordination-driven self-assembly is an efficient strategy for construction of discrete supramolecular architectures with pre-designed sizes and well-defined shapes, from two-dimensional (2D) polygons, three-dimensional (3D) prisms, bowls, cages and polyhedra, due to the directional and predictable metal-ligand coordination interactions.<sup>[19]</sup> The kinetic reversibility of the self-assembly process between a Lewis-base-containing donor and a Lewis-acidic acceptor allows the system to undergo error correction and self-repairing processes, leading to the formation of a product that is thermodynamically favorable. These advantages enable the construction of a series of discrete coordination complexes. In addition, functional moieties can be introduced to the assemblies by the direct incorporation into the starting units, pendant attachment, or host-guest encapsulation. Several examples show introduction of AIE-active fluorophores into supramolecular coordination complexes.<sup>[20]</sup>

TPE-based metallacycles or metallacages were obtained through the coordination interaction of TPE derivatives with metal ions. Stang and co-workers reported the construction of tetragonal prismatic platinum(II) metallacages by using TPE-based tetrapyridine ligands (Figure 3.4).<sup>[21]</sup> TPE-based ligands are held in a cofacial arrangement by four dicarboxylate ligands acting as edges of the prism. Both cages have emission in dilute solution and tunable visible-light emission in the aggregation state. With the modification of oxyalkyl chains on the carboxylate ligand backbones, the cages not only exhibit tunable visible-light emission by varying the solvent composition, but also result in white light emission when dissolved in THF.

### 3. Tetraphenylethylene-based macrocycles with adjustable CPL

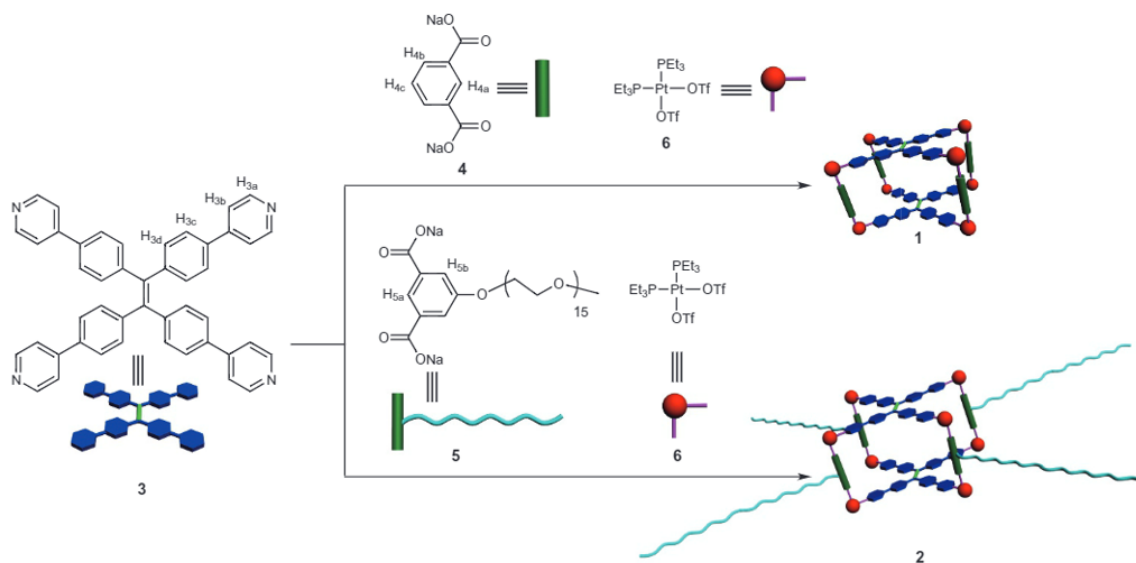


Figure 3.4: Heteroligation-directed self-assembly of TPE-based pyridyl ligand, carboxylate ligand and 90° Pt(II) acceptor in a 2:4:8 ratio to furnish tetragonal metallacages.<sup>[21]</sup> Copyright © 2015 Macmillan Published Limited.

Using the same TPE-based tetrapyridine ligand, Stang and co-workers also reported a discrete fused double metallarhomboid and a double triangle, both based on the shape complementarity and stoichiometric control of the building blocks through coordination-driven self-assembly (Figure 3.5).<sup>[22]</sup> TPE tetra-pyridine donors as the bridging components were combined with different pyridyl donors and platinum acceptors with the coordination angles of 120° or 180°. As the intramolecular motions of TPE units can be anchored not only by the molecular packing upon aggregation but also by the dative bonds, the assemblies exhibit fluorescence both in dilute solutions and in the aggregated state. The geometries differences of the assemblies with different strength and rigidity lead to different fluorescence enhancement behavior too, indicating the properties of supramolecular coordination complexes as well as the properties of the chromophore can be tuned by the resulting geometry.

### 3. Tetraphenylethylene-based macrocycles with adjustable CPL

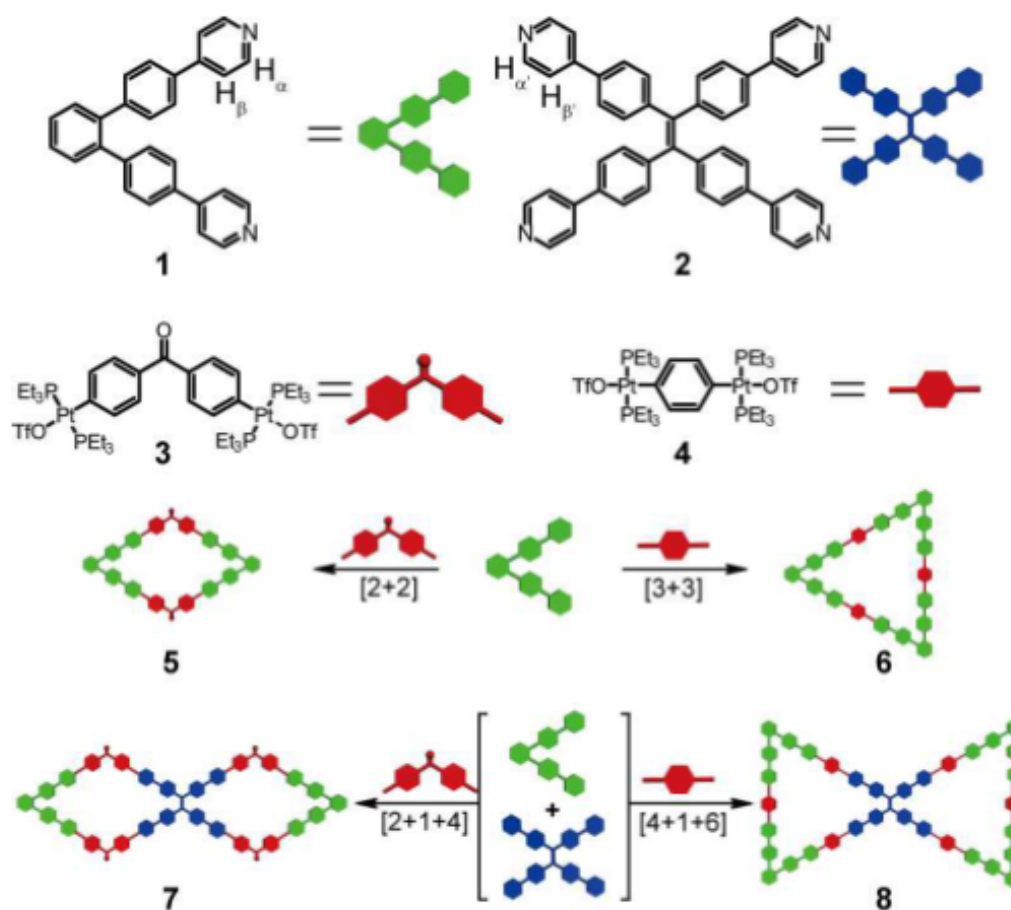


Figure 3.5: Syntheses of rhomboid 5, triangle 6, double rhomboid 7, and double triangle 8 via multicomponent coordination-driven self-assembly in a controlled ratio.<sup>[22]</sup> Copyright © 2016 American Chemical Society.

Owing to the metal centers, coordination assemblies have often a charged nature. The charged structure shows attractive interactions with molecules having the opposite charge. The Yang group reported a 120° bipyridine ligand with TPE as the pendant and self-assembly with 120° diplatinum (II) acceptors to form a discrete macrocycle (Figure 3.6).<sup>[23]</sup> The hierarchical self-assembly of positively charged *tris*-TPE metallacycles with negatively charged heparin, a polysaccharide with many sulfate and carboxylate groups, driven by multiple electrostatic interactions was investigated. The higher-order aggregates of entangled necklace networks exhibited typical AIE behaviour and could act as heparin sensor.



### 3. Tetraphenylethylene-based macrocycles with adjustable CPL

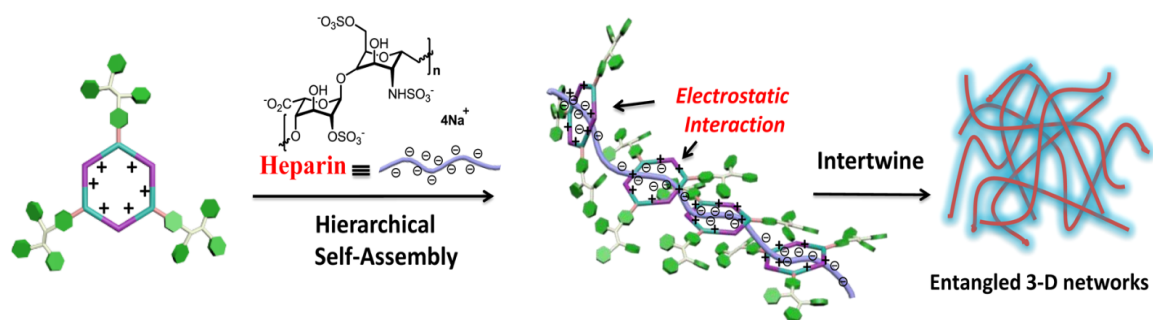


Figure 3.6: Schematic representation of the hierarchical self-assembly and aggregation mode between *tris*-TPE metallacycle and heparin.<sup>[23]</sup> Copyright © 2015 American Chemical Society.

Although lots of light-emitting TPE-based Pt(II) metallacycles and metallacages have been explored, examples based on Pd(II) cations have been proven to be quite challenging due to well-known heavy metal effect for fluorescence quenching.<sup>[24]</sup>

In Mukherjee group, a water soluble AIE active TPE-Pd- trigonal prism has been synthesized through coordination-driven self-assembly of a tetraimidazole ligand with *cis*-protected Pd(II) acceptor (Figure 3.7).<sup>[25]</sup> Conjugated aromatic TPE ligands act as the walls of the prism. Photoproperties of the prism were examined. The ligand shows weak emission in dilute solution, while fluorescence enhancements were found in assemblies due to the restriction of the motions of the phenyl rings. The emission maximum underwent a redshift, arising from a metal-to-ligand charge-transfer process upon coordination. Interestingly, the prism has a confined hydrophobic cavity that was successfully used in catalysis.

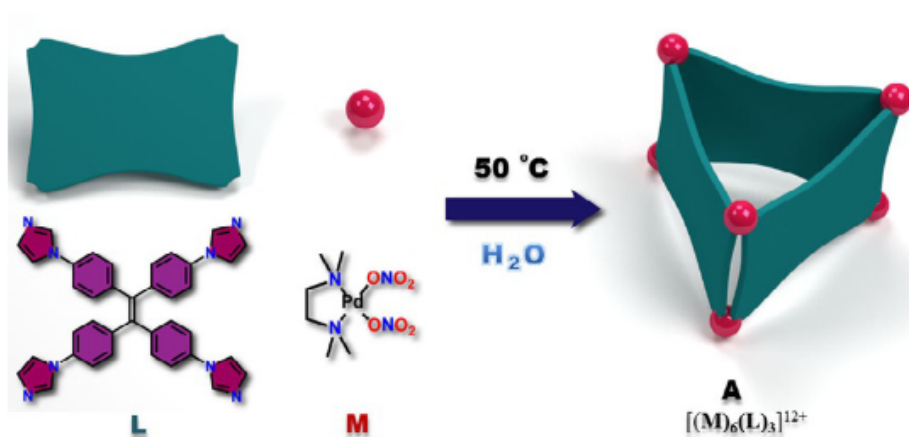


Figure 3.7: Schematic representation of 3D molecular prism.<sup>[25]</sup> Copyright © 2017 Wiley-VCH Verlag GmbH & Co. KGaA, Weinheim.

### 3. Tetraphenylethylene-based macrocycles with adjustable CPL

The Sun group reported the self-assembly of fluorescent TPE-based Pd(II) capsules.<sup>[26,27]</sup> A ditopic TPE-based pyridine ligand reacts with 0.5 equiv. of Pd(NO<sub>3</sub>)<sub>2</sub> to obtain an AIE-active capsule Pd<sub>2</sub>L<sub>4</sub>, with the encapsulation of two nitrate ions, which is due to the hydrogen-bonding and electrostatic interactions (Figure 3.8 a). The emission of capsule can also be turned on by the encapsulation of anions such as HCO<sub>3</sub><sup>-</sup>, so called encapsulation-induced emission (EIE). Coordination-enhanced emission of supramolecular complexes was also studied by using bidentate and tetradentate TPE-based pyridine ligands, self-assembled with *cis*-Pd(en)](NO<sub>3</sub>)<sub>2</sub> (Figure 3.8 b). The assembly with four arms coordinated to Pd(II) ions, yet holds the strong emission properties not only in dilute solution but also in the aggregation state. On the contrary, when using the ditopic ligand, the system shows lower emission intensity in dilute solution due to the intramolecular motion of two unrestricted phenyl rings (Figure 3.8 c).

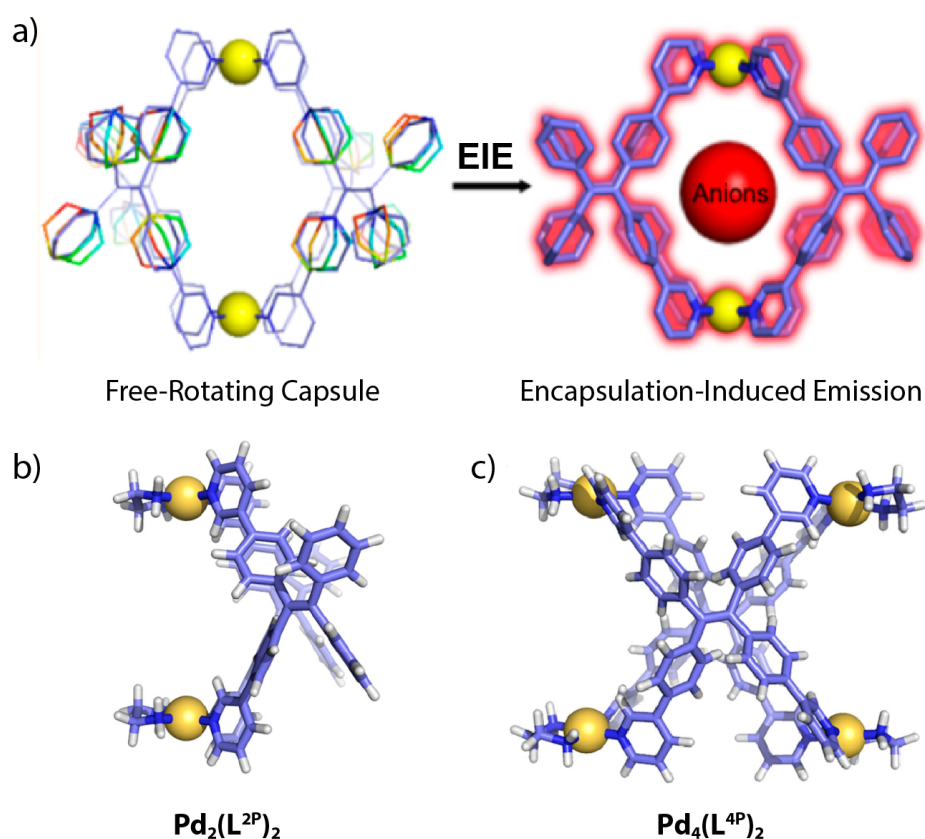


Figure 3.8: a) Coordination-directed self-assembly of a lantern-type Pd<sub>2</sub>L<sub>4</sub> capsule with encapsulation-induced emission.<sup>[26]</sup> Simulated molecular structures from b) bidentate ligand and c) tetradentate ligand self-assembled with *cis*-protected Pd(II) ions.<sup>[27]</sup> Copyright © 2017 American Chemical Society.

### 3. Tetraphenylethylene-based macrocycles with adjustable CPL

#### 3.1.4 Chiral TPE-based supramolecular assemblies

TPE-based supramolecular assemblies have been used for fluorescence probes, catalysis, bioimaging agents. Among those functions and applications, the possibility to introduce chirality in such assemblies has drawn an increasing interest for chiral recognition and as CPL-active materials.

Generally, chiral TPE derivatives are constructed by introducing chiral moieties at the periphery of TPE units.<sup>[28]</sup> Alternatively, self-assembly of achiral molecules into larger supramolecular structures such as helices or fibers, has been carried out exploring the possibility to induce chirality to the system. Several CPL-active AIE systems are constructed via noncovalent bond interactions of AIEgen units with other chiral molecules.<sup>[29]</sup> The Zheng group reported the self-assembly of TPE tetracycle (*m*-TPE-TC) treated with 4-dodecylbenzenesulfonic acid (DSA) through acid-base interaction (Figure 3.9).<sup>[30]</sup> TPE-based acid-base complexes (*M/P*-TPE-TC-DSA) with helical chirality can self-assemble into supramolecular helical nanofibers in the aggregate state. Interestingly, the CD signal of the nanofibers shows a sign inversion from solution to the solid state. Furthermore, the CPL signals of *M/P*-TPE-TC-DSA are significantly magnified after the formation of helical nanofibers. A secondary self-assembly was carried out by the addition of one enantiomer of tartaric acid. The different stimuli response for two enantiomers of tartaric acid, one aroused no CPL change, another one furnishes a larger enhancement due to the further self-assembly of the helices, are showing a great potential for chiral recognition.

### 3. Tetraphenylethylene-based macrocycles with adjustable CPL

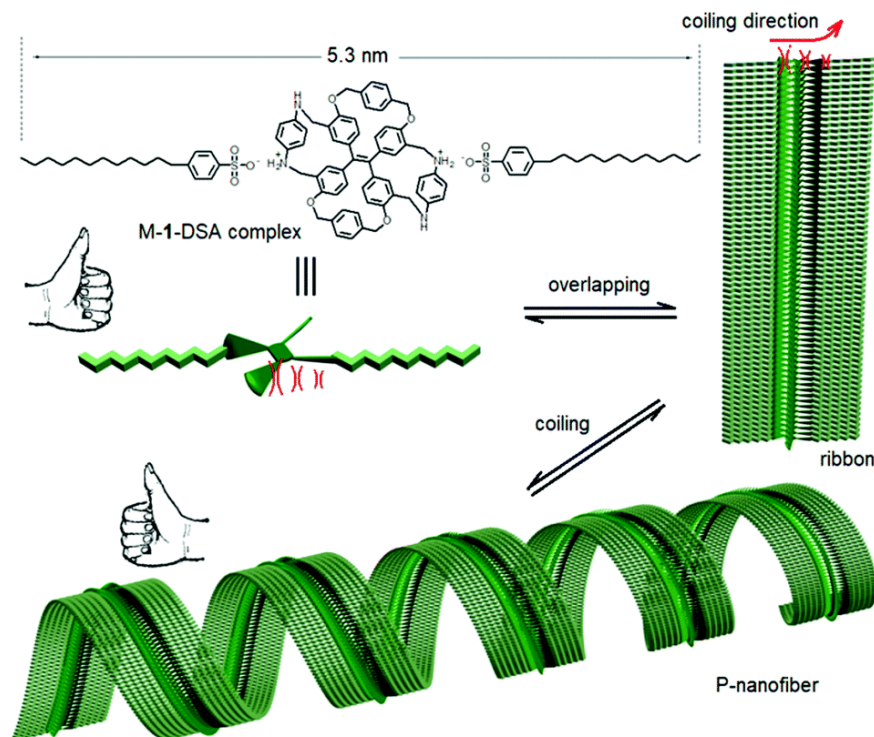


Figure 3.9: The helices formation mechanism of P-/M- macrocycles<sup>[30]</sup> Copyright © The Society of Chemistry 2020

Moreover, Tang and co-workers reported a TPE-derivative where four phenyl rings can be twisted against the C=C and oriented in the same direction in the crystal structure, showing CD signals in the solid state<sup>[31]</sup> Propeller-like TPE can exhibit clockwise (*M*) or anticlockwise (*P*) rotational configurations due to the steric hindrance between the phenyl rings. Strategies for constructing chiral macrocycles or cages through immobilizing the conformation of TPE were also developed.

Based on this, the Zheng group firstly reported the immobilization of a propeller-like conformation of TPE units exploring AIE, chiral recognition and enhanced chiroptical properties resulting from the formation of helical chirality (Figure 3.10).<sup>[32]</sup> TPE is completely fixed by four intramolecular cyclization to form a tetracycle. Such a compound does not only show strong emission in the solid state but also in the solution-state, proving the AIE mechanism of RIR. Left-handed helical (*M*) or right-handed helical (*P*) TPE cores was observed from crystal structures in one-unit cell and packed into column structures, showing CPL signals with mirror image.

### 3. Tetraphenylethylene-based macrocycles with adjustable CPL

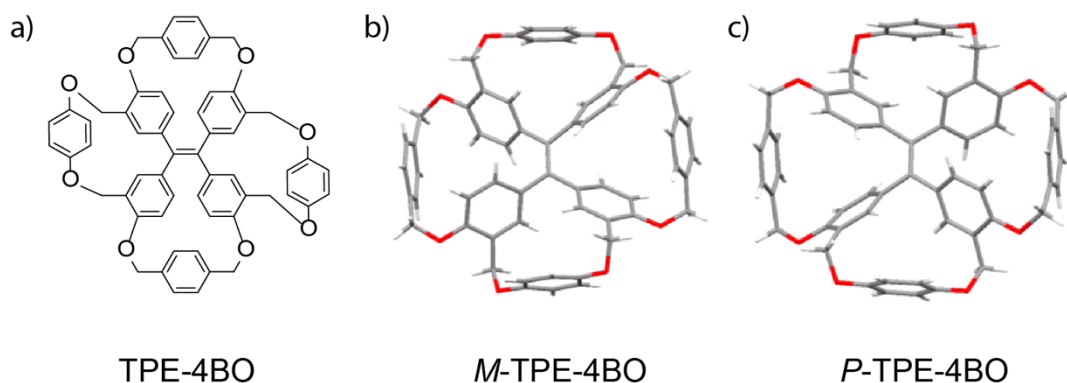


Figure 3.10: a) Chemical structure of macrocycle TPE-4BO. Crystal structures of b) *M*-TPE-4BO and c) *P*-TPE-4BO.<sup>[32]</sup> Copyright © 2016 American Chemical Society.

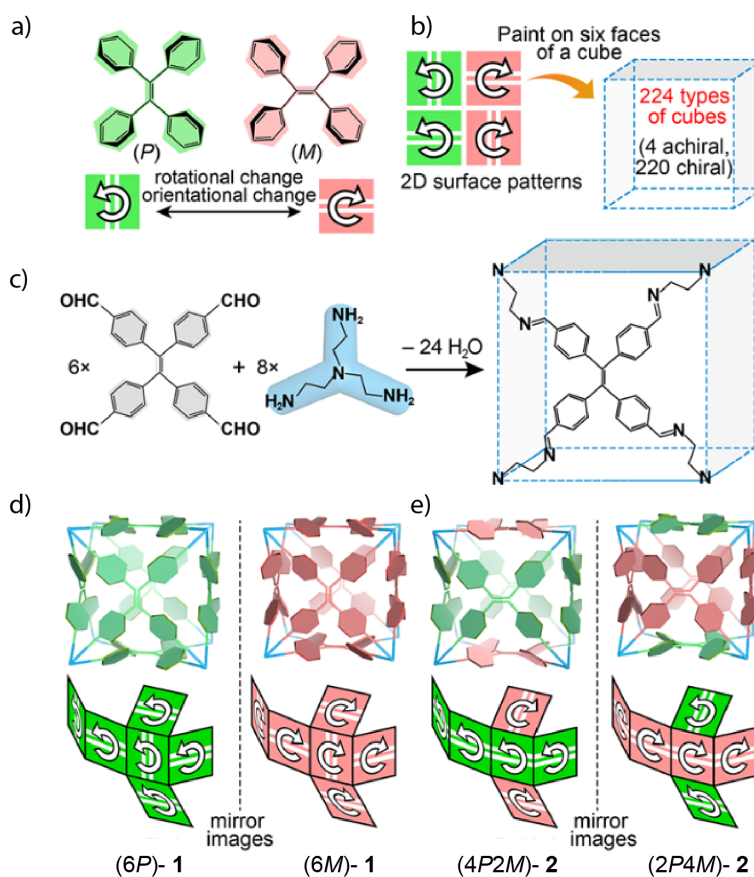


Figure 3.11: Synthesis of chiral cubes with different facial rotational and orientational configurations. (A) The TPE motif exhibits two rotational modes (*P* or *M*) of the phenyl groups and two orientational modes (horizontal or vertical) of the vinyl group in two dimensions. (B) Rotational and orientational modes of the TPE motif generate 224 types of cubes when they are painted on the six faces of a cube. Nevertheless, only four types of cubes were found in the experimental product (D, E). (C) Schematic of synthesis of organic cubes from six TPE faces and eight triamine vertices. (D, E) Cartoons to show the TPE configurations in the homodirectional cubes (6*P*)-1 and (6*M*)-1, and the heterodirectional cubes (4*P*2*M*)-2 and (2*P*4*M*)-2.<sup>[33]</sup> Copyright © 2017 American Chemical Society.

### 3. Tetraphenylethylene-based macrocycles with adjustable CPL

The Cao group reported a chiral TPE-based cube-like organic cage (Figure 3.11).<sup>[33]</sup> Face-rotating cubes (FRCs) were constructed by the reversible covalent condensation reaction of six tetragonal TPE ligands, perched on each face, and eight amine building blocks, composing the eight vertices. The intramolecular flipping of TPE units is restricted by the conjugation between phenyl rings and imine bonds. The cage chirality is originated from the cubic faces constructed from the rectangular TPE motifs, which is restricted in different configurations. These FRCs also show CPL properties.

#### 3.2 Synthesis of TPE-based ligands and macrocycles

In this chapter, the formation of binuclear tetraphenylethylene-based chiral salen metallamacrocycles developed during this thesis will be described. The macrocycle **R** is formed by the condensation reaction of TPE-based salicylaldehyde ligands and chiral diamines. The complexes **M<sub>2</sub>R** (M=Zn(II), Co(III)) were obtained in good yields by metalation of **R** with the corresponding acetate salts as the metal source. The formation of **M<sub>2</sub>R** was confirmed by <sup>1</sup>H NMR spectroscopy, DOSY, FT-IR, UV-Vis, and single crystal X-ray diffraction. The aggregation-induced emission of the metal salen complexes will be discussed. The chiral properties of macrocycles are also studied. The assemblies possess good CD and CPL properties. Due to the formation of helical chirality in the aggregated state, the CD and CPL signals of the assemblies are enhanced and reversed compared to the monomer.

The chiral TPE salen macrocycles were synthesized according to the synthetic procedure depicted in Figure 3.12. Firstly, 4,4'-(2,2-diphenylethene-1,1-diyl)bis(bromobenzene) (**2Br-TPE**) was synthesized following a literature procedure in two steps.<sup>[34]</sup> Two bromines were introduced in the *para*- position of two *gem*-located phenyl rings. The TPE based salicylaldehyde ligand **L** was obtained by Suzuki coupling reaction of **2Br-TPE** and a pinacol ester salicylaldehyde compound in a good yield.

The ligand was treated with excess (1*S*,2*S*)-1,2-diphenylethane-1,2-diamine to form the chiral macrocycle by a condensation reaction (Figure 3.12). Acetic acid acts as a catalyst in this reaction. In general, condensation reactions of aldehydes and amines are often performed in methanol or ethanol.<sup>[35]</sup> Due to the poor solubility of

### 3. Tetraphenylethylene-based macrocycles with adjustable CPL

**L** in methanol, this reaction was done in a mixture of anhydrous dichloromethane and methanol (v/v, 1:1). The solution became turbid after stirring at room temperature for a few minutes. Pure macrocycle **s-R** was obtained after precipitation by addition of diethyl ether to the resulting mixture. The isomer **r-R** is synthesized following the same procedure by using (1*R*,2*R*)-1,2-diphenylethane-1,2-diamine. The structure of **R** was confirmed by <sup>1</sup>H NMR (Figure 3.12). Compared with the free ligand, the proton signals of most of the phenyl rings showed an upfield shift. The proton signal at  $\delta = 8.34$  ppm assigned to the protons He on the imine bonds newly appeared after the reaction, indicating the formation of a Schiff base.

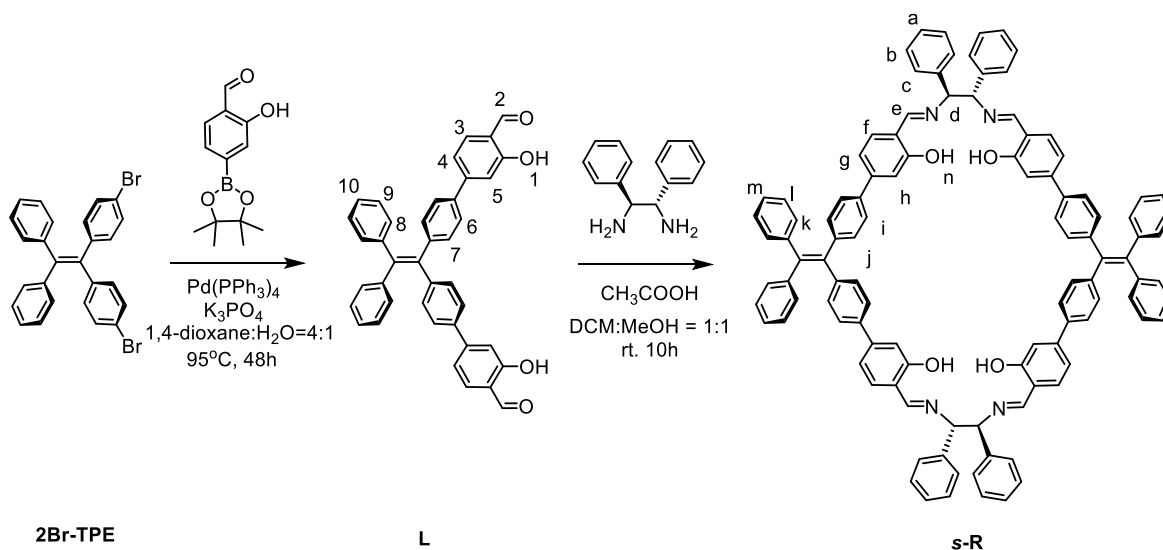


Figure 3.12: Synthesis route of TPE-based chiral macrocycle.

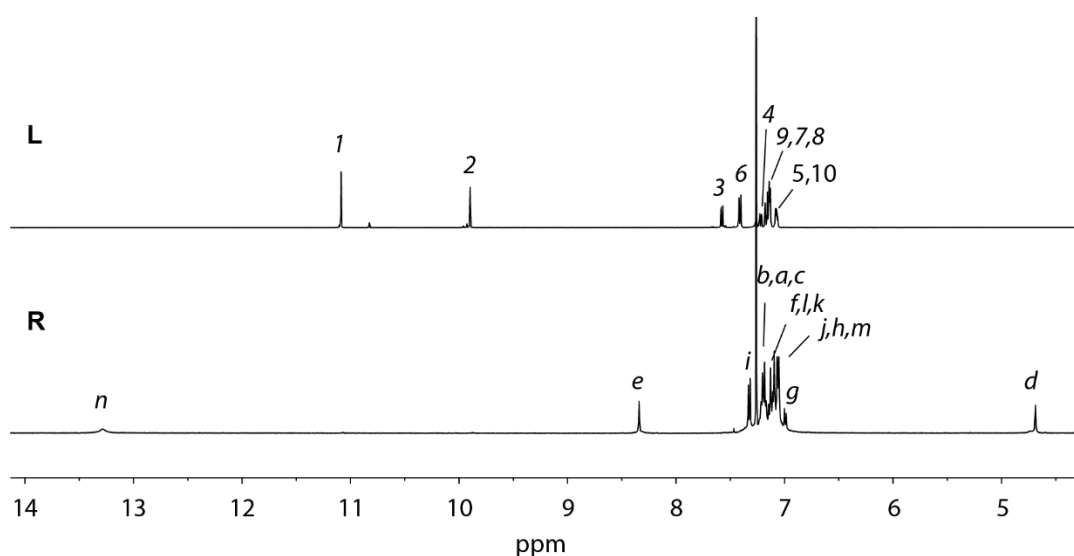


Figure 3.13: stacked <sup>1</sup>H NMR spectra of **L** and **R** (600 MHz, 298 K, CDCl<sub>3</sub>).

### 3. Tetraphenylethylene-based macrocycles with adjustable CPL

#### 3.3 Self-assembly of metal salen macrocycles

As the second most abundant transition metal ion and essential for human health, Zn(II) ions have drawn considerable interest.<sup>[36]</sup> Zn(II) complexes supported by Schiff base ligands have been investigated for their intriguing catalytic, photophysical and aggregation properties.<sup>[37]</sup> Here, a Zn(II)-based macrocycle was obtained by self-assembly of TPE-based salen macrocycle **R** with Zn(II).

**TPE-R** is poorly soluble in DMSO, but when the suspension of 1 equiv. of **R** in DMSO-*d*<sub>6</sub> was treated with 2.0 equiv. of Zn(OAc)<sub>2</sub> at room temperature, the yellow suspension turned into a clear solution after 10 minutes. In the <sup>1</sup>H NMR spectrum of the obtained solution, a new set of signals was observed (Figure 3.14). The signal of proton H<sub>n</sub> disappeared indicating the self-assembly of **R** with Zn(II). DMSO has a high boiling point which hinders isolation of the obtained macrocycle as a solid. Hence, the same metalation reaction was also performed in CHCl<sub>3</sub> for 2h. After evaporating the residual chloroform **Zn<sub>2</sub>R** was obtained as a yellow powder.

The diffusion-ordered spectroscopy (DOSY) spectrum of **Zn<sub>2</sub>R** confirmed the formation of a single compound which showed a diffusion coefficient of  $9.54 \times 10^{-11}$  m<sup>2</sup>/s with hydrodynamic radius of 11.5 Å (Figure 3.49). While a hydrodynamic radius of **L** was calculated to be 6.95 Å, which further confirms the expected larger size of **Zn<sub>2</sub>R**. Further, **Co(III)<sub>2</sub>R** was also synthesized following the same procedure, but using Co(OAc)<sub>2</sub> as a metal source, in a chloroform/acetonitrile mixture. Notably, the kinetically labile Co(II) could be easily converted into kinetically stable state, Co(III), by atmospheric oxidation.<sup>[38]</sup> For this reason, NH<sub>4</sub>PF<sub>6</sub> was added as electrolyte to balance the whole charge. As a result, the turbid grey-green solution became a clear reddish-brown solution because the change in the oxidation-state changed the solubility and the optical properties of the complex. The <sup>1</sup>H NMR spectrum of **Co(III)<sub>2</sub>R** showed broadened signals probably due to some residual paramagnetic Co(II)<sub>2</sub>R. The structure of binuclear metal salen macrocycle **Co(III)<sub>2</sub>R** was confirmed by the ESI-MS showing a prominent peak at *m/z* 805.7257, corresponding to positively charged complex [**Co(III)<sub>2</sub>R**]<sup>2+</sup>, supporting the oxidation of Co(II) to Co(III) (Figure 3.15)



### 3. Tetraphenylethylene-based macrocycles with adjustable CPL

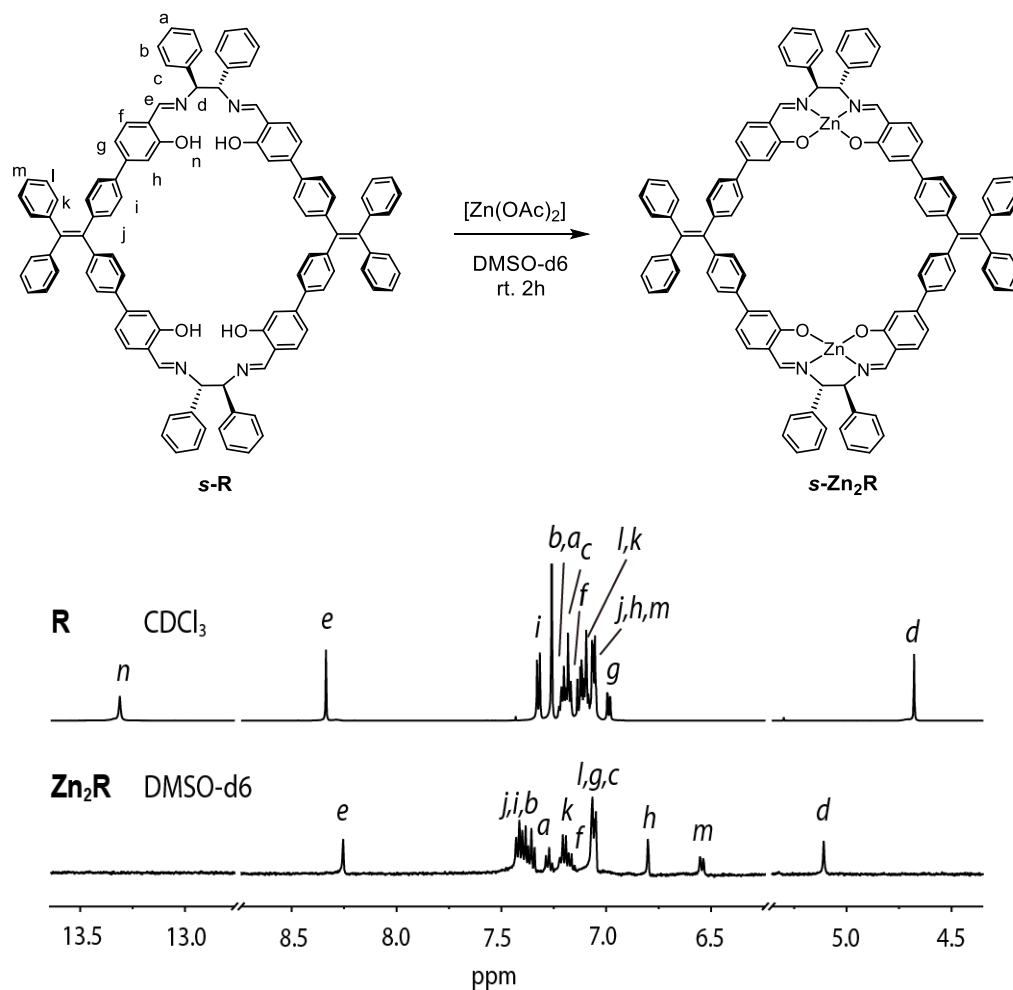


Figure 3.14: Self-assembly of **Zn<sub>2</sub>R** and  $^1\text{H}$  NMR spectra of **R** in  $\text{CDCl}_3$  and **Zn<sub>2</sub>R** in  $\text{DMSO-d}_6$  (600 MHz, 298 K).

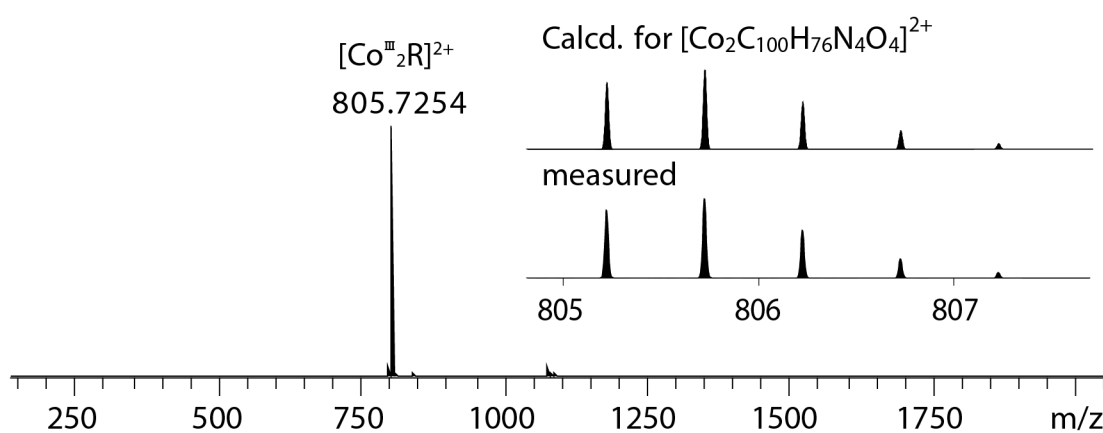


Figure 3.15: ESI-MS spectra of **Co(III)<sub>2</sub>R**, with insets showing the calculated and measured isotopic patterns of  $[\text{Co(III)}_2\text{R}]^{2+}$ .

### 3. Tetraphenylethylene-based macrocycles with adjustable CPL

Fourier transform infrared (FT-IR) spectra were recorded to further confirm the structure of the assembly (Figure 3.16), **R** displays a characteristic band at  $1625\text{ cm}^{-1}$ , corresponding to vibration of C=N bonds, indicating the formation of Schiff base.<sup>[39,40]</sup> The band at  $3030\text{ cm}^{-1}$  is assigned to the stretching vibration of C-H of aromatic rings. The band at  $2856\text{ cm}^{-1}$  is attributed to the vibration of the OH group. As for **Zn<sub>2</sub>R** and **Co(III)<sub>2</sub>R**, the bands from the OH groups disappeared, proving the coordination of metal ions.

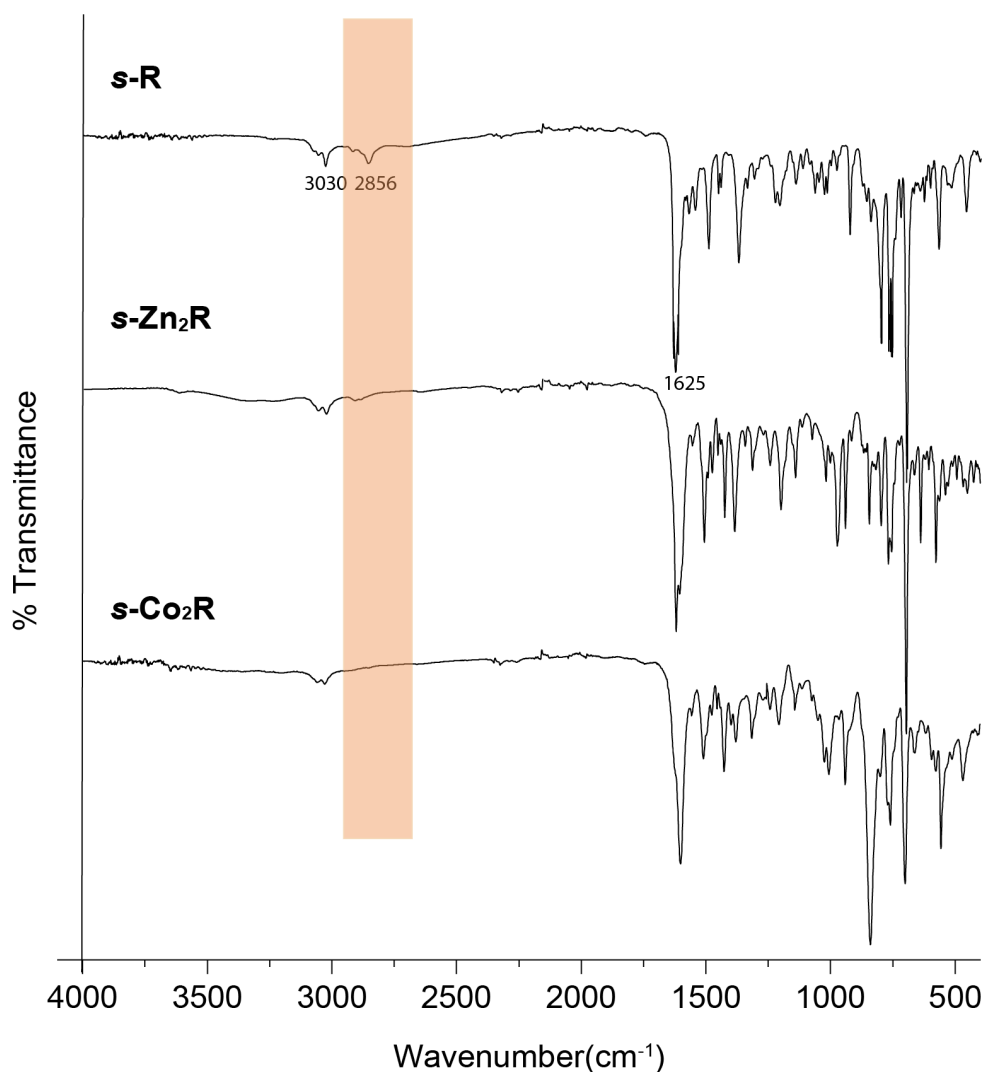


Figure 3.16: FT-IR spectra of **R**, **Zn<sub>2</sub>R** and **Co(III)<sub>2</sub>R**.

Colorless block-shaped single crystals of **r-Zn<sub>2</sub>R** and red block-shaped single crystals of **s-Co(III)<sub>2</sub>R** suitable for X-ray diffraction analysis were obtained by slow vapor diffusion of diethyl ether to DMF and dioxane to acetonitrile solutions of the compounds, respectively.

### 3. Tetraphenylethylene-based macrocycles with adjustable CPL

By crystallographic analysis, the structure of each macrocycle was unambiguously revealed. In the crystal structure of *r*-Zn<sub>2</sub>R (Figure 3.17 a), the Zn(II) centers were found to be coordinated by the N<sub>2</sub>O<sub>2</sub> coordination-sites of the salen units and one DMF molecule in the apical position forming a square pyramid geometry. The N<sub>2</sub>O<sub>2</sub> coordination-sites and the Zn(II) centers are located on the same plane. The Zn···Zn distance in the solid-state was estimated to be 13.664 Å. In addition, the longest C···C distance in the solid-state was estimated to be 25.941 Å. In addition, the longest C···C distance between the two salen-units was calculated to be 25.941 Å. The outer phenyl rings of the TPE units were found to have a dihedral angle of 45°. The longest C···C distance from one TPE backbone to the other backbone was determined to be 23.981 Å. The unit-cell of the crystals was found to have a chiral space group C<sub>2</sub>. The C-C bonds of the salen units showed a distortion, possessing a chirality center (Figure 3.17 b). Two four-blade propeller-shaped TPE units show *P* and *M* configuration, respectively. In the solid state, the metallacycle showed a columnar packing. The TPE-backbone are stacked together and the intramolecular rotational motion seems to be restricted. Porous channels exist in the columnar assembly in the solid-state (Figure 3.17 c).

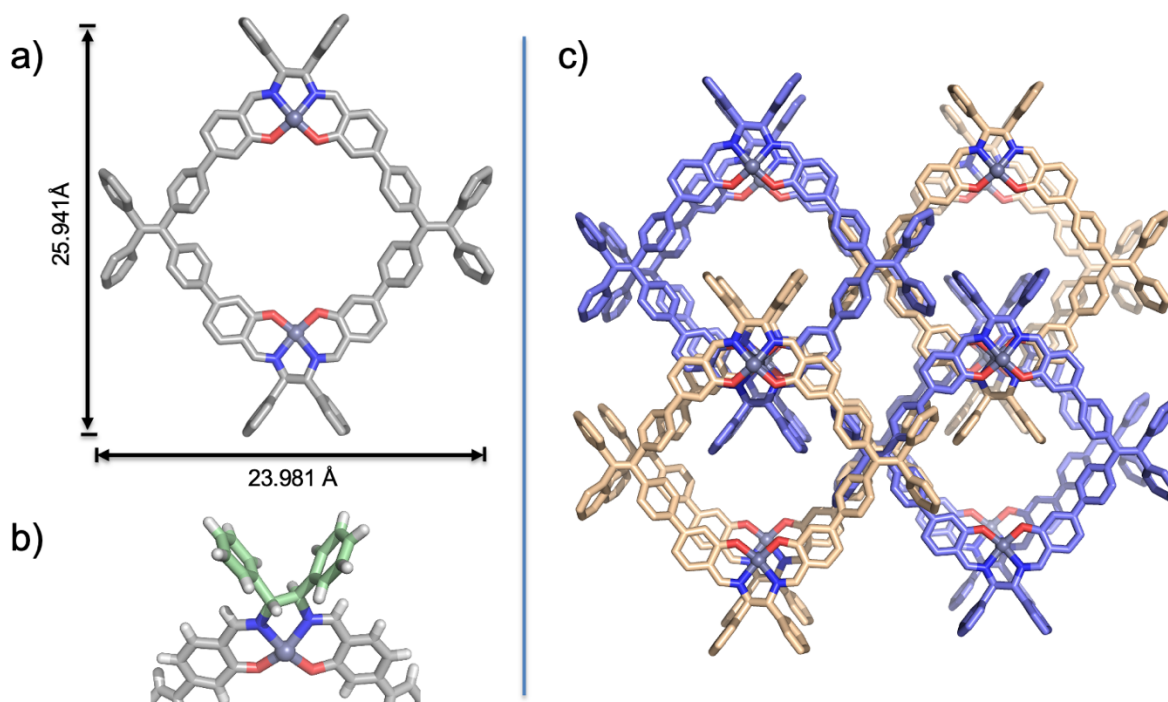


Figure 3.17: a) Preliminary single crystal X-ray structure of *r*-Zn<sub>2</sub>R. Color code for C: gray, N: blue; O: red; Zn: dark purple) b) Partly structure of salen and c) packing structures of *r*-Zn<sub>2</sub>R in top view (Solvent molecules and hydrogens are not shown for clarity).

### 3. Tetraphenylethylene-based macrocycles with adjustable CPL

The crystal structure of **Co(III)<sub>2</sub>R** (Figure 3.60) shows that two Co(III) are coordinated octahedrally by the N<sub>2</sub>O<sub>2</sub> coordination-sites. The other two coordination sites on the axial position of each Co(III) coordinated by one H<sub>2</sub>O molecule and one CH<sub>3</sub>CN molecule. The unit-cell of the crystals was found to have the *P2*<sub>1</sub> space group. The Co(III)•••Co(III) distance was estimated to be 14.521 Å. **Co(III)<sub>2</sub>R** has a different packing structure as **Zn<sub>2</sub>R** (Figure 3.60), which is tilted, due to the different coordination geometry of metal ions.

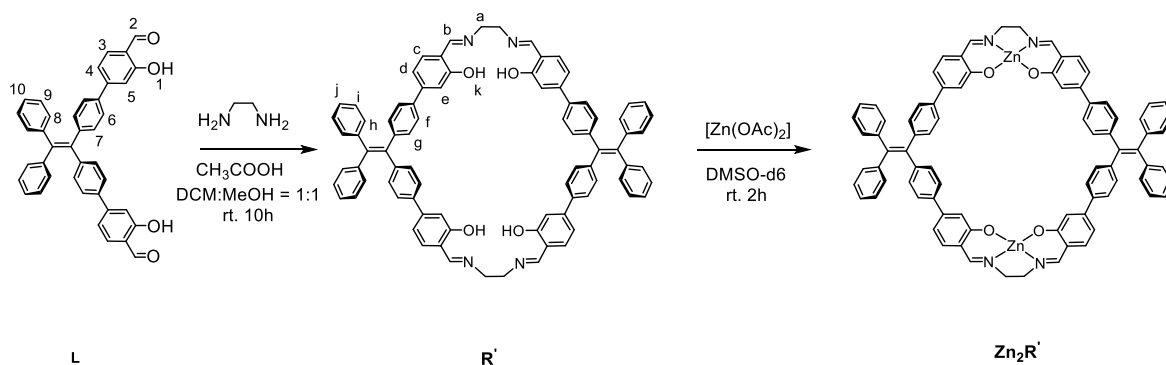


Figure 3.18 Synthesis route of **Zn<sub>2</sub>R'**.

As a control to investigate the chiroptical properties of the resulting complex, an achiral macrocycle was also synthesized by the condensation reaction of the TPE-based salicylaldehyde ligand with ethylenediamine (Figure 3.18). After coordinating with Zn(II), the obtained assembly **Zn<sub>2</sub>R'** structure is confirmed by <sup>1</sup>H NMR. The <sup>1</sup>H NMR signals were assigned with the aid of COSY measurements (Figure 3.42). In the <sup>1</sup>H NMR spectrum of **Zn<sub>2</sub>R'**, a clear single set of signals lacking of the protons H<sub>k</sub>, are indicating the deprotonation and the formation of the desired Zn(II)-macrocyclic. The DOSY spectrum of **Zn<sub>2</sub>R'** confirmed the formation of a single product which showed that all signals from the compound have a diffusion coefficient at  $1.11 \times 10^{-10} \text{ m}^2/\text{s}$  with a hydrodynamic radius of 9.85 Å (Figure 3.55). **Co(III)<sub>2</sub>R'** was synthesized following the same procedure by using Co(OAc)<sub>2</sub> as a metal source in a chloroform/acetonitrile mix solvent (Figure 3.18). The formation of **Co(III)<sub>2</sub>R'** was confirmed by ESI-MS showing a strong peak at *m/z* 653.1620 with a perfect isotopic pattern assignable to  $[\text{Co}(\text{III})_2\text{R}']^{2+}$  (Figure 3.20).

### 3. Tetraphenylethylene-based macrocycles with adjustable CPL

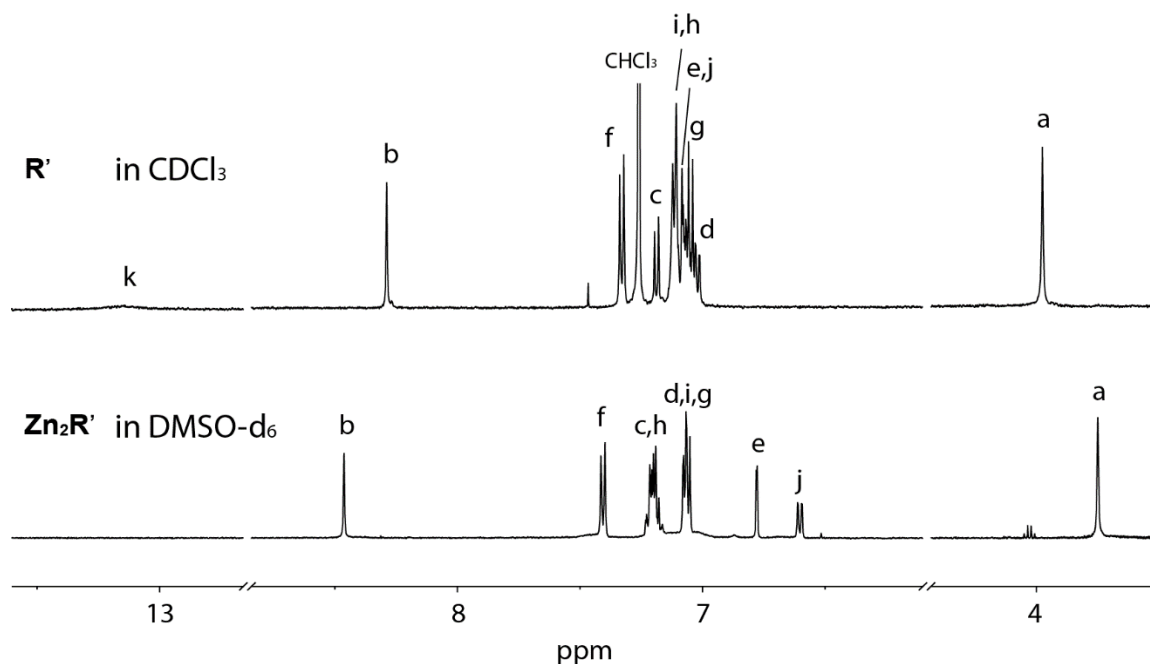


Figure 3.19: Stacked <sup>1</sup>H NMR spectra of **R'** in CDCl<sub>3</sub> and **Zn<sub>2</sub>R'** in DMSO-d<sub>6</sub> (500 MHz, 298 K).

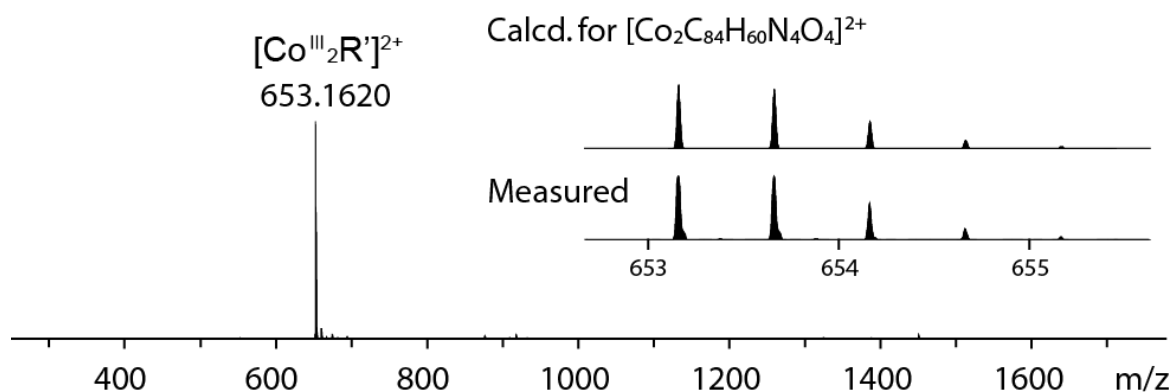


Figure 3.20: ESI-MS spectrum of **[Co(III)<sub>2</sub>R']<sup>2+</sup>** with measured and simulated isotopic patterns of **[Co(III)<sub>2</sub>R']<sup>2+</sup>**.

The structure of the achiral macrocycle was confirmed by single crystal X-ray structure analysis. A colorless square-shaped single crystal of **R'** was obtained by slow evaporation of chloroform. The system crystallized in the *P*-1 space group. The N<sub>2</sub>O<sub>2</sub> coordination-sites were found to be slightly twisting, probably owing to the flexibility of the ethylene chain. The longest C•••C distance of two salen-units of the macrocycle was calculated to 18.896 Å. Besides, the longest C•••C distance of the TPE units was found to be around 23.487 Å (Figure 3.21).

### 3. Tetraphenylethylene-based macrocycles with adjustable CPL

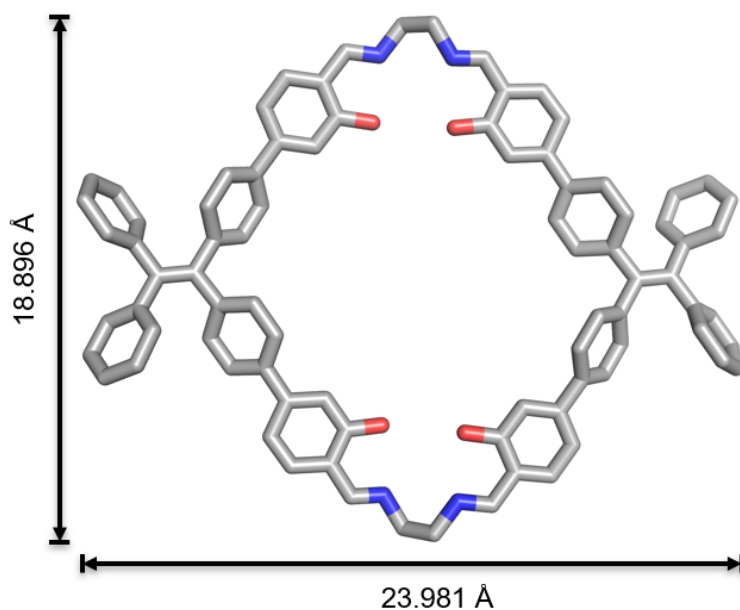


Figure 3.21: Preliminary single crystal X-ray structures of **R'** (Solvent molecules and hydrogens are not shown for clarity).

#### 3.4 Chiroptical properties study in solution

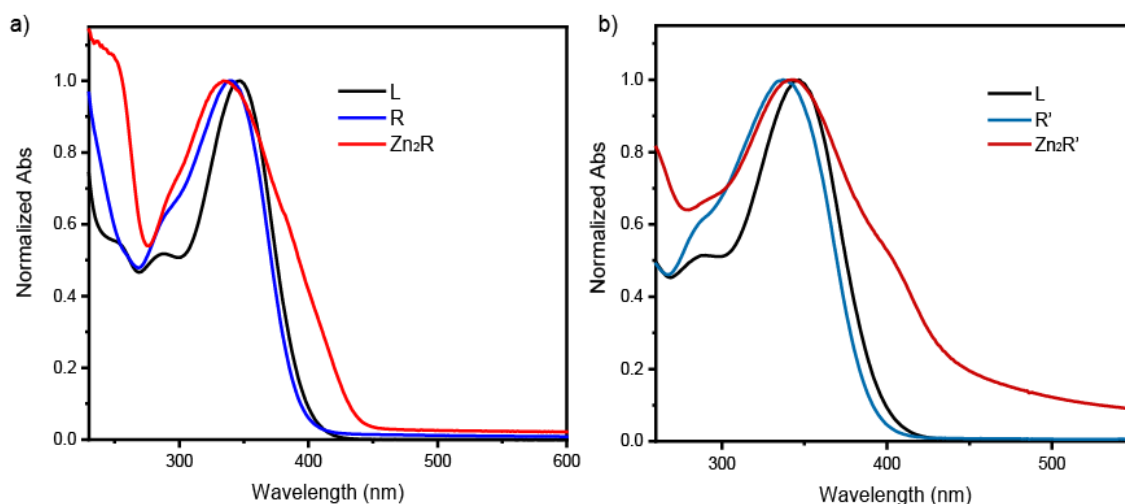


Figure 3.22: UV-Vis absorption spectra of a) **L**, **R**, **Zn<sub>2</sub>R** b) **L**, **R'**, **Zn<sub>2</sub>R'** in THF. Spectra were normalized to fraction folded values between 1 and 0.

UV-Vis absorption measurement of the compounds was performed in THF (Figure 3.22). In the UV-Vis spectrum, ligands displayed a broad absorption band for the  $\pi$ - $\pi^*$  transitions centered at 347 nm with a molar absorption coefficient ( $\epsilon$ ) of  $7.53 \times 10^4 \text{ M}^{-1}\text{cm}^{-1}$ . After forming the macrocyclic structure, the maximum absorption band of **R** and **R'** shifted to 339 nm and 337 nm, respectively, compared with the free ligand.

### 3. Tetraphenylethylene-based macrocycles with adjustable CPL

Metal-organic macrocycles/cages usually show a red shift compared with corresponding ligands.<sup>[41]</sup> From the absorption spectra, as reported, we can see that the maximum absorption wavelength of **Zn<sub>2</sub>R'** exhibits an absorption band centered at 343 nm with  $\epsilon = 5.18 \times 10^4 \text{ M}^{-1}\text{cm}^{-1}$ , showing a red shift compared with metal free salen macrocycle **R'**. On the other hand, the maximum absorption wavelength of **Zn<sub>2</sub>R** showed a hypsochromic shift comparing to free macrocycle **R**. The maximum absorption of **Zn<sub>2</sub>R** shifted from 339 nm to 334 nm. The shoulder at around 400 nm of **Zn<sub>2</sub>R** and **Zn<sub>2</sub>R'** is attributed to the coordination of the salen-motifs with Zn(II).<sup>[42]</sup>

The fluorescence spectra of **L**, **R'**, **R**, **Zn<sub>2</sub>R'** and **Zn<sub>2</sub>R** in THF are shown in Figure 3.23 a. As expected, the TPE-based ligand and the metal-free salen-macrocycles have weak emission properties in THF because of nonradiative decay from the rotation of peripheral phenyl rings. After metalation of the macrocycles with Zn(II) ions, the emission of **Zn<sub>2</sub>R** emitted blue light under 365 nm UV light. The emission spectrum of **Zn<sub>2</sub>R** showed a blue shift from 525 nm to 470 nm and a 16-fold enhancement compared to the metal-free **R** probably due to the improved rigidity of the structure after metal-insertion. A similar phenomenon was also observed in the emission spectrum of **Zn<sub>2</sub>R'**. **Zn<sub>2</sub>R'** showed the maximum emission band at 480 nm and 9.5-fold enhancement compared with the emission intensity of free **R'**. Emission of **Co(III)<sub>2</sub>R'** is not shown due to complete quenching of the emission properties due to the heavy-atom effect.<sup>[43]</sup>

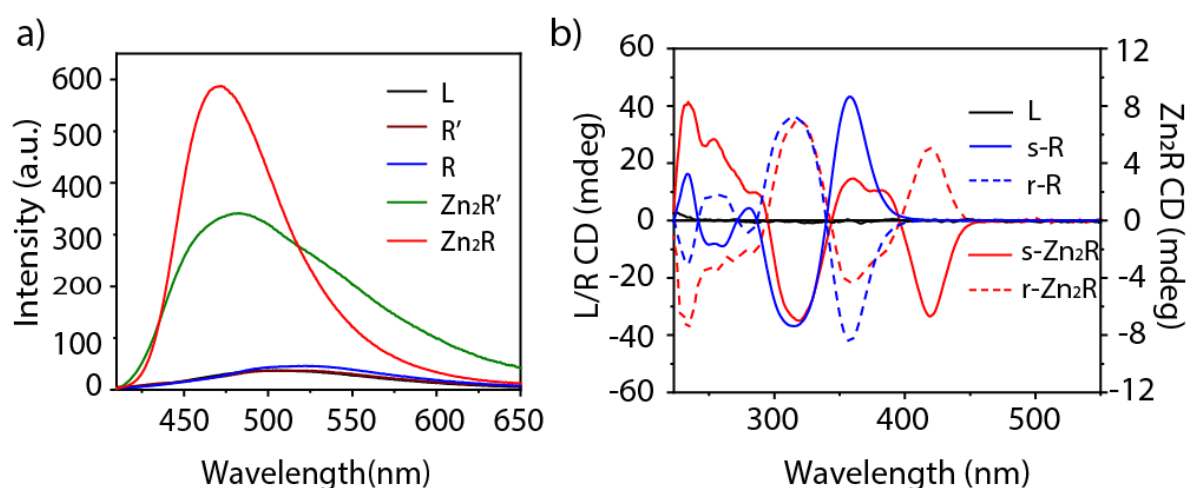


Figure 3.23: a) Emission spectra and b) CD spectra of ligand and macrocycles (in THF,  $c_L = 2 \times 10^{-5} \text{ M}$ ,  $c_R = 1 \times 10^{-5} \text{ M}$ ,  $c_{R'} = 1 \times 10^{-5} \text{ M}$ ,  $c_{Zn_2R} = 1 \times 10^{-5} \text{ M}$ ,  $c_{Zn_2R'} = 1 \times 10^{-5} \text{ M}$ , cuvette path length: 1 cm).

### 3. Tetraphenylethylene-based macrocycles with adjustable CPL

Table 3.1 Fluorescence spectra information of compounds.

	<b>L</b>	<b>R'</b>	<b>R</b>	<b>Zn<sub>2</sub>R'</b>	<b>Zn<sub>2</sub>R</b>
$\lambda_{\text{ex}}$ (nm)	360	360	360	360	360
$\lambda_{\text{em}}$ (nm)	500	525	525	480	470

The CD spectra of the macrocycles in THF assured the chiroptical properties (Figure 3.23b). While achiral **L** is CD silent, the synthesized macrocycles possessing the chiral salen-coordination sites showed mirror CD signals with Cotton effect at around  $\lambda = 350$  nm for the **s/r-R** and **s/r-Zn<sub>2</sub>R** enantiomeric couples, assigned to the absorbance bands of the TPE units, indicating that the chiral information from the coordination-sites is successfully transferred to the whole structure. In addition, **Zn<sub>2</sub>R** exhibits a Cotton effect also at 410 nm, which is attributed to the absorption of the chiral Zn(II)-salen parts.

#### 3.5 The investigation of AIE properties

To gain further insight into the light emitting behavior of the ligand and macrocycles, the fluorescence spectra of compounds in the aggregated state were recorded. Aggregation-induced emission experiments are usually performed in a mixed solution of a good solvent and a poor solvent with progressive increase of the latter.

Efforts to select an appropriate solvent system were therefore made for the examination of the AIE properties. Finally, the solvents system of THF/H<sub>2</sub>O was selected for the investigation of the AIE effect. THF is the good solvent for all compounds used in this chapter, while water is the poor solvent. The addition of water as a poor solvent induced aggregation of the substrates owing to lowering their solubility. After water was added, the absorption band of the compounds showed a bathochromic shift, similar to the *J* aggregation process already reported.<sup>[44]</sup>

**L** shows rather weak emission in THF, however, the emission intensity increased over the addition of water. When the fraction of water reached to 80%, the solution became turbid due to the formation of a precipitate. However, the intensity of the emission was dramatically increased by 75-fold when the water fraction up to 90% in comparison with the one in THF, which is a typical AIE behavior (



### 3. Tetraphenylethylene-based macrocycles with adjustable CPL

Figure 3.63). The emission wavelength showed a blue shift over the addition of water. According to the reported TPE-based AIE mechanism, the perpendicular conformation of the peripheral phenyl rings weakens  $\pi$ -electron conjugation and leads to a blue shift.<sup>[45]</sup>

The emission intensity of **R** gradually increases with the addition of water and is around 5-fold enhanced when the water fraction reached 90%, showing an AIE property (Figure 3.64). The emission wavelength showed a red shift at the beginning of the addition, which is probably caused by an intermolecular charge-transfer (CT) process, which involves to emission at the longer wavelength compared with the luminophores especially in polar solution.<sup>[46]</sup>

In the case of **Zn<sub>2</sub>R**, the emission decreased upon the addition of 10% of water, probably due to polarity-induced fluorescence quenching.<sup>[47]</sup> At the 50% water fraction, the metal-organic macrocycle shows a 2-fold enhanced emission, supporting the persistency of the AIE effect. However, the emission negligibly increased after the formation of a precipitate when the water content exceeded 50%.

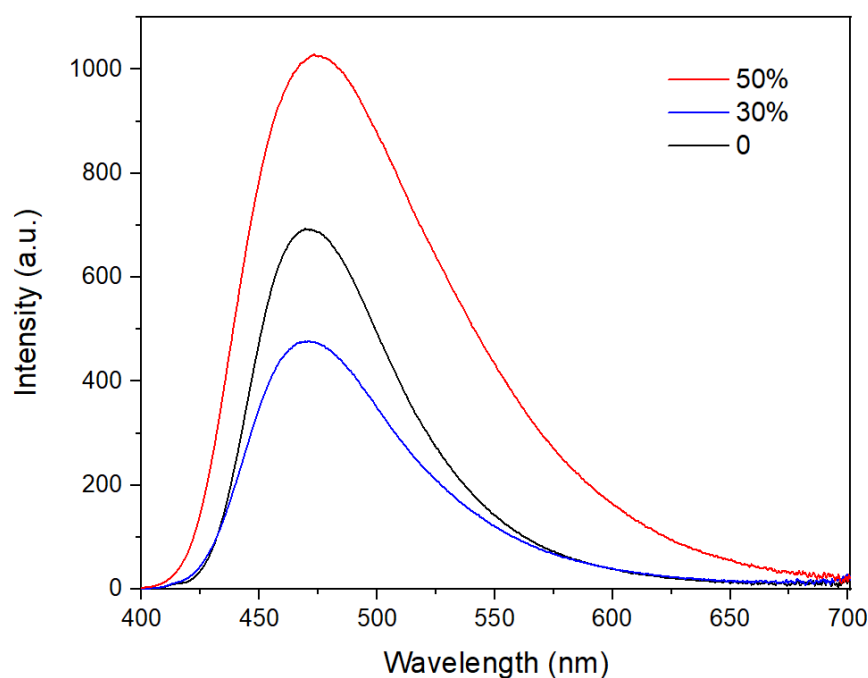


Figure 3.24: Emission spectra of **Zn<sub>2</sub>R** with increasing water fraction in THF/H<sub>2</sub>O mixtures. ( $\lambda_{\text{ex}} = 370 \text{ nm}$ ,  $c = 1 \times 10^{-5} \text{ M}$ ).

The fluorescence quantum yields ( $\Phi_{\text{F}}$ ) both in THF and the mixed solvent (THF:H<sub>2</sub>O = 10:90) were measured (Figure 3.66). In THF, the internal quantum yields of ligand

### 3. Tetraphenylethylene-based macrocycles with adjustable CPL

**L**, macrocycle **R** and metallacycle **Zn<sub>2</sub>R** are 1.86, 1.11 and 3.51%, respectively. On the other hand, the improvement of the quantum yields was observed in the mixed solvent system (THF:H<sub>2</sub>O = 10:90) to 21.23, 2.70 and 6.02%, respectively, further demonstrating the AIE character of the compounds.

In addition, dynamic light scattering (DLS) data for the **R** and **Zn<sub>2</sub>R** with the concentration of  $1 \times 10^{-5}$  M, with different content of water, was collected (Figure 3.70). It evidenced the formation of larger aggregates of macrocycles upon increasing fraction of water for both macrocycles.

The chiroptical properties of macrocycles in the aggregate-state were also studied. The CD signal of **R** showed a slight decrease over the addition of water at the beginning. When the water content exceeded 50%, the CD signal changed sign and was dramatically enhanced. **Zn<sub>2</sub>R** showed a similar behavior. The solution of **Zn<sub>2</sub>R** became turbid when the water was added and showed a reverse CD signal. With the increase of the water fraction, the signal intensity increased. The reversal of chirality can be assumed to be formation of supramolecular helices in the aggregated state as further confirmed by SEM measurement. The detail will be discussed later.

### 3. Tetraphenylethylene-based macrocycles with adjustable CPL

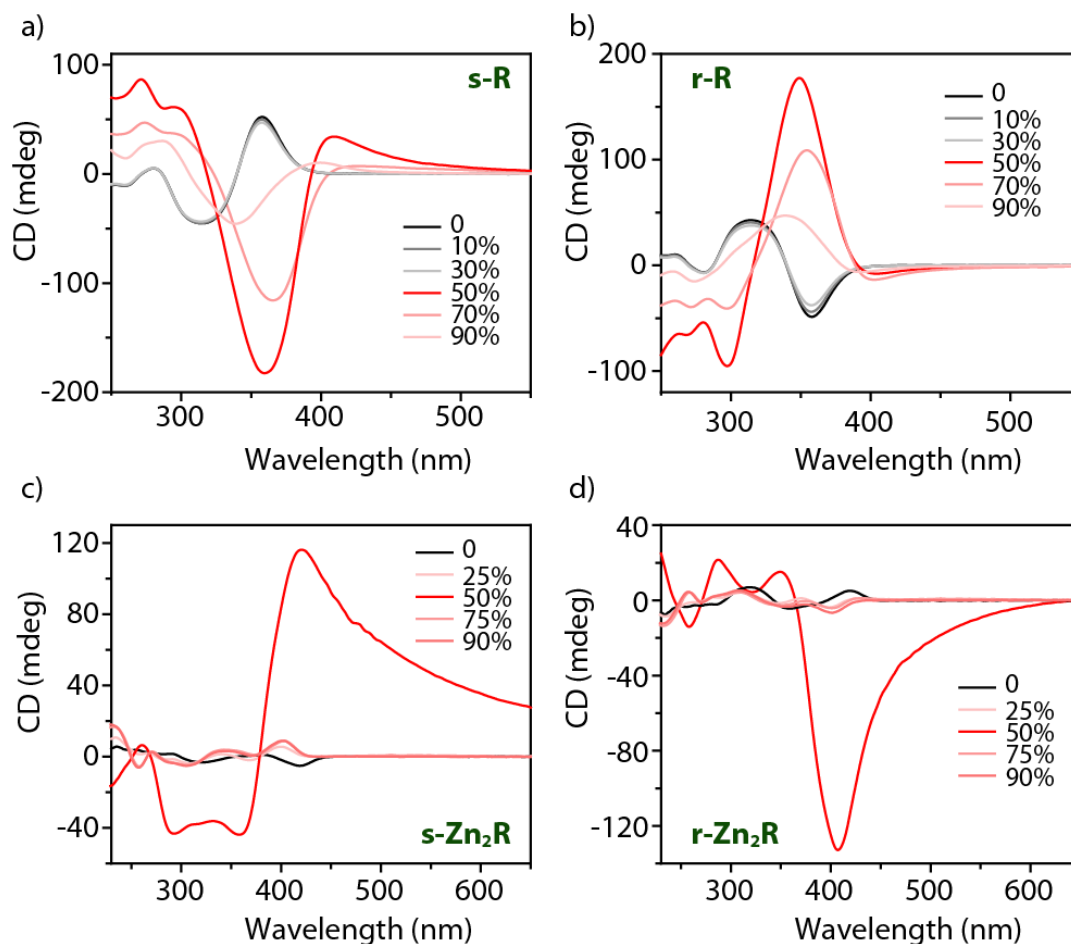


Figure 3.25: CD spectra spectra of (a) **s-R** (b) **r-R** (c) **s-Zn<sub>2</sub>R** (d) **r-Zn<sub>2</sub>R** in THF with different fraction of water ( $c = 1 \times 10^{-5}$  M, cuvette path length: 1 cm).

Furthermore, the combination of luminescence and chirality endowed **Zn<sub>2</sub>R** with a circularly polarized luminescence (CPL) property (Figure 3.26). CPL performance is generally estimated by the emission dissymmetry factor ( $g_{lum}$ ), which is calculated as  $g_{lum} = 2(I_L - I_R)/(I_L + I_R) = 2\Delta I/I$ , where  $I_L$  and  $I_R$  represent the emission intensities of left and right circularly polarized luminescence, respectively.<sup>[48]</sup> However, it is still a challenge to obtain CPL active materials with high  $g_{lum}$ . To increase the CPL  $g_{lum}$  value, one successful strategy is to make the chromophores assemble into an ordered aggregate, which can significantly amplify the CPL intensity up to one order of magnitude.<sup>[49]</sup>

**r-Zn<sub>2</sub>R** showed a negative CPL signal at 460 nm with  $g_{lum} = 1.2 \times 10^{-3}$  in THF (Figure 3.26). The CPL signal decreased when 25% water was added, presumably due to a mixed contribution of both monomeric **Zn<sub>2</sub>R** and supramolecular helical aggregates. On the other hand, after the addition of 50% of water, the CPL signal

### 3. Tetraphenylethylene-based macrocycles with adjustable CPL

was inverted and enhanced with a  $g_{lum}$  value of  $-2.1 \times 10^{-2}$ . Meanwhile, the emission wavelength shifted to the shorter wavelength, indicating of a conformation change in the aggregate state (Figure 3.26 b). Unfortunately, CPL analysis of **R** was hampered by the low sample stability due to the dynamic imine bonds.

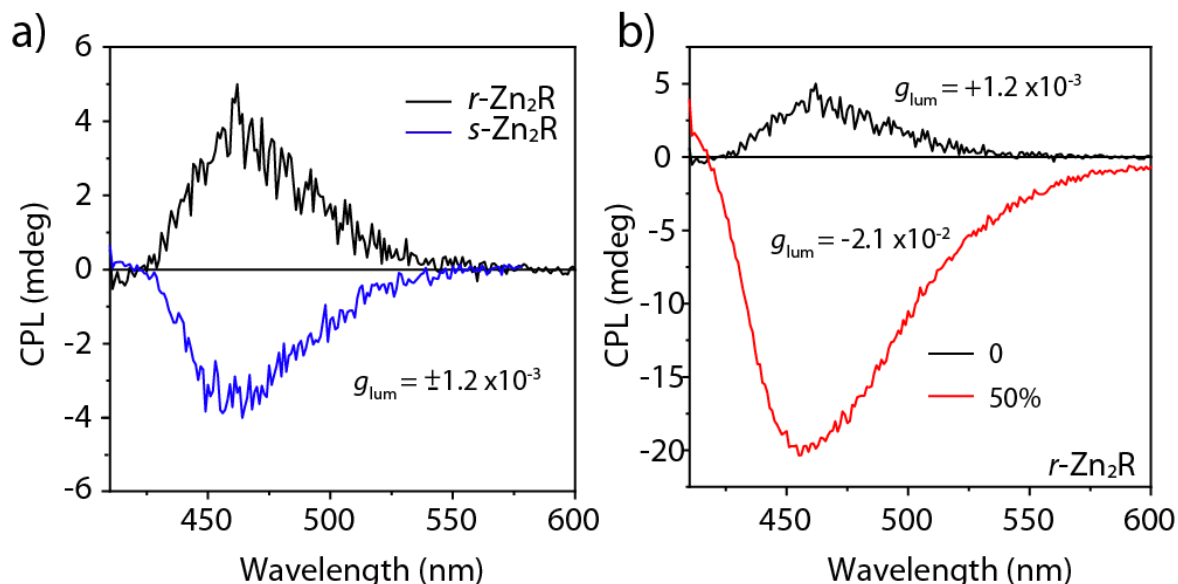


Figure 3.26: CPL spectra of a) *r*/*s*-Zn<sub>2</sub>R in THF b) *r*-Zn<sub>2</sub>R in THF and THF:H<sub>2</sub>O = 50:50.

Analogous results, but with mirror image CPL spectra, are obtained with **s**-Zn<sub>2</sub>R in pure THF or in THF/water, which showed a negative CPL signal at 460 nm with  $g_{lum} = -1.2 \times 10^{-3}$  in THF and boosted the  $g_{lum}$  up to  $2 \times 10^{-2}$  after the addition of 50% water (Figure 3.68, Figure 3.69). The inversion and increase of the CD and the CPL signals upon aggregation suggest the formation of higher ordered supramolecular structures. To prove this and gain further insight into the morphological features of the aggregated species, we performed Scanning Electron Microscopy (SEM) analysis (Figure 3.27). Samples of chiral macrocycles were prepared from  $1 \times 10^{-5}$  M solution in THF or THF: H<sub>2</sub>O = 50:50. Sample of achiral ring **R'** was prepared from  $1 \times 10^{-4}$  M THF solution. At first, both **R** and Zn<sub>2</sub>R in solely THF as solvent, only showed dispersed spheres, without aggregation into ordered aggregates. However, as previously reported, introducing chiral unit into AIEgens can form helical supramolecular self-assemblies.<sup>[50]</sup> SEM images of **R** from a THF/water (50:50, v: v) solvent mixture show the formation of helical fibers with a length of from 200 nm to 2 μm, approximately 120 nm wide and 35 nm thicknesses. Helices with left (*M*)- and right (*P*)- handedness were observed from **s**-**R** and **r**-**R**,

### 3. Tetraphenylethylene-based macrocycles with adjustable CPL

respectively with a twist half period of approximately 160 nm and 120 nm, respectively (Figure 3.27 b). As a control, achiral **R'** was also prepared for the SEM measurement. As expected, while it forms nanofibers, the achiral species aggregates in non-helical structures (Figure 3.72 e-f). SEM images of **Zn<sub>2</sub>R** from a THF/water (50:50, v: v) solvent mixture also proved the formation of aggregates (Figure 3.27).

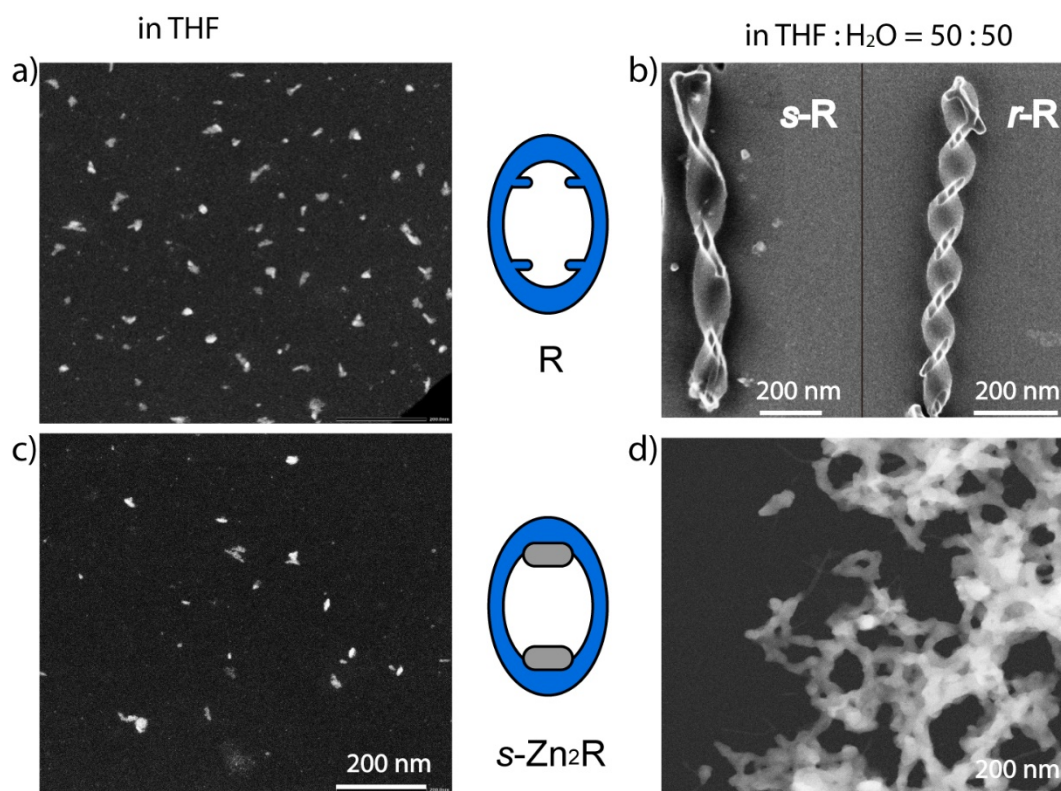


Figure 3.27: **bSEM** images of **R** a) in THF b) in THF: H<sub>2</sub>O = 50 : 50, and **Zn<sub>2</sub>R** in c) THF d) in THF:H<sub>2</sub>O = 50 : 50.

### 3.6 Conclusion and outlook

In conclusion, two enantiomers of a chiral macrocycles and an achiral macrocycle based on a TPE structure and a salen coordination-unit, were designed and synthesized by the condensation reaction of salicylaldehyde ligand and diamine building blocks. Upon the addition of Zn(II), the binuclear metallacycles *r*-/*s*- **Zn<sub>2</sub>R** and achiral **Zn<sub>2</sub>R'** were formed. The structures are characterized by <sup>1</sup>H NMR, DOSY, ESI-MS, single crystal X-ray structure analysis, FT-IR, UV-Vis, Fluorescence, CD, DLS, SEM and CPL analysis.

### 3. Tetraphenylethylene-based macrocycles with adjustable CPL

The chiroptical properties and AIE effect of ligand and macrocycles were studied in pure THF or in a THF/water mixture. Due to coordination-induced emission enhancement and AIE property, **Zn<sub>2</sub>R** does not only show strong emission in solution but also in the aggregate state. Helical chirality was generated in the aggregated state, which is supported by CD, CPL and SEM measurements, resulting in the amplification and reversal of the chiroptical properties. In addition, formation of supramolecular helices with *r/s*-**Zn<sub>2</sub>R** results in reverse and increasement of the CPL properties of one order of magnitude, with the  $g_{lum}$  value changing from  $\pm 1.2 \times 10^{-3}$  to  $\pm 2.1 \times 10^{-2}$ . This strategy shows how a modular approach can be used to incorporate multiple properties in a simple synthetic way. Here, the AIE behavior of a TPE chromophore is combined with chirality coming from the salen-unit and finally introducing Zn(II) cations allows a boost of the emission properties. The final properties result from a synergistic effect of all the selected building blocks, allowing to self-assemble a compound with strong emission and switchable chiroptical properties with potential application for chiral sensing and optical displays.

### 3. Tetraphenylethylene-based macrocycles with adjustable CPL

#### 3.7 Experimental part

##### 3.7.1 Materials

Unless otherwise stated, all chemicals and solvents were purchased from commercial companies (Abcr, Sigma Aldrich, Acros Organics, VWR and Chempur) and used as received. (1*S*,2*S*)-1,2-diphenylethane-1,2-diamine and (1*R*,2*R*)-1,2-diphenylethane-1,2-diamine were recrystallized from hexane.

##### 3.7.2 General Methods

###### NMR

NMR spectroscopic data was measured on the spectrometers Bruker AV 500 Avance NEO and Bruker AV 600 Avance III HD. Chemical shifts for <sup>1</sup>H and <sup>13</sup>C spectra are reported in ppm on the δ scale relative to proton resonance resulting from incomplete deuteration of the solvents (CDCl<sub>3</sub>: 7.26 ppm, 77.16 ppm, DMSO-*d*<sub>6</sub>: 2.5 ppm, 39.52 ppm, CD<sub>3</sub>CN: 1.94 ppm, 118.26 ppm). The chemical shift δ is given in ppm, the coupling constants *J* in Hz. The following abbreviations are used to describe signal multiplicity for <sup>1</sup>H NMR spectra: s: singlet, d: doublet, t: triplet, dd: doublet of doublets, m: multiplet. All spectra were recorded in standard 5 mm NMR tubes at 298 K if not stated otherwise.

###### DOSY

<sup>1</sup>H DOSY spectra were recorded with a *dstebpgp3s* pulse sequence with diffusion delays *D*<sub>20</sub> of 0.09-0.14 s and gradient powers *P*<sub>30</sub> of 900-2500 μs for each species optimized. The hydrodynamic radius was calculated according to Stokes-Einstein equation:

$$D = \frac{k_B T}{6\pi\eta r_H}$$

Where *D* is coefficient constant, *k<sub>B</sub>* is the Boltzmann constant, *T* is the absolute temperature, *η* is the viscosity of solvent, *r<sub>H</sub>* is the hydrodynamic radius.

###### ESI-MS

Electrospray ionization mass spectrometry (ESI-MS) experiments were performed on ESI-timsTOF (ESI-trapped ion mobility-time of flight) mass spectrometer by Bruker, equipped with and ESI source (positive/negative mode). An Agilent ESI low concentration tuning mix has been used for calibration of tims and TOF units. Mass

### 3. Tetraphenylethylene-based macrocycles with adjustable CPL

spectrometry data is given as mass/charge ratio (m/z) as well as the relative intensity with regard to the base peak (I = 100).

#### **X-Ray Analysis**

##### **Bruker D8 venture (in-house)**

Data collection for single crystal X-ray diffraction was performed on a Bruker D8 venture with a four-axle goniometer in  $\kappa$ -geometry, equipped with CuK $\alpha$  and MoK $\alpha$  Incoatec microfocus sources (I $\mu$ s 3.0) and a photon II detector. The crystal was covered with inert NVH oil and placed on the 0.2 mm nylon loop. The sample was cooled down to 100(2) K utilizing an Oxford Cryostream 800.

##### **P11@DESY (Synchrotron)**

Data collection for single crystal X-ray diffraction was performed on a one-axle goniometer equipped with a Pilatus 6M fast detector by Dectris at the macromolecular beamline PXI, Petra III, DESY, Hamburg. Therefore, a wavelength of  $\lambda = 0.6888 \text{ \AA}$  has been set on a nitrogen cooled double monochromator and the sample has been cooled to 80(2) K utilizing an Oxford Cryostream 800.

#### **UV-Vis**

UV-vis spectra were recorded on a DAD HP-8453 UV-Vis spectrometer. Cuvette path length 10 mm.

#### **Fluorescence**

Fluorescence spectra were recorded on a JASCO FP-8300 fluorimeter equipped with a (150W) Xe lamp as light source. Cuvette path length 10 mm in emission direction.

Internal fluorescence Quantum Yield (QY)  $\Phi_F$  is the number of photons for the fluorescence emitted from the sample divided by the number of photons for the excitation light absorbed by the sample.

$$\Phi_F = \frac{\text{emission photon number}}{\text{absorbent photon number}}$$

QY for fluorescence were determined on a Jasco FP-8300 fluorimeter with accessory of JASCO ILF-835 integrating sphere. Cuvette path length 3 mm was used. The absorption of the samples is around 0.05-0.1. All the fluorescence spectra



### 3. Tetraphenylethylene-based macrocycles with adjustable CPL

of samples and solvents were recorded with same slit widths. The integrated emission area was divided by integrated absorbed area to get internal fluorescence QY.

#### **FT-IR**

Fourier Transform Infrared (FT-IR) spectra were measured on Perkin Elmer Spectrum Two spectrometer in the 400-4,000  $\text{cm}^{-1}$  spectral region.

#### **CD**

Circular dichroism spectra were recorded on an Applied Photophysics Chirascan qCD Spectrometer with a temperature-controlled cuvette holder. The spectra were background-corrected and smoothed with a window size of 5.

#### **CPL**

Circularly polarized luminescence measurements were performed on a JASCO CPL-300 spectrophotometer equipped with a (150W) Xe lamp as light source. CPL spectra were recorded with excitation/emission bandwidth of 15 nm and emission bandwidth of 15 nm and averaged over 20 spectra.

#### **DLS**

Dynamic light scattering experiments were performed on a Malvern Zetasizer ZS nano instrument, with a single  $173^\circ$  scattering angle, and at  $25^\circ\text{C}$  temperature.

#### **STEM**

STEM measurements were done using a JEOL JEM-2800 with Schottky field emission cathode operated at 200 kV. SEM detectors are equipped for STEM images. Dual SDD X-ray detectors are used to capture EDS signals for elemental mapping with solid angle of 0.95 sr, and with 133 eV of spectral resolution.

### 3. Tetraphenylethylene-based macrocycles with adjustable CPL

#### 3.7.3 Synthesis of the macrocycles

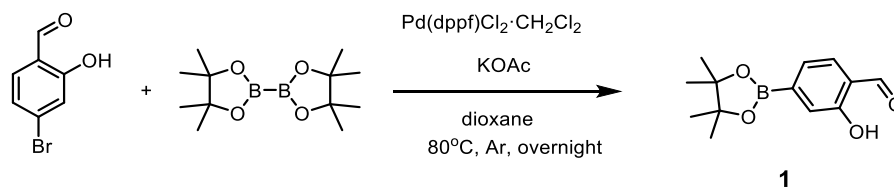


Figure 3.28: synthesis route of **1**

Pinacol ester salicylaldehyde compound **1**:

the synthesis of **1** was carried out according to the literature procedure.<sup>[51]</sup>

4-bromosalicylaldehyde (1.0 g, 4.97 mmol), Pin<sub>2</sub>B<sub>2</sub> (1.52g, 5.97 mmol), Pd(dppf)Cl<sub>2</sub>·CH<sub>2</sub>Cl<sub>2</sub> (203 mg, 0.249 mmol), and KOAc (1.46 g, 14.92 mmol) were combined in a 100 mL Schlenk tube, 15 mL anhydrous 1,4-dioxane were added. The mixture was degassed via freeze-thaw cycles and then heated at 85 °C under N<sub>2</sub> atmosphere for 5 h. After cooling to room temperature, the solvent was removed under vacuum. The residue was dissolved in CH<sub>2</sub>Cl<sub>2</sub> and washed with H<sub>2</sub>O and dried over MgSO<sub>4</sub>. The crude product was purified by column chromatography (dichloromethane: pentane = 1:1) to provide a white solid as aim product.

<sup>1</sup>H NMR (600 MHz, CDCl<sub>3</sub>): δ 10.83 (s, 1H), 9.93 (s, 1H), 7.54 (s, 1H), 7.42 (d, J = 8.4 Hz, 2H), 1.35 (s, 12H).

<sup>13</sup>C NMR (151 MHz, CDCl<sub>3</sub>): δ 197.16, 160.94, 132.96, 125.72, 124.20, 122.36, 84.78, 25.21.

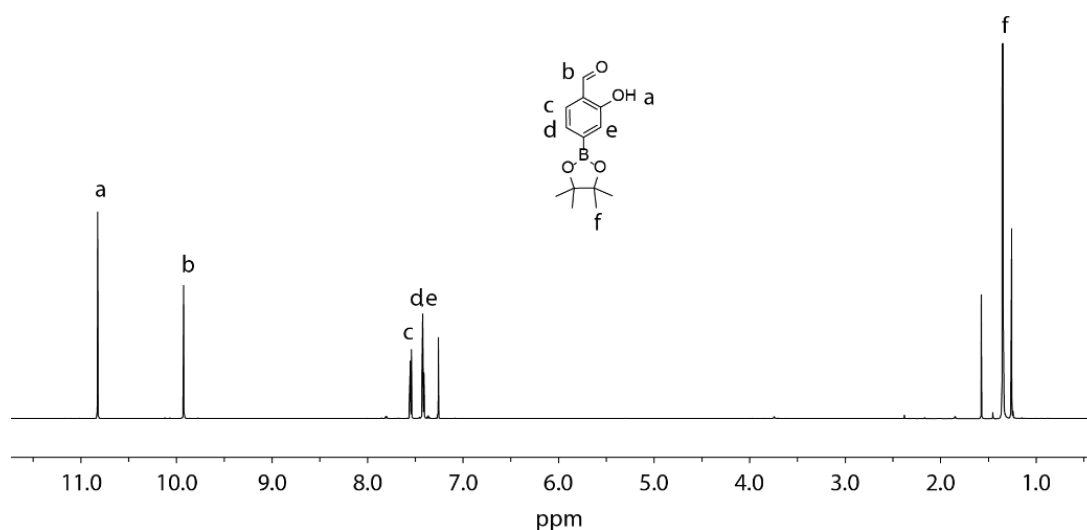


Figure 3.29: <sup>1</sup>H NMR spectrum of compound **1** (600 MHz, 298 K, CDCl<sub>3</sub>).

### 3. Tetraphenylethylene-based macrocycles with adjustable CPL

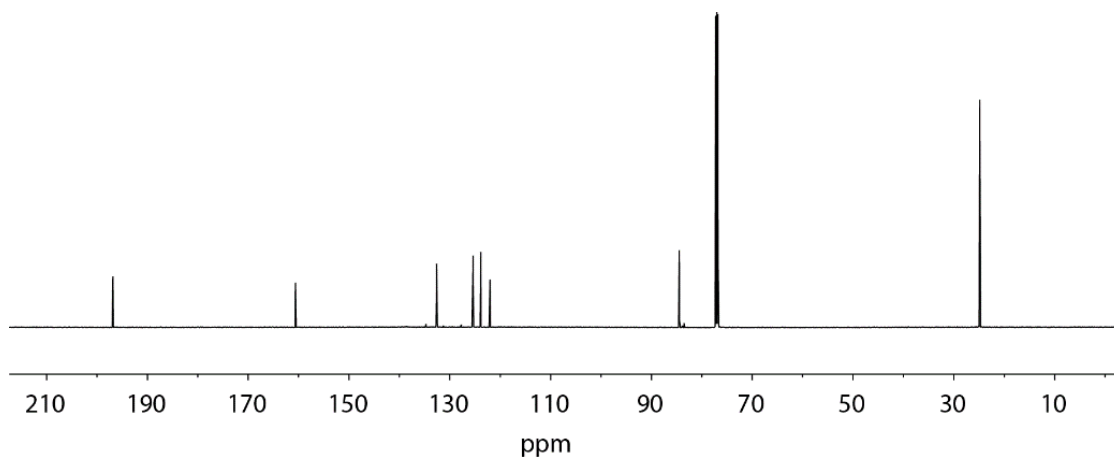


Figure 3.30:  $^{13}\text{C}$  NMR spectrum of compound **1** (151 MHz, 298 K,  $\text{CDCl}_3$ ).

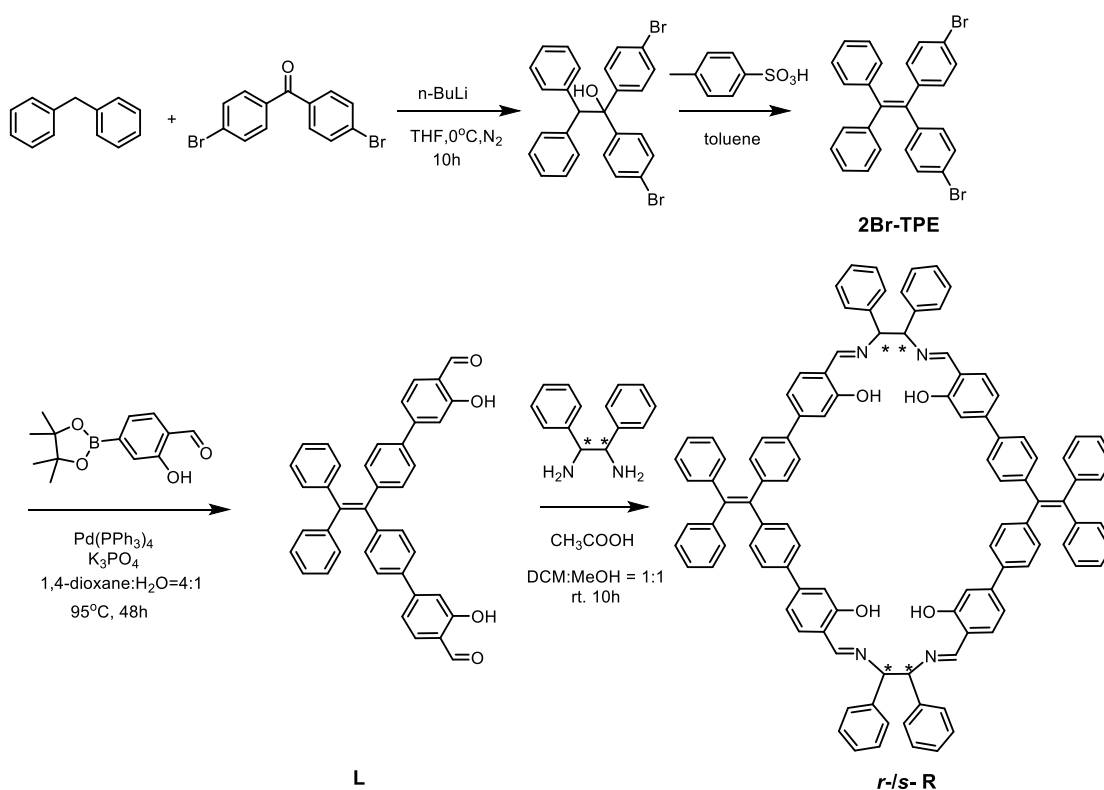


Figure 3.31: Synthesis route of **1**

Synthesis of compound **2Br-TPE**:

**2Br-TPE** was synthesized in two steps by following a reported procedure.<sup>[34]</sup>

Diphenylmethane (2.0 g, 11.9 mmol) and anhydrous tetrahydrofuran 15 mL were mixed in a 100 mL Schlenk tube and stirred under argon at  $0^\circ$ . A 2.5 M solution of *n*-butyllithium (4.8 mL, 762 mg, 12.88 mmol) in hexane was added into the Schlenk tube. After stirring for 1 h at  $0^\circ$ , 4-(4-bromophenyl) benzophenone (3.24 g, 9.5 mmol) was added and the reaction mixture was stirred for 10 h and the temperature to rise

### 3. Tetraphenylethylene-based macrocycles with adjustable CPL

gradually to room temperature. Then the reaction was quenched with  $\text{NH}_4\text{Cl}$  aq. The mixture was extracted with DCM. The organic layer was collected and dry over anhydrous  $\text{Na}_2\text{SO}_4$ . The solvent was evaporated and crude product was obtained as yellow oil. The crude product (2.0 g, 3.94 mmol) was dissolved in toluene, then 2 equiv *p*-toluene sulfonic acid was added, and the mixture was refluxed overnight at  $110^\circ\text{C}$  under argon. After cooling to room temperature, the mixture was concentrated and the crude product was purified by column chromatography and pentane as eluent to obtain the product as a white solid (1.43 g, yield 73.9%).

$^1\text{H}$  NMR (600 MHz,  $\text{CDCl}_3$ ):  $\delta$  7.23 (d,  $J$  = 8.6 Hz, 4H), 7.15 – 7.11 (m, 6H), 7.00 (dd,  $J$  = 6.6, 3.0 Hz, 4H), 6.87 (d,  $J$  = 8.5 Hz, 4H).

$^{13}\text{C}$  NMR (151 MHz,  $\text{CDCl}_3$ ):  $\delta$  143.02, 142.18, 138.36, 132.94, 131.14, 131.00, 127.92, 126.89, 120.71.

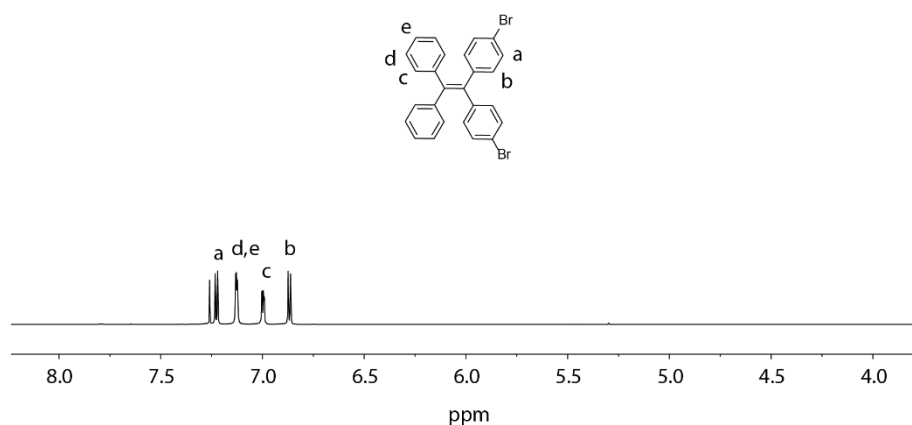


Figure 3.32:  $^1\text{H}$  NMR spectrum of compound **2Br-TPE** (600 MHz, 298 K,  $\text{CDCl}_3$ ).

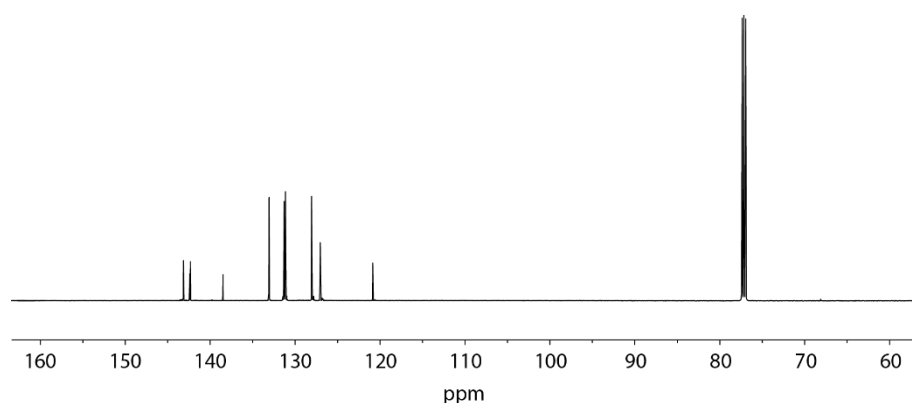


Figure 3.33:  $^{13}\text{C}$  NMR spectrum of compound **2** (151 MHz, 298 K,  $\text{CDCl}_3$ ).

### 3. Tetraphenylethylene-based macrocycles with adjustable CPL

#### Synthesis of **L**:

**2Br-TPE** (283 mg, 0.58 mmol, 1.0 equiv.), pinacol ester **1** (360 mg, 1.44 mmol, 2.5 equiv.), Pd(PPh<sub>3</sub>)<sub>4</sub> (66.7 mg, 0.058 mmol, 10 mol%) and K<sub>3</sub>PO<sub>4</sub> (440 mg, 2.08 mmol, 3.6 equiv.) were mixed in mixture solvents of a 1,4-dioxane: H<sub>2</sub>O = 4:1 (20 mL). The mixture was degassed (via freeze-thaw cycles) and then heated to 95 °C under N<sub>2</sub> atmosphere for 48 h. After cooling to room temperature, the solvents were removed under vacuum. Aqueous HCl (2 M, 50 mL) was added and the mixture extracted with CHCl<sub>3</sub> (3 × 30 mL), organic phases combined and dried over Na<sub>2</sub>SO<sub>4</sub>. The solvent was removed under reduced pressure. The crude product was purified by column chromatography (CHCl<sub>3</sub>: Pentane = 2:1) to provide the product as a bright yellow solid (212 mg, yield 64%).

<sup>1</sup>H NMR (600 MHz, DMSO-d<sub>6</sub>): δ 10.83 (s, 2H), 10.25 (s, 2H), 7.71 (d, J = 8.2 Hz, 2H), 7.52 (d, J = 8.5 Hz, 4H), 7.24 (dd, J = 8.1, 1.4 Hz, 2H), 7.20–7.12 (m, 12H), 7.05 (dd, J = 8.2, 1.3 Hz, 4H).

<sup>13</sup>C NMR (151 MHz, DMSO-d<sub>6</sub>): δ 191.26, 161.00, 146.99, 143.58, 142.96, 141.75, 139.24, 136.60, 131.55, 130.68, 129.99, 127.99, 126.88, 126.37, 121.23, 117.89, 114.58.

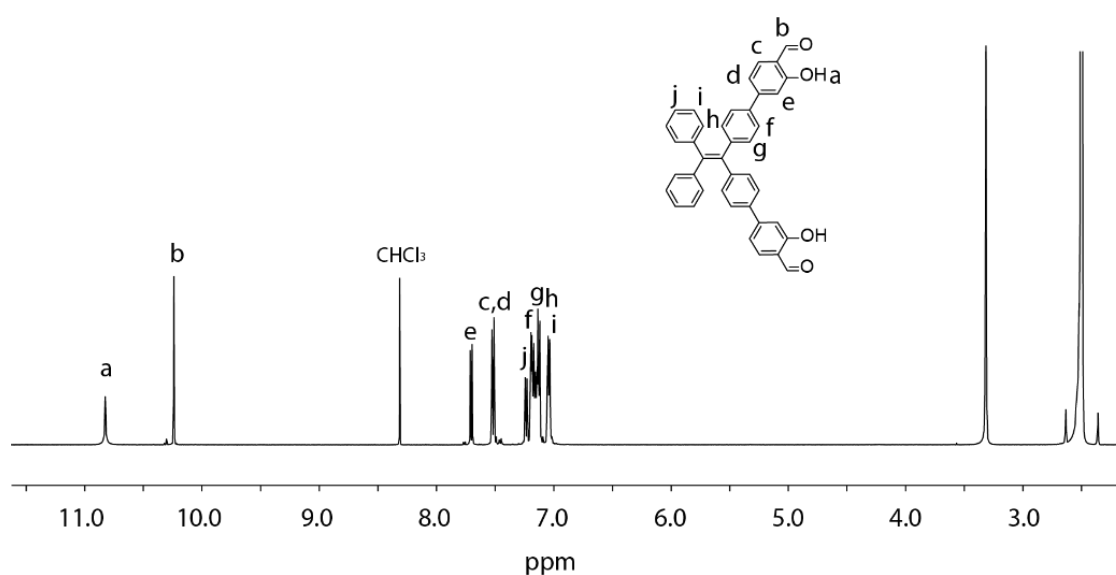


Figure 3.34: <sup>1</sup>H NMR spectrum of **L** (600 MHz, 298 K, DMSO-d<sub>6</sub>).

### 3. Tetraphenylethylene-based macrocycles with adjustable CPL

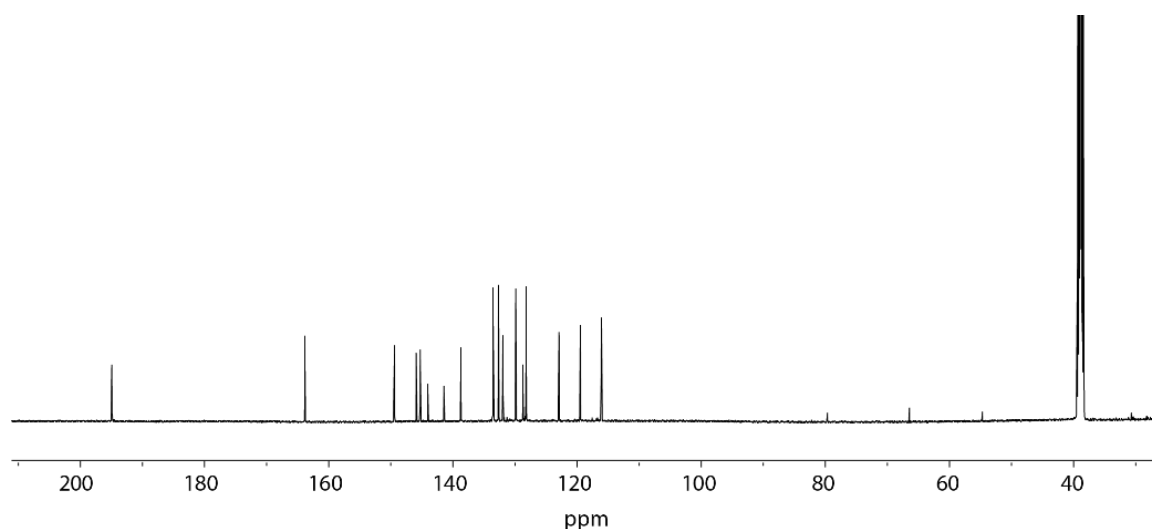


Figure 3.35:  $^{13}\text{C}$  NMR spectrum of **L** (151 MHz, 298 K,  $\text{DMSO-}d_6$ ).

#### Synthesis of **s-R**:

Ligand **L** (11.8 mg, 0.021 mmol, 1.0 equiv.) and (1*S*,2*S*)-(-)-1,2-diphenyl-1,2-ethanediamine (5.25 mg, 0.025 mmol, 1.2 equiv.) were dissolved in 2 mL DCM: MeOH=1:1. After addition of  $\text{CH}_3\text{COOH}$  (20  $\mu\text{L}$ ), the solution was stirred at room temperature for 10 h. Then, the solvent was removed under reduced pressure. The residue was washed with anhydrous methanol ( $3 \times 1$  mL) and dried in vacuum to provide the product as yellow powder in quantitative yield.

**r-R** was synthesised following the same procedure by using (1*R*,2*R*)-(-)-1,2-diphenyl-1,2-ethanediamine.

$^1\text{H}$  NMR (600 MHz,  $\text{CDCl}_3$ ):  $\delta$ 13.31 (s, 4H), 8.34 (s, 4H), 7.32 (d,  $J = 8.4$  Hz, 8H), 7.21–7.17 (m, 20H), 7.14–7.09 (m, 20H), 7.07–7.05 (m, 16H), 6.99 (dd,  $J = 8.0, 1.7$  Hz, 4H), 4.68 (s, 4H).

$^{13}\text{C}$  NMR (151 MHz,  $\text{CDCl}_3$ ):  $\delta$ 166.14, 161.41, 145.08, 143.93, 141.92, 140.21, 139.66, 138.14, 132.35, 132.20, 131.67, 128.76, 128.25, 128.13, 127.97, 126.97, 126.69, 117.86, 117.79, 80.73, 30.06.

HR ESI-MS: Calculated for  $\text{C}_{108}\text{H}_{80}\text{N}_4\text{O}_4$ ,  $m/z$  1498.6285  $[\text{M} + \text{H}]^+$ ,

found: 1498.6285

### 3. Tetraphenylethylene-based macrocycles with adjustable CPL

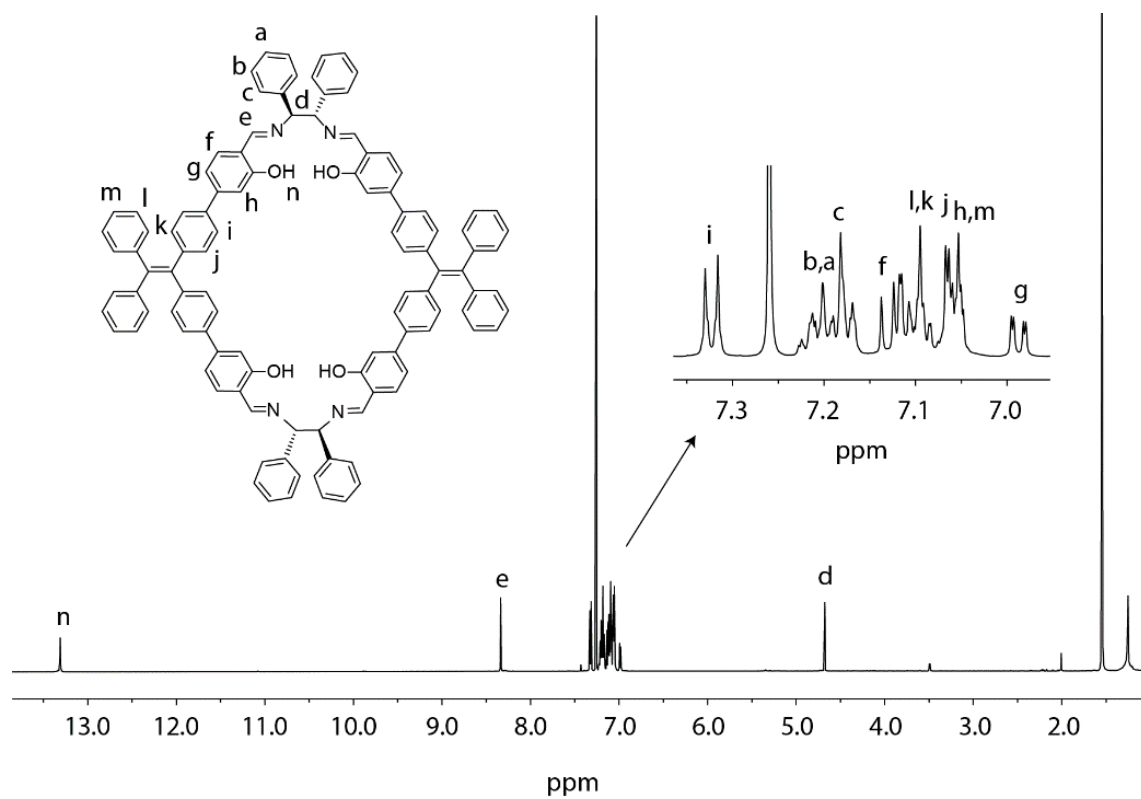


Figure 3.36: <sup>1</sup>H NMR spectrum of **R** (600 MHz, 298 K, CDCl<sub>3</sub>).

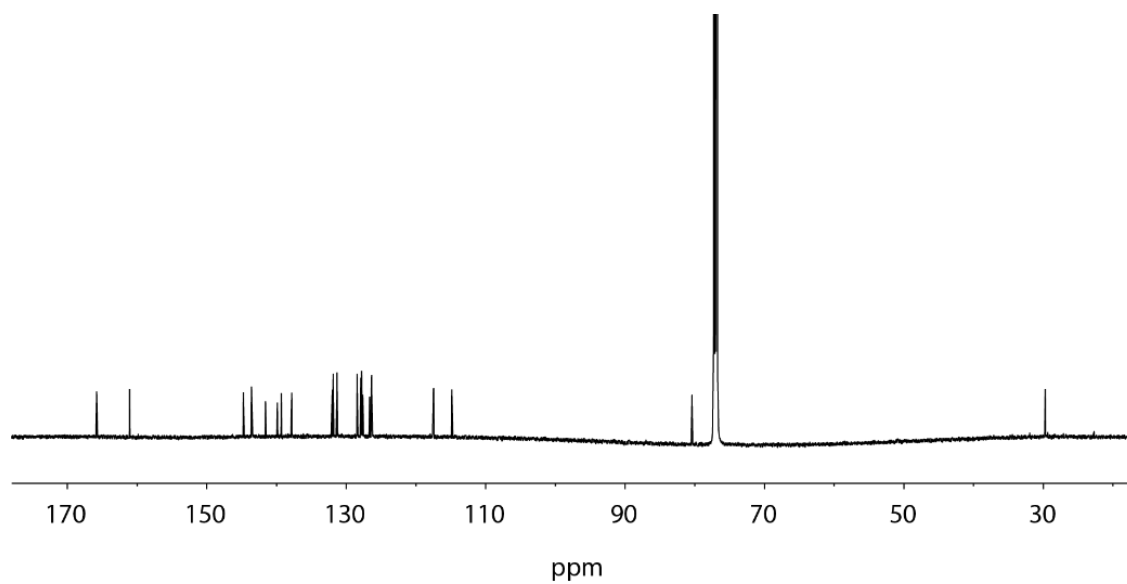


Figure 3.37: <sup>13</sup>C NMR spectrum of **R** (151 MHz, 298 K, CDCl<sub>3</sub>).

### 3. Tetraphenylethylene-based macrocycles with adjustable CPL

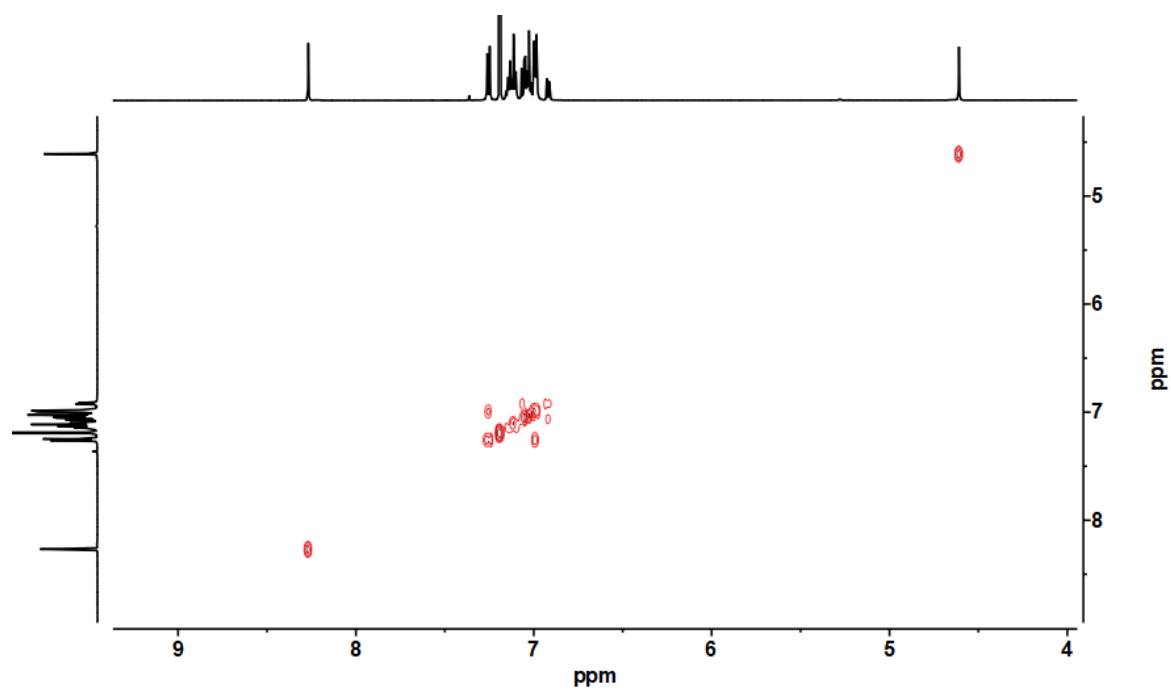


Figure 3.38:  $^1\text{H}$ - $^1\text{H}$  COSY spectrum of **R** (600 MHz, 298 K,  $\text{CDCl}_3$ ).

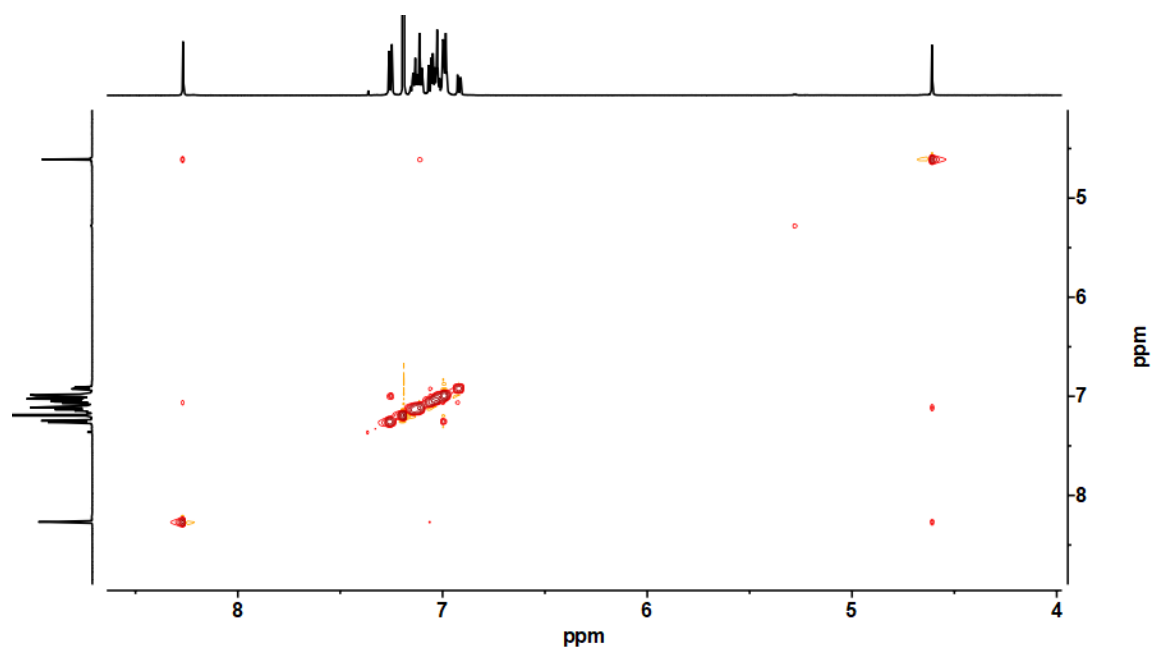


Figure 3.39:  $^1\text{H}$ - $^1\text{H}$  NOESY spectrum of **R** (600 MHz, 298 K,  $\text{CDCl}_3$ ).



### 3. Tetraphenylethylene-based macrocycles with adjustable CPL

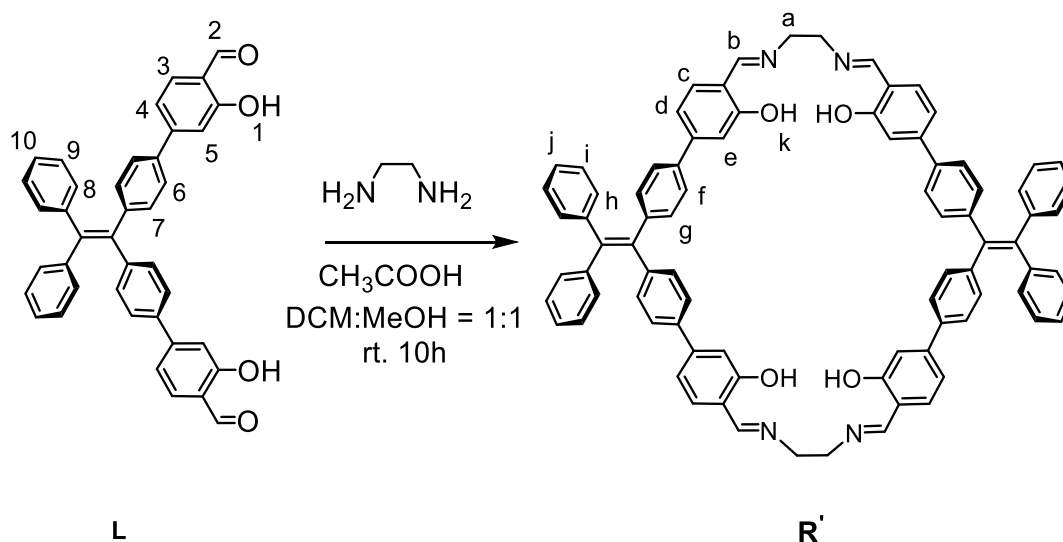


Figure 3.40: Synthesis route of **R'**

#### Synthesis of **R'**:

Ligand **L** (10 mg, 0.017 mmol, 1.0 equiv.) and ethanediamine (1.26 mg, 0.021 mmol, 1.2 equiv.) were dissolved in 2ml DCM: MeOH=1:1. Then the solution was stirred at room temperature for 10h. Then, the precipitate was collected by centrifugation and washed with anhydrous methanol ( $3 \times 1$  mL). The product was dried in vacuum to provide the product as yellow powder in quantitative yield.

$^1\text{H}$  NMR (500 MHz,  $\text{CDCl}_3$ ):  $\delta$  13.15 (s, 4H), 8.29 (s, 4H), 7.33 (d,  $J = 8.3$  Hz, 8H), 7.19 (d,  $J = 8.0$  Hz, 4H), 7.13 – 7.09 (m, 16H), 7.09 – 7.06 (m, 8H), 7.06 – 7.04 (d, 8H), 7.02 (dd,  $J = 8.0, 1.7$  Hz, 4H), 3.98 (s, 8H).

### 3. Tetraphenylethylene-based macrocycles with adjustable CPL

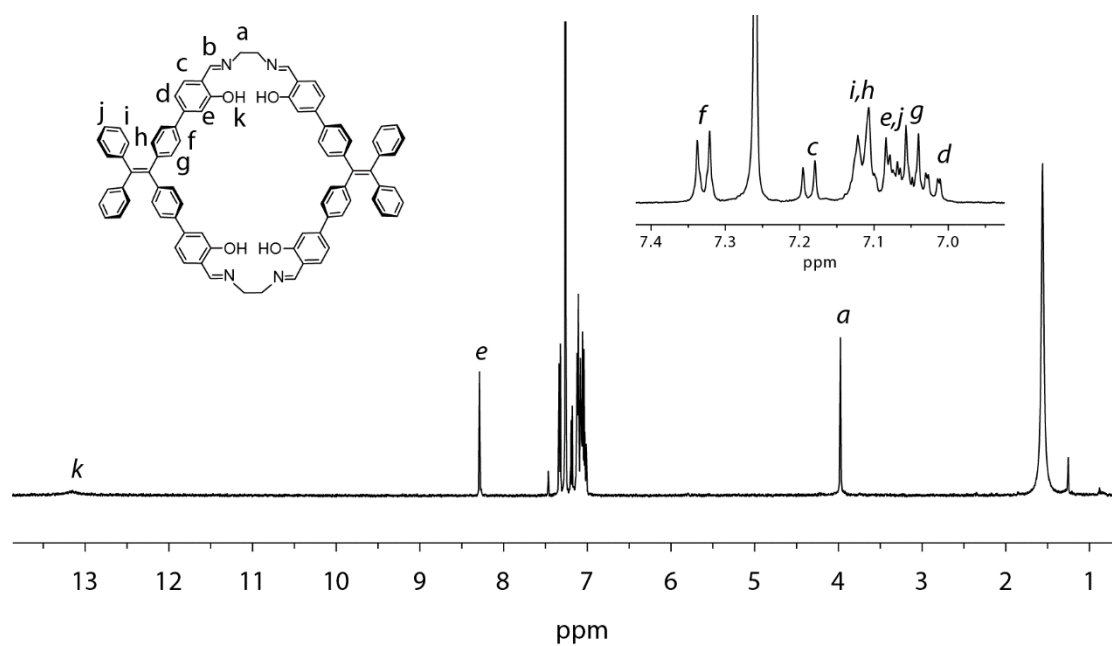


Figure 3.41:  $^1\text{H}$  NMR spectrum of **R'** (500 MHz, 298 K,  $\text{CDCl}_3$ ).

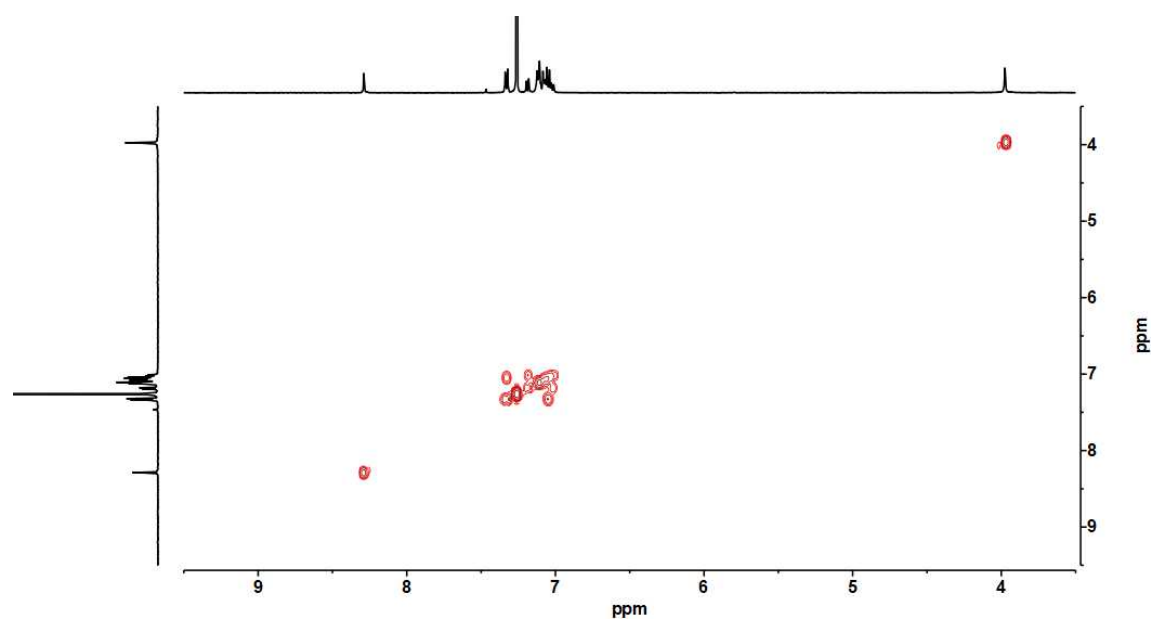


Figure 3.42:  $^1\text{H}$ - $^1\text{H}$  COSY spectrum of **R** (500 MHz, 298 K,  $\text{CDCl}_3$ ).

### 3. Tetraphenylethylene-based macrocycles with adjustable CPL

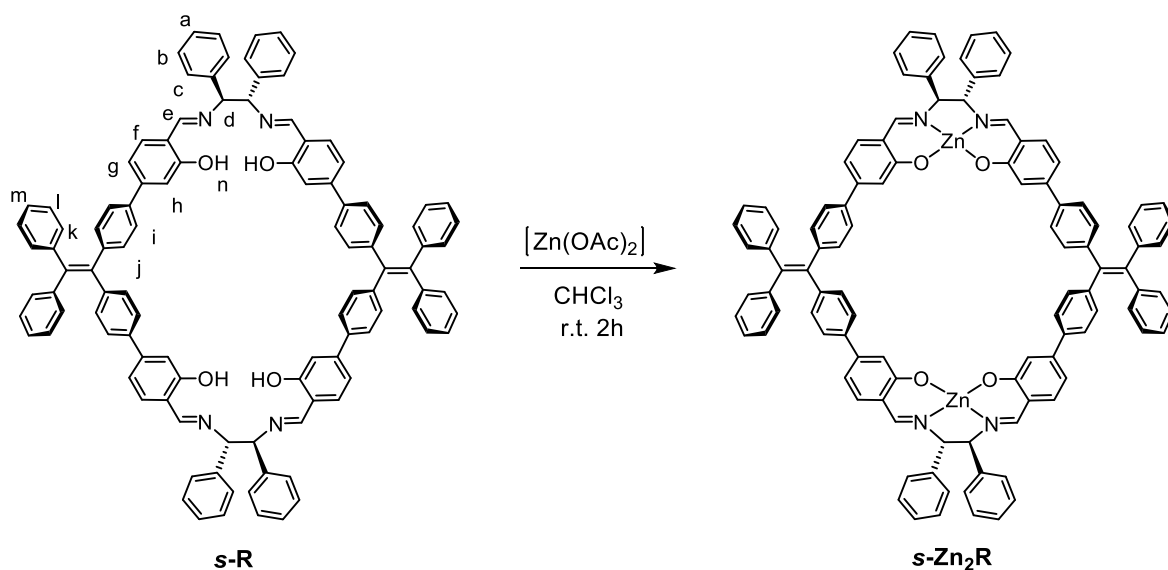


Figure 3.43: Self-assembly of **s-Zn<sub>2</sub>R**

**R** (1 equiv.) was dissolved in  $\text{CHCl}_3$ , stock solution of  $[\text{Zn}(\text{OAc})_2]$  (20 mg/mL, 2 equiv.) in DMSO was added and stir at room temperature for 2 h. After the reaction, solvents were removed and the crude product was dissolved in a minimal amount of DCM and precipitated with  $\text{Et}_2\text{O}$  to give the product (90% yield) as yellow solid.

$^1\text{H}$  NMR: (600 MHz,  $\text{DMSO}-d_6$ )  $\delta$  8.25 (s, 4H), 7.44 –7.41 (m, 8H), 7.40 (d,  $J = 8.3$  Hz, 8H), 7.36 (t,  $J = 7.7$  Hz, 8H), 7.29 –7.26 (m, 4H), 7.21 (dd,  $J = 8.0, 6.4$  Hz, 8H), 7.19 –7.15 (m, 4H), 7.08 –7.04 (m, 20H), 6.81 (d,  $J = 1.7$  Hz, 4H), 6.55 (dd,  $J = 8.0, 1.8$  Hz, 4H), 5.11 (s, 4H).

$^{13}\text{C}$  NMR: (176 MHz,  $\text{DMSO}-d_6$ )  $\delta$  171.24, 169.27, 144.80, 143.51, 142.81, 141.23, 140.73, 139.34, 138.77, 135.56, 131.74, 130.84, 128.53, 128.05, 127.74, 127.51, 126.83, 126.26, 120.83, 118.50, 111.38, 72.40.

### 3. Tetraphenylethylene-based macrocycles with adjustable CPL

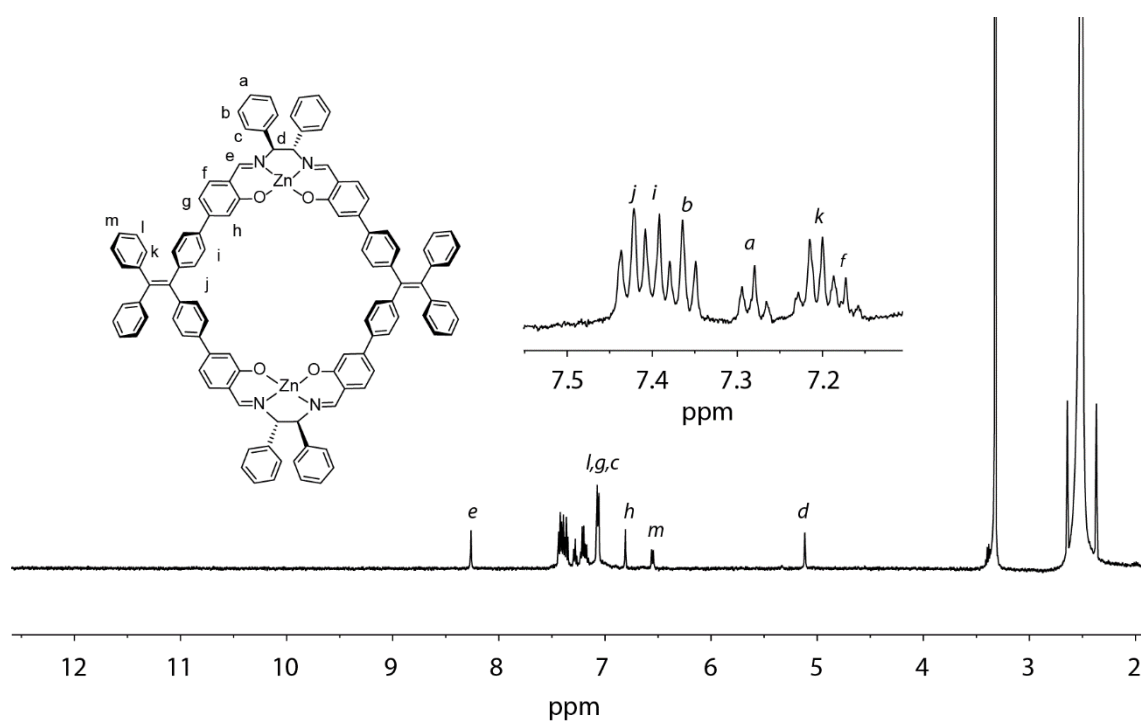


Figure 3.44:  $^1\text{H}$  NMR spectrum of  $\text{Zn}_2\text{R}$  (500 MHz, 298 K,  $\text{DMSO-}d_6$ ).

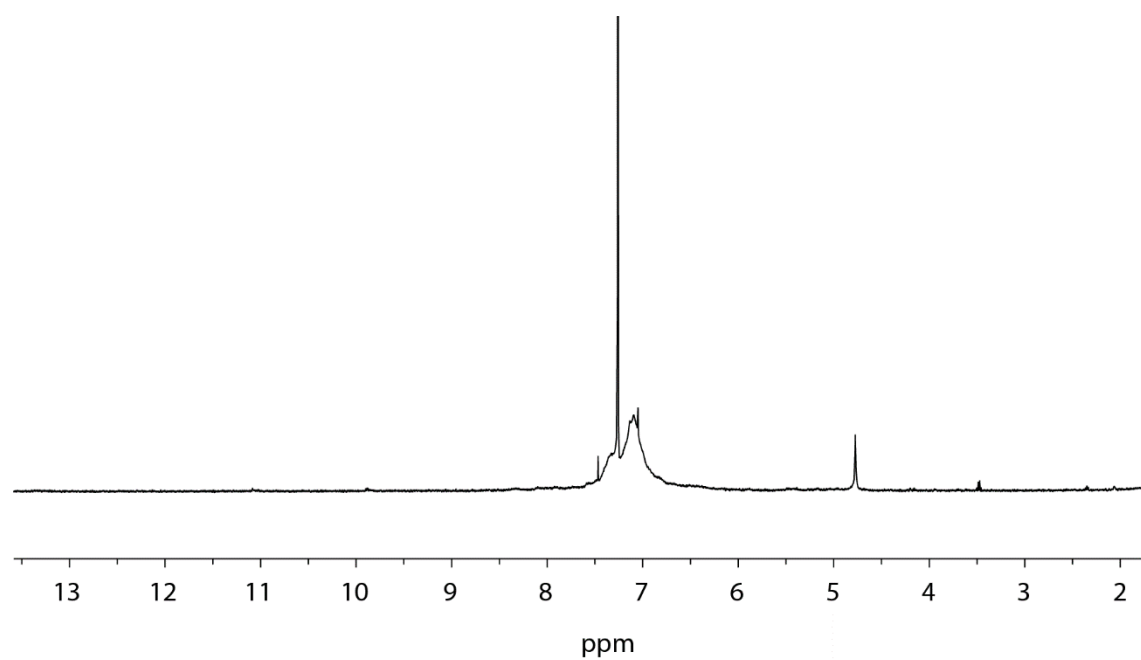


Figure 3.45:  $^1\text{H}$  NMR spectrum of  $\text{Zn}_2\text{R}$  (500 MHz, 298 K,  $\text{CDCl}_3$ ).

### 3. Tetraphenylethylene-based macrocycles with adjustable CPL

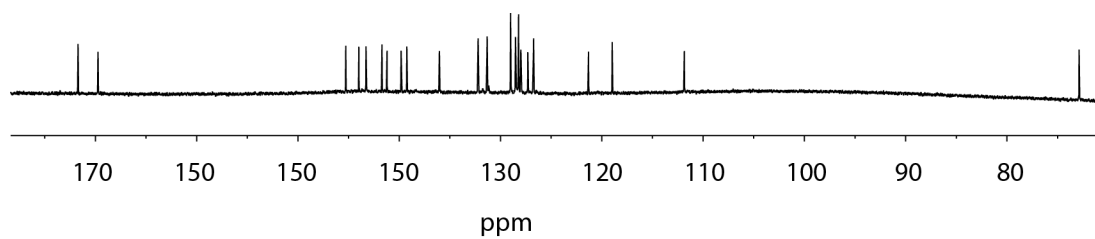


Figure 3.46:  $^{13}\text{C}$  NMR spectrum of  $\text{Zn}_2\text{R}$  (500 MHz, 298 K,  $\text{DMSO-}d_6$ ).

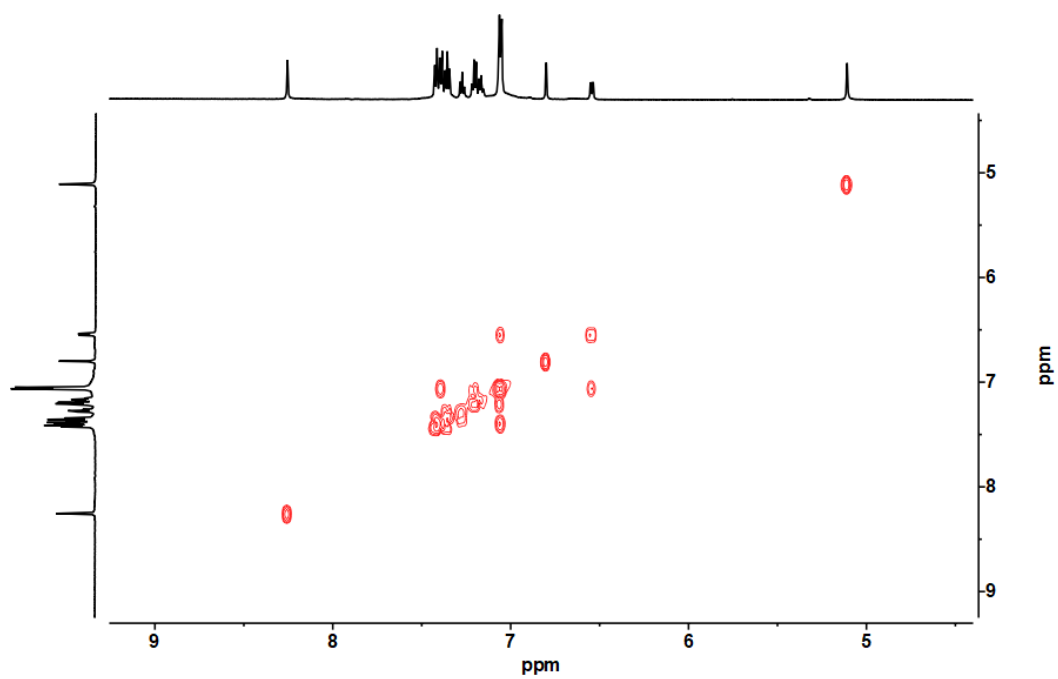


Figure 3.47:  $^1\text{H}$ - $^1\text{H}$  COSY spectrum of  $\text{Zn}_2\text{R}$  (500 MHz, 298 K,  $\text{DMSO-}d_6$ ).

### 3. Tetraphenylethylene-based macrocycles with adjustable CPL

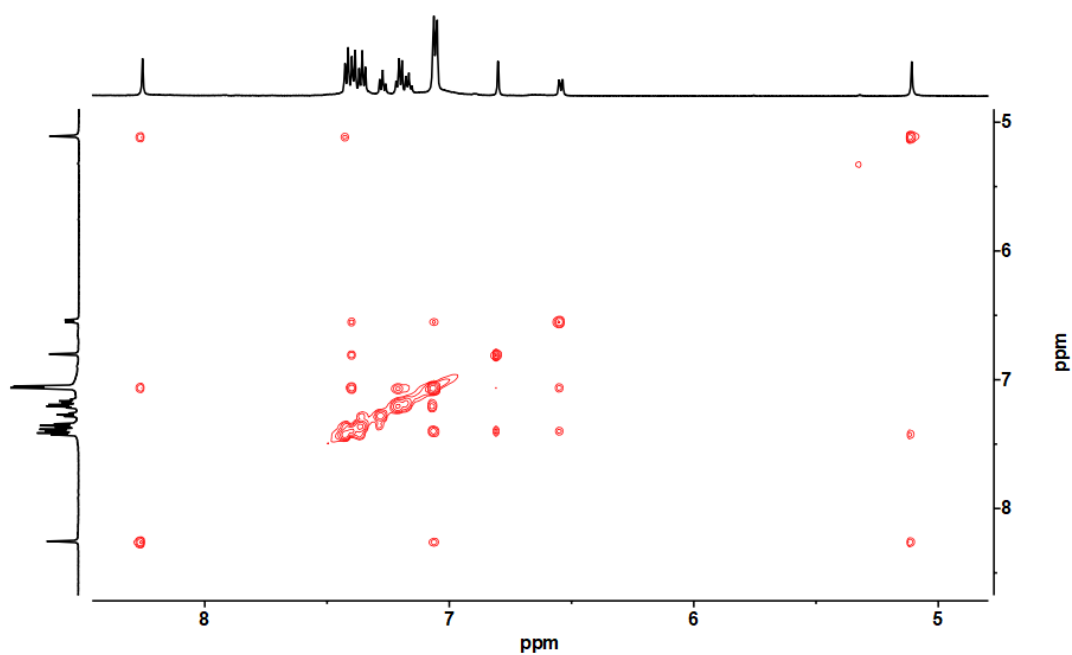


Figure 3.48: <sup>1</sup>H-<sup>1</sup>H NOESY spectrum of **Zn<sub>2</sub>R** (500 MHz, 298 K, DMSO-*d*<sub>6</sub>).

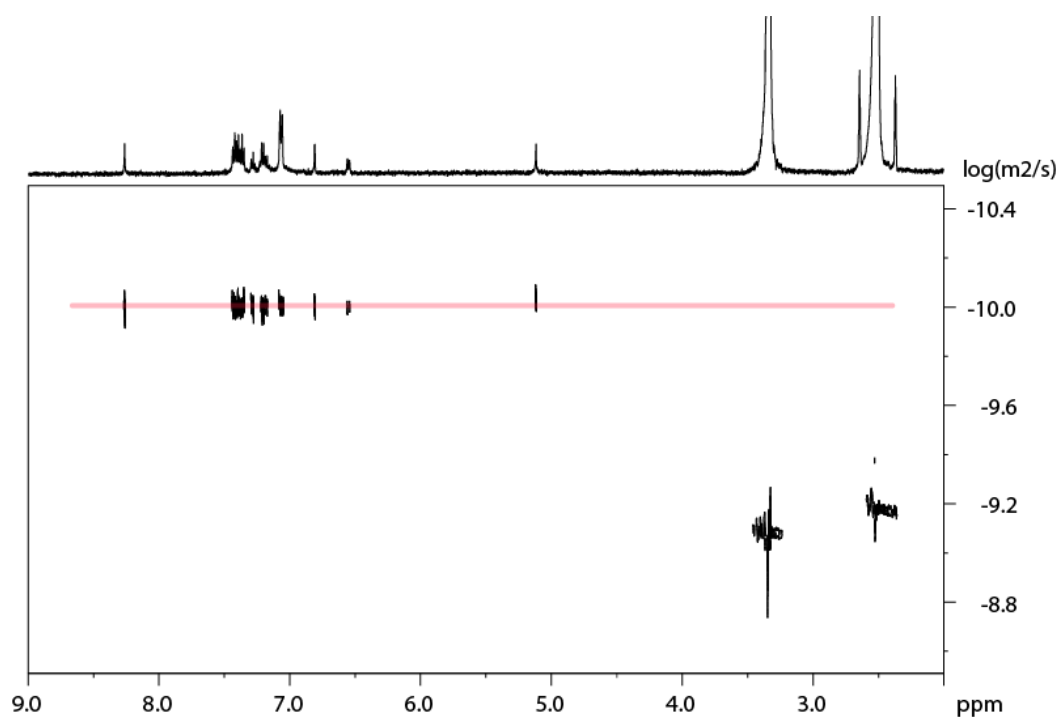


Figure 3.49: DOSY spectrum of **Zn<sub>2</sub>R** (600 MHz, 298 K, DMSO-*d*<sub>6</sub>). Diffusion coefficient:  $D = 9.54 \times 10^{-11} \text{ m}^2\text{s}^{-1}$ ,  $r = 11.47 \text{ \AA}$ .

### 3. Tetraphenylethylene-based macrocycles with adjustable CPL

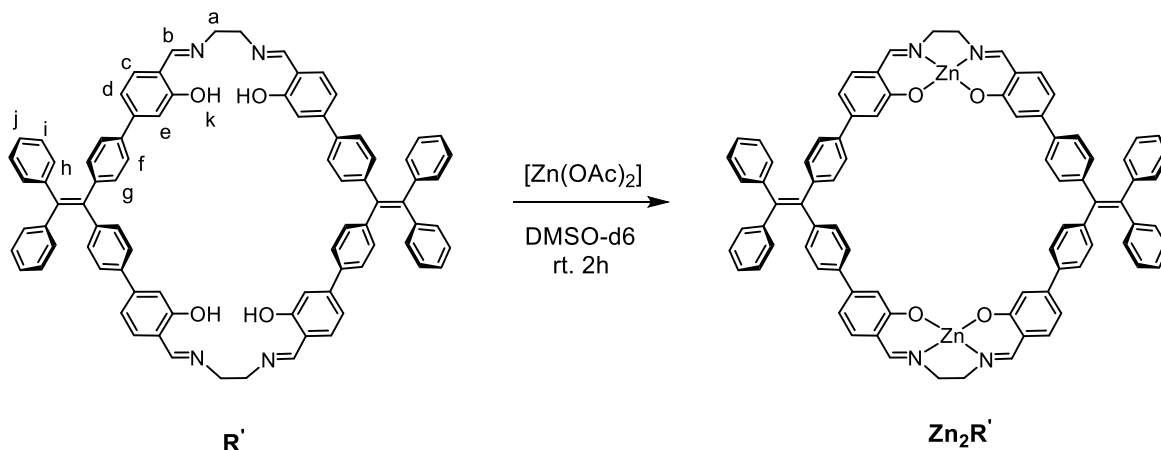


Figure 3.50: Self-assembly of  $Zn_2R'$ .

$R'$  (1 equiv.) was dissolved in  $CHCl_3$ , a stock solution of  $[Zn(OAc)_2]$  (20 mg/mL, 2 equiv.) in DMSO was added and stir at room temperature for 2 h. After the reaction, solvents were removed and the crude product was dissolved in a minimal amount of DCM and precipitated with  $Et_2O$  to give the product as yellow solid.

$^1H$  NMR (500 MHz,  $DMSO-d_6$ ):  $\delta$  8.47 (s, 4H), 7.41 (d,  $J = 8.2$  Hz, 4H), 7.21 (dd,  $J = 7.6, 4.1$  Hz, 12H), 7.09 (d,  $J = 1.8$  Hz, 4H), 7.08 – 7.05 (m, 16H), 6.79 (d,  $J = 1.8$  Hz, 4H), 6.61 (dd,  $J = 8.0, 1.8$  Hz, 4H), 3.76 (s, 8H).

$^{13}C$  NMR (151 MHz,  $DMSO-d_6$ ):  $\delta$  170.94, 167.58, 144.04, 143.58, 142.71, 140.64, 139.42, 138.78, 135.22, 131.75, 130.88, 128.05, 126.19, 120.71, 118.56, 111.10, 55.59.

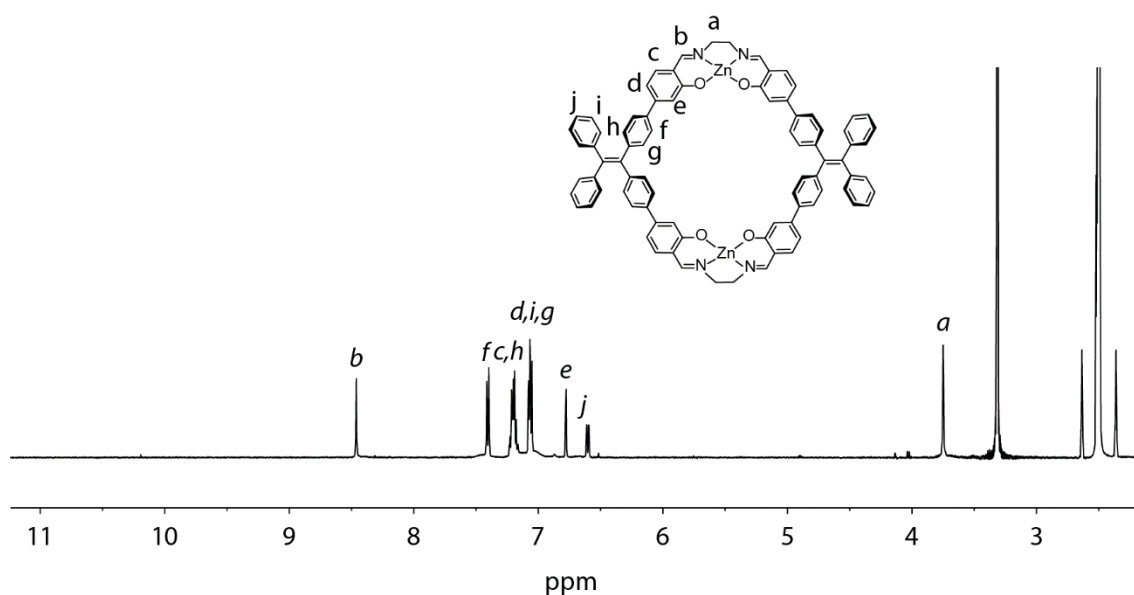


Figure 3.51:  $^1H$  NMR spectrum of  $Zn_2R'$  (600 MHz, 298 K,  $CDCl_3$ ).

### 3. Tetraphenylethylene-based macrocycles with adjustable CPL

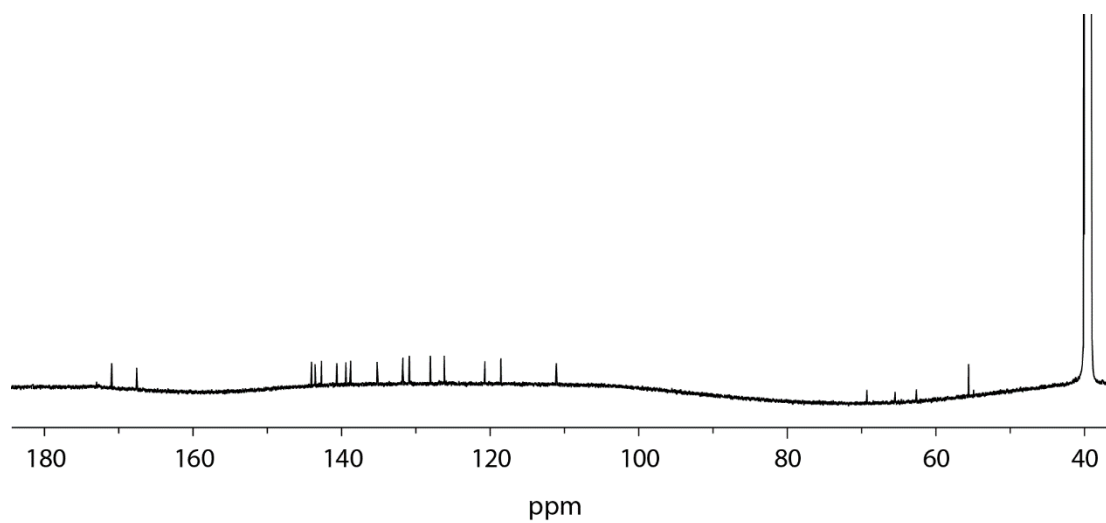


Figure 3.52:  $^{13}\text{C}$  NMR spectrum of  $\text{Zn}_2\mathbf{R}'$  (600 MHz, 298 K,  $\text{CDCl}_3$ ).

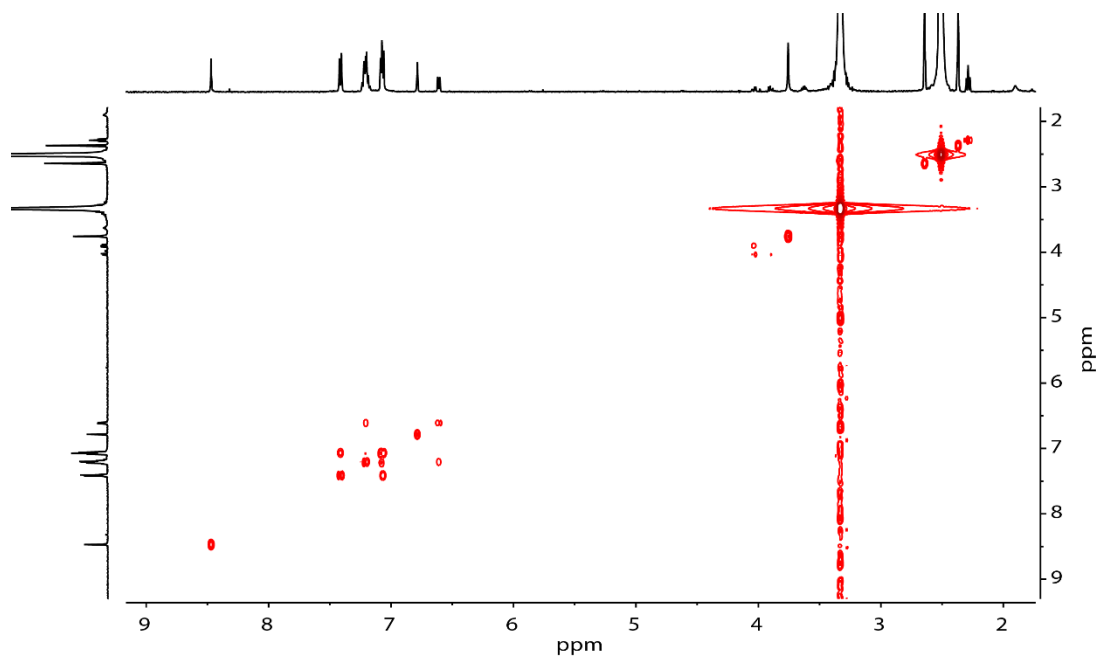


Figure 3.53:  $^1\text{H}$ - $^1\text{H}$  COSY spectrum of  $\mathbf{ZnR}'$  (600 MHz, 298 K,  $\text{DMSO-}d_6$ ).



### 3. Tetraphenylethylene-based macrocycles with adjustable CPL

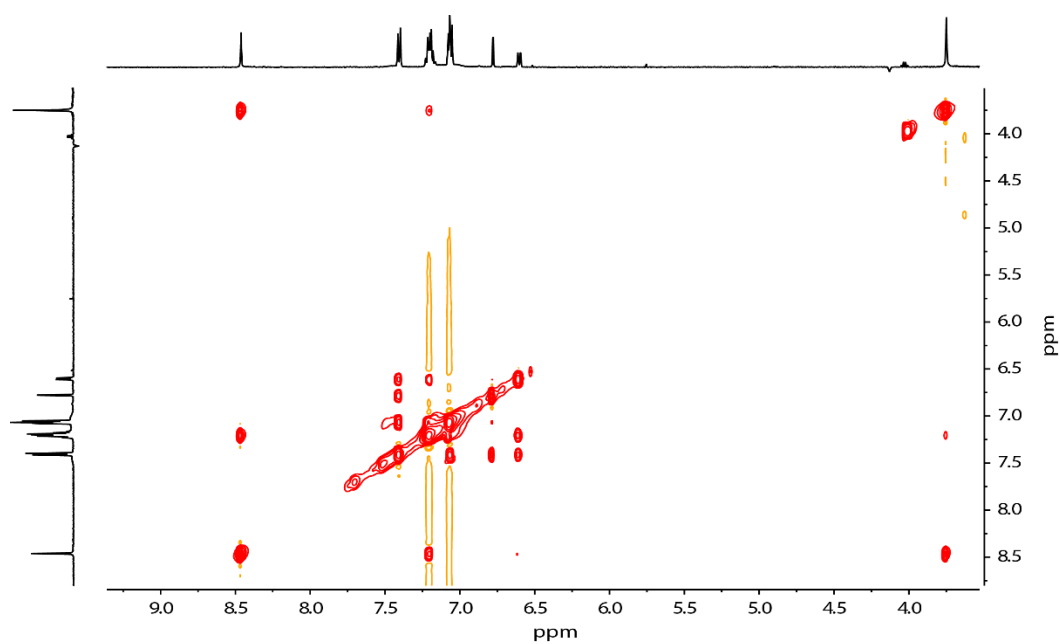


Figure 3.54: <sup>1</sup>H-<sup>1</sup>H NOESY spectrum of **ZnR'** (600 MHz, 298 K, DMSO-*d*<sub>6</sub>).

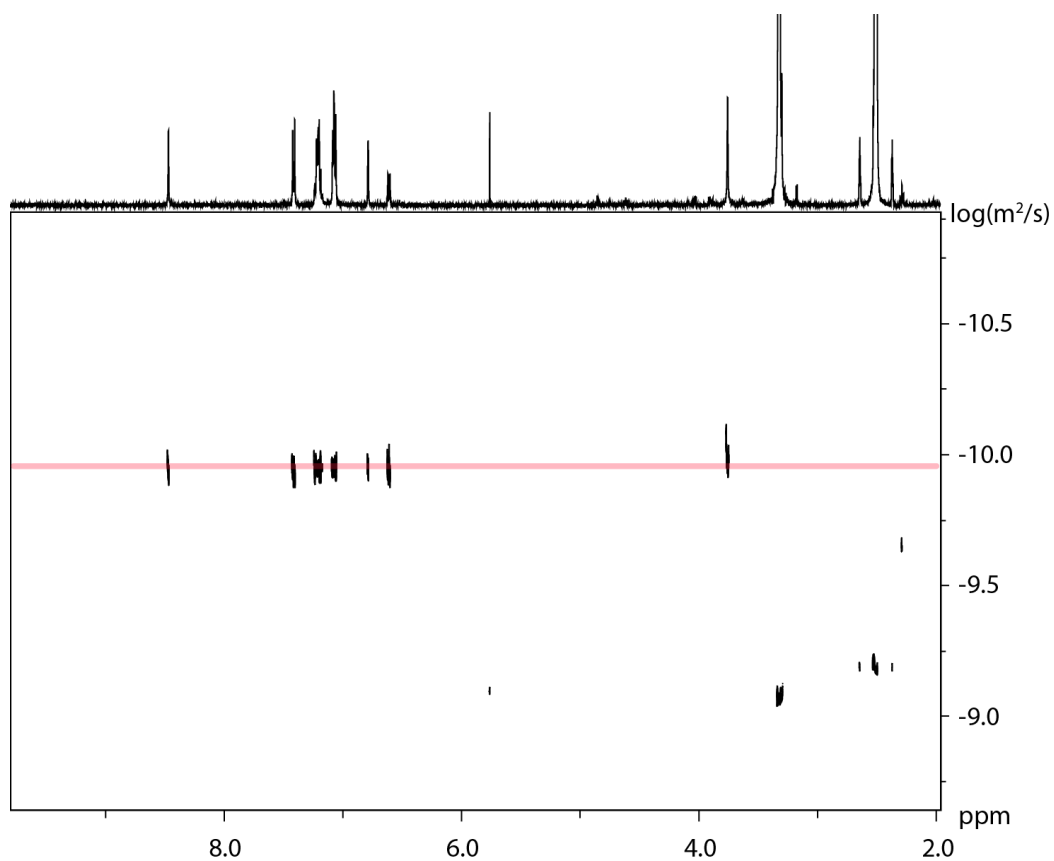


Figure 3.55: DOSY spectrum of **ZnR'** (600 MHz, 298 K, DMSO-*d*<sub>6</sub>). Diffusion coefficient:  $D = 1.11 \times 10^{-10} \text{ m}^2\text{s}^{-1}$ ,  $r = 9.84 \text{ \AA}$ .

### 3. Tetraphenylethylene-based macrocycles with adjustable CPL

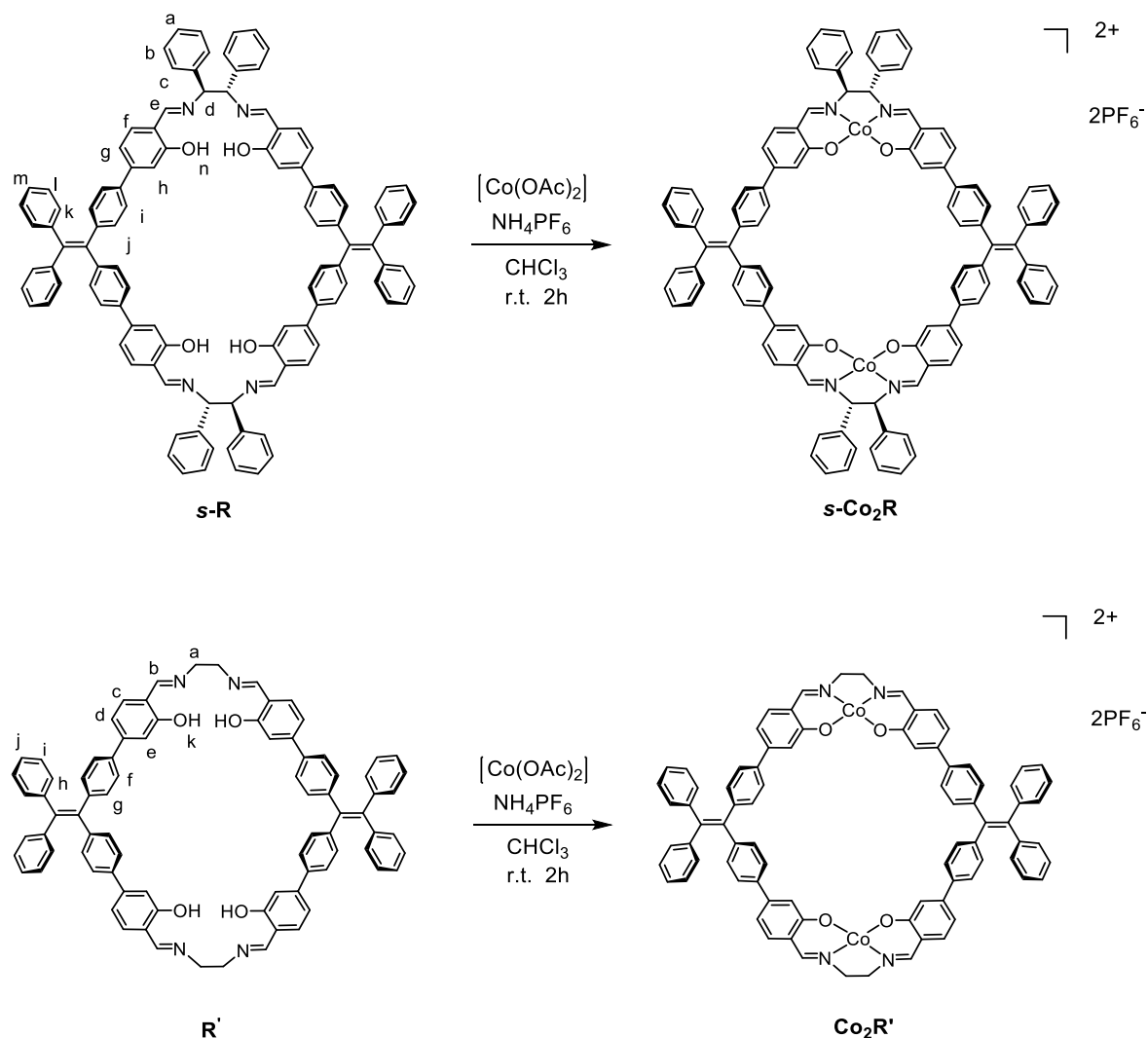


Figure 3.56: Self-assembly of  $\text{Co}(\text{III})_2\text{R}$  and  $\text{Co}(\text{III})_2\text{R}'$

**R** (1 equiv.) was dissolved in  $\text{CHCl}_3$ , a stock solution of  $[\text{Co}(\text{OAc})_2]$  (20 mg/mL, 2 equiv.) in DMSO was added and stirred at room temperature for 2 h. After stirring for 15 min under aerobic condition, the  $\text{NH}_4\text{PF}_6$  was added and stirred for 6 h at room temperature (Figure 3.56). After the reaction, solvents were removed and the crude product was dissolved in a minimal amount of DCM and precipitated with  $\text{Et}_2\text{O}$  to give the product as dark red solid.

### 3. Tetraphenylethylene-based macrocycles with adjustable CPL

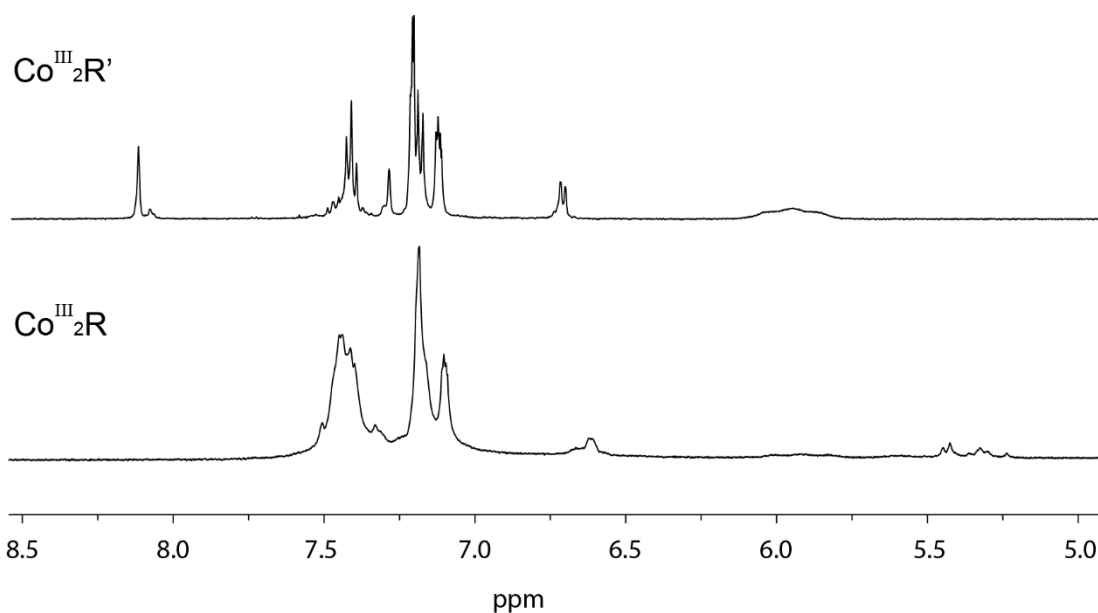


Figure 3.57:  $^1\text{H}$  NMR spectra of  $\text{Co(III)}_2\text{R}$  and  $\text{Co(III)}_2\text{R}'$  in  $\text{CD}_3\text{CN}$  (600 MHz, 298 K).

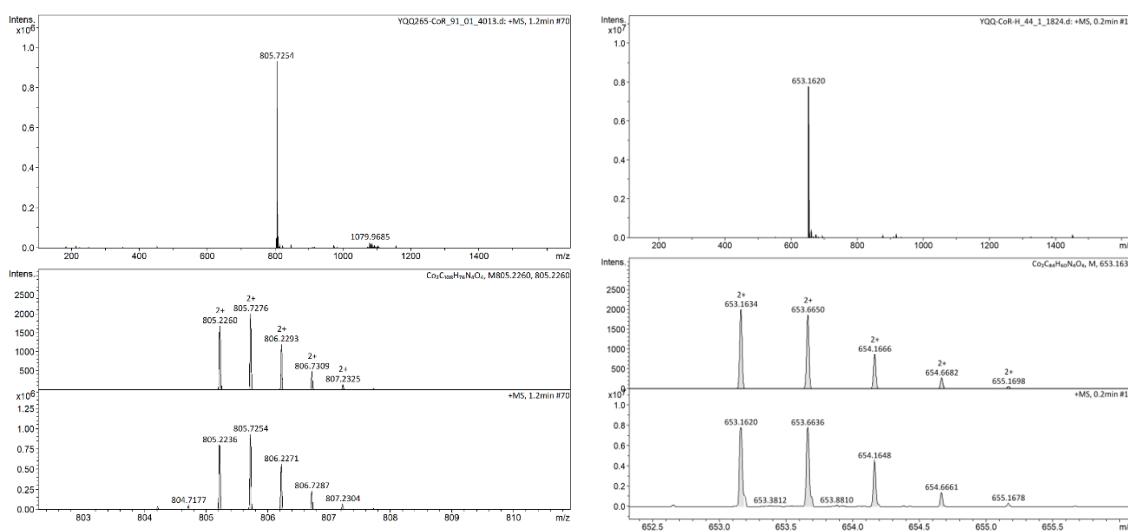


Figure 3.58: ESI-MS of  $\text{Co(III)}_2\text{R}$  and  $\text{Co(III)}_2\text{R}'$ .

#### 3.7.4 Crystallography information

The X-ray structures were measured by Dr. Jacopo Tessorolo and Dr. Julian Holstein, solved and preliminarily refined by Dr. Julian Holstein and Shota Hasegawa.

##### Crystal structure of $\text{R}'$

Colorless square shape single crystal of  $\text{R}'$  was obtained by slow evaporation of chloroform from NMR tubes. A single crystal in mother liquor was mounted onto a 0.2 mm nylon loop using NVH oil. Data were collected in-house on a Bruker D8

### 3. Tetraphenylethylene-based macrocycles with adjustable CPL

Venture diffractometer equipped with an INCOATEC micro focus sealed tube ( $I\mu\text{s}$  3.0) using  $\text{CuK}\alpha$  for radiation at 100 K. The resolution was cut off at 1.60 Å after which the signal to noise ratio has dropped below  $I/\sigma(I) < 2.0$ . The data was integrated with APEX3. The structures were solved by intrinsic phasing/direct methods using SHELXT<sup>[52]</sup> and refined with SHELXL (2018/2)<sup>[53]</sup> for full-matrix least-squares routines on  $F^2$  and ShelXle<sup>[54]</sup> as a graphical user interface. The SQUEEZE<sup>[55]</sup> method provided by the program PLATON<sup>[56]</sup> was used to improve the contrast of the electron density map the structure.

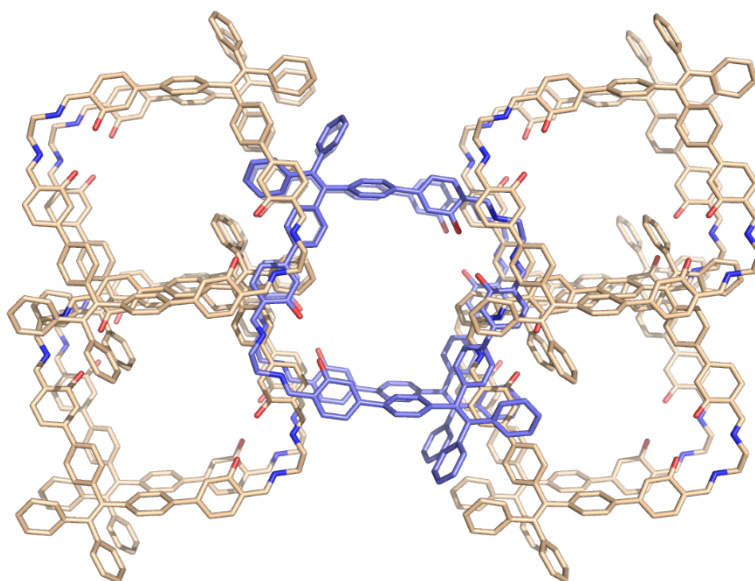


Figure 3.59: The packing structures of **R'** in top view (Solvent molecules and hydrogens are not shown for clarity).

#### Crystal structure of ***r*-Zn<sub>2</sub>R** and ***s*-Co(III)<sub>2</sub>R**

Colorless square-shaped single crystal of ***r*-Zn<sub>2</sub>R** and red block single crystal ***s*-Co(III)<sub>2</sub>R** were obtained by slow diffusion of diethyl ether into DMF solution. A single crystal in mother liquor was mounted onto a 0.2 mm nylon loop using NVH oil. Data were collected on macromolecular beamline PXI, Petra III, DESY, Hamburg. Therefore, a wavenumber of  $\lambda = 0.6888$  Å has been set on a nitrogen cooled double monochromator and the sample has been cooled to 80(2) K utilizing an Oxford Cryostream 800. The data were integrated and reduction with XDS.<sup>[57]</sup> The structures were solved by intrinsic phasing/direct methods using SHELXT<sup>[52]</sup> and refined with SHELXL (2018/2)<sup>[53]</sup> for full-matrix least-squares routines on  $F^2$  and ShelXle<sup>[54]</sup> as a graphical user interface. The SQUEEZE<sup>[55]</sup> method provided by the

### 3. Tetraphenylethylene-based macrocycles with adjustable CPL

program PLATON<sup>[56]</sup> was used to improve the contrast of the electron density map of the structure.

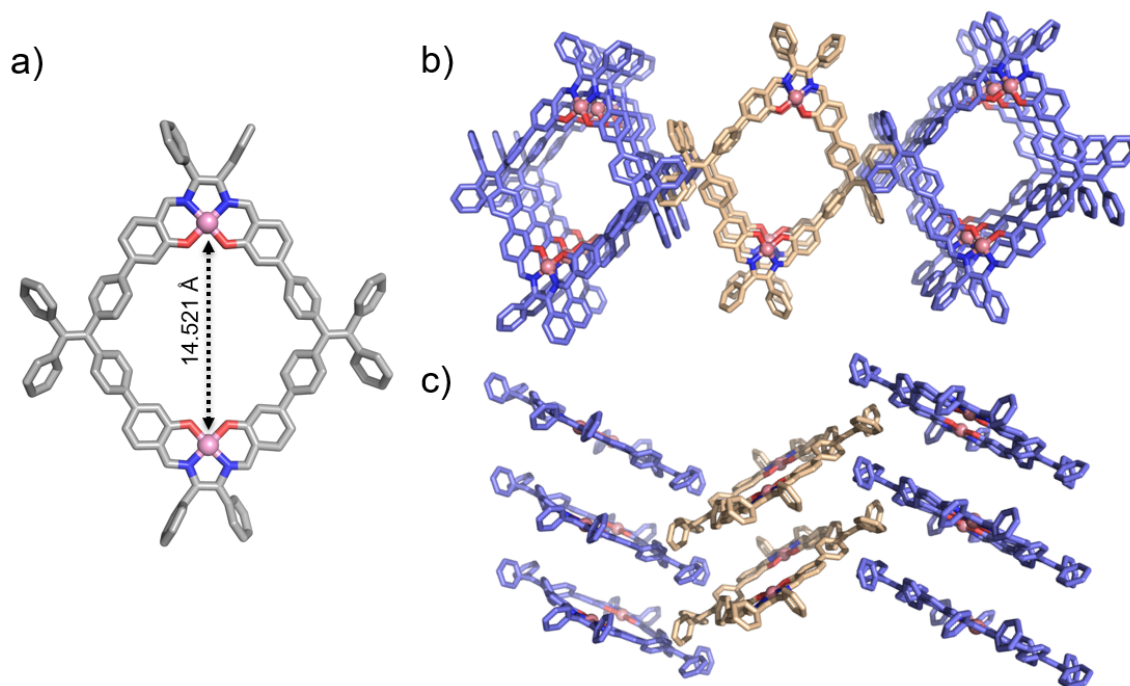


Figure 3.60: a) The preliminary single crystal X-ray structure and b) the packing structures of **s-Co(III)<sub>2</sub>R** in top and c) in side view (Solvent molecules and hydrogens are not shown for clarity).

#### 3.7.5 UV-vis spectra

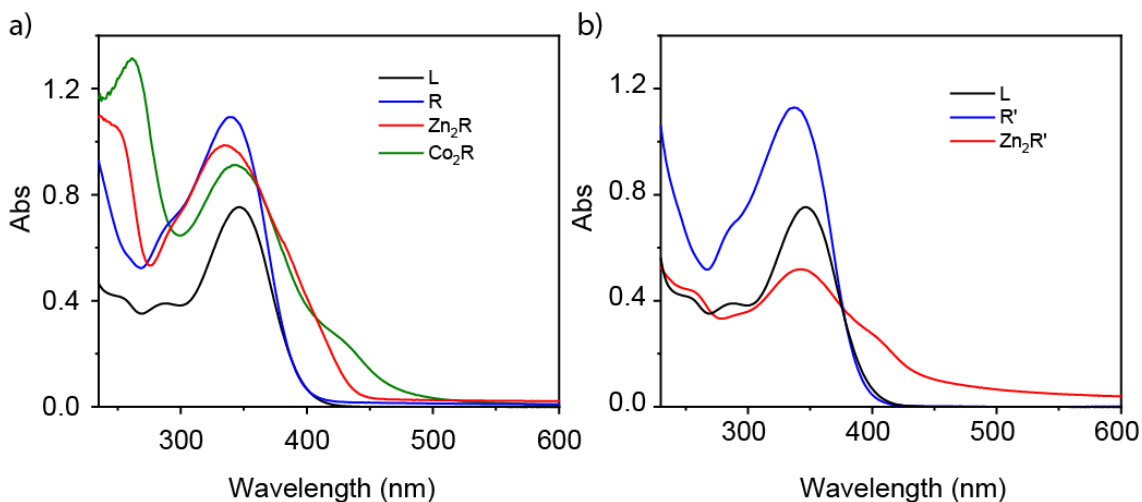


Figure 3.61: UV-Vis spectra of compounds performed in THF ( $c_L = 2 \times 10^{-5}$  M,  $c_R = 1 \times 10^{-5}$  M,  $c_{R'} = 1 \times 10^{-5}$  M,  $c_{Zn_2R} = 1 \times 10^{-5}$  M,  $c_{Zn_2R'} = 1 \times 10^{-5}$  M, cuvette path length: 1 cm).

AIE experiments were performed in the mixture solution of THF and water with different fraction of water.

### 3. Tetraphenylethylene-based macrocycles with adjustable CPL

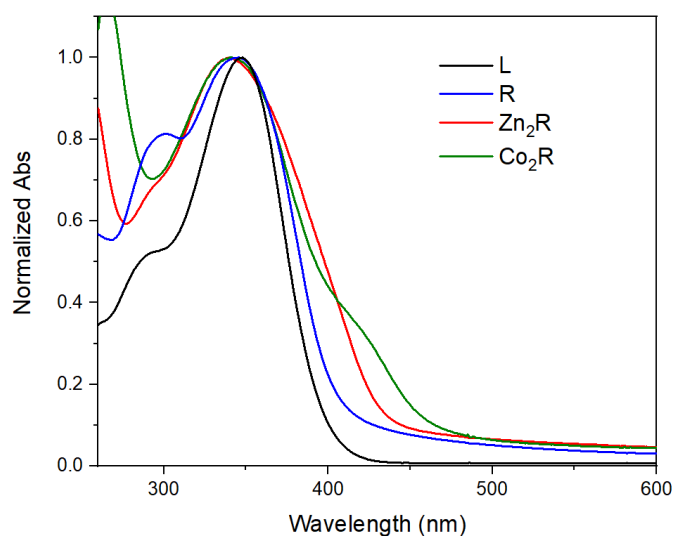


Figure 3.62: Normalized absorption spectra of compounds in THF:H<sub>2</sub>O = 50: 50.

Table 3.1. Absorption of compounds in THF

	L	R	R'	Zn <sub>2</sub> R	Co(III) <sub>2</sub> R	Zn <sub>2</sub> R'
$\lambda_{\max}/\text{nm}$	347	339	337	334	343	343
Abs	0.75297	1.09278	1.1296	0.9869	0.91231	0.51853
$\epsilon/(\text{M}^{-1}\text{cm}^{-1})$	75297	109278	112960	98690	91231	51853

#### 3.7.6 Fluorescence spectra

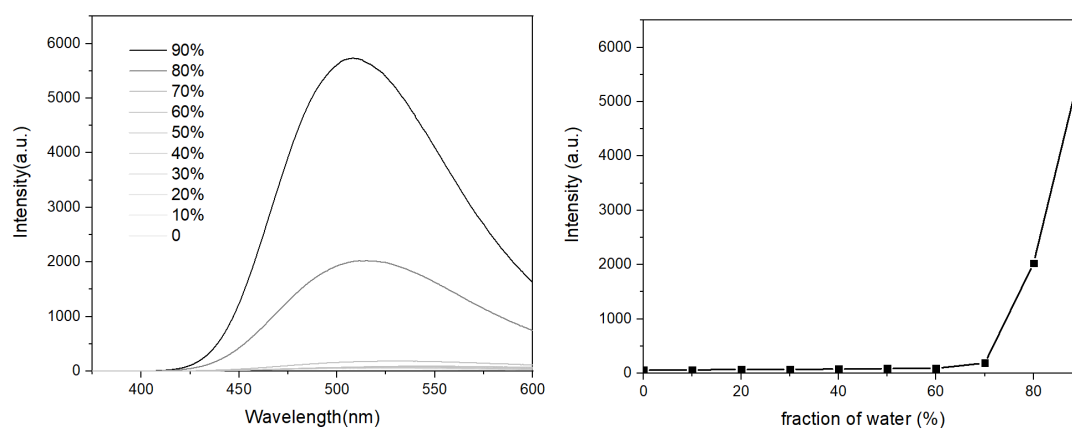


Figure 3.63: Emission spectra of **L** in mixture solution of THF and H<sub>2</sub>O with different content of water.

### 3. Tetraphenylethylene-based macrocycles with adjustable CPL

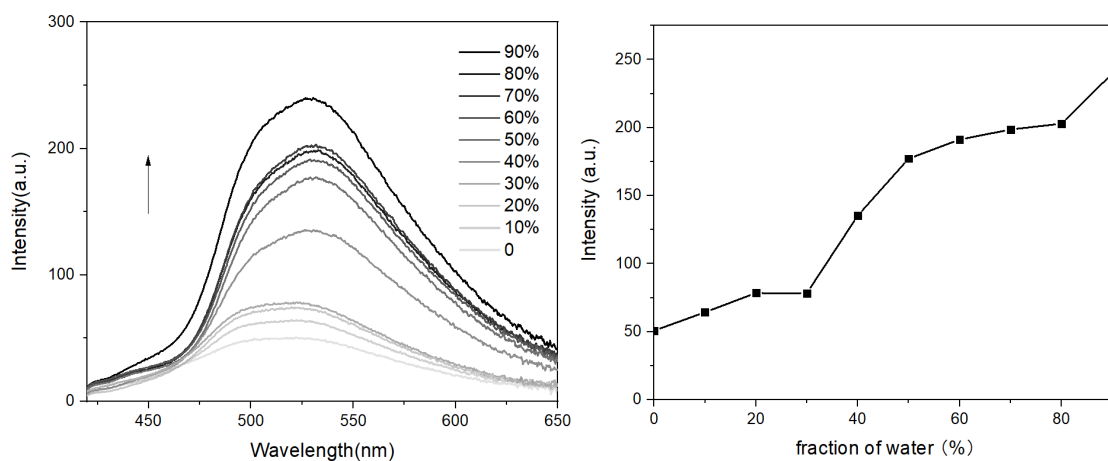


Figure 3.64: Emission spectra of **R** in mixture solution of THF and H<sub>2</sub>O with different content of water.

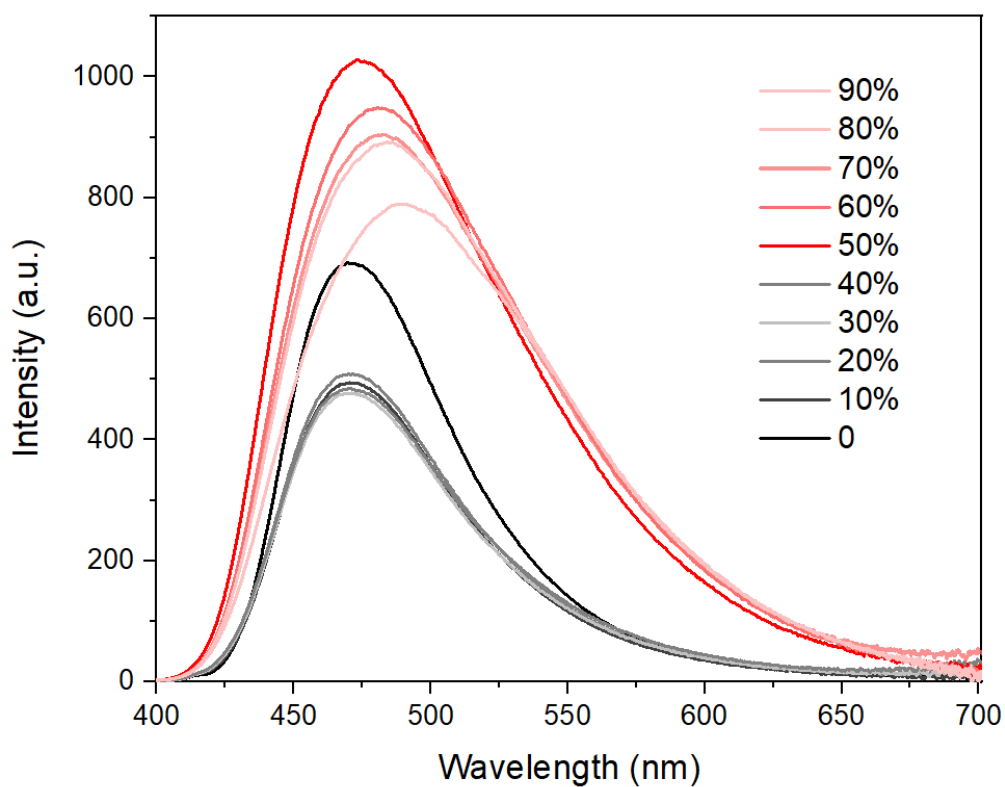


Figure 3.65: Emission spectra of **Zn<sub>2</sub>R** in mixture solution of THF and H<sub>2</sub>O with different content of water.

### 3. Tetraphenylethylene-based macrocycles with adjustable CPL

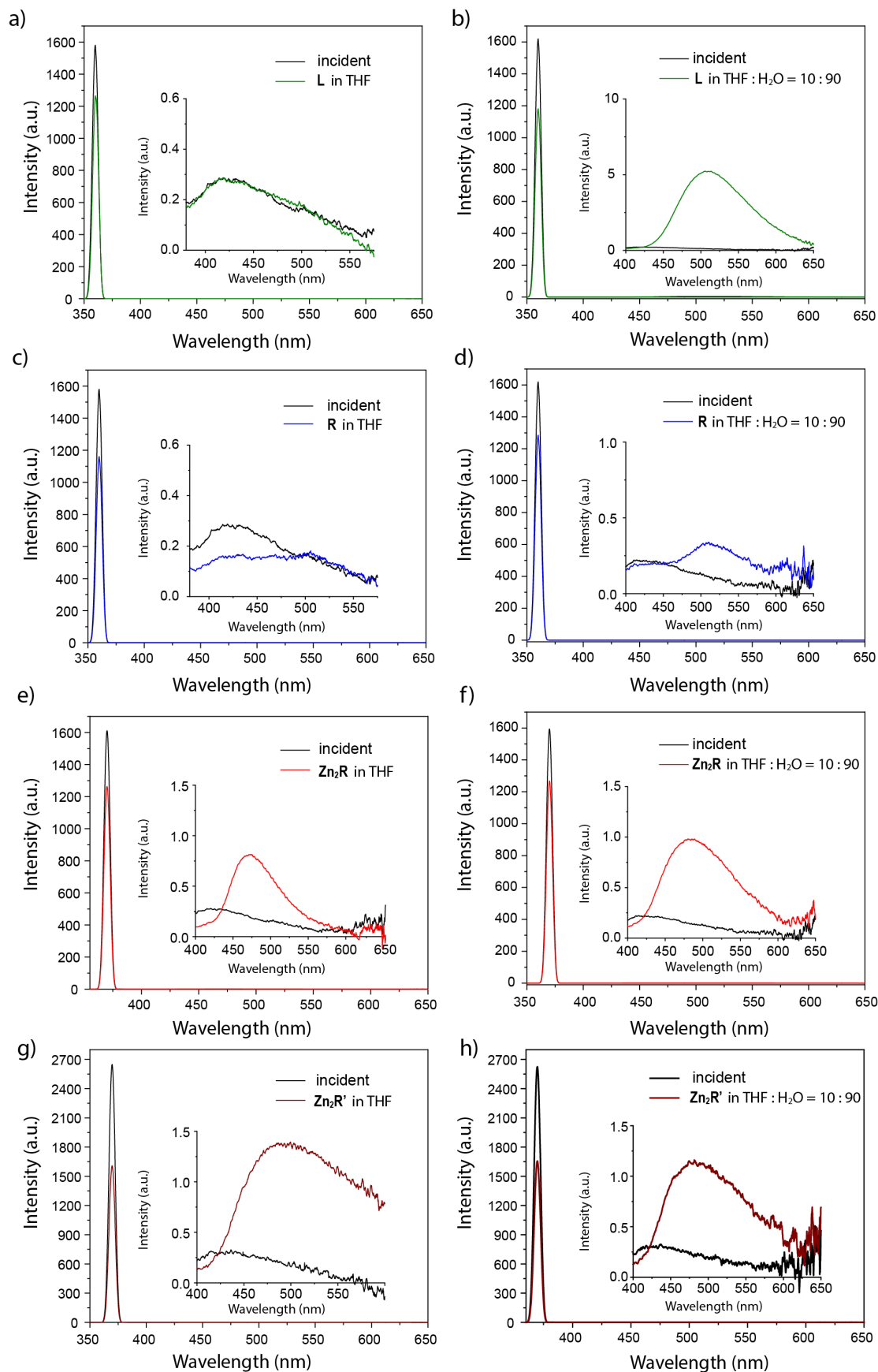


Figure 3.66: Quantum yield spectra of L, R,  $Zn_2R$  and  $Zn_2R'$  in THF and THF:H<sub>2</sub>O = 10 : 90, respectively.



### 3. Tetraphenylethylene-based macrocycles with adjustable CPL

Table 3.2 Luminescent quantum yield of compounds

	$\Phi_F$ (in THF)	$\Phi_F$ (in THF: H <sub>2</sub> O=10: 90)
<b>L</b>	1.86	21.23
<b>R</b>	1.11	2.70
<b>Zn<sub>2</sub>R</b>	3.51	6.02
<b>Zn<sub>2</sub>R'</b>	3.38	3.51

#### 3.7.7 CD spectra

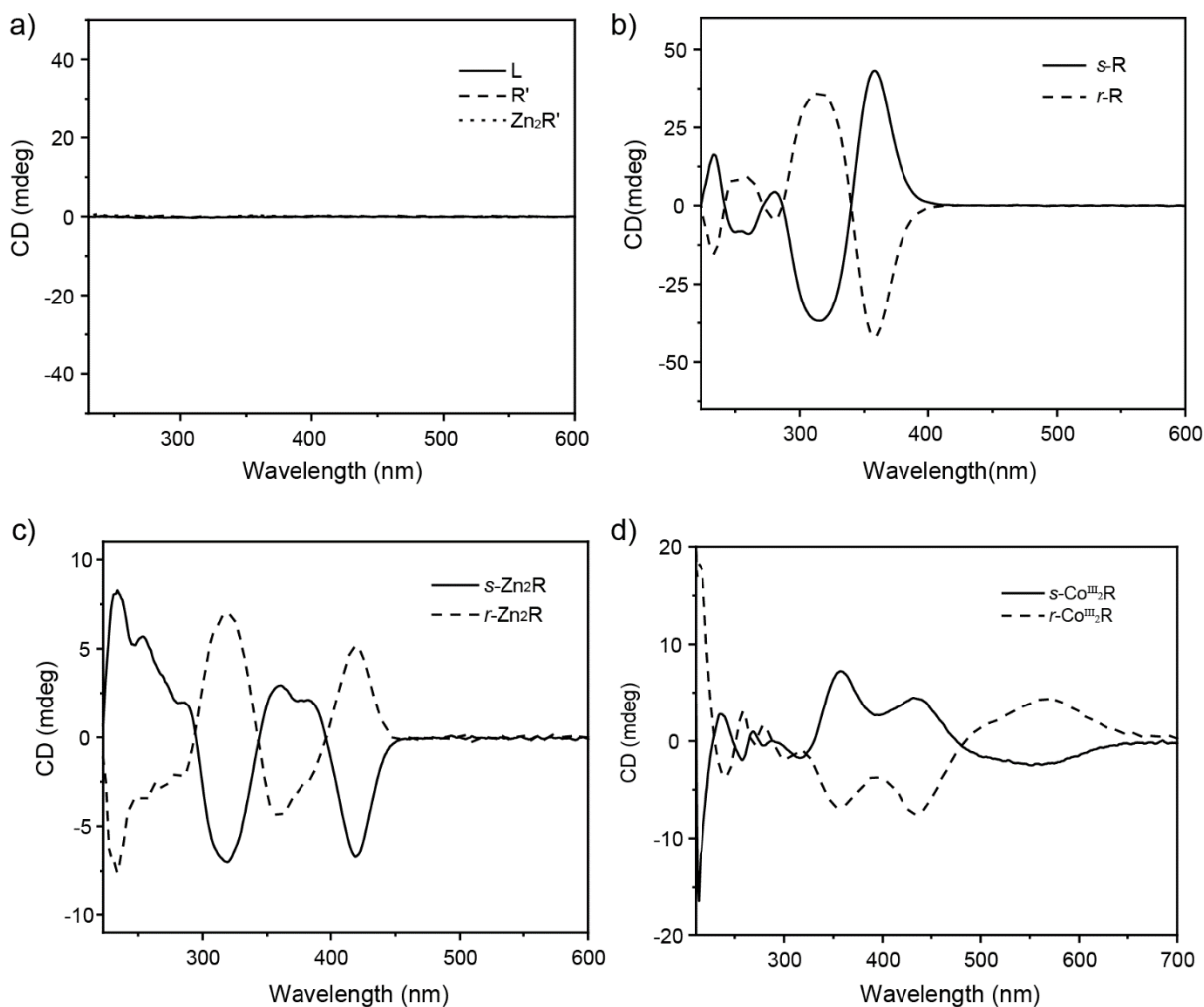


Figure 3.67: CD spectra of a) **L**, **R'**, **Zn<sub>2</sub>R'** b) **s-/r- R** c) **s-/r- Zn<sub>2</sub>R** and d) **s-/r- Co(III)<sub>2</sub>R** in THF ( $c = 1 \times 10^{-5}$  M).

### 3. Tetraphenylethylene-based macrocycles with adjustable CPL

#### 3.7.8 CPL spectra

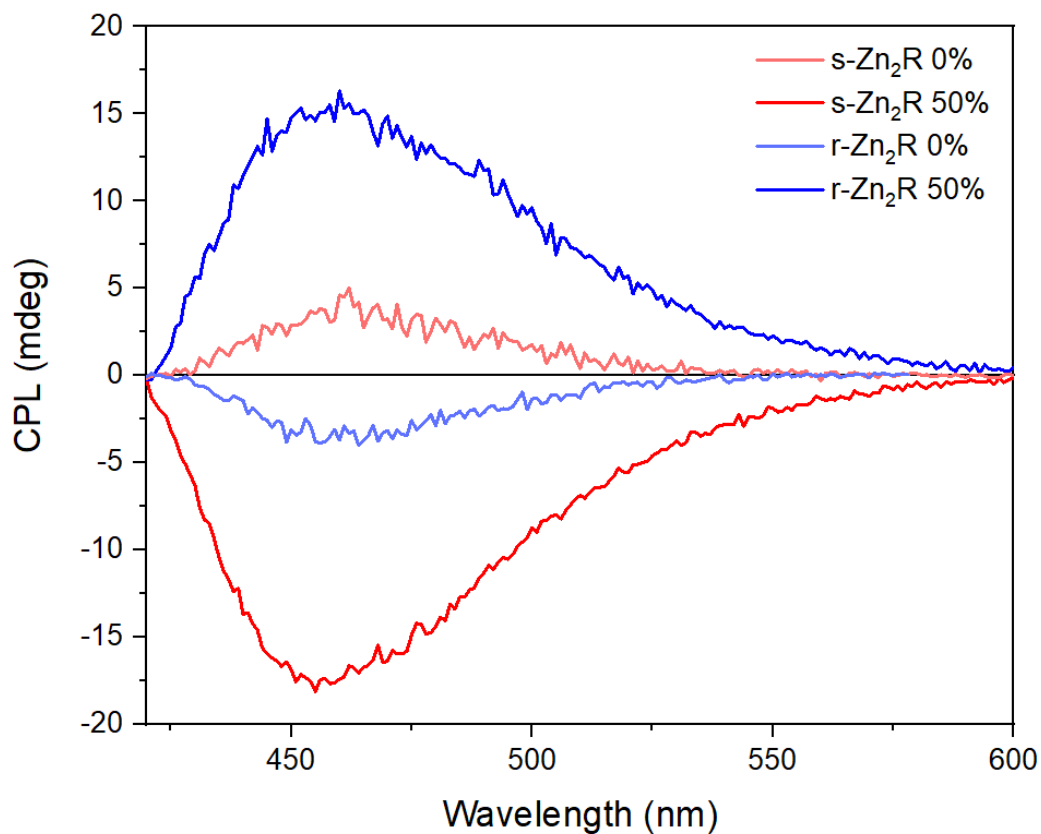


Figure 3.68: CPL spectra of **s-/r-Zn<sub>2</sub>R** in THF and in THF:H<sub>2</sub>O=50:50.

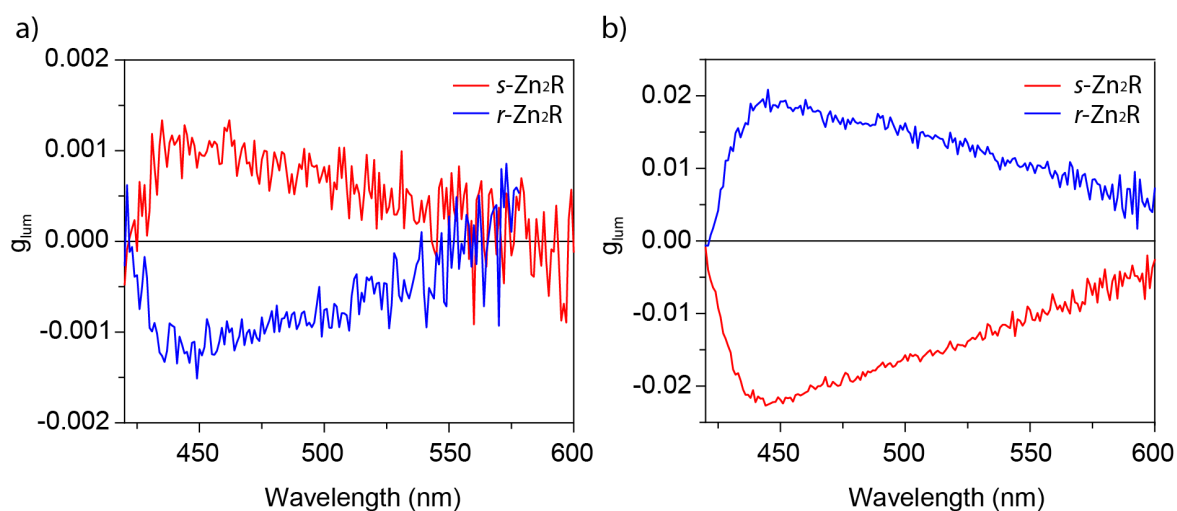


Figure 3.69:  $g_{lum}$  spectra of **s-/r-Zn<sub>2</sub>R** a) in THF and b) in THF: H<sub>2</sub>O = 50:50 ( $c = 1 \times 10^{-5}$  M).

### 3. Tetraphenylethylene-based macrocycles with adjustable CPL

#### 3.7.9 DLS and SEM

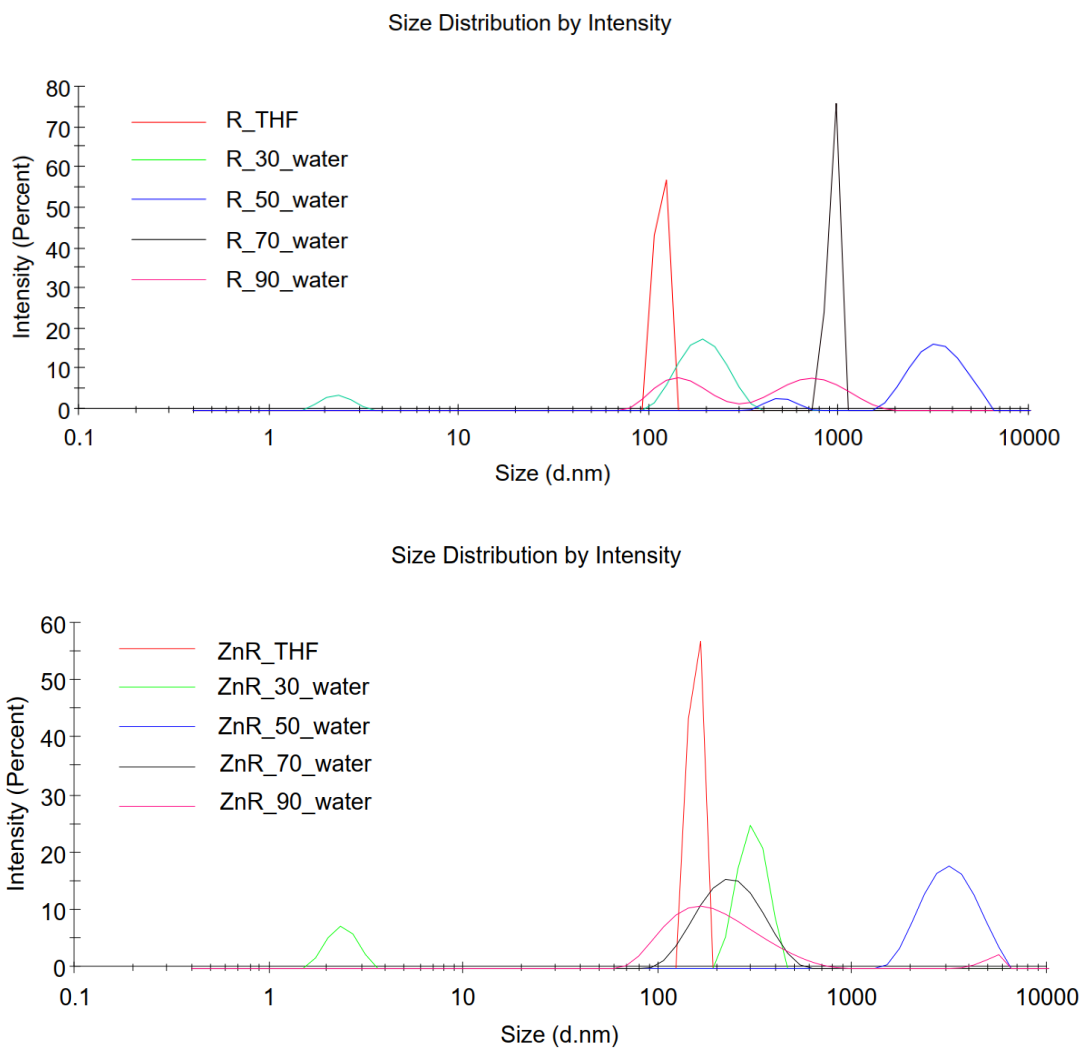


Figure 3.70: DLS of **R** and **Zn<sub>2</sub>R** in THF and water with different diffraction of water.

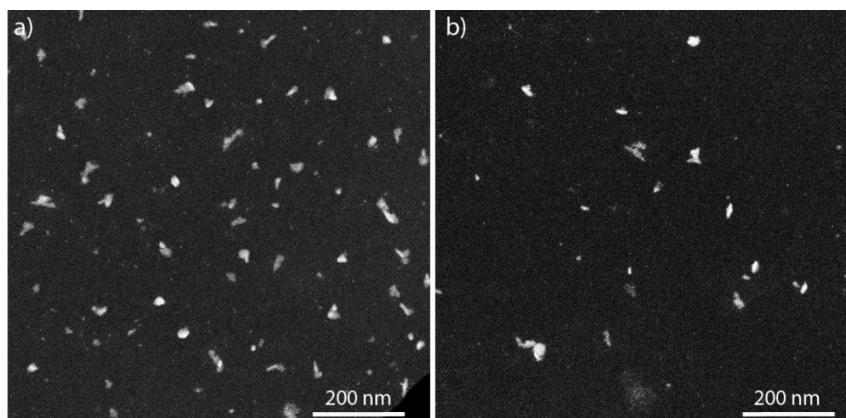


Figure 3.71: SEM image of **s-R** and **s-Zn<sub>2</sub>R** in THF.

### 3. Tetraphenylethylene-based macrocycles with adjustable CPL

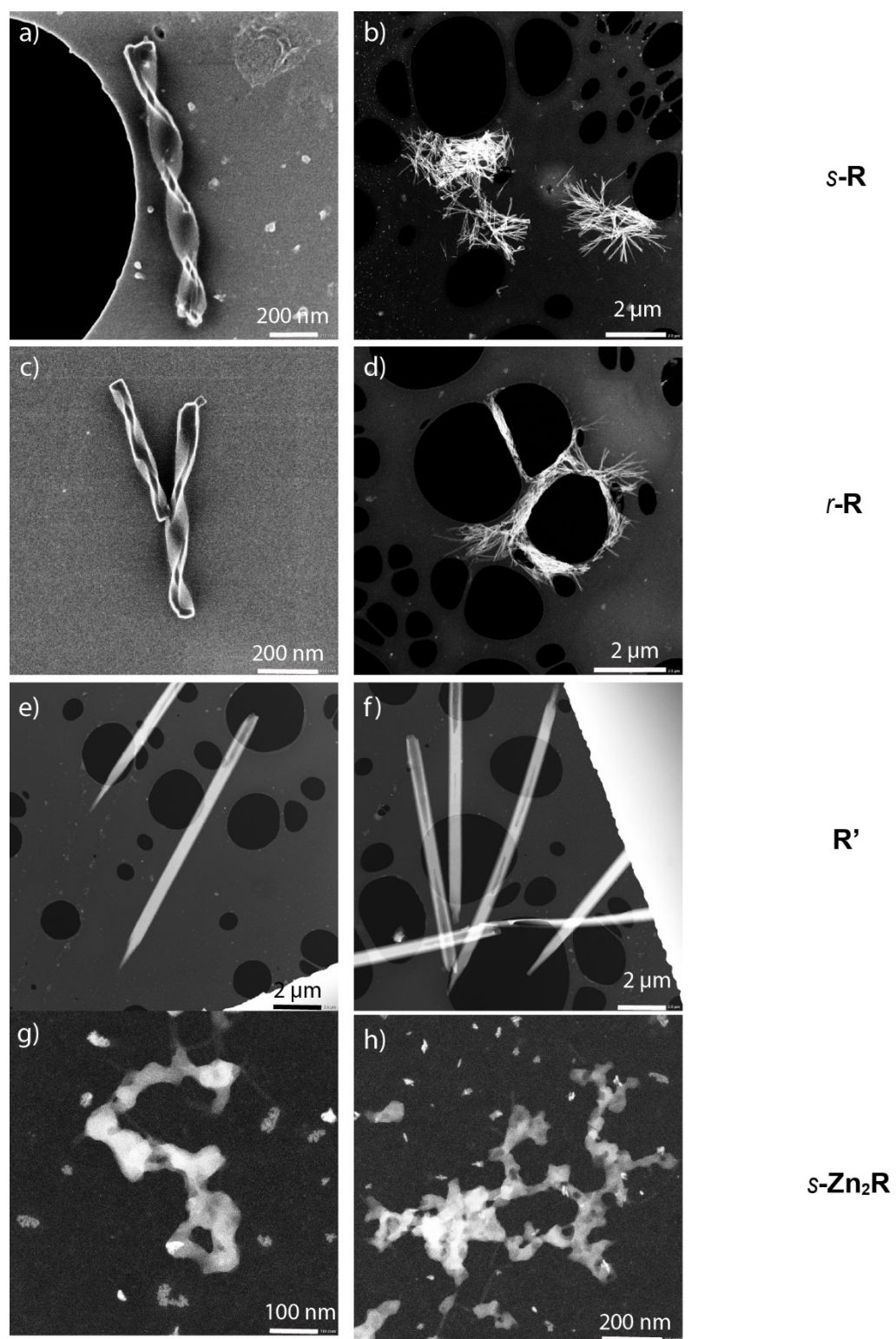


Figure 3.72: SEM images of compounds in THF: H<sub>2</sub>O=50:50.

### 3. Tetraphenylethylene-based macrocycles with adjustable CPL

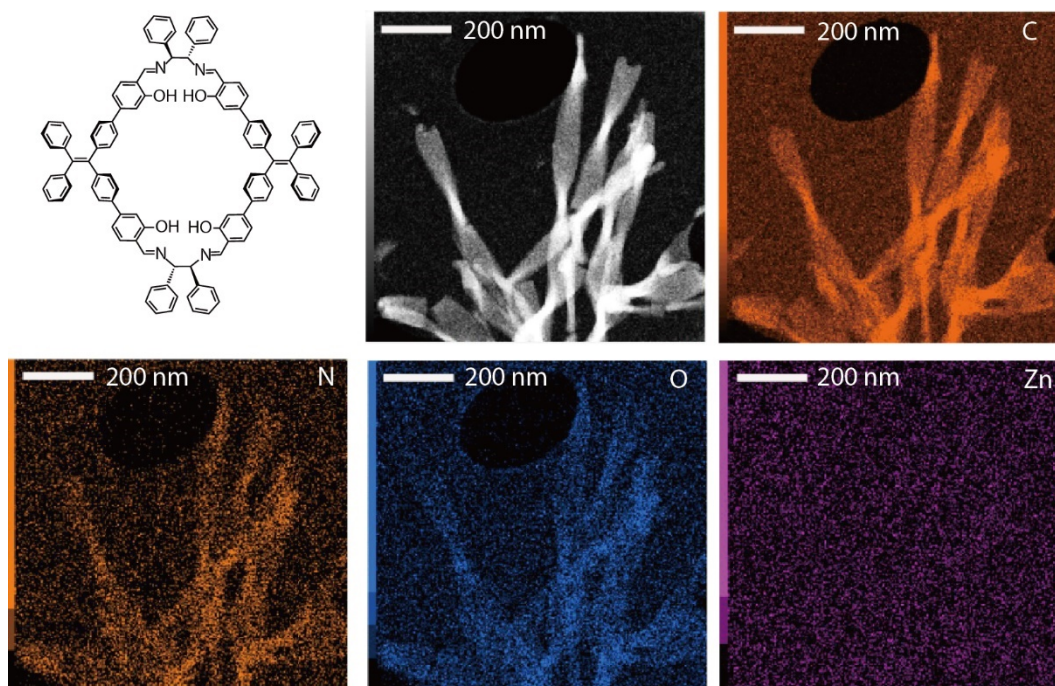


Figure 3.73: EDS mapping of **s-R** with the element mapping of C,N,O,Zn

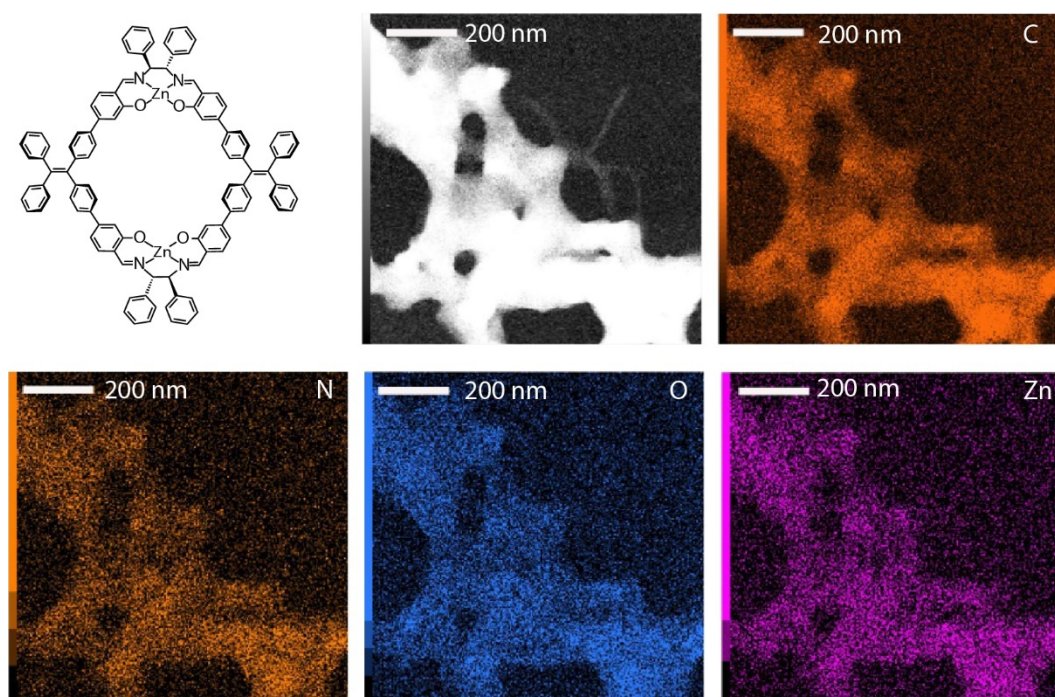


Figure 3.74: EDS mapping of **s-Zn<sub>2</sub>R** with the element mapping of C, N, O, Zn.

### 3. Tetraphenylethylene-based macrocycles with adjustable CPL

#### 3.8 References

- [1] R. Hu, N. L. C. Leung, B. Z. Tang, *Chem. Soc. Rev.* **2014**, *43*, 4494–4562.
- [2] Z. Zhao, J. W. Y. Lam, B. Z. Tang, *J. Mater. Chem.* **2012**, *22*, 23726–23740.
- [3] J. Liu, H. Zhang, L. Hu, J. Wang, J. W. Y. Lam, L. Blancafort, B. Z. Tang, *J. Am. Chem. Soc.* **2022**, *144*, 7901–7910.
- [4] Y. Xu, L. Chen, Z. Guo, A. Nagai, D. Jiang, *J. Am. Chem. Soc.* **2011**, *133*, 17622–17625.
- [5] N. B. Shustova, T.-C. Ong, A. F. Cozzolino, V. K. Michaelis, R. G. Griffin, M. Dincă, *J. Am. Chem. Soc.* **2012**, *134*, 15061–15070.
- [6] H.-T. Feng, Y.-X. Yuan, J.-B. Xiong, Y.-S. Zheng, B. Z. Tang, *Chem. Soc. Rev.* **2018**, *47*, 7452–7476.
- [7] C. Mu, Z. Zhang, Y. Hou, H. Liu, L. Ma, X. Li, S. Ling, G. He, M. Zhang, *Angew. Chem. Int. Ed.* **2021**, *60*, 12293–12297.
- [8] B. Kilbas, S. Mirtschin, R. Scopelliti, K. Severin, *Chem. Sci.* **2011**, *3*, 701–704.
- [9] Y.-X. Yuan, J.-H. Jia, Y.-P. Song, F.-Y. Ye, Y.-S. Zheng, S.-Q. Zang, *J. Am. Chem. Soc.* **2021**, *144*, 5389–5399.
- [10] A. Fürstner, G. Seidel, C. Kopiske, C. Krüger, R. Mynott, *Liebigs. Ann.* **1996**, *1996*, 655–662.
- [11] S. Song, Y.-S. Zheng, *Org. Lett.* **2013**, *15*, 820–823.
- [12] C. Zhang, Z. Wang, S. Song, X. Meng, Y.-S. Zheng, X.-L. Yang, H.-B. Xu, *J. Org. Chem.* **2014**, *79*, 2729–2732.
- [13] J.-B. Xiong, Y.-X. Yuan, L. Wang, J.-P. Sun, W.-G. Qiao, H.-C. Zhang, M. Duan, H. Han, S. Zhang, Y.-S. Zheng, *Org. Lett.* **2018**, *20*, 373–376.
- [14] H.-T. Feng, S. Song, Y.-C. Chen, C.-H. Shen, Y.-S. Zheng, *J. Mater. Chem. C.* **2013**, *2*, 2353–2359.
- [15] K. Li, G. Jiang, F. Zhou, L. Li, Z. Zhang, Z. Hu, N. Zhou, X. Zhu, *Polym. Chem.* **2017**, *8*, 2686–2692.
- [16] C. Zhang, Z. Wang, L. Tan, T. Zhai, S. Wang, B. Tan, Y. Zheng, X. Yang, H. Xu, *Angew. Chem. Int. Ed.* **2015**, *54*, 9244–9248.
- [17] J. Jiao, Z. Li, Z. Qiao, X. Li, Y. Liu, J. Dong, J. Jiang, Y. Cui, *Nat. Commun.* **2018**, *9*, 4423.
- [18] N. B. Shustova, B. D. McCarthy, M. Dincă, *J. Am. Chem. Soc.* **2011**, *133*, 20126–20129.
- [19] M. Zhang, G. Feng, Z. Song, Y.-P. Zhou, H.-Y. Chao, D. Yuan, T. T. Y. Tan, Z. Guo, Z. Hu, B. Z. Tang, B. Liu, D. Zhao, *J. Am. Chem. Soc.* **2014**, *136*, 7241–7244.
- [20] S. Saha, I. Regeni, G. H. Clever, *Coord. Chem. Rev.* **2018**, *374*, 1–14.
- [21] Y. Li, J. Zhang, H. Li, Y. Fan, T. He, H. Qiu, S. Yin, *Adv. Opt. Mater.* **2020**, *8*, 1902190.
- [22] X. Yan, T. R. Cook, P. Wang, F. Huang, P. J. Stang, *Nat. Chem.* **2015**, *7*, 342–348.
- [23] Z. Zhou, X. Yan, M. L. Saha, M. Zhang, M. Wang, X. Li, P. J. Stang, *J. Am. Chem. Soc.* **2016**, *138*, 13131–13134.

### 3. Tetraphenylethylene-based macrocycles with adjustable CPL

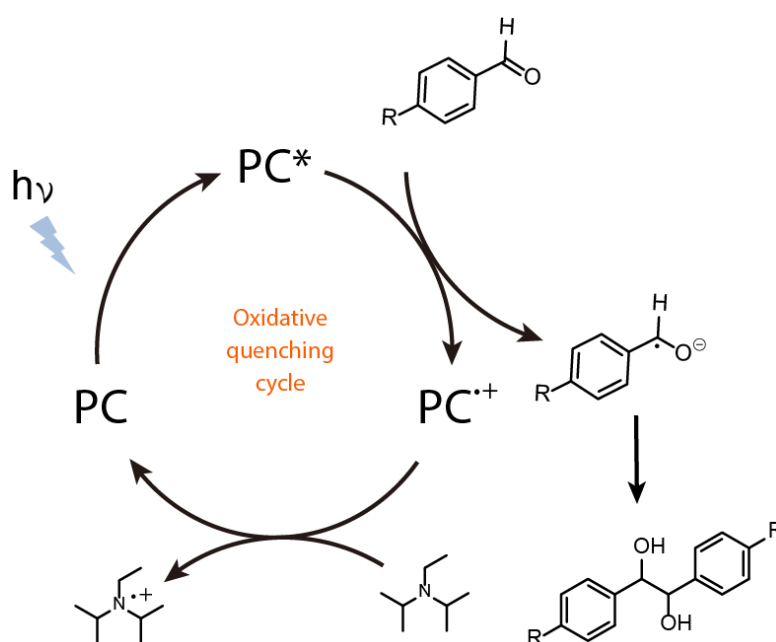
- [24] L.-J. Chen, Y.-Y. Ren, N.-W. Wu, B. Sun, J.-Q. Ma, L. Zhang, H. Tan, M. Liu, X. Li, H.-B. Yang, *J. Am. Chem. Soc.* **2015**, *137*, 11725–11735.
- [25] P. Das, A. Kumar, P. Howlader, P. S. Mukherjee, *Chem. Eur. J.* **2017**, *23*, 12565–12574.
- [26] T. Zhang, G.-L. Zhang, Q.-Q. Yan, L.-P. Zhou, L.-X. Cai, X.-Q. Guo, Q.-F. Sun, *Inorg Chem* **2017**, *57*, 3596–3601.
- [27] Q.-Q. Yan, S.-J. Hu, G.-L. Zhang, T. Zhang, L.-P. Zhou, Q.-F. Sun, *Molecules* **2018**, *23*, 363.
- [28] H. Li, X. Zheng, H. Su, J. W. Y. Lam, K. S. Wong, S. Xue, X. Huang, X. Huang, B. S. Li, B. Z. Tang, *Sci. Rep.* **2016**, *6*, 19277.
- [29] Q. Ye, D. Zhu, L. Xu, X. Lu, Q. Lu, *J. Mater. Chem. C.* **2016**, *4*, 1497–1503.
- [30] Y.-X. Yuan, M. Hu, K.-R. Zhang, T.-T. Zhou, S. Wang, M. Liu, Y.-S. Zheng, *Mater Horizons* **2020**, *7*, 3209–3216.
- [31] Y. Hong, J. W. Y. Lam, B. Z. Tang, *Chem. Soc. Rev.* **2011**, *40*, 5361–5388.
- [32] J.-B. Xiong, H.-T. Feng, J.-P. Sun, W.-Z. Xie, D. Yang, M. Liu, Y.-S. Zheng, *J. Am. Chem. Soc.* **2016**, *138*, 11469–11472.
- [33] H. Qu, Y. Wang, Z. Li, X. Wang, H. Fang, Z. Tian, X. Cao, *J. Am. Chem. Soc.* **2017**, *139*, 18142–18145.
- [34] X. Zhou, H. Li, Z. Chi, X. Zhang, J. Zhang, B. Xu, Y. Zhang, S. Liu, J. Xu, *New. J. Chem.* **2011**, *36*, 685–693.
- [35] P. G. Cozzi, *Chem. Soc. Rev.* **2004**, *33*, 410–421.
- [36] J. Guan, P. Zhang, T. Wei, Q. Lin, H. Yao, Y. Zhang, *Rsc. Adv.* **2014**, *4*, 35797–35802.
- [37] S. Ullmann, R. Schnorr, C. Laube, B. Abel, B. Kersting, *Dalton. Trans.* **2018**, *47*, 5801–5811.
- [38] F. Tosi, M. C. A. Stuart, S. J. Wezenberg, B. L. Feringa, *Angew. Chem. Int. Ed.* **2019**, *131*, 15077–15081.
- [39] V. Bressi, Z. Akbari, M. Montazerzohori, A. Ferlazzo, D. Iannazzo, C. Espro, G. Neri, *Sensors* **2022**, *22*, 900.
- [40] J. S. Danilova, S. M. Avdoshenko, M. P. Karushev, A. M. Timonov, E. Dmitrieva, *J. Mol. Struct.* **2021**, *1241*, 130668
- [41] Y. Sun, P. J. Stang, *Aggreg.* **2021**, *2*, e94.
- [42] P. G. Cozzi, L. S. Dolci, A. Garelli, M. Montalti, L. Prodi, N. Zaccheroni, *New. J. Chem.* **2003**, *27*, 692–697.
- [43] L. Fabbrizzi, M. Licchelli, P. Pallavicini, A. Perotti, A. Taglietti, D. Sacchi, *Chem. Eur. J.* **1996**, *2*, 75–82.
- [44] F. Würthner, T. E. Kaiser, C. R. Saha-Möller, *Angew. Chem. Int. Ed.* **2011**, *50*, 3376–3410.
- [45] E. P. J. Parrott, N. Y. Tan, R. Hu, J.A. Zeitler, B. Z. Tang, E. Pickwell-MacPherson, *Mater. Horizons.* **2013**, *1*, 251–258.
- [46] R. Hu, E. Lager, A. Aguilar-Aguilar, J. Liu, J. W. Y. Lam, H. H. Y. Sung, I. D. Williams, Y. Zhong, K. S. Wong, E. Peña-Cabrera, B. Z. Tang, *J. Phys. Chem. C.* **2009**, *113*, 15845–15853.

### 3. Tetraphenylethylene-based macrocycles with adjustable CPL

- [47] H. Wu, L. Du, J. Luo, Z. Wang, D. L. Phillips, A. Qin, B. Z. Tang, *J. Mater. Chem. C*. **2022**, *10*, 8174–8180.
- [48] G. Longhi, E. Castiglioni, J. Koshoubu, G. Mazzeo, S. Abbate, *Chirality*. **2016**, *28*, 696–707.
- [49] X.-Y. Luo, M. Pan, *Coord. Chem. Rev.* **2022**, *468*, 214640.
- [50] L. Yang, X. Dou, C. Ding, C. Feng, *J. Phys. Chem. Lett.* **2021**, 1155–1161.
- [51] F. Mamiya, N. Ousaka, E. Yashima, *Angew. Chem. Int. Ed.* **2015**, *54*, 14442–14446.
- [52] G. M. Sheldrick, *Acta Crystallogr Sect. Found. Adv.* **2015**, *71*, 3–8.
- [53] G. M. Sheldrick, *Acta Crystallogr Sect. C*. **2015**, *71*, 3–8.
- [54] C. B. Hübschle, G. M. Sheldrick, B. Dittrich, *J. Appl. Crystallogr.* **2011**, *44*, 1281–1284.
- [55] A. L. Spek, *Acta Crystallogr Sect C*. **2015**, *71*, 9–18.
- [56] A. L. Spek, *Acta Crystallogr Sect D*. **2009**, *65*, 148–155.
- [57] W. Kabsch, *Acta Crystallogr. Sect. D*. **2010**, *66*, 125–132.



## 4 Phenoxazine-based macrocycles for photoredox catalysis





## 4. Phenoxazine-based macrocycles for Photoredox catalysis

### 4.1 Introduction

#### 4.1.1 Photocatalysis

As an environmentally friendly method to synthesize a compound, photoredox catalysis has been intensively studied and widely used for synthetic chemistry. One of the most important concepts of photoredox catalysis is to convert light energy into chemical energy. Generally, a reaction using a photoredox catalyst absorbing visible light does not require high energy UV radiation and the reaction occurs under mild conditions to avoid unexpected by-products. Photoredox catalysis provides a new methodology which traditional organic reactions often can not achieve. In recent years, photoredox catalysis has become the forefront in organic chemistry.<sup>[1]</sup>

Photoredox catalysis has emerged as a powerful methodology enabling to form covalent bonds under milder reaction conditions to many thermal reactions. Photoredox catalysis is initiated by excitation of the photoredox catalyst followed by single electron transfer (SET) to or from the substrate to convert the absorbed light to chemical energy. The general mechanism of photoredox catalysts are depicted in Figure 4.1. The photoinduced electron transfer (PET) cycles of photoredox catalysis are usually categorized as oxidative quenching cycle and reductive quenching cycle. In an oxidative quenching cycle, the photoredox catalyst (PC) is excited upon irradiation and generates a relatively long-lived triplet excited state through a rapid intersystem crossing (ISC). The excited PC\* is quenched by donating an electron to a substrate or an oxidant (electron acceptor) in the reaction system and consequently generates a reactive intermediate as a radical from the substrate. For closing the catalytic cycle, a subsequent electron transfer from a reductant to PC<sup>•+</sup> is required to restore the catalyst. On the other hand, in the reductive quenching cycle, PC\* is reduced by an electron donor and forms PC<sup>•-</sup>. In photoredox reactions, relatively high energy states are achieved catalytically, and thus, a strong oxidant or reductant is often not needed unlikely to conventional organic reactions. In addition, as shown in Figure 4.1, photoredox reactions have a "redox-neutral" reaction mechanism overall.

#### 4. Phenoxazine-based macrocycles for Photoredox catalysis

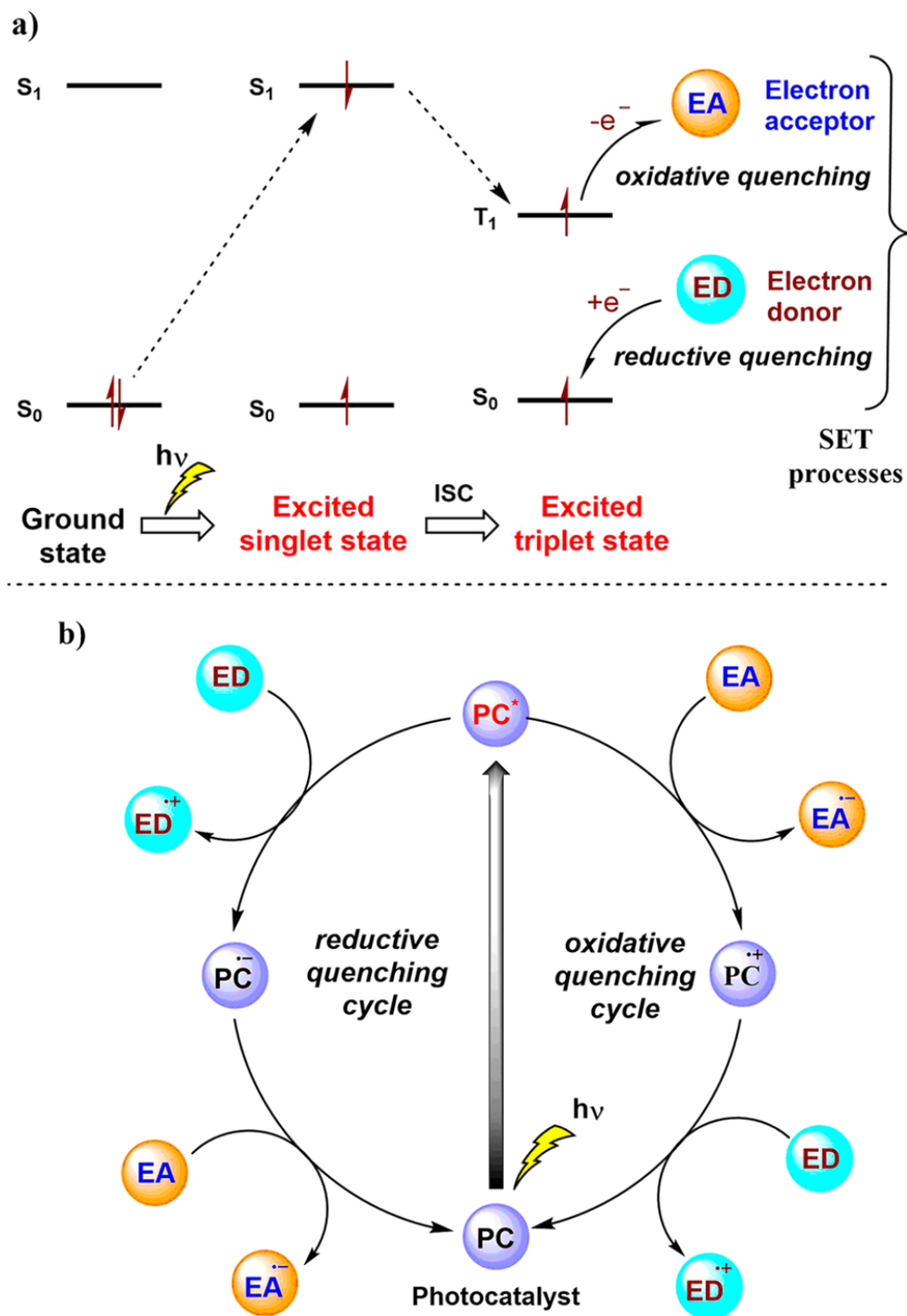


Figure 4.1: General mechanistic paradigm: (a) simplified orbital energy level diagram for the activation; (b) typical catalytic cycles of a photoredox catalyst.<sup>[2]</sup> Copyright © 2021, American Chemical Society.

### 4.1.2 Supramolecular Photocatalysis

Supramolecular catalysis has attracted considerable attention owing to the unique reactivities. Although many catalytic reactions in host-guest systems have been reported, supramolecular photoredox catalysis has not been explored extensively. In particular, photo-active supramolecular entities have been paid attention due to the potential to be utilized in a photoredox reaction.

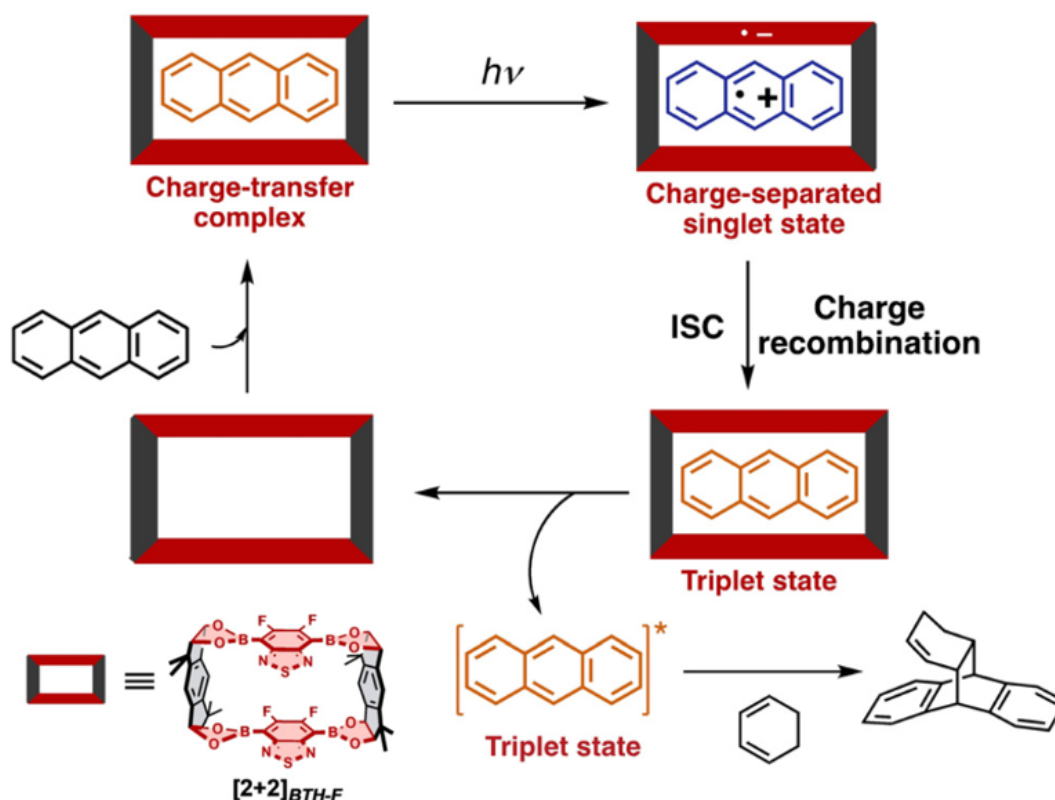


Figure 4.2: Proposed mechanism of the [4+2] cycloaddition in the presence of the host under visible light irradiation.<sup>[3]</sup> Copyright © 2020 Wiley-VCH Verlag GmbH & Co. KGaA, Weinheim

Iwasawa and co-workers reported visible-light-induced [4+2] cycloaddition reaction via charge-transfer excitation of a supramolecular host-guest complex.<sup>[3]</sup> The macrocyclic boronic ester  $[2+2]_{BTH-F}$  was constructed via multiple condensation reactions of racemic indacene tetrol and highly electron-deficient difluorobenzothiadiazole diboronic acid.<sup>[4]</sup> Anthracene can be encapsulated in the macrocycle through  $\pi$ - $\pi$  interactions. The host-guest complex undergoes a charge transfer excitation and yields a charge-separated singlet state upon visible-light irradiation. Then, anthracene in a triplet excited state is obtained in the cavity through intersystem crossing (ISC) and is

#### 4. Phenoxazine-based macrocycles for Photoredox catalysis

released into the solution. A subsequent photocycloaddition reaction of the released anthracene in the triplet excited state with dienes/alkenes proceeds efficiently.

Ruthenium and Iridium complexes have been demonstrated to show good properties as photoredox catalysts in the last decades. Ligands incorporating phosphorescent Ru(II) or Ir(III) complexes in their backbone as photoactive units have been shown to form metallacycles and metallacages.<sup>[5]</sup> Such metallacycles or cages have a well-defined cavity which can be used to bind a molecule Würthner and co-workers reported a self-assembled trigonal metalla-supramolecular macrocycle based on [Ru(bda)] building blocks (bda = 2,2'-bipyridine-6,6'-dicarboxylic acid), which has been used for water oxidation catalysis.<sup>[6]</sup> Two bpb linkers (bpb = 1,4-bis(pyrid-3-yl) benzene) are coordinated axially on both sides of the Ru(II) centers to form the [3+3] macrocycle [Ru(bda)bpb]<sub>3</sub>. In the water oxidation reaction system, the metallamacrocycle acts as a catalytic oxidant, [Ru(bpy)<sub>3</sub>]Cl<sub>2</sub> as photosensitizer (P) and Na<sub>2</sub>S<sub>2</sub>O<sub>8</sub> as a supporting oxidant to make the reaction catalytic (Figure 4.3). The reaction proceeds via a water nucleophilic attack mechanism. The coordination environment accelerates the rate of water oxidation with more than one order of magnitude enhancement, attributed to the preorganization of water molecules in the macrocyclic cavity.

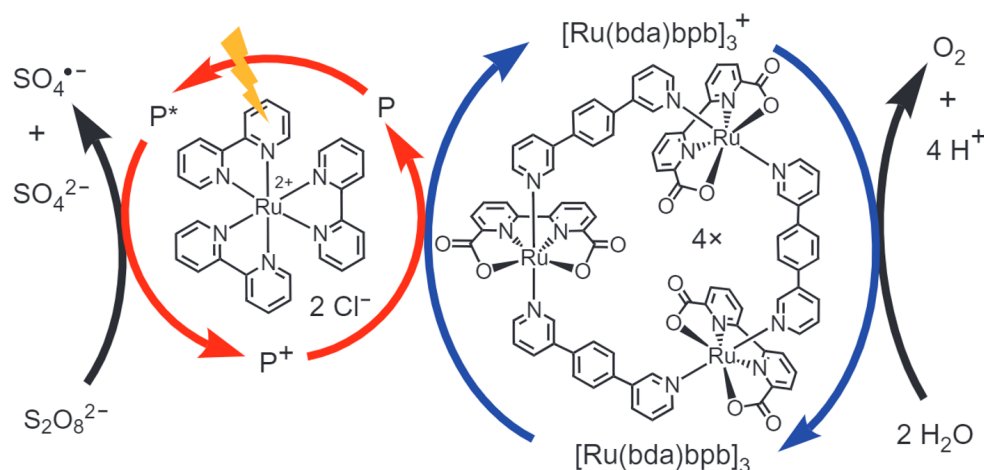


Figure 4.3: The structure of the [Ru(bda)bpb]<sub>3</sub> macrocycle and the proposed photocatalytic water oxidation process.<sup>[6]</sup> Copyright © 2016 Macmillan Publishers Limited.

In most cases, stereoselectivity is not expected in photoredox catalysis,<sup>[7]</sup> however, tremendous efforts to achieve stereoselectivity in photoredox reactions have been made in the last decades.<sup>[8-11]</sup> The combination of the inherent cavity and the

#### 4. Phenoxazine-based macrocycles for Photoredox catalysis

implemented chirality on supramolecular cages provide asymmetric catalysis. Su and co-workers have reported a photoredox-active and chiral Ru(II) metallaligand based on homochiral heterometallic octahedral cage  $[\text{Pd}_6(\text{RuL}_3)_6]^{28+}$ . The molecular design endows the resulting assembly with a photoactivity and a chiral space. A regio- and enantioselective biaryl coupling photoreaction in the cage was demonstrated and an unusual 1,4-coupling reaction was achieved. The homochiral cage with the confined nano-space enables to preorganize the substrates giving enantio-selectivity in the coupling reaction.

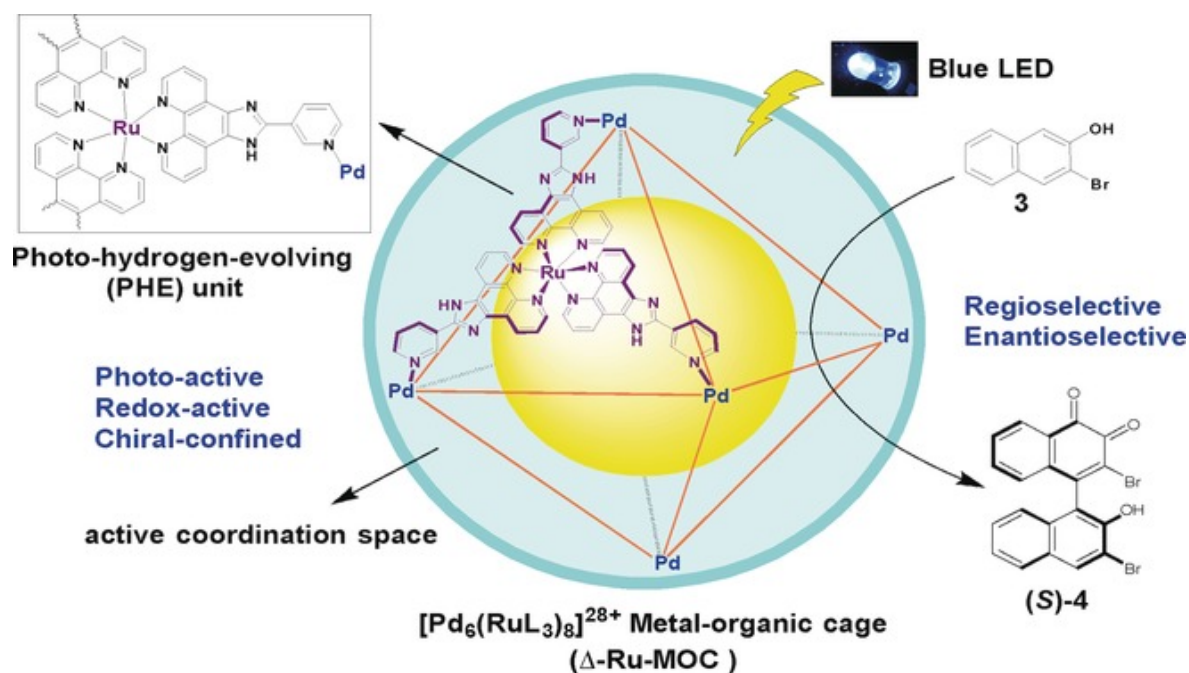


Figure 4.4: Schematic representation of homochiral  $\Delta$ -Ru-MOC structure with photoredox-active site and chiral-confined space based on  $\text{RuL}_3$  metallaligand. Photoinduced biaryl coupling reaction was proceeded with unique selectivity.<sup>[12]</sup> Copyright © 2017 Wiley-VCH Verlag GmbH & Co. KGaA, Weinheim.

Crowley and co-workers have developed a series of heterometallic architectures.<sup>[13,14]</sup> They obtained a heterometallic  $\text{Pd}_3\text{Pt}_6$  “donut”-shaped cage, which can be used for a photo-induced [4+2] cycloaddition reaction of anthracene with singlet  $\text{O}_2$ .<sup>[15]</sup> The low-symmetry and flexible pyridine ligand has different orthogonal binding sites. The bidentate binding sites of two of the ligands bind a square planar Pt(II) in a head-to-tail arrangement. The remaining monodentate coordination site is available to coordinate to Pd(II) to form the heterometallic cage. The analogue of  $\text{Pd}_3\text{Pt}_6$ , homonuclear cage  $\text{Pd}_9$ , can be also synthesized together with impurities. The cage consists of three planar cationic panels allowing the encapsulation of a planar aromatic

#### 4. Phenoxazine-based macrocycles for Photoredox catalysis

guest. The photocatalytic properties of **Pd<sub>3</sub>Pt<sub>6</sub>** were studied. **Pd<sub>3</sub>Pt<sub>6</sub>** acts as a molecular container and photosensitizer, which promotes the light-induced excitation of <sup>3</sup>O<sub>2</sub> to <sup>1</sup>O<sub>2</sub> and results in the formation of the endoperoxide with an enhanced reaction rate.

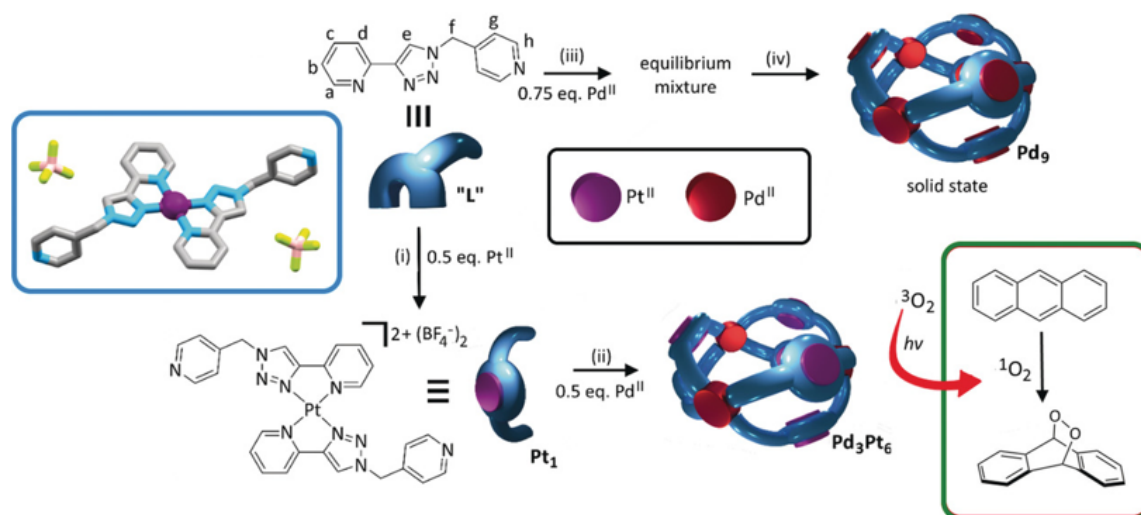


Figure 4.5: a) Scheme of the stepwise self-assembly of low-symmetry pyridine ligand with Pd(II) or Pt(II)/Pd(II) to form homometallic cage **Pd<sub>9</sub>** and heterometallic cage **Pd<sub>3</sub>Pt<sub>6</sub>**. Blue box: X-ray crystal structure of **Pt<sub>1</sub>**. Green box: photocatalytic conversion of anthracene to its endoperoxide.<sup>[15]</sup> Copyright © 2018 Wiley-VCH Verlag GmbH & Co. KGaA, Weinheim.

An increase in the complexity of supramolecular architectures can lead to the emergence of a new feature. Clever group has reported a series of interpenetrated double cages comprising of Pd(II) ions and banana-shaped pyridine ligands.<sup>[16–22]</sup> The catenated structure features three consecutive pockets, initially containing BF<sub>4</sub><sup>-</sup>. Recently, an acridone-based interpenetrated double cage with photocatalytic activity has been reported.<sup>[23]</sup> Double Cage [**3BF<sub>4</sub>@Pd<sub>4</sub>L<sub>8</sub>**] was formed via self-assembly of the acridone-based bis-monodentate ligand and Pd(II). After the addition of halides, the small chloride anions replace BF<sub>4</sub><sup>-</sup> in the outer pockets, resulting in a larger middle pocket. This enables encapsulation of neutral guest molecules within the middle pocket. The ligand is light sensitive and not suitable for photocatalysis, while, the cage is more robust against light. The double cage acts as a photosensitizer to generate singlet oxygen, which subsequently reacts with 1,3-cyclohexadiene in a [2+4] manner.



#### 4. Phenoxazine-based macrocycles for Photoredox catalysis

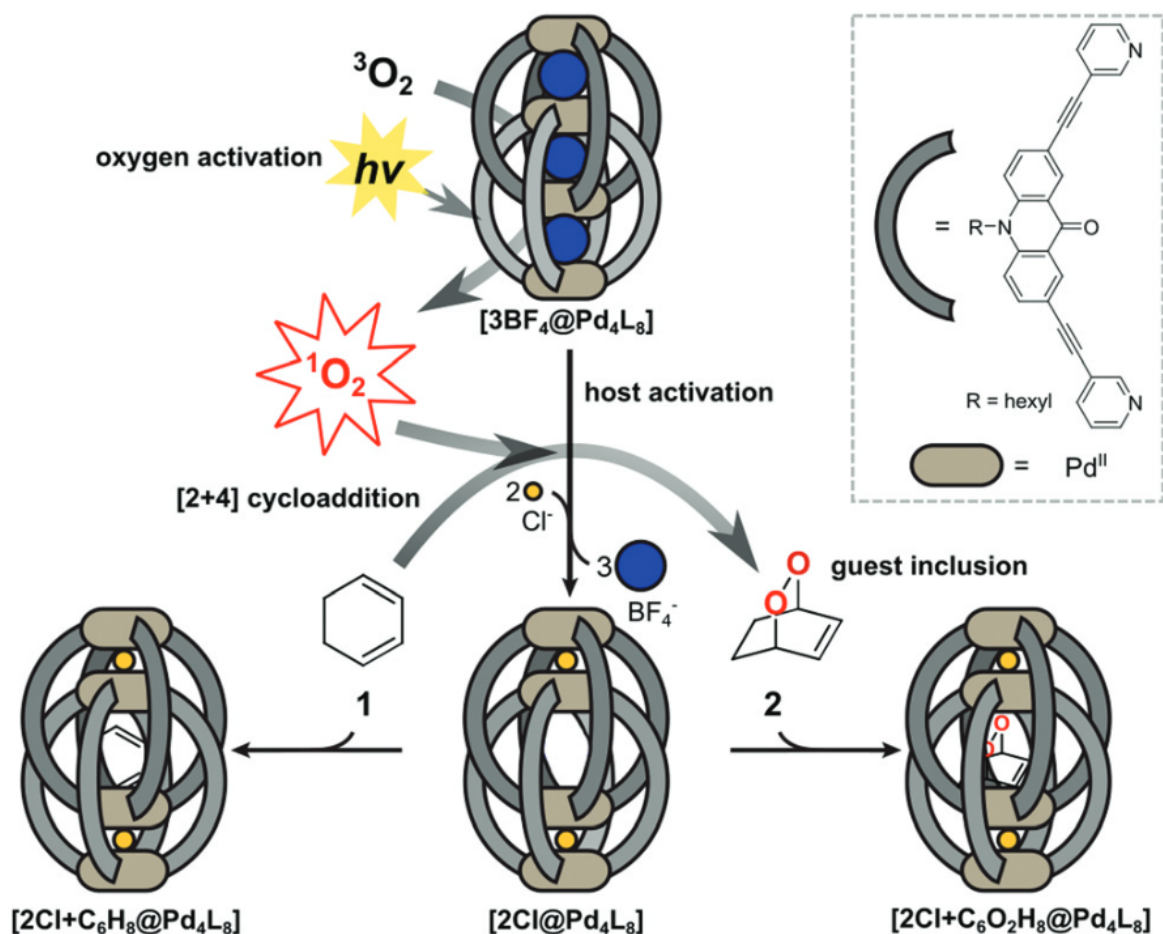


Figure 4.6: Scheme of guest inclusion behaviour and catalytic function of the acridone-based interpenetrated double cages. The cage has three pockets and are filled with one BF<sub>4</sub><sup>-</sup> counter anions, each. The addition of Cl<sup>-</sup> anions triggered the conformation change, the outer two BF<sub>4</sub><sup>-</sup> can be exchanged by two Cl<sup>-</sup> anions and obtained an enlarged inner pocket, followed by uptake of neutral guest molecules and photocatalysis.<sup>[23]</sup> Copyright © The Royal Society of Chemistry 2020.

#### 4.2 Design of phenoxazine-based ligand macrocycles

Based on the research and the established concepts shown in the last chapters, synthesis and investigation of metallamacrocycles designed for photoredox catalysis has been conducted. In this chapter, the formation and a photoredox catalytic property of binuclear phenoxazine-based chiral metallamacrocycles will be described. *N*-aryl phenoxazine, the backbone of the ligand, is known as a photoredox catalyst.<sup>[24–26]</sup> The macrocycle **R<sup>PZ</sup>** was synthesized by a condensation reaction of phenoxazine-based salicylaldehyde ligand and a chiral diamine. The complexes of **M<sub>2</sub>R<sup>PZ</sup>** (M=Zn(II), Co(III)) were obtained in a quantitative yield by metalation of **R<sup>PZ</sup>** with the corresponding

#### 4. Phenoxazine-based macrocycles for Photoredox catalysis

acetate salts as a metal source. The formation of  $M_2R^{PZ}$  was confirmed by  $^1H$  NMR spectroscopy, DOSY, ESI-MS, FT-IR, and UV-Vis. Then, the photophysical properties of the synthesized ligand and macrocycles were investigated. The phenoxazine-based salen macrocycle as a photoredox catalyst exhibits absorption in the visible region, high molar absorptivity, oxidation reversibility, and a charge transfer excited state, which are required for being a good catalyst in photoredox reactions. Further, an ability as a photoredox catalyst in catalytic pinacol coupling reactions has been investigated.

Phenoxazine derivatives have been utilized in photoredox catalysis as an organic catalyst. The phenoxazine core is electron-rich, i.e.  $E^0(\text{phenoxazine}^{\cdot-}/\text{phenoxazine}) = \sim 0.6$  V vs SCE (calomel reference electrode).<sup>[26]</sup> Miyake and co-workers have studied the absorption, charge transfer and redox potential properties of phenoxazine derivatives modified by different substituents for photoredox catalysts through experimental and computational analyses.<sup>[27]</sup> Phenoxazine could be modified by *N*-aryl substituents or phenoxazine core substituents (Figure 4.7). To reduce catalyst loadings, PCs that strongly absorb visible light and efficiently generate long-lived triplet excitons are ideal. The maximum wavelength of absorption of phenoxazine with two core-substituents shows a red shift, attributed to the stabilizing of energies of the  $\pi^*$  orbitals. The strong charge-transfer character of the lowest singlet excited (S1) is a key factor to effectively populate the lowest triplet excited state ( $T_1$ ).<sup>[28]</sup> *N*-naphthyl phenoxazine can access a charge transfer (CT) excited state, which is supposed to give superior performance in photoredox reactions, while, *N*-phenyl phenoxazine can only achieve this by a suitable core substituent. A photoredox catalyst should exhibit high reducing power in its excited state along with an appropriate ground-state oxidation potential for the effective reduction of its radical cation. The reduction potentials can be tunable by installation of electro-donating or electro-withdrawing core substituents.

#### 4. Phenoxazine-based macrocycles for Photoredox catalysis

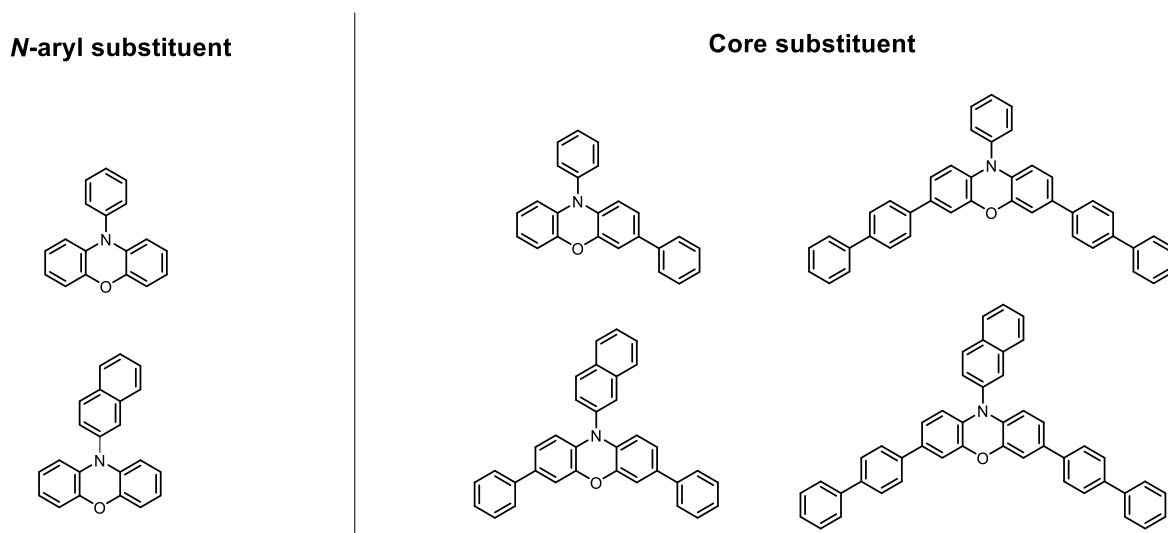


Figure 4.7: Structures of phenoxazine derivatives with different N-aryl substituent and one / two core substituent.

Here, a *N*-aryl phenoxazine-based ligand was designed and investigated in the formation of macrocycles. Firstly, **2Br-PZ** with naphthalene *N*-substituent on the phenoxazine core was synthesized following the literature in two steps from 10-phenoxazine.<sup>[27]</sup> Phenoxazine-based ligand **L<sup>PZ</sup>** was designed and synthesized by Suzuki-coupling of **2Br-PZ** and pinacol ester salicylaldehyde compound (Figure 4.8). The ligand was fully characterized by <sup>1</sup>H NMR, COSY, NOESY, DOSY and ESI-MS.

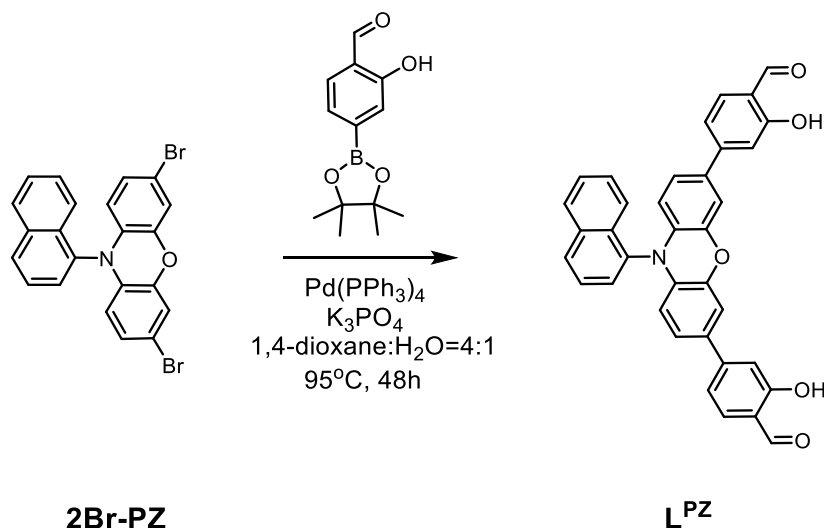


Figure 4.8: Synthesis route of ligand **L<sup>PZ</sup>**.

#### 4. Phenoxazine-based macrocycles for Photoredox catalysis

The ligand was treated with excess (1*S*,2*S*)-1,2-diphenylethane-1,2-diamine to form a chiral macrocycle by condensation reaction in a mixture of methanol and dichloromethane (Figure 4.9). The solution became turbid after stirring at room temperature for few minutes. Pure macrocycle **s-R<sup>PZ</sup>** was obtained after purification. The isomer **r-R<sup>PZ</sup>** was synthesized following the same procedure by using (1*R*,2*R*)-1,2-diphenylethane-1,2-diamine. The structure of **R<sup>PZ</sup>** was firstly confirmed by <sup>1</sup>H NMR. Compared with the free ligand, the proton signals of phenyl ring showed upfield shift ( $\Delta\delta[\text{H}_{3/f}] = 0.29$  ppm,  $\Delta\delta[\text{H}_{4/g}] = 0.15$  ppm,  $\Delta\delta[\text{H}_{5/h}] = 0.08$  ppm). The proton signal at  $\delta = 8.57$  ppm, assignable to proton He of the imine moiety was observed, indicating the formation of the Schiff-base moiety.

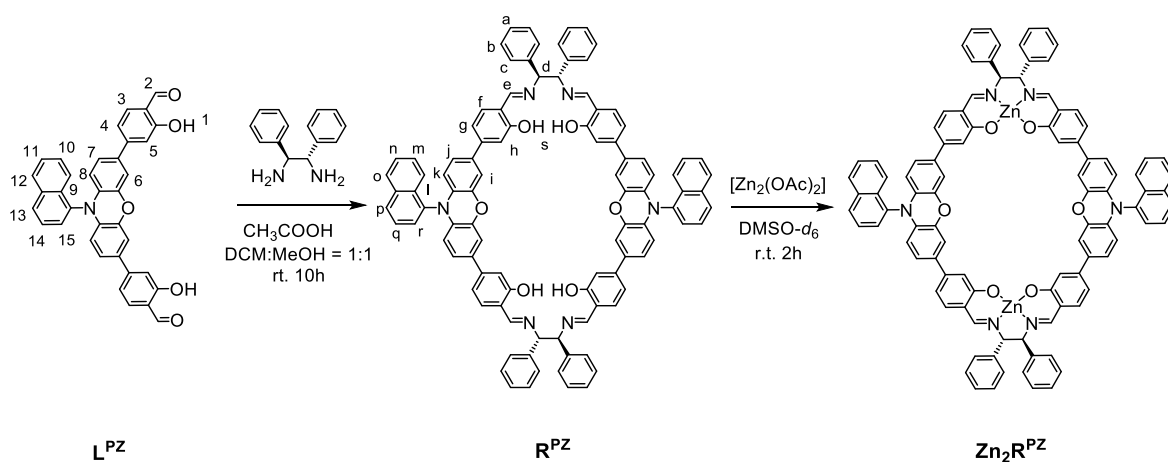


Figure 4.9: synthesis route of macrocycles **R<sup>PZ</sup>** and **Zn<sub>2</sub>R<sup>PZ</sup>**.

Zn(II) complexes based on Schiff base ligands are well investigated due to their intriguing catalytic, photophysical and aggregation properties. Here, the Zn macrocycle was obtained by coordination of phenoxazine-based salen macrocycle with Zn(II) ions. after purification, the obtained compound was characterized by <sup>1</sup>H NMR and the observed signals were assigned by COSY and NOESY. In the <sup>1</sup>H NMR spectrum of **Zn<sub>2</sub>R**, a single set of signals with chemical shifts compared with the metal-free salen ring was observed (Figure 4.10), suggesting the formation of metal complexes. The signal of proton Hs disappeared after metalation, indicating of the deprotonation of the OH groups on **R**. The protons from salen moieties showed upfield shift ( $\Delta\delta[\text{H}_e] = 0.39$  ppm,  $\Delta\delta[\text{H}_f] = 0.36$  ppm,  $\Delta\delta[\text{H}_h] = 1.33$  ppm) compared with **R**, consistent with coordination of N<sub>2</sub>O<sub>2</sub> to Zn(II).

#### 4. Phenoxazine-based macrocycles for Photoredox catalysis

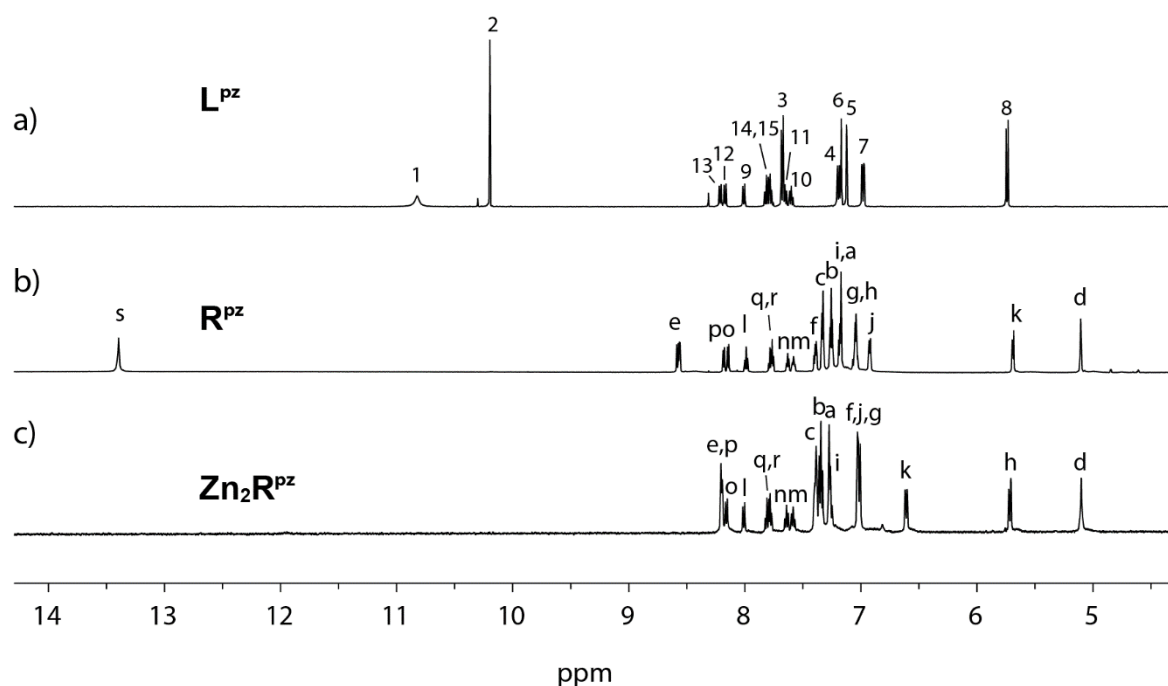


Figure 4.10: <sup>1</sup>H NMR spectra of a) **L<sup>PZ</sup>**, b) **R<sup>PZ</sup>** and c) **Zn<sub>2</sub>R<sup>PZ</sup>** (500 MHz, 298 K, DMSO-*d*<sub>6</sub>).

The diffusion-ordered spectroscopy (DOSY) spectrum of **Zn<sub>2</sub>R<sup>PZ</sup>** confirmed the formation of a single species (Figure 4.36). The diffusion coefficient was estimated to be  $1.0 \times 10^{-10}$  m<sup>2</sup>/s with a hydrodynamic radius of 10.9 Å, while the hydrodynamic radius of **L** was calculated to be 6.62 Å with the diffusion coefficient of  $1.65 \times 10^{-10}$  m<sup>2</sup>/s (Figure 4.28). To further confirm the structure of the metal salen ring, **Co(III)<sub>2</sub>R<sup>PZ</sup>** was also synthesized following the same procedure to **Zn<sub>2</sub>R<sup>PZ</sup>** using Co(OAc)<sub>2</sub> as a metal source in a mixed solvents of chloroform and acetonitrile. NH<sub>4</sub>PF<sub>6</sub> was added into the self-assembly system to provide a counter anion and the turbid greenish solution became red-brown. The composition of binuclear metal salen macrocycle **Co(III)<sub>2</sub>R<sup>PZ</sup>** was confirmed by ESI-MS (Figure 4.11). The ESI-MS analysis revealed only one peak at *m/z* 782.6910, corresponding to positively charged complex **[Co(III)<sub>2</sub>R<sup>PZ</sup>]<sup>2+</sup>**, suggesting oxidation of the Co(II) to Co(III) occurred during the reaction.

#### 4. Phenoxazine-based macrocycles for Photoredox catalysis

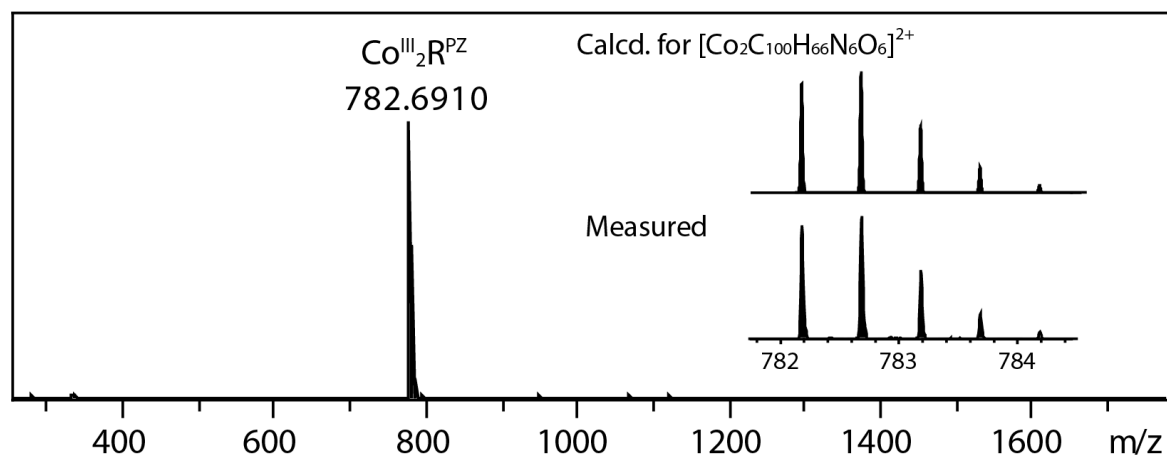


Figure 4.11: ESI-MS of  $\text{Co(III)}_2\text{R}^{\text{PZ}}$ , with insets showing the calculated and measured isotopic patterns of  $[\text{Co(III)}_2\text{R}^{\text{PZ}}]^{2+}$ .

FT-IR spectra were measured to further confirm the structure of the assembly (Figure 4.37).  $\text{R}^{\text{PZ}}$  displays characteristic bands at  $3059\text{ cm}^{-1}$ ,  $1620\text{ cm}^{-1}$  and  $1490\text{ cm}^{-1}$ , corresponding to molecular vibrations of the aromatic rings, C=N and C-N bonds, respectively.<sup>[29]</sup> The band at  $2852\text{ cm}^{-1}$  is attributed to the vibration of -OH group. The band from the vibration of the OH group disappeared after coordination with Zn(II), indicating of the formation of desired  $\text{Zn}_2\text{R}^{\text{PZ}}$ .

#### 4.3 Photophysical properties of $\text{Zn}_2\text{R}^{\text{PZ}}$

To investigate the absorption properties of the prepared metallamacrocycles, UV-vis absorption spectra of the macrocycles in DMSO were measured (Figure 4.12 a). Comparing to ligand  $\text{L}^{\text{PZ}}$ , the maximum absorption wavelength of metal free macrocycle  $\text{R}^{\text{PZ}}$  and Zn salen macrocycle displayed a blue shift from  $428\text{ nm}$  to  $409\text{ nm}$  and  $413\text{ nm}$ , respectively. All of the compounds showed absorption in the visible region, allowing the desired photoredox catalysis by visible light irradiation. Especially,  $\text{Zn}_2\text{R}^{\text{PZ}}$  has a higher molar absorptivity ( $\epsilon$ ) (table 4.1), which should increase the population of the catalyst in the excited state.

#### 4. Phenoxazine-based macrocycles for Photoredox catalysis

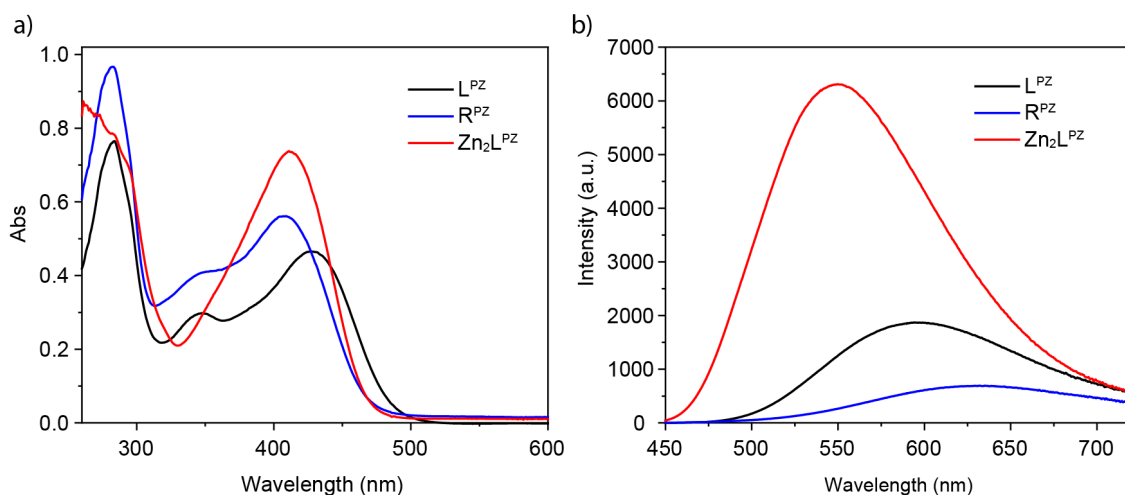


Figure 4.12: a) Absorption spectra and b) emission spectra of the ligand and the macrocycles (in DMSO,  $c_L = 2 \times 10^{-5}$  M,  $c_R = 1 \times 10^{-5}$  M,  $c_{Zn_2R} = 1 \times 10^{-5}$  M, cuvette path length: 1 cm).

Table 4.1: Absorption and fluorescence information

		$L^{PZ}$	$R^{PZ}$	$Zn_2R^{PZ}$
Absorption	$\lambda_{max}$ (nm)	428	409	413
	$\epsilon$ ( $M^{-1}cm^{-1}$ )	46529	56139	73566
Fluorescence	$\lambda_{ex}$ (nm)	410	410	410
	$\lambda_{em}$ (nm)	600	635	550
	$E_{S_1}$ (eV)	2.07	1.95	2.25

The fluorescence spectra of the compounds were measured (Figure 4.12 b).  $Zn_2R^{PZ}$  showed a strong emission with a blue shift compared with the metal-free macrocycle. The emission should come from the radiative decay from the  $S_1$  state since the spectrum was measured in the presence of oxygen. A singlet excited state energy  $E_{S_1}$  is commonly determined by a maximum wavelength of emission which is supposed to correspond to the radiative decay from the  $S_1$  state.

As shown in Figure 4.13, all of the PCs have a large Stokes shift ( $\Delta\lambda_L = 172$  nm,  $\Delta\lambda_R = 226$  nm,  $\Delta\lambda_{Zn_2R} = 137$  nm). Among the PCs,  $R^{PZ}$  showed the largest Stokes shift. In order to investigate the electronic state of the PCs, DFT calculations were carried out for the PCs in both the ground state and the triplet state at the  $\omega$ B97X/def2svp level of theory (Figure 4.13). The highest occupied molecular orbital (HOMO) of  $L^{PZ}$  was suggested to distribute on the benzyl aldehyde moiety, while the lowest occupied molecular orbital (LUMO) is mainly localized on the phenoxazine core. For  $R^{PZ}$ , the

#### 4. Phenoxazine-based macrocycles for Photoredox catalysis

HOMO is implied to localize on the phenoxazine core (donor). Meanwhile, the LUMO of  $\mathbf{R}^{\text{PZ}}$  should be localized on the naphthalene moieties. In stark contrast, the distribution of the LUMO of  $\mathbf{Zn}_2\mathbf{R}^{\text{PZ}}$  to the whole macrocycle structure was suggested. Among the PCs,  $\mathbf{R}^{\text{PZ}}$  seems to have a possibility to form an excited CT state.

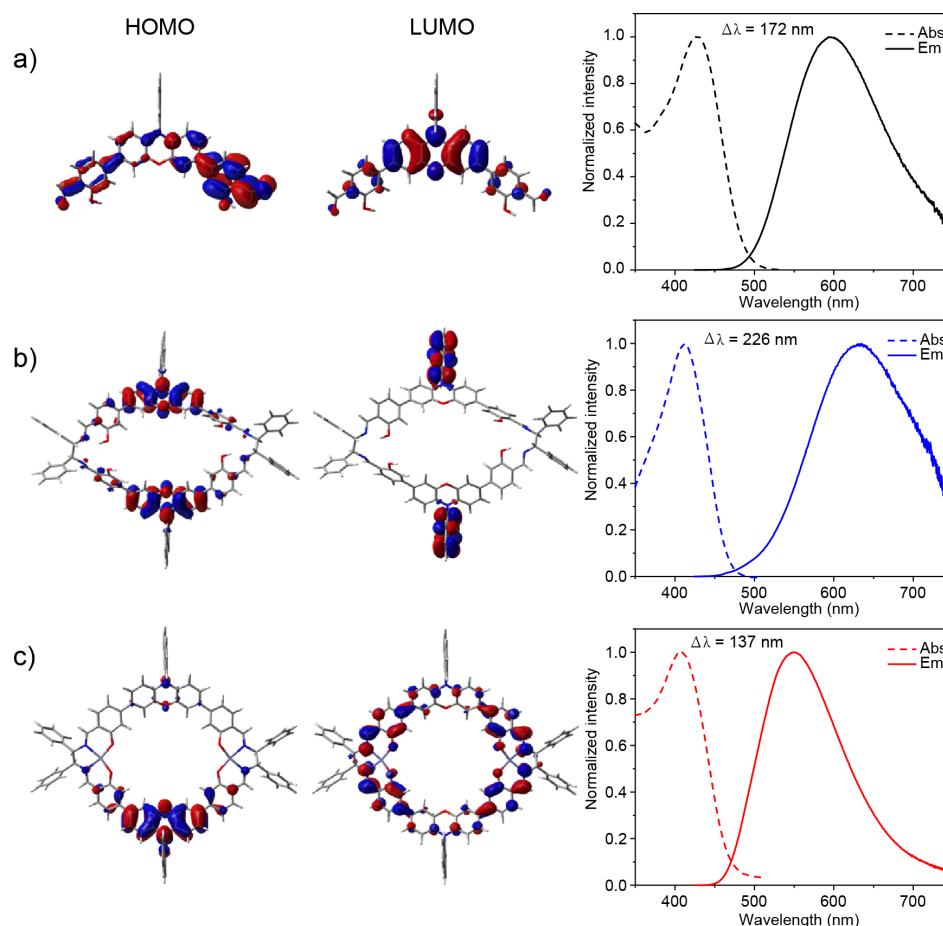


Figure 4.13: The calculated HOMO, LUMO and overlays of absorption and emission spectra of a)  $\mathbf{L}^{\text{PZ}}$ , b)  $\mathbf{R}^{\text{PZ}}$ , and c)  $\mathbf{Zn}_2\mathbf{R}^{\text{PZ}}$  (in DMSO)

CD spectra were measured to investigate the chiroptical properties of the macrocycles (Figure 4.14). All the enantiomers were synthesized by using commercially available enantiopure 1,2-diphenylethane-1,2-diamine.  $\mathbf{L}^{\text{PZ}}$  is CD silent because it is achiral. While, chiral  $\mathbf{R}^{\text{PZ}}$  (*s*- $\mathbf{R}^{\text{PZ}}$  and *r*- $\mathbf{R}^{\text{PZ}}$ ) showed a strong Cotton effect at around 380 nm in a mirror image fashion formation, suggesting the successful implementation of chirality. Similarly, chiral  $\mathbf{Zn}_2\mathbf{R}^{\text{PZ}}$  (*s*- $\mathbf{Zn}_2\mathbf{R}^{\text{PZ}}$  and *r*- $\mathbf{Zn}_2\mathbf{R}^{\text{PZ}}$ ) showed mirrored CD signals with a strong Cotton effect at around 440 nm. The introduced chirality on the PCs should be useful in asymmetric catalysis. Applications in asymmetric catalysis will be tried in due course.



#### 4. Phenoxazine-based macrocycles for Photoredox catalysis

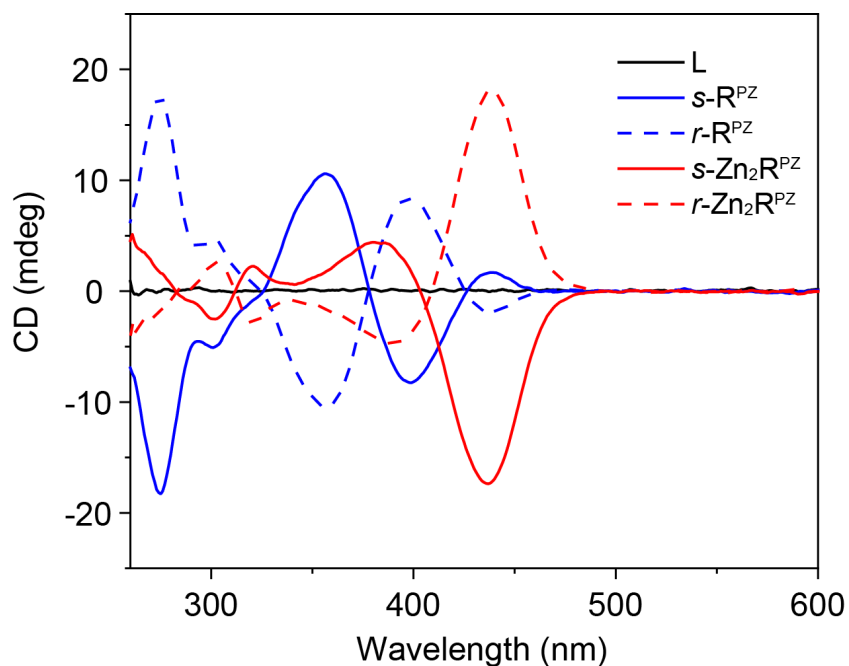


Figure 4.14: CD spectra of ligand and macrocycles (in DMSO,  $c_L = 2 \times 10^{-5}$  M,  $c_R = 1 \times 10^{-5}$  M,  $c_{Zn_2R} = 1 \times 10^{-5}$  M, cuvette path length: 1 cm).

Phenoxazine derivatives are known to undergo the oxidative quenching cycle.<sup>[30]</sup> In the oxidative quenching catalytic cycle, excited  $PC^*$  is oxidized to a radical cation  $PC^{+\bullet}$  after giving one electron to a substrate. To complete the catalytic cycle, PC needs to be regenerate by the reduction of  $PC^{+\bullet}$ . Cyclic voltammetry (CV) measurements were performed to investigate redox properties of the synthesized PC. The difference between the anodic ( $E_{pa}$ ) and cathodic ( $E_{pc}$ ) peak potentials  $\Delta E_p$  and the ratio of peak anodic current  $i_{pa}$  to peak current  $i_{pc}$  were shown in table 4.3. Compared to the theoretical value of  $\Delta E_p = 59$  mV and  $i_{pa}/i_{pc} = 1$  for a reversible system, CV applied to  $R^{PZ}$  and  $Zn_2R^{PZ}$  to analyze their oxidation potentials showed a quasi-reversible wave in DMSO (Figure 4.15), implying a reversible  $PC^{+\bullet}/PC$  state.<sup>[25]</sup> CV of  $L^{PZ}$  was also performed at different scan rates ranging from 20 mV/s to 100 mV/s (Figure 4.43). A linear relationship between the anodic peak current ( $I_a$ ) and square root of the scan rate ( $V^{1/2}$ ) was observed, indicating that the electron transfer process is diffusion-controlled. The ground state oxidation potentials of the PCs ( $E^0_{ox}$ ) were approximated from the half wave potential  $E^0_{1/2}$ . They were obtained from the voltammograms as the half sum of anodic ( $E_{pa}$ ) and cathodic ( $E_{pc}$ ) peak potentials, where  $E^0_{ox, PC^{+\bullet}/PC} \approx E_{1/2, PC^{+\bullet}/PC} = (E_{pa} + E_{pc}) / 2$ <sup>[27]</sup> As shown in Table 4.2,  $Zn_2R^{PZ}$  is more easily oxidized ( $E_{1/2} = \sim 0.47$  V vs  $Ag^+/Ag$ ) than  $L^{PZ}$  ( $E_{1/2} = \sim 0.52$  V vs  $Ag^+/Ag$ ).

#### 4. Phenoxazine-based macrocycles for Photoredox catalysis

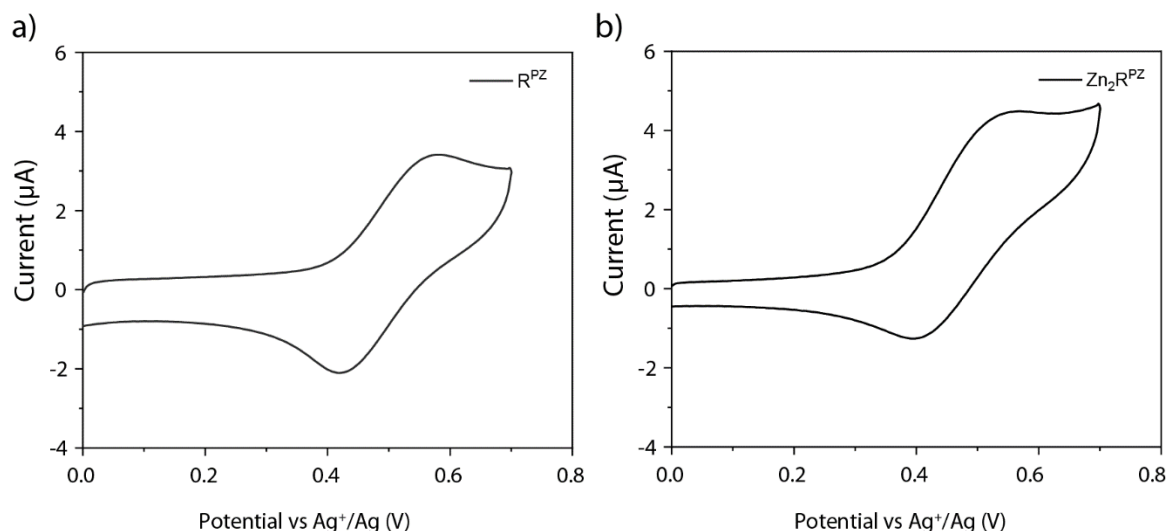


Figure 4.15: Cyclic voltammograms of a)  $\mathbf{R}^{\text{PZ}}$  and b)  $\mathbf{Zn}_2\mathbf{R}^{\text{PZ}}$  measured with scan rate: 100 mV/s in DMSO solution (0.5 mM) with 0.1 M TBAPF<sub>6</sub> as an electrolyte.

Table 4.2: Cyclic voltammetry results

	$E_{\text{pa}}$ (V)	$E_{\text{pc}}$ (V)	$\Delta E_{\text{p}}$ (mV)	$E_{1/2}$ vs $\text{Ag}^+/\text{Ag}$ (V)	$i_{\text{pa}}/i_{\text{pc}}$
$\mathbf{L}^{\text{PZ}}$	0.57	0.47	100	0.52	1.68
$\mathbf{R}^{\text{PZ}}$	0.56	0.42	140	0.49	1.28
$\mathbf{Zn}_2\mathbf{R}^{\text{PZ}}$	0.54	0.40	140	0.47	1.37

In the reaction, PC acts as excited state reductant. The triplet excited state reduction potentials of the PCs are estimated by:  $E_{\text{ox},\text{T}1}^*(\text{PC}^{*+}/\text{PC}^*) = E_{\text{ox}}^0 - E_{\text{T}1}^*$ , where  $E_{\text{T}1}^*$  is the triplet energy, which is often read from the maximum wavelength of phosphorescence and is approximated by the singlet energies  $E_{\text{S}1}^*$  ( $E_{\text{S}1}^*$  was calculated using the maximum wavelength of emission).<sup>[28]</sup>  $E_{\text{ox},\text{T}1}^*$  is more negative means the catalyst is more strongly reducing in the excited state. As shown in Table 4.3,  $\mathbf{Zn}_2\mathbf{R}^{\text{PZ}}$  is the strongest excited state reductant ( $E_{\text{ox},\text{T}1}^* = -1.78$  V vs  $\text{Ag}^+/\text{Ag}$ ).

Table 4.3: Oxidation potentials of cyclic voltammetry, singlet energy and calculated triplet state reduction potentials of PCs.

	$E_{1/2}$ vs $\text{Ag}^+/\text{Ag}$ (V)	$E_{\text{S}1}$ (eV)	$E_{\text{red},\text{T}1}^*$ (V)
$\mathbf{L}^{\text{PZ}}$	0.52	2.07	-1.55
$\mathbf{R}^{\text{PZ}}$	0.49	1.95	-1.46
$\mathbf{Zn}_2\mathbf{R}^{\text{PZ}}$	0.47	2.25	-1.78

#### 4.4 Photoredox catalysis

PCs can convert visible light into chemical energy through oxidation/reduction from the catalysts in excited states. As a result of the oxidation/reduction, the substrate forms a reactive radical species. For instance, pinacol coupling reactions occur catalyzed by PCs via formation of a ketyl radical as an intermediate. The generation of a ketyl radical by visible light was first reported by Kellogg and co-workers in 1979.<sup>[31]</sup> After then, a variety of photoredox reactions have been used for C-C bond formation with aldehydes and ketones as substrates.<sup>[32]</sup>

A photocatalytic pinacol coupling has been reported by Rueping and co-workers.<sup>[33]</sup> Pinacol coupling is a reductive coupling reaction of carbonyl compounds proceeding through formation and dimerization of two ketyl radicals to obtain 1,2-diols in one step. Pinacol coupling is a useful method to synthesize a diol-motif. In particular, [Ir(III)] and [Ru(II)] complexes, organic dyes, and semi-conductors have been used in photoredox-mediated pinacol coupling. Normally, homo-coupling reactions of such ketyl radicals is neither diastereo- nor enantio-selective due to loss of the stereo information by in the intermediate the radical state. On the other hand, asymmetric pinacol coupling reactions can be achieved with high enantiocontrol by choosing an appropriate chiral catalyst.<sup>[32]</sup>

Pinacol coupling reactions of simple aldehydes have been chosen as a test reaction to examine the photocatalytic ability of the synthesized ligand and macrocycles (Figure 4.16).

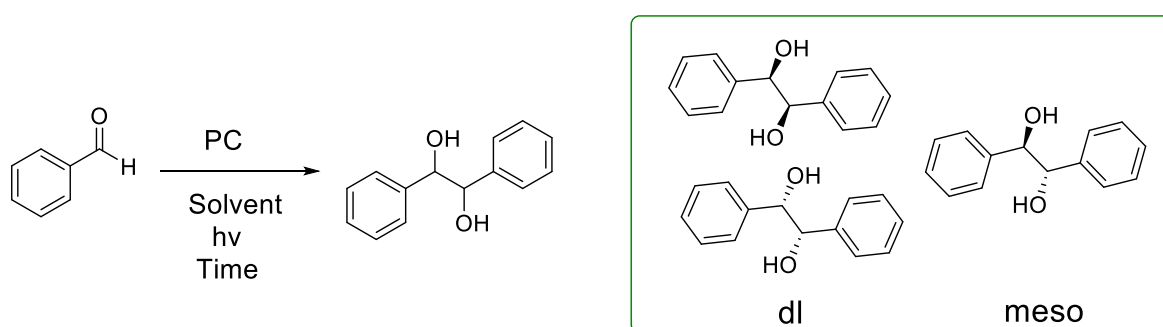


Figure 4.16: Scheme of pinacol coupling reaction of benzaldehyde via photocatalysis

Firstly, 4-(Trifluoromethyl)benzaldehyde (**S-CF<sub>3</sub>**) was chosen as a substrate to find an optimal condition for the photoredox pinacol coupling reaction (Table 4.4). The

#### 4. Phenoxazine-based macrocycles for Photoredox catalysis

reaction was performed in two solvents, DMSO-*d*<sub>6</sub> and CD<sub>3</sub>CN. DIPEA was used as a sacrificial oxidant. Since all the PCs (**L**<sup>PZ</sup>, **R**<sup>PZ</sup>, **Zn<sub>2</sub>R**<sup>PZ</sup>) have a maximum absorption at around 420 nm, a LED light source (420 nm) was used for the irradiation.

In DMSO, 2.5 mol% PCs was loaded (5 mol% for ligand to balance the number of phenoxazine core) in a reaction system in the presence of DIPEA. The results are summarized in Table 4.3. As a result, all the reactions yielded a complete conversion after irradiating for 16 h. The PCs have shown a good performance for the photoredox reaction. However, no diastereo-selectivity was observed confirmed by <sup>1</sup>H NMR integration ratio of the signal of the *dll* and *meso* 1,2-diol products. Formation of the products was not observed in the <sup>1</sup>H NMR spectrum without the LED irradiation. The reactions without any PC only gave traces of the 1,2-diol product suggesting a crucial role of the PCs for the reaction. In addition, DIPEA was proven to play an important role for the reaction. The yields reached only 31%-52% in the absence of DIPEA.

The reaction completed with a shorter reaction time (10 h) using **R**<sup>PZ</sup> or **Zn<sub>2</sub>R**<sup>PZ</sup> as a photoredox catalyst. On the other hand, with **L**<sup>PZ</sup>, only 65% yield was obtained after 10 h, indicating the less efficient catalytic ability of **L**<sup>PZ</sup> than the macrocycles. When the reaction time was even shortened to 5 h, the reaction loading **R**<sup>PZ</sup> or **Zn<sub>2</sub>R**<sup>PZ</sup> yielded only 14% of the desired products.

Since PCs have a limited solubility in CD<sub>3</sub>CN, all the reaction in CD<sub>3</sub>CN have a lower yield than in DMSO. Therefore, the further substrate scope study has been conducted in DMSO.

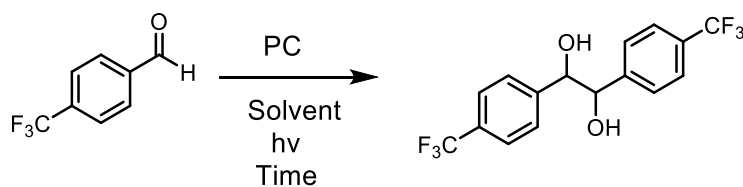


Table 4.4: Optimization of photoredox-catalyzed pinacol coupling of **S-CF3**.

Entry	PC <sup>a</sup>	DIPEA (eq)	Solvent	Light (nm)	Time (h)	Yield <sup>b</sup> (%)	<i>meso</i> : <i>dl</i> <sup>c</sup>
1	-	6	DMSO- <i>d</i> <sub>6</sub>	420	16	2.4	53.9:46.1
2	<b>L</b> <sup>PZ</sup>	-	DMSO- <i>d</i> <sub>6</sub>	420	16	35	53.6:46.4

#### 4. Phenoxazine-based macrocycles for Photoredox catalysis

3	<b>L<sup>PZ</sup></b>	6	DMSO- <i>d</i> <sub>6</sub>	420	16	100	52.7:47.3
4	<b>L<sup>PZ</sup></b>	6	DMSO- <i>d</i> <sub>6</sub>	daylight	16	-	-
5	<b>L<sup>PZ</sup></b>	6	DMSO- <i>d</i> <sub>6</sub>	dark	16	-	-
6	-	6	CD <sub>3</sub> CN	420	16	-	-
7	<b>L<sup>PZ</sup></b>	-	CD <sub>3</sub> CN	420	16	-	-
8	<b>L<sup>PZ</sup></b>	6	CD <sub>3</sub> CN	420	16	26	53.6:46.4
9	<b>L<sup>PZ</sup></b>	6	CD <sub>3</sub> CN	daylight	16	-	-
10	<b>L<sup>PZ</sup></b>	6	CD <sub>3</sub> CN	dark	16	-	-
11	<b>L<sup>PZ</sup></b>	6	DMSO- <i>d</i> <sub>6</sub>	420	10	65	50.8:49.2
12	<b>R<sup>PZ</sup></b>	-	DMSO- <i>d</i> <sub>6</sub>	420	16	31	51.6:48.4
13	<b>R<sup>PZ</sup></b>	6	DMSO- <i>d</i> <sub>6</sub>	420	16	100	51.2:48.8
14	<b>R<sup>PZ</sup></b>	6	DMSO- <i>d</i> <sub>6</sub>	420	10	100	51.8:48.2
15	<b>R<sup>PZ</sup></b>	6	DMSO- <i>d</i> <sub>6</sub>	daylight	16	-	-
16	<b>R<sup>PZ</sup></b>	6	DMSO- <i>d</i> <sub>6</sub>	dark	16	-	-
17	<b>R<sup>PZ</sup></b>	-	CD <sub>3</sub> CN	420	16	-	-
18	<b>R<sup>PZ</sup></b>	6	CD <sub>3</sub> CN	420	16	45	54.5:45.5
19	<b>R<sup>PZ</sup></b>	6	CD <sub>3</sub> CN	daylight		-	-
20	<b>Zn<sub>2</sub>R<sup>PZ</sup></b>	-	DMSO- <i>d</i> <sub>6</sub>	420	16	52	53.8:46.2
21	<b>Zn<sub>2</sub>R<sup>PZ</sup></b>	6	DMSO- <i>d</i> <sub>6</sub>	420	16	100	51.4:48.2
22	<b>Zn<sub>2</sub>R<sup>PZ</sup></b>	6	DMSO- <i>d</i> <sub>6</sub>	daylight	16	-	-
23	<b>Zn<sub>2</sub>R<sup>PZ</sup></b>	6	DMSO- <i>d</i> <sub>6</sub>	420	10	100	51.0:49.0
24	<b>Zn<sub>2</sub>R<sup>PZ</sup></b>	6	CD <sub>3</sub> CN	420	16	-	-
25	<b>Zn<sub>2</sub>R<sup>PZ</sup></b>	6	CD <sub>3</sub> CN	daylight	16	-	-

<sup>a</sup> If no mentioned, the amount of PC used for the photocatalysis: **L<sup>PZ</sup>**- 5 mol%; **R<sup>PZ</sup>** - 2.5 mol%; **Zn<sub>2</sub>R<sup>PZ</sup>**- 2.5 mol%.

<sup>b</sup> Yields were estimated by <sup>1</sup>H NMR analyses using 1,3,5-trimethoxybenzene as an internal standard.

<sup>c</sup> The absolute configuration of product was determined according to the literature and the ratio was determined by the <sup>1</sup>H NMR integration ratio.

The pinacol coupling reaction with different substrates was also performed under the optimized reaction condition (Figure 4.17). As a result, consistent results were obtained for all the substrates (Table 4.5). All the PCs were found to work well as in the photoredox pinacol coupling reaction with the variety of substrates. In addition, **R<sup>PZ</sup>** and **Zn<sub>2</sub>R<sup>PZ</sup>** showed a higher reaction rate compared with the ligand.

#### 4. Phenoxazine-based macrocycles for Photoredox catalysis

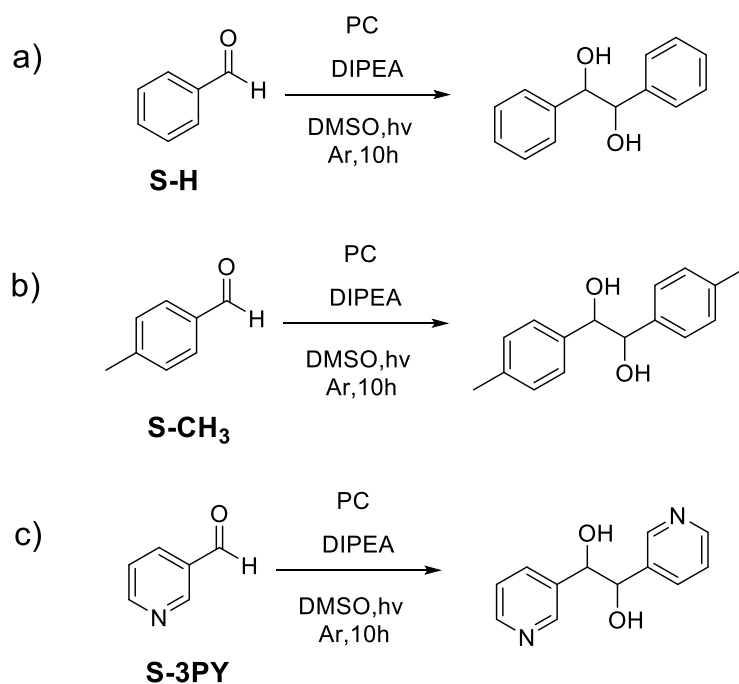
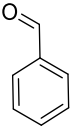
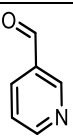
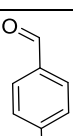


Figure 4.17: Scope of pinacol coupling reaction of other aldehydes derivative as substrates.

Table 4.5: Photoredox-catalyzed pinacol coupling of aldehydes.

Substrate	PC	DIPEA(eq)	Light (nm)	yield	<i>meso:dl</i>
	-	6	420, 16h	trace	52.6:47.4
	<b>L<sup>PZ</sup></b>	6	420, 16h	100	50.8:49.2
	<b>R<sup>PZ</sup></b>	6	420, 16h	100	51.8:48.2
	<b>Zn<sub>2</sub>R<sup>PZ</sup></b>	6	420, 16h	92	46.8:53.2
	-	6	420, 10h	trace	50.8:49.2
	<b>L<sup>PZ</sup></b>	6	420, 10h	65	51.6:48.4
	<b>R<sup>PZ</sup></b>	6	420, 10h	94	51.9:48.1
	<b>Zn<sub>2</sub>R<sup>PZ</sup></b>	6	420, 10h	100	52.4:47.6
	<b>L<sup>PZ</sup></b>	6	420, 10h	82	48.8:51.2
	<b>R<sup>PZ</sup></b>	6	420, 10h	100	49.7:50.3
	<b>Zn<sub>2</sub>R<sup>PZ</sup></b>	6	420, 10h	100	49.5:50.5

#### 4. Phenoxazine-based macrocycles for Photoredox catalysis

Based on these results and corresponding literature,<sup>[7]</sup> we propose the reaction mechanism as depicted in Figure 4.18. In the reaction system, upon the irradiation with visible light, the PC was excited to PC\*. Aldehydes should be reduced to a corresponding reactive ketal radical by a single electron transfer from the PC\*, and consequently, a C-C bond is formed. After dimerization and protonation, the 1,2-diols should be obtained. The generated PC<sup>•+</sup> should be restored to the ground state by reduction with DIPEA.

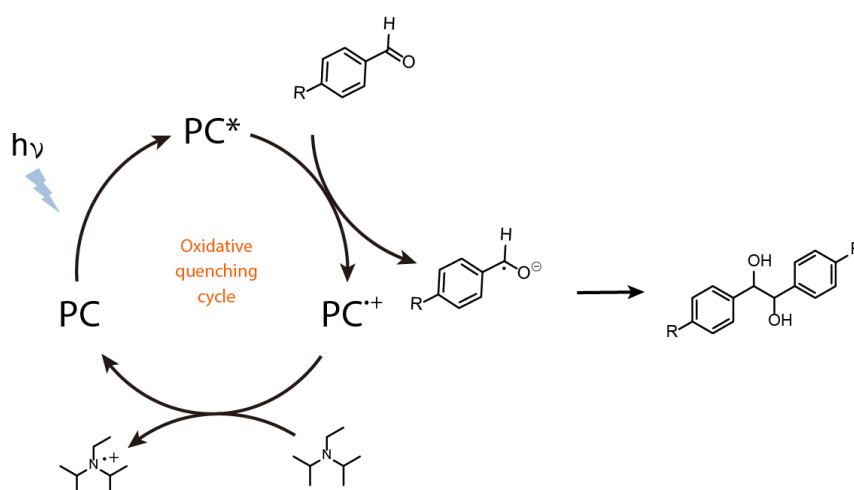


Figure 4.18: Proposed catalytic cycle for the photoredox-catalyzed pinacol coupling of aldehydes.

#### 4.5 Conclusion

A phenoxazine-based ligand, as metal free macrocycle and a Zn(II) salen macrocycle were designed and synthesized. Taking advantage of redox reversibility and strong visible-light absorption of the synthesized molecules, the photoredox-catalyzed pinacol coupling of aldehydes was achieved with high conversion with relatively low catalyst loading under mild reaction condition. Further investigations will be performed aiming for an asymmetric reaction using **Zn<sub>2</sub>R<sup>PZ</sup>** by taking advantage of the chirality implemented on the structure.

## 4. Phenoxazine-based macrocycles for Photoredox catalysis

### 4.6 Experimental part

#### 4.6.1 Materials

Unless otherwise stated, all chemicals and solvents were purchased from commercial companies (Abcr, Sigma Aldrich, Acros Organics, VWR and Chempur) and used as received.

#### 4.6.2 General Methods

##### NMR

NMR spectroscopic data was measured on the spectrometers Bruker AV 500 Avance NEO and Bruker AV 600 Avance III HD. Chemical shifts for  $^1\text{H}$  and  $^{13}\text{C}$  spectra are reported in ppm on the  $\delta$  scale relative to proton resonance resulting from incomplete deuteration of the solvents ( $\text{CDCl}_3$ : 7.26 ppm,  $\text{DMSO-d}_6$ : 2.5 ppm,  $\text{CD}_3\text{CN}$ : 1.94 ppm). The chemical shift  $\delta$  is given in ppm, the coupling constants  $J$  in Hz. The following abbreviations are used to describe signal multiplicity for  $^1\text{H}$  NMR spectra: s: singlet, d: doublet, t: triplet, dd: doublet of doublets, m: multiplet. All spectra were recorded in standard 5 mm NMR tubes at 298 K if not stated otherwise.

##### DOSY

$^1\text{H}$  DOSY spectra were recorded with a `dstebpgp3s` pulse sequence with diffusion delays  $D_{20}$  of 0.09-0.14 s and gradient powers  $P_{30}$  of 900-2500  $\mu\text{s}$  for each species optimized.<sup>[34]</sup> The hydrodynamic radius was calculated according to Stokes-Einstein equation<sup>[35]</sup>:

$$D = \frac{k_B T}{6\pi\eta r_H}$$

Where  $D$  is diffusional coefficient, calculated by using STEJSKAL-TANNER-Equation,  $k_B$  is the Boltzmann constant,  $T$  is the absolute temperature,  $\eta$  is the viscosity of solvent,  $r_H$  is the hydrodynamic radius.

##### ESI-MS

Electrospray ionization mass spectrometry (ESI-MS) experiments were performed on ESI-timsTOF (ESI-trapped ion mobility-time of flight) mass spectrometer by Bruker, equipped with and ESI source (positive/negative mode). An Agilent ESI low concentration tuning mix has been used for calibration of tims and TOF units. Mass



#### 4. Phenoxazine-based macrocycles for Photoredox catalysis

spectrometry data is given as mass/charge ratio ( $m/z$ ) as well as the relative intensity with regard to the base peak ( $I = 100$ ).

##### **UV-Vis**

UV-vis spectra were recorded on a DAD HP-8453 UV-Vis spectrometer. Cuvette path length 10 mm.

##### **Fluorescence**

Fluorescence spectra were recorded on a JASCO FP-8300 fluorimeter equipped with a (150W) Xe lamp as light source. Cuvette path length 10 mm in emission direction.

##### **FT-IR**

Fourier Transform Infrared (FT-IR) spectra were measured on Perkin Elmer Spectrum Two spectrometer in the 400-4,000  $\text{cm}^{-1}$  spectral region.

##### **CD**

Circular dichroism spectra were recorded on an Applied Photophysics Chirascan qCD Spectrometer with a temperature-controlled cuvette holder. The spectra were background-corrected and smoothed with a window size of 5.

##### **CV**

Cyclic voltammetry experiments were recorded on Metrohm Autolab PGSTAT101 potentiostat and analysed by using NOVA software ver. 2.1. All experiments were carried out by using a one compartment electrolysis cell consisting of a glassy carbon working electrode, a platinum wire counter electrode, and  $\text{Ag}^+/\text{Ag}$  reference electrode under  $\text{N}_2$  atmosphere. To a DMSO solution of each sample, 0.1 M tetrabutylammonium hexafluorophosphate ( $n\text{-Bu}_4\text{NPF}_6$ ) as supporting electrolyte.

## 4. Phenoxazine-based macrocycles for Photoredox catalysis

### 4.6.3 Synthesis of the macrocycles

#### Synthesis of 3,7-dibromo-1-naphthly-10-phenoxazine (**2Br-PZ**)

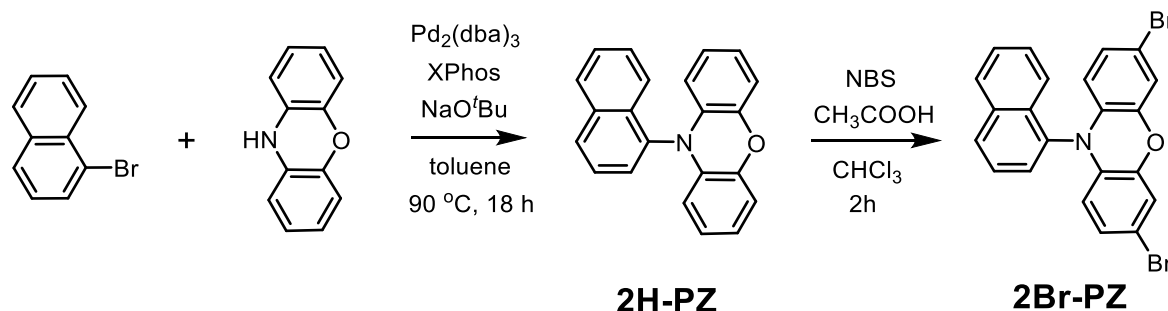


Figure 4.19: Synthesis route of **2Br-PZ**

The synthesis procedures of **2Br-PZ** were following the literature procedure.<sup>[27]</sup>

Phenoxazine (0.8 g, 4.37 mmol, 1 equiv.), 2-bromonaphthalene (1.22 mL, 8.74 mmol, 2.0 equiv.), sodium tert-butoxide (590 mg, 6.13 mmol, 1.4 equiv.) and XPhos (312 mg, 0.66 mmol, 0.15 equiv.) were combined in a 250 mL Schlenk tube and cycled under nitrogen and vacuum three times.  $\text{Pd}_2(\text{dba})_3$  was added under Ar. Then 20 mL degassed anhydrous toluene was added. The mixture was stirred at  $90\text{ }^\circ\text{C}$  for 18 h. After cooling to room temperature, the toluene was removed under reduced pressure. The reaction mixture was mixed with water (30 mL) and extracted with  $\text{CH}_2\text{Cl}_2$  (30 mL  $\times$  3). The organic layer was collected and dried over  $\text{MgSO}_4$ . The solvent was removed. The resulting solid was recrystallized from  $\text{CH}_2\text{Cl}_2/\text{MeOH}$  at  $-40\text{ }^\circ\text{C}$  to afford the product.

$^1\text{H}$  NMR (500 MHz,  $\text{DMSO}-d_6$ ):  $\delta$  8.15 (d,  $J = 8.3$  Hz, 1H), 8.12 (d,  $J = 6.8$  Hz, 1H), 7.92 (d,  $J = 8.4$  Hz, 1H), 7.79 – 7.72 (m, 1H), 7.67 (dd,  $J = 7.2, 1.2$  Hz, 1H), 7.61 (ddd,  $J = 8.1, 6.8, 1.3$  Hz, 1H), 7.54 (ddd,  $J = 8.2, 6.8, 1.3$  Hz, 1H), 6.78 (dd,  $J = 7.9, 1.5$  Hz, 2H), 6.65 (td,  $J = 7.7, 1.5$  Hz, 2H), 6.54 (td,  $J = 7.7, 1.5$  Hz, 2H), 5.60 (dd,  $J = 8.0, 1.5$  Hz, 2H).

$^{13}\text{C}$  NMR (151 MHz,  $\text{DMSO}-d_6$ ):  $\delta$  143.07, 135.35, 133.91, 133.74, 130.25, 129.40, 129.21, 129.08, 127.53, 127.23, 126.90, 123.79, 122.44, 121.47, 115.35, 113.00.

#### 4. Phenoxazine-based macrocycles for Photoredox catalysis

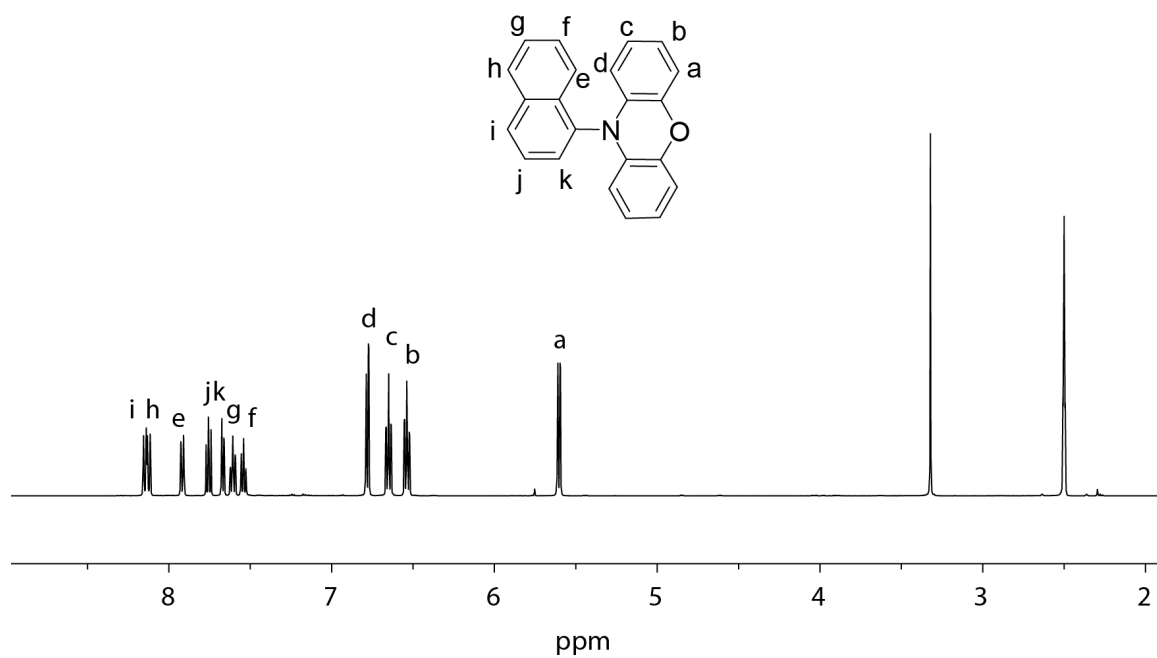


Figure 4.20: <sup>1</sup>H NMR spectrum of **2H-PZ** (500 MHz, 298 K, DMSO-*d*<sub>6</sub>).

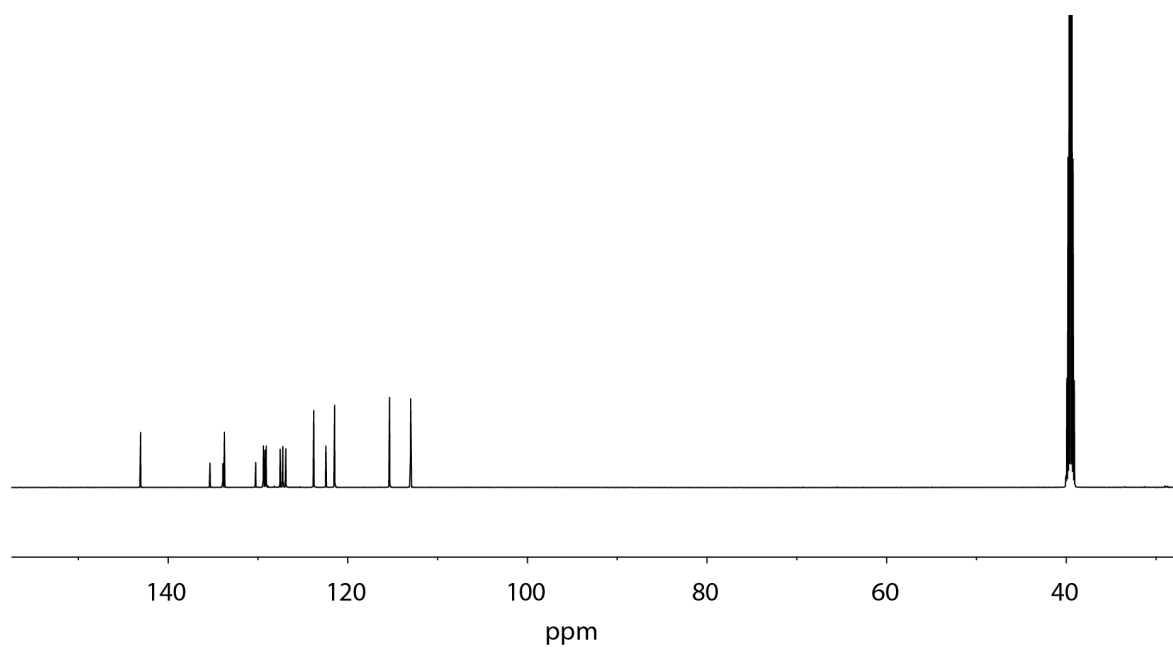


Figure 4.21: <sup>13</sup>C NMR spectrum of **2H-PZ** (126 MHz, 298 K, DMSO-*d*<sub>6</sub>).

#### 4. Phenoxazine-based macrocycles for Photoredox catalysis

**2H-PZ** (500 mg, 1.60 mmol, 1 equiv.) was dissolved in 20 mL of acetic acid and 20 mL of chloroform in a 250 mL flask. NBS (635 mg, 3.56 mmol, 2.2 equiv.) was added portion-wise over 20 mins. The mixture was stirred at room temperature for 2 h. The reaction mixture was mixed with water. The organic layer was collected and dried over  $\text{MgSO}_4$ . Solvent was removed under reduced pressure and **2Br-PZ** was yield as brown solid

$^1\text{H}$  NMR (500 MHz,  $\text{DMSO-}d_6$ ):  $\delta$  8.17 (dd,  $J = 8.4, 1.1$  Hz, 1H), 8.13 (dd,  $J = 8.1, 1.3$  Hz, 1H), 7.93 (dd,  $J = 8.4, 1.1$  Hz, 1H), 7.76 (dd,  $J = 8.2, 7.2$  Hz, 1H), 7.70 (dd,  $J = 7.3, 1.2$  Hz, 1H), 7.63 (ddd,  $J = 8.1, 6.8, 1.3$  Hz, 1H), 7.60 – 7.54 (m, 1H), 6.99 (d,  $J = 2.2$  Hz, 2H), 6.75 (dd,  $J = 8.6, 2.2$  Hz, 2H), 5.52 (d,  $J = 8.5$  Hz, 2H).

$^{13}\text{C}$  NMR (126 MHz,  $\text{DMSO-}d_6$ ):  $\delta$  143.60, 135.36, 133.00, 132.91, 129.87, 129.77, 129.19, 129.04, 127.87, 127.33, 127.12, 126.80, 122.27, 118.11, 114.59, 112.10.

HR ESI-MS: Calculated for  $\text{C}_{22}\text{H}_{13}\text{NOBr}_2$ ,  $m/z$  467.9417  $[\text{M} + \text{H}]^+$ ,  
found: 467.9243

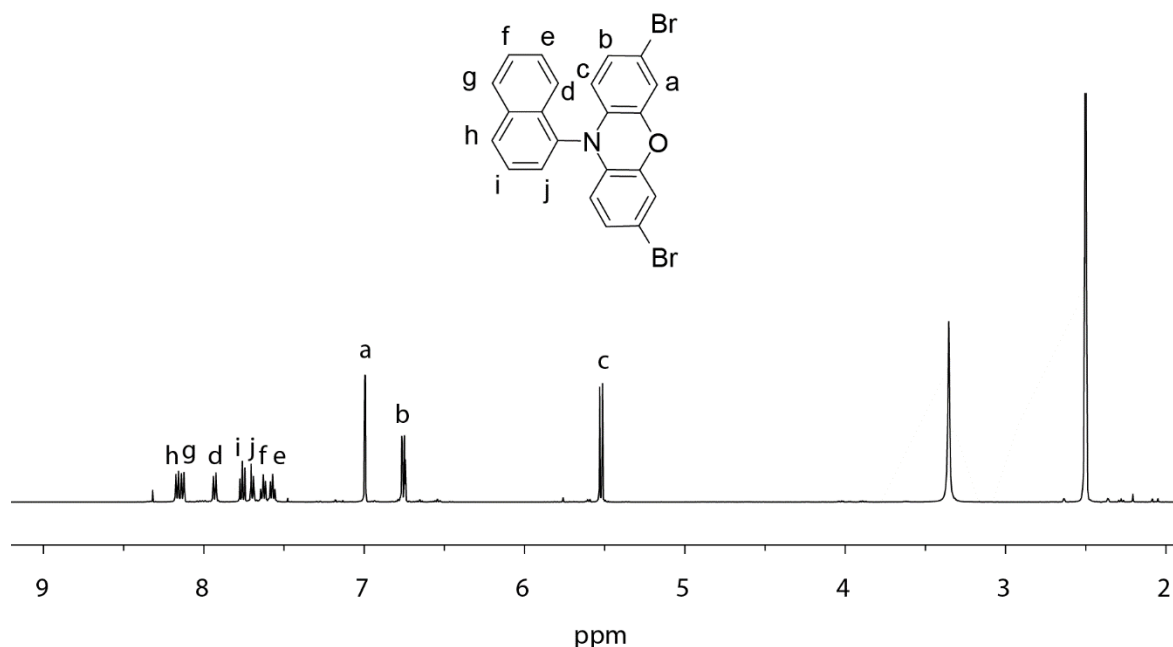


Figure 4.22:  $^1\text{H}$  NMR spectrum of **2Br-PZ** (500 MHz, 298 K,  $\text{DMSO-}d_6$ ).

#### 4. Phenoxazine-based macrocycles for Photoredox catalysis

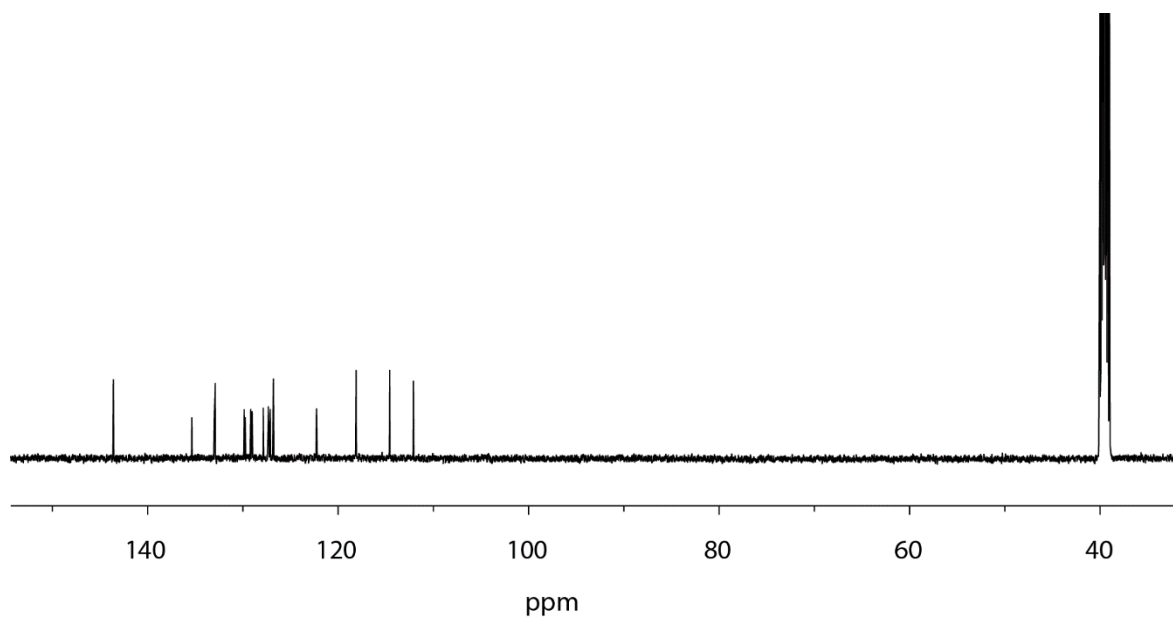


Figure 4.23:  $^{13}\text{C}$  NMR spectrum of **2Br-PZ** (126 MHz, 298 K, DMSO- $d_6$ ).

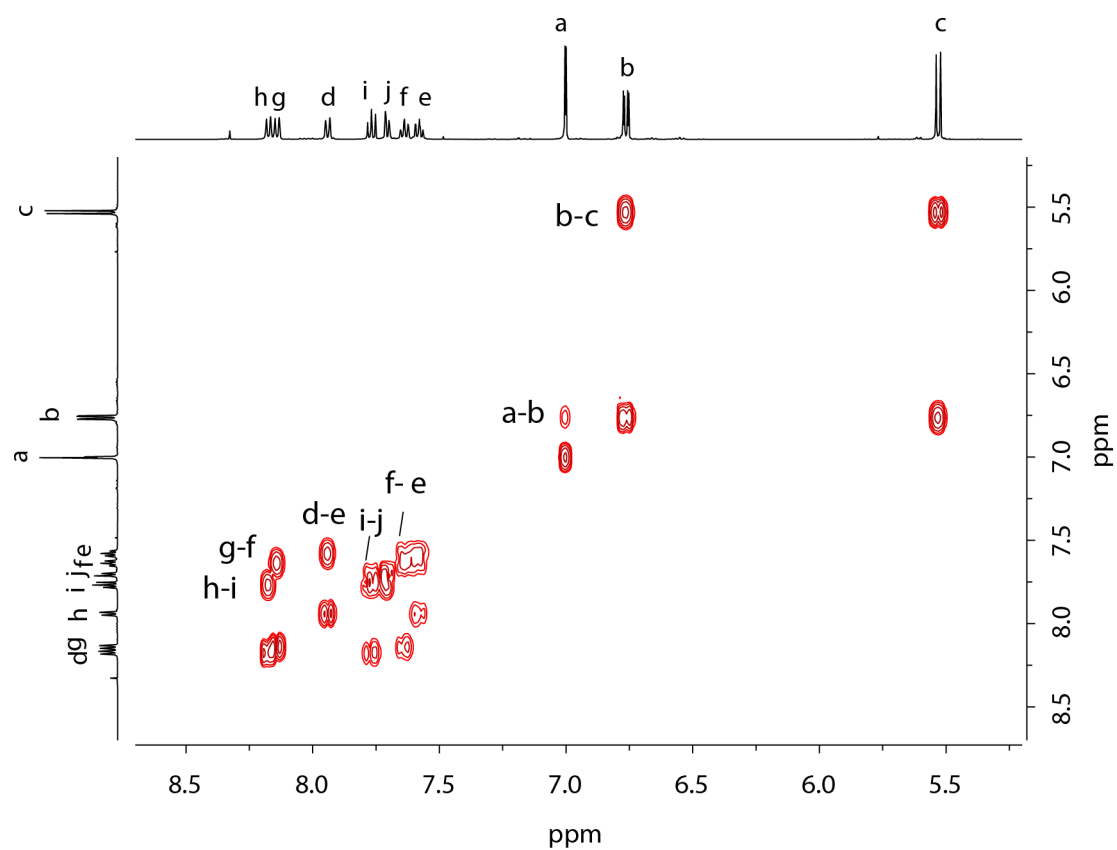
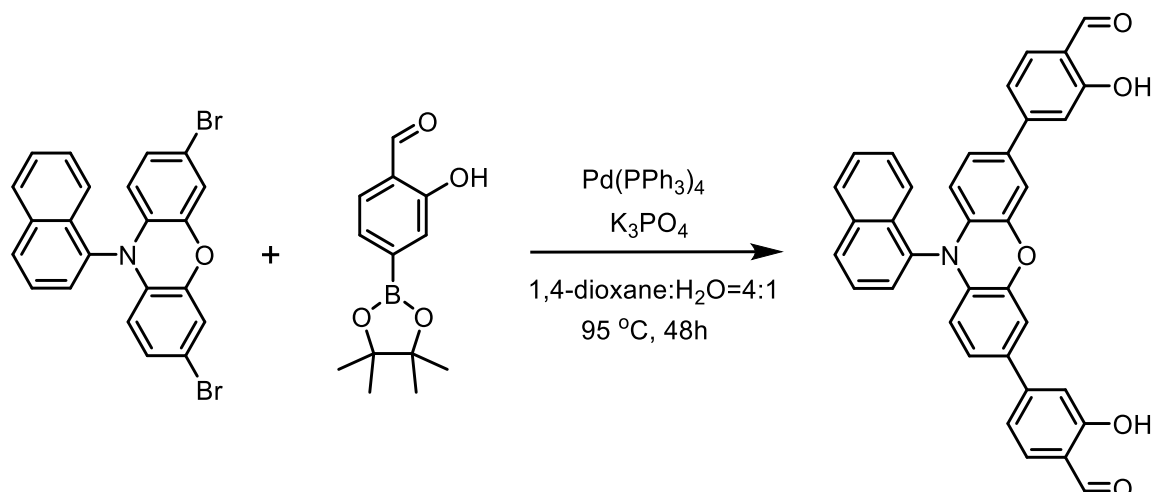


Figure 4.24:  $^1\text{H}$ - $^1\text{H}$  COSY spectrum of **2Br-PZ** (500 MHz, 298 K, DMSO- $d_6$ ).

#### 4. Phenoxazine-based macrocycles for Photoredox catalysis

##### Synthesis of L<sup>PZ</sup>



**2Br-PZ** (150 mg, 0.32 mmol, 1 equiv.), pinacol ester (200 mg, 0.8 mmol, 2.5 equiv.), K<sub>3</sub>PO<sub>4</sub> (245 mg, 1.16 mmol, 3.6 equiv.) were combined in a 100 mL Schlenk tube and cycled three times under vacuum and nitrogen. Then Tetrakis-(triphenylphosphine)palladium(0) (37 mg, 0.032 mmol, 0.1 equiv.) was added inside under Ar atmosphere. 20 mL degassed mixture solvents of 1,4-dioxane and water were added. The reaction was stirred at 95 °C for 48 h. After cooling down to room temperature, the solvents were evaporated. Then 30 mL 2 M HCl was added and extracted with CH<sub>2</sub>Cl<sub>2</sub> (30 mL × 3). The organic phase was collected and dried over MgSO<sub>4</sub>. Solvent was removed under reduced pressure. The crude product was purified by column chromatography (Chloroform:pentane = 2:1). The product was isolated as reddish brown solid (98 mg, Yield 55.5%).

<sup>1</sup>H NMR (500 MHz, DMSO-*d*<sub>6</sub>): δ 10.82 (s, 2H), 10.20 (s, 2H), 8.21 (d, *J* = 8.1 Hz, 1H), 8.17 (d, *J* = 8.2 Hz, 1H), 8.03 – 7.97 (m, 1H), 7.84 – 7.79 (m, 1H), 7.77 (dd, *J* = 7.2, 1.4 Hz, 1H), 7.68 (d, *J* = 8.2 Hz, 2H), 7.66 – 7.63 (m, 1H), 7.60 (ddd, *J* = 8.2, 6.8, 1.3 Hz, 1H), 7.19 (dd, *J* = 8.2, 1.7 Hz, 2H), 7.17 (d, *J* = 2.1 Hz, 2H), 7.12 (d, *J* = 1.7 Hz, 2H), 6.98 (dd, *J* = 8.4, 2.1 Hz, 2H), 5.74 (d, *J* = 8.4 Hz, 2H).

<sup>13</sup>C NMR (151 MHz, DMSO-*d*<sub>6</sub>): δ 191.37, 161.03, 146.44, 143.42, 135.32, 133.80, 133.20, 132.18, 130.20, 129.97, 129.83, 129.18, 129.01, 127.89, 127.31, 127.13, 122.75, 122.33, 120.87, 117.30, 113.66, 113.64, 113.61.

HR ESI-MS: Calculated for C<sub>36</sub>H<sub>23</sub>NO<sub>5</sub>, *m/z* 550.1649 [M + H]<sup>+</sup>,  
found: 550.1517

#### 4. Phenoxazine-based macrocycles for Photoredox catalysis

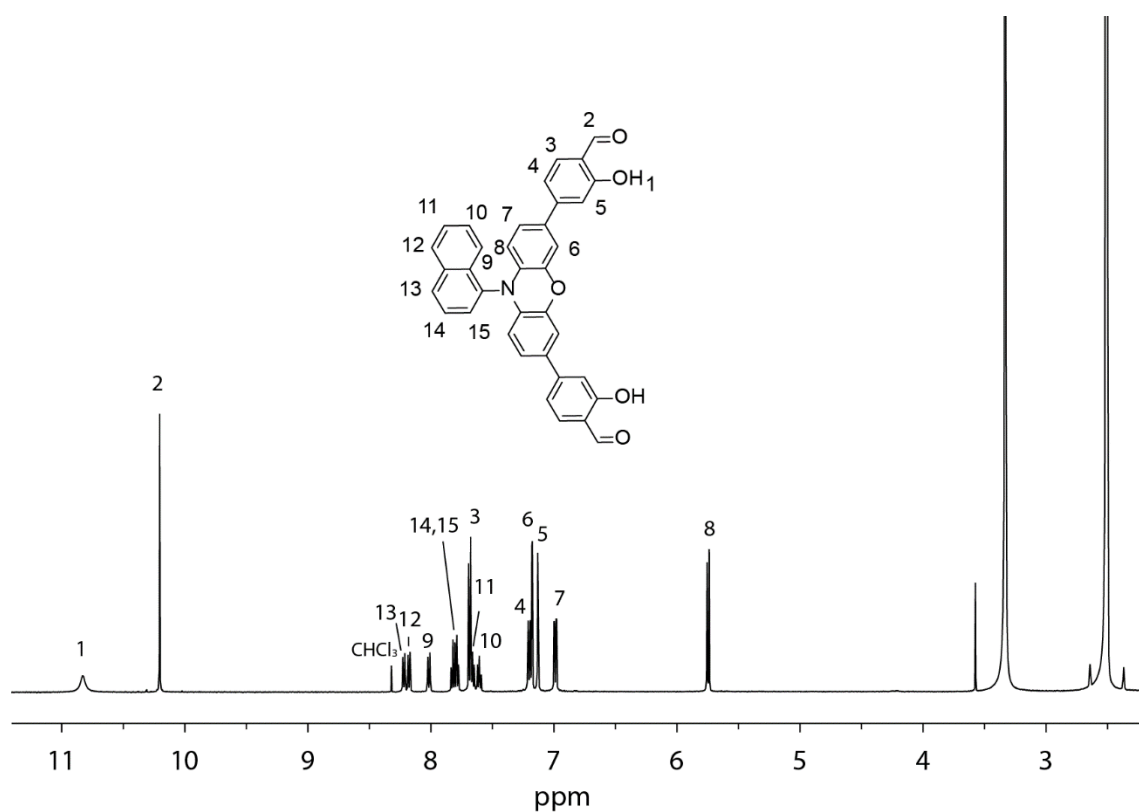


Figure 4.25:  $^1\text{H}$  NMR spectrum of  $\text{L}^{\text{PZ}}$  (500 MHz, 298 K,  $\text{DMSO-}d_6$ ).

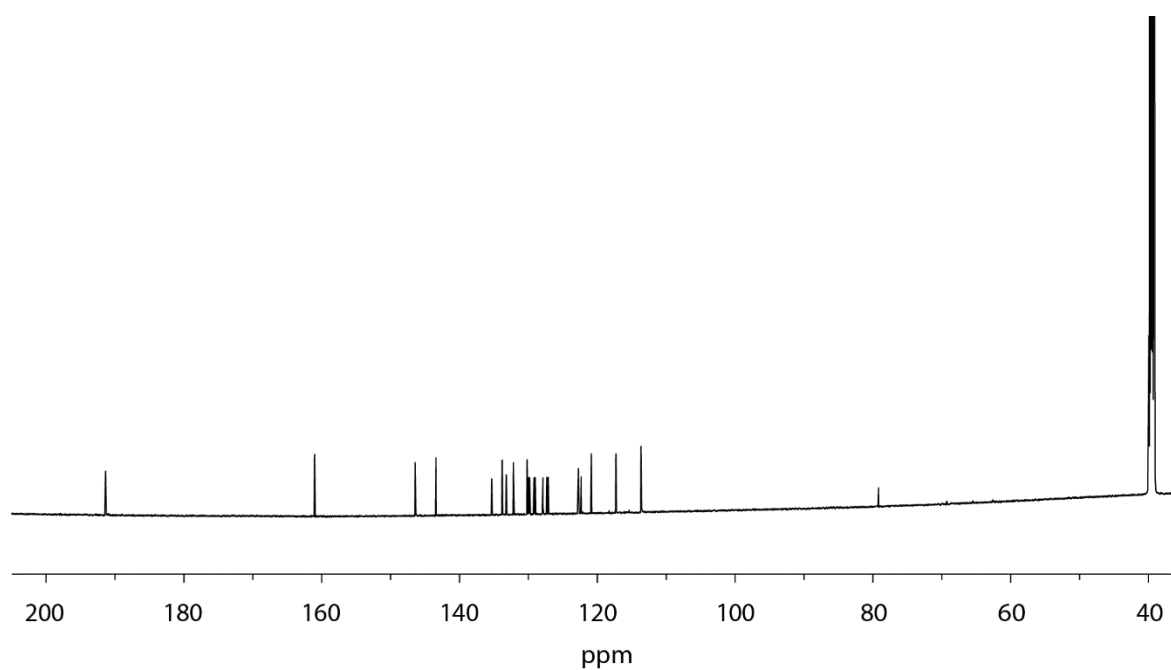


Figure 4.26:  $^{13}\text{C}$  NMR spectrum of  $\text{L}^{\text{PZ}}$  (151 MHz, 298 K,  $\text{DMSO-}d_6$ ).

#### 4. Phenoxazine-based macrocycles for Photoredox catalysis

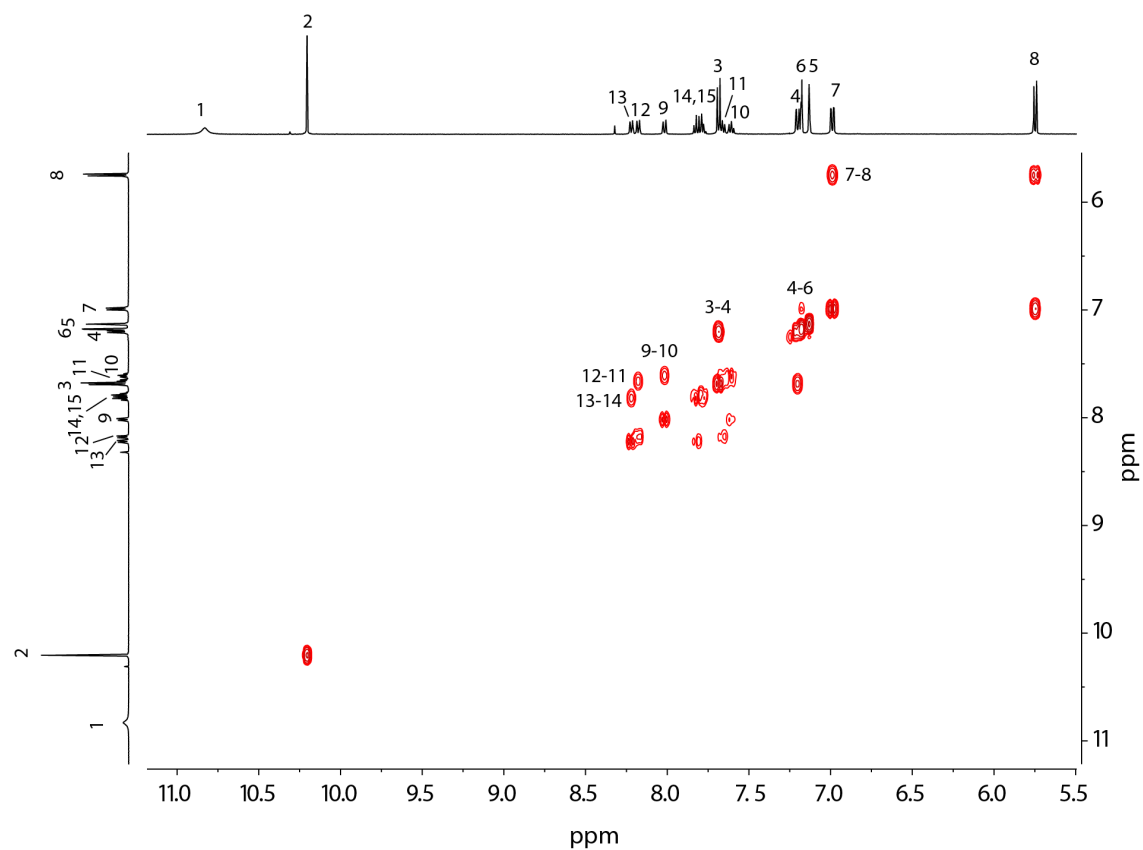


Figure 4.27:  $^1\text{H}$ - $^1\text{H}$  COSY spectrum of  $\text{L}^{\text{PZ}}$  (500 MHz, 298 K,  $\text{DMSO-}d_6$ ).

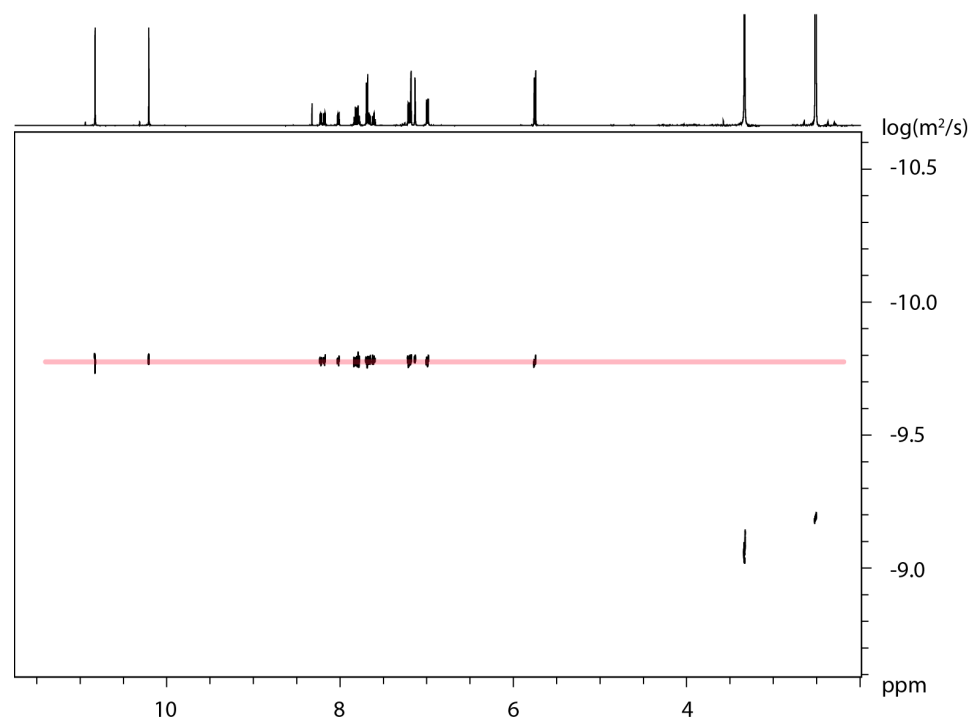
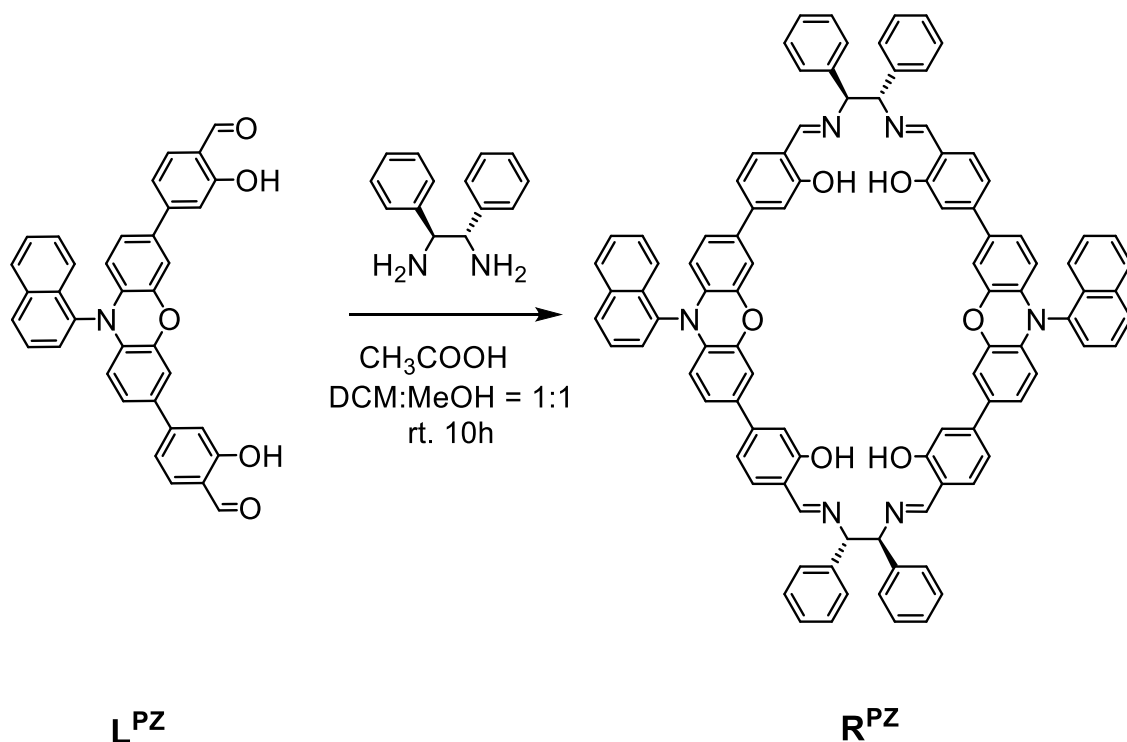


Figure 4.28: DOSY spectra of  $\text{L}^{\text{PZ}}$  (500 MHz, 298 K,  $\text{DMSO-}d_6$ ). Diffusion coefficient:  $D = 1.65 \times 10^{-10} \text{ m}^2\text{s}^{-1}$ ,  $r = 6.62 \text{ \AA}$ .



#### 4. Phenoxazine-based macrocycles for Photoredox catalysis

##### Synthesis of $R^{PZ}$



Ligand  $L^{PZ}$  (10 mg, 18.2  $\mu\text{mol}$ , 1.0 equiv.) and (1*S*,2*S*)-(-)-1,2-diphenyl-1,2-ethanediamine (4.7 mg, 21.9  $\mu\text{mol}$ , 1.2 equiv.) were dissolved in 2 mL mixture solvent of DCM/MeOH (1:1). After addition of  $\text{CH}_3\text{COOH}$  (20  $\mu\text{L}$ ), the solution was stirred at room temperature for 10 h. Then, the solvent was removed under reduced pressure. The residue was washed with anhydrous methanol ( $3 \times 1 \text{ mL}$ ) and dried under vacuum to provide the product as yellow powder in quantitative yield.

$^1\text{H}$  NMR (700 MHz,  $\text{DMSO-}d_6$ ):  $\delta$  13.40 (s, 4H), 8.62 – 8.52 (m, 4H), 8.18 (d,  $J = 8.1$  Hz, 2H), 8.14 (d,  $J = 7.6$  Hz, 2H), 8.01 – 7.96 (m, 2H), 7.78 (td,  $J = 7.6, 1.4$  Hz, 2H), 7.76 (dt,  $J = 7.3, 1.6$  Hz, 2H), 7.63 (ddt,  $J = 8.3, 6.7, 1.6$  Hz, 2H), 7.58 (dddd,  $J = 8.2, 6.8, 3.3, 1.3$  Hz, 2H), 7.39 (dt,  $J = 8.2, 5.1$  Hz, 4H), 7.33 (d,  $J = 6.8$  Hz, 8H), 7.26 (t,  $J = 7.6$  Hz, 8H), 7.19 (d,  $J = 7.4$  Hz, 4H), 7.17 (d,  $J = 2.1$  Hz, 4H), 7.05 (t,  $J = 2.2$  Hz, 4H), 7.04 (d,  $J = 4.2$  Hz, 4H), 6.92 (dd,  $J = 8.4, 2.3$  Hz, 4H), 5.69 (dt,  $J = 8.4, 2.7$  Hz, 4H), 5.11 (t,  $J = 2.8$  Hz, 4H).

$^{13}\text{C}$  NMR (151 MHz,  $\text{DMSO-}d_6$ ):  $\delta$  165.78, 160.71, 143.36, 143.17, 140.18, 135.28, 133.51, 133.41, 132.92, 132.21, 130.11, 129.70, 129.13, 129.04, 128.37, 127.94, 127.84, 127.45, 127.26, 127.07, 122.38, 122.25, 117.37, 116.66, 114.17, 113.50, 113.40, 77.54.

#### 4. Phenoxazine-based macrocycles for Photoredox catalysis

HR ESI-MS: Calculated for  $C_{100}H_{70}N_6O_6$ ,  $m/z$  726.7767  $[M + 2H]^{2+}$ ,  
found: 726.7740

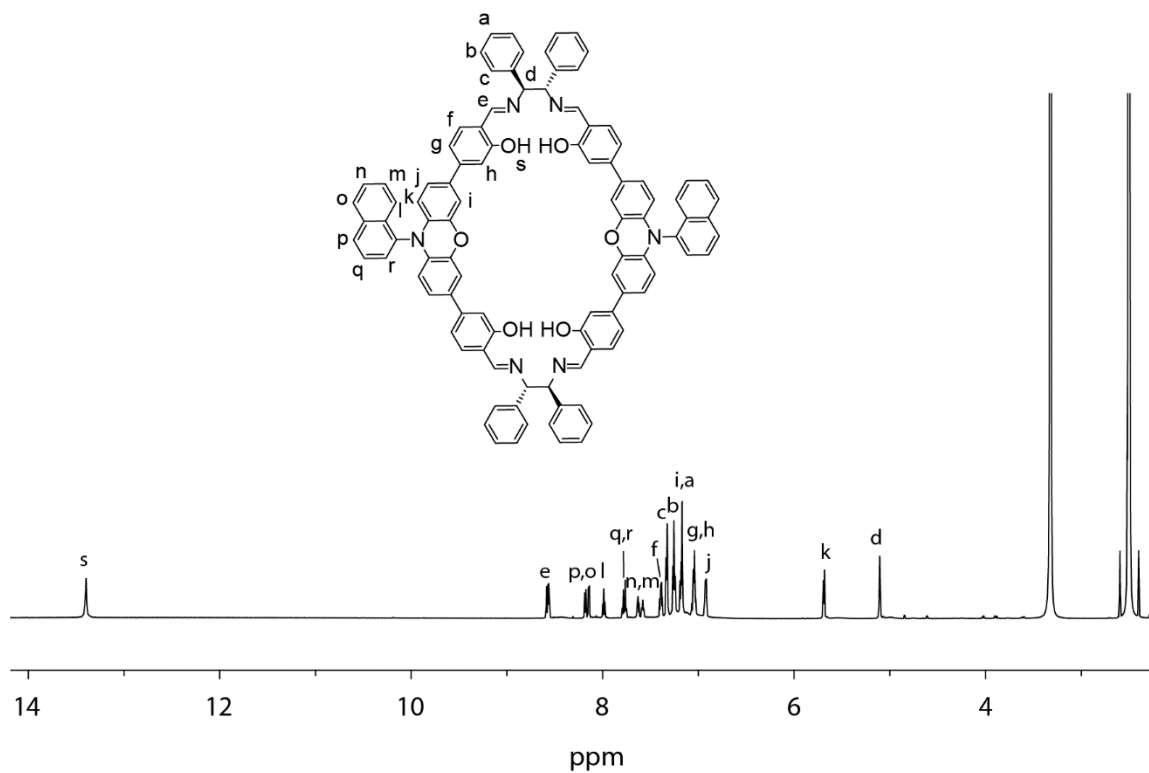


Figure 4.29:  $^1H$  NMR spectrum of  $R^{PZ}$  (700 MHz, 298 K,  $DMSO-d_6$ ).

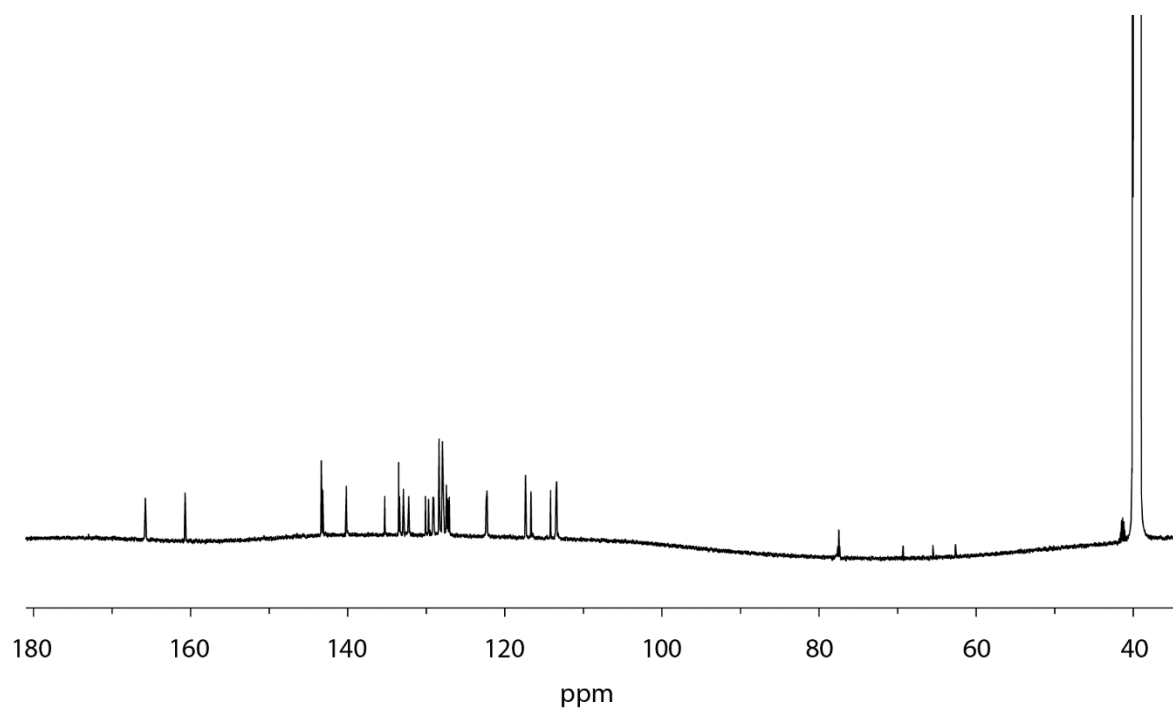


Figure 4.30:  $^{13}C$  NMR spectrum of  $R^{PZ}$  (151 MHz, 298 K,  $DMSO-d_6$ ).

#### 4. Phenoxazine-based macrocycles for Photoredox catalysis

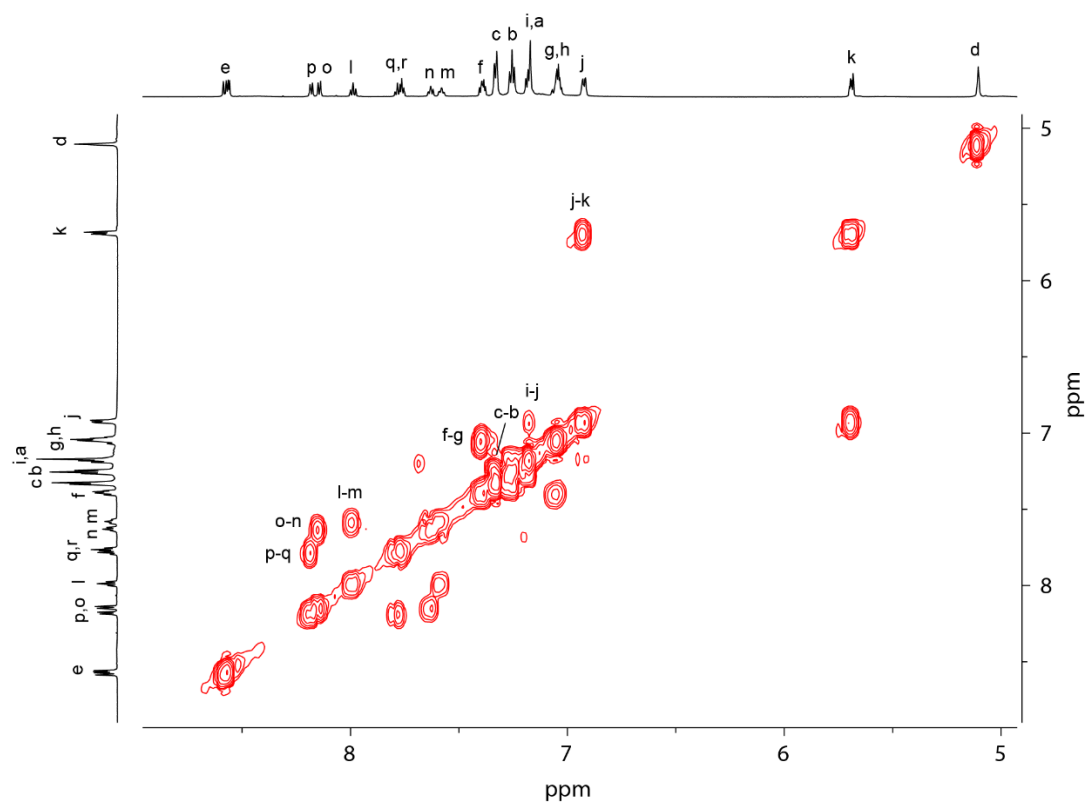


Figure 4.31:  $^1\text{H}$ - $^1\text{H}$  COSY spectrum of  $\text{R}^{\text{PZ}}$  (500 MHz, 298 K,  $\text{DMSO-d}_6$ ).

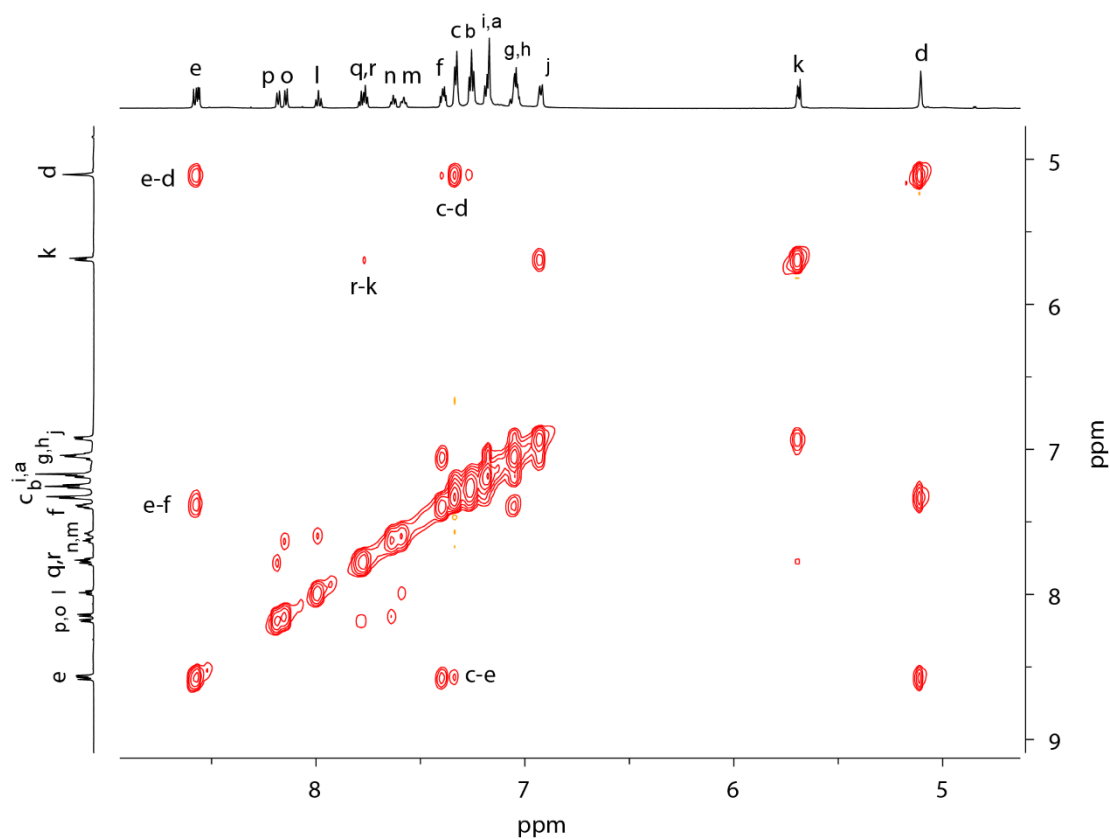
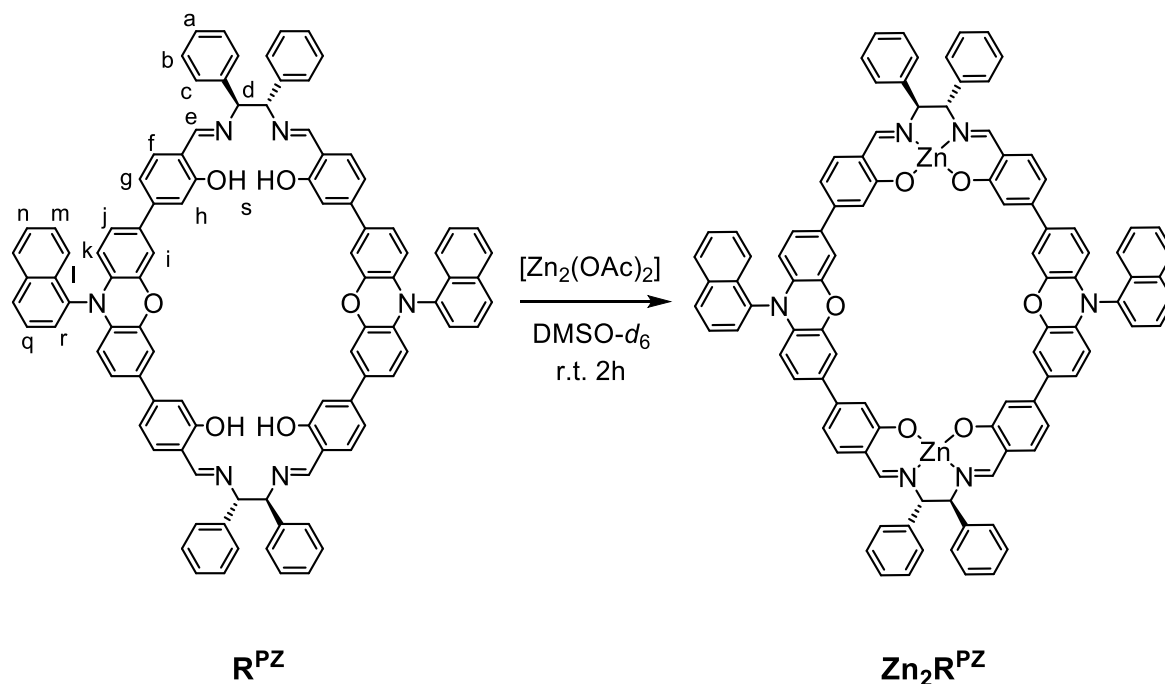


Figure 4.32:  $^1\text{H}$ - $^1\text{H}$  NOESY spectrum of  $\text{R}^{\text{PZ}}$  (500 MHz, 298 K,  $\text{DMSO-d}_6$ ).

#### 4. Phenoxazine-based macrocycles for Photoredox catalysis

##### Self-assembly of $\text{Zn}_2\text{R}^{\text{PZ}}$ .



$\text{R}^{\text{PZ}}$  (5 mg, 3.44  $\mu\text{mol}$ , 1 equiv.) was dissolved in  $\text{CHCl}_3$ ,  $[\text{Zn}(\text{OAc})_2]$  (86  $\mu\text{L}$ , 20 mg/mL, 2 equiv. in DMSO) was added. The mixture was stirred at room temperature for 2 h. After reaction, solvents were removed and crude product was dissolved in a minimal amount of DCM and precipitated with  $\text{Et}_2\text{O}$  to give the product (4.3 mg, 79.1% yield) as yellow solid.

$^1\text{H}$  NMR (500 MHz,  $\text{DMSO-}d_6$ ):  $\delta$  8.20 (dd,  $J = 5.4, 2.2$  Hz, 6H), 8.16 (d,  $J = 8.2$  Hz, 2H), 8.01 (d,  $J = 8.3$  Hz, 2H), 7.81 (t,  $J = 7.6$  Hz, 2H), 7.78 (dd,  $J = 7.4, 1.6$  Hz, 2H), 7.66 – 7.62 (m, 2H), 7.58 (dd,  $J = 8.6, 6.5$  Hz, 2H), 7.42 – 7.37 (m, 8H), 7.34 (t,  $J = 7.6$  Hz, 8H), 7.30 – 7.23 (m, 8H), 7.05 – 6.98 (m, 12H), 6.61 (dd,  $J = 8.2, 1.8$  Hz, 4H), 5.71 (dd,  $J = 8.3, 2.0$  Hz, 4H), 5.10 (s, 4H).

#### 4. Phenoxazine-based macrocycles for Photoredox catalysis

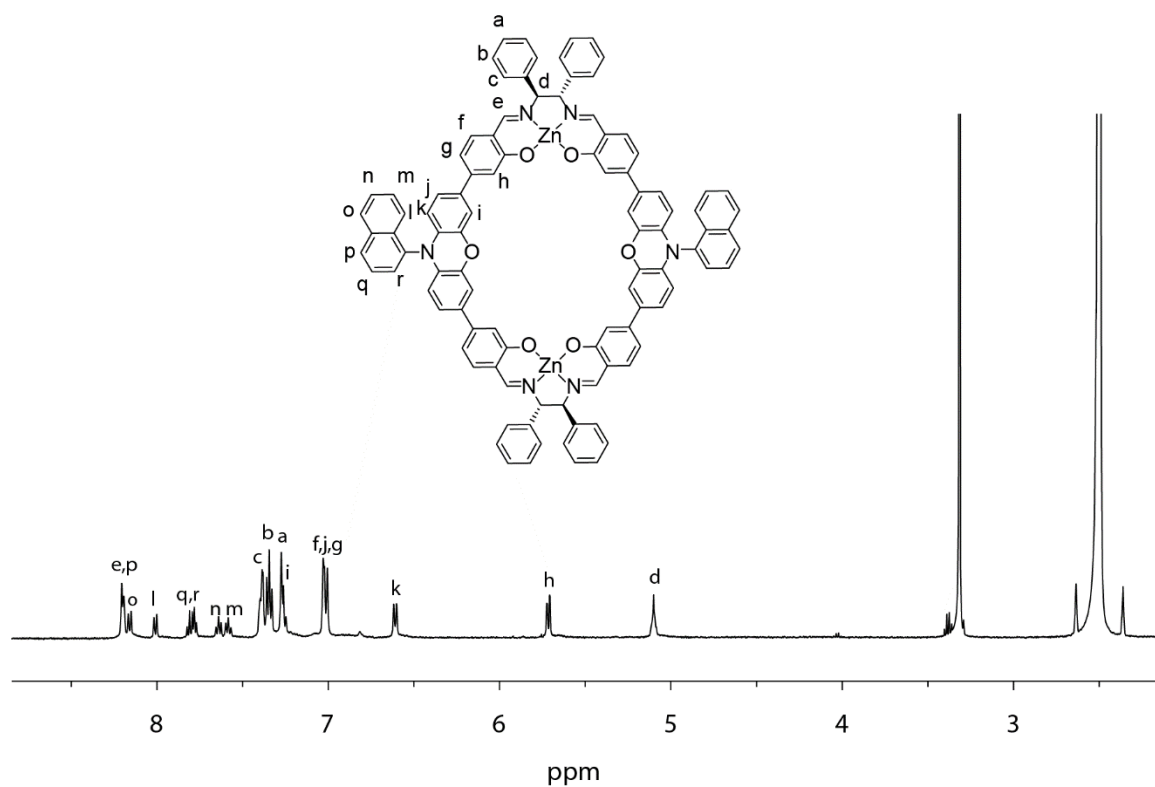


Figure 4.33:  $^1\text{H}$  NMR spectrum of  $\text{Zn}_2\text{R}^{\text{PZ}}$  (500 MHz, 298 K,  $\text{DMSO-}d_6$ ).

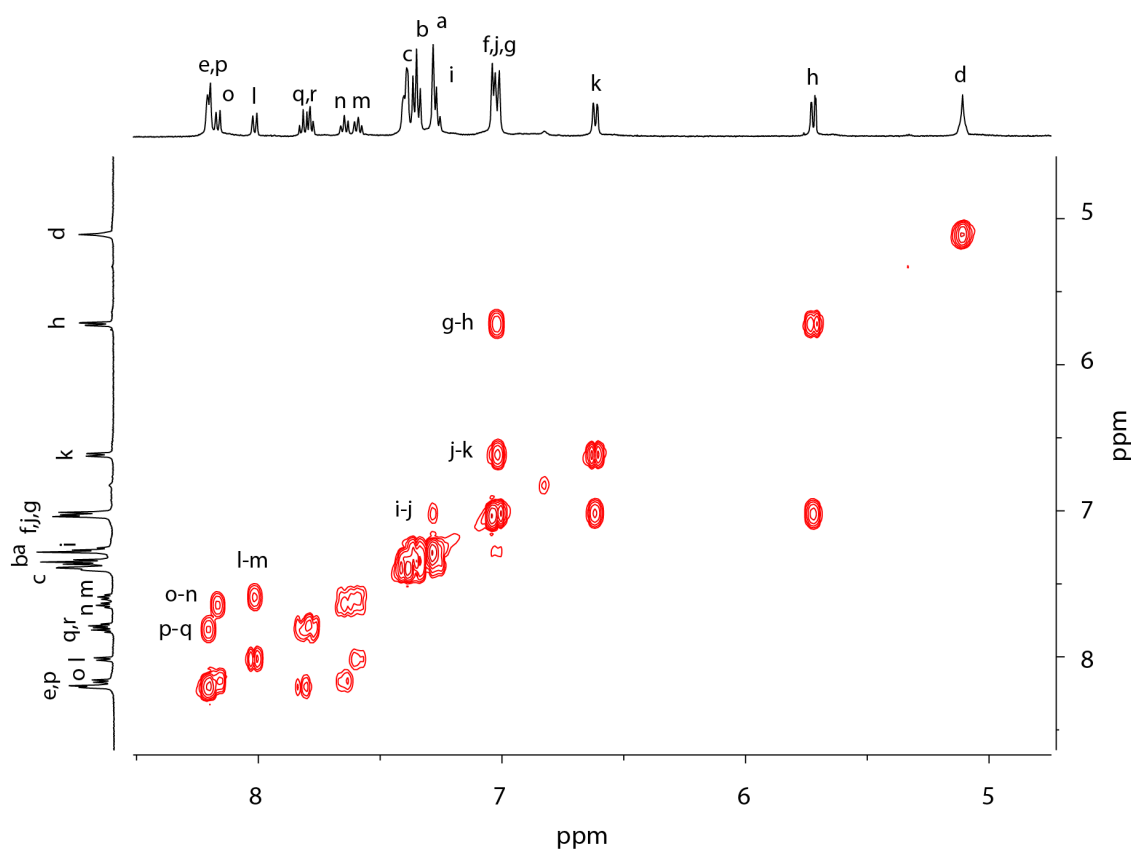


Figure 4.34:  $^1\text{H}$ - $^1\text{H}$  COSY spectrum of  $\text{Zn}_2\text{R}^{\text{PZ}}$  (500 MHz, 298 K,  $\text{DMSO-}d_6$ ).

#### 4. Phenoxazine-based macrocycles for Photoredox catalysis

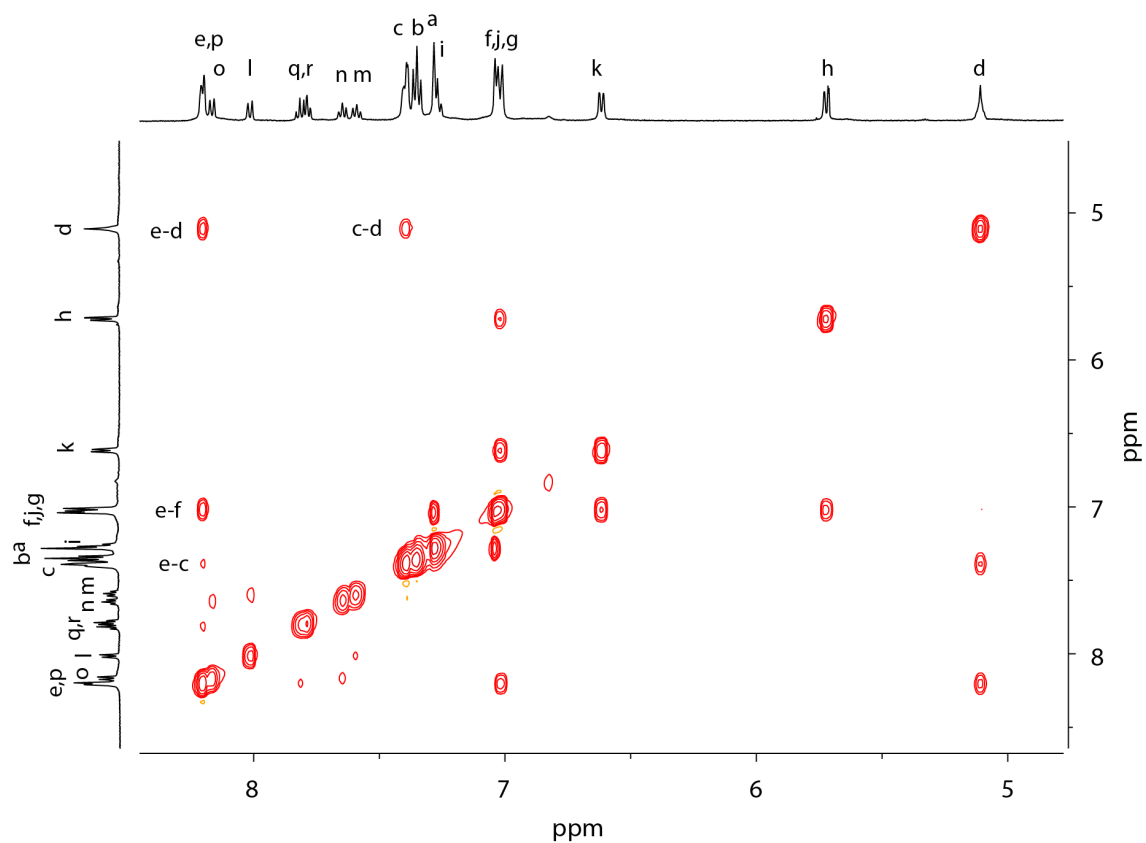


Figure 4.35:  $^1\text{H}$ - $^1\text{H}$  NOESY spectrum of  $\text{Zn}_2\text{R}^{\text{PZ}}$  (500 MHz, 298 K,  $\text{DMSO-d}_6$ ).

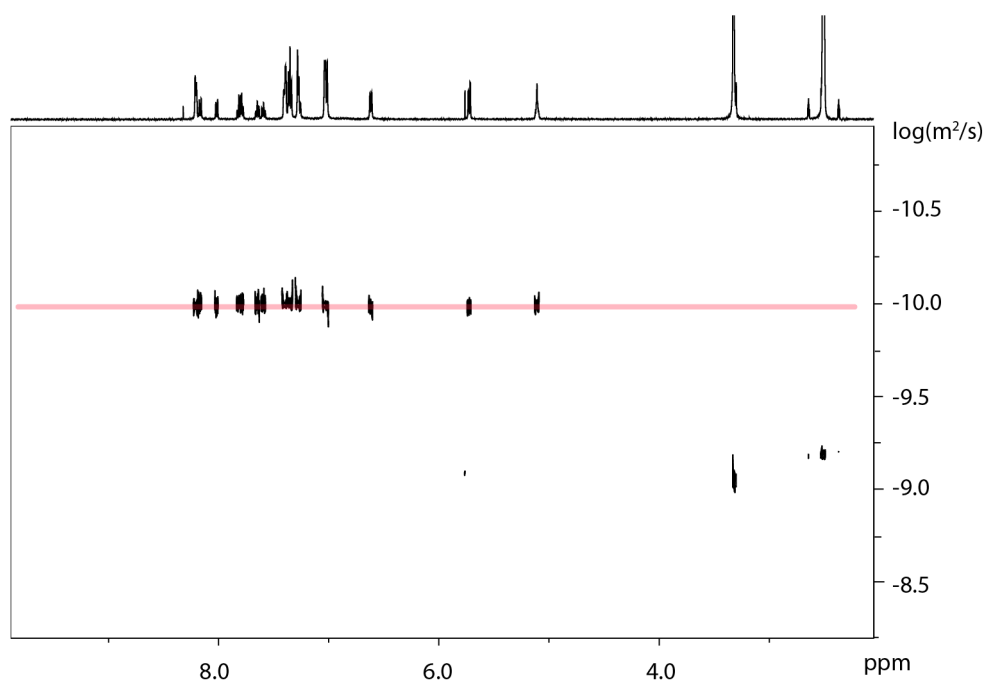


Figure 4.36: DOSY spectra of  $\text{Zn}_2\text{R}^{\text{PZ}}$  (500 MHz, 298 K,  $\text{DMSO-d}_6$ ). Diffusion coefficient:  $D = 1.0 \times 10^{-10} \text{ m}^2\text{s}^{-1}$ ,  $r = 10.9 \text{ \AA}$ .

#### 4. Phenoxazine-based macrocycles for Photoredox catalysis

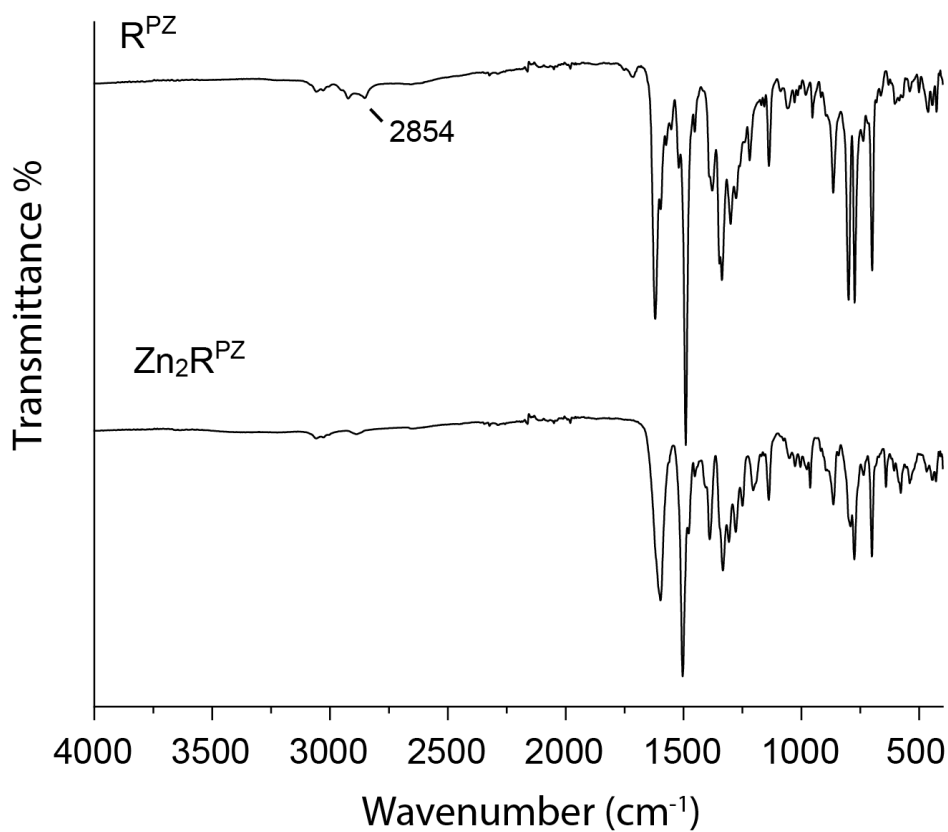


Figure 4.37: FT-IR spectra of  $R^{PZ}$  and  $Zn_2R^{PZ}$ .

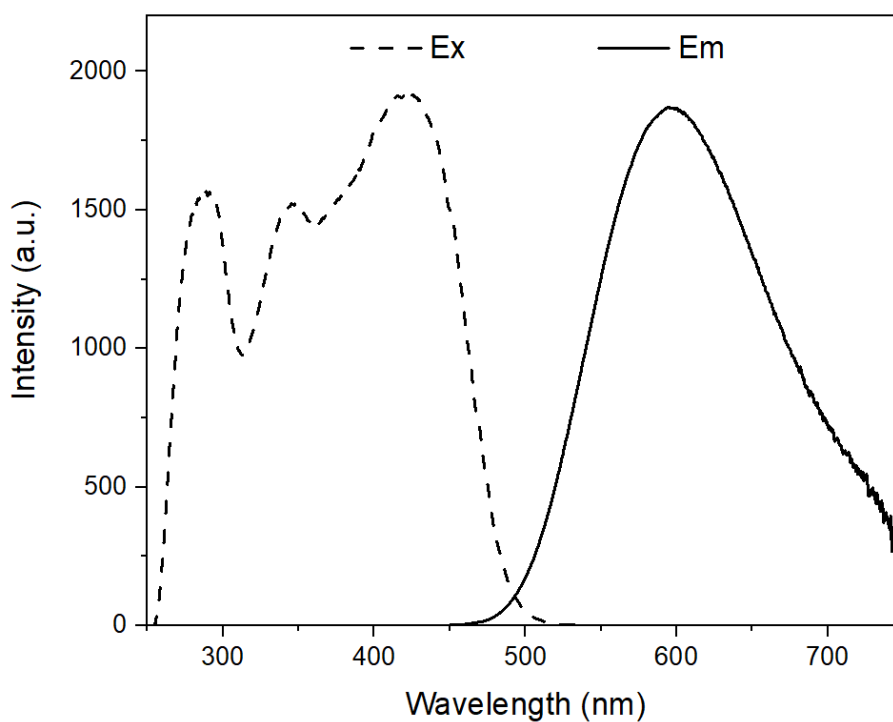


Figure 4.38: Excitation and emission spectra of  $L^{PZ}$  ( $c = 2 \times 10^{-5}$  M,  $\lambda_{ex} = 410$  nm,  $\lambda_{em} = 600$  nm).

#### 4. Phenoxazine-based macrocycles for Photoredox catalysis

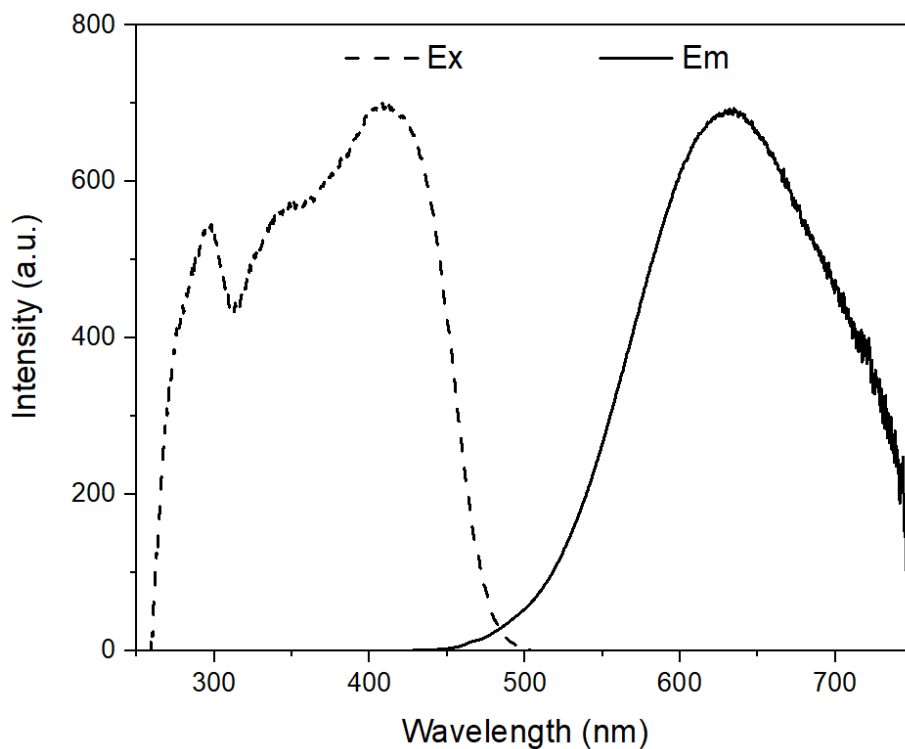


Figure 4.39: Excitation and emission spectra of  $R^{PZ}$  ( $c = 1 \times 10^{-5}$  M,  $\lambda_{ex} = 410$  nm,  $\lambda_{em} = 635$  nm).

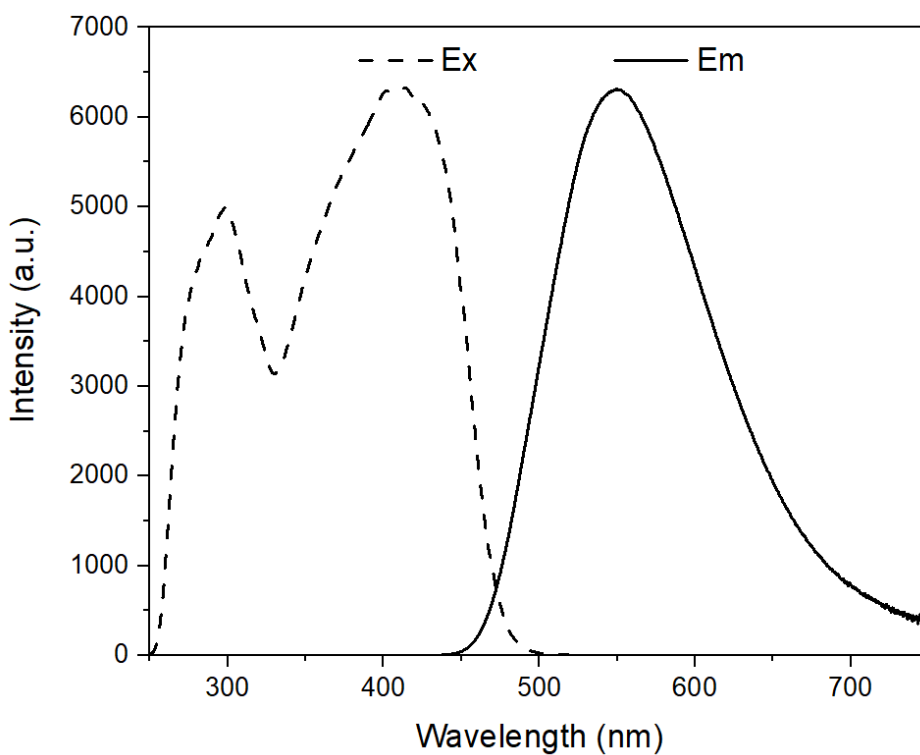


Figure 4.40: Excitation and emission spectra of  $Zn_2R^{PZ}$  ( $c = 1 \times 10^{-5}$  M,  $\lambda_{ex} = 410$  nm,  $\lambda_{em} = 550$  nm).



#### 4. Phenoxazine-based macrocycles for Photoredox catalysis

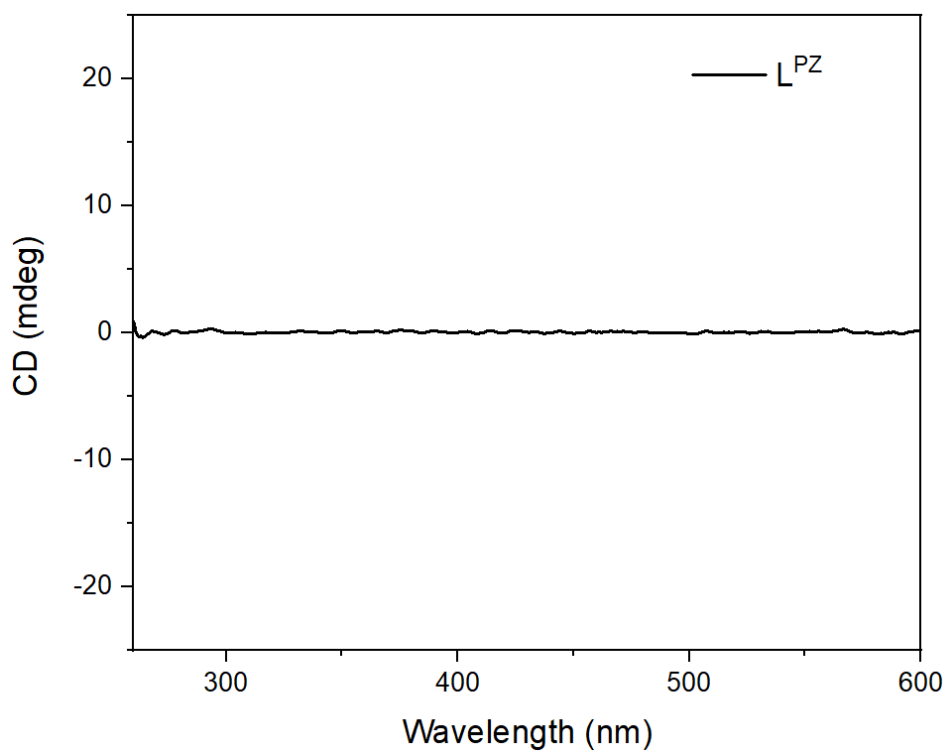


Figure 4.41: CD spectrum of ligand  $L^{PZ}$  in DMSO ( $c = 2 \times 10^{-5}$  M, cuvette path: 1 cm).

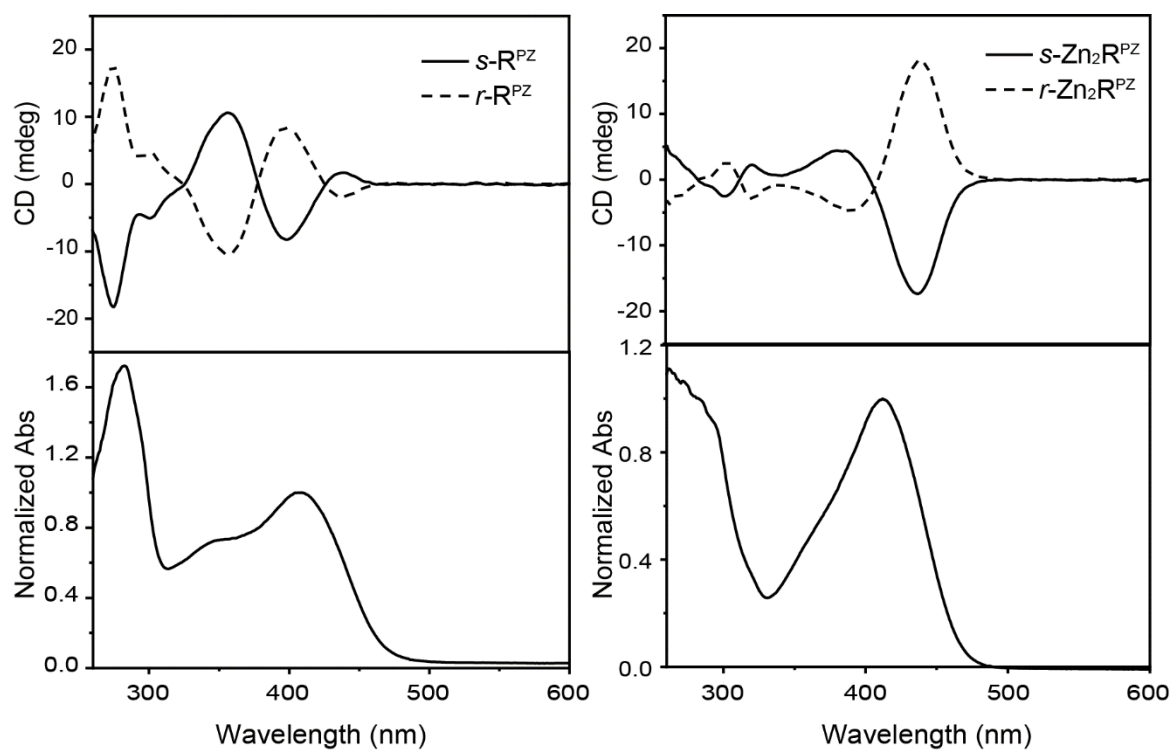


Figure 4.42: CD spectra and normalized UV spectra of a)  $R^{PZ}$  and b)  $Zn_2R^{PZ}$  in DMSO ( $c = 1 \times 10^{-5}$  M, cuvette path length: 1 cm).

#### 4. Phenoxazine-based macrocycles for Photoredox catalysis

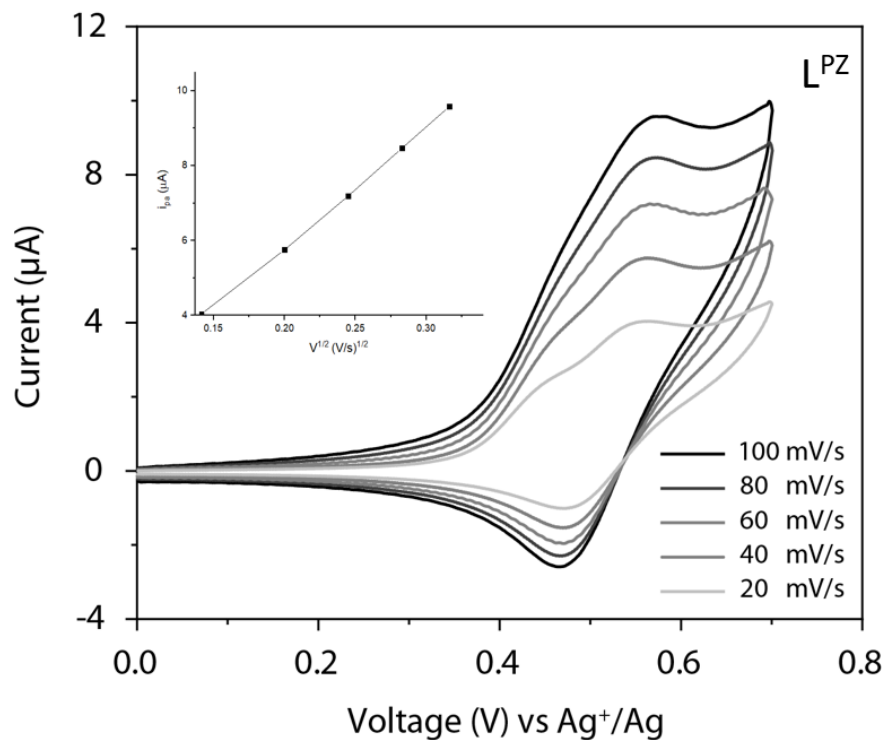


Figure 4.43: Cyclic voltammograms of  $L^{PZ}$  vs  $\text{Ag}^+/\text{Ag}$  at different scan rate (1.0 mM  $L^{PZ}$  in DMSO containing 0.1 M  $\text{TBAPF}_6$  on a glassy carbon working electrode at variable scan rates from 20 to 100  $\text{mV/s}$ . Inset, corresponding linear relationship between the anodic peak current ( $I_a$ ) and square root of the scan rate ( $V^{1/2}$ ).

#### 4.6.4 Photoredox catalytic pinacol coupling reaction

General procedure for photoredox catalytic pinacol coupling experiments:

All the stock solutions of the compounds were prepared in DMSO- $d_6$ .

Aldehyde derivatives (50 mM, 200  $\mu$ L, 1 equiv.), DIPEA (500 mM, 120  $\mu$ L, 6 eq), **L<sup>PZ</sup>** (10 mM, 50  $\mu$ L, 5 mol%) were combined in HPLC vials. 150  $\mu$ L DMSO- $d_6$  was added. The mixture was degassed and irradiated with 420 nm blue LED light at room temperature. After the irradiation, 1,3,5-trimethoxybenzene was added as an internal standard to determine the NMR yield of the products.

Aldehyde (50 mM, 200  $\mu$ L, 1 equiv.), DIPEA (500 mM, 120  $\mu$ L, 6 eq), **R<sup>PZ</sup>** or **Zn<sub>2</sub>R<sup>PZ</sup>** (5 mM, 50  $\mu$ L, 2.5 mol%) were mixed in a HPLC vial. 150  $\mu$ L DMSO- $d_6$  was added. The mixture was degassed and irradiated with 420 nm blue LED light at room temperature. After the irradiation, 1,3,5-trimethoxybenzene was added as an internal standard to determine the yield of the products by <sup>1</sup>H NMR.

Aldehyde (50 mM, 200  $\mu$ L, 1 equiv.), **R<sup>PZ</sup>** or **Zn<sub>2</sub>R<sup>PZ</sup>** (5 mM, 50  $\mu$ L, 2.5 mol%) were mixed in HPLC vials. 270  $\mu$ L DMSO- $d_6$  was added. The mixture was degassed and irradiated with 420 nm blue LED light at room temperature. After the irradiation, 1,3,5-trimethoxybenzene was added as an internal standard to determine the yield of the products by <sup>1</sup>H NMR.

#### 4. Phenoxazine-based macrocycles for Photoredox catalysis

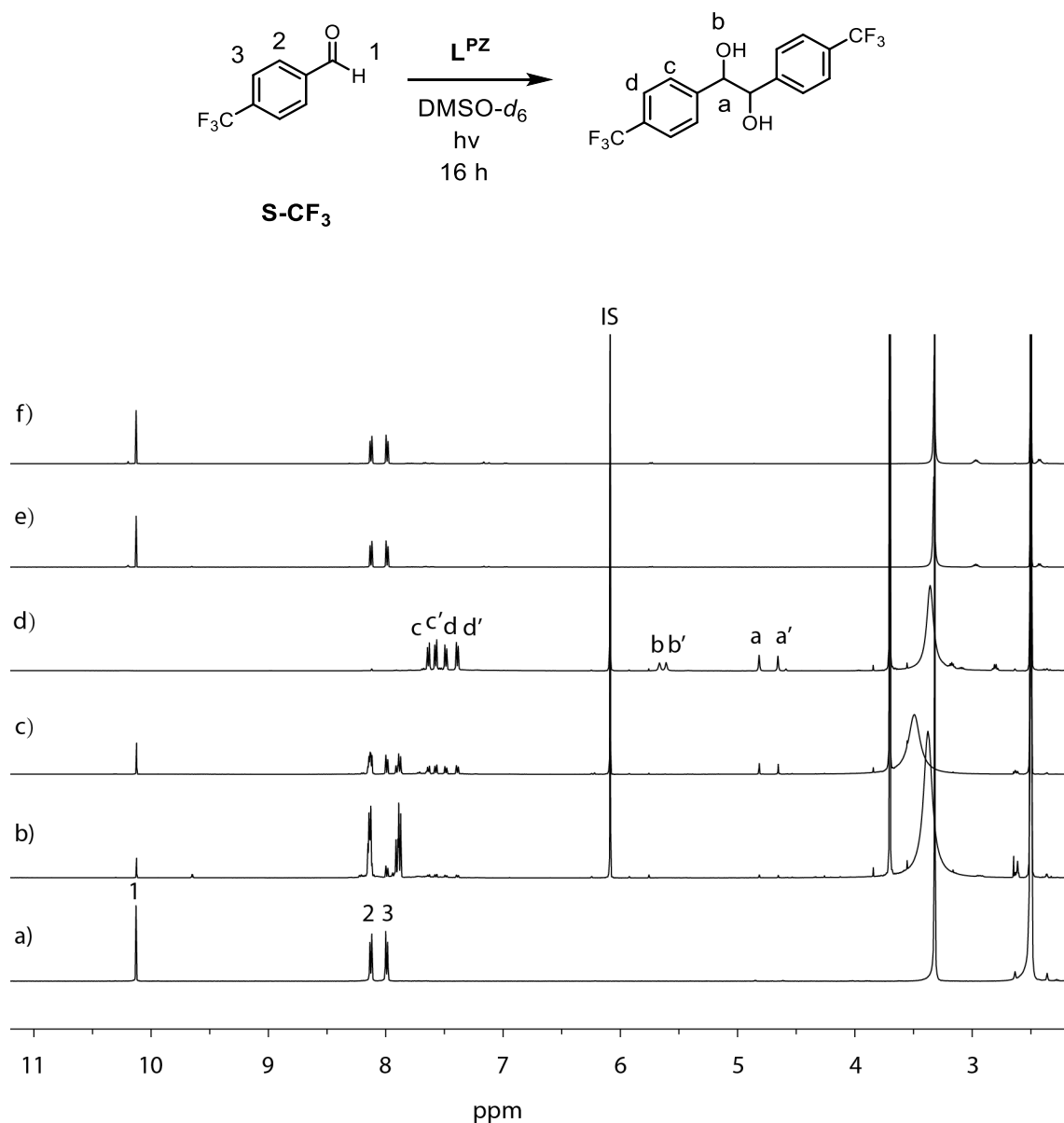


Figure 4.44: <sup>1</sup>H NMR spectra of a) substrate **S-CF<sub>3</sub>** and photocatalysis products under the condition b) 6 eq DIPEA, 420 nm blue LED light, 16 h; c) 5 mol% **L<sup>PZ</sup>**, 420 nm blue LED light, 16h; d) 5 mol% **L<sup>PZ</sup>**, 6 eq DIPEA, 420 nm blue LED light, 16 h; e) 5 mol% **L<sup>PZ</sup>**, 6 eq DIPEA, daylight, 16 h; f) 5 mol% **L<sup>PZ</sup>**, 6 eq DIPEA, dark, 16 h (500 MHz, 298 K, DMSO-*d*<sub>6</sub>). IS = 1,3,5-trimethoxybenzene.

#### 4. Phenoxazine-based macrocycles for Photoredox catalysis

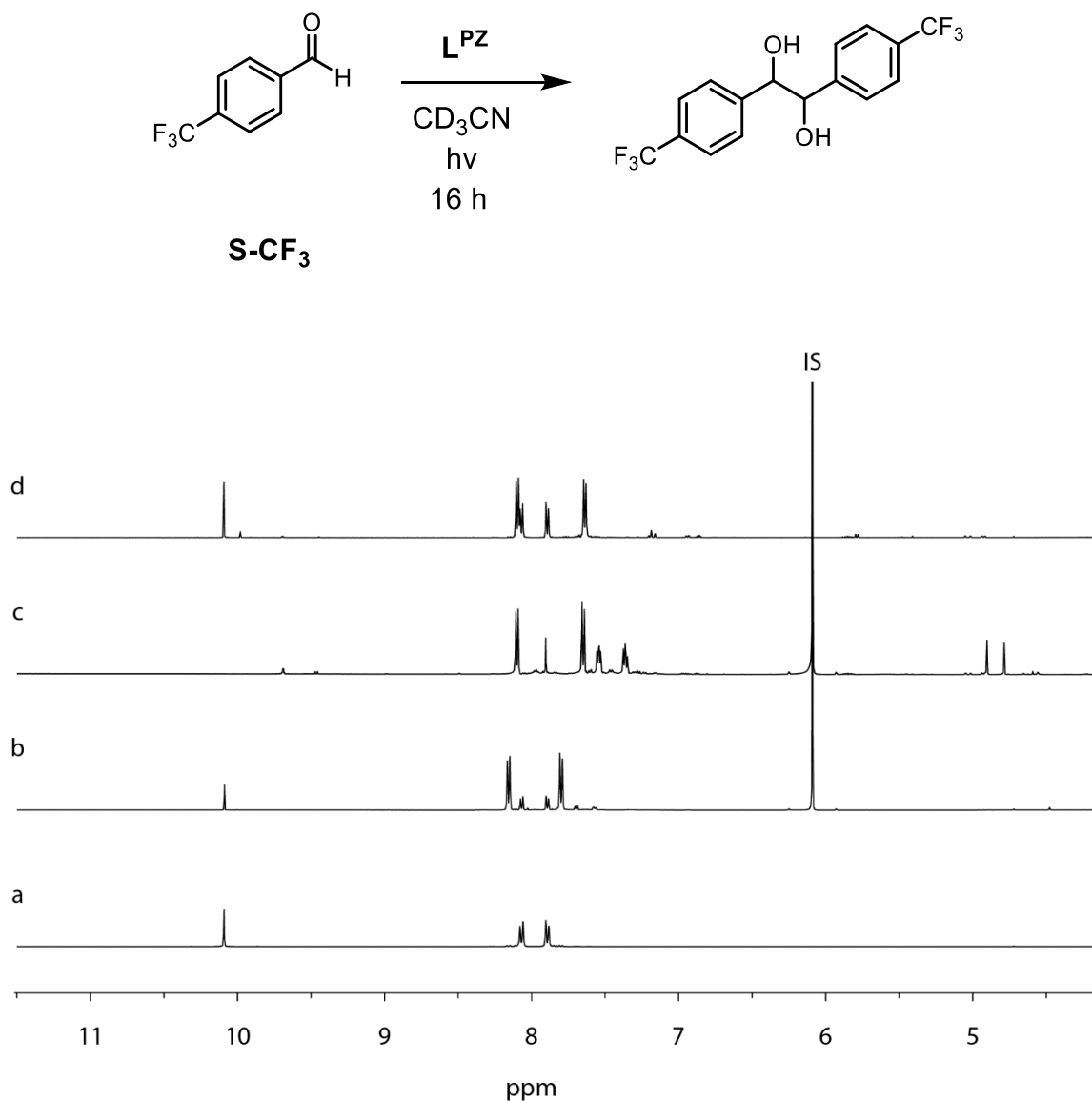


Figure 4.45:  $^1H$  NMR spectra of a) substrate **S-CF<sub>3</sub>** and photocatalysis products under the condition b) 6 eq DIPEA, 420 nm blue LED light, 16 h; c) 2.5 mol% **R<sup>PZ</sup>**, 420 nm blue LED light, 16 h; d) 2.5 mol% **R<sup>PZ</sup>**, 6 eq DIPEA, 420 nm blue LED light, 16 h (500 MHz, 298 K,  $DMSO-d_6$ ). IS = 1,3,5-trimethoxybenzene.

#### 4. Phenoxazine-based macrocycles for Photoredox catalysis

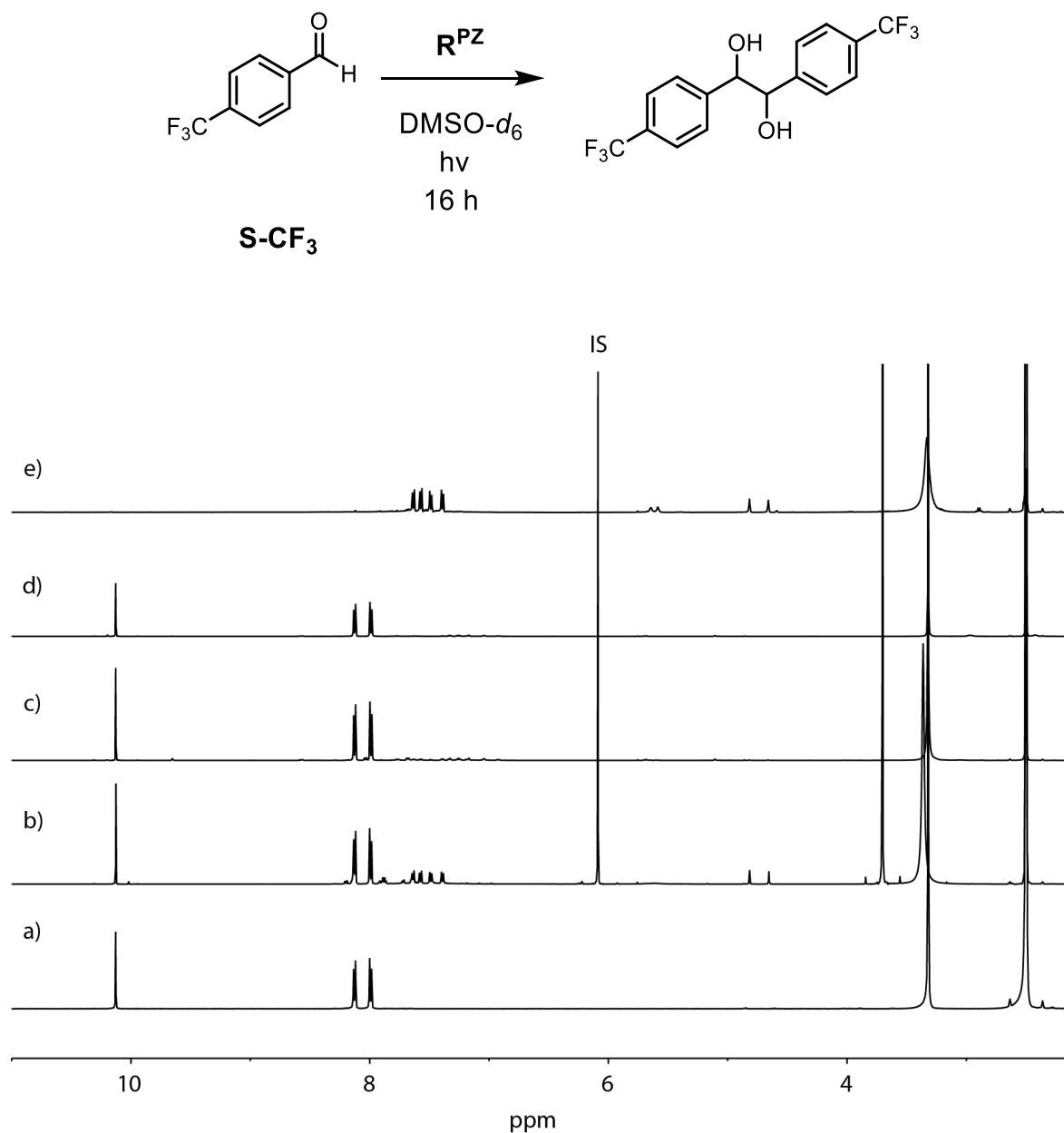
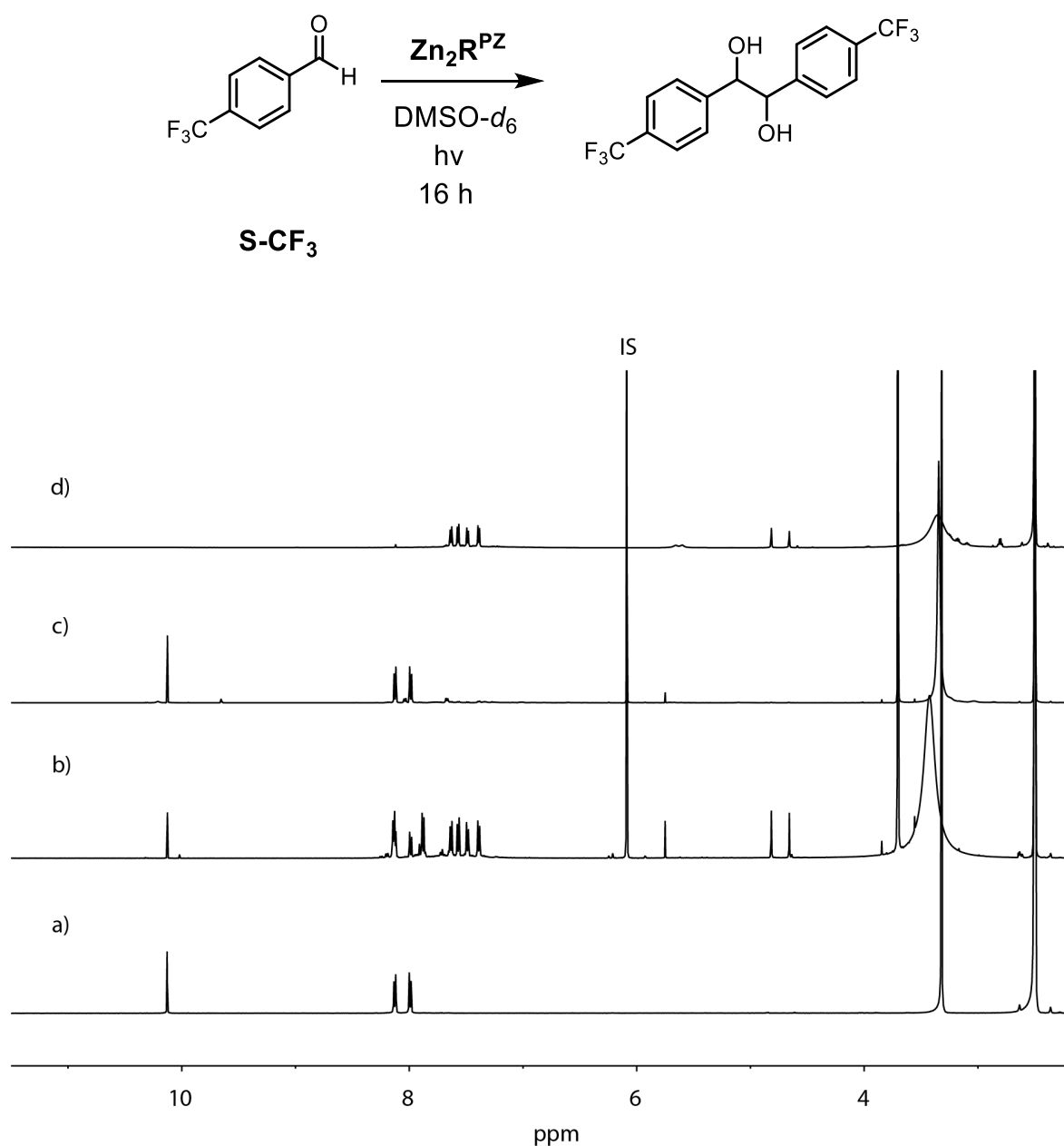


Figure 4.46: <sup>1</sup>H NMR spectra of a) substrate **S-CF<sub>3</sub>** and photocatalysis products under the condition b) 2.5 mol% **R<sup>PZ</sup>**, 420 nm blue LED light, 16h; c) 2.5 mol% **R<sup>PZ</sup>**, 6 eq DIPEA, daylight, 16 h; d) 2.5 mol% **R<sup>PZ</sup>**, 6 eq DIPEA, dark, 16 h (500 MHz, 298 K, DMSO-*d*<sub>6</sub>) ; e) 2.5 mol% **R<sup>PZ</sup>**, 6 eq DIPEA, 420 nm blue LED light, 16 h (600 MHz, 298 K, DMSO-*d*<sub>6</sub>). IS = 1,3,5-trimethoxybenzene.

#### 4. Phenoxazine-based macrocycles for Photoredox catalysis



#### 4. Phenoxazine-based macrocycles for Photoredox catalysis

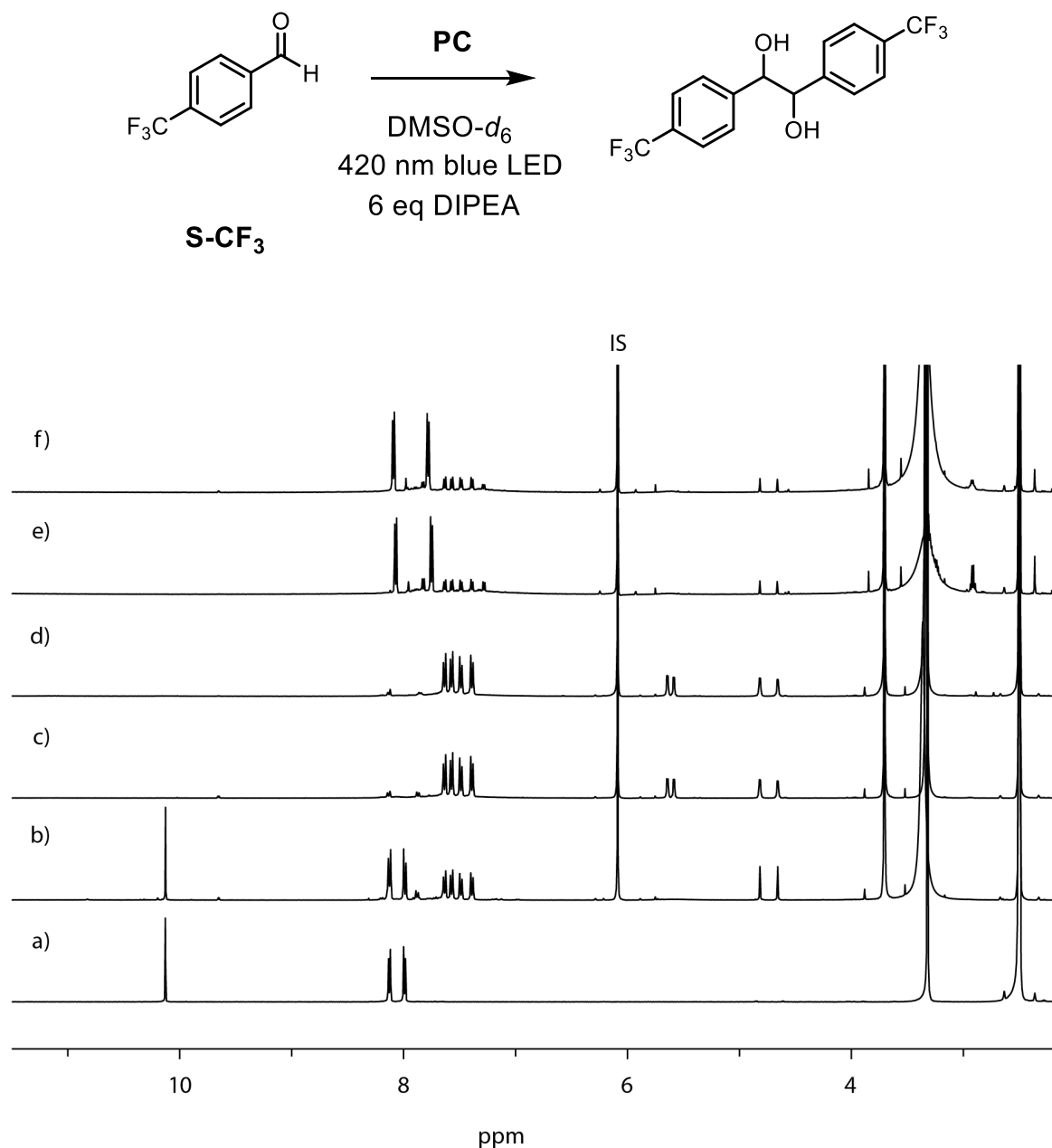


Figure 4.48: <sup>1</sup>H NMR spectra of a) substrate **S-CF<sub>3</sub>** (500 MHz, 298 K, DMSO-*d*<sub>6</sub>) and photocatalysis products under the condition b) 2.5 mol% **L<sup>PZ</sup>**, 6 eq DIPEA, 420 nm blue LED light, 10 h (400 MHz, 298 K, DMSO-*d*<sub>6</sub>); c) 2.5 mol% **R<sup>PZ</sup>**, 6 eq DIPEA, 420 nm blue LED light, 10 h (400 MHz, 298 K, DMSO-*d*<sub>6</sub>); d) 2.5 mol% **Zn<sub>2</sub>R<sup>PZ</sup>**, 6 eq DIPEA, 420 nm blue LED light, 10 h (400 MHz, 298 K, DMSO-*d*<sub>6</sub>); e) 2.5 mol% **R<sup>PZ</sup>**, 6 eq DIPEA, 420 nm blue LED light, 5 h (500 MHz, 298 K, DMSO-*d*<sub>6</sub>); f) 2.5 mol% **Zn<sub>2</sub>R<sup>PZ</sup>**, 6 eq DIPEA, 420 nm blue LED light, 5 h (500 MHz, 298 K, DMSO-*d*<sub>6</sub>). IS = 1,3,5-trimethoxybenzene.



#### 4. Phenoxazine-based macrocycles for Photoredox catalysis

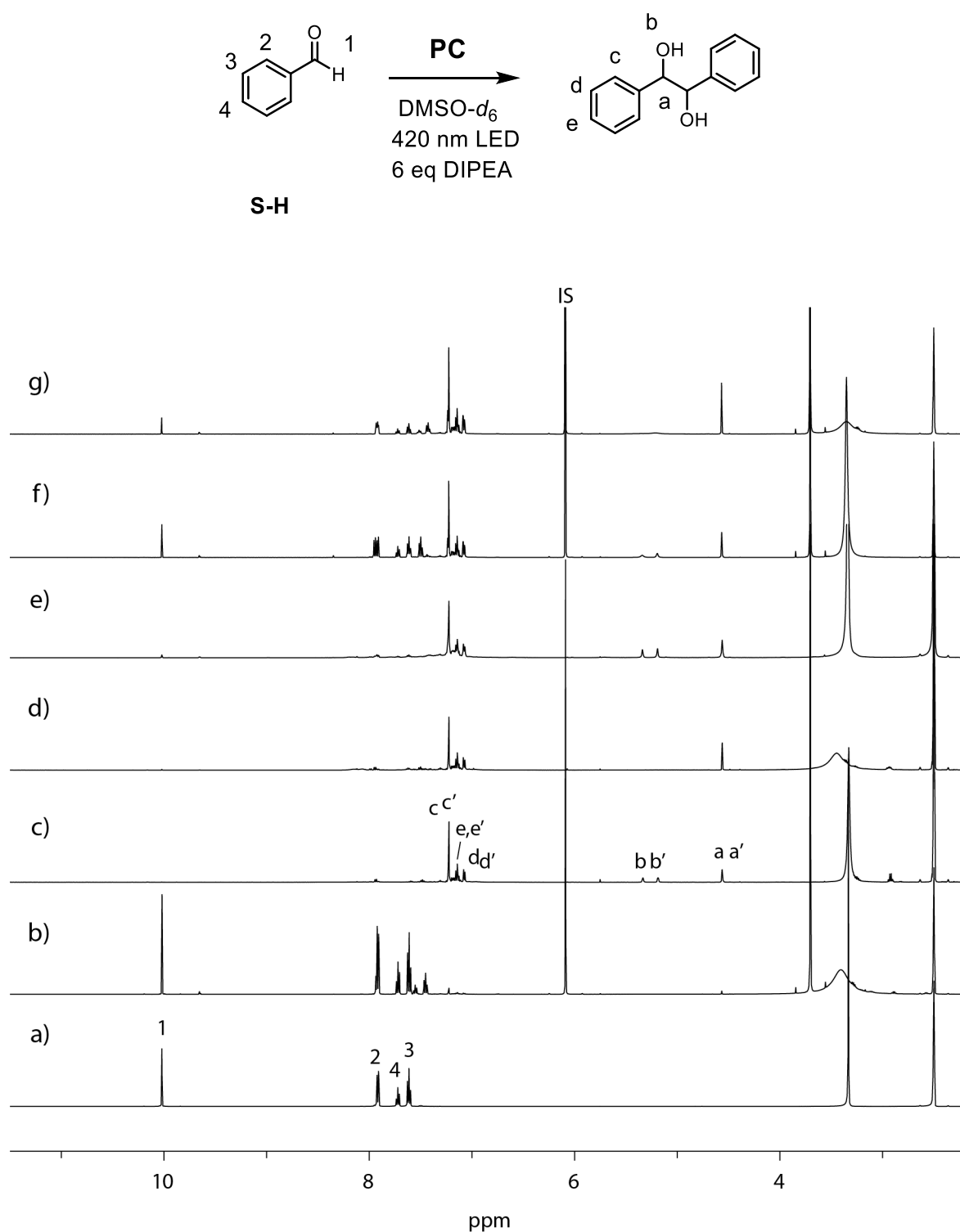


Figure 4.49:  $^1\text{H NMR}$  spectra of a) substrate **S-H** and photocatalysis products under the condition b) 6 eq DIPEA, 420 nm blue LED light, 16 h; c) 5 mol% **L<sup>PZ</sup>**, 6 eq DIPEA, 420 nm blue LED light, 16 h; d) 2.5 mol% **R<sup>PZ</sup>**, 6 eq DIPEA, 420 nm blue LED light, 16 h; e) 2.5 mol% **Zn<sub>2</sub>R<sup>PZ</sup>**, 6 eq DIPEA, 420 nm blue LED light, 16 h; f) 2.5 mol% **L<sup>PZ</sup>**, 6 eq DIPEA, 420 nm blue LED light, 5 h; g) 2.5 mol% **Zn<sub>2</sub>R<sup>PZ</sup>**, 6 eq DIPEA, 420 nm blue LED light, 5 h (500 MHz, 298 K,  $\text{DMSO-}d_6$ ). IS = 1,3,5-trimethoxybenzene.

#### 4. Phenoxazine-based macrocycles for Photoredox catalysis

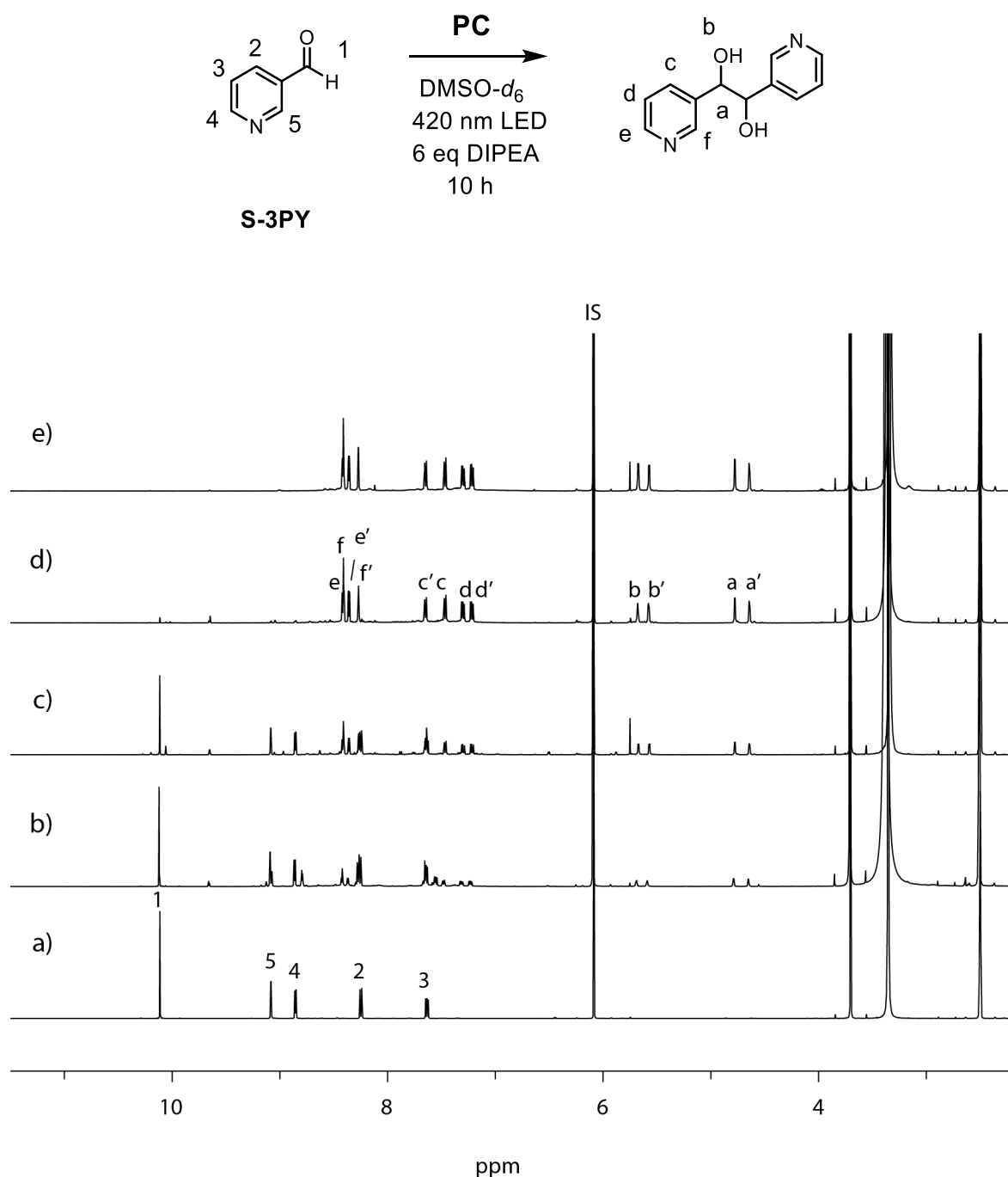


Figure 4.50:  $^1\text{H NMR}$  spectra of a) substrate **S-3PA** and photocatalysis products under the condition b) 6 eq DIPEA, 420 nm blue LED light, 10 h; c) 5 mol% **L<sup>PZ</sup>**, 6 eq DIPEA, 420 nm blue LED light, 10 h; d) 2.5 mol% **R<sup>PZ</sup>**, 6 eq DIPEA, 420 nm blue LED light, 10 h; e) 2.5 mol% **Zn<sub>2</sub>R<sup>PZ</sup>**, 6 eq DIPEA, 420 nm blue LED light, 10 h (500 MHz, 298 K,  $\text{DMSO-}d_6$ ). IS = 1,3,5-trimethoxybenzene.

#### 4. Phenoxazine-based macrocycles for Photoredox catalysis

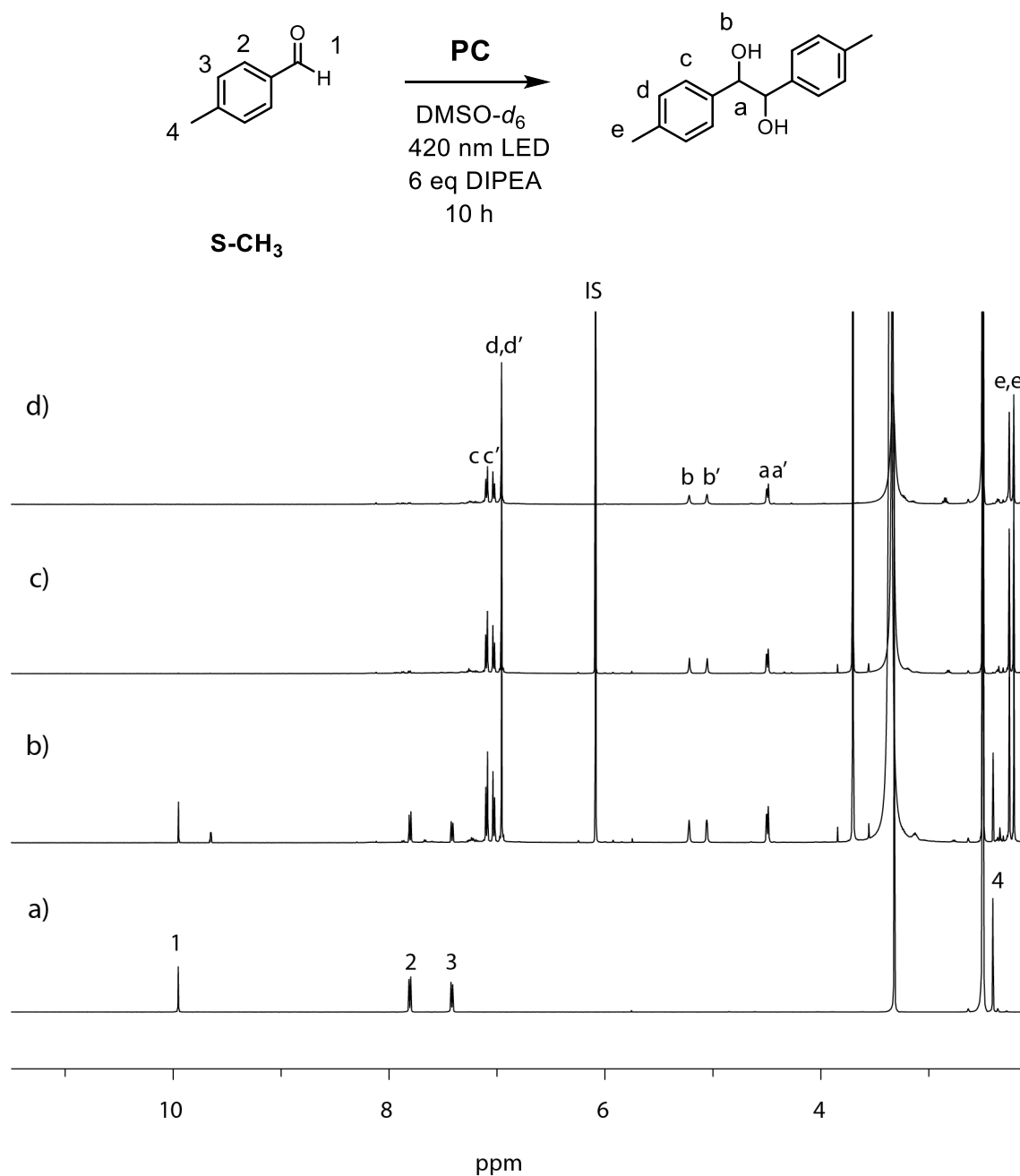


Figure 4.51: <sup>1</sup>H NMR spectra of a) substrate **S-CH<sub>3</sub>** and photocatalysis products under the condition b) 5 mol% **L<sup>PZ</sup>**, 6 eq DIPEA, 420 nm blue LED light, 10 h; c) 5 mol% **L<sup>PZ</sup>**, 6 eq DIPEA, 420 nm blue LED light, 10 h; d) 2.5 mol% **Zn<sub>2</sub>L<sup>PZ</sup>**, 420 nm blue LED light, 6 eq DIPEA, 10 h (500 MHz, 298 K, DMSO-*d*<sub>6</sub>).

## 4. Phenoxazine-based macrocycles for Photoredox catalysis

### 4.6.5 Theoretical studies

All the calculations were performed using Gaussian ver B01 at the  $\omega$ B97X/def2svp level of theory in the gas phase. Geometry optimization and frequency calculations were performed for  $L^{PZ}$ ,  $R^{PZ}$ , and  $Zn_2R^{PZ}$  in ground state (multiplicity:0, charge: 0), doublet state (multiplicity:2, charge: +1), and triplet state (multiplicity:3, charge: 0).

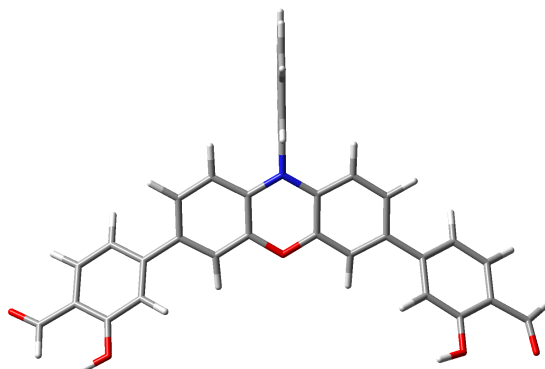


Figure 4.52: The optimized geometry of  $L^{PZ}$  in the ground state

Standard orientation:											
Center	Atomic	Atomic	Coordinates								
Number	Number	Type	X	Y	Z						
1	6	0	-2.464022	1.572500	0.597337	18	6	0	-6.027521	-3.438978	0.307042
2	6	0	-1.206051	0.971287	0.543272	19	6	0	-7.147469	-2.888663	-0.344110
3	6	0	-1.148440	-0.413764	0.303787	20	6	0	-7.070068	-1.567403	-0.816565
4	6	0	-2.302160	-1.156685	0.128421	21	6	0	-5.927659	-0.808954	-0.654370
5	6	0	-3.568190	-0.552744	0.183127	22	6	0	-8.400179	-3.638253	-0.557002
6	6	0	-3.625845	0.821566	0.419274	23	8	0	-5.986175	-4.690468	0.807602
7	7	0	-0.011887	1.686517	0.711893	24	8	0	-9.378061	-3.198190	-1.108110
8	6	0	1.209207	1.025704	0.516122	25	6	0	5.965418	-0.560093	-0.808240
9	6	0	1.208198	-0.360703	0.277723	26	6	0	7.137029	-1.280032	-0.988619
10	8	0	0.045409	-1.083068	0.240459	27	6	0	7.299043	-2.578833	-0.492910
11	6	0	2.439843	1.682861	0.542108	28	6	0	6.226676	-3.163582	0.212451
12	6	0	3.630353	0.984794	0.339342	29	6	0	5.045445	-2.435961	0.393903
13	6	0	3.629039	-0.390808	0.104448	30	6	0	8.591459	-3.263021	-0.740287
14	6	0	2.390549	-1.050821	0.076565	31	8	0	8.904202	-4.369741	-0.388694
15	6	0	-4.804757	-1.357645	-0.000616	32	8	0	6.363939	-4.403623	0.703134
16	6	0	4.896720	-1.138943	-0.106180	33	6	0	-0.041279	3.096848	0.928217
17	6	0	-4.871650	-2.667364	0.470861	34	6	0	-0.073785	3.982095	-0.196785
						35	6	0	-0.102743	5.383665	0.042438
						36	6	0	-0.098667	5.861876	1.383794
						37	6	0	-0.067369	4.989879	2.441126
						38	6	0	-0.038376	3.592015	2.208922
						39	6	0	-0.078325	3.508085	-1.538736
						40	6	0	-0.110177	4.390574	-2.588793

#### 4. Phenoxazine-based macrocycles for Photoredox catalysis

41	6	0	-0.139005	5.788751	-2.353330	54	1	0	5.863410	0.441266	-1.232445
42	6	0	-0.135334	6.271801	-1.069839	55	1	0	7.968638	-0.832465	-1.543794
43	1	0	-2.535385	2.644723	0.790423	56	1	0	4.231003	-2.892149	0.967129
44	1	0	-2.188638	-2.224278	-0.073963	57	1	0	9.309315	-2.625147	-1.322947
45	1	0	-4.593962	1.323426	0.491090	58	1	0	5.553727	-4.658589	1.156996
46	1	0	2.466977	2.757397	0.733655	59	1	0	-0.121188	6.942055	1.556327
47	1	0	4.577095	1.528414	0.390033	60	1	0	-0.064637	5.365123	3.467614
48	1	0	2.319816	-2.122092	-0.126613	61	1	0	-0.013442	2.890566	3.046979
49	1	0	-4.033605	-3.121327	1.004607	62	1	0	-0.056288	2.430734	-1.721704
50	1	0	-7.950584	-1.168283	-1.327533	63	1	0	-0.113621	4.015442	-3.615635
51	1	0	-5.882673	0.206262	-1.055095	64	1	0	-0.164321	6.479750	-3.200137
52	1	0	-8.424545	-4.693582	-0.171628	65	1	0	-0.157573	7.349268	-0.880918
53	1	0	-6.820286	-5.147735	0.665793						

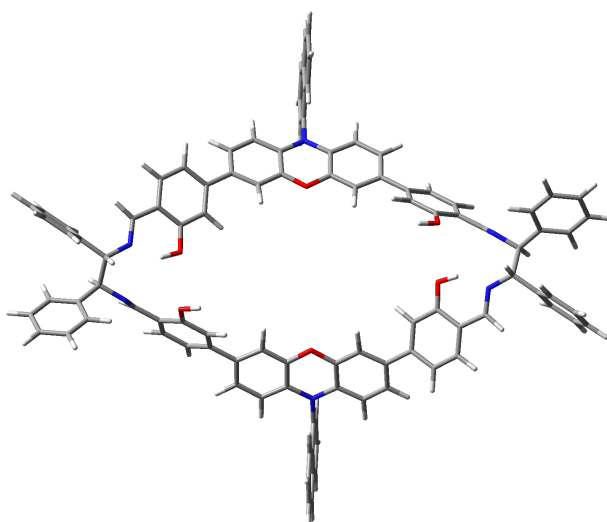


Figure 4.53: The optimized geometry of  $R^{PZ}$  in the ground state

Standard orientation:						8	6	0	1.026351	5.623805	-1.995829
-----						9	6	0	1.040062	4.499729	-1.150132
Center	Atomic	Atomic	Coordinates			10	8	0	-0.117185	3.933992	-0.685489
		(Angstroms)				11	6	0	2.252530	6.127376	-2.431321
Number	Number	Type	X	Y	Z	12	6	0	3.452230	5.527441	-2.047457
-----						13	6	0	3.465996	4.408755	-1.213283
1	6	0	-2.640694	6.229980	-2.039817	14	6	0	2.231853	3.907922	-0.770034
2	6	0	-1.383556	5.673041	-1.804401	15	6	0	-4.936695	3.976634	-0.015452
3	6	0	-1.310862	4.545886	-0.966487	16	6	0	4.742871	3.767307	-0.800736
4	6	0	-2.449285	4.007772	-0.392946	17	6	0	-5.033700	2.601283	0.185726
5	6	0	-3.715465	4.565839	-0.629092	18	6	0	-6.175900	2.020136	0.758007
6	6	0	-3.786941	5.683842	-1.461686	19	6	0	-7.259414	2.854577	1.130873
7	7	0	-0.203813	6.188748	-2.362248	20	6	0	-7.145170	4.238597	0.929393

#### 4. Phenoxazine-based macrocycles for Photoredox catalysis

21	6	0	-6.011758	4.802266	0.370594	63	8	0	6.182865	2.084420	2.126371
22	6	0	-8.482345	2.293711	1.707391	64	8	0	6.197522	-0.702194	0.927633
23	8	0	-6.197839	0.702230	0.927203	65	7	0	8.623263	-1.036010	1.854836
24	7	0	-8.623250	1.036253	1.855014	66	6	0	10.087943	0.910580	1.670069
25	6	0	-9.785531	0.405072	2.450479	67	6	0	9.785494	-0.404855	2.450436
26	6	0	-10.087953	-0.910335	1.669993	68	6	0	-0.248183	7.328517	-3.217926
27	7	0	-8.848682	-1.629473	1.513107	69	6	0	0.248174	-7.328630	-3.217634
28	6	0	-8.444580	-1.886446	0.341341	70	6	0	-0.175188	8.640602	-2.649185
29	6	0	-7.168516	-2.544959	0.010683	71	6	0	-0.220102	9.763568	-3.520565
30	6	0	-6.071970	-2.612645	0.894895	72	6	0	-0.336073	9.552059	-4.923939
31	6	0	-4.883121	-3.218350	0.477000	73	6	0	-0.404377	8.283829	-5.440126
32	6	0	-4.742909	-3.767367	-0.800574	74	6	0	-0.359735	7.161093	-4.576389
33	6	0	-5.831094	-3.692918	-1.681323	75	6	0	0.359763	-7.161013	-4.576071
34	6	0	-7.008768	-3.083029	-1.271645	76	6	0	0.404429	-8.283613	-5.439985
35	8	0	-6.183031	-2.084446	2.126444	77	6	0	0.336109	-9.551917	-4.923987
36	6	0	-3.466024	-4.408874	-1.213000	78	6	0	0.220099	-9.763630	-3.520643
37	6	0	-2.231893	-3.908281	-0.769435	79	6	0	0.175165	-8.640798	-2.649087
38	6	0	-1.040105	-4.500126	-1.149470	80	6	0	0.147356	-11.071626	-2.962958
39	6	0	-1.026368	-5.623994	-1.995451	81	6	0	0.035767	-11.251274	-1.607975
40	6	0	-2.252528	-6.127323	-2.431267	82	6	0	-0.008531	-10.129518	-0.741290
41	6	0	-3.452230	-5.527370	-2.047431	83	6	0	0.059334	-8.855950	-1.247017
42	8	0	0.117120	-3.934613	-0.684494	84	6	0	-0.059385	8.855543	-1.247078
43	6	0	1.310836	-4.546270	-0.965855	85	6	0	0.008469	10.129030	-0.741152
44	6	0	1.383554	-5.673197	-1.804073	86	6	0	-0.035816	11.250920	-1.607666
45	7	0	0.203791	-6.188981	-2.361809	87	6	0	-0.147375	11.071480	-2.962678
46	6	0	2.449278	-4.008127	-0.392377	88	6	0	8.482449	-2.293470	1.707169
47	6	0	3.715504	-4.565937	-0.628895	89	6	0	-11.103546	-1.752359	2.424901
48	6	0	3.787003	-5.683712	-1.461789	90	6	0	-11.022609	1.271789	2.590219
49	6	0	2.640739	-6.229870	-2.039870	91	6	0	11.103551	1.752502	2.425074
50	6	0	4.936768	-3.976651	-0.015387	92	6	0	11.022576	-1.271561	2.590141
51	6	0	5.033552	-2.601329	0.186101	93	6	0	12.469030	1.647591	2.146984
52	6	0	6.175790	-2.020084	0.758208	94	6	0	13.400756	2.389072	2.872173
53	6	0	7.259533	-2.854410	1.130665	95	6	0	12.975400	3.248134	3.883827
54	6	0	7.145521	-4.238400	0.928863	96	6	0	11.613738	3.363005	4.162861
55	6	0	6.012097	-4.802156	0.370173	97	6	0	10.683060	2.621185	3.438011
56	6	0	5.831163	3.693007	-1.681362	98	6	0	11.634930	-1.838823	1.464470
57	6	0	7.008835	3.083184	-1.271590	99	6	0	12.791637	-2.604041	1.591223
58	6	0	7.168471	2.545092	0.010737	100	6	0	13.357636	-2.813242	2.849557
59	6	0	6.071831	2.612637	0.894833	101	6	0	12.756570	-2.256528	3.975716
60	6	0	4.882963	3.218244	0.476832	102	6	0	11.595752	-1.493937	3.844009
61	6	0	8.444511	1.886588	0.341494	103	6	0	-10.682994	-2.620992	3.437870
62	7	0	8.848694	1.629780	1.513270	104	6	0	-11.613608	-3.362911	4.162689

#### 4. Phenoxazine-based macrocycles for Photoredox catalysis

105	6	0	-12.975279	-3.248203	3.883591	145	1	0	7.066363	-0.456412	1.343264
106	6	0	-13.400688	-2.389221	2.871901	146	1	0	10.521819	0.626704	0.686888
107	6	0	-12.469014	-1.647631	2.146738	147	1	0	9.468967	-0.079898	3.457283
108	6	0	-11.595685	1.494206	3.844124	148	1	0	-0.369783	10.422959	-5.585424
109	6	0	-12.756480	2.256824	3.975912	149	1	0	-0.493437	8.129956	-6.518569
110	6	0	-13.357623	2.813528	2.849793	150	1	0	-0.413654	6.146971	-4.980948
111	6	0	-12.791726	2.604284	1.591415	151	1	0	0.413694	-6.146829	-4.980479
112	6	0	-11.635049	1.839039	1.464584	152	1	0	0.493518	-8.129571	-6.518402
113	1	0	-2.725003	7.099781	-2.694550	153	1	0	0.369834	-10.422727	-5.585591
114	1	0	-2.323132	3.143360	0.262951	154	1	0	0.182044	-11.932633	-3.637277
115	1	0	-4.757041	6.132577	-1.689160	155	1	0	-0.019637	-12.260230	-1.190504
116	1	0	2.268659	7.006550	-3.078685	156	1	0	-0.097636	-10.283306	0.337415
117	1	0	4.394364	5.961575	-2.391533	157	1	0	0.025398	-7.991033	-0.579660
118	1	0	2.172358	3.020233	-0.135787	158	1	0	-0.025457	7.990529	-0.579847
119	1	0	-4.231288	1.925949	-0.120624	159	1	0	0.097553	10.282652	0.337577
120	1	0	-7.979213	4.880609	1.232703	160	1	0	0.019575	12.259812	-1.190041
121	1	0	-5.940374	5.885671	0.251131	161	1	0	-0.182048	11.932591	-3.636863
122	1	0	-9.267892	3.016385	1.998673	162	1	0	9.268059	-3.016087	1.998425
123	1	0	-7.066579	0.456605	1.343136	163	1	0	12.809402	0.971215	1.356289
124	1	0	-9.469079	0.080037	3.457324	164	1	0	14.465945	2.295763	2.642502
125	1	0	-10.521803	-0.626350	0.686829	165	1	0	13.704847	3.832656	4.451642
126	1	0	-9.055030	-1.607854	-0.545357	166	1	0	11.271708	4.041859	4.949436
127	1	0	-4.052510	-3.281140	1.188258	167	1	0	9.611905	2.719849	3.634483
128	1	0	-5.740750	-4.082111	-2.698100	168	1	0	11.199091	-1.681501	0.472092
129	1	0	-7.845928	-3.006129	-1.973249	169	1	0	13.256288	-3.039213	0.701930
130	1	0	-5.310385	-2.049136	2.531715	170	1	0	14.267679	-3.411153	2.950102
131	1	0	-2.172389	-3.020737	-0.134985	171	1	0	13.194066	-2.413216	4.965538
132	1	0	-2.268651	-7.006337	-3.078848	172	1	0	11.132710	-1.050245	4.730971
133	1	0	-4.394345	-5.961342	-2.391760	173	1	0	-9.611831	-2.719534	3.634371
134	1	0	2.323110	-3.143905	0.263764	174	1	0	-11.271541	-4.041719	4.949288
135	1	0	4.757129	-6.132255	-1.689529	175	1	0	-13.704674	-3.832802	4.451394
136	1	0	2.725060	-7.099499	-2.694827	176	1	0	-14.465876	-2.296047	2.642167
137	1	0	4.230934	-1.926079	-0.119889	177	1	0	-12.809442	-0.971331	1.356002
138	1	0	7.979750	-4.880328	1.231838	178	1	0	-11.132584	1.050531	4.731065
139	1	0	5.940933	-5.885542	0.250405	179	1	0	-13.193887	2.413540	4.965769
140	1	0	5.740904	4.082270	-2.698120	180	1	0	-14.267650	3.411456	2.950389
141	1	0	7.846080	3.006373	-1.973103	181	1	0	-13.256436	3.039453	0.702152
142	1	0	4.052269	3.280975	1.187996	182	1	0	-11.199310	1.681682	0.472167
143	1	0	9.054898	1.607808	-0.545185						
144	1	0	5.310174	2.048775	2.531513						

#### 4. Phenoxazine-based macrocycles for Photoredox catalysis

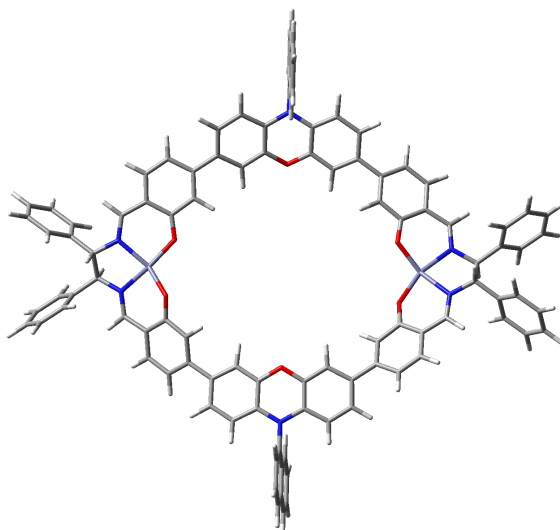


Figure 4.54: The optimized geometry of  $\text{Zn}_2\text{R}^{\text{PZ}}$  in the ground state

Standard orientation:						22	6	0	8.277503	2.430777	-0.759971
-----						23	8	0	6.025122	1.426759	0.890329
Center	Atomic	Atomic	Coordinates			24	7	0	8.442944	1.161424	-0.597078
			(Angstroms)			25	6	0	9.675776	0.464272	-0.946114
Number	Number	Type	X	Y	Z	26	6	0	9.839227	-0.738469	0.039703
-----						27	7	0	8.543661	-1.402994	0.146550
1	6	0	2.544455	7.749055	0.861408	28	6	0	8.390628	-2.684900	0.123888
2	6	0	1.297855	7.127955	0.950740	29	6	0	7.135543	-3.388483	0.097487
3	6	0	1.255524	5.726921	0.839879	30	6	0	5.862039	-2.741655	-0.037901
4	6	0	2.405888	4.990944	0.626204	31	6	0	4.712364	-3.582792	-0.083029
5	6	0	3.660518	5.612510	0.527863	32	6	0	4.775226	-4.962682	-0.031617
6	6	0	3.706171	7.002091	0.654568	33	6	0	6.051246	-5.583850	0.068698
7	7	0	0.096531	7.831906	1.135839	34	6	0	7.180734	-4.806166	0.132600
8	6	0	-1.119340	7.138025	1.022425	35	8	0	5.686705	-1.469143	-0.124435
9	6	0	-1.095722	5.735982	0.917458	36	6	0	3.528569	-5.780135	-0.077186
10	8	0	0.079378	5.034768	0.945076	37	6	0	2.334071	-5.239424	-0.581669
11	6	0	-2.364062	7.769172	1.009362	38	6	0	1.164658	-5.974709	-0.604616
12	6	0	-3.544270	7.029107	0.908734	39	6	0	1.125466	-7.298753	-0.133288
13	6	0	-3.519156	5.636913	0.808235	40	6	0	2.307735	-7.842265	0.369061
14	6	0	-2.264981	5.006616	0.813063	41	6	0	3.486167	-7.093938	0.395857
15	6	0	4.878371	4.796400	0.267714	42	8	0	0.049238	-5.377119	-1.129910
16	6	0	-4.761620	4.822680	0.708414	43	6	0	-1.168115	-5.937542	-0.845787
17	6	0	4.964941	3.498956	0.737529	44	6	0	-1.271140	-7.271052	-0.411672
18	6	0	6.052495	2.630595	0.430932	45	7	0	-0.090312	-7.999724	-0.186844
19	6	0	7.108770	3.177373	-0.374453	46	6	0	-2.293973	-5.155331	-1.027102
20	6	0	7.026432	4.528524	-0.796419	47	6	0	-3.578785	-5.678512	-0.815606
21	6	0	5.947255	5.326353	-0.504206	48	6	0	-3.685225	-7.014934	-0.427874



#### 4. Phenoxazine-based macrocycles for Photoredox catalysis

49	6	0	-2.548354	-7.798270	-0.217495	91	6	0	11.011521	-1.614745	-0.354336
50	6	0	-4.776351	-4.808122	-0.965342	92	6	0	10.926009	1.321668	-0.966428
51	6	0	-4.733593	-3.501023	-0.520695	93	6	0	-10.944144	1.417474	0.109456
52	6	0	-5.835983	-2.604662	-0.634304	94	6	0	-10.910477	-1.305262	-1.151025
53	6	0	-7.030545	-3.120930	-1.242260	95	6	0	-11.116789	2.368216	-0.905296
54	6	0	-7.055629	-4.472750	-1.673541	96	6	0	-12.258917	3.162935	-0.947248
55	6	0	-5.970602	-5.306524	-1.551295	97	6	0	-13.249031	3.017965	0.025633
56	6	0	-5.956410	5.242279	1.352889	98	6	0	-13.086653	2.077640	1.039474
57	6	0	-7.071423	4.442187	1.290481	99	6	0	-11.939280	1.284631	1.079758
58	6	0	-7.073372	3.190484	0.623893	100	6	0	-11.806068	-1.216616	-2.218617
59	6	0	-5.881585	2.757323	-0.051013	101	6	0	-12.955202	-2.007206	-2.255713
60	6	0	-4.757043	3.629793	0.009679	102	6	0	-13.219762	-2.901821	-1.222248
61	6	0	-8.300962	2.437345	0.625127	103	6	0	-12.329855	-3.003251	-0.151988
62	7	0	-8.435845	1.225922	0.201855	104	6	0	-11.186070	-2.210541	-0.117310
63	8	0	-5.763871	1.652856	-0.705213	105	6	0	11.050363	-2.254718	-1.600519
64	8	0	-5.698783	-1.410287	-0.173409	106	6	0	12.142104	-3.038250	-1.964341
65	7	0	-8.394441	-1.110442	-1.098452	107	6	0	13.216248	-3.193088	-1.086934
66	6	0	-9.715928	0.529563	0.138166	108	6	0	13.187824	-2.563505	0.154522
67	6	0	-9.680884	-0.420251	-1.105124	109	6	0	12.090328	-1.781743	0.516426
68	6	0	0.106575	9.250938	1.271965	110	6	0	11.721745	1.392792	-2.111482
69	6	0	-0.153778	-9.361408	0.232593	111	6	0	12.891035	2.154160	-2.122335
70	6	0	0.077968	10.076706	0.101976	112	6	0	13.275730	2.857504	-0.984025
71	6	0	0.088979	11.489454	0.265302	113	6	0	12.485727	2.797589	0.165006
72	6	0	0.127775	12.038895	1.578497	114	6	0	11.321193	2.035102	0.172938
73	6	0	0.154383	11.223713	2.680261	115	1	0	2.608378	8.834976	0.958540
74	6	0	0.143658	9.815211	2.523292	116	1	0	2.297537	3.909836	0.517155
75	6	0	-0.044931	-10.363489	-0.699709	117	1	0	4.665332	7.523760	0.605707
76	6	0	-0.104169	-11.724333	-0.308055	118	1	0	-2.411596	8.857996	1.079704
77	6	0	-0.271751	-12.053248	1.011989	119	1	0	-4.498594	7.561423	0.887555
78	6	0	-0.388082	-11.041056	2.006977	120	1	0	-2.175539	3.919469	0.762987
79	6	0	-0.329045	-9.673880	1.619754	121	1	0	4.177133	3.066820	1.358782
80	6	0	-0.561771	-11.360500	3.383548	122	1	0	7.846803	4.931518	-1.400995
81	6	0	-0.670637	-10.369679	4.325386	123	1	0	5.892985	6.345376	-0.893101
82	6	0	-0.611065	-9.007162	3.936553	124	1	0	9.086631	3.021792	-1.224611
83	6	0	-0.444697	-8.665829	2.618063	125	1	0	9.536929	0.028549	-1.952549
84	6	0	0.038871	9.531431	-1.212164	126	1	0	10.059301	-0.299714	1.030015
85	6	0	0.012177	10.356662	-2.307948	127	1	0	9.287292	-3.327999	0.098498
86	6	0	0.023250	11.765814	-2.148158	128	1	0	3.759338	-3.053902	-0.140809
87	6	0	0.060693	12.316981	-0.892980	129	1	0	6.140369	-6.671521	0.071199
88	6	0	-8.249740	-2.364384	-1.368235	130	1	0	8.161981	-5.289025	0.203194
89	30	0	6.970588	-0.074645	0.153716	131	1	0	2.288985	-4.226959	-0.986311
90	30	0	-6.851878	0.091244	-0.463243	132	1	0	2.307493	-8.865354	0.751055

#### 4. Phenoxazine-based macrocycles for Photoredox catalysis

133	1	0	4.380317	-7.552969	0.822906	158	1	0	0.001634	12.410766	-3.030775
134	1	0	-2.150605	-4.125101	-1.360986	159	1	0	0.069320	13.403358	-0.762366
135	1	0	-4.671104	-7.451020	-0.245754	160	1	0	-9.128442	-2.942708	-1.702924
136	1	0	-2.655777	-8.833685	0.112820	161	1	0	-10.341518	2.499359	-1.667584
137	1	0	-3.840033	-3.098251	-0.037563	162	1	0	-12.377235	3.902347	-1.744062
138	1	0	-7.978234	-4.851588	-2.127732	163	1	0	-14.146582	3.641529	-0.007491
139	1	0	-6.012860	-6.334056	-1.920024	164	1	0	-13.856810	1.957858	1.806259
140	1	0	-5.977742	6.175442	1.919844	165	1	0	-11.818425	0.543871	1.876531
141	1	0	-7.992135	4.761138	1.791977	166	1	0	-11.605178	-0.511797	-3.031644
142	1	0	-3.867212	3.288622	-0.524151	167	1	0	-13.646682	-1.920993	-3.098243
143	1	0	-9.185594	2.971373	1.014871	168	1	0	-14.119122	-3.523061	-1.249161
144	1	0	-9.780785	-0.123015	1.028016	169	1	0	-12.528401	-3.706416	0.661518
145	1	0	-9.694500	0.233457	-1.996261	170	1	0	-10.491544	-2.307825	0.723826
146	1	0	0.135984	13.127093	1.692574	171	1	0	10.210689	-2.149705	-2.295700
147	1	0	0.184195	11.653008	3.685024	172	1	0	12.155030	-3.532638	-2.939574
148	1	0	0.164929	9.158559	3.396852	173	1	0	14.074716	-3.806823	-1.373068
149	1	0	0.088373	-10.092337	-1.750063	174	1	0	14.024882	-2.678870	0.848396
150	1	0	-0.015353	-12.506908	-1.065954	175	1	0	12.075191	-1.285375	1.491885
151	1	0	-0.318475	-13.101712	1.321499	176	1	0	11.426087	0.838189	-3.007696
152	1	0	-0.606610	-12.413879	3.676343	177	1	0	13.503231	2.196283	-3.027274
153	1	0	-0.803615	-10.626279	5.379849	178	1	0	14.190817	3.455927	-0.990398
154	1	0	-0.698549	-8.224134	4.694396	179	1	0	12.778805	3.350992	1.061387
155	1	0	-0.399042	-7.615133	2.320379	180	1	0	10.702689	2.005576	1.076193
156	1	0	0.030298	8.445463	-1.335589	-----					
157	1	0	-0.018071	9.926681	-3.312629						

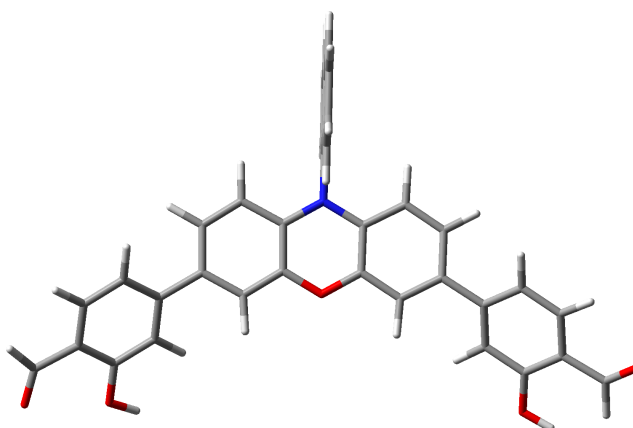


Figure 4.55: The optimized geometry of  $L^{PZ+}$

Standard orientation:

Center Atomic Atomic Coordinates  
(Angstroms)

#### 4. Phenoxazine-based macrocycles for Photoredox catalysis

Number	Number	Type	X	Y	Z							
						41	6	0	-0.152201	5.940531	-2.223388	
						42	6	0	-0.146361	6.338378	-0.911349	
1	6	0	-2.463888	1.558775	0.562954	43	1	0	-2.528353	2.625732	0.782124	
2	6	0	-1.195835	0.949649	0.444323	44	1	0	-2.196745	-2.252149	-0.212786	
3	6	0	-1.141218	-0.435495	0.168067	45	1	0	-4.578104	1.288048	0.523368	
4	6	0	-2.300835	-1.190443	0.019987	46	1	0	2.454882	2.742423	0.731953	
5	6	0	-3.549744	-0.586036	0.138344	47	1	0	4.560204	1.500610	0.435995	
6	6	0	-3.605164	0.804993	0.409796	48	1	0	2.331740	-2.146361	-0.254629	
7	7	0	-0.014391	1.651392	0.584215	49	1	0	-4.000282	-3.159649	0.945875	
8	6	0	1.195821	1.005323	0.421714	50	1	0	-7.976659	-1.149189	-1.237164	
9	6	0	1.200451	-0.380974	0.147273	51	1	0	-5.899706	0.217868	-1.007651	
10	8	0	0.044135	-1.069800	0.032936	52	1	0	-8.459485	-4.675779	-0.114299	
11	6	0	2.436168	1.673187	0.515199	53	1	0	-6.803568	-5.166542	0.683205	
12	6	0	3.608379	0.973299	0.341526	54	1	0	5.879007	0.474435	-1.161634	
13	6	0	3.613055	-0.419424	0.072769	55	1	0	7.997970	-0.779622	-1.442548	
14	6	0	2.391550	-1.081275	-0.021485	56	1	0	4.205667	-2.931912	0.914414	
15	6	0	-4.797660	-1.375725	-0.013483	57	1	0	9.358127	-2.571444	-1.212729	
16	6	0	4.893980	-1.147940	-0.104225	58	1	0	5.569743	-4.699644	1.124054	
17	6	0	-4.849596	-2.690970	0.443124	59	1	0	-0.127210	6.838046	1.747025	
18	6	0	-6.018112	-3.452736	0.309993	60	1	0	-0.064466	5.152329	3.562372	
19	6	0	-7.149023	-2.881111	-0.300862	61	1	0	-0.011686	2.711288	2.996650	
20	6	0	-7.081987	-1.557950	-0.759621	62	1	0	-0.063683	2.548821	-1.831817	
21	6	0	-5.931387	-0.803038	-0.619926	63	1	0	-0.126984	4.256172	-3.600245	
22	6	0	-8.425396	-3.618643	-0.486282	64	1	0	-0.180345	6.684709	-3.023012	
23	8	0	-5.966662	-4.704105	0.794192	65	1	0	-0.169642	7.400602	-0.652452	
24	8	0	-9.399627	-3.143304	-1.006210							
25	6	0	5.971676	-0.535782	-0.756370							
26	6	0	7.155064	-1.245601	-0.921649							
27	6	0	7.310446	-2.548818	-0.447243							
28	6	0	6.227576	-3.164894	0.218496							
29	6	0	5.030885	-2.455335	0.374669							
30	6	0	8.623910	-3.222060	-0.669838							
31	8	0	8.915748	-4.334007	-0.328148							
32	8	0	6.376115	-4.406007	0.686633							
33	6	0	-0.044712	3.065021	0.886936							
34	6	0	-0.080012	3.995849	-0.193791							
35	6	0	-0.110156	5.379237	0.139941							
36	6	0	-0.103694	5.770947	1.508587							
37	6	0	-0.068991	4.839994	2.515829							
38	6	0	-0.039015	3.460546	2.200541							
39	6	0	-0.086601	3.608857	-1.563310							
40	6	0	-0.121933	4.561207	-2.550715							

#### 4. Phenoxazine-based macrocycles for Photoredox catalysis

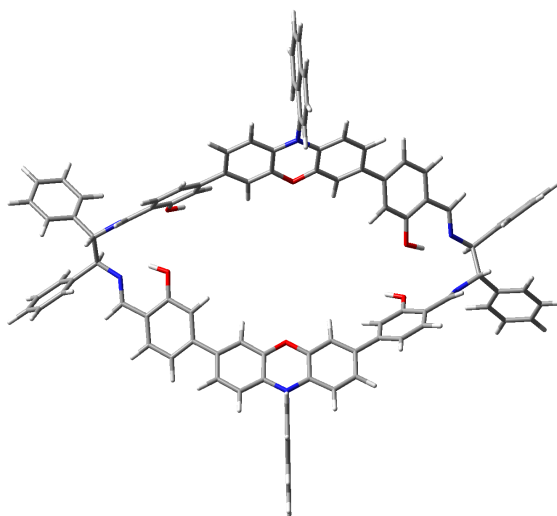


Figure 4.56: The optimized geometry of  $R^{PZ++}$

Standard orientation:						19	6	0	-7.253372	2.814626	1.150160
-----						20	6	0	-7.139987	4.196988	0.938433
Center	Atomic	Atomic	Coordinates			21	6	0	-6.009771	4.755519	0.367102
(Angstroms)						22	6	0	-8.473605	2.256805	1.736141
Number	Number	Type	X	Y	Z	23	8	0	-6.201032	0.657856	0.953640
-----						24	7	0	-8.611011	0.999256	1.892235
1	6	0	-2.652108	6.156126	-2.082706	25	6	0	-9.774928	0.367647	2.487068
2	6	0	-1.393569	5.602016	-1.846420	26	6	0	-10.093319	-0.930309	1.684377
3	6	0	-1.317766	4.485874	-0.994026	27	7	0	-8.857721	-1.656137	1.508788
4	6	0	-2.453324	3.955736	-0.408084	28	6	0	-8.434251	-1.850694	0.334629
5	6	0	-3.720633	4.510173	-0.646517	29	6	0	-7.146329	-2.501821	0.011927
6	6	0	-3.795743	5.617699	-1.492687	30	6	0	-6.060428	-2.561240	0.914617
7	7	0	-0.217479	6.109754	-2.416994	31	6	0	-4.858885	-3.146160	0.504751
8	6	0	1.014083	5.558700	-2.038357	32	6	0	-4.708383	-3.691120	-0.775662
9	6	0	1.033066	4.447800	-1.175220	33	6	0	-5.784496	-3.632860	-1.668990
10	8	0	-0.122455	3.875407	-0.712220	34	6	0	-6.971160	-3.029485	-1.269162
11	6	0	2.238786	6.063165	-2.478114	35	8	0	-6.202285	-2.050385	2.144121
12	6	0	3.441302	5.477747	-2.081255	36	6	0	-3.425972	-4.313841	-1.179606
13	6	0	3.459693	4.375374	-1.225834	37	6	0	-2.207411	-3.839422	-0.696834
14	6	0	2.227650	3.873975	-0.777554	38	6	0	-1.015272	-4.444907	-1.080321
15	6	0	-4.938222	3.927602	-0.020648	39	6	0	-1.001853	-5.542777	-1.969811
16	6	0	4.737787	3.748292	-0.797104	40	6	0	-2.236343	-6.022444	-2.457590
17	6	0	-5.035337	2.552694	0.190913	41	6	0	-3.410686	-5.419830	-2.068308
18	6	0	-6.173168	1.978181	0.773986	42	8	0	0.135758	-3.941747	-0.581679

#### 4. Phenoxazine-based macrocycles for Photoredox catalysis

43	6	0	1.321480	-4.503432	-0.907039	85	6	0	-0.009907	10.052742	-0.794533
44	6	0	1.383168	-5.608837	-1.786600	86	6	0	-0.057053	11.174305	-1.661172
45	7	0	0.210626	-6.105063	-2.321344	87	6	0	-0.169842	10.994129	-3.015926
46	6	0	2.471208	-3.965146	-0.340000	88	6	0	8.534515	-2.332504	1.679620
47	6	0	3.721029	-4.512128	-0.626818	89	6	0	-11.111467	-1.781437	2.423376
48	6	0	3.780916	-5.622957	-1.508150	90	6	0	-11.006199	1.238186	2.649285
49	6	0	2.649532	-6.160620	-2.077503	91	6	0	11.051705	1.755726	2.486025
50	6	0	4.957125	-3.950678	-0.031448	92	6	0	11.053914	-1.292967	2.597990
51	6	0	5.044806	-2.585093	0.236531	93	6	0	12.422014	1.694756	2.219572
52	6	0	6.201655	-2.023739	0.801254	94	6	0	13.323006	2.458098	2.960767
53	6	0	7.295896	-2.876536	1.103463	95	6	0	12.861017	3.293874	3.975731
54	6	0	7.186853	-4.246170	0.835753	96	6	0	11.493991	3.364245	4.242936
55	6	0	6.043538	-4.791570	0.272337	97	6	0	10.593661	2.600672	3.502692
56	6	0	5.822251	3.642093	-1.679138	98	6	0	11.687023	-1.810147	1.459604
57	6	0	6.998963	3.041180	-1.254318	99	6	0	12.849971	-2.568127	1.573453
58	6	0	7.160787	2.537935	0.042520	100	6	0	13.400798	-2.818761	2.830866
59	6	0	6.069444	2.644506	0.930418	101	6	0	12.779624	-2.310720	3.969118
60	6	0	4.881997	3.242430	0.497989	102	6	0	11.612612	-1.555616	3.850771
61	6	0	8.440702	1.894583	0.383989	103	6	0	-10.701329	-2.643233	3.446157
62	7	0	8.807275	1.567507	1.551138	104	6	0	-11.638737	-3.390707	4.156270
63	8	0	6.184252	2.162681	2.180363	105	6	0	-12.995869	-3.287051	3.852142
64	8	0	6.220625	-0.721619	1.027083	106	6	0	-13.410360	-2.433867	2.831155
65	7	0	8.645486	-1.084175	1.889132	107	6	0	-12.472064	-1.687012	2.120264
66	6	0	10.070522	0.890511	1.711544	108	6	0	-11.557681	1.454487	3.913879
67	6	0	9.806828	-0.440050	2.477368	109	6	0	-12.711444	2.223258	4.068915
68	6	0	-0.264753	7.251837	-3.272153	110	6	0	-13.326389	2.791342	2.956040
69	6	0	0.249446	-7.224994	-3.233422	111	6	0	-12.782186	2.587654	1.687297
70	6	0	-0.193114	8.562966	-2.701493	112	6	0	-11.632447	1.816260	1.536824
71	6	0	-0.240978	9.685857	-3.573045	113	1	0	-2.738831	7.018336	-2.746947
72	6	0	-0.358402	9.474691	-4.976371	114	1	0	-2.324208	3.102783	0.262156
73	6	0	-0.425435	8.206889	-5.493824	115	1	0	-4.766347	6.064943	-1.720924
74	6	0	-0.377812	7.084157	-4.630393	116	1	0	2.250712	6.932158	-3.139028
75	6	0	0.362646	-6.982453	-4.578670	117	1	0	4.381416	5.912298	-2.430403
76	6	0	0.401735	-8.068989	-5.485276	118	1	0	2.173253	3.000127	-0.123800
77	6	0	0.325988	-9.355550	-5.015194	119	1	0	-4.234005	1.876611	-0.116648
78	6	0	0.207947	-9.627216	-3.622675	120	1	0	-7.970757	4.842359	1.242805
79	6	0	0.167840	-8.545471	-2.698811	121	1	0	-5.939103	5.837935	0.239407
80	6	0	0.128181	-10.958504	-3.124904	122	1	0	-9.260304	2.978200	2.024961
81	6	0	0.014467	-11.198373	-1.779806	123	1	0	-7.071422	0.431129	1.382194
82	6	0	-0.024972	-10.117211	-0.863237	124	1	0	-9.454554	0.023859	3.486268
83	6	0	0.049724	-8.821171	-1.307611	125	1	0	-10.523781	-0.624695	0.707287
84	6	0	-0.076091	8.778759	-1.299609	126	1	0	-9.016655	-1.523508	-0.552907

#### 4. Phenoxazine-based macrocycles for Photoredox catalysis

127	1	0	-4.038173	-3.204240	1.227214	169	1	0	13.333507	-2.961950	0.675126
128	1	0	-5.688187	-4.017349	-2.687018	170	1	0	14.316868	-3.408747	2.921219
129	1	0	-7.800582	-2.955294	-1.979094	171	1	0	13.207353	-2.498171	4.957667
130	1	0	-5.340359	-1.961798	2.564048	172	1	0	11.135131	-1.148833	4.747699
131	1	0	-2.150926	-2.974924	-0.032489	173	1	0	-9.633968	-2.732362	3.666684
132	1	0	-2.250095	-6.879011	-3.133404	174	1	0	-11.306510	-4.063260	4.952231
133	1	0	-4.358156	-5.820219	-2.435000	175	1	0	-13.730788	-3.874613	4.409279
134	1	0	2.359245	-3.124878	0.347779	176	1	0	-14.472067	-2.348563	2.583942
135	1	0	4.753878	-6.049531	-1.760529	177	1	0	-12.804026	-1.013881	1.323321
136	1	0	2.721326	-7.008801	-2.760140	178	1	0	-11.083733	1.002705	4.790951
137	1	0	4.233984	-1.896518	-0.013368	179	1	0	-13.132440	2.376094	5.066291
138	1	0	8.031767	-4.896199	1.084580	180	1	0	-14.230822	3.394040	3.075154
139	1	0	5.983030	-5.868587	0.100500	181	1	0	-13.258540	3.032044	0.808985
140	1	0	5.731166	4.004078	-2.705821	182	1	0	-11.214439	1.664489	0.535795
141	1	0	7.835621	2.945893	-1.954228						
142	1	0	4.055645	3.337616	1.210985						
143	1	0	9.093620	1.695057	-0.493745						
144	1	0	5.336068	2.249028	2.627844						
145	1	0	7.103489	-0.484289	1.430263						
146	1	0	10.523005	0.634650	0.729380						
147	1	0	9.486529	-0.135382	3.488948						
148	1	0	-0.394363	10.345846	-5.637236						
149	1	0	-0.515707	8.054001	-6.572213						
150	1	0	-0.430699	6.070191	-5.035593						
151	1	0	0.422290	-5.953479	-4.943958						
152	1	0	0.492154	-7.872378	-6.555836						
153	1	0	0.355536	-10.198288	-5.711673						
154	1	0	0.159088	-11.787988	-3.836935						
155	1	0	-0.046453	-12.224090	-1.407962						
156	1	0	-0.115917	-10.320565	0.206783						
157	1	0	0.018146	-7.997318	-0.589096						
158	1	0	-0.039830	7.915422	-0.630258						
159	1	0	0.080009	10.207389	0.283953						
160	1	0	-0.002966	12.183291	-1.243958						
161	1	0	-0.206778	11.854936	-3.690172						
162	1	0	9.341377	-3.052900	1.908498						
163	1	0	12.791219	1.038054	1.425200						
164	1	0	14.392575	2.401145	2.740590						
165	1	0	13.566352	3.895727	4.555407						
166	1	0	11.124214	4.025354	5.031834						
167	1	0	9.518354	2.665842	3.690947						
168	1	0	11.267181	-1.616039	0.466641						

#### 4. Phenoxazine-based macrocycles for Photoredox catalysis

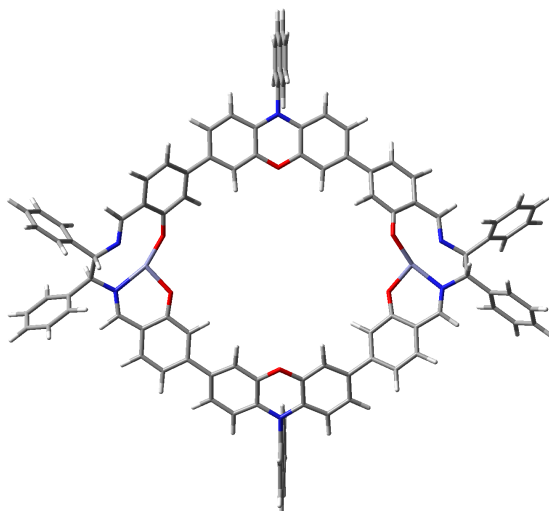


Figure 4.57: The optimized geometry of  $\text{Zn}_2\text{R}^{\text{PZ}^{2+}}$

Standard orientation:						19	6	0	7.148630	3.193013	-0.289442
-----						20	6	0	7.082582	4.542292	-0.697082
Center	Atomic	Atomic	Coordinates			21	6	0	5.989474	5.341955	-0.437704
			(Angstroms)			22	6	0	8.341918	2.445338	-0.643577
Number	Number	Type	X	Y	Z	23	8	0	6.029411	1.423602	0.914852
-----						24	7	0	8.477132	1.175719	-0.515742
1	6	0	2.555503	7.737333	0.818973	25	6	0	9.715126	0.465466	-0.839479
2	6	0	1.294096	7.102487	0.817274	26	6	0	9.846727	-0.743523	0.140957
3	6	0	1.256447	5.698672	0.658527	27	7	0	8.542937	-1.399707	0.209043
4	6	0	2.419267	4.955598	0.496584	28	6	0	8.380229	-2.681867	0.164698
5	6	0	3.662376	5.583953	0.486657	29	6	0	7.123224	-3.377051	0.102752
6	6	0	3.702551	6.992333	0.655103	30	6	0	5.852023	-2.729142	-0.046252
7	7	0	0.102640	7.791355	0.951751	31	6	0	4.703288	-3.565513	-0.116503
8	6	0	-1.100007	7.111621	0.894316	32	6	0	4.761835	-4.947081	-0.075069
9	6	0	-1.083178	5.707343	0.736652	33	6	0	6.035766	-5.570057	0.035538
10	8	0	0.082293	5.032661	0.642024	34	6	0	7.165361	-4.796078	0.123331
11	6	0	-2.354076	7.754995	0.980798	35	8	0	5.677653	-1.451256	-0.121860
12	6	0	-3.514610	7.015548	0.916371	36	6	0	3.515286	-5.762289	-0.137696
13	6	0	-3.496192	5.604690	0.765021	37	6	0	2.320276	-5.212334	-0.631559
14	6	0	-2.258960	4.969547	0.682753	38	6	0	1.150580	-5.946314	-0.665087
15	6	0	4.897720	4.789691	0.274456	39	6	0	1.111041	-7.278175	-0.215359
16	6	0	-4.749353	4.812343	0.698947	40	6	0	2.294262	-7.831191	0.274610
17	6	0	4.960835	3.484951	0.731736	41	6	0	3.472800	-7.084318	0.312170
18	6	0	6.069001	2.625818	0.468167	42	8	0	0.034275	-5.339341	-1.178657

#### 4. Phenoxazine-based macrocycles for Photoredox catalysis

43	6	0	-1.182594	-5.904619	-0.900223	85	6	0	0.005658	10.398325	-2.434685
44	6	0	-1.284106	-7.244502	-0.484966	86	6	0	0.018027	11.802461	-2.237568
45	7	0	-0.104257	-7.976463	-0.274977	87	6	0	0.060539	12.320671	-0.968890
46	6	0	-2.308886	-5.120570	-1.067736	88	6	0	-8.277990	-2.338507	-1.320256
47	6	0	-3.593215	-5.646330	-0.857959	89	30	0	6.980838	-0.095721	0.189663
48	6	0	-3.698116	-6.987780	-0.487197	90	30	0	-6.876240	0.097002	-0.473271
49	6	0	-2.560827	-7.774020	-0.292887	91	6	0	11.020613	-1.626144	-0.233132
50	6	0	-4.791339	-4.774958	-0.989788	92	6	0	10.968666	1.316175	-0.847549
51	6	0	-4.738430	-3.463160	-0.557094	93	6	0	-10.952956	1.423513	0.253660
52	6	0	-5.840430	-2.568469	-0.653091	94	6	0	-10.940113	-1.291667	-1.041182
53	6	0	-7.052368	-3.087055	-1.222966	95	6	0	-11.188760	2.355117	-0.766273
54	6	0	-7.087669	-4.443034	-1.643918	96	6	0	-12.331828	3.149381	-0.751586
55	6	0	-5.999725	-5.274954	-1.543892	97	6	0	-13.258822	3.022547	0.284030
56	6	0	-5.907169	5.230476	1.398093	98	6	0	-13.033279	2.101127	1.303170
57	6	0	-7.031054	4.432096	1.356068	99	6	0	-11.885204	1.308234	1.286810
58	6	0	-7.065520	3.205484	0.658914	100	6	0	-11.851056	-1.218888	-2.096888
59	6	0	-5.908706	2.774209	-0.073972	101	6	0	-12.992404	-2.021321	-2.111891
60	6	0	-4.773828	3.636616	-0.030804	102	6	0	-13.232790	-2.910878	-1.068224
61	6	0	-8.309175	2.454401	0.681360	103	6	0	-12.327130	-2.996130	-0.009823
62	7	0	-8.441837	1.248049	0.264970	104	6	0	-11.191000	-2.191884	0.003147
63	8	0	-5.823299	1.691004	-0.757514	105	6	0	11.092748	-2.241241	-1.490258
64	8	0	-5.685699	-1.365379	-0.208027	106	6	0	12.183885	-3.035873	-1.830897
65	7	0	-8.424490	-1.081588	-1.056188	107	6	0	13.222828	-3.226438	-0.918789
66	6	0	-9.722297	0.540719	0.226202	108	6	0	13.160541	-2.621890	0.333784
67	6	0	-9.715756	-0.398724	-1.024238	109	6	0	12.063970	-1.828582	0.672550
68	6	0	0.113573	9.225075	1.124496	110	6	0	11.737362	1.434384	-2.007265
69	6	0	-0.166590	-9.348001	0.116319	111	6	0	12.906931	2.195315	-2.013263
70	6	0	0.080538	10.054755	-0.036097	112	6	0	13.318378	2.850261	-0.855579
71	6	0	0.092841	11.463137	0.166883	113	6	0	12.555742	2.742655	0.308374
72	6	0	0.136765	11.979545	1.492923	114	6	0	11.390756	1.980736	0.311668
73	6	0	0.167226	11.144453	2.580755	115	1	0	2.611217	8.819165	0.950789
74	6	0	0.155356	9.741056	2.394536	116	1	0	2.322530	3.878794	0.346643
75	6	0	-0.062945	-10.329641	-0.837960	117	1	0	4.670121	7.498810	0.669577
76	6	0	-0.120923	-11.698330	-0.474700	118	1	0	-2.393560	8.840228	1.088417
77	6	0	-0.281802	-12.054320	0.839165	119	1	0	-4.475025	7.533399	0.962736
78	6	0	-0.392616	-11.063238	1.855833	120	1	0	-2.177684	3.885046	0.591912
79	6	0	-0.335140	-9.688091	1.497449	121	1	0	4.150440	3.040194	1.314449
80	6	0	-0.559353	-11.412094	3.226108	122	1	0	7.925782	4.954629	-1.261569
81	6	0	-0.663238	-10.441816	4.189598	123	1	0	5.954786	6.365177	-0.817895
82	6	0	-0.605395	-9.071415	3.829473	124	1	0	9.178770	3.042734	-1.046149
83	6	0	-0.445610	-8.701754	2.517787	125	1	0	9.577255	0.036710	-1.848246
84	6	0	0.036150	9.542073	-1.362981	126	1	0	10.046920	-0.317580	1.140941



#### 4. Phenoxazine-based macrocycles for Photoredox catalysis

127	1	0	9.274066	-3.328201	0.151285	169	1	0	-12.507447	-3.695617	0.810889
128	1	0	3.751924	-3.035069	-0.183779	170	1	0	-10.484212	-2.278191	0.835422
129	1	0	6.124184	-6.657512	0.029683	171	1	0	10.280732	-2.109877	-2.213470
130	1	0	8.143924	-5.282132	0.204143	172	1	0	12.224249	-3.511053	-2.814742
131	1	0	2.274502	-4.193820	-1.020507	173	1	0	14.080632	-3.848981	-1.186733
132	1	0	2.293971	-8.860706	0.638540	174	1	0	13.969870	-2.766392	1.054351
133	1	0	4.366376	-7.552795	0.729696	175	1	0	12.022106	-1.353265	1.657714
134	1	0	-2.165652	-4.087071	-1.391170	176	1	0	11.422422	0.915974	-2.918469
135	1	0	-4.682328	-7.427529	-0.305514	177	1	0	13.499639	2.273089	-2.928564
136	1	0	-2.666907	-8.813918	0.023060	178	1	0	14.235226	3.445759	-0.857531
137	1	0	-3.834378	-3.058094	-0.096309	179	1	0	12.873106	3.254866	1.220713
138	1	0	-8.021031	-4.826164	-2.071065	180	1	0	10.797902	1.910042	1.229868
139	1	0	-6.052642	-6.304575	-1.904712						
140	1	0	-5.907064	6.146389	1.992824						
141	1	0	-7.929539	4.744251	1.899135						
142	1	0	-3.911598	3.301634	-0.612111						
143	1	0	-9.187438	2.992332	1.079480						
144	1	0	-9.744570	-0.118689	1.112227						
145	1	0	-9.758608	0.258045	-1.912045						
146	1	0	0.145851	13.064390	1.631609						
147	1	0	0.200875	11.551660	3.593684						
148	1	0	0.179697	9.067283	3.255405						
149	1	0	0.065249	-10.037362	-1.883325						
150	1	0	-0.036422	-12.464927	-1.249068						
151	1	0	-0.327346	-13.108968	1.126686						
152	1	0	-0.602920	-12.471370	3.496539						
153	1	0	-0.790838	-10.721111	5.238842						
154	1	0	-0.688961	-8.305171	4.604760						
155	1	0	-0.401301	-7.644702	2.243026						
156	1	0	0.025999	8.461334	-1.529694						
157	1	0	-0.028733	9.996414	-3.450477						
158	1	0	-0.006726	12.469484	-3.102786						
159	1	0	0.070108	13.402688	-0.810174						
160	1	0	-9.163093	-2.922417	-1.625025						
161	1	0	-10.466240	2.469264	-1.581462						
162	1	0	-12.502811	3.871347	-1.554694						
163	1	0	-14.158468	3.643642	0.294106						
164	1	0	-13.755484	1.994371	2.116888						
165	1	0	-11.716566	0.580548	2.086967						
166	1	0	-11.668991	-0.519077	-2.918680						
167	1	0	-13.696553	-1.948807	-2.944977						
168	1	0	-14.125943	-3.541247	-1.077998						

#### 4. Phenoxazine-based macrocycles for Photoredox catalysis

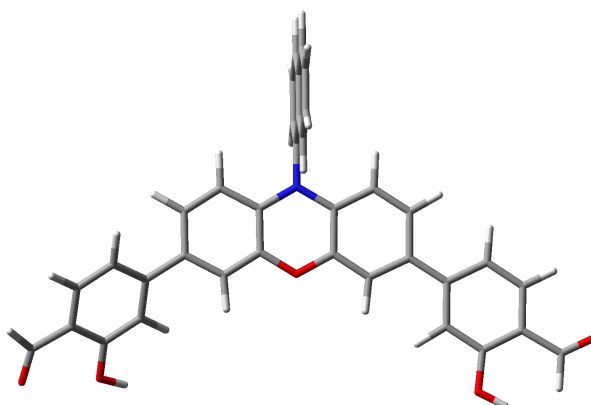


Figure 4.58: The optimized geometry of  $L^{PZ}$  in the triplet state

Standard orientation:						22	6	0	-8.438952	-3.641485	-0.304763
-----						23	8	0	-5.743809	-4.838529	-0.540139
Center	Atomic	Atomic	Coordinates			24	8	0	-9.544862	-3.154415	-0.208895
						25	6	0	5.982140	-0.582256	-0.713899
(Angstroms)						26	6	0	7.156147	-1.308377	-0.852832
Number	Number	Type	X	Y	Z	27	6	0	7.293008	-2.607565	-0.352455
-----						28	6	0	6.193445	-3.189142	0.313061
1	6	0	-2.493577	1.609203	0.553603	29	6	0	5.009323	-2.456334	0.451547
2	6	0	-1.205131	1.004937	0.449476	30	6	0	8.591991	-3.297910	-0.551992
3	6	0	-1.164150	-0.431059	0.187796	31	8	0	8.884635	-4.405512	-0.187865
4	6	0	-2.291468	-1.173569	0.060597	32	8	0	6.308934	-4.429098	0.806738
5	6	0	-3.607084	-0.585421	0.175504	33	6	0	-0.035561	3.110113	0.832122
6	6	0	-3.629695	0.876719	0.425985	34	6	0	-0.046654	4.018224	-0.271208
7	7	0	-0.017499	1.699310	0.574019	35	6	0	-0.059875	5.412451	0.009887
8	6	0	1.198922	1.036101	0.426912	36	6	0	-0.065093	5.851633	1.364253
9	6	0	1.192932	-0.347130	0.176141	37	6	0	-0.058276	4.951086	2.398161
10	8	0	0.034826	-1.051669	0.066764	38	6	0	-0.043323	3.560480	2.127818
11	6	0	2.440235	1.686532	0.513755	39	6	0	-0.047082	3.581837	-1.625927
12	6	0	3.620984	0.979032	0.355505	40	6	0	-0.058150	4.495475	-2.649158
13	6	0	3.615193	-0.404913	0.109560	41	6	0	-0.069087	5.886572	-2.373091
14	6	0	2.381943	-1.052366	0.023294	42	6	0	-0.070346	6.332579	-1.076514
15	6	0	-4.791924	-1.349793	0.055320	43	1	0	-2.558626	2.683904	0.737568
16	6	0	4.886892	-1.158472	-0.053149	44	1	0	-2.160231	-2.237543	-0.132972
17	6	0	-4.755506	-2.757377	-0.189051	45	1	0	-4.586599	1.389861	0.509708
18	6	0	-5.907380	-3.514442	-0.308760	46	1	0	2.468911	2.759004	0.715008
19	6	0	-7.183826	-2.905557	-0.190007	47	1	0	4.572401	1.508316	0.448313
20	6	0	-7.230839	-1.510464	0.052862	48	1	0	2.310299	-2.121193	-0.191430
21	6	0	-6.095520	-0.753665	0.172412						

#### 4. Phenoxazine-based macrocycles for Photoredox catalysis

49	1	0	-3.813076	-3.295636	-0.292007
50	1	0	-8.222496	-1.058734	0.141876
51	1	0	-6.199246	0.315219	0.359708
52	1	0	-8.354293	-4.746475	-0.497287
53	1	0	-6.597006	-5.276236	-0.608816
54	1	0	5.901584	0.420401	-1.139770
55	1	0	8.009685	-0.864447	-1.376573
56	1	0	4.172315	-2.908664	0.994444
57	1	0	9.333907	-2.663957	-1.107655
58	1	0	5.482838	-4.685186	1.230487
59	1	0	-0.076453	6.926609	1.566865
60	1	0	-0.064832	5.297182	3.434565
61	1	0	-0.038742	2.835238	2.945789
62	1	0	-0.043271	2.510429	-1.842442
63	1	0	-0.060810	4.150557	-3.686421
64	1	0	-0.078520	6.601708	-3.199782
65	1	0	-0.080957	7.404197	-0.856711

-----

#### 4. Phenoxazine-based macrocycles for Photoredox catalysis

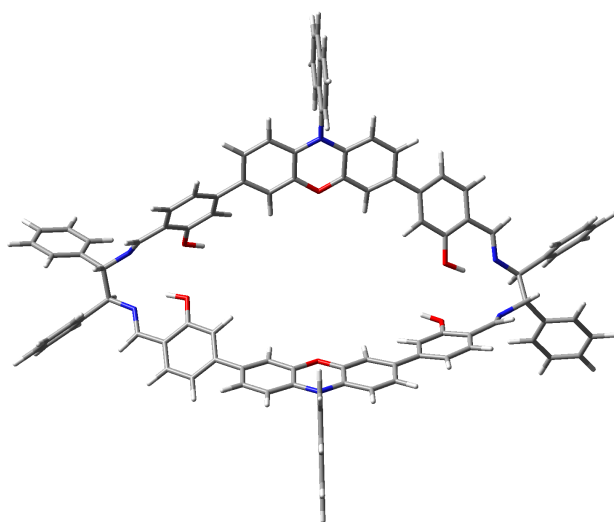


Figure 4.59: The optimized geometry of  $R^{Pz^{2+}}$  in the triplet state

Standard orientation:						
Center Number	Atomic Number	Atomic Type	Coordinates (Angstroms)			
			X	Y	Z	
						19 6 0 -7.311551 2.832996 0.919815
						20 6 0 -7.232504 4.202433 0.624739
						21 6 0 -6.098741 4.764783 0.063638
						22 6 0 -8.521830 2.280188 1.532590
						23 8 0 -6.171243 0.710471 0.899664
						24 7 0 -8.632640 1.034467 1.773287
						25 6 0 -9.764655 0.447430 2.468226
						26 6 0 -10.025862 -0.983339 1.909327
						27 7 0 -8.758710 -1.660320 1.801441
						28 6 0 -8.477157 -2.235143 0.702752
						29 6 0 -7.205932 -2.878573 0.377862
						30 6 0 -5.989218 -2.621165 1.066443
						31 6 0 -4.799909 -3.164261 0.611267
						32 6 0 -4.727541 -4.024459 -0.528995
						33 6 0 -5.969072 -4.298003 -1.188585
						34 6 0 -7.140451 -3.721895 -0.751775
						35 8 0 -6.020669 -1.821731 2.152314
						36 6 0 -3.499436 -4.557165 -0.988762
						37 6 0 -2.223591 -4.154093 -0.438145
						38 6 0 -1.052960 -4.639379 -0.916470
						39 6 0 -1.005058 -5.624997 -1.997784
						40 6 0 -2.253406 -6.054813 -2.541190
						41 6 0 -3.432098 -5.560312 -2.083517
						42 8 0 0.105255 -4.183434 -0.379484
1	6	0	-2.647036	6.164715	-2.254386	
2	6	0	-1.392683	5.632264	-1.955889	
3	6	0	-1.338020	4.533987	-1.079876	
4	6	0	-2.489714	4.003039	-0.527529	
5	6	0	-3.753649	4.535976	-0.826180	
6	6	0	-3.807358	5.623491	-1.699587	
7	7	0	-0.198485	6.145323	-2.486481	
8	6	0	1.022446	5.591770	-2.076300	
9	6	0	1.017439	4.492575	-1.197895	
10	8	0	-0.148762	3.944529	-0.736428	
11	6	0	2.258568	6.082220	-2.498895	
12	6	0	3.449202	5.491800	-2.074134	
13	6	0	3.444389	4.394846	-1.211327	
14	6	0	2.200354	3.909025	-0.779074	
15	6	0	-4.985694	3.951656	-0.228743	
16	6	0	4.711554	3.759480	-0.760819	
17	6	0	-5.051215	2.590149	0.059374	
18	6	0	-6.192132	2.012098	0.636757	

#### 4. Phenoxazine-based macrocycles for Photoredox catalysis

43	6	0	1.305056	-4.642079	-0.828017	85	6	0	-0.054941	10.112755	-0.929043
44	6	0	1.396658	-5.615446	-1.838086	86	6	0	-0.079057	11.219472	-1.815617
45	7	0	0.223858	-6.098788	-2.417510	87	6	0	-0.149127	11.016430	-3.170072
46	6	0	2.447565	-4.111132	-0.238778	88	6	0	8.473665	-2.282458	1.743567
47	6	0	3.718615	-4.539639	-0.623405	89	6	0	-10.967658	-1.739972	2.833578
48	6	0	3.809456	-5.528089	-1.618487	90	6	0	-11.033532	1.278688	2.494270
49	6	0	2.675366	-6.053881	-2.217360	91	6	0	10.992329	1.785760	2.633236
50	6	0	4.939825	-3.957428	-0.004548	92	6	0	10.973834	-1.252977	2.725876
51	6	0	4.990194	-2.600120	0.304723	93	6	0	12.366745	1.712102	2.391519
52	6	0	6.131810	-2.020404	0.880384	94	6	0	13.262616	2.463834	3.150659
53	6	0	7.254768	-2.841501	1.154054	95	6	0	12.791967	3.301640	4.160021
54	6	0	7.185939	-4.207834	0.843407	96	6	0	11.421100	3.385133	4.402887
55	6	0	6.057130	-4.769262	0.271590	97	6	0	10.526240	2.633173	3.644273
56	6	0	5.818510	3.672745	-1.617103	98	6	0	11.622183	-1.766169	1.594332
57	6	0	6.987503	3.070396	-1.173906	99	6	0	12.784953	-2.522581	1.719673
58	6	0	7.120394	2.549009	0.118628	100	6	0	13.321360	-2.776727	2.982574
59	6	0	6.004986	2.627861	0.978154	101	6	0	12.684840	-2.273698	4.114555
60	6	0	4.825184	3.227926	0.526953	102	6	0	11.518080	-1.520183	3.984004
61	6	0	8.392491	1.901873	0.482651	103	6	0	-10.462050	-2.432286	3.939520
62	7	0	8.764464	1.629035	1.661638	104	6	0	-11.323382	-3.092876	4.813305
63	8	0	6.091343	2.118104	2.219153	105	6	0	-12.700529	-3.072004	4.593051
64	8	0	6.114069	-0.719169	1.144673	106	6	0	-13.210855	-2.388645	3.490820
65	7	0	8.573948	-1.035592	1.981183	107	6	0	-12.348259	-1.728251	2.616743
66	6	0	10.014568	0.933709	1.840077	108	6	0	-11.621023	1.645935	3.706752
67	6	0	9.726019	-0.400763	2.592730	109	6	0	-12.811630	2.372842	3.734492
68	6	0	-0.223055	7.269084	-3.363752	110	6	0	-13.428848	2.747399	2.543596
69	6	0	0.293509	-7.097543	-3.442630	111	6	0	-12.848827	2.392195	1.324876
70	6	0	-0.173709	8.591120	-2.815857	112	6	0	-11.662233	1.663551	1.302435
71	6	0	-0.198406	9.698814	-3.707341	113	1	0	-2.717850	7.011633	-2.940021
72	6	0	-0.271660	9.462670	-5.109656	114	1	0	-2.375847	3.164095	0.162476
73	6	0	-0.318255	8.185421	-5.605679	115	1	0	-4.773169	6.052625	-1.977274
74	6	0	-0.293507	7.077806	-4.721826	116	1	0	2.289668	6.943536	-3.169286
75	6	0	0.378678	-6.716177	-4.757618	117	1	0	4.398476	5.916390	-2.410324
76	6	0	0.451274	-7.694227	-5.780213	118	1	0	2.125363	3.039418	-0.121852
77	6	0	0.436502	-9.027108	-5.458977	119	1	0	-4.220040	1.920512	-0.173607
78	6	0	0.346630	-9.452356	-4.103139	120	1	0	-8.093725	4.836834	0.860667
79	6	0	0.271841	-8.477328	-3.070486	121	1	0	-6.057504	5.840007	-0.124300
80	6	0	0.327455	-10.831300	-3.749196	122	1	0	-9.320978	3.004534	1.780833
81	6	0	0.237481	-11.217039	-2.436467	123	1	0	-7.040899	0.449341	1.303796
82	6	0	0.161284	-10.241561	-1.409681	124	1	0	-9.425172	0.293030	3.507829
83	6	0	0.177896	-8.904589	-1.716128	125	1	0	-10.518528	-0.878089	0.918617
84	6	0	-0.101039	8.830508	-1.414832	126	1	0	-9.218694	-2.257868	-0.126417

#### 4. Phenoxazine-based macrocycles for Photoredox catalysis

127	1	0	-3.895582	-2.931200	1.178904	155	1	0	0.222482	-12.278638	-2.175945
128	1	0	-5.996779	-4.934461	-2.073388	156	1	0	0.086900	-10.559706	-0.366521
129	1	0	-8.066904	-3.914973	-1.303091	157	1	0	0.115051	-8.154585	-0.923571
130	1	0	-5.137175	-1.471792	2.307241	158	1	0	-0.083088	7.977163	-0.732173
131	1	0	-2.157180	-3.410906	0.356126	159	1	0	0.000637	10.285205	0.149085
132	1	0	-2.251436	-6.801778	-3.338350	160	1	0	-0.041633	12.235616	-1.413882
133	1	0	-4.356807	-5.935054	-2.521170	161	1	0	-0.168302	11.865767	-3.859640
134	1	0	2.312633	-3.363537	0.546254	162	1	0	9.289255	-2.996660	1.963852
135	1	0	4.792389	-5.871663	-1.950184	163	1	0	12.742697	1.052954	1.602403
136	1	0	2.771439	-6.808549	-3.000301	164	1	0	14.335374	2.395448	2.949217
137	1	0	4.151213	-1.937082	0.079746	165	1	0	13.493288	3.894204	4.754292
138	1	0	8.052802	-4.838283	1.068620	166	1	0	11.043678	4.047318	5.187448
139	1	0	6.022293	-5.840583	0.060037	167	1	0	9.448290	2.707556	3.812271
140	1	0	5.750092	4.047590	-2.640877	168	1	0	11.211294	-1.572470	0.597737
141	1	0	7.840027	2.986374	-1.855943	169	1	0	13.277804	-2.914978	0.825675
142	1	0	3.980256	3.300838	1.220122	170	1	0	14.236297	-3.367242	3.082182
143	1	0	9.035853	1.648927	-0.388485	171	1	0	13.099264	-2.465347	5.108122
144	1	0	5.212349	2.097401	2.611642	172	1	0	11.026948	-1.119202	4.876169
145	1	0	6.989807	-0.468999	1.543699	173	1	0	-9.379480	-2.459669	4.092048
146	1	0	10.479083	0.676476	0.863653	174	1	0	-10.914511	-3.634159	5.671475
147	1	0	9.397597	-0.101058	3.603407	175	1	0	-13.375564	-3.593095	5.277949
148	1	0	-0.290401	10.321918	-5.786790	176	1	0	-14.288827	-2.370159	3.306796
149	1	0	-0.374880	8.012707	-6.683466	177	1	0	-12.755022	-1.188829	1.755178
150	1	0	-0.330680	6.056644	-5.110292	178	1	0	-11.145221	1.344545	4.645270
151	1	0	0.389419	-5.651301	-5.004489	179	1	0	-13.259612	2.644927	4.694232
152	1	0	0.518552	-7.376764	-6.823687	180	1	0	-14.362200	3.316940	2.562658
153	1	0	0.492641	-9.786650	-6.244366	181	1	0	-13.325961	2.684087	0.385003
154	1	0	0.384853	-11.578642	-4.546156	182	1	0	-11.213755	1.391162	0.341110

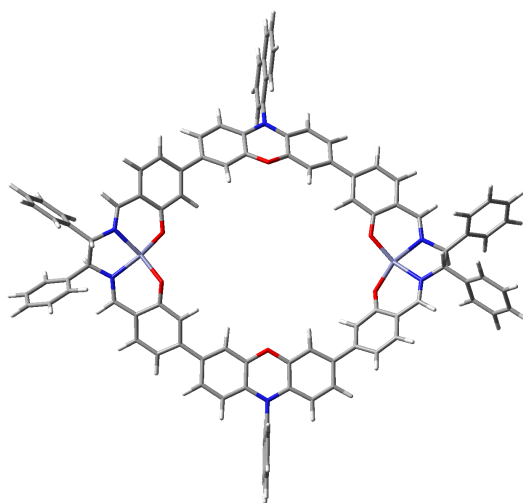


Figure 4.60: The optimized geometry of  $Zn_2R^{PZ}$  in the triplet state

#### 4. Phenoxazine-based macrocycles for Photoredox catalysis

Standard orientation:						37	6	0	2.260574	-5.110325	0.009426
-----						38	6	0	1.093690	-5.850612	0.005209
Center	Atomic	Atomic	Coordinates			39	6	0	1.117510	-7.251953	0.123085
(Angstroms)						40	6	0	2.364056	-7.866749	0.240226
Number	Number	Type	X	Y	Z	41	6	0	3.542629	-7.117813	0.235087
-----						42	8	0	-0.080045	-5.157401	-0.107019
1	6	0	2.583434	7.581638	0.887024	43	6	0	-1.261744	-5.848497	-0.092643
2	6	0	1.307756	7.086468	0.615050	44	6	0	-1.301549	-7.250000	0.019277
3	6	0	1.209595	5.840714	-0.030394	45	7	0	-0.096119	-7.960790	0.122123
4	6	0	2.338795	5.102630	-0.336143	46	6	0	-2.422954	-5.107802	-0.208900
5	6	0	3.622081	5.589977	-0.044516	47	6	0	-3.683008	-5.725248	-0.219159
6	6	0	3.722879	6.847180	0.552813	48	6	0	-3.726096	-7.115231	-0.102779
7	7	0	0.126448	7.769368	0.952715	49	6	0	-2.554643	-7.865762	0.020059
8	6	0	-1.097379	7.089728	0.843175	50	6	0	-4.909951	-4.897401	-0.372879
9	6	0	-1.132047	5.857363	0.166668	51	6	0	-4.972469	-3.638177	0.193390
10	8	0	-0.004224	5.325100	-0.400715	52	6	0	-6.068237	-2.749786	-0.006175
11	6	0	-2.295344	7.572938	1.369102	53	6	0	-7.149612	-3.229567	-0.820922
12	6	0	-3.482283	6.850465	1.232904	54	6	0	-7.090282	-4.547775	-1.340831
13	6	0	-3.518138	5.623888	0.566097	55	6	0	-6.008424	-5.370416	-1.139580
14	6	0	-2.309655	5.147850	0.030209	56	6	0	-6.046119	5.436705	0.608180
15	6	0	4.827761	4.767293	-0.334237	57	6	0	-7.181077	4.667011	0.542768
16	6	0	-4.771512	4.823833	0.452380	58	6	0	-7.142730	3.266661	0.317430
17	6	0	4.800794	3.401038	-0.122460	59	6	0	-5.870531	2.635377	0.113188
18	6	0	5.918449	2.553434	-0.367733	60	6	0	-4.715538	3.464954	0.206631
19	6	0	7.113404	3.182701	-0.855794	61	6	0	-8.400380	2.570613	0.247427
20	6	0	7.119378	4.586180	-1.054773	62	7	0	-8.556597	1.295776	0.113507
21	6	0	6.018669	5.372682	-0.811434	63	8	0	-5.700518	1.385887	-0.145350
22	6	0	8.355865	2.483540	-1.087857	64	8	0	-6.023859	-1.587880	0.548549
23	8	0	5.786582	1.292085	-0.117648	65	7	0	-8.467550	-1.189846	-0.869553
24	7	0	8.519983	1.208326	-1.023228	66	6	0	-9.854889	0.651548	-0.061489
25	6	0	9.804629	0.526039	-1.132440	67	6	0	-9.694255	-0.453866	-1.155593
26	6	0	9.841342	-0.619894	-0.060858	68	6	0	0.190351	9.025269	1.624866
27	7	0	8.548265	-1.274437	-0.041623	69	6	0	-0.103185	-9.376715	0.281078
28	6	0	8.405564	-2.551809	0.335716	70	6	0	0.099040	10.230338	0.858842
29	6	0	7.196162	-3.284477	0.241909	71	6	0	0.162608	11.477389	1.540084
30	6	0	5.949490	-2.799356	-0.429918	72	6	0	0.315172	11.490640	2.955261
31	6	0	4.800151	-3.635483	-0.451401	73	6	0	0.400692	10.319460	3.663589
32	6	0	4.752145	-4.904062	0.115431	74	6	0	0.337028	9.074690	2.990088
33	6	0	5.959723	-5.354878	0.719093	75	6	0	-0.054533	-10.194073	-0.821603
34	6	0	7.121924	-4.591449	0.770213	76	6	0	-0.060059	-11.603833	-0.675470
35	8	0	5.884273	-1.663492	-1.011489	77	6	0	-0.114005	-12.166302	0.573675
36	6	0	3.521246	-5.723703	0.120823	78	6	0	-0.165318	-11.350385	1.739531

#### 4. Phenoxazine-based macrocycles for Photoredox catalysis

79	6	0	-0.160200	-9.935276	1.598493	121	1	0	3.908329	2.909948	0.273221
80	6	0	-0.222128	-11.911903	3.046725	122	1	0	8.041370	5.049484	-1.423662
81	6	0	-0.271353	-11.105491	4.154885	123	1	0	6.049954	6.447988	-1.001534
82	6	0	-0.266248	-9.694512	4.010981	124	1	0	9.225245	3.126531	-1.311529
83	6	0	-0.212039	-9.122122	2.765378	125	1	0	9.813274	0.021439	-2.115440
84	6	0	-0.052664	10.219528	-0.556267	126	1	0	10.011235	-0.131393	0.920251
85	6	0	-0.136950	11.396337	-1.256001	127	1	0	9.274799	-3.098721	0.726300
86	6	0	-0.074250	12.641804	-0.579660	128	1	0	3.940426	-3.207884	-0.973087
87	6	0	0.071842	12.680171	0.783253	129	1	0	5.977723	-6.342269	1.191057
88	6	0	-8.316442	-2.444872	-1.129888	130	1	0	8.006477	-5.006881	1.261173
89	30	0	7.021061	-0.094354	-0.531959	131	1	0	2.156771	-4.025283	-0.055837
90	30	0	-6.986766	-0.028741	-0.022263	132	1	0	2.416189	-8.954224	0.326754
91	6	0	11.025984	-1.529537	-0.336082	133	1	0	4.494005	-7.651870	0.300835
92	6	0	11.034566	1.406516	-1.046011	134	1	0	-2.322161	-4.025870	-0.319004
93	6	0	-11.019540	1.568813	-0.377053	135	1	0	-4.689406	-7.631879	-0.087426
94	6	0	-10.951082	-1.294200	-1.267025	136	1	0	-2.614535	-8.951803	0.117911
95	6	0	-11.038278	2.337106	-1.548920	137	1	0	-4.158836	-3.256100	0.814473
96	6	0	-12.123628	3.157487	-1.844262	138	1	0	-7.931468	-4.901605	-1.947616
97	6	0	-13.211161	3.221086	-0.971990	139	1	0	-5.971707	-6.361147	-1.598169
98	6	0	-13.202672	2.463384	0.196003	140	1	0	-6.129087	6.514319	0.759482
99	6	0	-12.111546	1.645044	0.489851	141	1	0	-8.160780	5.143482	0.661700
100	6	0	-11.729697	-1.257213	-2.425385	142	1	0	-3.764489	2.940685	0.097290
101	6	0	-12.905335	-2.002776	-2.519999	143	1	0	-9.295362	3.214703	0.298417
102	6	0	-13.313738	-2.798930	-1.453331	144	1	0	-10.082826	0.123011	0.882176
103	6	0	-12.540997	-2.847691	-0.292123	145	1	0	-9.545365	0.074844	-2.114985
104	6	0	-11.369978	-2.100604	-0.200456	146	1	0	0.363279	12.455088	3.469824
105	6	0	11.021227	-2.385832	-1.444616	147	1	0	0.517775	10.337988	4.750206
106	6	0	12.123401	-3.187920	-1.727091	148	1	0	0.404252	8.138073	3.550550
107	6	0	13.250038	-3.145619	-0.904176	149	1	0	-0.011435	-9.738979	-1.814661
108	6	0	13.263825	-2.299501	0.201617	150	1	0	-0.021090	-12.237239	-1.565461
109	6	0	12.156195	-1.498614	0.482760	151	1	0	-0.118610	-13.253983	0.692862
110	6	0	11.936724	1.463863	-2.110543	152	1	0	-0.226080	-13.001190	3.150634
111	6	0	13.090374	2.244102	-2.029676	153	1	0	-0.315153	-11.547394	5.154016
112	6	0	13.353212	2.983190	-0.879211	154	1	0	-0.306300	-9.060274	4.900557
113	6	0	12.457271	2.938364	0.189721	155	1	0	-0.208338	-8.035041	2.652931
114	6	0	11.308944	2.155166	0.106522	156	1	0	-0.100243	9.256941	-1.071473
115	1	0	2.687785	8.551445	1.377717	157	1	0	-0.253294	11.377056	-2.342922
116	1	0	2.198340	4.138807	-0.830942	158	1	0	-0.142854	13.571669	-1.150742
117	1	0	4.706926	7.253805	0.800615	159	1	0	0.121062	13.637533	1.310866
118	1	0	-2.300137	8.525587	1.902557	160	1	0	-9.136755	-2.990826	-1.628645
119	1	0	-4.388932	7.255182	1.687591	161	1	0	-10.187633	2.304229	-2.237906
120	1	0	-2.258565	4.207578	-0.521336	162	1	0	-12.120983	3.752564	-2.761615



#### 4. Phenoxazine-based macrocycles for Photoredox catalysis

163	1	0	-14.064497	3.863897	-1.204622
164	1	0	-14.050340	2.506696	0.885214
165	1	0	-12.112018	1.048031	1.407295
166	1	0	-11.415405	-0.629458	-3.265228
167	1	0	-13.503878	-1.959426	-3.433959
168	1	0	-14.233956	-3.385063	-1.525251
169	1	0	-12.852799	-3.474210	0.548062
170	1	0	-10.765686	-2.156105	0.711179
171	1	0	10.134474	-2.434424	-2.084966
172	1	0	12.102883	-3.853964	-2.594256
173	1	0	14.115913	-3.775718	-1.125605
174	1	0	14.141593	-2.260504	0.852568
175	1	0	12.173111	-0.831615	1.350641
176	1	0	11.738245	0.879224	-3.014347
177	1	0	13.787339	2.271887	-2.871679
178	1	0	14.256289	3.596159	-0.813371
179	1	0	12.655048	3.517992	1.095652
180	1	0	10.611428	2.133060	0.950472

---



## 4. Phenoxazine-based macrocycles for Photoredox catalysis

## Energy comparison (energy in Hartree)

Ground state	L <sup>PZ</sup>	R <sup>PZ</sup>	Zn <sub>2</sub> R <sup>PZ</sup>
<i>E</i>	-1814.792727	-4628.213435	-8184.390656
<i>H</i>	-1814.254194	-4626.661939	-8182.882094
<i>G</i>	-1814.356076	-4626.887431	-8183.106352
•+	L <sup>PZ</sup>	R <sup>PZ</sup>	Zn <sub>2</sub> R <sup>PZ</sup>
<i>E</i>	-1814.550559	-4627.986509	-8184.172456
<i>H</i>	-1814.011839	-4626.434851	-8182.663160
<i>G</i>	-1814.113229	-4626.659955	-8182.886818
Triplet	L <sup>PZ</sup>	R <sup>PZ</sup>	Zn <sub>2</sub> R <sup>PZ</sup>
<i>E</i>	-1814.697043	-4628.115027	-8184.296959
<i>H</i>	-1814.161088	-4626.566804	-8182.791273
<i>G</i>	-1814.265110	-4626.794455	-8183.019258

## Energy difference between doublet state and triplet state (energy in Hartree)

•+–Triplet	L <sup>PZ</sup>	R <sup>PZ</sup>	Zn <sub>2</sub> R <sup>PZ</sup>
$\Delta E$	0.146484	0.128518	0.124503
$\Delta H$	0.149249	0.131953	0.128113
$\Delta G$	0.151881	0.134500	0.132440

## Energy difference between doublet state and triplet state (energy in eV)

•+–Triplet	L <sup>PZ</sup>	R <sup>PZ</sup>	Zn <sub>2</sub> R <sup>PZ</sup>
$\Delta E$	3.986035	3.497155	3.387901
$\Delta H$	4.061274	3.590626	3.486134
$\Delta G$	4.132895	3.659933	3.603878

#### 4. Phenoxazine-based macrocycles for Photoredox catalysis

##### Visualization of molecular orbitals

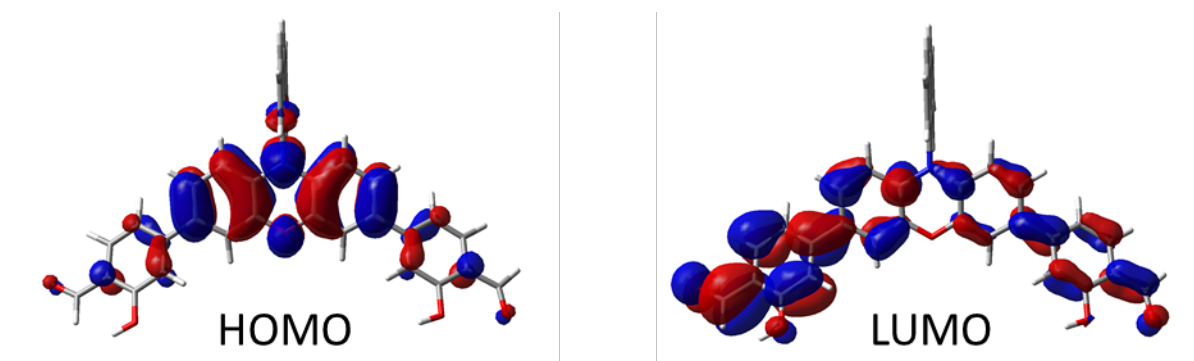


Figure 4.61: The HOMO and the LUMO of  $L^{PZ}$

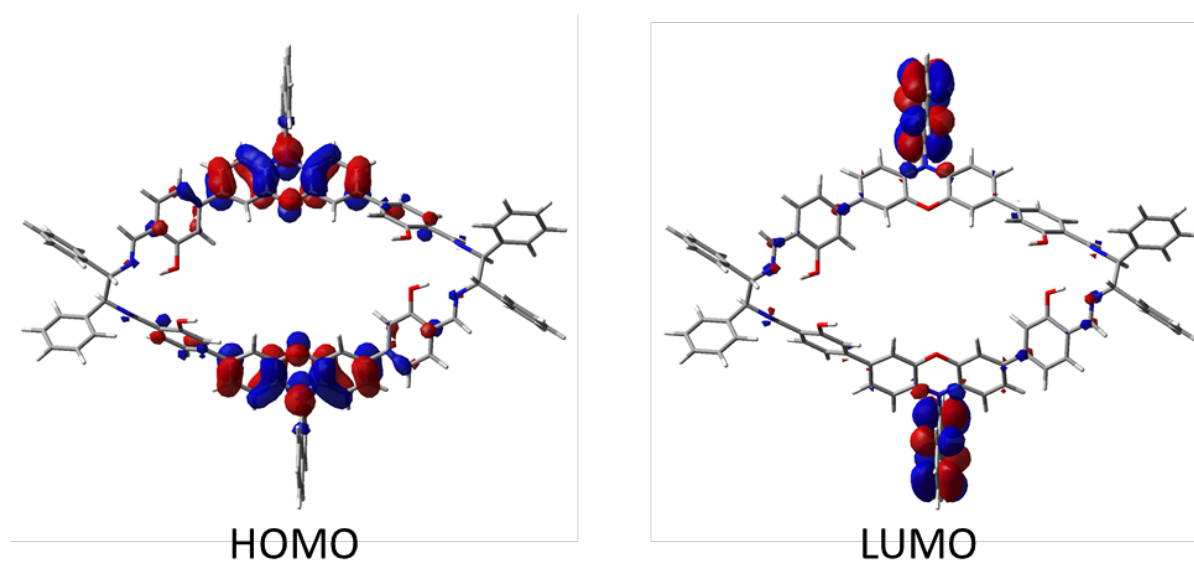


Figure 4.62: The HOMO and the LUMO of  $R^{PZ}$

## 4. Phenoxazine-based macrocycles for Photoredox catalysis

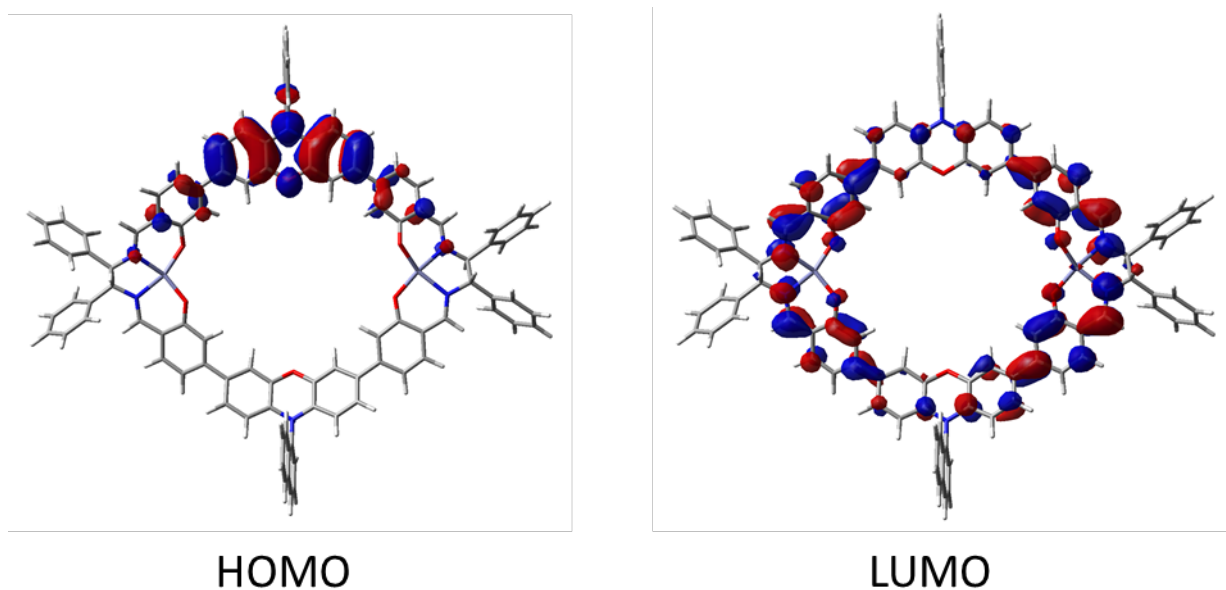


Figure 4.63: The HOMO and the LUMO of  $\text{Zn}_2\text{R}^{\text{PZ}}$

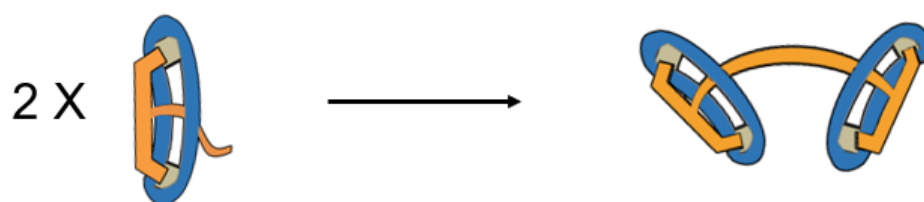
### 4.7 References

- [1] M. H. Shaw, J. Twilton, D. W. C. MacMillan, *J. Org. Chem.* **2016**, *81*, 6898–6926.
- [2] A. Bhattacharyya, S. D. Sarkar, A. Das, *Acs. Catal.* **2021**, *11*, 710–733.
- [3] T. Uchikura, M. Oshima, M. Kawasaki, K. Takahashi, N. Iwasawa, *Angew. Chem. Int. Ed.* **2020**, *59*, 7403–7408.
- [4] T. Uchikura, K. Ono, K. Takahashi, N. Iwasawa, *Angew. Chem. Int. Ed.* **2018**, *57*, 2130–2133.
- [5] D. R. Martir, E. Zysman-Colman, *Chem. Commun.* **2018**, *55*, 139–158.
- [6] M. Schulze, V. Kunz, P. D. Frischmann, F. Würthner, *Nat. Chem.* **2016**, *8*, 576–583.
- [7] C. K. Prier, D. A. Rankic, D. W. C. MacMillan, *Chem. Rev.* **2013**, *113*, 5322–5363.
- [8] T. Hamada, H. Ishida, S. Usui, Y. Watanabe, K. Tsumura, K. Ohkubo, *J. Chem. Soc. Chem. Commun.* **1993**, *0*, 909–911.
- [9] D. A. Nicewicz, D. W. C. MacMillan, *Science* **2008**, *322*, 77–80.
- [10] J. Du, K. L. Skubi, D. M. Schultz, T. P. Yoon, *Science* **2014**, *344*, 392–396.
- [11] H. Huo, X. Shen, C. Wang, L. Zhang, P. Röse, L.-A. Chen, K. Harms, M. Marsch, G. Hilt, E. Meggers, *Nature* **2014**, *515*, 100–103.
- [12] J. Guo, Y. Xu, K. Li, L. Xiao, S. Chen, K. Wu, X. Chen, Y. Fan, J. Liu, C. Su, *Angew. Chem. Int. Ed.* **2017**, *56*, 3852–3856.
- [13] D. Preston, R. A. J. Tucker, A. L. Garden, J. D. Crowley, *Inorg. Chem.* **2016**, *55*, 8928–8934.
- [14] L. S. Lisboa, J. A. Findlay, L. J. Wright, C. G. Hartinger, J. D. Crowley, *Angew. Chem. Int. Ed.* **2020**, *59*, 11101–11107.

#### 4. Phenoxazine-based macrocycles for Photoredox catalysis

- [15] D. Preston, J. J. Sutton, K. C. Gordon, J. D. Crowley, *Angew. Chem. Int. Ed.* **2018**, *57*, 8659–8663.
- [16] M. Frank, M. D. Johnstone, G. H. Clever, *Chem. Eur. J.* **2016**, *22*, 14104–14125.
- [17] R. Zhu, J. Ding, L. Jin, H. Pang, *Coord. Chem. Rev.* **2019**, *389*, 119–140.
- [18] R. Zhu, I. Regeni, J. J. Holstein, B. Dittrich, M. Simon, S. Prévost, M. Gradzielski, G. H. Clever, *Angew. Chem. Int. Ed.* **2018**, *57*, 13652–13656.
- [19] M. Frank, L. Krause, R. Herbst-Irmer, D. Stalke, G. H. Clever, *Dalton. Trans.* **2014**, *43*, 4587–4592.
- [20] R. Zhu, J. Lübben, B. Dittrich, G. H. Clever, *Angew. Chem. Int. Ed.* **2015**, *54*, 2796–2800.
- [21] M. Frank, J. Ahrens, I. Bejenke, M. Krick, D. Schwarzer, G. H. Clever, *J. Am. Chem. Soc.* **2016**, *138*, 8279–8287.
- [22] S. Löffler, J. Lübben, L. Krause, D. Stalke, B. Dittrich, G. H. Clever, *J. Am. Chem. Soc.* **2015**, *137*, 1060–1063.
- [23] S. Pullen, S. Löffler, A. Platzek, J. J. Holstein, G. H. Clever, *Dalton. Trans.* **2020**, *49*, 9404–9410.
- [24] B. L. Ramsey, R. M. Pearson, L. R. Beck, G. M. Miyake, *Macromolecules* **2017**, *50*, 2668–2674.
- [25] Y. Du, R. M. Pearson, C. Lim, S. M. Sartor, M. D. Ryan, H. Yang, N. H. Damrauer, G. M. Miyake, *Chem. Eur. J.* **2017**, *23*, 10962–10968.
- [26] S. M. Sartor, Y. M. Lattke, B. G. McCarthy, G. M. Miyake, N. H. Damrauer, *J. Phys. Chem.* **2019**, *123*, 4727–4736.
- [27] B. G. McCarthy, R. M. Pearson, C.-H. Lim, S. M. Sartor, N. H. Damrauer, G. M. Miyake, *J. Am. Chem. Soc.* **2018**, *140*, 5088–5101.
- [28] V. K. Singh, C. Yu, S. Badgajar, Y. Kim, Y. Kwon, D. Kim, J. Lee, T. Akhter, G. Thangavel, L. S. Park, J. Lee, P. C. Nandajan, R. Wannemacher, B. Milián-Medina, L. Lüer, K. S. Kim, J. Gierschner, M. S. Kwon, *Nat. Catal.* **2018**, *1*, 794–804.
- [29] J. S. Danilova, S. M. Avdoshenko, M. P. Karushev, A. M. Timonov, E. Dmitrieva, *J. Mol. Struct.* **2021**, *1241*, 130668
- [30] A. L. Berger, K. Donabauer, B. König, *Chem. Sci.* **2018**, *9*, 7230–7235.
- [31] T. J. V. Bergen, D. M. Hedstrand, W. H. Kruizinga, R. M. Kellogg, *J. Org. Chem.* **1979**, *44*, 4953–4962.
- [32] F. Calogero, G. Magagnano, S. Potenti, F. Pasca, A. Fermi, A. Gualandi, P. Ceroni, G. Bergamini, P. G. Cozzi, *Chem. Sci.* **2022**, *13*, 5973–5981.
- [33] M. Nakajima, E. Fava, S. Loescher, Z. Jiang, M. Rueping, *Angew. Chem. Int. Ed.* **2015**, *54*, 8828–8832.
- [34] J. E. Tanner, E. O. Stejskal, *J. Chem. Phys.* **1968**, *49*, 1768–1777.
- [35] R. Manjunath, *Hist Math* **1975**, *2*, 73.

## 5 Coordination-driven construction of [3]rotaxane based on hierarchical assembly







## 5. Coordination-driven construction of [3]rotaxane based on hierarchical assembly

### 5.1 Introduction

Mechanically interlocked molecules (MIMs) are composed of multiple molecular fragments held together by mechanical bonds.<sup>[1,2]</sup> Those components cannot be separated without breaking the covalent structure of at least one of the constituents. MIMs have been attracting great interest for their application in artificial molecular machines, catalysis, and so on.<sup>[3]</sup> One of the archetypal examples is rotaxanes. A rotaxane consists of a macrocycle as the wheel and a linear component, namely the axle. The axle threads through the wheel and is often terminated by a bulky group as stopper to prevent dethreading (Figure 5.1).



Figure 5.1: Graphical representation of a simple [2]rotaxane.<sup>[4]</sup> Copyright © 2017 Wiley-VCH Verlag GmbH & Co. KGaA, Weinheim.

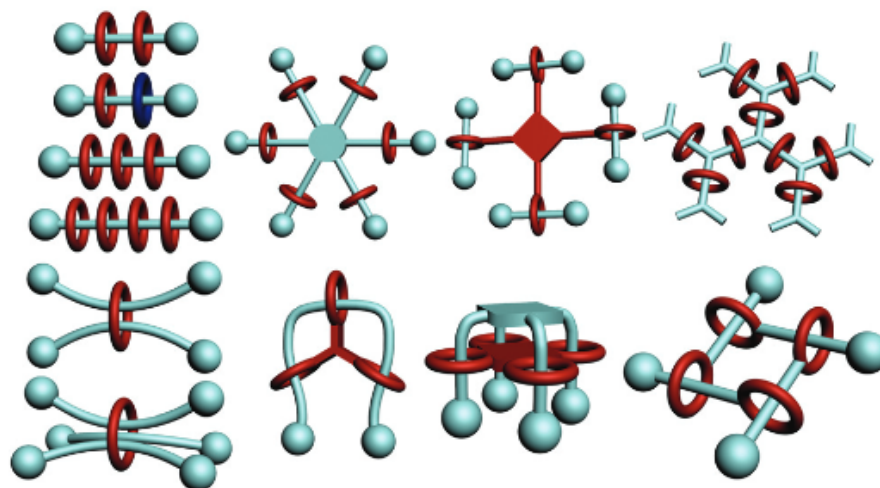


Figure 5.2: Schematic representation of various rotaxane architectures with multiple macrocycle or multiple axles.<sup>[5]</sup> Copyright © The Royal Society of Chemistry 2020.

Since Sauvage, Stoddart *et al.* pioneered the formation of rotaxane, in the past few decades, various types of rotaxanes with increasing number of components have been synthesized (Figure 5.2).<sup>[5]</sup> Those rotaxanes consist of (i) one dumbbell and multiple macrocycles, (ii) one macrocycle and multiple dumbbells, (iii) multiple

## 5. Coordination-driven construction of [3]rotaxane based on hierarchical assembly

dumbbells and multiple macrocycles. The approaches for generating rotaxanes have raised considerable interest for the development of MIMs. Recently, template-directed synthesis, such as by hydrogen bond<sup>[6]</sup> or metal cation templates,<sup>[7]</sup> was widely explored. The active metal template strategy has been developed by Leigh and co-workers (Figure 5.3).<sup>[2,8]</sup> The metal ion is endotopically binding within the cavity of the macrocycle. Two “half-thread” units generate the rotaxane thread under the metal-based catalysis and directed through the macrocycle. Goldup and coworkers further investigated the copper(I)-catalysed azide-alkyne cycloaddition (AT-CuAAC) based active-metal-template approach.<sup>[9–11]</sup>

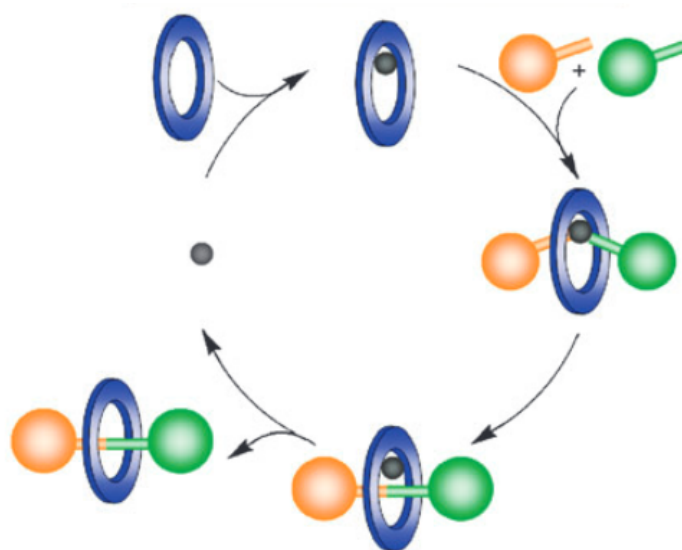


Figure 5.3: Schematic illustration of the catalytic active metal template synthesis of [2]rotaxane.<sup>[2]</sup> Copyright © The Royal Society of Chemistry.

## 5. Coordination-driven construction of [3]rotaxane based on hierarchical assembly

### 5.2 Ligand design and synthesis

To increase complexity and functionality of architectures and develop coordination cages mimicking enzymes, rational approaches for the construction of compounds composed of multiple building blocks have emerged.<sup>[12]</sup> In our previous work, a series of salen macrocycle bridged homo- and heteroleptic cages have been developed based on hierarchical assembly and shape complementarity (Figure 5.4).<sup>[13]</sup> A salen macrocycle was designed and synthesized to form a binuclear metalla-macrocycle. Two shape complementary ligands were further combined with the metal salen macrocycle to assemble heteroleptic cages. The fluorene-based bis-pyridine ligand self-assembles with macrocycle **R<sup>ACR</sup>** with methyl groups on the backbone pointing into the cavity (Figure 5.4). Furthermore, it consists of one macrocycle in this system. It is a promising approach to develop new rotaxanes by connecting the two ligands and followed by detaching the ligands from the macrocycle.

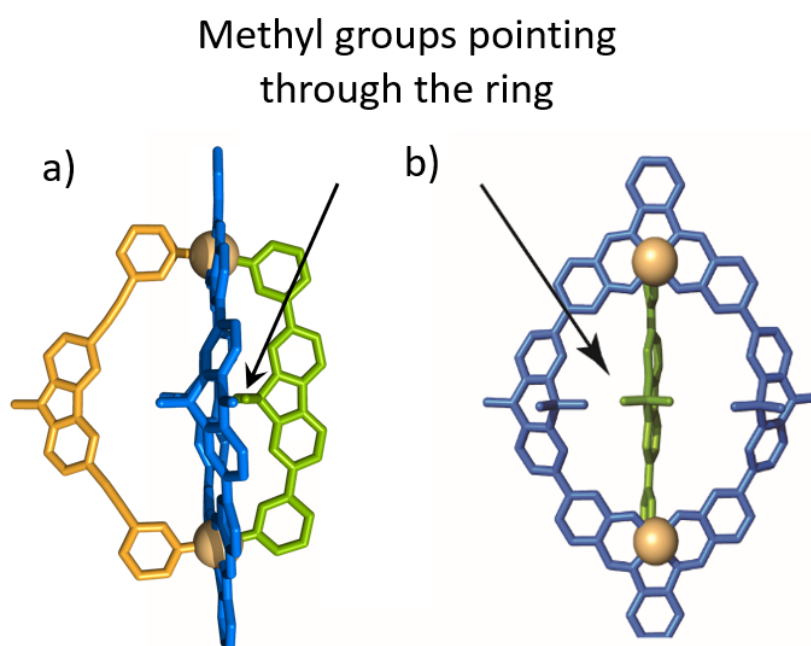


Figure 5.4: a) X-ray structure and b) partial X-ray structure of heteroleptic cage self-assembly from salen macrocycle with shape-complementary fluorene ligands

In this chapter, a new approach for the construction of a [3]rotaxane based on coordination-driven self-assembly is described. Firstly, a salen macrocycle was synthesised and further coordinated with Co(II) ions. Co(II) could be easily oxidized

## 5. Coordination-driven construction of [3]rotaxane based on hierarchical assembly

to octahedral coordinated Co(III) thus having two remaining coordination sites on the axial position of the octahedral coordination center. Then, the binuclear Co(III) salphen macrocycle was combined with a 2,7-carbazole-based ligand, modified with a functional group on the nitrogen atom of the backbone. The combination of the two building blocks lead to the formation of a bowl-like structure. Connecting two bowls together can be achieved by a reaction on the chain of the two outer ligands creating an axle, while the ligands act as stoppers. By using a ligand with a bulky group, the macrocycles should stay threaded on the axle after removing the coordinating metal ions or addition of a competing ligand to displace the pyridyl ligand from the ring.

First, a hydro acridine-based salicylaldehyde ligand **L<sup>ACR</sup>** was synthesized by Suzuki-coupling reaction of 2,7-dibromo-10-hexyl-9,9-dimethyl-9,10-dihydro-acridine and 4-formyl-3-hydroxyphenylboronic acid pinacol ester. The alkyl chain on the backbone of ligand increased the solubility of the ligand. Following a similar procedure previously described in Chapter 3 and 4, the macrocycle was obtained by condensation reaction of **L<sup>ACR</sup>** and *o*-phenylenediamine (Figure 5.5). The formation of the macrocycle was firstly confirmed by <sup>1</sup>H NMR analysis (Figure 5.6). One set of signals was observed in the <sup>1</sup>H NMR spectrum of the compound. Compared with the free ligand, the proton signal of the -OH group undergoes a downfield shift ( $\Delta\delta[H_{1/q}] = 2.28$  ppm). The proton signals of the phenyl ring have a slight shift ( $\Delta\delta[H_{8/i}] = 0.11$  ppm,  $\Delta\delta[H_{5/f}] = 0.16$  ppm). The formation of the Schiff base was further confirmed by the proton signal at  $\delta=8.76$  ppm, which was assigned to the proton Hc of the imine group.

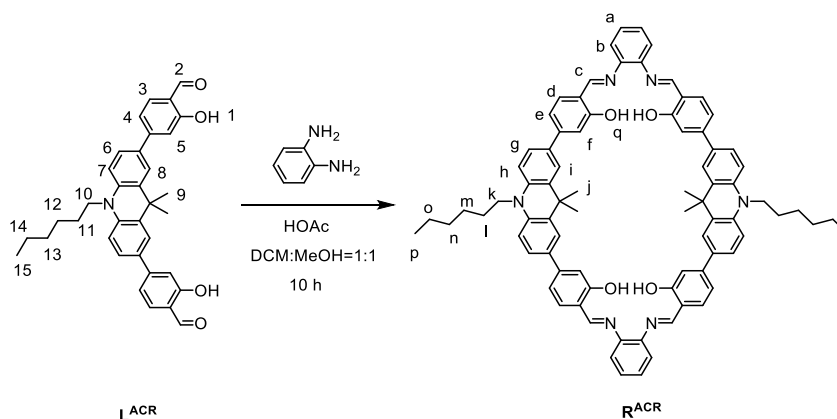


Figure 5.5: Synthetic route to salphen macrocycle **R<sup>ACR</sup>**.

## 5. Coordination-driven construction of [3]rotaxane based on hierarchical assembly

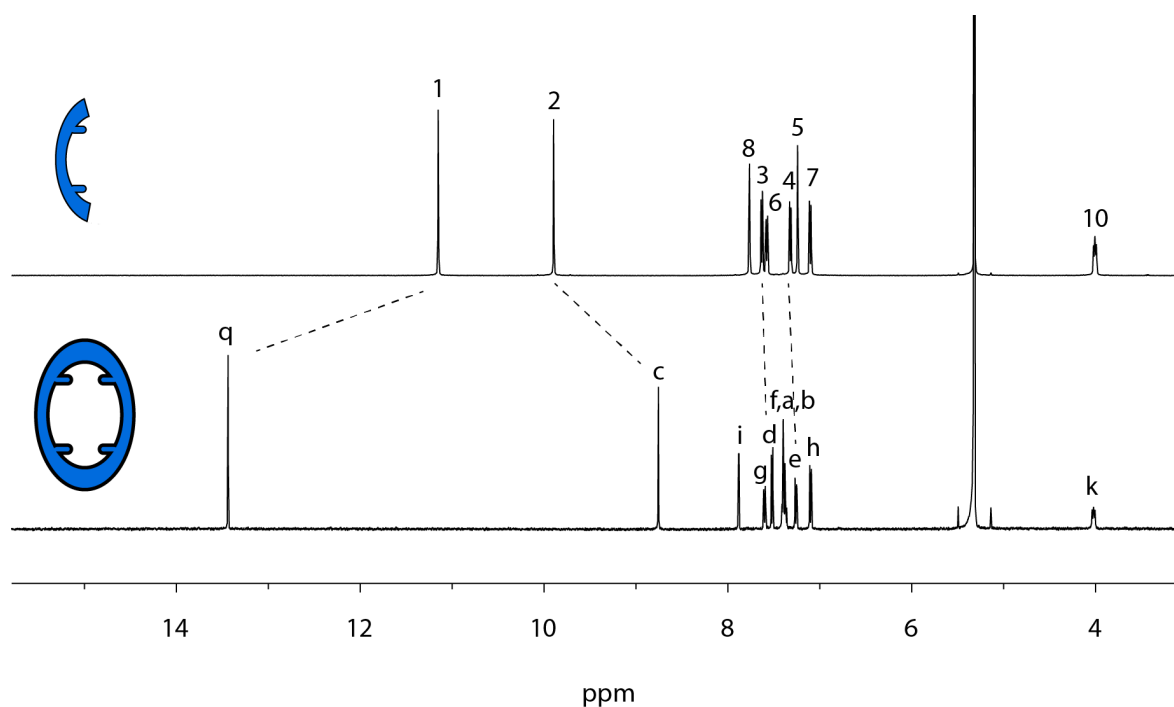


Figure 5.6:  $^1\text{H}$  NMR spectrum of  $\text{L}^{\text{ACR}}$  and  $\text{R}^{\text{ACR}}$  (500 MHz, 298 K,  $\text{CD}_2\text{Cl}_2$ ).

Yellow rod shape single crystals of  $\text{R}^{\text{ACR}}$  suitable for x-ray diffraction analysis were obtained by slow evaporation of a DCM solution of the ring. The compound crystallized in the  $P-1$  space group. From the crystal structure, we can observe that  $\text{L}^{\text{ACR}}$  is slightly twisted. As a consequence,  $\text{N}_2\text{O}_2$  moieties are not in the same plane. The four methyl substituents of the backbones point toward different directions. The longest distance between two phenyl rings of the salphen units is 24.817 Å.

## 5. Coordination-driven construction of [3]rotaxane based on hierarchical assembly

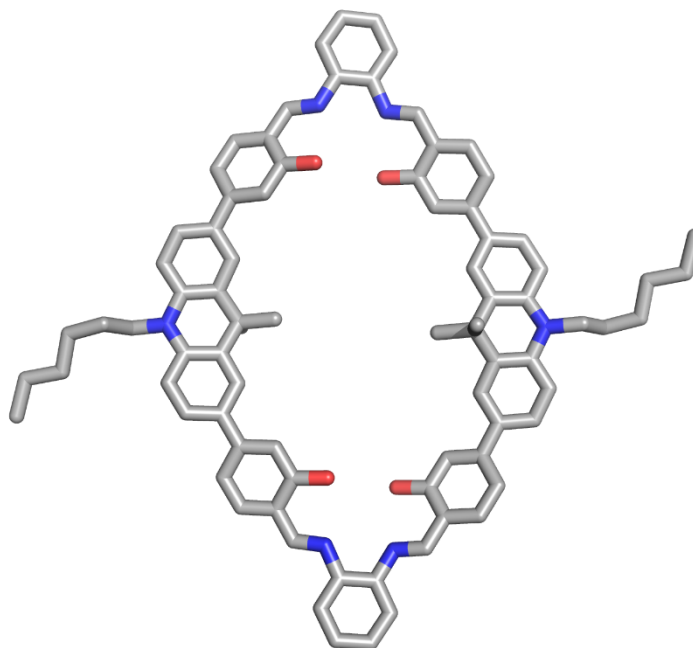


Figure 5.7: Single crystal X-ray structure of  $\mathbf{R}^{\text{ACR}}$  (Solvent molecules and hydrogens are omitted for clarity. Color code for C: gray, N: blue; O: red).

To introduce functional groups on the backbone which can be used for further reaction between two bowls, we designed carbazole-based bis-monodentate pyridine ligands ( $\mathbf{L}^{\text{R}}$  and  $\mathbf{L}^{\text{NH}_2}$ ) (Figure 5.8 a). It has been observed that fluorene-based ligands can adopt two different binding modes. One is concave with the substituents pointing in the same direction than the nitrogen donors, the other is convex with the substituents pointing in the opposite direction than the coordination vectors (Figure 5.8 b).<sup>[14]</sup> In our case, the concave binding is a crucial precondition for the construction of the rotaxane. To explore the influence of the flexibility of substituents, two types of ligands were prepared.  $\mathbf{L}^{\text{R}}$  bears a flexible chain with a terminal alkyne.  $\mathbf{L}^{\text{NH}_2}$  bears a rigid phenyl ring on the backbone with an amine group in the para position.

## 5. Coordination-driven construction of [3]rotaxane based on hierarchical assembly

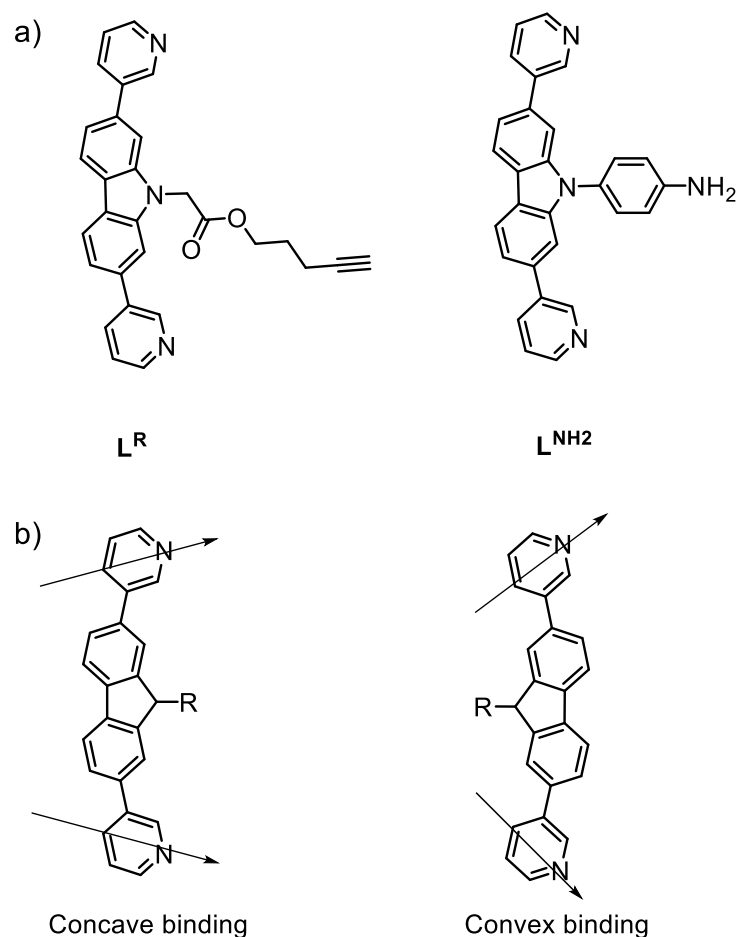


Figure 5.8: a) Designed carbazole-based pyridine ligands with flexible or rigid chains on the backbone. b) Schematic representation of the two binding modes of fluorene-based pyridine ligands.

### 5.3 Formation of the bowl

The macrocycle contains two Co(III) ions with free coordination sites in the axial position, allowing to combine with one or two bis-monodentate ligands on the side to form a bowl or cage like structure. As regard of the length and binding angle of ligand  $L^R$ , as well as the distance of Co(III)•••Co(III), the macrocycle is supposed to be bent and combined with only one  $L^R$  to form a bowl rather than a cage. For the self-assembly of the bowl (Figure 5.9), firstly, a 1:2 mixture of macrocycle  $R^{ACR}$  and Co(OAc)<sub>2</sub>, in a mixed solvent of CHCl<sub>3</sub> and CH<sub>3</sub>CN (v:v, 1:1) was prepared, accompanying with oxidation of Co(II) to Co(III), leads to the formation of [Co(III)<sub>2</sub>R<sup>ACR</sup>]<sup>2+</sup>. The formation of the metallamacrocycle was confirmed by <sup>1</sup>H NMR (Figure 5.10 c) and ESI-MS (Figure 5.49). Then 1 equiv. of  $L^R$  was added and the reaction mixture was heated at 60 °C overnight. Afterwards, the crude product was

## 5. Coordination-driven construction of [3]rotaxane based on hierarchical assembly

purified by precipitation. As expected, a pure  $[\text{Co(III)}_2\text{R}^{\text{ACR}}\text{L}^{\text{R}}]^{2+}$  (**Bowl-1**) assembly was obtained.

The structure of **Bowl-1** was confirmed using NMR spectroscopy, mass spectrometry and X-ray crystallography. The diamagnetic Co(III) ions allow the assembly to give a series of clear and sharp signals in  $^1\text{H}$  NMR (Figure 5.10 d). All the proton signals were assigned with the aid of 2D NMR ( $^1\text{H}$ - $^1\text{H}$  COSY and  $^1\text{H}$ - $^1\text{H}$  NOESY). The integration shows a 1:1 ratio of proton signals assigned to macrocycle and  $\text{L}^{\text{R}}$ . After coordination with Co(III) ions, a significantly downfield shift of the proton signals from ligand  $\text{L}^{\text{R}}$  was observed in  $^1\text{H}$  NMR. Meanwhile, by comparison with the  $^1\text{H}$  NMR spectrum of  $\text{CoR}^{\text{ACR}}$ , the proton signals of the macrocycle were split into two sets of signals with a 1:1 ratio, suggesting that an asymmetrical environment in macrocycle was caused by combination with  $\text{L}^{\text{R}}$ . As mentioned above, the ligand can adopt two different binding modes. The substituents of the ligand could point through the macrocycle or stay outside and toward one side of the acridine units on the macrocycle. Therefore, the NOESY spectrum was checked carefully. However, no  $^1\text{H}$ - $^1\text{H}$  interaction between the substituent of  $\text{L}^{\text{R}}$  and  $\text{CoR}^{\text{ACR}}$  could be observed.

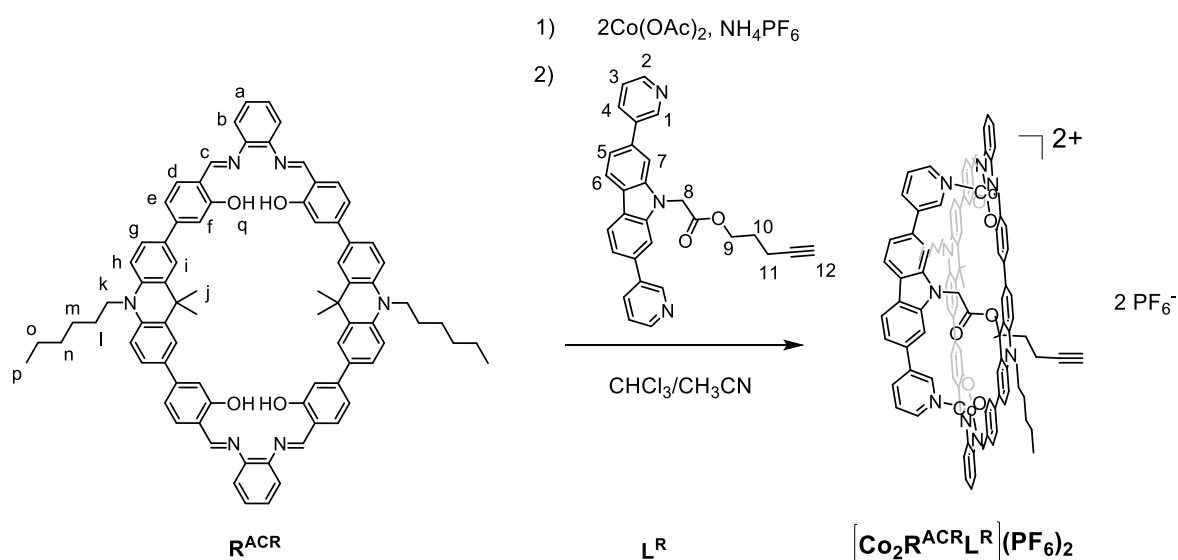


Figure 5.9: Hierarchical self-assembly of  $\text{R}^{\text{ACR}}$ , Co(II), and  $\text{L}^{\text{R}}$  to form **Bowl-1**



## 5. Coordination-driven construction of [3]rotaxane based on hierarchical assembly

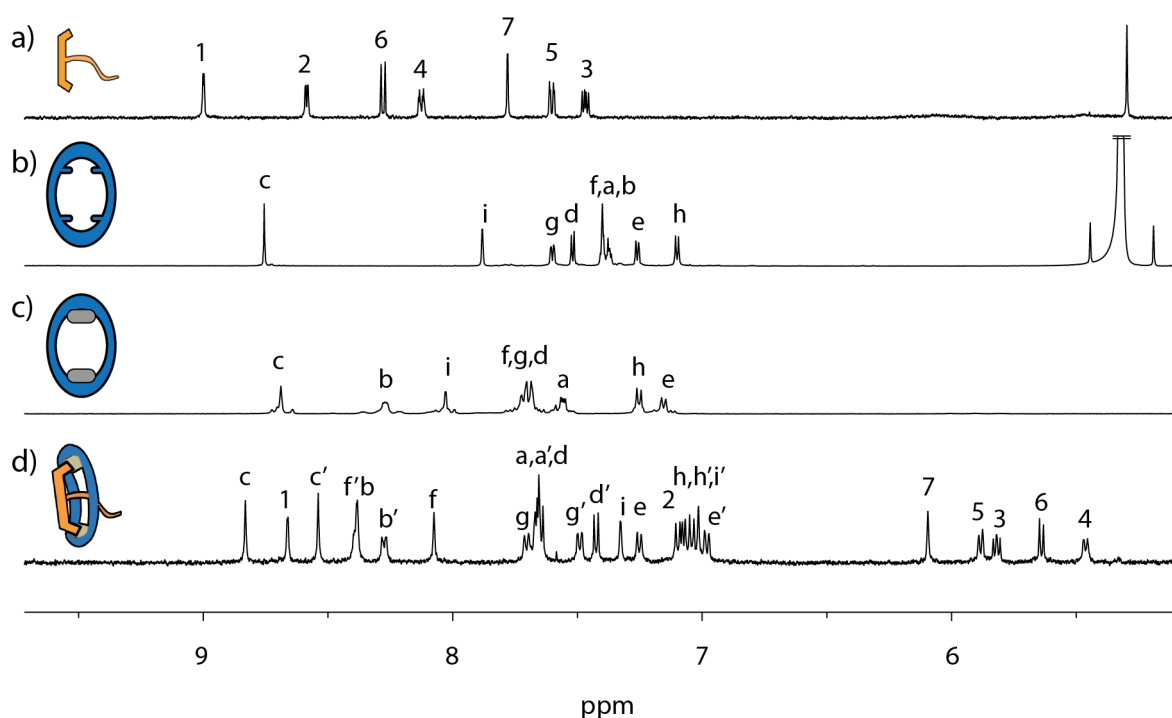


Figure 5.10:  $^1\text{H}$  NMR spectra of a) ligand  $\text{L}^{\text{R}}$  (500 MHz, 298 K,  $\text{CD}_3\text{CN}$ ), b) macrocycle  $\text{R}^{\text{ACR}}$  (700 MHz, 298 K,  $\text{CD}_2\text{Cl}_2$ ), c) metallamacrocycle  $\text{Co}_2\text{R}^{\text{ACR}}$  (500 MHz, 298 K,  $\text{CD}_3\text{CN}$ ) and d) bowl  $\text{Co}_2\text{R}^{\text{ACR}}\text{L}^{\text{R}}$  (500 MHz, 298 K,  $\text{CD}_3\text{CN}$ ).

As shown in the DOSY spectrum (Figure 5.11 a), all signals from the assembly have the same diffusion coefficient at  $4.75 \times 10^{-10} \text{ m}^2/\text{s}$  indicating the formation of one single species with hydrodynamic radius of 13.4 Å. The structure of assembly is further confirmed by ESI-MS (Figure 5.11 b). ESI-MS analysis gave a prominent peak at  $m/z = 885.3081$ , which is consistent with the calculated isotopic pattern for of  $[\text{Co}_2\text{R}^{\text{ACR}}\text{L}^{\text{R}}]^{2+}$ . Small peaks were observed at  $m/z = 893.8024$  and  $m/z = 902.3319$ , corresponding to  $[\text{Co}_2\text{R}^{\text{ACR}}\text{L}^{\text{R}}(\text{OH})]^{2+}$  and  $[\text{Co}_2\text{R}^{\text{ACR}}\text{L}^{\text{R}}(\text{OH})_2]^{2+}$ , respectively.

## 5. Coordination-driven construction of [3]rotaxane based on hierarchical assembly

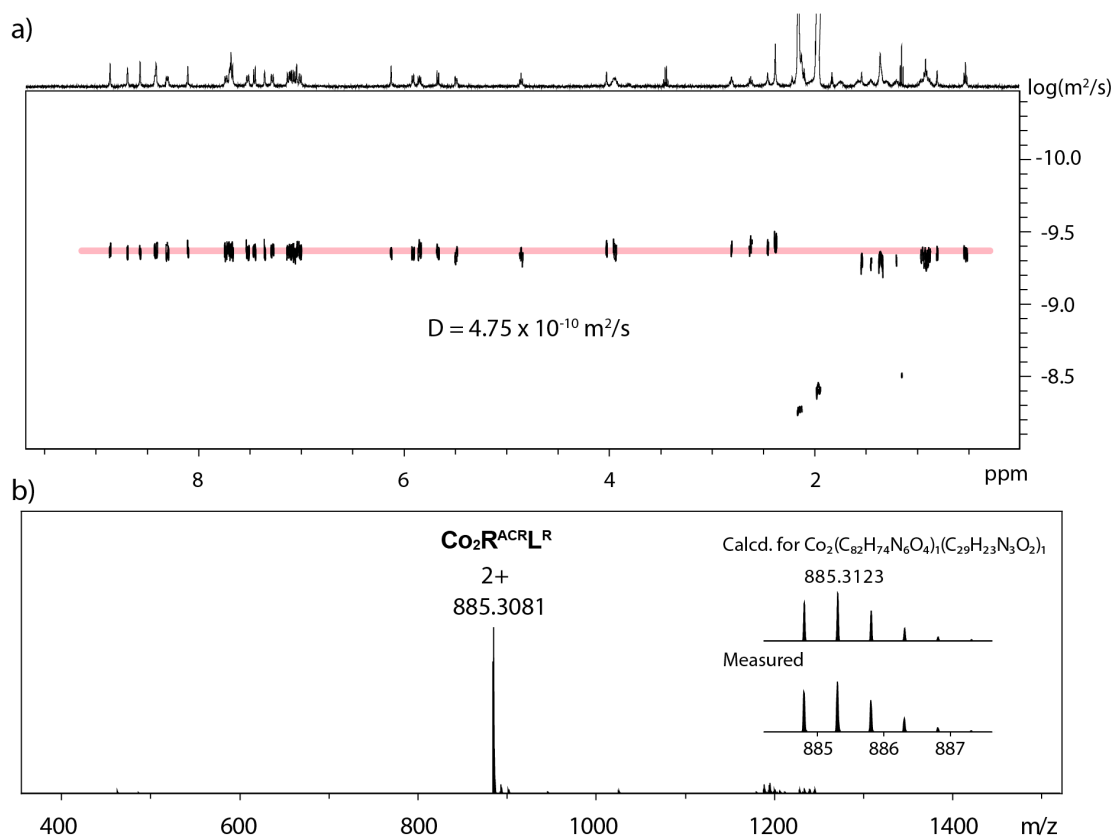


Figure 5.11: a) DOSY spectrum of  $\text{Co}_2\text{R}^{\text{ACR}}\text{L}^{\text{R}}$  (500 MHz, 289 K,  $\text{CD}_3\text{CN}$ ), diffusion coefficient  $D = 4.75 \times 10^{-10} \text{ m}^2\text{s}^{-1}$ ,  $r_H = 13.4 \text{ \AA}$ . b) ESI-MS of  $\text{Co}_2\text{R}^{\text{ACR}}\text{L}^{\text{R}}$ , with insets showing the calculated and measured isotopic patterns of  $[\text{Co}_2\text{R}^{\text{ACR}}\text{L}^{\text{R}}]^{2+}$ .

However, it was still unclear if the substituent on the backbone of  $\text{L}^{\text{A}}$  was pointing through the macrocycle or in the opposite direction. Fortunately, the efforts to grow single crystals suitable for X-ray diffraction were successful and red plate shape single crystals of **Bowl-1** were obtained by slow vapor diffusion of ethyl acetate into an acetonitrile solution. The structure of **Bowl-1** was unambiguously confirmed by single-crystal X-ray analysis (Figure 5.12). Two of the methyl groups are directed toward the cavity of the macrocycle, while the other two methyl groups of the salen ring backbone point to the outside of macrocycle, leading to a bent conformation of the macrocycle. The crystal structure shows that  $\text{L}^{\text{R}}$  coordinates with two Co(III) ions on one side of the macrocycle. Because of the bent conformation of the macrocycle, a second ligand  $\text{L}^{\text{R}}$  could not coordinate to the remaining two coordination sites of the Co(III) center. Two water molecules thus saturated the free coordination sites. The largest distance between two phenyl rings of salen units was found to be

5. Coordination-driven construction of [3]rotaxane based on hierarchical assembly

24.486 Å, which is a little shorter than the length in the metal free macrocycle. The Co...Co distance is 14.375 Å.

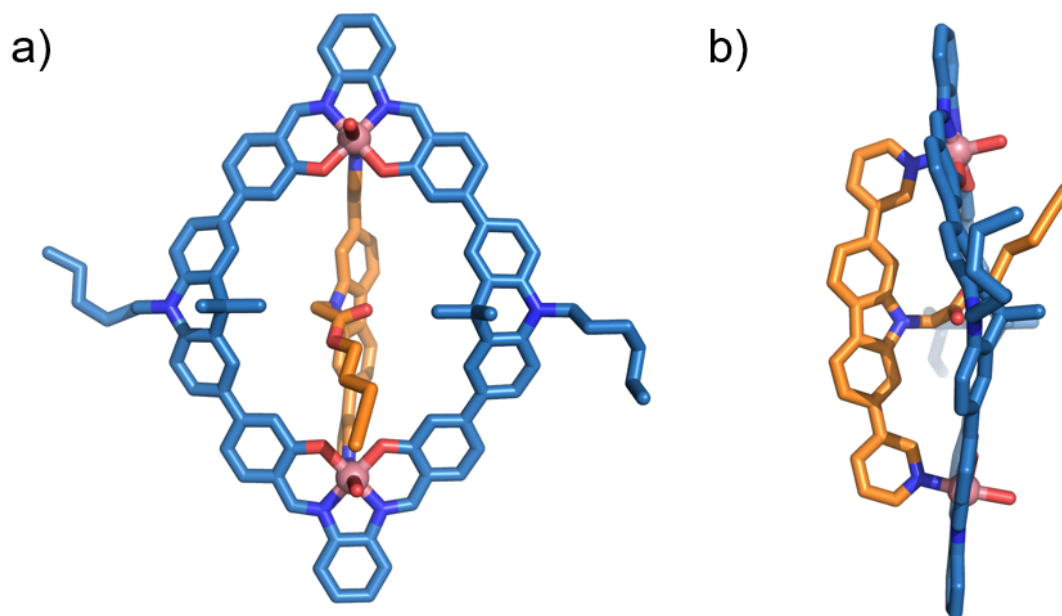


Figure 5.12: X-ray crystal structure of  $\text{Co}_2\text{R}^{\text{ACR}}\text{L}^{\text{R}}$  from a) front and b) side view. (Solvent molecules and hydrogen are not shown for clarity. Color code for N: blue; O: red; Co: pink).

To investigate the self-assembly of the macrocycle and ligand with a more rigid substituent, a bis-monodentate pyridine ligand with phenyl ring substituent, ligand  $\text{L}^{\text{NO}_2}$ , was prepared. Following the same procedure used for **Bowl-1**, the self-assembly of macrocycle, Co(II), and  $\text{L}^{\text{NO}_2}$  resulted in a bowl structure  $[\text{Co}_2\text{R}^{\text{ACR}}\text{L}^{\text{NO}_2}]^{2+}$  (**Bowl-2**) (Figure 5.13). The signals of the  $^1\text{H}$  spectrum are similar to those of **Bowl-1**, all the proton signals of  $\text{L}^{\text{NO}_2}$  having a dramatic downfield shift and the signals of macrocycle splitting into two sets of signals, indicating that  $\text{L}^{\text{NO}_2}$  has the same coordination mode than  $\text{L}^{\text{R}}$ . The substituent on the backbone of  $\text{L}^{\text{NO}_2}$  was inferred to similarly point through the macrocycle. ESI-MS analysis gave prominent signals at  $m/z = 883.7928$ , corresponding to  $[\text{Co}_2\text{R}^{\text{ACR}}\text{L}^{\text{NO}_2}]^{2+}$  species.

## 5. Coordination-driven construction of [3]rotaxane based on hierarchical assembly

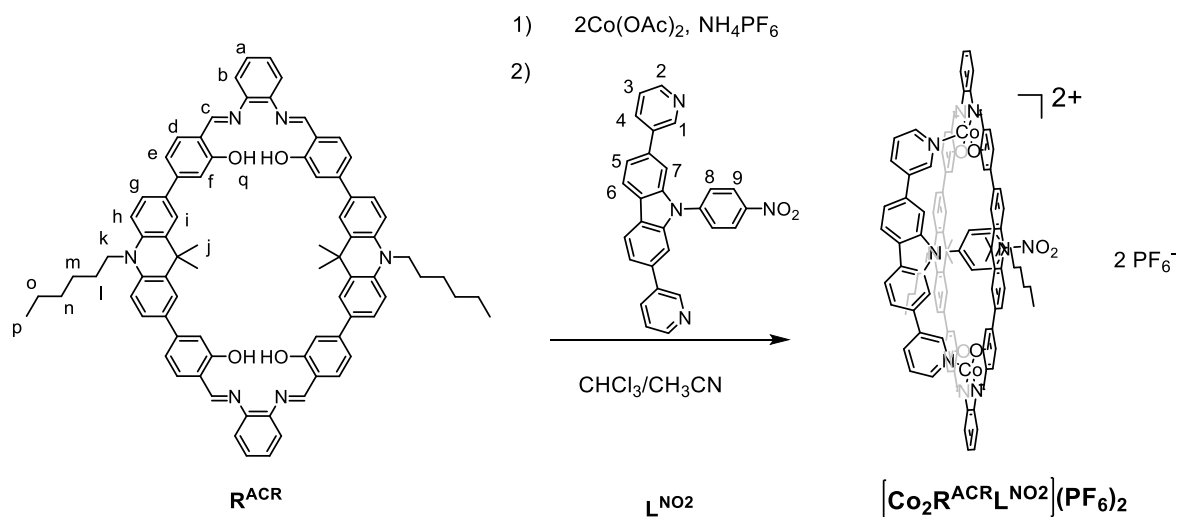


Figure 5.13: Self-assembly of  $\text{R}^{\text{ACR}}$ ,  $\text{Co}^{2+}$ , and  $\text{L}^{\text{NO}_2}$  to form  $\text{Co}_2\text{R}^{\text{ACR}}\text{L}^{\text{NO}_2}$  (Bowl-2).

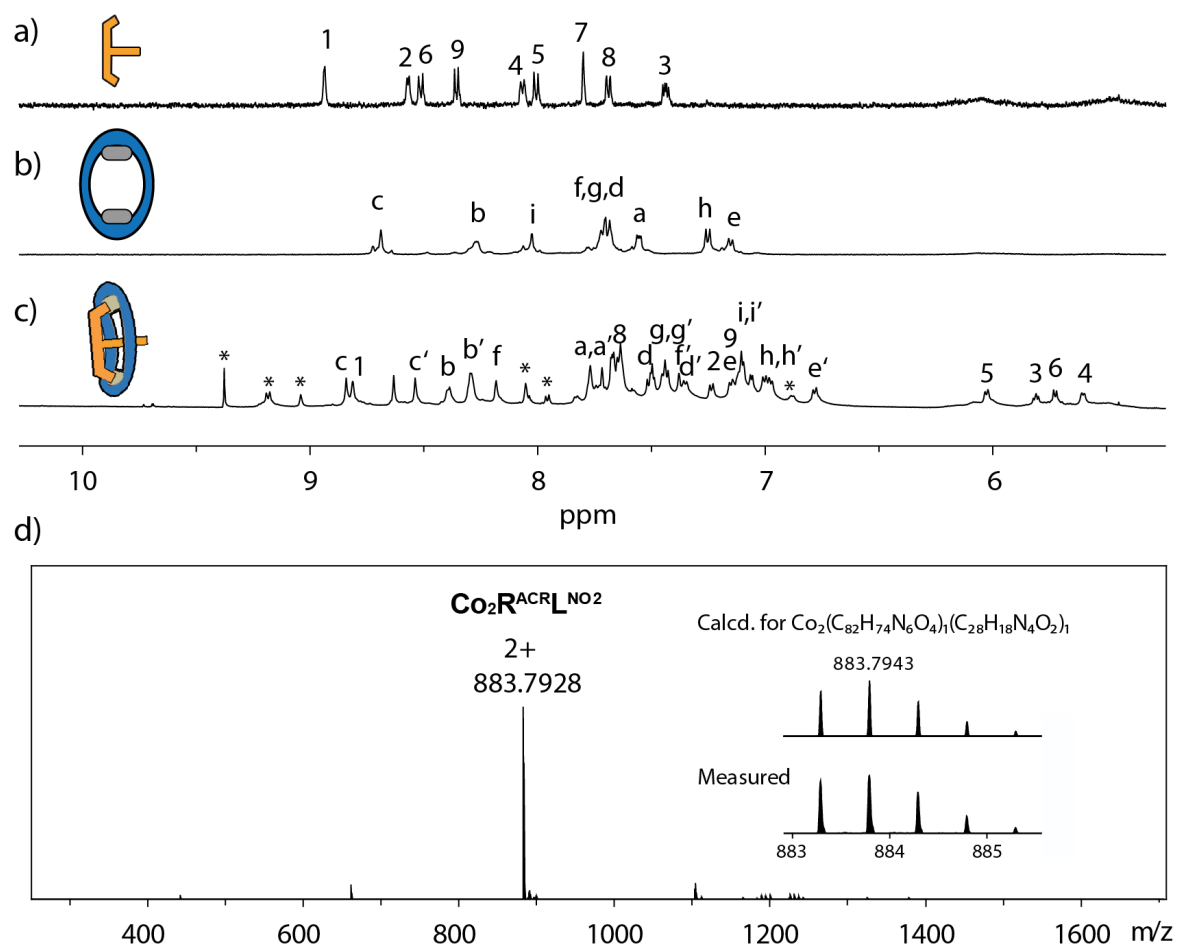


Figure 5.14:  $^1\text{H}$  NMR spectra of a) ligand  $\text{L}^{\text{NO}_2}$  (500 MHz, 298 K,  $\text{CD}_3\text{CN}$ ), b) metallamacrocycle  $\text{Co}_2\text{R}^{\text{NO}_2}$  (500 MHz, 298 K,  $\text{CD}_3\text{CN}$ ), and c) bowl  $\text{Co}_2\text{R}^{\text{ACR}}\text{L}^{\text{NO}_2}$  (600 MHz, 298 K,  $\text{CD}_3\text{CN}$ ). d) ESI-MS of  $\text{Co}_2\text{R}^{\text{ACR}}\text{L}^{\text{NO}_2}$ , with insets showing the calculated and measured isotopic patterns of  $[\text{Co}_2\text{R}^{\text{ACR}}\text{L}^{\text{NO}_2}]^{2+}$ .

## 5. Coordination-driven construction of [3]rotaxane based on hierarchical assembly

Red block crystals of  $\text{Co}_2\text{R}^{\text{ACR}}\text{L}^{\text{NO}_2}$  were obtained from the slow diffusion of ethyl acetate into acetonitrile (Figure 5.15).  $\text{L}^{\text{R}}$  coordinates with two Co(III) ions on the same side of the macrocycle. Two water molecules saturate the free coordination sites. The largest distance between two phenyl rings of salphen units is 24.485 Å and Co...Co distance is 14.390 Å.

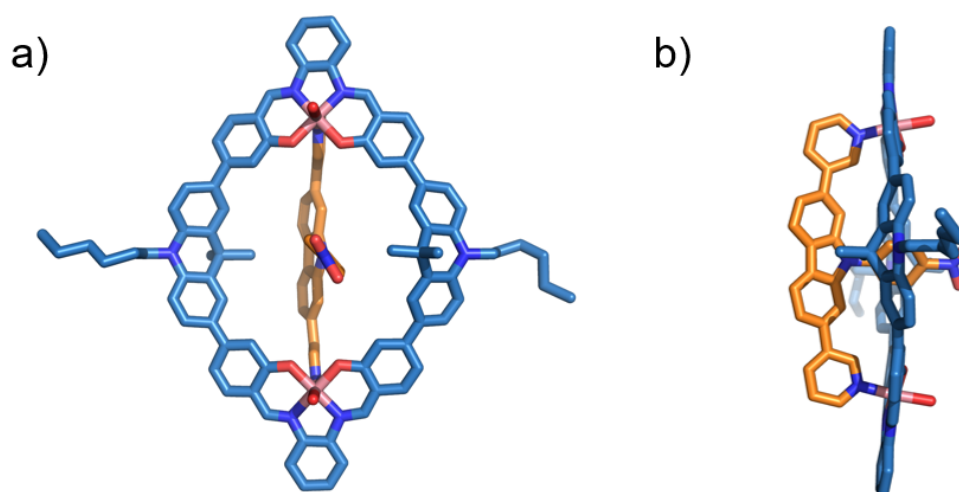


Figure 5.15: Preliminary single crystal X-ray structure of  $\text{Co}_2\text{R}^{\text{ACR}}\text{L}^{\text{NO}_2}$  from a) front and b) side view. (Solvent molecules and hydrogen are not shown for clarity. Color code for N: blue; O: red; Co: pink).

To achieve the reaction of two bowls and the formation of rotaxane, the ligand  $\text{L}^{\text{NH}_2}$  with a functional imine group was then synthesized. It could be used for the condensation reaction with an aldehyde group. As depicted in Figure 5.16, the self-assembly of macrocycle, Co(II), and  $\text{L}^{\text{NH}_2}$  in a 1:2:1 ratio was performed following the same procedure described previously, affording  $[\text{Co}_2\text{R}^{\text{ACR}}\text{L}^{\text{NH}_2}]^{2+}$  (**Bowl-3**). The assembly was characterized by NMR spectroscopy and ESI-MS (Figure 5.17). The proton signals of  $^1\text{H}$  spectrum are similar to those of **Bowl-1**, all the proton signals of  $\text{L}^{\text{NH}_2}$  having a consequent downfield shift. Moreover, the signals of the macrocycle also split into two sets, indicating that the substituent on the backbone of  $\text{L}^{\text{NH}_2}$  probably points through the macrocycle. DOSY spectrum (Figure 5.80) shows that all signals from the assembly have the same diffusion coefficient at  $4.17 \times 10^{-10} \text{ m}^2/\text{s}$ , indicating the formation of one single species with hydrodynamic radius of 15.2 Å. ESI-MS analysis further confirmed the formation of **Bowl-3**, showing a prominent signal at  $m/z = 868.8060$ , corresponding to the  $[\text{Co}_2\text{R}^{\text{ACR}}\text{L}^{\text{NH}_2}]^{2+}$  species.

## 5. Coordination-driven construction of [3]rotaxane based on hierarchical assembly

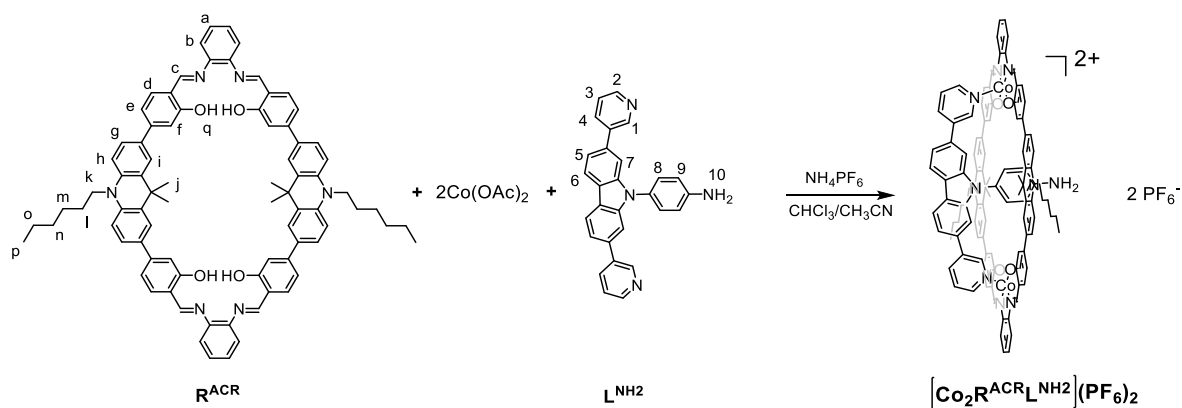


Figure 5.16: Self-assembly of  $\text{R}^{\text{ACR}}$ ,  $\text{Co}(\text{II})$ , and  $\text{L}^{\text{NH}_2}$  to form  $\text{Co}_2\text{R}^{\text{ACR}}\text{L}^{\text{NH}_2}$  (Bowl-3).

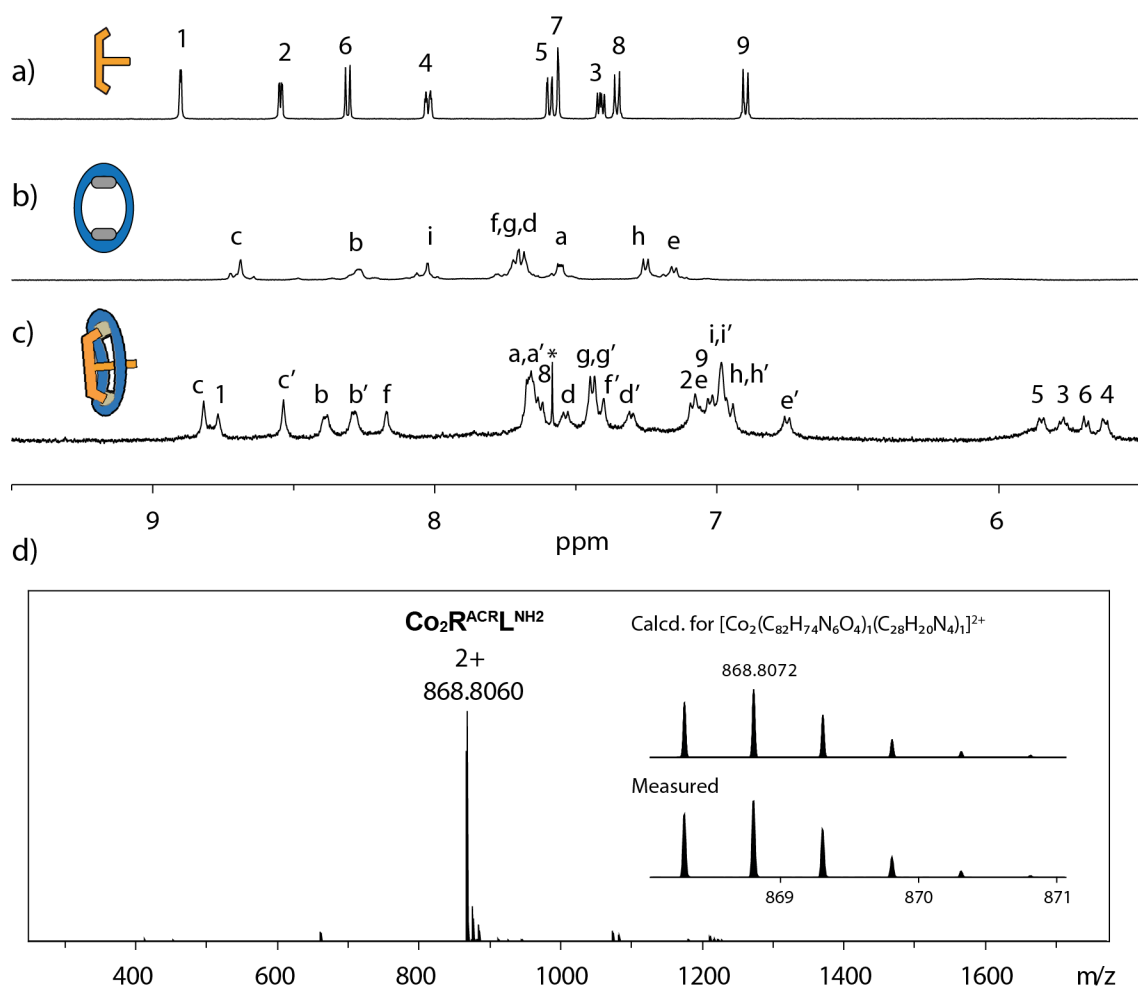


Figure 5.17:  $^1\text{H}$  NMR spectra of a) ligand  $\text{L}^{\text{NH}_2}$ , b) metalla-macrocycle  $\text{Co}_2\text{R}^{\text{NH}_2}$ , bowl  $\text{Co}_2\text{R}^{\text{ACR}}\text{L}^{\text{NH}_2}$  (500 MHz, 298 K,  $\text{CD}_3\text{CN}$ ). d) ESI-MS of  $\text{Co}_2\text{R}^{\text{ACR}}\text{L}^{\text{NH}_2}$ , with insets showing the calculated and measured isotopic patterns of  $[\text{Co}_2\text{R}^{\text{ACR}}\text{L}^{\text{NH}_2}]^{2+}$ .

## 5. Coordination-driven construction of [3]rotaxane based on hierarchical assembly

### 5.4 Formation of an axle

With the aim of forming a rotaxane derived from two bowls, two types of linkers were designed and synthesized. One is a bis-sulfonate compound with two azide functionalities (**2N<sub>3</sub>**) which enable the derivatization by click chemistry. Furthermore, the sulfonate anions can stabilize the macrocycle after the ligand was detached via electrostatic interactions. We designed another dialdehyde compound (**2CHO**) to connect two **Bowl-3** via a condensation reaction. To investigate the conditions of formation of the rotaxane, the reactions between free ligands and linkers to form the axle of the rotaxane were studied first.

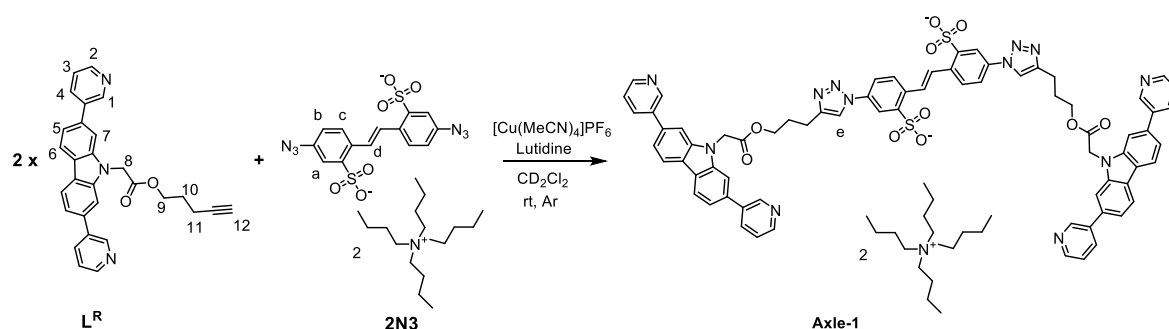


Figure 5.18: Synthetic route to **Axle-1**.

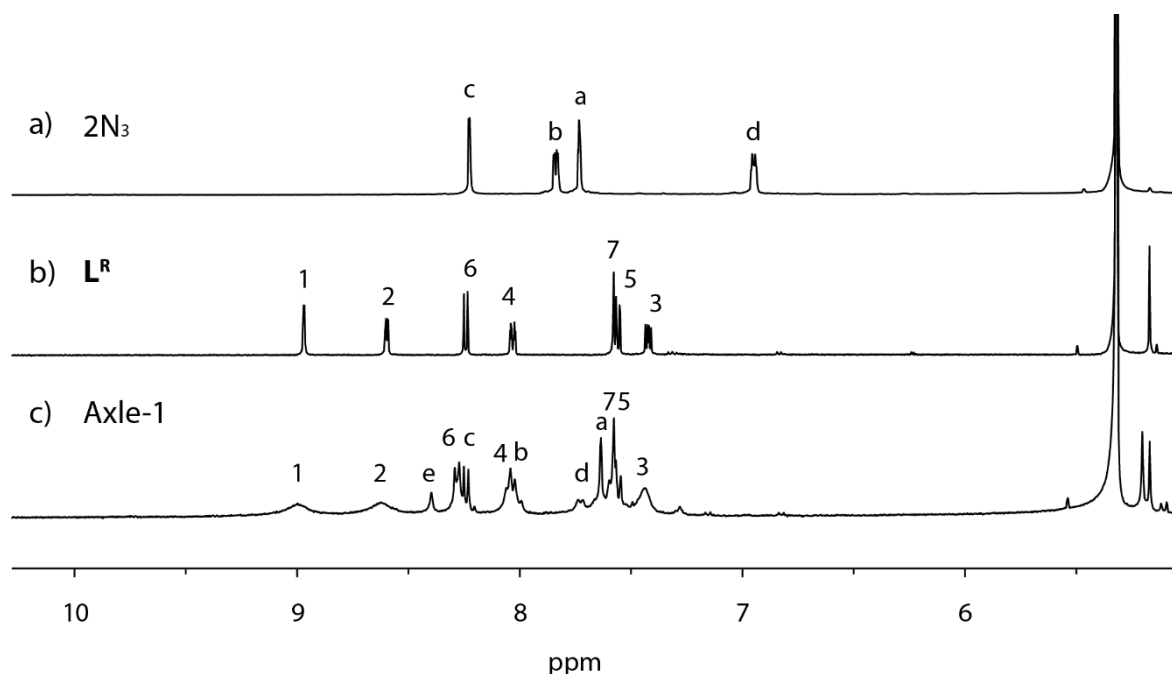


Figure 5.19: <sup>1</sup>H NMR spectra of a) **2N<sub>3</sub>** (600 MHz, 298 K, CD<sub>2</sub>Cl<sub>2</sub>), b) **L<sup>R</sup>** (500 MHz, 298 K, CD<sub>2</sub>Cl<sub>2</sub>), and c) **Axle-1** (400 MHz, 298 K, CD<sub>2</sub>Cl<sub>2</sub>).

## 5. Coordination-driven construction of [3]rotaxane based on hierarchical assembly

The Cu(I)-catalyzed reaction of **L<sup>R</sup>** and **2N<sub>3</sub>** in a 2:1 ratio was performed under argon atmosphere in anhydrous DCM (Figure 5.18). The formation of the axle was confirmed by <sup>1</sup>H NMR and ESI-MS analysis. A new set of signals was observed in <sup>1</sup>H NMR spectrum and proton signals of **2N<sub>3</sub>** present a clear shift. Due to the presence of residual copper cations and the possible coordination to the pyridine units of the ligand, the proton signals of *H<sub>1</sub>* and *H<sub>2</sub>* are broadened. A new proton signal at  $\delta=8.40$ , assigned to the proton on the triazole, was observed, thus indicating that the click reaction was successfully achieved. The ESI-MS measured in negative mode showed a prominent signal at 702.2026, corresponding to the [**Axle-1**]<sup>2-</sup> (Figure 5.20).

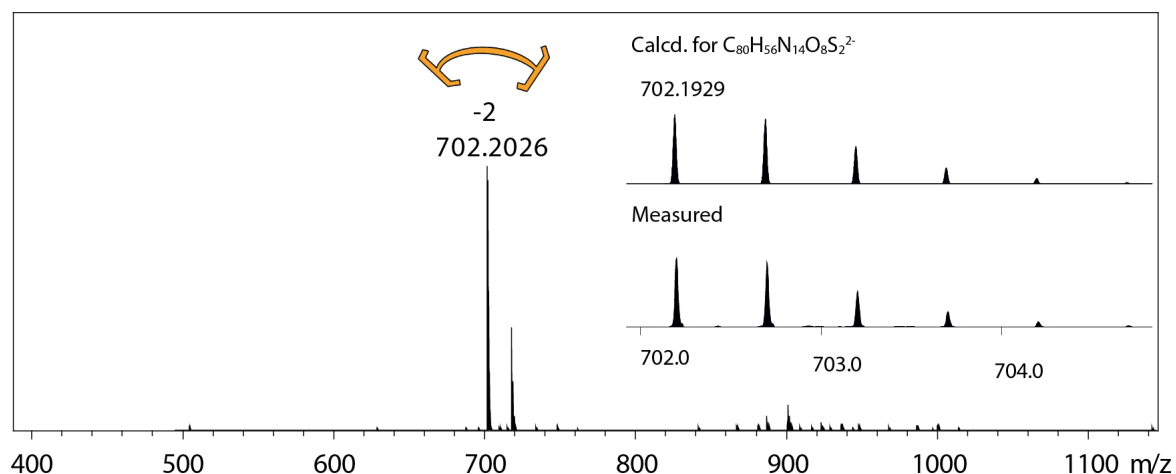


Figure 5.20: ESI-MS of **Axle-1**, with insets showing the calculated and measured isotopic patterns of [**Axle-1**]<sup>2-</sup>.

In addition, the **L<sup>NH<sub>2</sub></sup>**-based axle (**Axle-2**) was also successfully synthesized. First, the dialdehyde linker (**2CHO**) was prepared by Suzuki-coupling reaction of 1,4-dibromobenzene with (4-formylphenyl)boronic acid. Mixing **L<sup>NH<sub>2</sub></sup>** and **2CHO** in a 2:1 ratio in methanol/dichloromethane (1:1, v/v) in presence of acetic acid resulted in the formation of a precipitate. The precipitate was washed by methanol and characterized by <sup>1</sup>H NMR. The spectrum showed a new set of proton signals. The proton signals of **2CHO** have a clear downfield shift ( $\Delta\delta[\text{H}_7] = 0.32$  ppm,  $\Delta\delta[\text{H}_8] = 0.18$  ppm,  $\Delta\delta[\text{H}_9] = 0.50$  ppm.). The proton signals at  $\delta=3.93$  ppm and  $\delta=10.08$  ppm respectively assigned to the proton on -NH<sub>2</sub> and -CHO group disappeared, and a



## 5. Coordination-driven construction of [3]rotaxane based on hierarchical assembly

new signal at  $\delta=8.68$  ppm appeared, suggesting the formation of C=N bond between **L<sup>NH2</sup>** and **2CHO**.

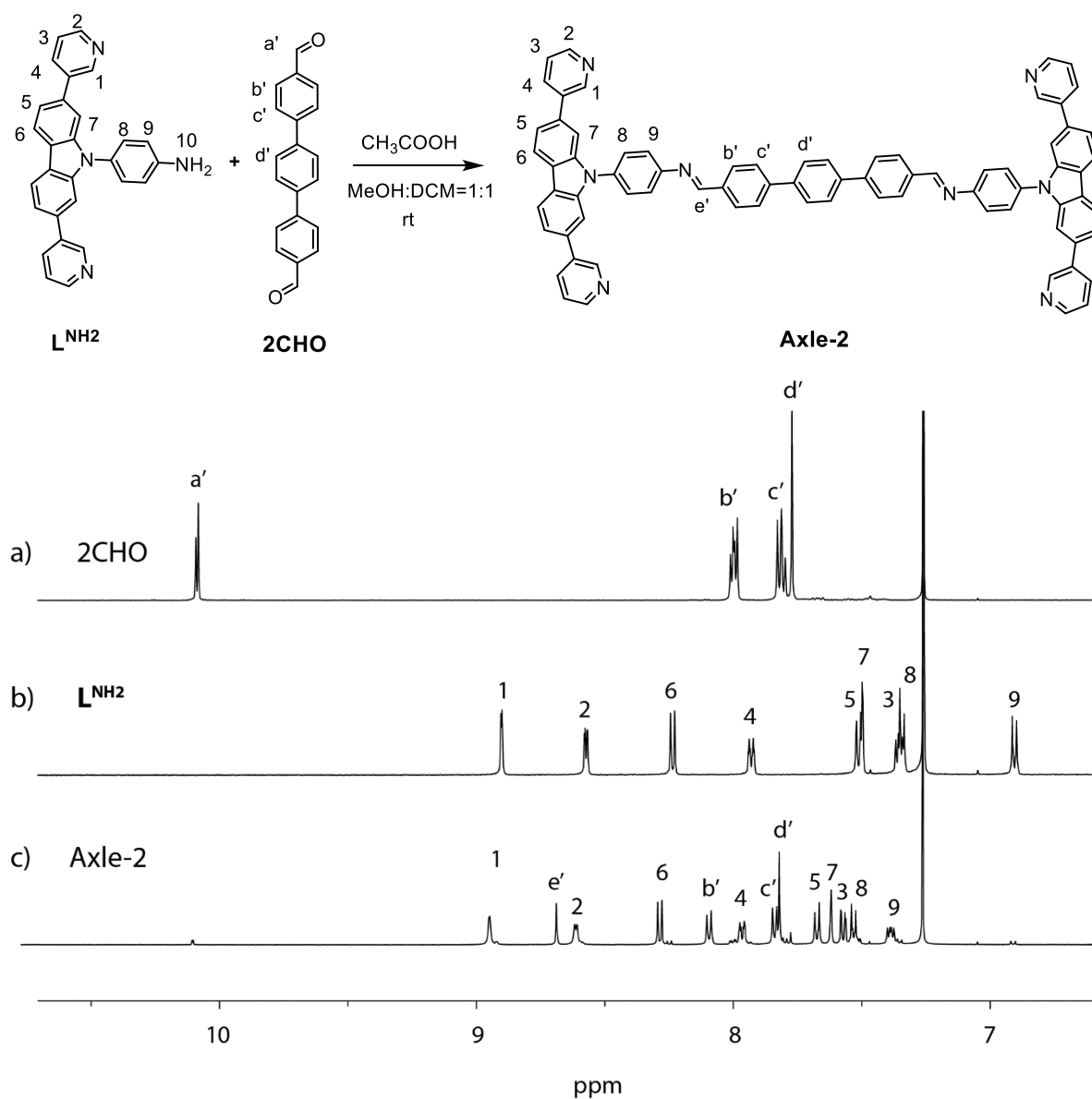


Figure 5.21: <sup>1</sup>H NMR spectra of a) **2CHO**, b) **L<sup>NH2</sup>** and c) **Axle-2** (500 MHz, 298 K, CD<sub>2</sub>Cl<sub>2</sub>).

### 5.5 Formation of rotaxanes

Inspired by those results, the construction of the rotaxanes by combination of both bowl and linkers was investigated. As shown in Figure 5.22, the bowl was firstly obtained by the self-assembly of the macrocycle with Co(II) and ligand (**L<sup>R</sup>** or **L<sup>NH2</sup>**). Then it was reacted with the linker in a 2:1 ratio. **Bowl-1** was reacted with **2N<sub>3</sub>** via CuAAC click reaction (Figure 5.22 a) and **Bowl-2** was reacted with **2CHO** via

5. Coordination-driven construction of [3]rotaxane based on hierarchical assembly condensation reaction (Figure 5.22 b). After purification by precipitate, the  $^1\text{H}$  NMR spectra of the product showed a clear set of signals still attributed to the bowls without new signals and no shift. However, the potential formation of the [3]rotaxane resulting from **Bowl-2** was observed in ESI-MS spectrum (Figure 5.22 c). It demonstrates the self-assembly of metallamacrocycle and **Axle-2** and exhibits promising prospect to generate [3]rotaxane.

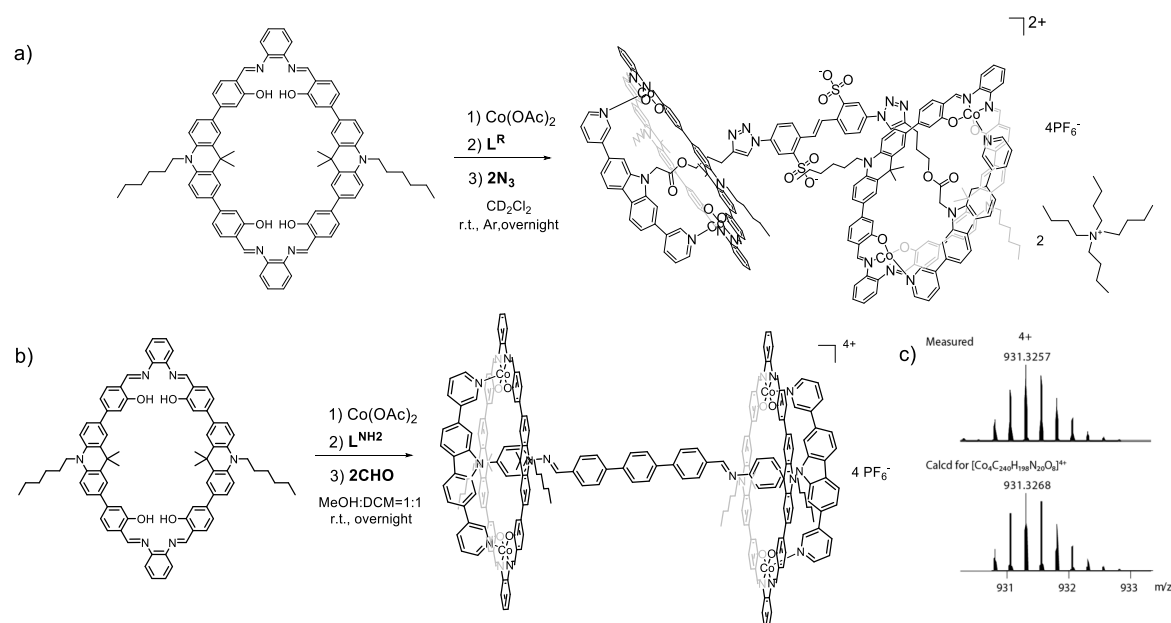


Figure 5.22: Synthesis route to a)  $[(\text{Bow-1})_2(\text{Axle-1})]$ , b)  $[(\text{Bow-2})_2(\text{Axle-2})]$  and ESI-MS spectrum of  $[(\text{Bow-2})_2(\text{Axle-2})]^{4+}$  with showing the calculated and measured isotopic patterns  $[(\text{Bow-2})_2(\text{Axle-2})]^{4+}$ .

Eventually, the optimization of the reaction conditions for the click reaction is still on the way and the challenge remains in the purification of the products. Then the motion of macrocycle by the addition of a competing ligand  $\text{L}'$  to displace the pyridyl ligand from the macrocycle could be investigated (Figure 5.23).

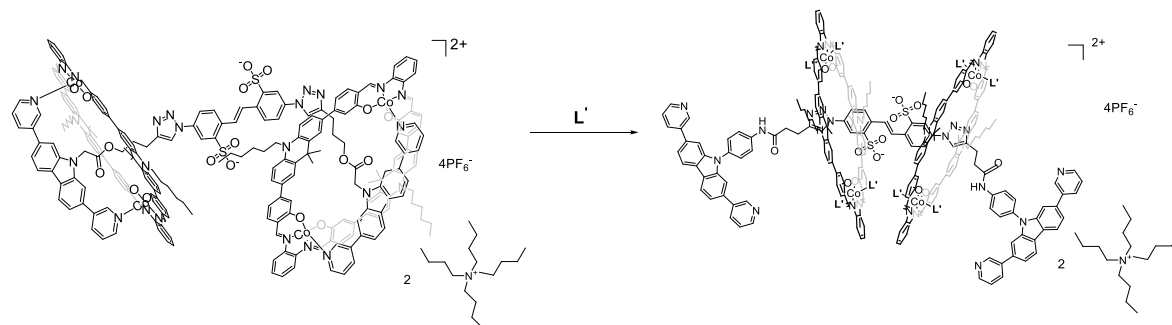


Figure 5.23: Scheme of [3]rotaxane with the detachment of ligand from the macrocycle.

## 5. Coordination-driven construction of [3]rotaxane based on hierarchical assembly

### 5.6 Formation of a heteroleptic cage

The molecular recognition and encapsulation properties of supramolecular cages have been widely exploited.<sup>[15–19]</sup> For the purpose of increasing the complexity and functionality of these discrete self-assembled architectures, it is possible to use the shape complementarity approach, combining geometrically distinct ligands through integrative self-sorting, to form heteroleptic cages.<sup>[12,20]</sup> Multi-components integrative self-sorting based on shape complementarity is a powerful tool to form heteroleptic cages with multiple functions. Here, we plan to combine a metallic active site on the backbone of ligand **A** with a shape complementary functional ligand **C** by coordinating them both to a binuclear cobalt macrocycle **Co(III)<sub>2</sub>B** (Figure 5.24). Finally, the catalytic properties of the assembled cage will be investigated.

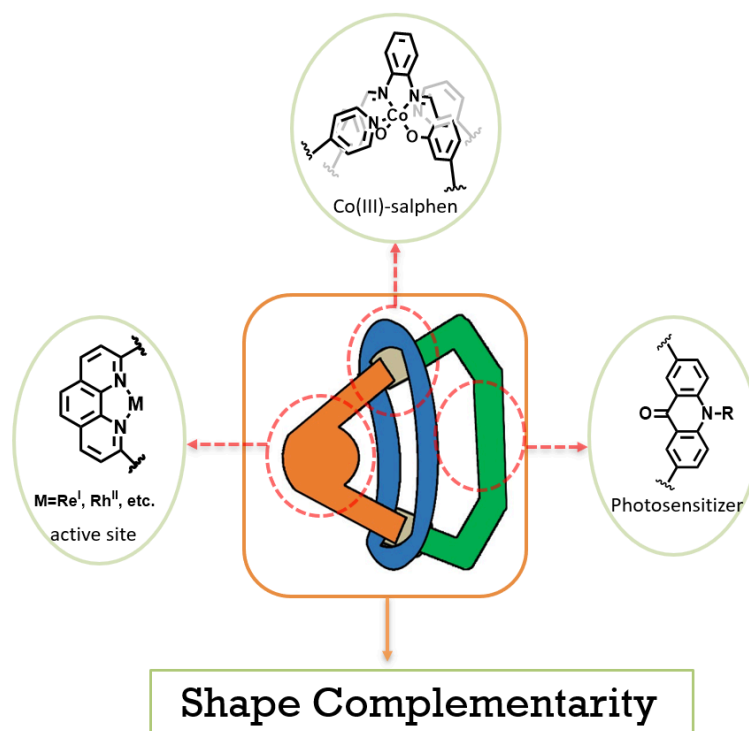
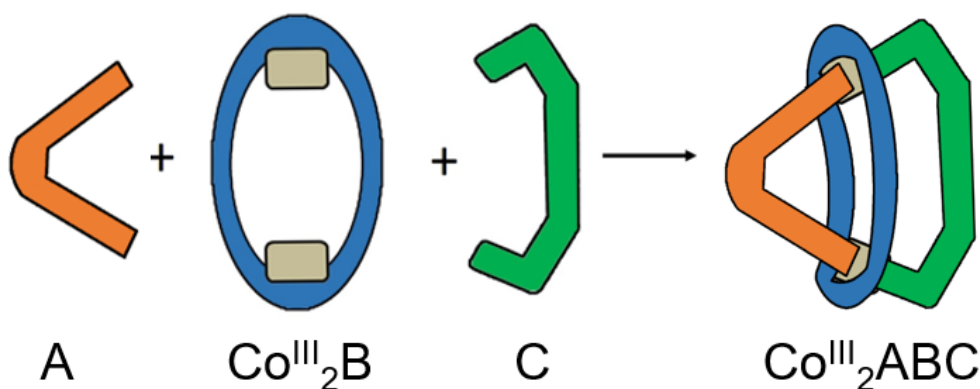
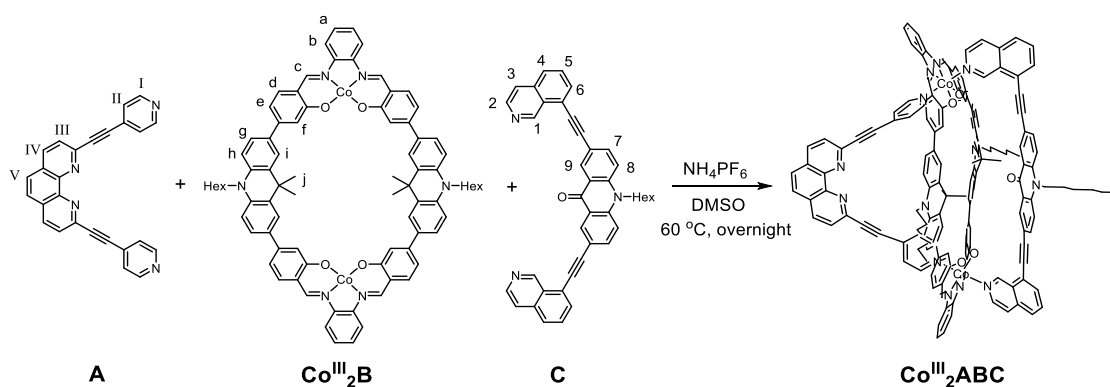


Figure 5.24: Schematic illustration of the structure of functional heteroleptic cage (Color code for **A**: orange, **B**: blue, **C**: green,  $\text{Co}^{\text{III}}$ : gray).

Here, two bis-monodentate ligands with shape-complementarity were prepared. Phenanthroline-based pyridine ligand **A** was synthesized by Sonogashira coupling reaction of 2,9-dibromo-1,10-phenanthroline and 4-ethynylpyridine. Acridone-based isoquinoline ligand **C** was prepared following the reported literature procedure.<sup>[20]</sup>

## 5. Coordination-driven construction of [3]rotaxane based on hierarchical assembly

Macrocycle  $R^{ACR}$  (which is named **B** here) was combined with  $Co(OAc)_2$  in DMSO to afford metallamacrocycle  $Co(III)_2B$ . Afterwards, one equivalent of ligand **A** and one equivalent of ligand **C** were added. With the addition of  $NH_4PF_6$ , the mixture was stirred at 60 °C overnight. The product was purified by precipitation and characterized by NMR and ESI-MS. The  $^1H$  NMR at room temperature showed very broad signals, probably due to dynamics of the structure. To overcome this problem, the  $^1H$  NMR spectrum was measured at higher temperature (353 K) and then clearer and sharp signals were observed (Figure 5.26). Because of the presence of small impurities and the overlapping on some signals in the spectrum, the assignment of the signals presents difficulties. The proton signals of ligand **C** and macrocycle **B** have clear shift in comparison with their free analogues. However, the signals of **A** can still be observed in the spectrum and don't present any shift, indicating the presence of free ligand. Then DOSY spectrum was recorded (Figure 5.83) and two sets of signals were observed. The signals of the ligand have a different diffusion coefficient than the signals from the assembly.



## 5. Coordination-driven construction of [3]rotaxane based on hierarchical assembly

Figure 5.25: Schematic representation of the self-assembly of ligands to form heteroleptic cage **Co(III)<sub>2</sub>ABC**.

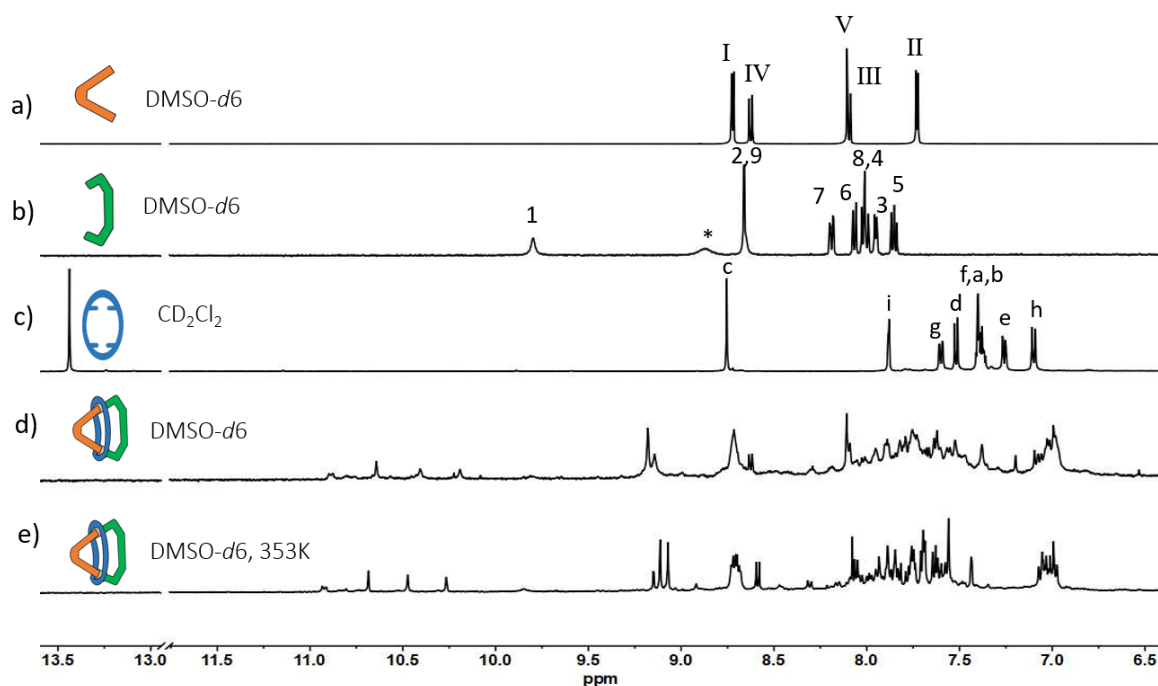
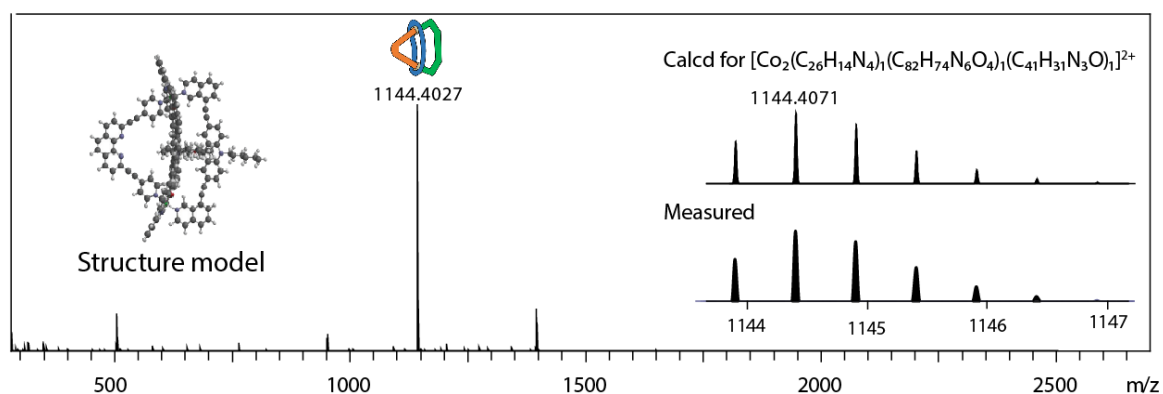


Figure 5.26: <sup>1</sup>H NMR spectra of a) ligand **A** (500 MHz, 298 K, DMSO-*d*<sub>6</sub>), b) ligand **C** (500 MHz, 298 K, DMSO-*d*<sub>6</sub>), c) macrocycle **B** (500 MHz, 298 K, CD<sub>2</sub>Cl<sub>2</sub>), d) cage **Co(III)<sub>2</sub>ABC** (500 MHz, 298 K, DMSO-*d*<sub>6</sub>), and e) **Co(III)<sub>2</sub>ABC** (500 MHz, 353 K, DMSO-*d*<sub>6</sub>).

Interestingly, ESI-MS showed a prominent peak at  $m/z = 1144.4027$  corresponding to the **[Co(III)<sub>2</sub>ABC]<sup>2+</sup>** species, thus indicating the formation of the heteroleptic cage (Figure 5.27). Therefore, we considered the NMR results again, complicated probably due to interaction between the ligand **A** and Co(III) being weak in DMSO solution. Unfortunately, despite many efforts, we did not manage to grow crystals suitable for measurement.



## 5. Coordination-driven construction of [3]rotaxane based on hierarchical assembly

Figure 5.27: ESI-MS and structure model of ( $PM_6$ ) of  $\text{Co(III)}_2\text{ABC}$ , with insets showing the calculated and measured isotopic patterns of  $[\text{Co(III)}_2\text{ABC}]^{2+}$ .

The backbone of ligand **A** was designed with a phenanthroline moiety bearing two chelating nitrogens which can coordinate with catalytically active metal complexes, such as rhenium complexes. Rhenium complexes linking to a bipyridine have been reported for photocatalytic  $\text{CO}_2$  reduction, which is a promising approach for alleviating climate change and energy shortage.<sup>[21]</sup> In a previous work, we have demonstrated that acridone-based ligand **C** can also act as a photosensitizer.<sup>[22]</sup> Therefore, the metalla-ligand with an active site was prepared from ligand **A** and  $\text{Re}(\text{CO})_5\text{Cl}$  to give a functional heteroleptic cage for photocatalytic  $\text{CO}_2$  reduction (Figure 5.28).

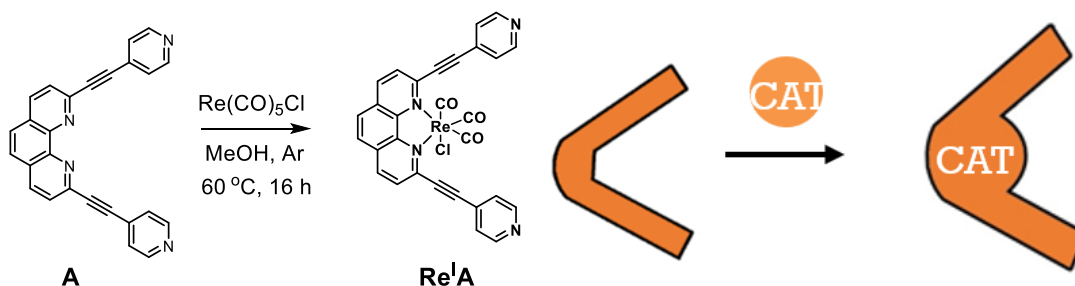


Figure 5.28: Methods to introduce catalyst complex in the cage.

Then, we investigate the formation of the multi-functional heteroleptic cage. Two methods were explored: i) post-synthetic modification. The  $\text{Re}(\text{CO})_5\text{Cl}$  was added into the solution of  $\text{Co(III)}_2\text{ABC}$ . ii) pre-modification. The  $\text{Re}^{\text{I}}\text{A}$  was successfully prepared. Then self-assembly was performed with  $\text{Co(III)}_2\text{B}$  and ligand **C**.

## 5. Coordination-driven construction of [3]rotaxane based on hierarchical assembly

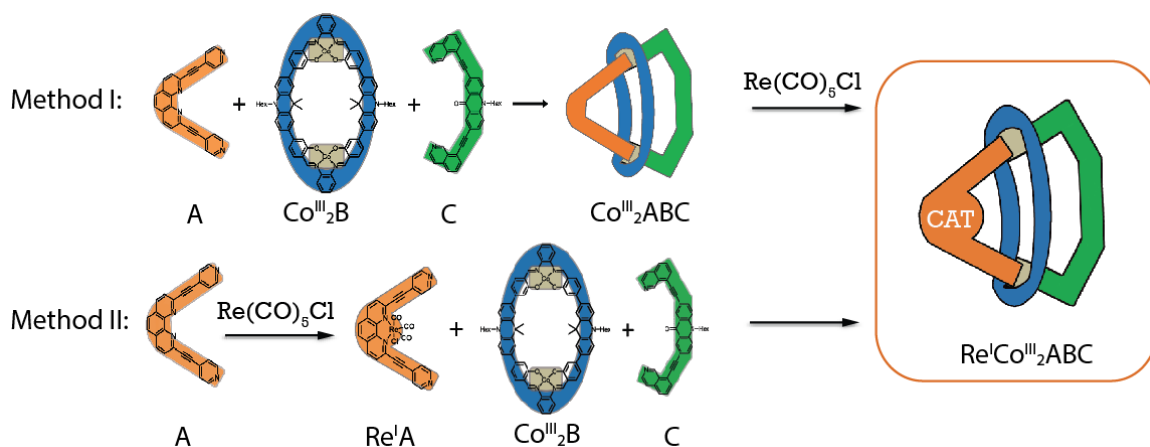


Figure 5.29: Methods to introduce catalyst complex in the cage and the formation of functional heteroleptic cage.

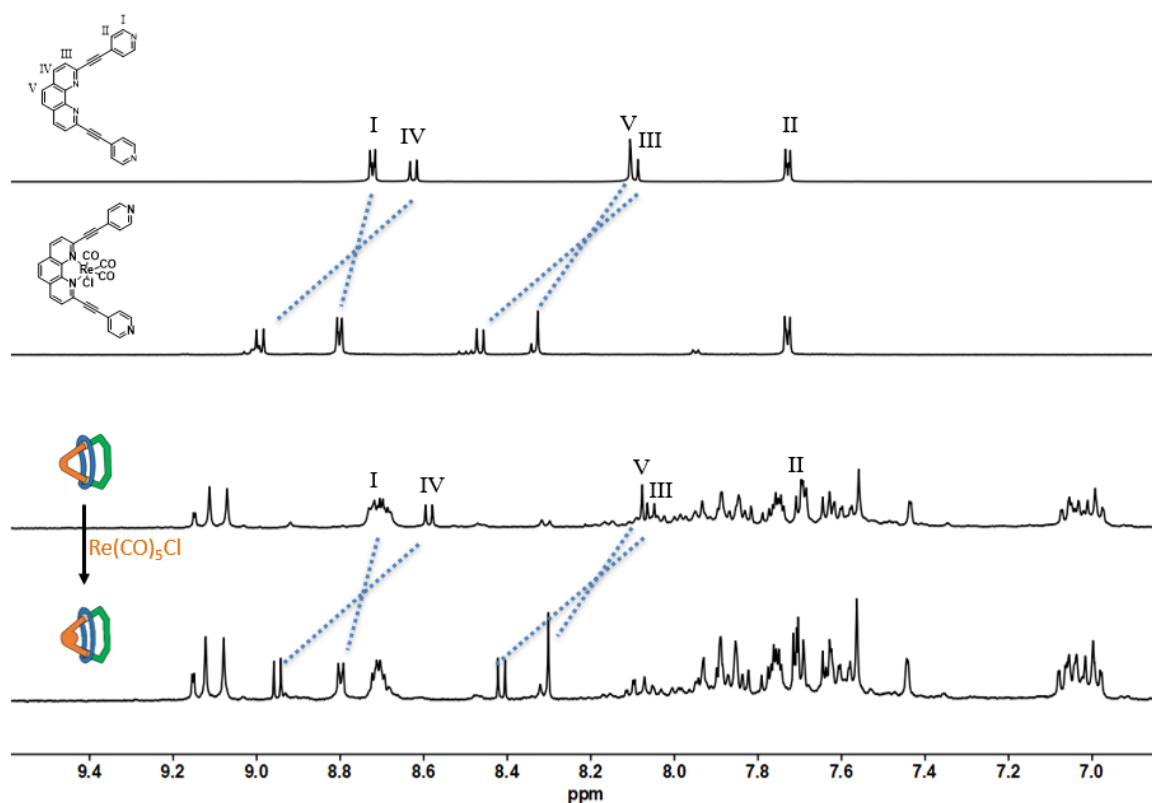


Figure 5.30:  $^1\text{H}$  NMR spectra of ligand **A**,  $\text{Re}^{\text{I}}\text{A}$  (500 MHz, 298 K,  $\text{DMSO}-d_6$ ) and cage  $\text{Co}^{\text{III}}_2\text{ABC}$ ,  $\text{Re}^{\text{I}}\text{Co}^{\text{III}}_2\text{ABC}$  (500 MHz, 353 K,  $\text{DMSO}-d_6$ ).

The formation of  $\text{Re}^{\text{I}}\text{A}$  was confirmed by  $^1\text{H}$  NMR and ESI-MS. One equivalent of  $\text{Re}(\text{CO})_5\text{Cl}$  was added in a degassed  $\text{Co}^{\text{III}}_2\text{ABC}$  DMSO solution. The mixture was heated at 90 °C overnight. The structure was characterized by NMR and ESI-MS.

## 5. Coordination-driven construction of [3]rotaxane based on hierarchical assembly

Comparing with  $^1\text{H}$  NMR spectrum of  $\text{Co(III)}_2\text{ABC}$ , the proton signals assigned to **A** were shifted and the signals of  $\text{Re(I)A}$  were observed, suggesting the successful self-assembly of **A** and  $\text{Re(I)}$  complex in this system. However, the signals of the  $\text{Re(I)A}$  motif in the assembly have the same chemical shifts than free  $\text{Re(I)A}$  complex, thus likely indicating the presence of the free complex in solution. ESI-MS showed a prominent peak at  $m/z = 1297.3507$  corresponding to  $[\text{Re(I)Co(III)}_2\text{ABC}]^{2+}$  species, indicating the formation of the functional heteroleptic cage (Figure 5.31). The peak at  $m/z = 953.3390$  corresponding to the  $[\text{Co(III)}_2\text{BC}]^{2+}$  species was also observed. It suggests that ligand **C** has a stronger binding with  $\text{Co(III)}$ . Similar results were obtained by utilizing method II to form the functional heteroleptic cage. Those results showed that the functional heteroleptic cage was formed, but further purification still needs to be done.

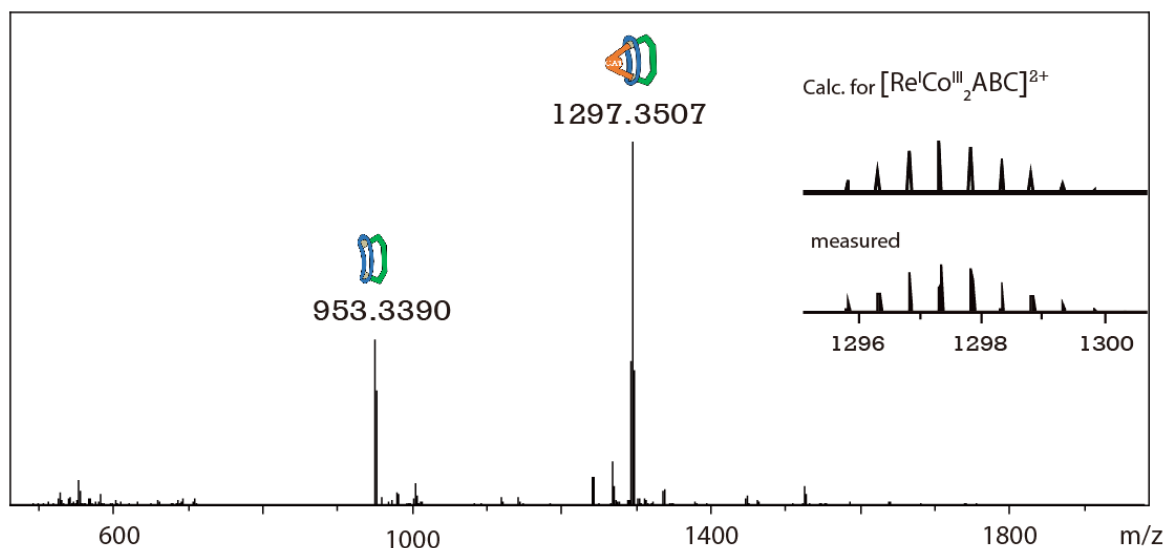


Figure 5.31: ESI-MS of  $\text{Re(I)Co(III)}_2\text{ABC}$ , with insets showing the calculated and measured isotopic patterns of  $[\text{Re(I)Co(III)}_2\text{ABC}]^{2+}$ .

The combination of photocatalyst and photosensitizer, with a defined cavity in the functional heteroleptic cage, is promising to perform a  $\text{CO}_2$  photocatalytic reduction reaction (Figure 5.32). The cavity of the cage is expected to stabilize the transition state or  $\text{CO}_2$  adduct to improve reactivity and selectivity.<sup>[23]</sup> The study of catalytic activity of cage should be studied next.



## 5. Coordination-driven construction of [3]rotaxane based on hierarchical assembly

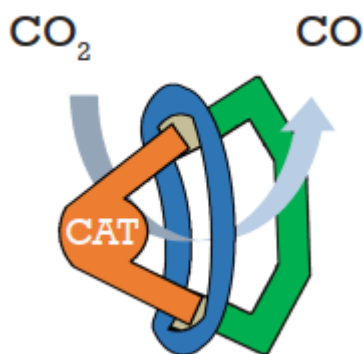


Figure 5.32: Proposed photocatalytic reduction of CO<sub>2</sub> to CO.

### 5.7 Conclusion

Herein, two kinds of carbazole-based ligands ( $L^R$  and  $L^{NH_2}$ ) with different flexibility of were synthesized and self-assembled with the binuclear cobalt macrocycle. The bowl-shape structures were obtained and fully characterized by NMR spectroscopy, mass spectroscopy and X-ray crystallography. The substituent on the backbone can react with a linker in order to connect two bowls. And it was observed that the substituents of the carbazole ligand point towards the inside of the macrocycle. It provides the possibility that the macrocycle thread on the axle after the connection of two bowls. The formation of the rotaxane was confirmed by ESI-MS. The reaction condition needs to be improved to increase the yield and the purity. Finally, studies of the detachment of ligand from the macrocycle to achieve its motion should be studied next.

### 5.8 Experiment Part

#### 5.8.1 Materials

Unless otherwise stated, all chemicals and solvents were purchased from commercial companies (Abcr, Sigma Aldrich, Acros Organics, VWR and Chempur) and used as received. 4,4'-Diazido-stilbene-2,2'-bis-sulfonic acid bis-tetrabutylammonium salt (**2N<sub>3</sub>**) was prepared following the reported literature.<sup>[24]</sup>

## 5. Coordination-driven construction of [3]rotaxane based on hierarchical assembly

### 5.8.2 General Methods

#### NMR

NMR spectroscopic data was measured on the spectrometers Bruker AV 500 Avance NEO, Bruker AV 600 Avance III HD and Bruker AV 700 Avance III HD. Chemical shifts for  $^1\text{H}$  and  $^{13}\text{C}$  spectra are reported in ppm on the  $\delta$  scale relative to proton resonance resulting from incomplete deuteration of the solvents ( $\text{CDCl}_3$ : 7.26 ppm, 77.16 ppm,  $\text{DMSO-}d_6$ : 2.5 ppm, 39.52 ppm,  $\text{CD}_3\text{CN}$ : 1.94 ppm, 118.26 ppm,  $\text{CD}_2\text{Cl}_2$ : 5.32 ppm). The chemical shift  $\delta$  is given in ppm, the coupling constants  $J$  in Hz. The following abbreviations are used to describe signal multiplicity for  $^1\text{H}$  NMR spectra: s: singlet, d: doublet, t: triplet, dd: doublet of doublets, m: multiplet. All spectra were recorded in standard 5 mm NMR tubes at 298 K if not stated otherwise.

#### DOSY

$^1\text{H}$  DOSY spectra were recorded with a dstebpgp3s pulse sequence with diffusion delays D20 of 0.09-0.14 s and gradient powers P30 of 900-2500  $\mu\text{s}$  for each species optimized. The hydrodynamic radius was calculated according to Stokes-Einstein equation:

$$D = \frac{k_B T}{6\pi\eta r_H}$$

Where  $D$  is coefficient constant,  $k_B$  is the Boltzmann constant,  $T$  is the absolute temperature,  $\eta$  is the viscosity of solvent,  $r_H$  is the hydrodynamic radius.

#### ESI-MS

Electrospray ionization mass spectrometry (ESI-MS) experiments were performed on ESI-timsTOF (ESI-trapped ion mobility-time of flight) mass spectrometer by Bruker, equipped with and ESI source (positive/negative mode). An Agilent ESI low concentration tuning mix has been used for calibration of tims and TOF units. Mass spectrometry data is given as mass/charge ratio ( $m/z$ ) as well as the relative intensity with regard to the base peak ( $I = 100$ ).

#### X-Ray Analysis

## 5. Coordination-driven construction of [3]rotaxane based on hierarchical assembly

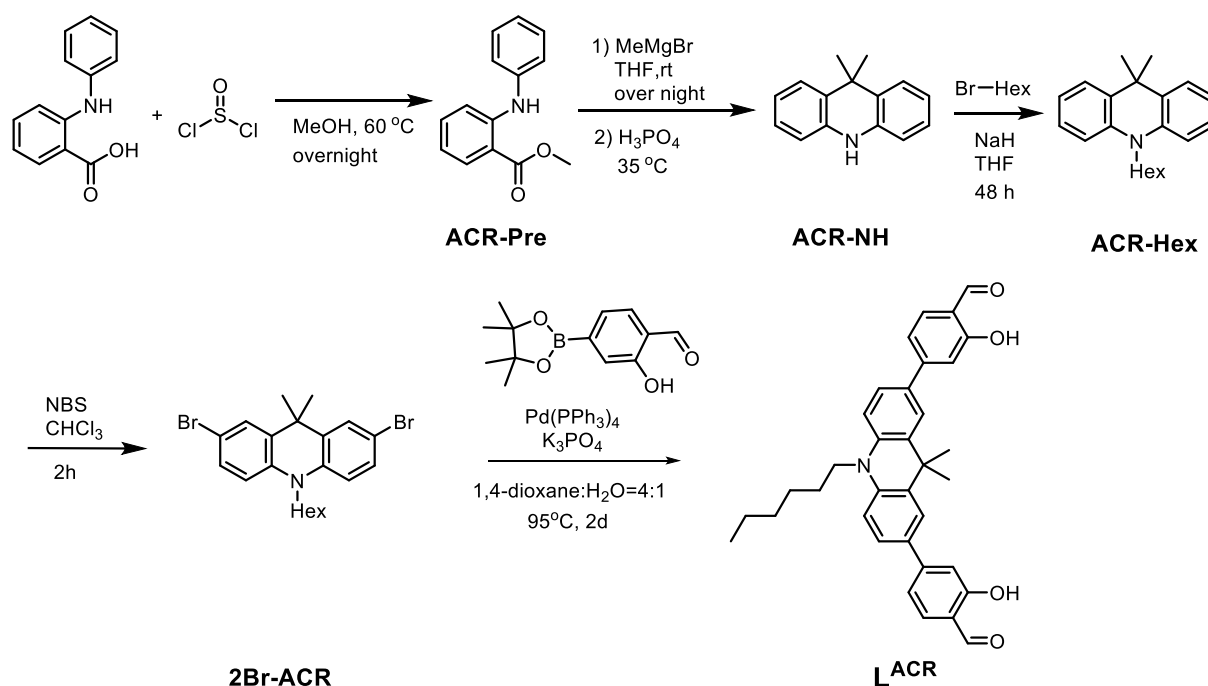
### Bruker D8 venture (in-house)

Data collection for single crystal X-ray diffraction was performed on a Bruker D8 venture with a four-axle goniometer in  $\kappa$ -geometry, equipped with CuK $\alpha$  and MoK $\alpha$  Incoatec microfocus sources ( $\lambda$  3.0) and a photon II detector. The crystal was covered with inert NVH oil and placed on the 0.2 mm nylon loop. The sample was cooled down to 100(2) K utilizing an Oxford Cryostream 800.

### P11@DESY (Synchrotron)

Data collection for single crystal X-ray diffraction was performed on a one-axle goniometer equipped with a Pilatus 6M fast detector by Dectris at the macromolecular beamline PXI, Petra III, DESY, Hamburg. Therefore, a wavelength of  $\lambda = 0.6888 \text{ \AA}$  has been set on a nitrogen cooled double monochromator and the sample has been cooled to 80(2) K utilizing an Oxford Cryostream 800.

### 5.8.3 Synthesis of the ligands



#### Synthesis of methyl 2-(phenylamino)benzoate (**ACR-pre**)

2-(phenylamino)benzoic acid (1 g, 4.7 mmol, 1 equiv.) was dissolved in 35 mL  $\text{MeOH}$ ,  $\text{SOCl}_2$  (3 mL) was added dropwise with stirring. The mixture was stirred at  $60^\circ\text{C}$  overnight. After cooling to room temperature, the excessive  $\text{SOCl}_2$  was removed under reduced pressure. The residue was extracted with  $\text{DCM}$  and saturated  $\text{NaCl}$  (aq.). The organic phase was combined and dried over  $\text{MgSO}_4$ . The

## 5. Coordination-driven construction of [3]rotaxane based on hierarchical assembly

crude product was purified by column chromatography (pentane:  $\text{CHCl}_3 = 2:1$ ) to give light yellow oil as product (0.95 g, 89.1% yield).

$^1\text{H}$  NMR (500 MHz,  $\text{DMSO-}d_6$ )  $\delta$  9.32 (s, 1H), 7.89 (dd,  $J = 8.0, 1.7$  Hz, 1H), 7.45 – 7.37 (m, 1H), 7.36 (t,  $J = 6.9$  Hz, 1H), 7.23 (t,  $J = 8.0$  Hz, 3H), 7.12 – 7.04 (m, 1H), 6.87 – 6.75 (m, 1H), 3.84 (s, 3H).

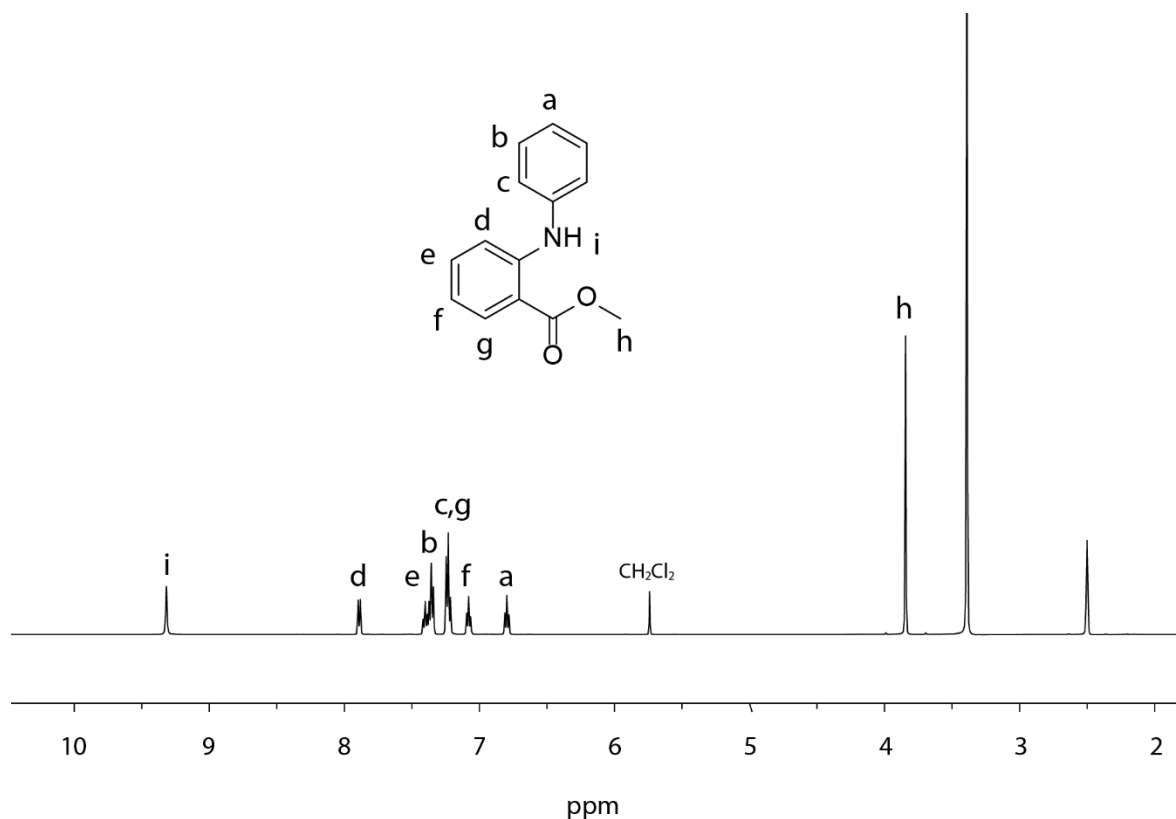


Figure 5.33:  $^1\text{H}$  NMR spectrum of **ACR-pre** (500 MHz, 298 K,  $\text{DMSO-}d_6$ ).

### Synthesis of 9,9-dimethyl-9,10-dihydroacridine (**ACR-NH**)

**ACR-Pre** (1 g, 4.4 mmol, 1 equiv.) was dissolved in anhydrous THF and cooled in an ice bath.  $\text{MeMgBr}$  (1.84 g, 15.4 mmol, 3.5 equiv.) was added dropwise over a period of 15 min. Then the reaction mixture was stirred at room temperature for 18 h and then quenched by saturated  $\text{NH}_4\text{Cl}$  solution. The mixture was extracted with DCM. The organic phase was combined and dried over  $\text{MgSO}_4$ . The solvent was removed. Under Ar atmosphere, 3 mL  $\text{H}_3\text{PO}_4$  was added to the crude product and stirred at 35 °C for 2 h.  $\text{NH}_4\text{Cl}$  aq solution was added and then poured into water at 0 °C. The white solid was collected by filtration (510 mg, 55.4% yield).

## 5. Coordination-driven construction of [3]rotaxane based on hierarchical assembly

$^1\text{H}$  NMR (700 MHz,  $\text{CDCl}_3$ ):  $\delta$  7.38 (dd,  $J = 7.8, 1.4$  Hz, 2H), 7.15 – 7.05 (m, 2H), 6.92 (t,  $J = 7.6$  Hz, 2H), 6.70 (d,  $J = 7.9$  Hz, 2H), 6.13 (s, 2H), 1.59 (s, 6H).

$^{13}\text{C}$  NMR (176 MHz,  $\text{CDCl}_3$ ):  $\delta$  138.62, 129.28, 126.86, 125.63, 120.75, 113.56, 36.35, 30.68.

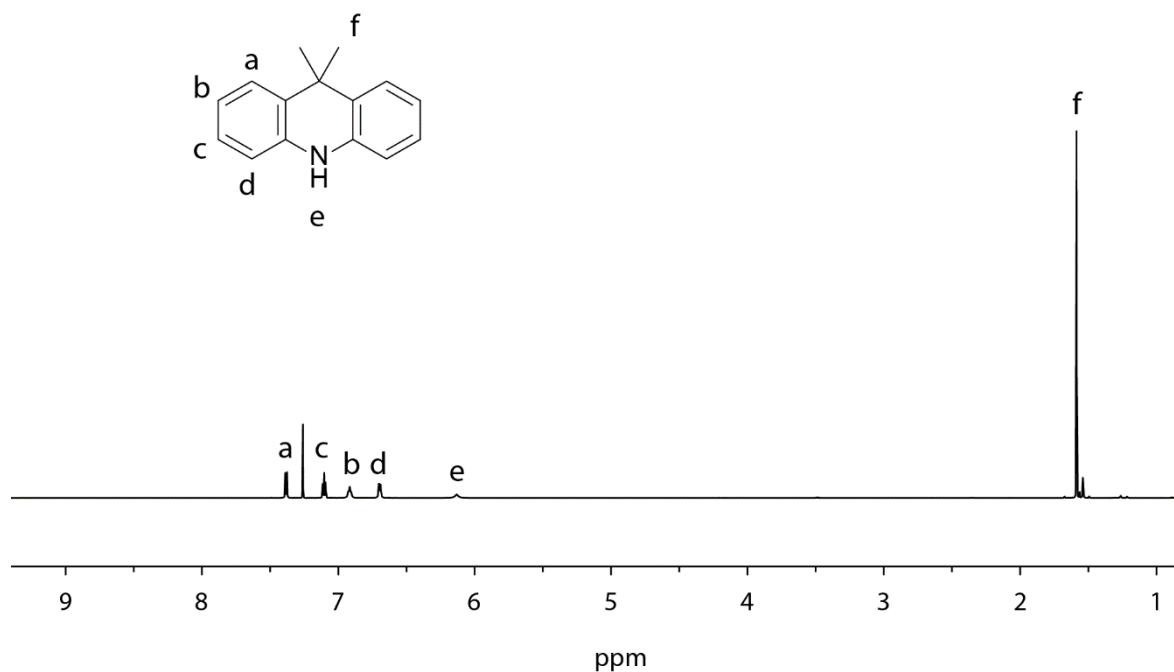
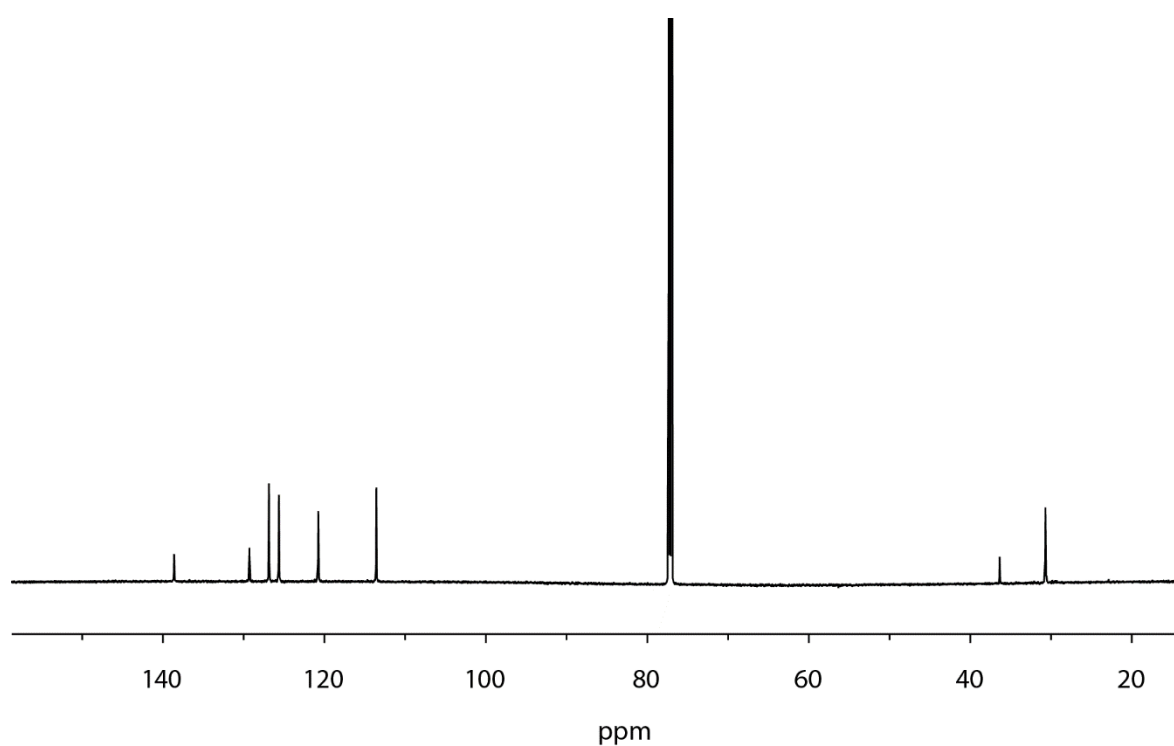


Figure 5.34:  $^1\text{H}$  NMR spectrum of **ACR-NH** (700 MHz, 298 K,  $\text{CDCl}_3$ ).



## 5. Coordination-driven construction of [3]rotaxane based on hierarchical assembly

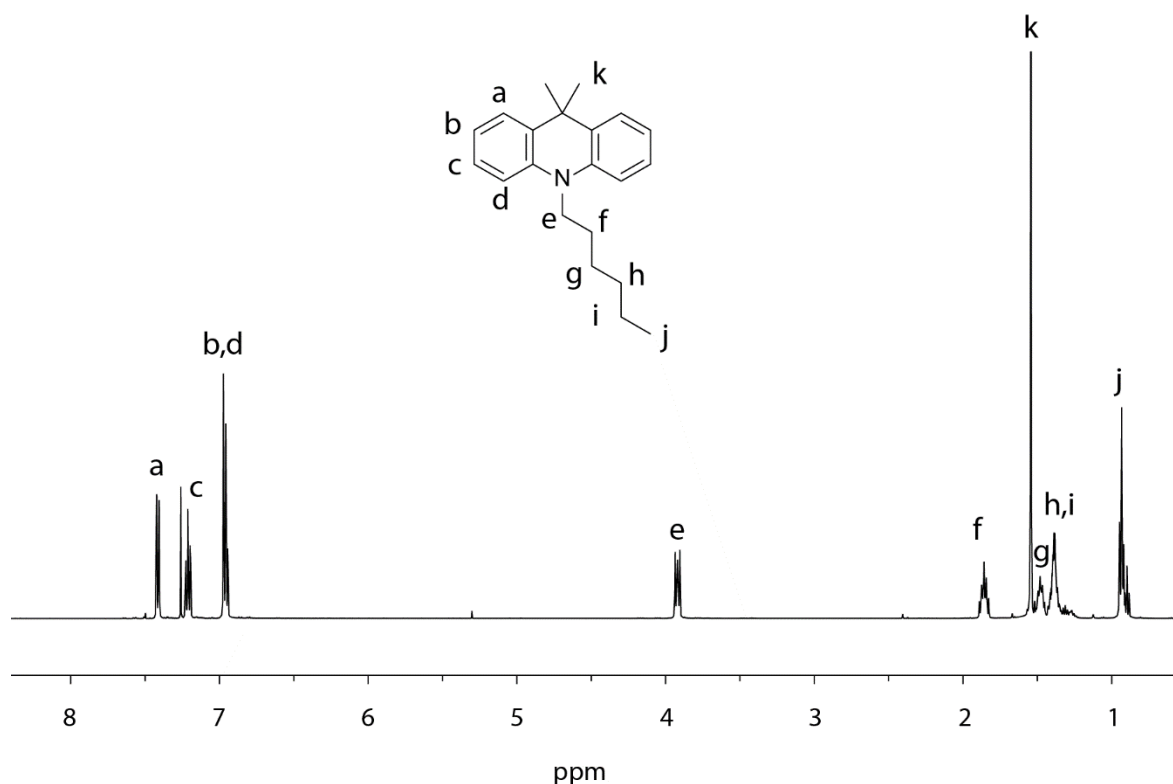
Figure 5.35:  $^{13}\text{C}$  NMR spectrum of **ACR-NH** (176 MHz, 298 K,  $\text{CDCl}_3$ ).

### Synthesis of 10-hexyl-9,9-dimethyl-9,10-dihydroacridine (**ACR-Hex**)

**ACR-NH** (800 mg, 3.82 mmol, 1 equiv.) was dissolved in 20 mL anhydrous THF. NaH (275 mg, 11.47 mmol, 3 equiv. 60% dispersion in mineral oil) was added portion-wise over 10 min at 0 °C. After stirring at room temperature for 1h, 1-bromohexane (757 mg, 4.59 mmol, 1.2 equiv.) was added. The reaction mixture was stirred at 65 °C for 2 days. The  $\text{NH}_4\text{Cl}$  (aq.) was added slowly to quench the excess of NaH and the reaction mixture was extracted with  $\text{CH}_2\text{Cl}_2$ . The organic phase was combined and dried over  $\text{MgSO}_4$ . Solvents were removed under reduced pressure and the crude product was purified by column chromatography (DCM: pentane = 1:20). The product was isolated as yellow oil (704 mg, 62.8% yield).

$^1\text{H}$  NMR (500 MHz,  $\text{CDCl}_3$ ):  $\delta$  7.42 (dd,  $J = 8.1, 1.5$  Hz, 2H), 7.24 – 7.18 (m, 2H), 6.98 – 6.93 (m, 4H), 3.97 – 3.86 (m, 2H), 1.86 (p,  $J = 7.7$  Hz, 2H), 1.54 (s, 6H), 1.52 – 1.43 (m, 2H), 1.39 (tt,  $J = 7.9, 3.9$  Hz, 4H), 0.93 (t,  $J = 7.1$  Hz, 3H).

$^{13}\text{C}$  NMR (126 MHz,  $\text{CDCl}_3$ ):  $\delta$  140.76, 132.34, 126.70, 124.53, 120.37, 112.59, 46.17, 36.35, 31.75, 29.04, 27.10, 26.07, 22.86, 14.19.



## 5. Coordination-driven construction of [3]rotaxane based on hierarchical assembly

Figure 5.36:  $^1\text{H}$  NMR spectrum of **ACR-Hex** (500 MHz, 298 K,  $\text{CDCl}_3$ ).

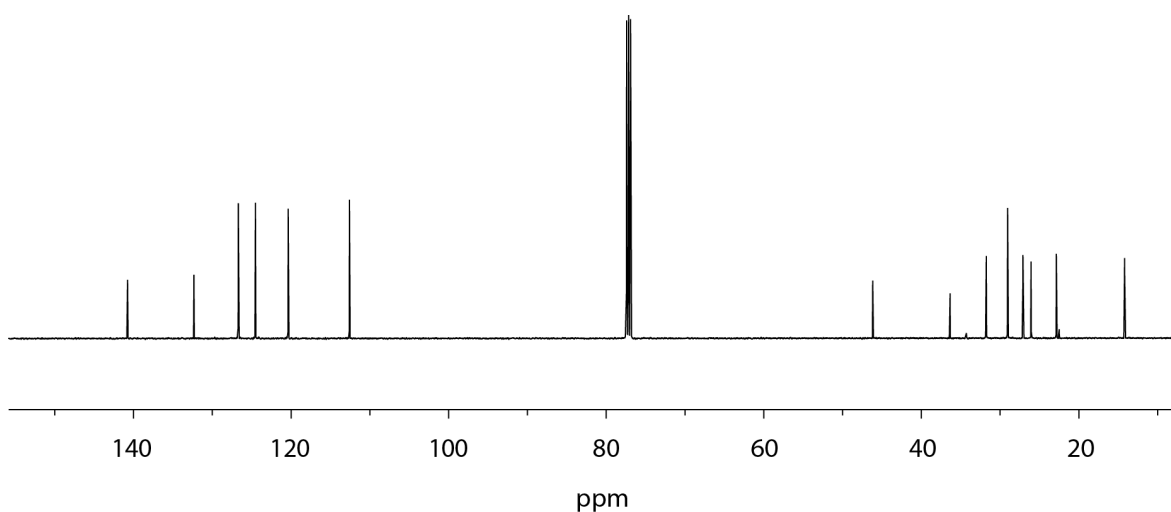


Figure 5.37:  $^{13}\text{C}$  NMR spectrum of **ACR-Hex** (126 MHz, 298 K,  $\text{CDCl}_3$ ).

Synthesis of 2,7-dibromo-10-hexyl-9,9-dimethyl-9,10-dihydroacridine (**2Br-Hex**)  
**Hex-ACR** (450 mg, 1.53 mmol, 1 equiv.) and NBS (546 mg, 3.07 mmol, 2 equiv.) were dissolved in 15 mL  $\text{CHCl}_3$  and stirred at room temperature for 2 h. the reaction was monitored by TLC. After the reaction, the solvent was removed under reduced pressure and the residue was purified by column chromatography (pentane) (508 mg, 73.4% yield).

$^1\text{H}$  NMR (500 MHz,  $\text{CDCl}_3$ ):  $\delta$  7.45 (d,  $J = 2.3$  Hz, 2H), 7.29 (dd,  $J = 8.7, 2.3$  Hz, 2H), 6.80 (d,  $J = 8.7$  Hz, 2H), 3.88 – 3.76 (m, 2H), 1.82 – 1.74 (m, 2H), 1.48 (s, 6H), 1.44 (t,  $J = 7.4$  Hz, 2H), 1.36 (qq,  $J = 4.4, 2.2$  Hz, 4H), 0.94 – 0.89 (m, 3H).

$^{13}\text{C}$  NMR (126 MHz,  $\text{CDCl}_3$ ):  $\delta$  139.53, 134.05, 129.58, 127.53, 114.37, 113.20, 46.28, 36.64, 31.65, 28.69, 26.97, 25.80, 22.81, 14.17.

## 5. Coordination-driven construction of [3]rotaxane based on hierarchical assembly

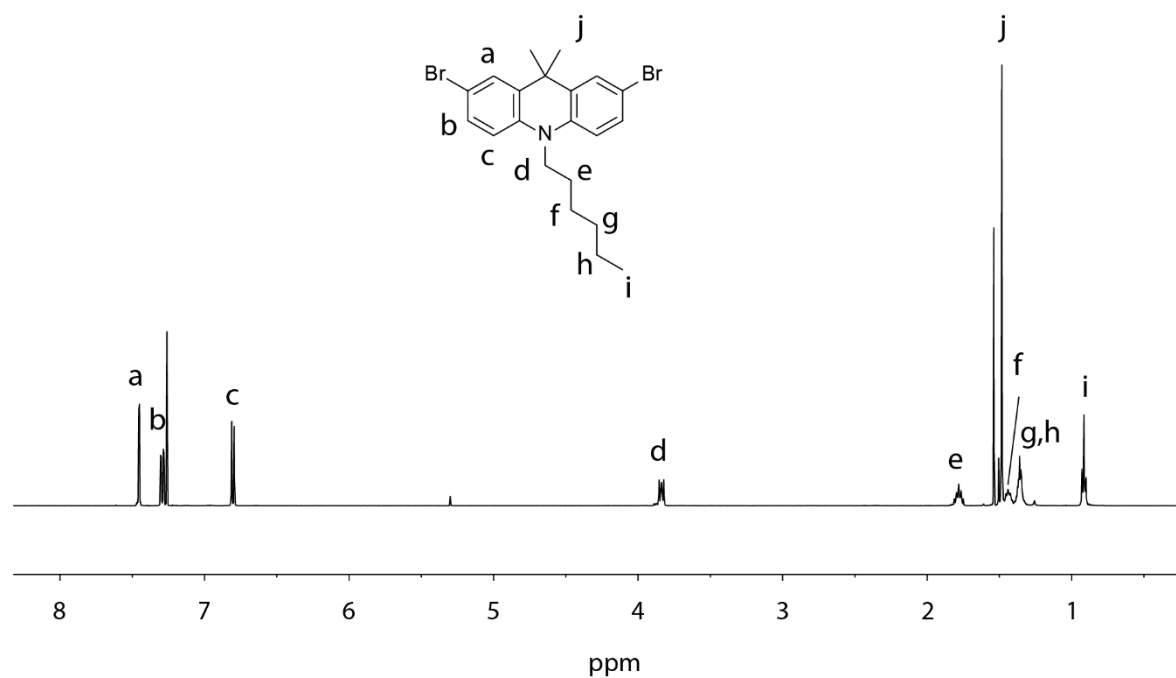


Figure 5.38: <sup>1</sup>H NMR spectrum of **2Br-Hex** (500 MHz, 298 K, CDCl<sub>3</sub>).

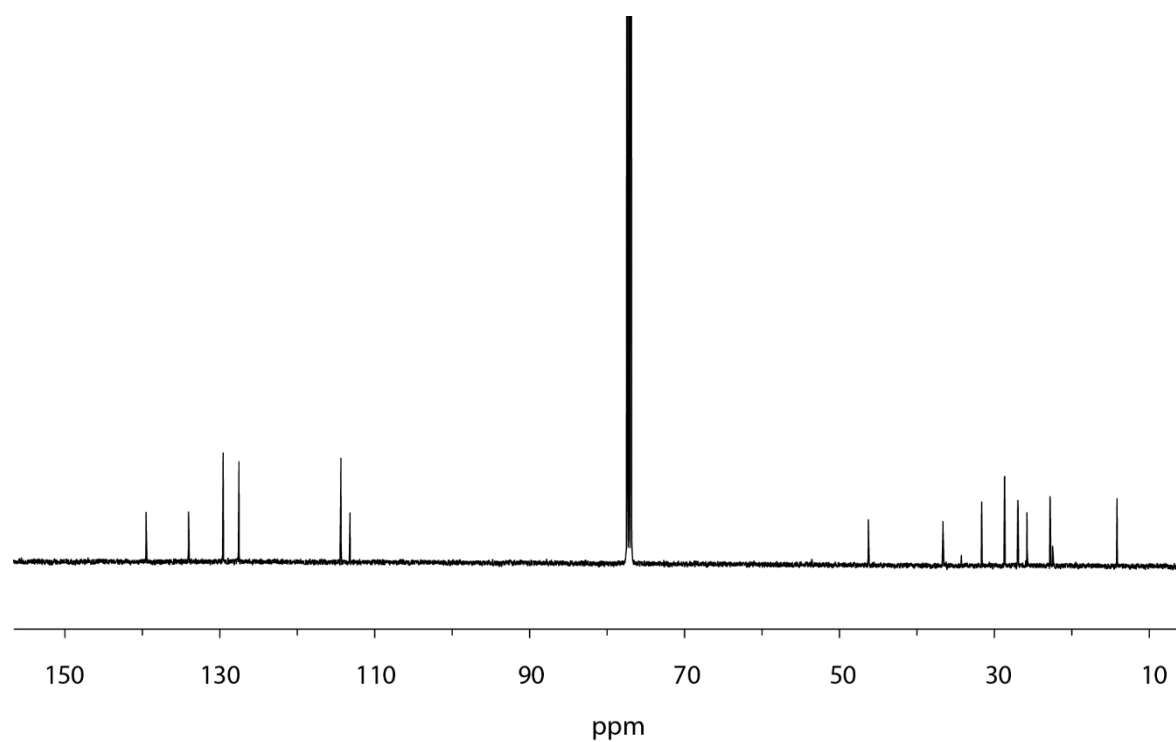


Figure 5.39: <sup>13</sup>C NMR spectrum of **2Br-Hex** (126 MHz, 298 K, CDCl<sub>3</sub>).



## 5. Coordination-driven construction of [3]rotaxane based on hierarchical assembly

### Synthesis of **L<sup>ACR</sup>**

**2Br-Hex** (350 mg, 0.75 mmol, 1.0 equiv.), pinacol ester (467 mg, 1.88 mmol, 2.5 equiv.), Pd(PPh<sub>3</sub>)<sub>4</sub> (87 mg, 0.075 mmol, 10 mol%) and K<sub>3</sub>PO<sub>4</sub> (575 mg, 2.71 mmol, 3.6 equiv.) were combined in a 100 mL Schlenk tube. The mixture was degassed and refilled with argon for three times. 20 mL degassed solvents (1,4-dioxane:H<sub>2</sub>O = 4:1) were added. The reaction mixture was stirred at 95 °C for 48 h. After cooling to room temperature, the solvent was removed under reduced pressure. HCl solution (aq. 2M, 50 ml) was added and extracted with CHCl<sub>3</sub> (3 × 30ml), combine the organic phase and dried over Na<sub>2</sub>SO<sub>4</sub>. The solvent was removed under reduced pressure. The crude product was purified by column chromatography (CHCl<sub>3</sub>:pentane = 2:1) to provide a bright yellow solid as aim product (228 mg, 54 % yield).

<sup>1</sup>H NMR (500 MHz, CD<sub>2</sub>Cl<sub>2</sub>): δ 11.15 (s, 2H), 9.90 (s, 2H), 7.77 (d, *J* = 2.2 Hz, 2H), 7.63 (d, *J* = 8.1 Hz, 2H), 7.58 (dd, *J* = 8.6, 2.3 Hz, 2H), 7.32 (dd, *J* = 8.0, 1.7 Hz, 2H), 7.24 (d, *J* = 1.7 Hz, 2H), 7.11 (d, *J* = 8.6 Hz, 2H), 4.06 – 3.79 (m, 2H), 1.89 (p, *J* = 7.7 Hz, 2H), 1.53 (m, 2H), 1.46 – 1.36 (m, 4H), 0.94 (t, *J* = 7.0 Hz, 6H).

<sup>13</sup>C NMR (126 MHz, CD<sub>2</sub>Cl<sub>2</sub>): δ 196.32, 162.41, 149.93, 141.20, 134.56, 132.86, 131.49, 126.27, 124.20, 119.51, 118.43, 114.64, 113.70, 46.71, 36.88, 31.98, 29.80, 27.20, 26.36, 23.12, 14.21.

HR ESI-MS: calculated for [C<sub>35</sub>H<sub>36</sub>NO<sub>4</sub>]<sup>2+</sup> *m/z* 534.2639 [M + 2H]<sup>2+</sup>  
found: 534.2631

## 5. Coordination-driven construction of [3]rotaxane based on hierarchical assembly

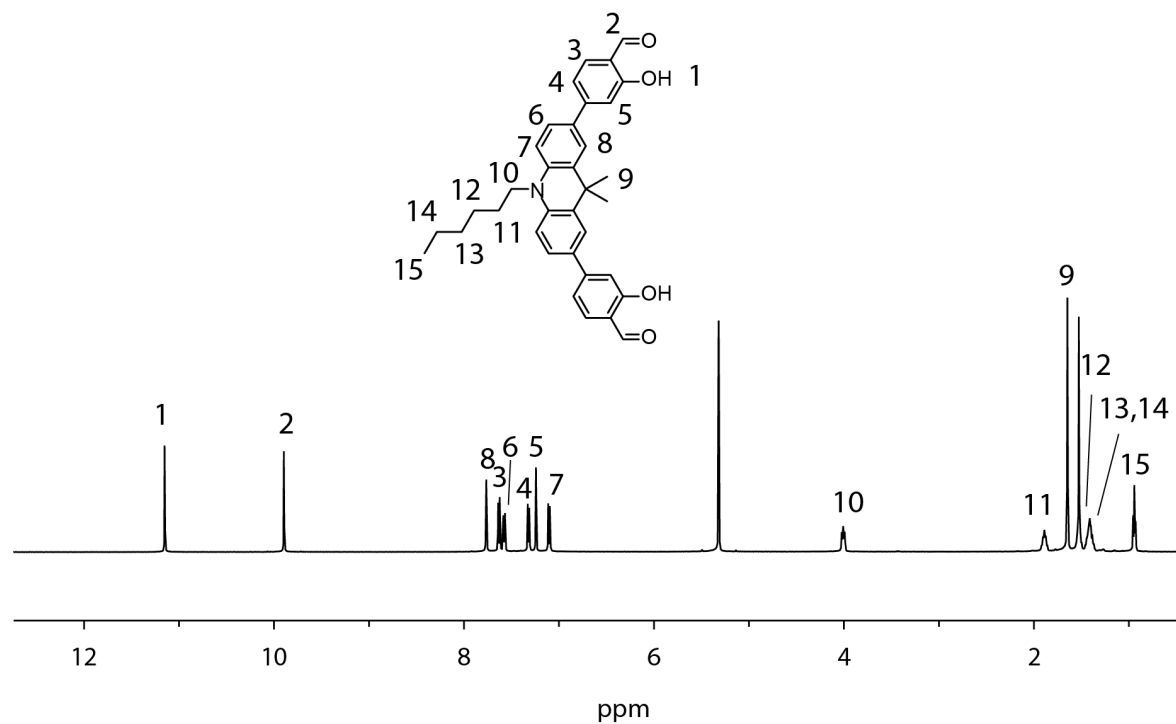


Figure 5.40:  $^1H$  NMR spectrum of  $L^{ACR}$  (500 MHz, 298 K,  $CD_2Cl_2$ ).

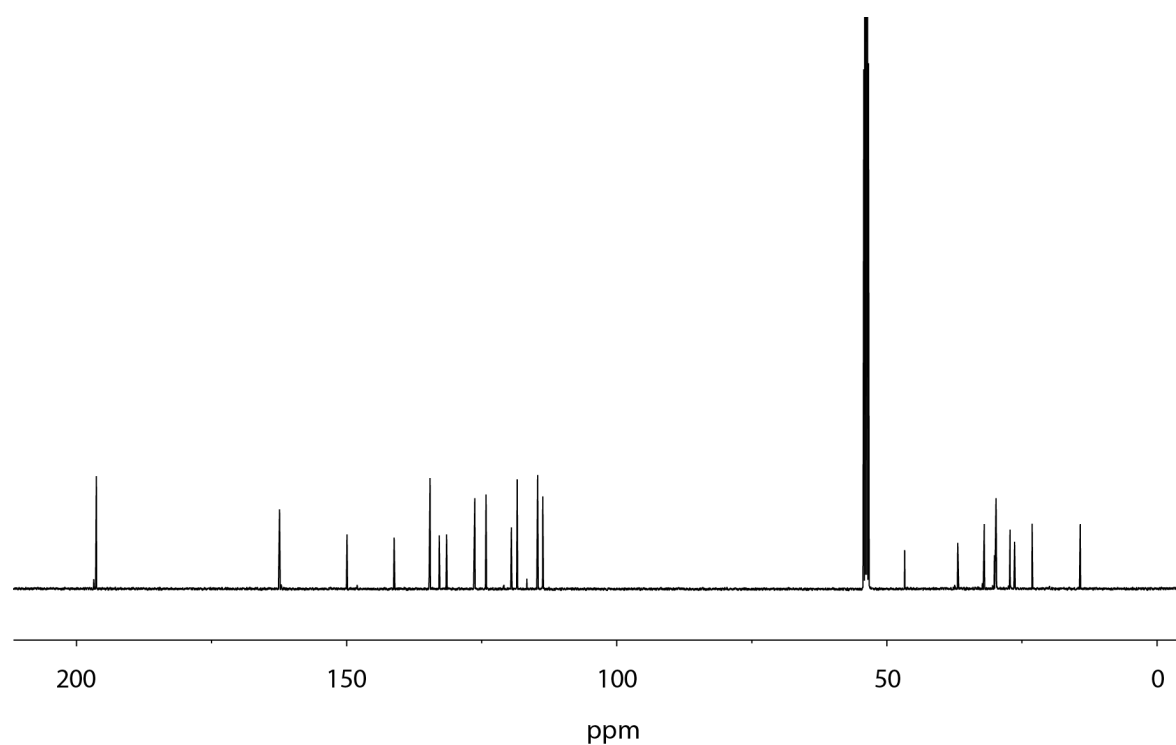


Figure 5.41:  $^{13}C$  NMR spectrum of  $L^{ACR}$  (126 MHz, 298 K,  $CD_2Cl_2$ ).

## 5. Coordination-driven construction of [3]rotaxane based on hierarchical assembly

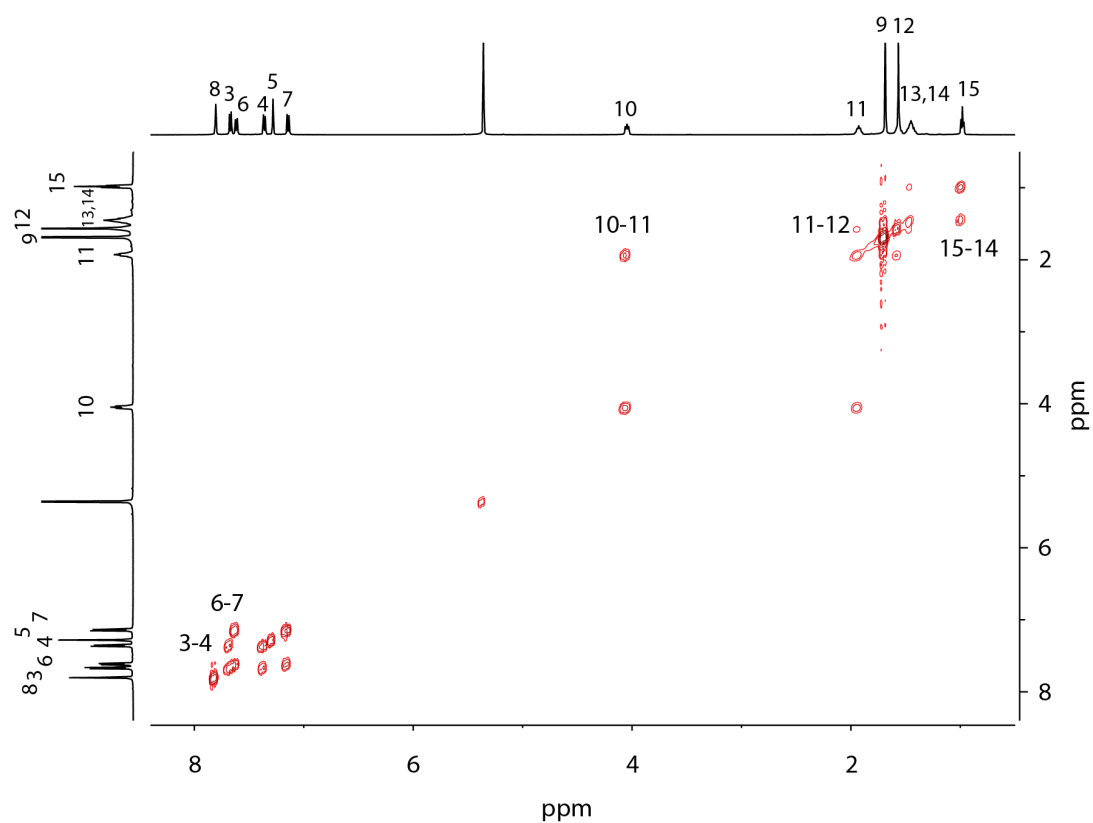


Figure 5.42:  $^1\text{H}$ - $^1\text{H}$  COSY NMR spectrum of  $\text{L}^{\text{ACR}}$  (500 MHz, 298 K,  $\text{CD}_2\text{Cl}_2$ ).

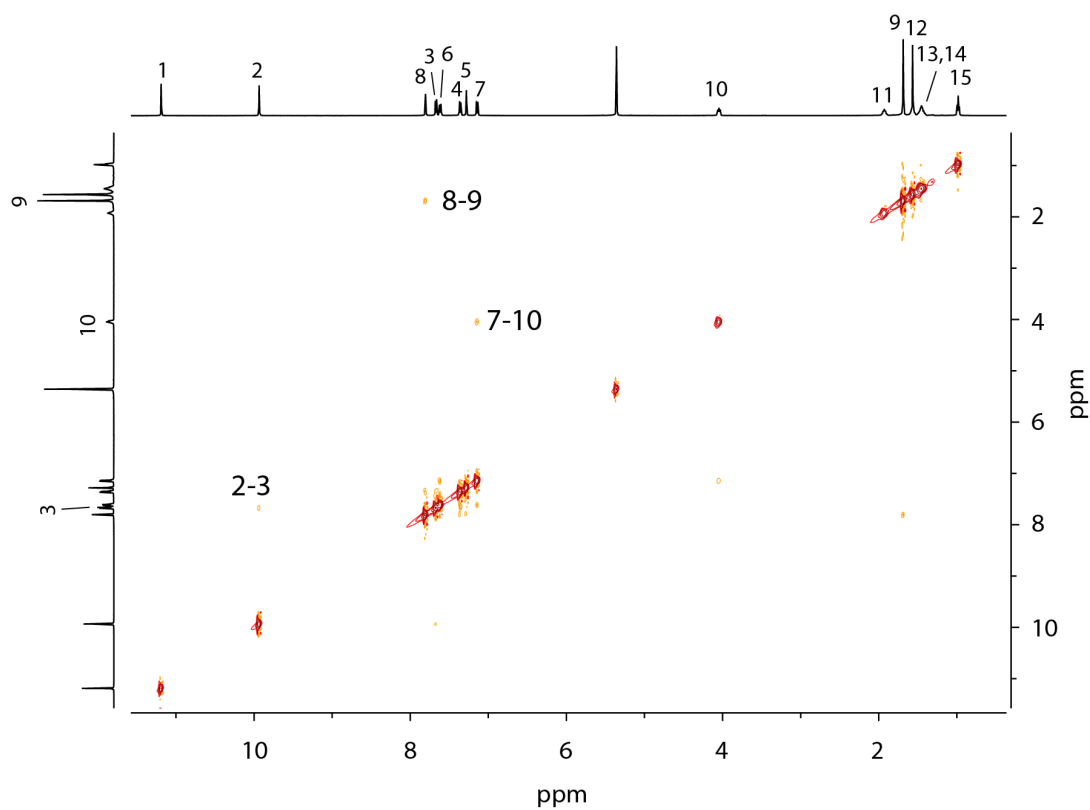
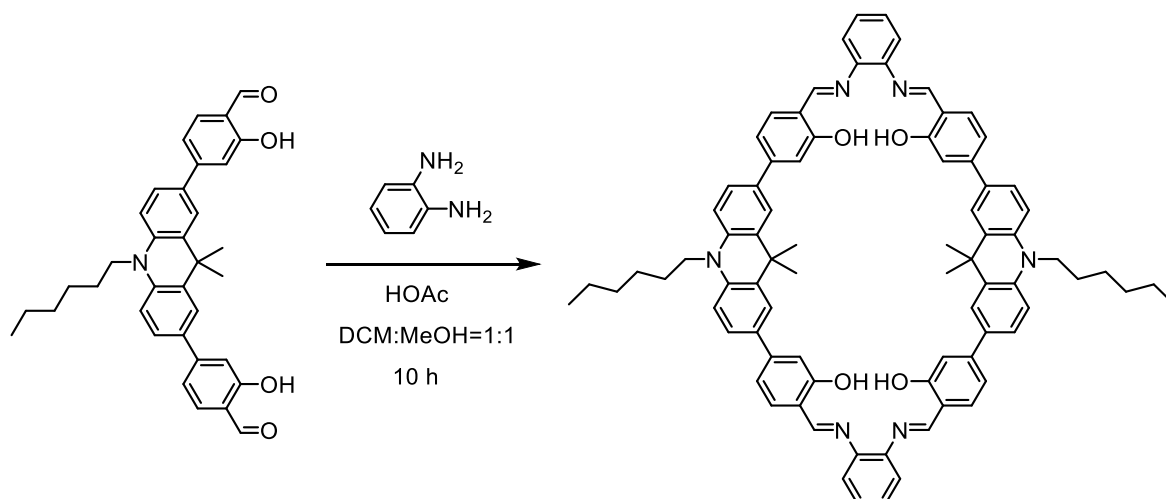


Figure 5.43:  $^1\text{H}$ - $^1\text{H}$  NOESY NMR spectrum of  $\text{L}^{\text{ACR}}$  (500 MHz, 298 K,  $\text{CD}_2\text{Cl}_2$ ).

## 5. Coordination-driven construction of [3]rotaxane based on hierarchical assembly

### 5.8.4 Synthesis of macrocycle R<sup>ACR</sup>



LACR (15 mg, 0.028 mmol, 1 equiv.) was dissolved in 2 mL DCM and MeOH mixture solvents (v:v = 1:1). 1,2-benzenediamine (3.65 mg, 0.033 mmol, 1.2 equiv.) was added. After addition of acetic acid (35  $\mu$ L), the reaction was stirred at room temperature for 10 h. The solvent was removed under reduced procedure. The crude product was washed with anhydrous MeOH (3 $\times$ 1 mL) and dried in vacuum to provide the product as yellow powder in quantitative yield.

<sup>1</sup>H NMR (700 MHz, CDCl<sub>3</sub>):  $\delta$  13.49 (s, 4H), 8.73 (s, 4H), 7.86 (d,  $J$  = 2.2 Hz, 4H), 7.56 (dd,  $J$  = 8.4, 2.1 Hz, 4H), 7.49 (d,  $J$  = 1.7 Hz, 4H), 7.46 (d,  $J$  = 7.9 Hz, 4H), 7.38 – 7.35 (m, 4H), 7.34 (dt,  $J$  = 5.4, 3.7 Hz, 4H), 7.21 (dd,  $J$  = 8.0, 1.7 Hz, 4H), 7.05 (d,  $J$  = 8.4 Hz, 4H), 4.03 – 3.99 (m, 4H), 1.91 (t,  $J$  = 7.9 Hz, 4H), 1.71 (s, 12H), 1.47 – 1.36 (m, 8H), 1.26 (s, 4H), 0.95 (t,  $J$  = 7.2 Hz, 6H).

<sup>13</sup>C NMR (176 MHz, CDCl<sub>3</sub>):  $\delta$  162.54, 162.06, 146.17, 142.92, 140.50, 132.78, 132.70, 132.21, 127.84, 125.37, 124.33, 119.16, 117.90, 117.26, 115.33, 112.94, 46.34, 36.79, 31.75, 29.69, 27.09, 26.08, 22.88, 14.21.

## 5. Coordination-driven construction of [3]rotaxane based on hierarchical assembly

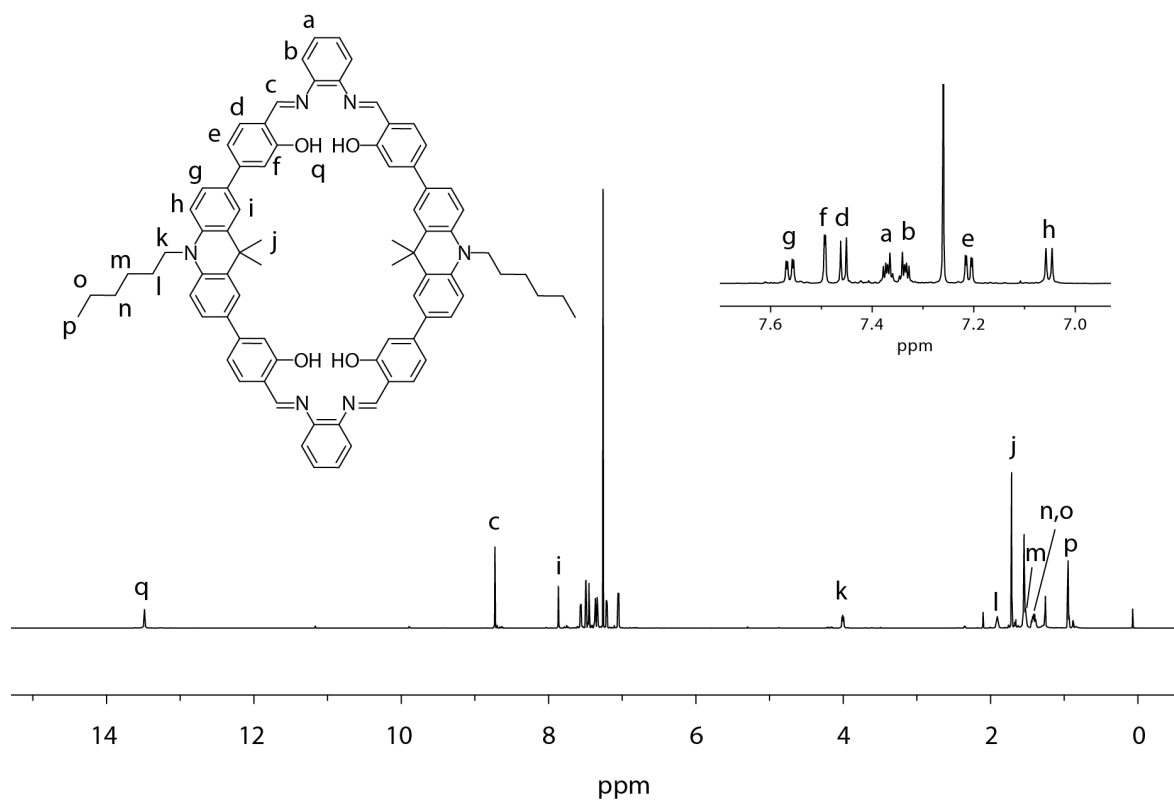


Figure 5.44:  $^1H$  NMR spectrum of  $R^{ACR}$  (700 MHz, 298 K,  $CDCl_3$ ).

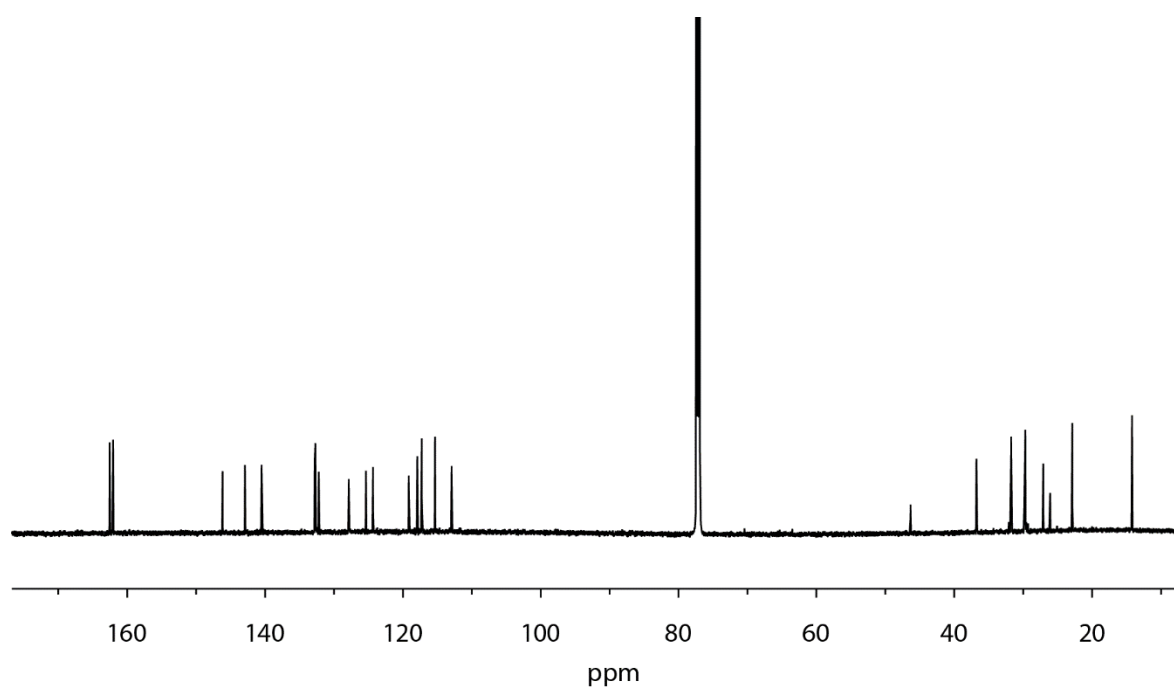


Figure 5.45:  $^{13}C$  NMR spectrum of  $R^{ACR}$  (176 MHz, 298 K,  $CDCl_3$ ).

## 5. Coordination-driven construction of [3]rotaxane based on hierarchical assembly

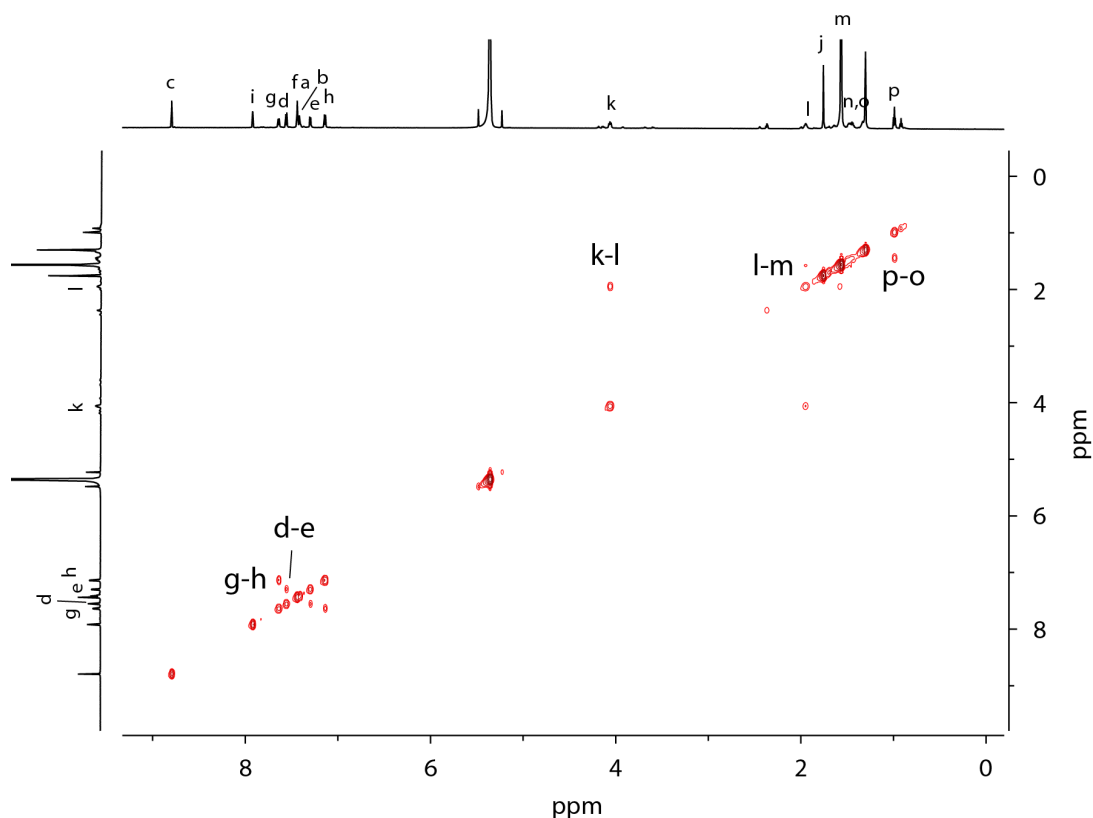


Figure 5.46:  $^1\text{H}$ - $^1\text{H}$  COSY NMR spectrum of  $\text{R}^{\text{ACR}}$  (700 MHz, 298 K,  $\text{CD}_2\text{Cl}_2$ ).

### 5.8.5 Self-assembly of $\text{Co}_2\text{R}^{\text{ACR}}$

$\text{R}^{\text{ACR}}$  (5 mg, 3.44  $\mu\text{mol}$ , 1 equiv.) was dissolved in  $\text{CHCl}_3$  and  $\text{CH}_3\text{CN}$  (2 mL, 1:1) mixture solvents,  $[\text{Co}(\text{OAc})_2]$  (122  $\mu\text{L}$ , 20 mg/mL in DMSO, 2 equiv.) was added. After stirring 15 min,  $\text{NH}_4\text{PF}_6$  (1.35 mg, 2 equiv.) was added. The mixture was stirred at room temperature for 2 h. After reaction, solvents were removed and crude product was dissolved in a minimal amount of DCM and precipitated with  $\text{Et}_2\text{O}$  to give red powder as product (4.2 mg, 77.3% yield).

$^1\text{H}$  NMR (500 MHz,  $\text{CD}_3\text{CN}$ ):  $\delta$  8.69 (s, 4H), 8.27 (d,  $J = 6.0$  Hz, 4H), 8.03 (d,  $J = 2.2$  Hz, 4H), 7.74 – 7.66 (m, 12H), 7.56 (dd,  $J = 6.2, 3.2$  Hz, 4H), 7.25 (d,  $J = 8.5$  Hz, 4H), 7.15 (d,  $J = 8.5$  Hz, 4H), 4.10 (d,  $J = 8.4$  Hz, 4H), 1.90 (s, 4H), 1.72 – 1.66 (m, 4H), 1.56 (s, 4H), 1.41 (d,  $J = 14.6$  Hz, 4H), 0.99 – 0.92 (m, 6H).

HR ESI-MS: calculated for  $[\text{Co}_2\text{C}_{82}\text{H}_{74}\text{N}_6\text{O}_4]^{2+}$ ,  $m/z$  662.2212  $[\text{M}]^{2+}$   
found: 662.2183

## 5. Coordination-driven construction of [3]rotaxane based on hierarchical assembly

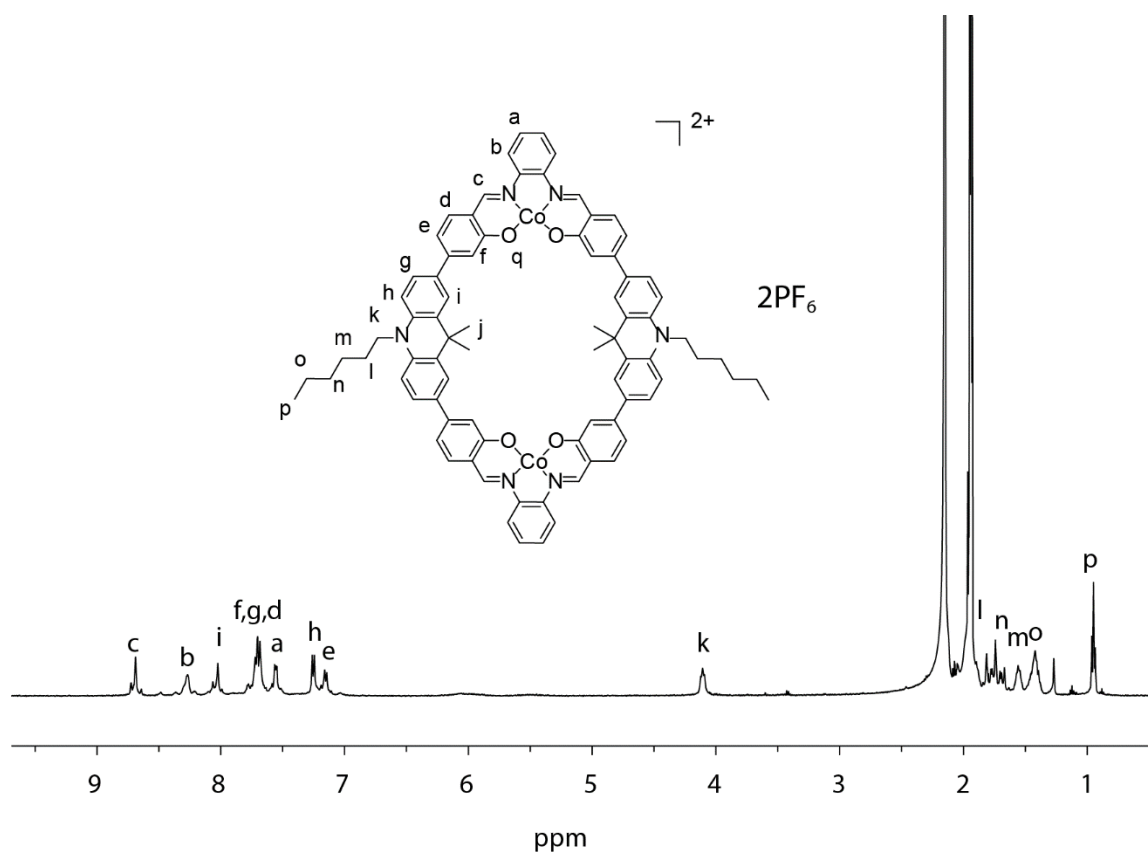


Figure 5.47:  $^1\text{H}$  NMR spectrum of  $\text{Co}_2\text{R}^{\text{ACR}}$  (500 MHz, 298 K,  $\text{CD}_3\text{CN}$ ).

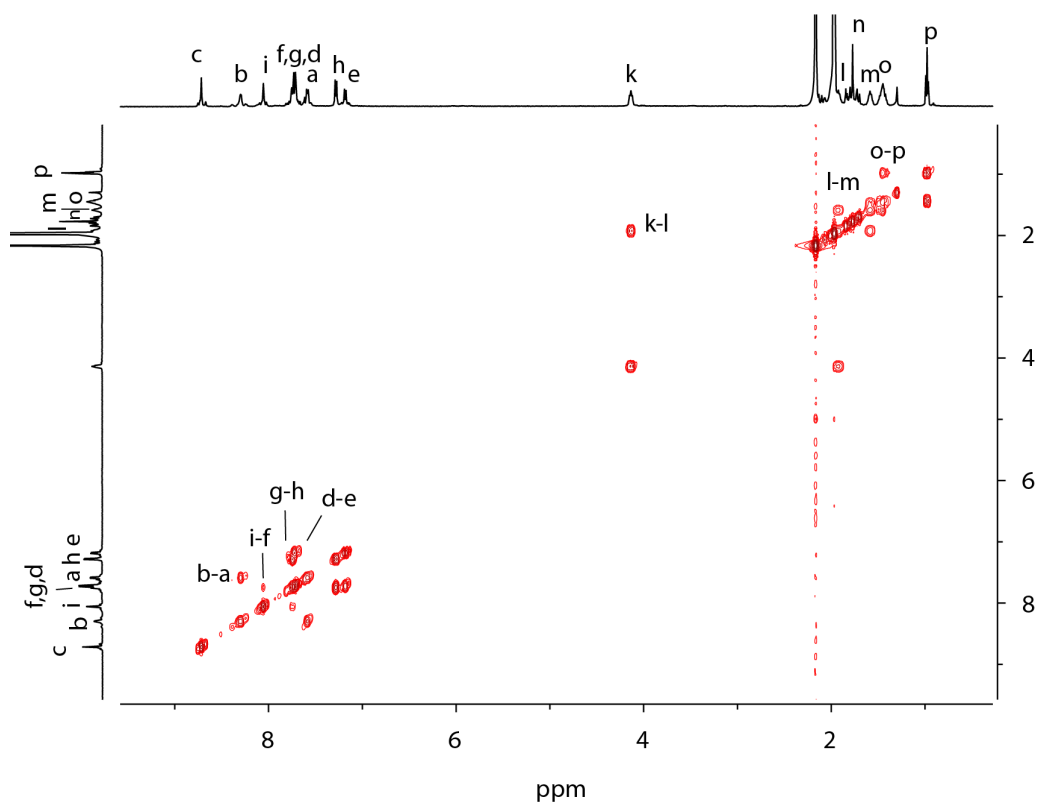


Figure 5.48:  $^1\text{H}$ - $^1\text{H}$  COSY NMR spectrum of  $\text{Co}_2\text{R}^{\text{ACR}}$  (500 MHz, 298 K,  $\text{CD}_3\text{CN}$ ).

## 5. Coordination-driven construction of [3]rotaxane based on hierarchical assembly

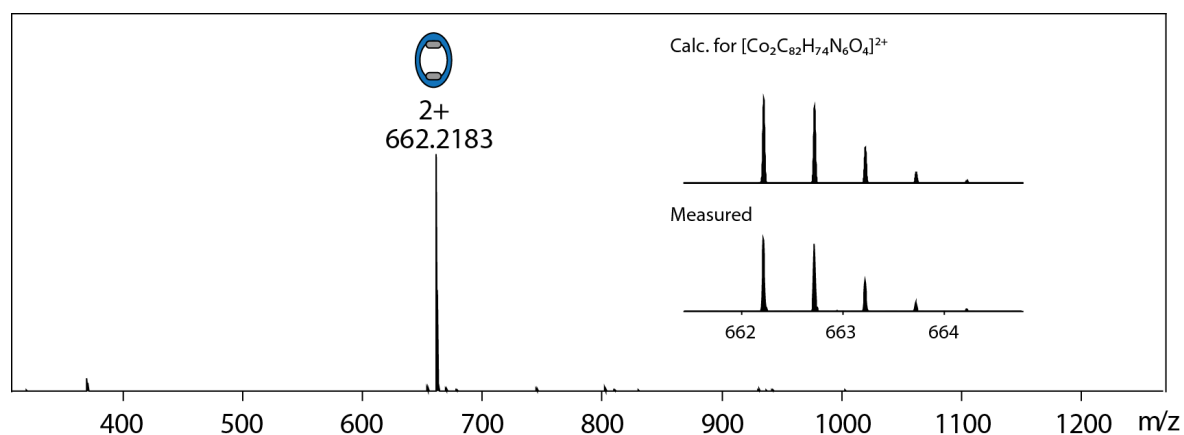


Figure 5.49: ESI-MS of  $\text{Co}_2\text{R}^{\text{ACR}}$ , with insets showing the calculated and measured isotopic patterns of  $[\text{Co}_2\text{R}^{\text{ACR}}]^{2+}$ .

### 5.8.6 Synthesis of $\text{L}^{\text{R}}$

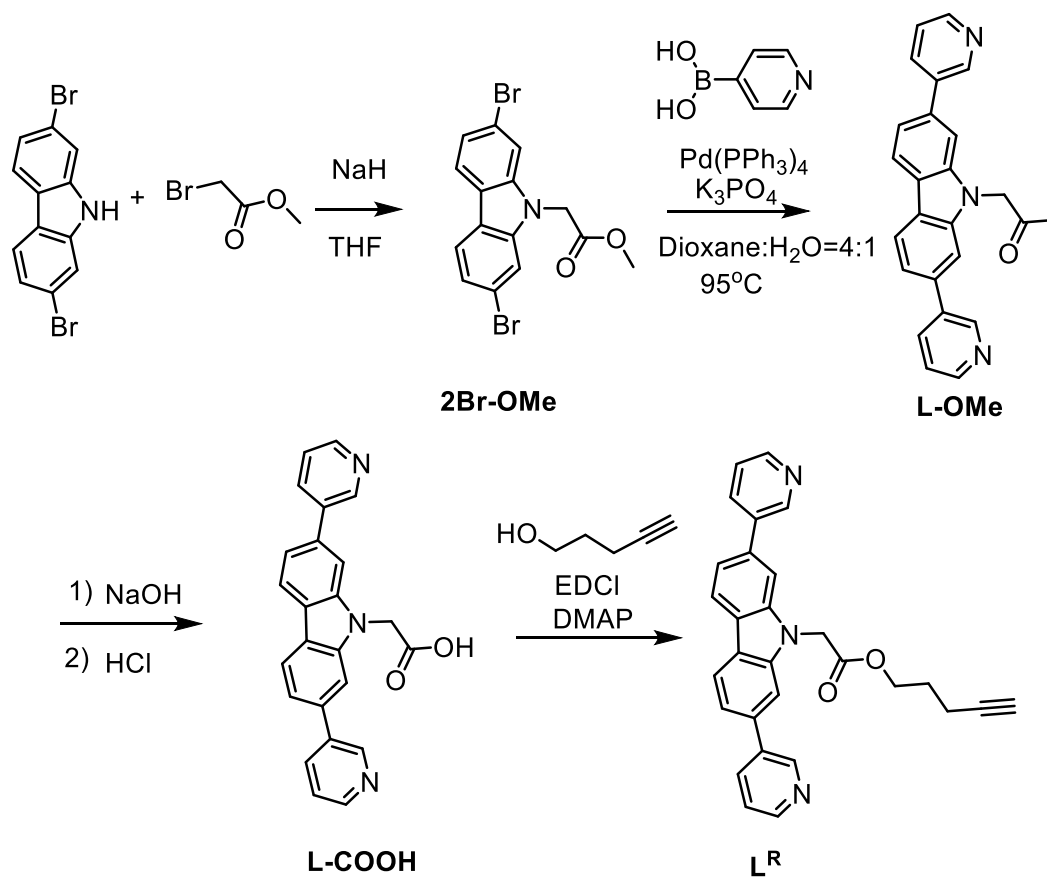


Figure 5.50: Synthesis route of  $\text{L}^{\text{R}}$ .



## 5. Coordination-driven construction of [3]rotaxane based on hierarchical assembly

### Synthesis of **2Br-OMe**

2,7-dibromo-9H-carbazole (1.1 g, 3.38 mmol, 1 equiv.) was dissolved in 10 mL dry THF, then NaH (162 mg, 6.77 mmol, 2 equiv. 60% dispersion in mineral oil) was added to the solution slowly in ice bath and stirred at 0° for 1 h. Then methyl 2-bromoacetate (1.04 g, 6.77 mmol, 2 equiv.) was added. The mixture was stirred at 55° overnight. The reaction was quenched with saturated NH<sub>4</sub>Cl (aqueous), and extracted with CH<sub>2</sub>Cl<sub>2</sub>. The organic phase was dried over MgSO<sub>4</sub>, filtered and the solvent removed in vacuo. The residue was purified by column chromatography (CH<sub>2</sub>Cl<sub>2</sub>: pentane=1:4) to afford white solid (1.25 g, 93.0% yield.)

<sup>1</sup>H NMR (500 MHz, CDCl<sub>3</sub>): δ 7.90 (d, *J* = 8.3 Hz, 2H), 7.47 (d, *J* = 1.6 Hz, 2H), 7.39 (dd, *J* = 8.3, 1.6 Hz, 2H), 4.93 (s, 2H), 3.78 (s, 3H).

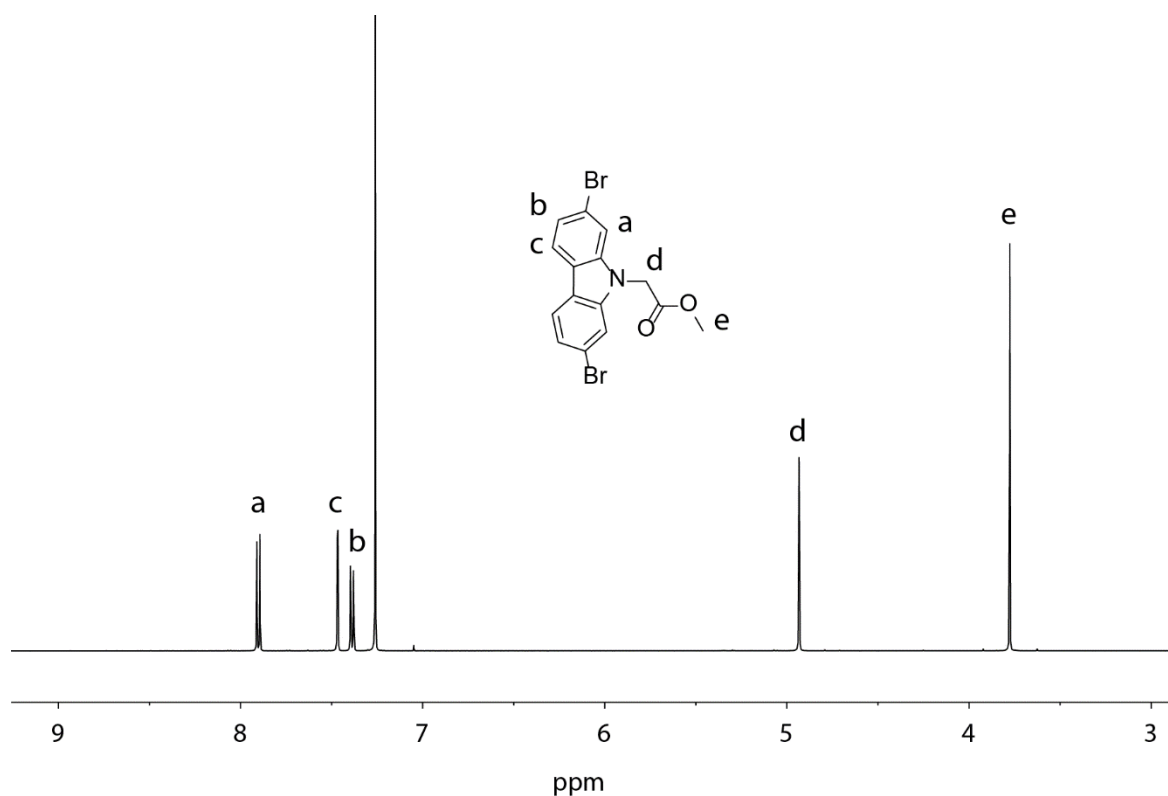


Figure 5.51: <sup>1</sup>H NMR of **2Br-OMe** (500 MHz, 298 K, CDCl<sub>3</sub>).

## 5. Coordination-driven construction of [3]rotaxane based on hierarchical assembly

### Synthesis of **L-OMe**

**2Br-OMe** (600 mg, 1.51 mmol, 1 equiv.), 4-pyridineboronic acid (557 mg, 4.53 mmol, 3 equiv.), Pd(PPh<sub>3</sub>)<sub>4</sub> (105 mg, 0.091 mmol, 6 mol%), and K<sub>3</sub>PO<sub>4</sub> (1.15 g, 5.44 mmol, 3.6 equiv.) was combined in a 100 mL Schenk flask and cycled three times under vacuum and refilled with argon. 20 mL degassed of 1,4-dioxane and water (v:v=4:1) were added. The reaction mixture was stirred at 95 °C for 48 h. After cooling down to room temperature, the solvents were evaporated and a little amount of DCM was added then filtered. The solid was washed by water and dried under vacuum (385 mg, 67.5% yield).

<sup>1</sup>H NMR (600 MHz, CD<sub>3</sub>CN): δ 9.00 (dd, *J* = 2.5, 0.9 Hz, 2H), 8.28 (dd, *J* = 8.1, 0.6 Hz, 2H), 8.13 (ddd, *J* = 7.9, 2.4, 1.6 Hz, 2H), 7.83 – 7.74 (m, 2H), 7.60 (dd, *J* = 8.0, 1.5 Hz, 2H), 7.47 (ddd, *J* = 7.9, 4.8, 0.9 Hz, 2H), 5.30 (s, 1H), 3.73 (s, 3H).

<sup>13</sup>C NMR (151 MHz, CD<sub>3</sub>CN) δ 170.12, 149.45, 142.93, 137.82, 137.08, 135.55, 124.70, 123.35, 122.19, 120.20, 108.78, 53.06, 45.06.

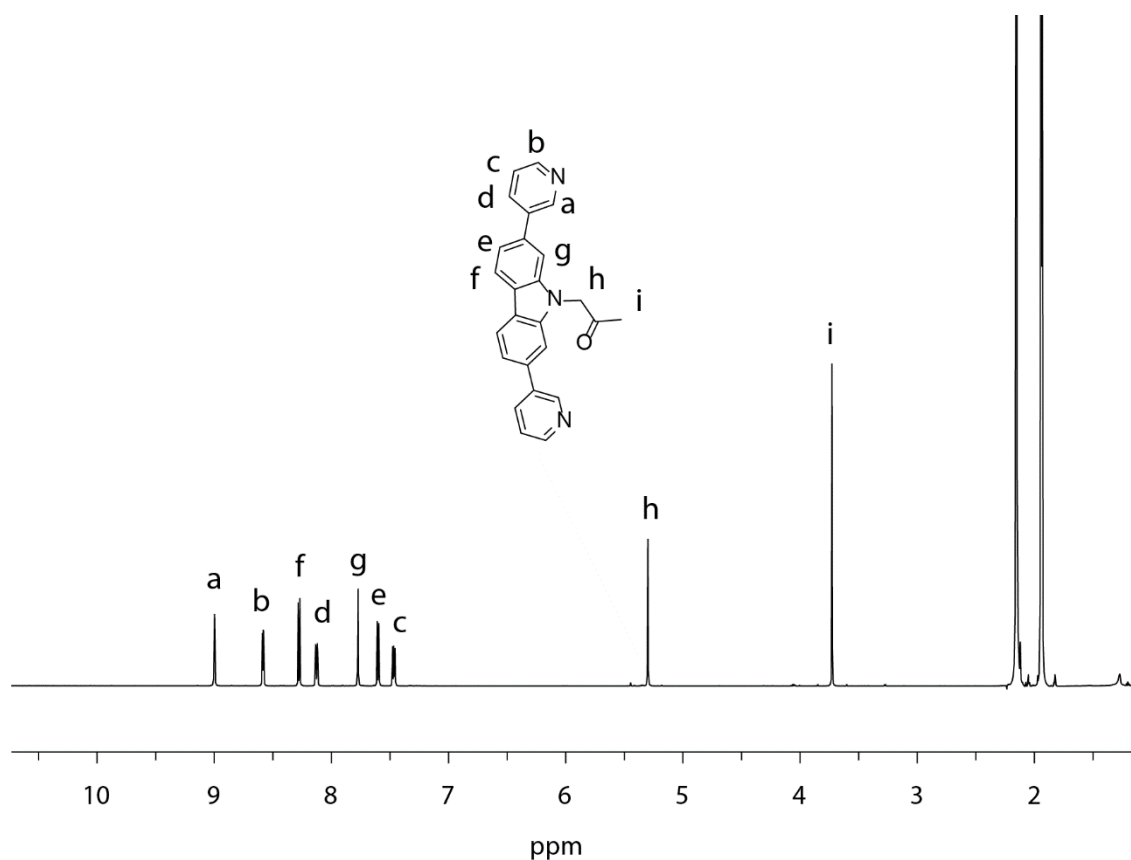


Figure 5.52: <sup>1</sup>H NMR of **L-OMe** (500 MHz, 298 K, CD<sub>3</sub>CN).

## 5. Coordination-driven construction of [3]rotaxane based on hierarchical assembly

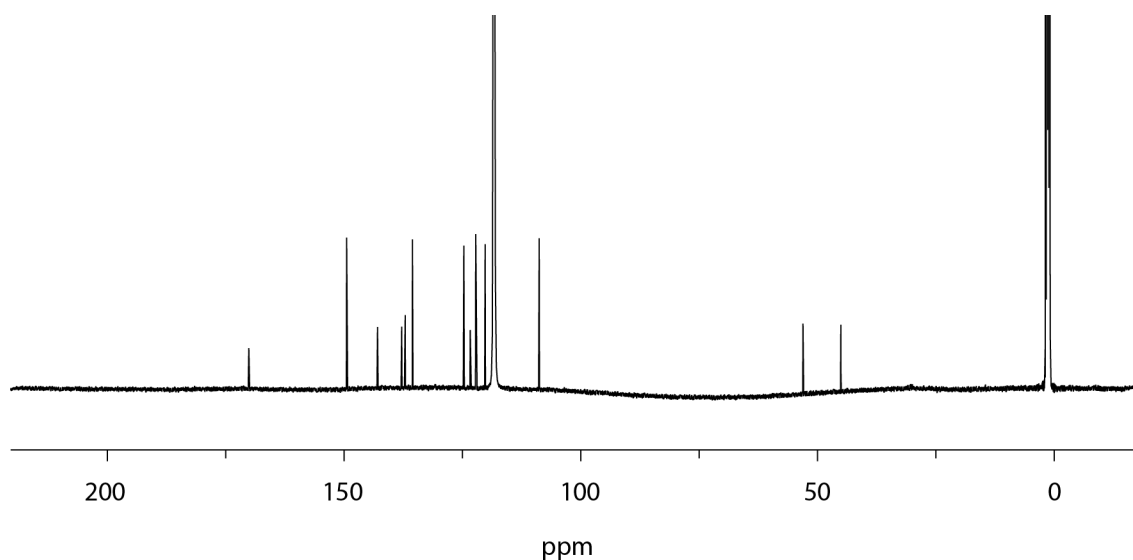


Figure 5.53:  $^{13}\text{C}$  NMR of **L-OMe** (500 MHz, 298 K,  $\text{CD}_3\text{CN}$ ).

### Synthesis of **L-COOH**

**L-OMe** (200 mg, 0.53 mmol, 1 equiv.) was dissolved in a mixture solvents of MeOH and DCM, NaOH (43 mg, 1.1 mmol, 2 equiv.) was added. The mixture was stirred at room temperature overnight. Then 2 M HCl aq was added dropwise and a yellow precipitate formed. The precipitate was collected by filtration and washed by water to give as product.

$^1\text{H}$  NMR (500 MHz,  $\text{DMSO}-d_6$ ):  $\delta$  13.06 (s, 1H), 9.07 (d,  $J = 2.4$  Hz, 2H), 8.60 (dd,  $J = 4.8, 1.6$  Hz, 2H), 8.32 (d,  $J = 8.1$  Hz, 2H), 8.24 (dt,  $J = 7.9, 2.0$  Hz, 2H), 8.02 (d,  $J = 1.5$  Hz, 2H), 7.63 (dd,  $J = 8.1, 1.5$  Hz, 2H), 7.54 (dd,  $J = 8.0, 4.7$  Hz, 2H), 5.42 (s, 2H).

$^{13}\text{C}$  NMR (151 MHz,  $\text{DMSO}-d_6$ ):  $\delta$  169.48, 148.39, 148.14, 141.84, 136.36, 135.19, 134.59, 124.04, 122.01, 121.34, 118.76, 108.03, 52.31.

## 5. Coordination-driven construction of [3]rotaxane based on hierarchical assembly

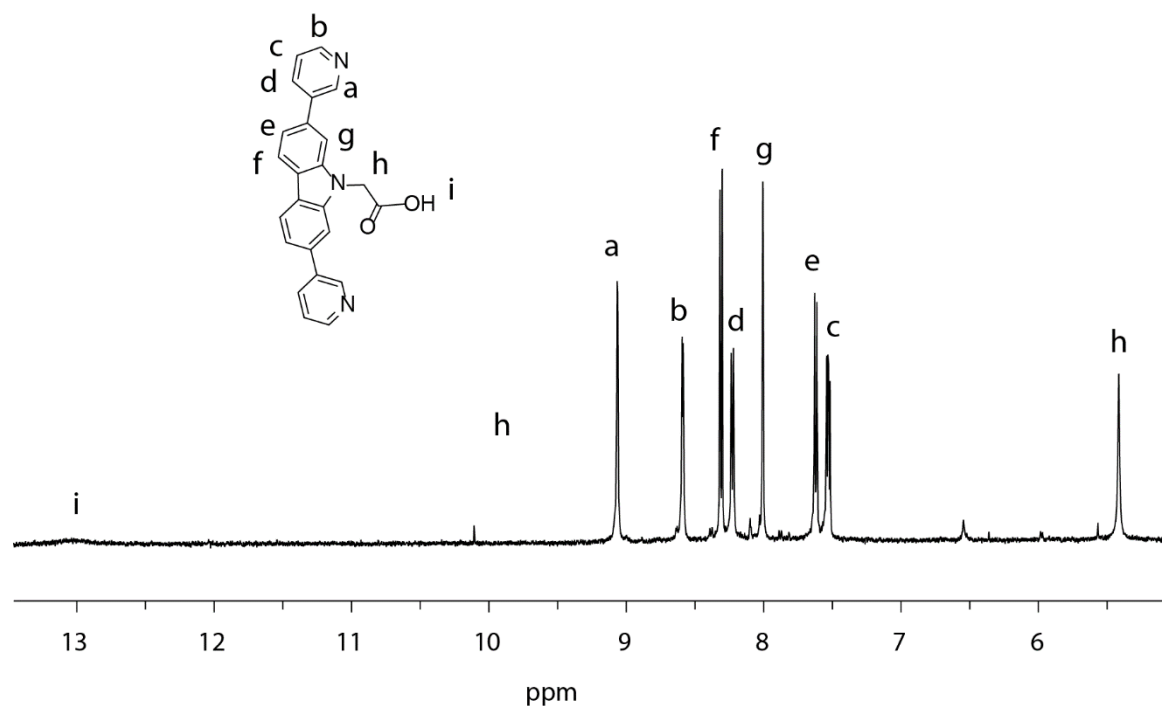


Figure 5.54:  $^1\text{H}$  NMR of **L-COOH** (500 MHz, 298 K,  $\text{DMSO-}d_6$ ).

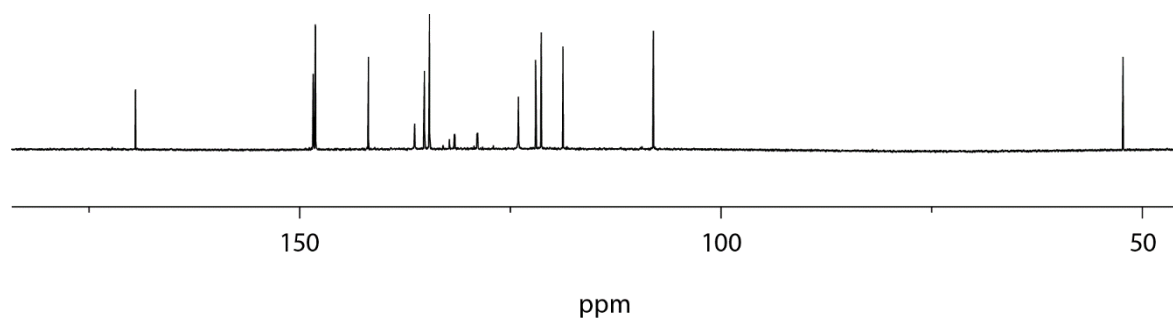


Figure 5.55:  $^{13}\text{C}$  NMR of **L-COOH** (151 MHz, 298 K,  $\text{DMSO-}d_6$ ).

### Synthesis of **L<sup>R</sup>**

**L-COOH** (50 mg, 0.13 mmol, 1 equiv.), 4-pentyn-1-ol (13.3 mg, 0.16 mmol, 1.2 equiv.), EDCI (75 mg), DMAP (16 mg) were combined in a 10 mL round flask. 2 mL anhydrous DCM was added. The reaction mixture was stirred at room temperature for 2 days. The product was purified by column chromatography (DCM: EtOAc =1:5) to afford the product (16 mg, 27% yield).

$^1\text{H}$  NMR (500 MHz,  $\text{DMSO-}d_6$ ):  $\delta$  9.06 (dd,  $J = 2.4, 0.9$  Hz, 2H), 8.59 (dd,  $J = 4.7, 1.6$  Hz, 2H), 8.32 (d,  $J = 8.2$  Hz, 2H), 8.25 – 8.18 (m, 2H), 8.02 (d,  $J = 1.5$  Hz, 2H), 7.63

## 5. Coordination-driven construction of [3]rotaxane based on hierarchical assembly

(dd,  $J = 8.2, 1.5$  Hz, 2H), 7.53 (ddd,  $J = 7.9, 4.7, 0.9$  Hz, 2H), 5.57 (s, 2H), 4.17 (t,  $J = 6.3$  Hz, 2H), 2.76 (t,  $J = 2.7$  Hz, 1H), 2.17 (td,  $J = 7.1, 2.7$  Hz, 2H), 1.74 (t,  $J = 6.7$  Hz, 2H).

$^{13}\text{C}$  NMR (151 MHz,  $\text{DMSO-}d_6$ )  $\delta$  169.08, 148.45, 148.16, 141.95, 136.47, 135.30, 134.73, 124.16, 122.11, 121.45, 118.89, 108.08, 83.62, 71.73, 63.76, 62.32, 27.32, 25.60.

HR ESI-MS: calculated for  $[\text{C}_{29}\text{H}_{23}\text{N}_3\text{O}_2]^+$   $m/z$  446.1863  $[\text{M} + \text{H}]^+$

found: 446.1830

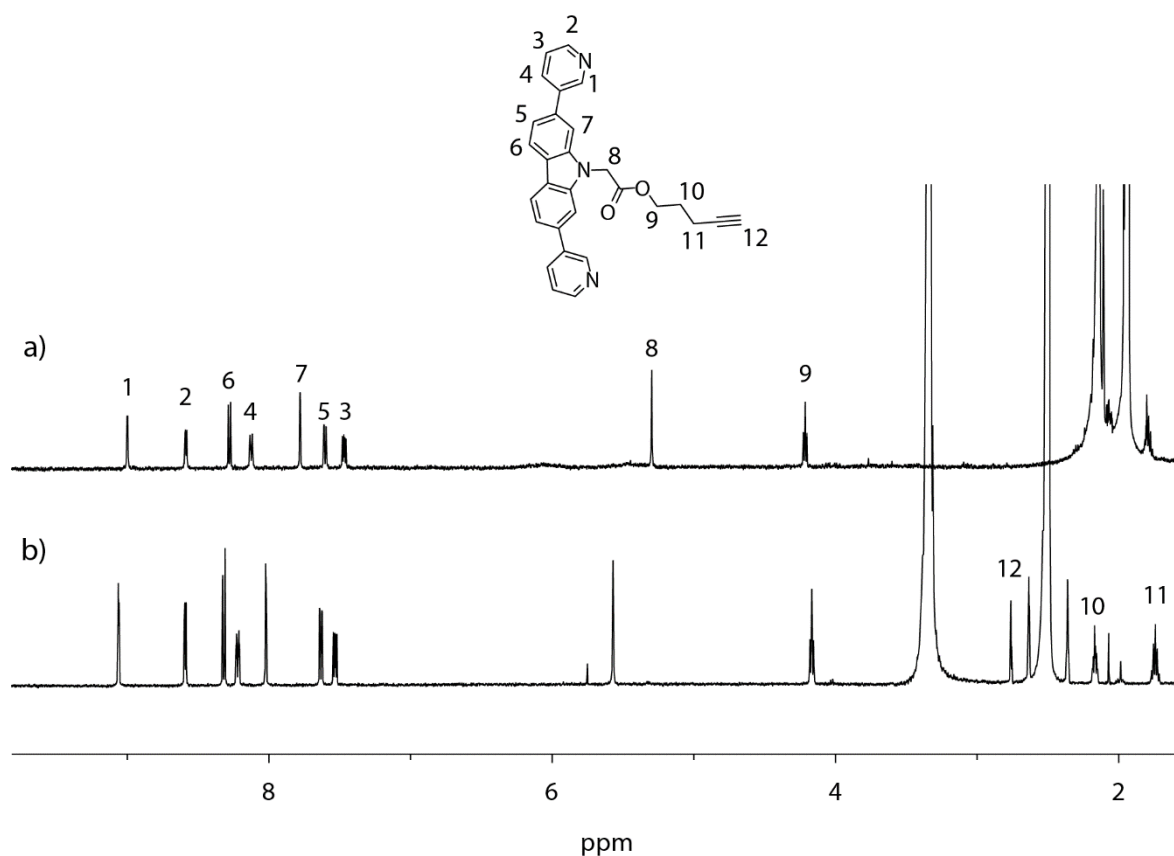


Figure 5.56:  $^1\text{H}$  NMR of  $\text{L}^{\text{R}}$  in a)  $\text{CD}_3\text{CN}$ , and b)  $\text{DMSO-}d_6$  (500 MHz, 298 K).

## 5. Coordination-driven construction of [3]rotaxane based on hierarchical assembly

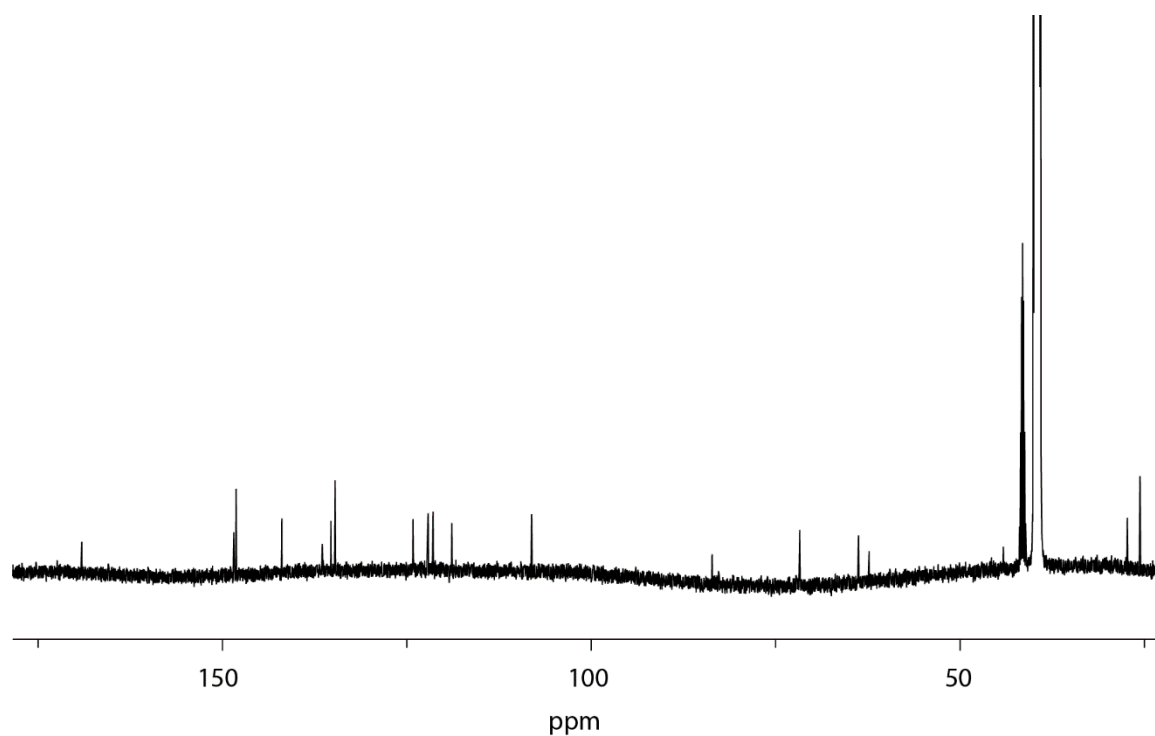


Figure 5.57:  $^{13}\text{C}$  NMR spectrum of  $\text{L}^{\text{R}}$  (151 MHz, 298 K,  $\text{DMSO-}d_6$ ).

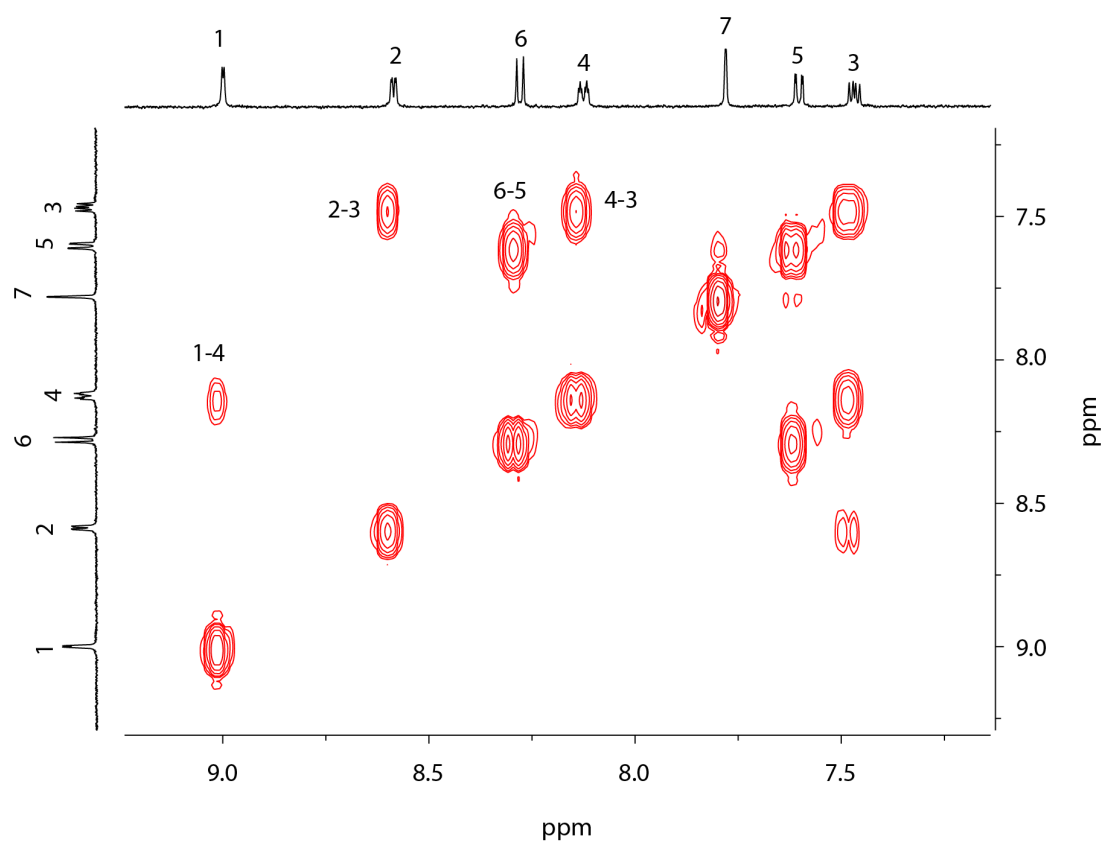


Figure 5.58:  $^1\text{H}$ - $^1\text{H}$  COSY NMR spectrum of  $\text{L}^{\text{R}}$  (600 MHz, 298 K,  $\text{CD}_3\text{CN}$ ).

## 5. Coordination-driven construction of [3]rotaxane based on hierarchical assembly

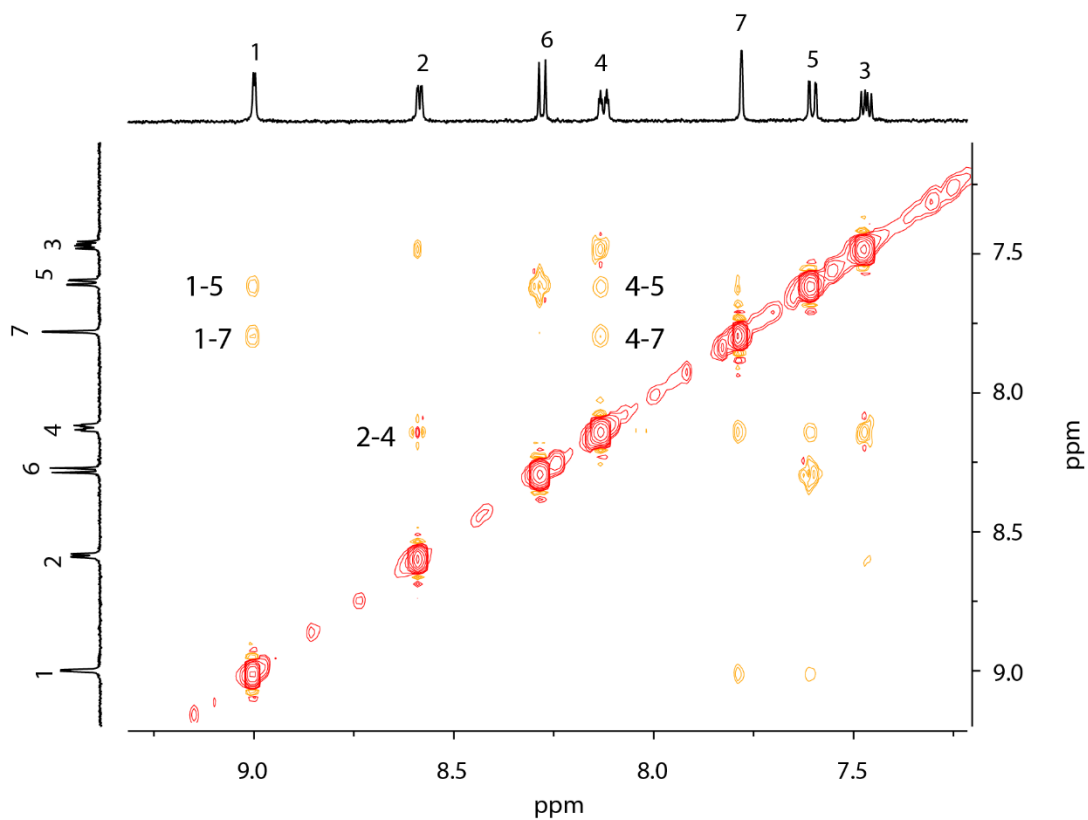
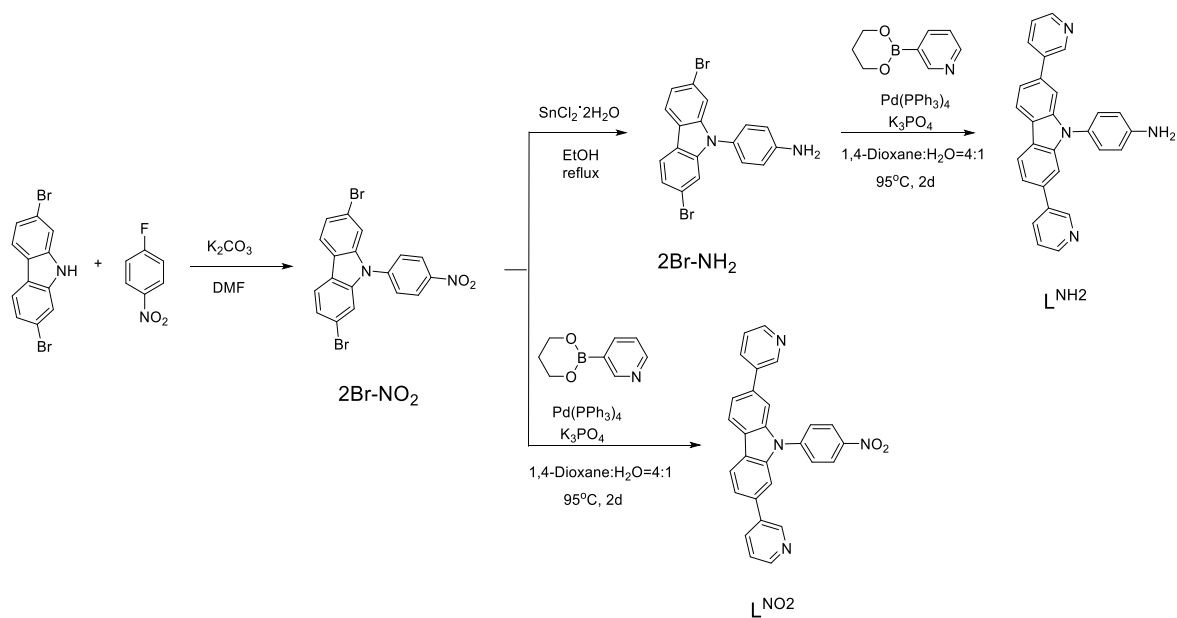


Figure 5.59:  $^1\text{H}$ - $^1\text{H}$  NOESY NMR spectrum of  $\text{L}^{\text{R}}$  (600 MHz, 298 K,  $\text{CD}_3\text{CN}$ ).

### 5.8.7 Synthesis of $\text{L}^{\text{NO}_2}$ and $\text{L}^{\text{NH}_2}$



## 5. Coordination-driven construction of [3]rotaxane based on hierarchical assembly

### Synthesis of 2,7- dibromo-9-(4-nitrophenyl)-9H-carbazol (**2Br-NO<sub>2</sub>**)<sup>[25]</sup>

2,7-dibromocabazole (1g, 3.08 mmol, 1 equiv.), 4-fluoronitrobenzene (1.3 g, 9.23 mmol, 3 equiv.) and K<sub>2</sub>CO<sub>3</sub> (2.13 g, 15.38 mmol, 5 equiv.) were combined in a 100 mL Schlenk tube. 10 mL DMF was added. The reaction mixture was stirred at 150 °C overnight. After cooling to room temperature, the solution was poured into 50 mL H<sub>2</sub>O. The yellow solid was washed by water and collected by filtration (1.31 g, 95.4% yield).

<sup>1</sup>H NMR (500 MHz, DMSO-*d*<sub>6</sub>): δ 8.52 (d, *J* = 9.0 Hz, 2H), 8.28 (d, *J* = 8.3 Hz, 2H), 8.00 (d, *J* = 9.0 Hz, 2H), 7.64 (d, *J* = 1.6 Hz, 2H), 7.54 (dd, *J* = 8.4, 1.7 Hz, 2H).

<sup>13</sup>C NMR (126 MHz, DMSO-*d*<sub>6</sub>): δ 146.30, 141.56, 140.61, 127.70, 126.35, 125.86, 122.73, 121.90, 119.76, 112.80.

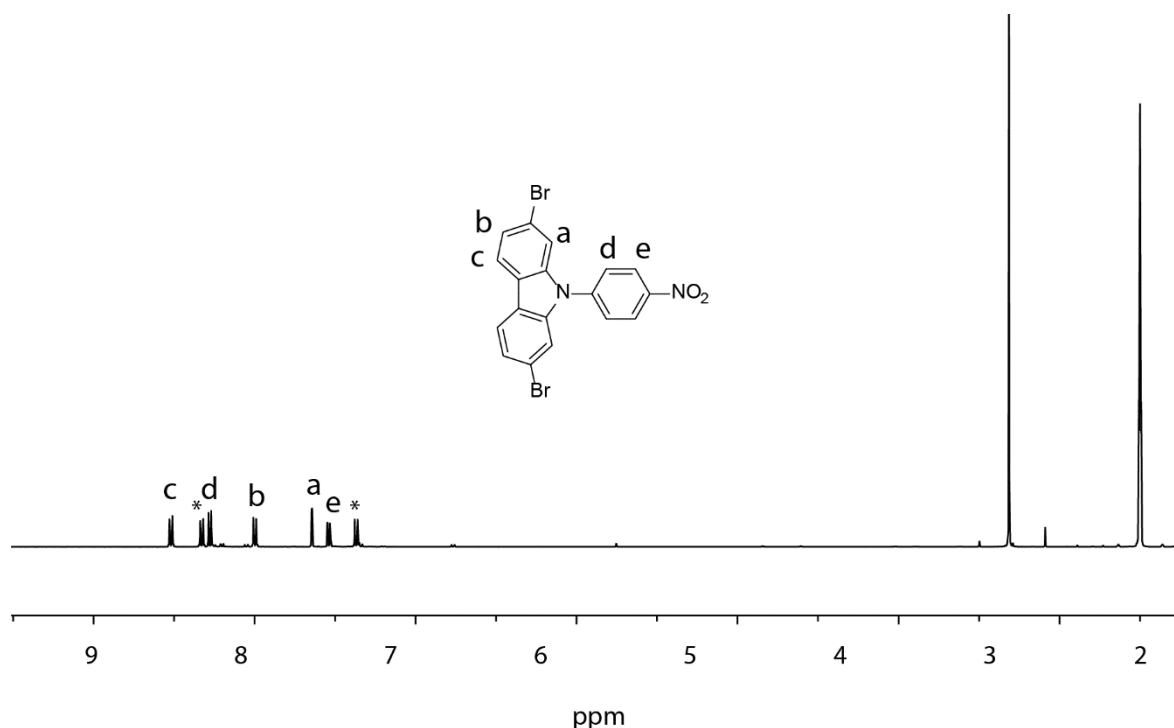


Figure 5.60: <sup>1</sup>H NMR spectrum of **2Br-NO<sub>2</sub>** (500 MHz, 298 K, DMSO-*d*<sub>6</sub>).



## 5. Coordination-driven construction of [3]rotaxane based on hierarchical assembly

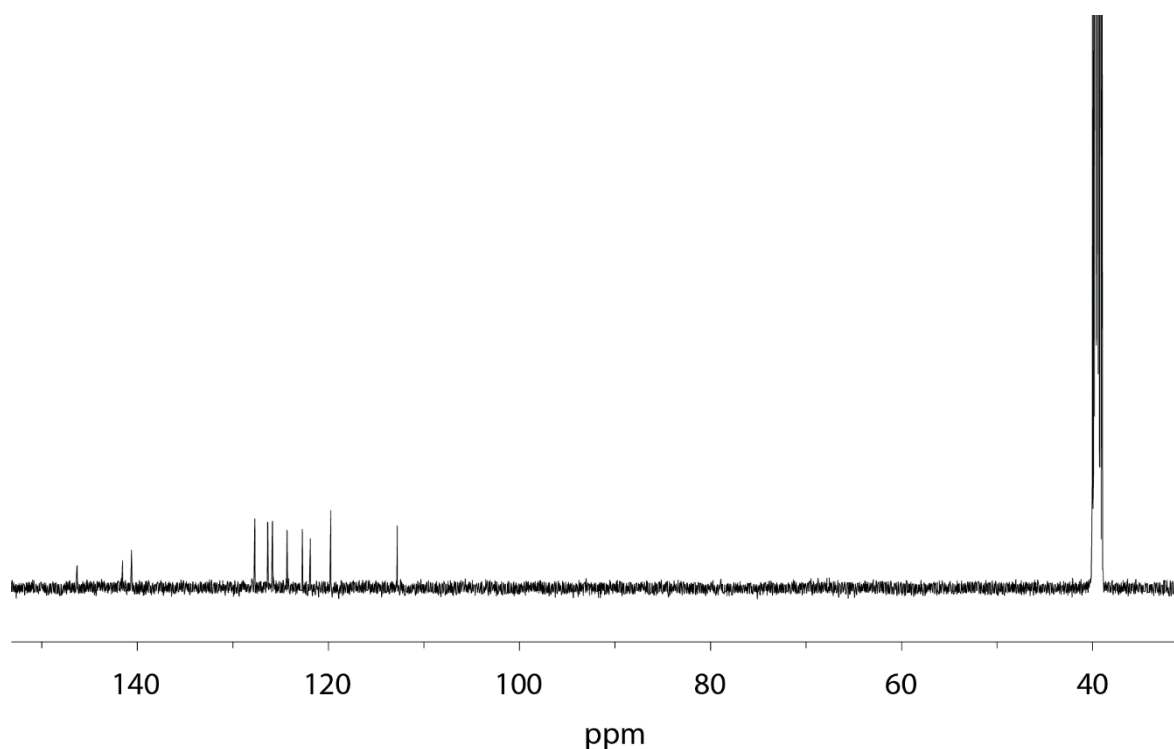


Figure 5.61: <sup>13</sup>C NMR spectrum of **2Br-NO<sub>2</sub>** (126 MHz, 298 K, DMSO-*d*<sub>6</sub>).

Synthesis of 4-(2,7-dibromo-9H-carbazol-9-yl)phenylamine (**2Br-NH<sub>2</sub>**)<sup>[25]</sup>

**2Br-NO<sub>2</sub>** (410 mg, 0.92 mmol, 1 equiv.), SnCl<sub>2</sub> • 2H<sub>2</sub>O (1.04g, 4.6 mmol, 5 equiv.) were combined in a 250 mL flask. 10 mL ethanol was added. The reaction mixture was stirred at 80 °C overnight and then cooled to room temperature. Most of ethanol was removed in vacuum. Saturated NaOH (aq.) was poured into the solution slowly at 0 °C. The product was washed by water and collected by filtration (350 mg, 91.5% yield).

<sup>1</sup>H NMR (500 MHz, DMSO-*d*<sub>6</sub>): δ 8.21 (d, *J* = 8.3 Hz, 2H), 7.42 (dd, *J* = 8.3, 1.7 Hz, 2H), 7.31 (d, *J* = 1.7 Hz, 2H), 7.19 (d, *J* = 8.6 Hz, 2H), 6.80 (d, *J* = 8.6 Hz, 2H), 5.54 (s, 2H).

<sup>13</sup>C NMR (126 MHz, DMSO-*d*<sub>6</sub>): δ 148.14, 142.17, 128.71, 127.84, 122.81, 122.51, 120.83, 119.22, 114.68, 112.36.

## 5. Coordination-driven construction of [3]rotaxane based on hierarchical assembly

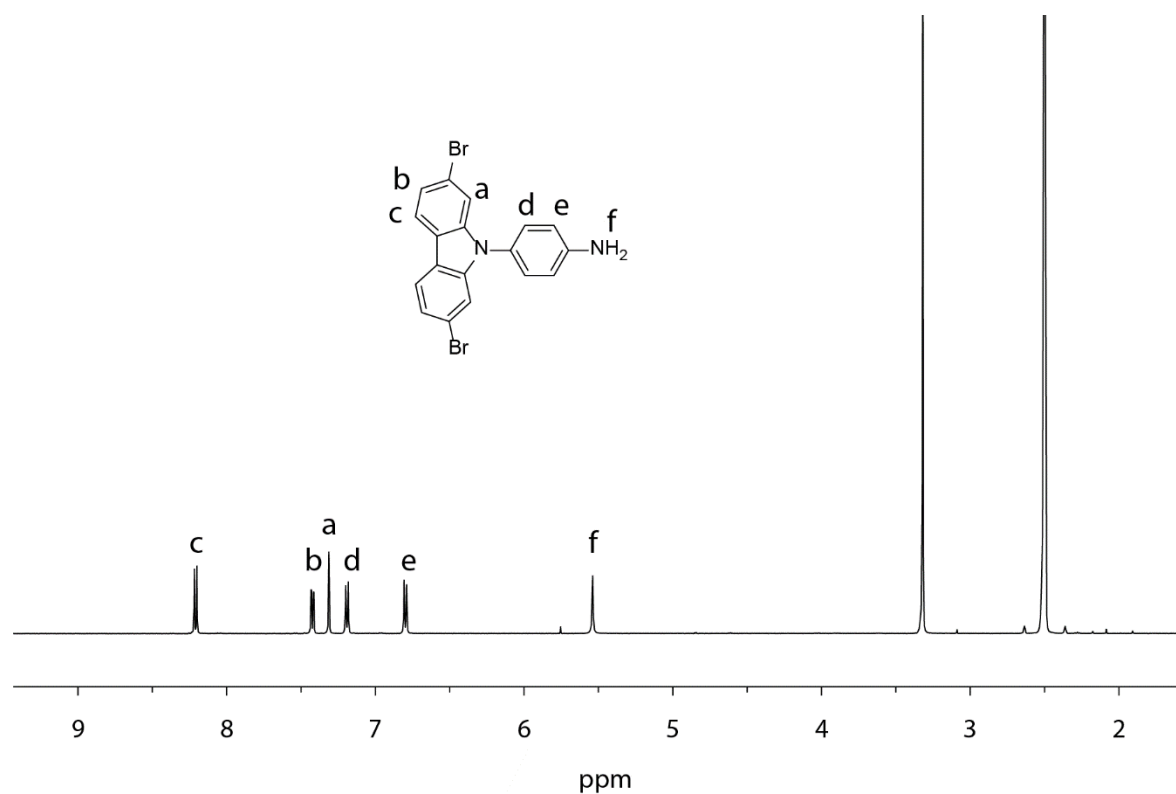


Figure 5.62:  $^1\text{H}$  NMR spectrum of **2Br-NH<sub>2</sub>** (500 MHz, 298 K, DMSO-*d*<sub>6</sub>).

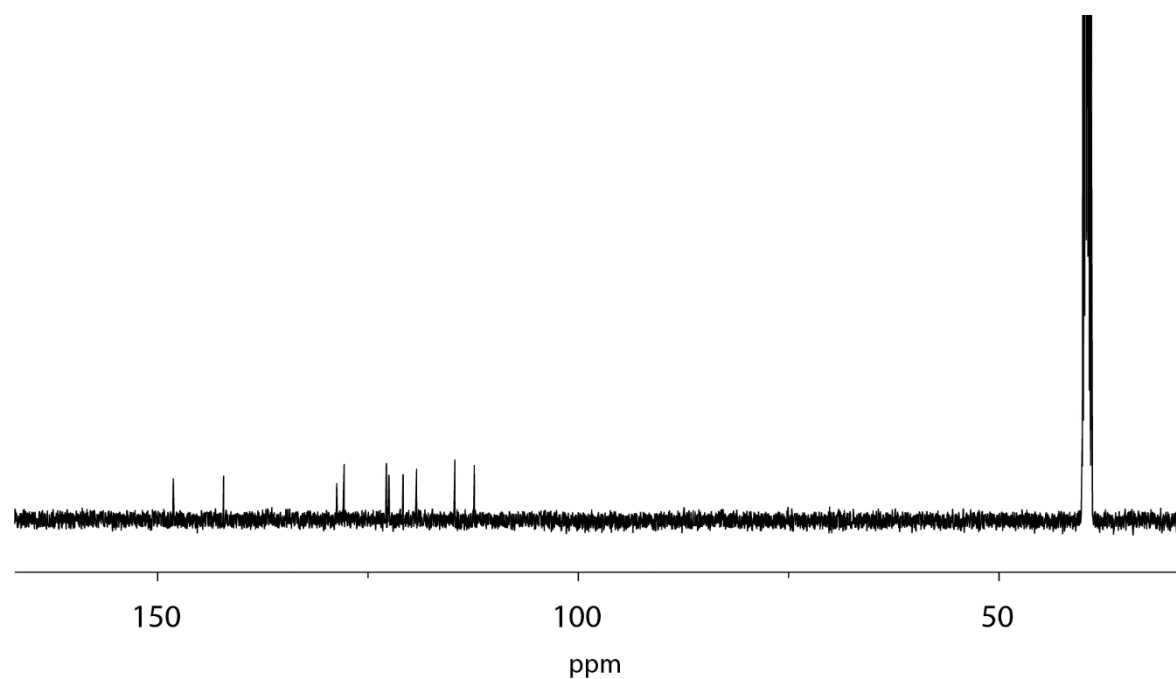


Figure 5.63:  $^{13}\text{C}$  NMR spectrum of **2Br-NH<sub>2</sub>** (126 MHz, 298 K, DMSO-*d*<sub>6</sub>).

## 5. Coordination-driven construction of [3]rotaxane based on hierarchical assembly

### Synthesis of **L-NO<sub>2</sub>**

**2Br-NO<sub>2</sub>** (150 mg, 0.34 mmol, 1 equiv.), 3-(1,3,2-dioxaborinan-2-yl)pyridine (164 mg, 1.01 mmol, 3 equiv.), Pd(PPh<sub>3</sub>)<sub>4</sub> (23 mg, 0.02 mmol, 0.06 mol%) and K<sub>3</sub>PO<sub>4</sub> (257 mg, 1.21 mmol, 3.6 equiv.) were combined in a 100 mL Schlenk tube and cycled three times under vacuum and argon. 20 mL degassed mixture solvents of 1,4-dioxane and water (v:v=4:1) were added. The reaction was stirred at 95 °C for 48 h. After cooling down to room temperature, the solvents were evaporated. 5 mL CH<sub>2</sub>Cl<sub>2</sub> was added and the yellow solid was collected by filtration and washed by water. The product was dried under vacuum to give a red powder in 59.2% yield (88 mg).

<sup>1</sup>H NMR (500 MHz, DMSO-*d*<sub>6</sub>): δ 9.00 (d, *J* = 2.4 Hz, 2H), 8.59 (dd, *J* = 4.8, 1.6 Hz, 2H), 8.53 (d, *J* = 9.0 Hz, 2H), 8.47 (d, *J* = 8.1 Hz, 2H), 8.22 – 8.16 (m, 2H), 8.16 (d, *J* = 8.9 Hz, 2H), 7.84 (d, *J* = 1.4 Hz, 2H), 7.75 (dd, *J* = 8.1, 1.5 Hz, 2H), 7.51 (ddd, *J* = 8.0, 4.8, 0.8 Hz, 2H).

<sup>13</sup>C NMR (151 MHz, DMSO-*d*<sub>6</sub>): δ 148.44, 148.07, 145.71, 142.51, 140.55, 136.05, 134.67, 127.48, 125.81, 123.88, 122.90, 121.73, 120.58, 108.42.

HR ESI-MS: calculated for [C<sub>28</sub>H<sub>18</sub>N<sub>4</sub>O<sub>2</sub>]<sup>+</sup> *m/z* 443.1503 [M + H]<sup>+</sup>  
found: 443.1493

## 5. Coordination-driven construction of [3]rotaxane based on hierarchical assembly

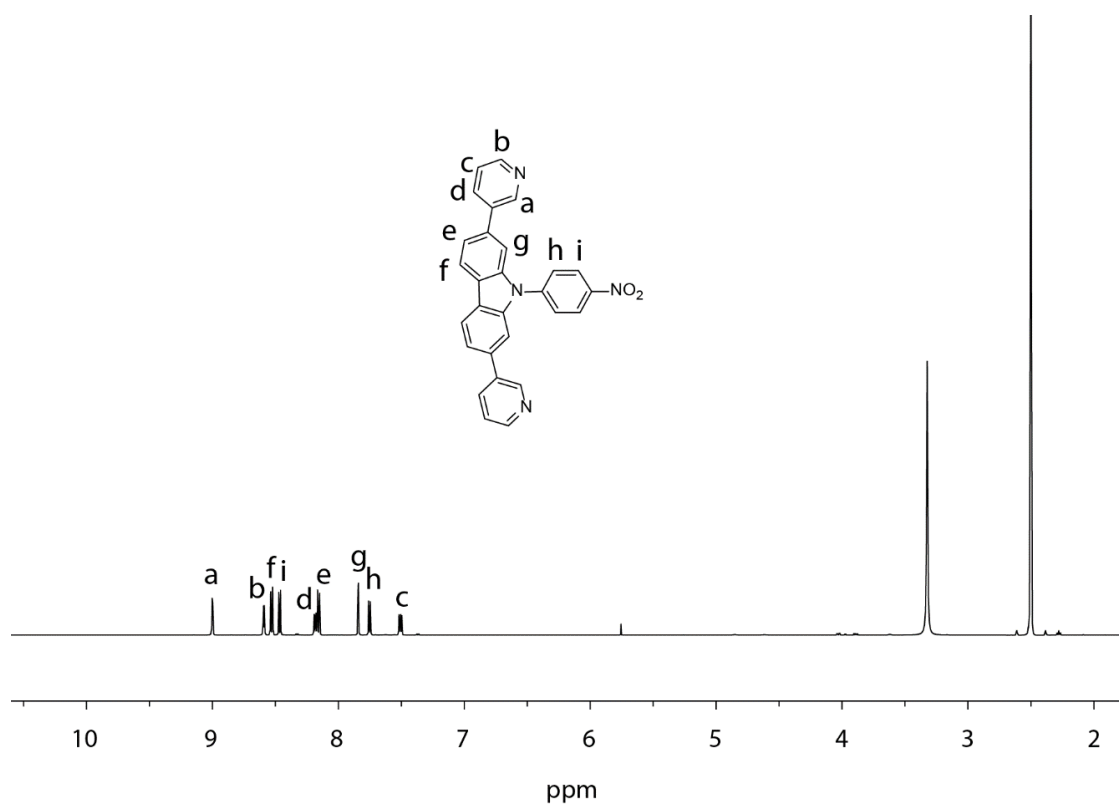


Figure 5.64:  $^1\text{H}$  NMR spectrum of  $\text{L}^{\text{NO}_2}$  (500 MHz, 298 K,  $\text{DMSO-}d_6$ ).

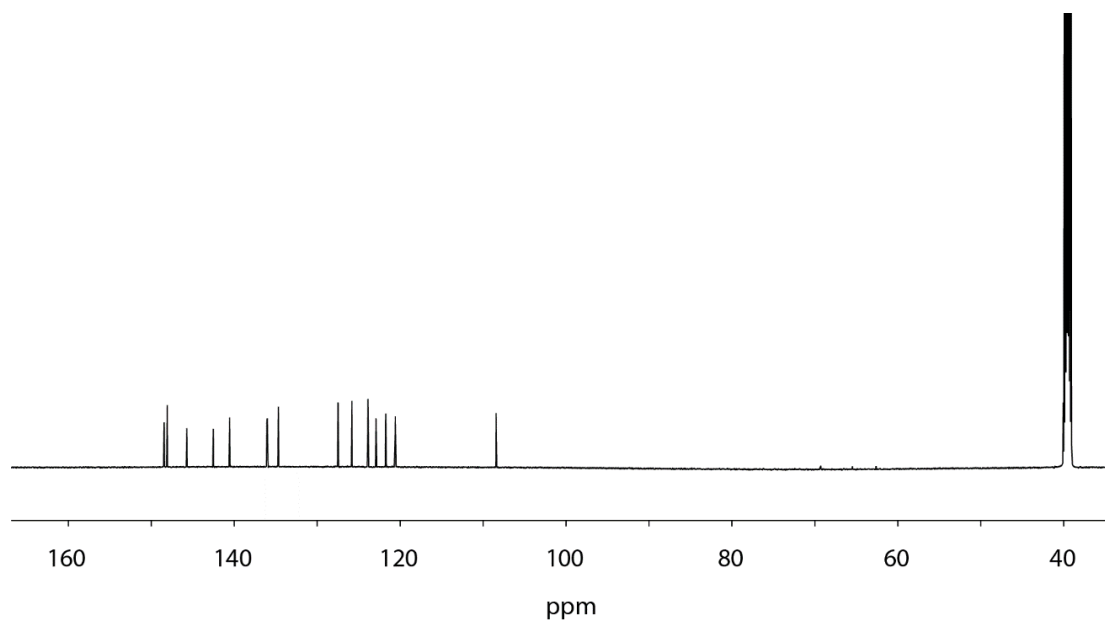


Figure 5.65:  $^{13}\text{C}$  NMR spectrum of  $\text{L}^{\text{NO}_2}$  (151 MHz, 298 K,  $\text{DMSO-}d_6$ ).

## 5. Coordination-driven construction of [3]rotaxane based on hierarchical assembly

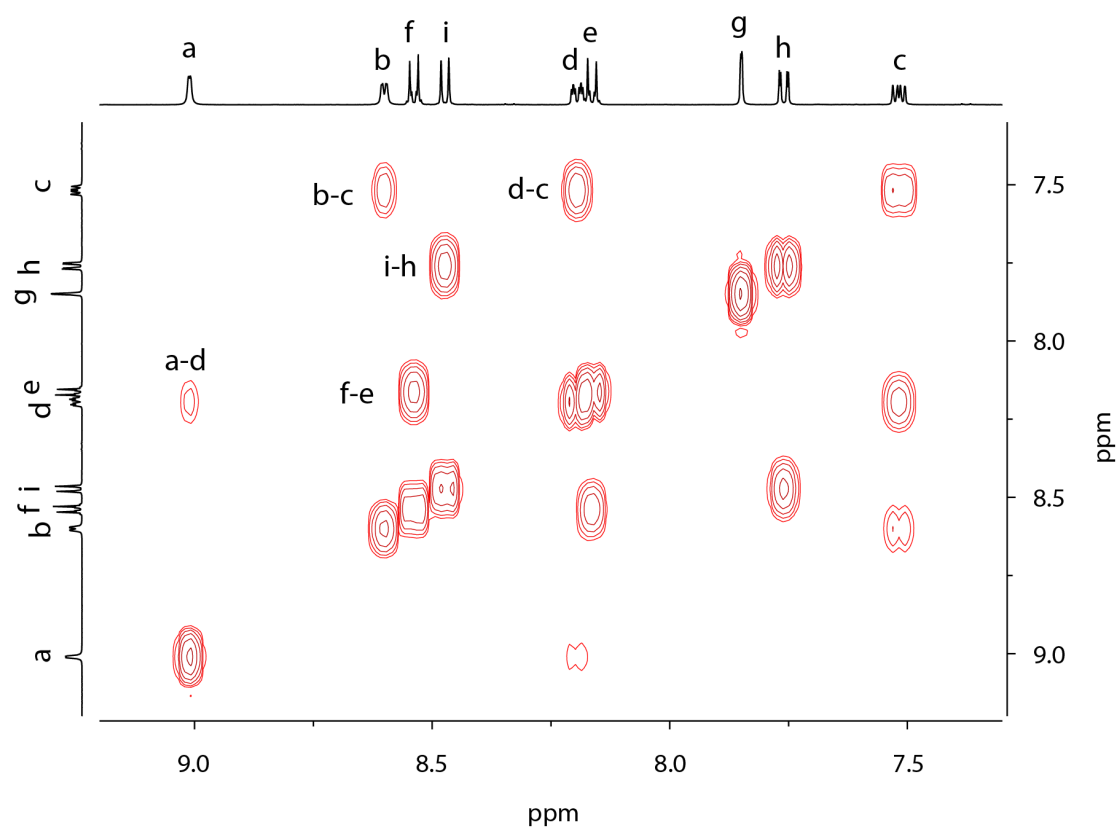


Figure 5.66:  $^1\text{H}$ - $^1\text{H}$  COSY NMR spectrum of of  $\text{L}^{\text{NO}_2}$  (500 MHz, 298 K,  $\text{DMSO-d}_6$ ).

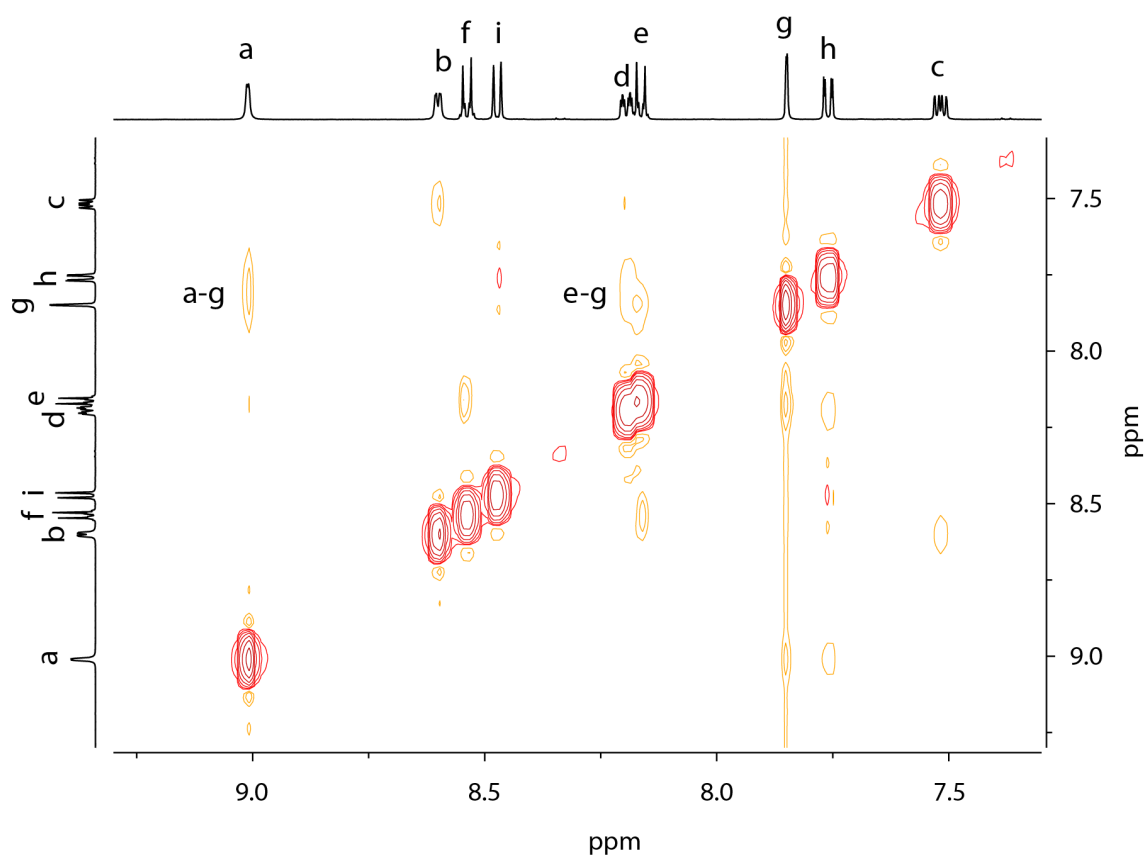


Figure 5.67:  $^1\text{H}$ - $^1\text{H}$  NOESY NMR spectrum of of  $\text{L}^{\text{NO}_2}$  (500 MHz, 298 K,  $\text{DMSO-d}_6$ ).

## 5. Coordination-driven construction of [3]rotaxane based on hierarchical assembly

### Synthesis of ligand **L<sup>NH2</sup>**

**2Br-NH<sub>2</sub>** (500 mg, 1.2 mmol, 1 equiv.), 3-(1,3,2-dioxaborinan-2-yl)pyridine (490 mg, 3.0 mmol, 2.5 equiv.), Pd(PPh<sub>3</sub>)<sub>4</sub> (83 mg, 0.07 mmol, 0.06 mol%) and K<sub>3</sub>PO<sub>4</sub> (918 mg, 4.33 mmol, 3.6 equiv.) were combined in a 100 mL Schlenk tube and cycled three times under vacuum and argon. 20 mL degassed mixture solvents of 1,4-dioxane and water (v:v=4:1) were added. The reaction was stirred at 95 °C for 48 h. After cooling down to room temperature, the solvents were evaporated and 30 mL water was added and then extracted with CH<sub>2</sub>Cl<sub>2</sub>. The organic layer was combined and dried over MgSO<sub>4</sub>. The solvent was removed in vacuum. The residue was purified by column chromatography (DCM:pentane=50:1) to afford the product (300 mg, 60.5% yield.)

<sup>1</sup>H NMR (700 MHz, CD<sub>3</sub>CN): δ 8.90 (dd, *J* = 2.4, 0.9 Hz, 2H), 8.55 (dd, *J* = 4.7, 1.6 Hz, 2H), 8.30 (dd, *J* = 8.1, 0.6 Hz, 2H), 8.02 (ddd, *J* = 7.9, 2.4, 1.6 Hz, 2H), 7.59 (dd, *J* = 8.0, 1.6 Hz, 2H), 7.56 (dd, *J* = 1.6, 0.7 Hz, 2H), 7.41 (ddd, *J* = 7.9, 4.8, 0.9 Hz, 2H), 7.35 (d, *J* = 8.6 Hz, 2H), 6.90 (d, *J* = 8.6 Hz, 2H), 4.46 (s, 2H).

<sup>13</sup>C NMR (176 MHz, CD<sub>3</sub>CN): δ 149.28, 149.07, 143.70, 137.88, 136.99, 135.42, 129.27, 126.87, 124.62, 123.21, 122.07, 120.13, 116.29, 109.27.

HR ESI-MS: calculated for [C<sub>28</sub>H<sub>20</sub>N<sub>4</sub>]<sup>+</sup> *m/z* 413.1761 [M + H]<sup>+</sup>  
found: 431.1759

## 5. Coordination-driven construction of [3]rotaxane based on hierarchical assembly

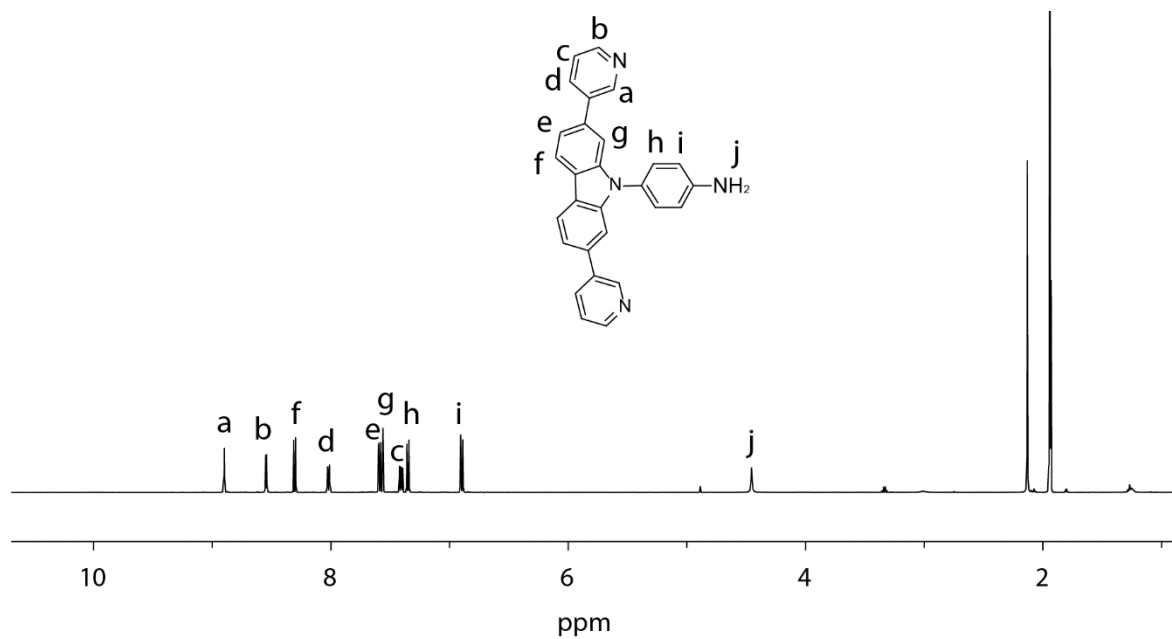


Figure 5.68:  $^1H$  NMR spectrum of  $L^{NH_2}$  (700 MHz, 298 K,  $CD_3CN$ ).

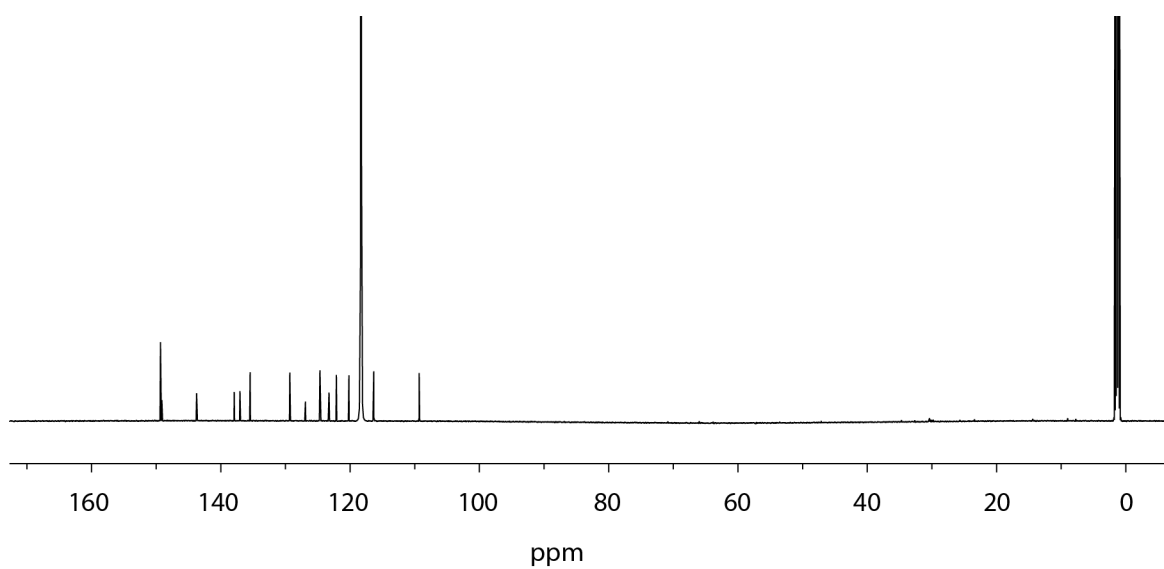


Figure 5.69:  $^{13}C$  NMR spectrum of  $L^{NH_2}$  (176 MHz, 298 K,  $CD_3CN$ ).

## 5. Coordination-driven construction of [3]rotaxane based on hierarchical assembly

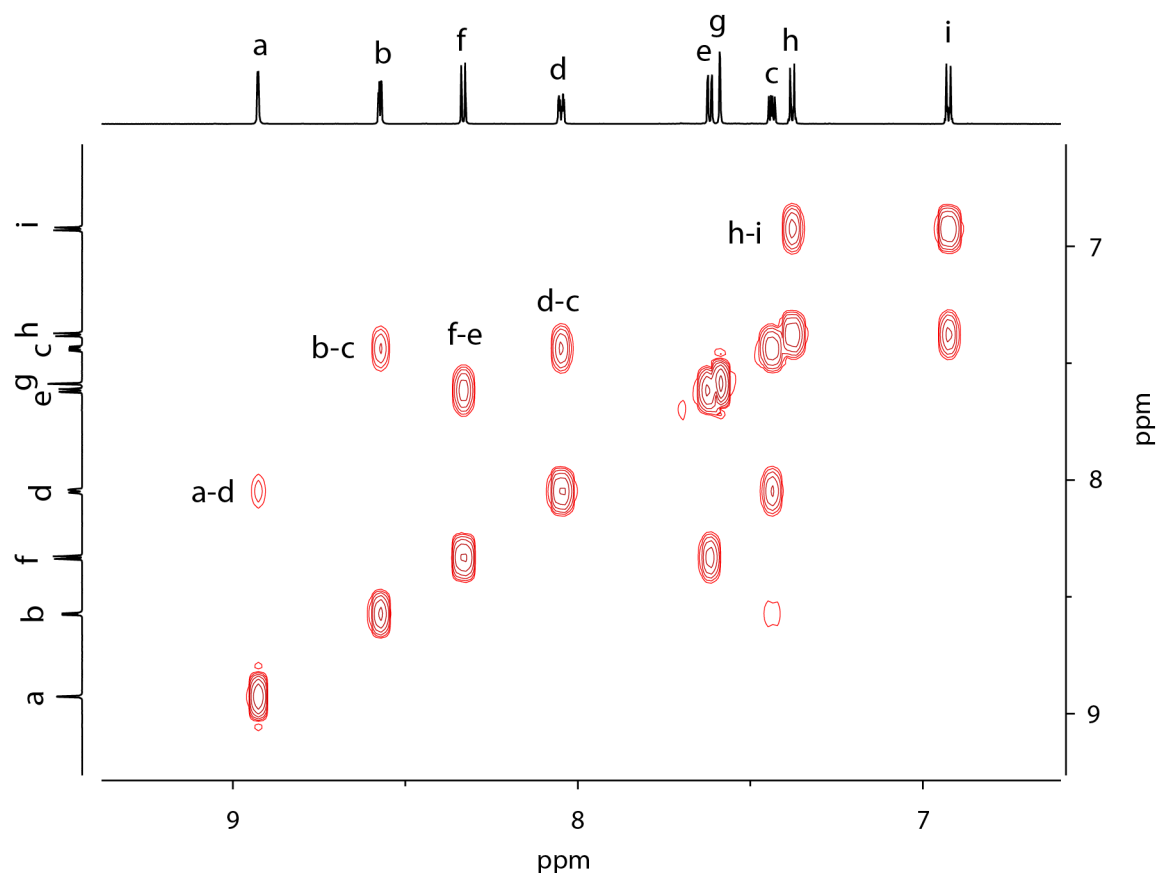
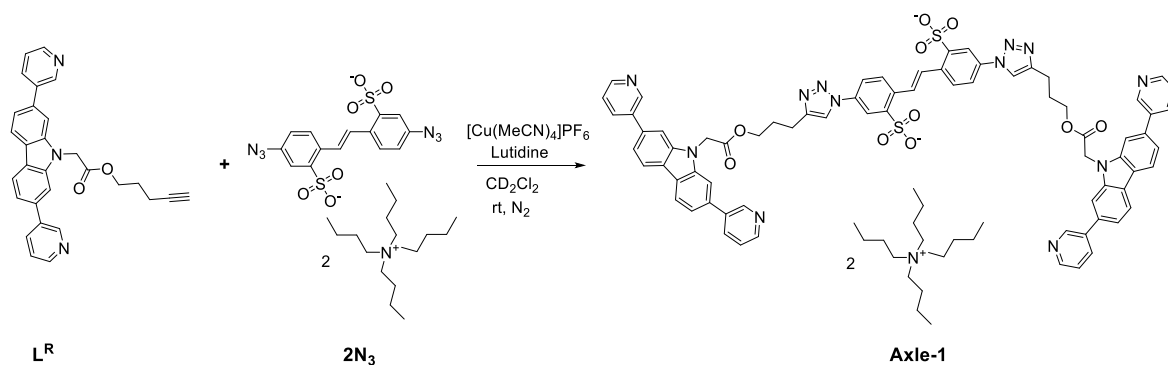


Figure 5.70:  $^1\text{H}$ - $^1\text{H}$  COSY NMR spectrum of  $\text{L}^{\text{NH}_2}$  (700 MHz, 298 K,  $\text{CD}_3\text{CN}$ ).

### 5.8.8 2 Synthesis of Axle-1



$2\text{N}_3$  (10.8 mg, 11.9  $\mu\text{mol}$ , 1 equiv.),  $\text{L}^{\text{R}}$  (2.65 mg, 5.95  $\mu\text{mol}$ , 0.5 equiv.),  $[\text{Cu}(\text{MeCN})_4]\text{PF}_6$  (0.27 mg, 6 mol%), lutidine (7.7 mg, 71.4  $\mu\text{mol}$ ) were combined in a 10 mL Schlenk flask and cycled three times under vacuum and refilled with argon. 3 mL degassed  $\text{CH}_3\text{CN}$  and  $\text{CH}_2\text{Cl}_2$  (v:v=1:2) mixture solvents were added. The reaction was stirred at 50  $^\circ\text{C}$  overnight. After cooling down to room temperature, the solvents were evaporated. The residue was resolved in  $\text{CH}_2\text{Cl}_2$  and washed with 10%

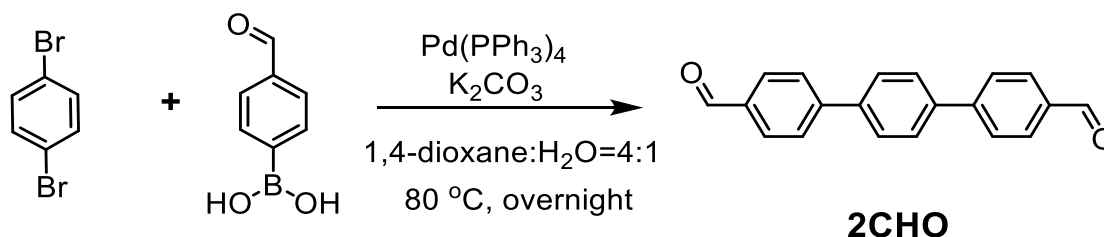


5. Coordination-driven construction of [3]rotaxane based on hierarchical assembly ammonia aq. Organic phase was collected and the solvent was removed by evaporation to give the product.

HR ESI-MS: Calculated for  $[C_{100}H_{70}N_6O_6]^{2-}$ ,  $m/z$  702.1929  $[M]^{2-}$ ,  
found: 702.2026

### 5.8.9 Synthesis of Axle-2

Synthesis of **2CHO**



1,4-dobromobenzene (0.50 g, 2.12 mmol, 1 equiv.), (4-formylphenyl)boronic acid (0.95 g, 6.36 mmol, 3 equiv.),  $Pd(PPh_3)_4$  (122 mg, 0.1 mmol, 5 mol%), and  $K_2CO_3$  (1.05 g, 7.63 mmol, 3.6 equiv.) were combined in a 100 mL Schlenk flask and cycled three times under vacuum and refilled with argon. 20 mL degassed 1,4-dioxane and water (v:v=4:1) mixture solvents were added. The reaction was stirred at 80 °C overnight. After cooling down to room temperature, the solvents were evaporated and 30 mL water was added and then extracted with  $CH_2Cl_2$ . The organic layer was combined and dried over  $MgSO_4$ . The solvent was removed in vacuum. The residue was purified by column chromatography (DCM:pentane=2:1) to afford the product (485 mg, 79.9% yield.)

$^1H$  NMR (500 MHz,  $CDCl_3$ ):  $\delta$  10.08 (s, 2H), 8.00 – 7.98 (m, 4H), 7.85 – 7.80 (m, 4H), 7.77 (d,  $J$  = 0.7 Hz, 4H).

$^{13}C$  NMR (151 MHz,  $CDCl_3$ ):  $\delta$  191.99, 146.41, 139.93, 135.61, 130.53, 128.15, 127.78.

## 5. Coordination-driven construction of [3]rotaxane based on hierarchical assembly

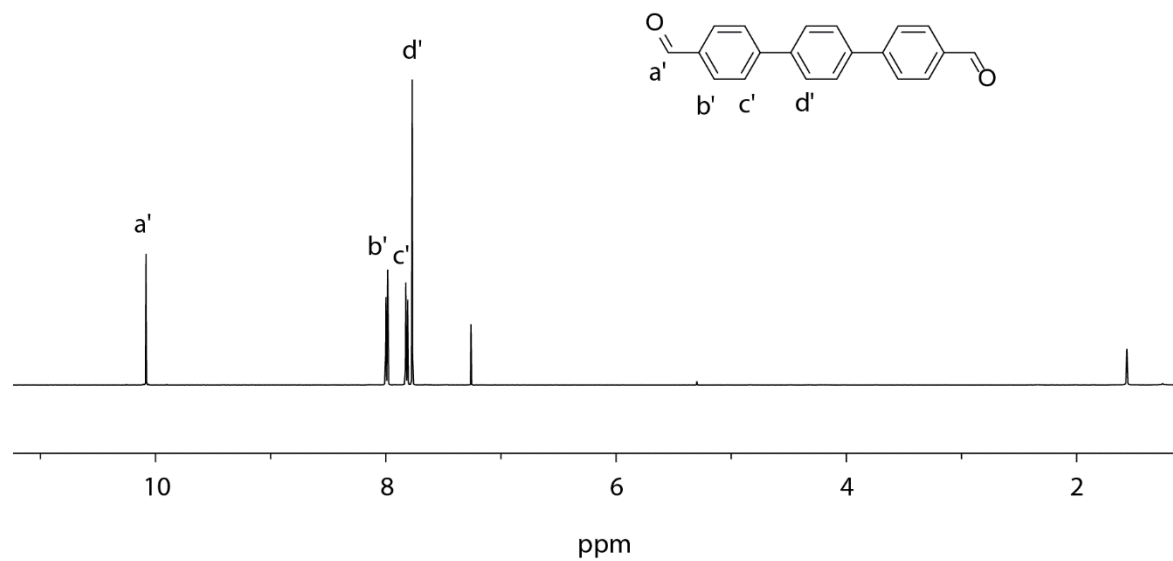


Figure 5.71: <sup>1</sup>H NMR spectrum of **2CHO** (500 MHz, 298 K, CDCl<sub>3</sub>).

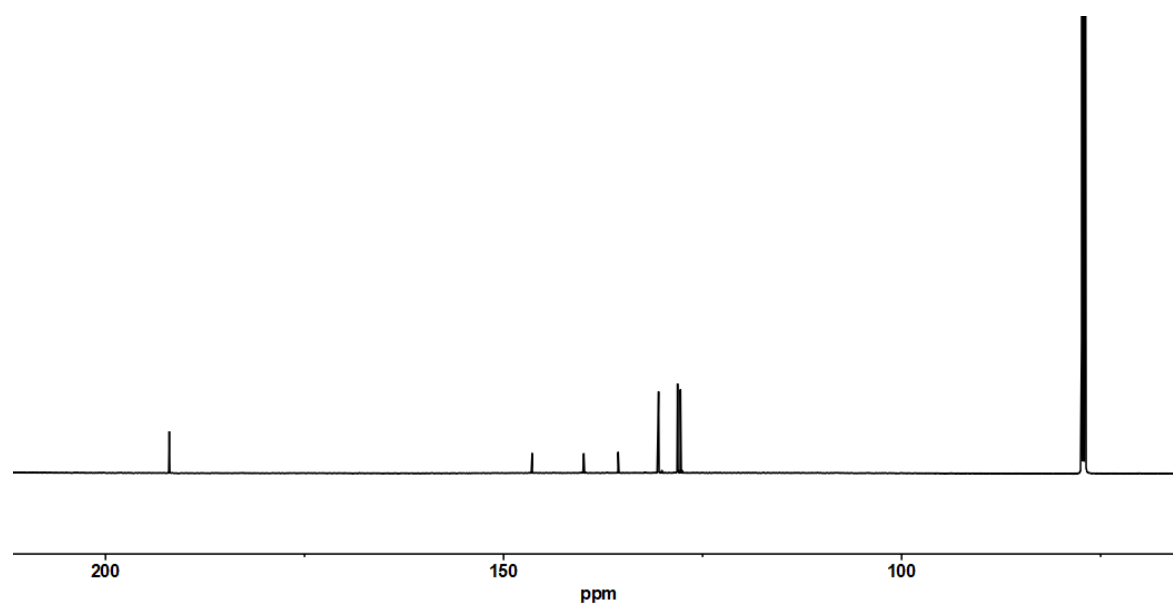
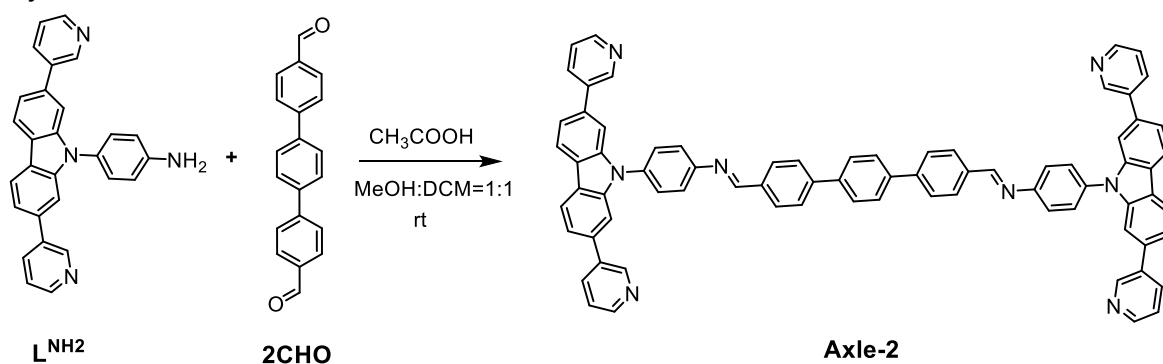


Figure 5.72: <sup>13</sup>C NMR spectrum of **2CHO** (151 MHz, 298 K, CDCl<sub>3</sub>).

### Synthesis of **Axle-2**



5. Coordination-driven construction of [3]rotaxane based on hierarchical assembly

**2CHO** (2.86 mg, 10  $\mu\text{mol}$ , 1 equiv), **L<sup>NH2</sup>** (10.3 mg, 25  $\mu\text{mol}$ , 2.5 equiv.) were dissolved in 2 mL mixture solvents of DCM / MeOH (v:v=1:1). 20  $\mu\text{l}$  acetic acid was added. The mixture was stirred at room temperature overnight. After reaction the precipitate was collected and washed by anhydrous MeOH to give a yellow product (4.3 mg, 40% yield).

$^1\text{H}$  NMR (500 MHz,  $\text{CDCl}_3$ ):  $\delta$  8.94 (d,  $J = 2.4$  Hz, 4H), 8.68 (s, 2H), 8.60 (dd,  $J = 4.9$ , 1.5 Hz, 4H), 8.28 (d,  $J = 8.2$  Hz, 4H), 8.12 – 8.06 (m, 4H), 7.96 (ddd,  $J = 7.9$ , 2.4, 1.6 Hz, 4H), 7.85 – 7.82 (m, 4H), 7.82 (s, 2H), 7.69 – 7.65 (m, 4H), 7.62 (d,  $J = 1.6$  Hz, 4H), 7.57 (dd,  $J = 8.1$ , 1.5 Hz, 4H), 7.55 – 7.52 (m, 4H), 7.38 (dd,  $J = 8.0$ , 4.8 Hz, 5H).

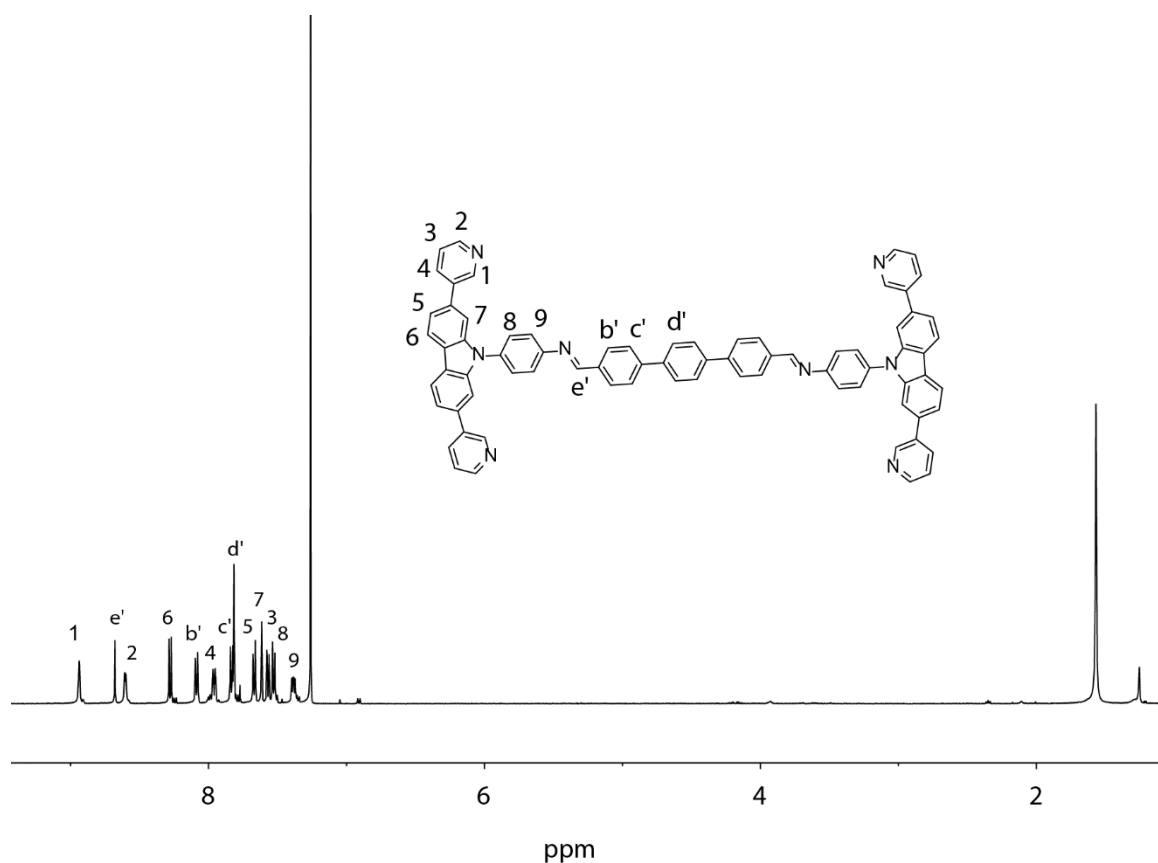
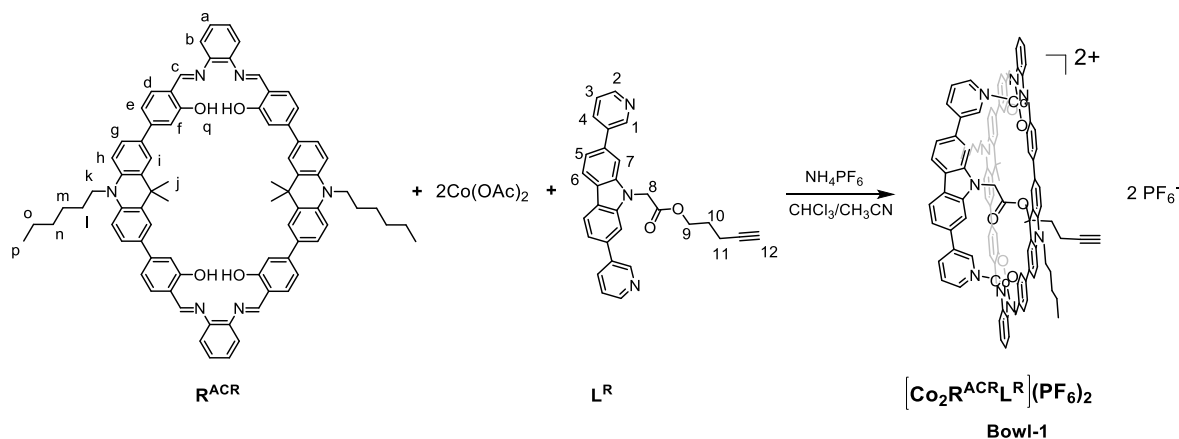


Figure 5.73:  $^1\text{H}$  NMR spectrum of **Axle-2** (500 MHz, 298 K,  $\text{CDCl}_3$ ).

## 5. Coordination-driven construction of [3]rotaxane based on hierarchical assembly

### 5.8.10 Self-assembly of bowl



$R^{ACR}$  (2 mg, 1.65  $\mu$ mol, 1 equiv.), and  $Co_2(OAc)_2$  (48.8  $\mu$ L, 20 mg/mL in DMSO solution, 2 equiv.) were dissolved in 2 mL  $CH_3CN/CHCl_3$  (v:v=1:1) and stirred at room temperature for 15 min.  $L^R$  (0.74 mg, 1.65  $\mu$ mol, 1 equiv.) and  $NH_4PF_6$  (0.54 mg, 3.3  $\mu$ mol, 2 equiv.) was added. The reaction mixture was heated at 70  $^{\circ}C$  overnight. Afterwards, the solvent was removed under reduced pressure. The residue was dissolved in a minimal amount of DCM and precipitated with  $Et_2O$  to provide 1.2 mg product (41.1% yield).

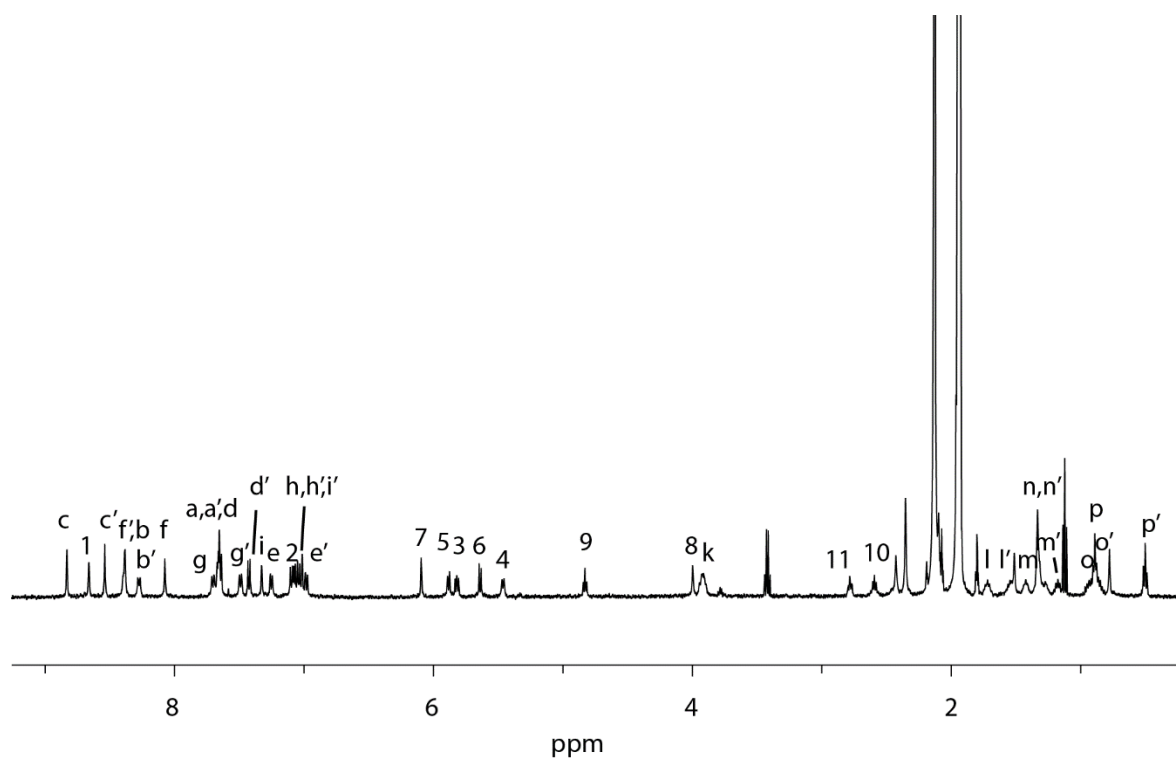


Figure 5.74:  $^1H$  NMR spectrum of **Bowl-1** (500 MHz, 298 K,  $CD_3CN$ ).

## 5. Coordination-driven construction of [3]rotaxane based on hierarchical assembly

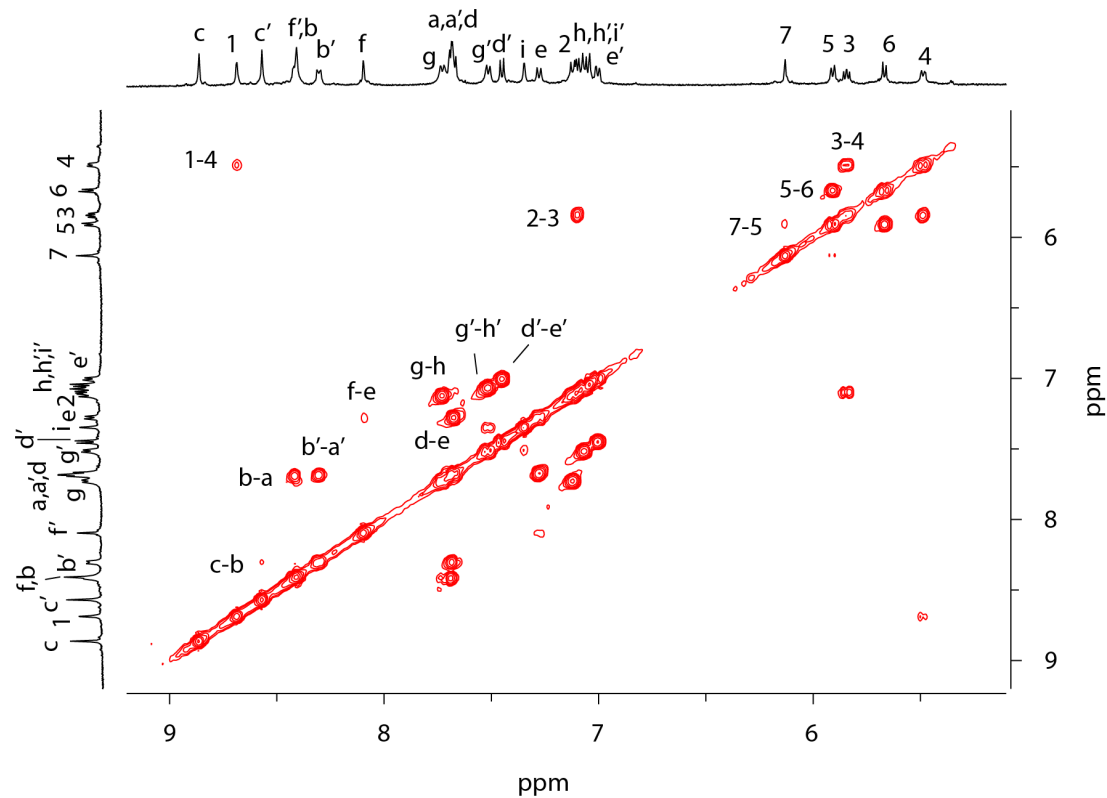


Figure 5.75:  $^1\text{H}$ - $^1\text{H}$  COSY NMR spectrum of **Bowl-1** (500 MHz, 298 K,  $\text{CD}_3\text{CN}$ ).

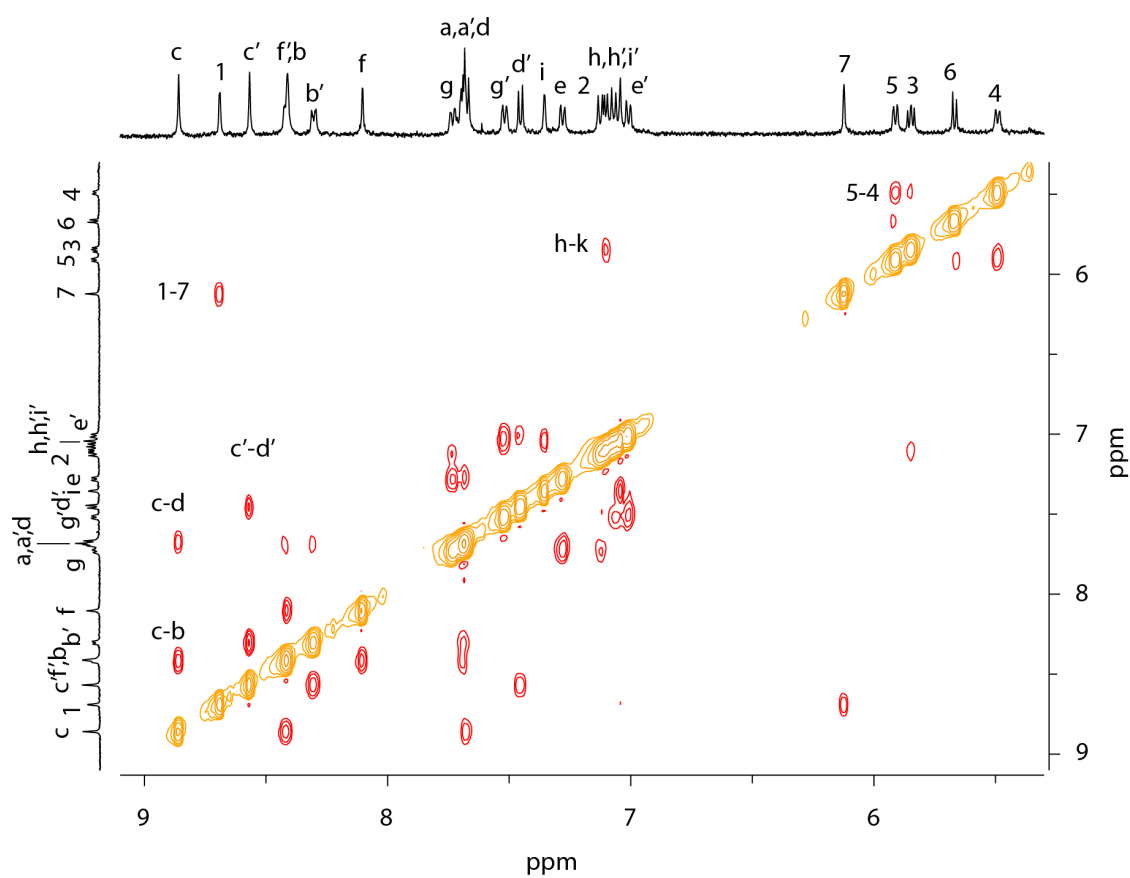
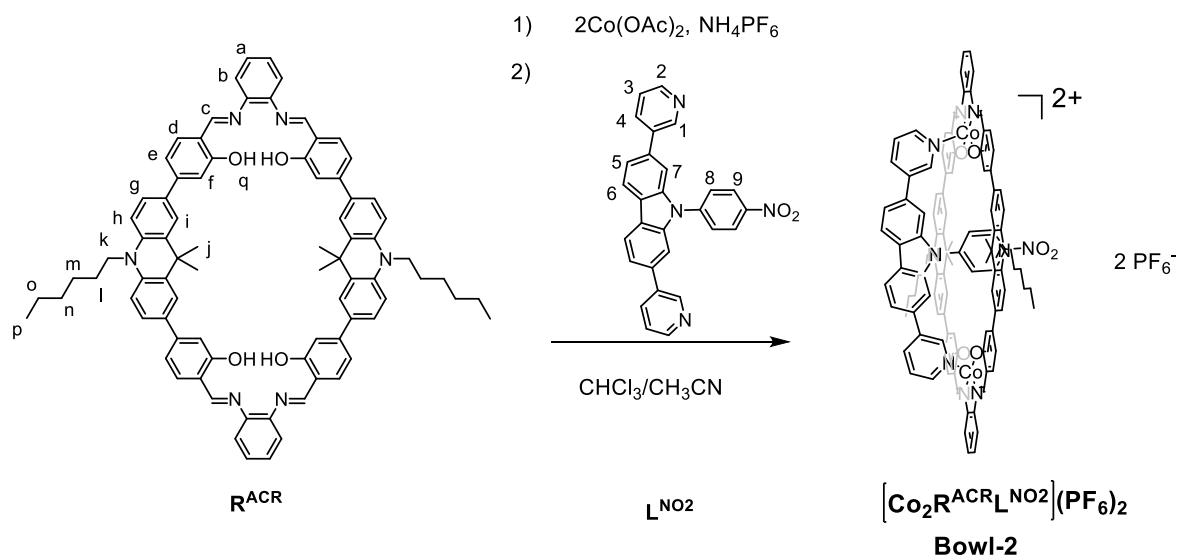
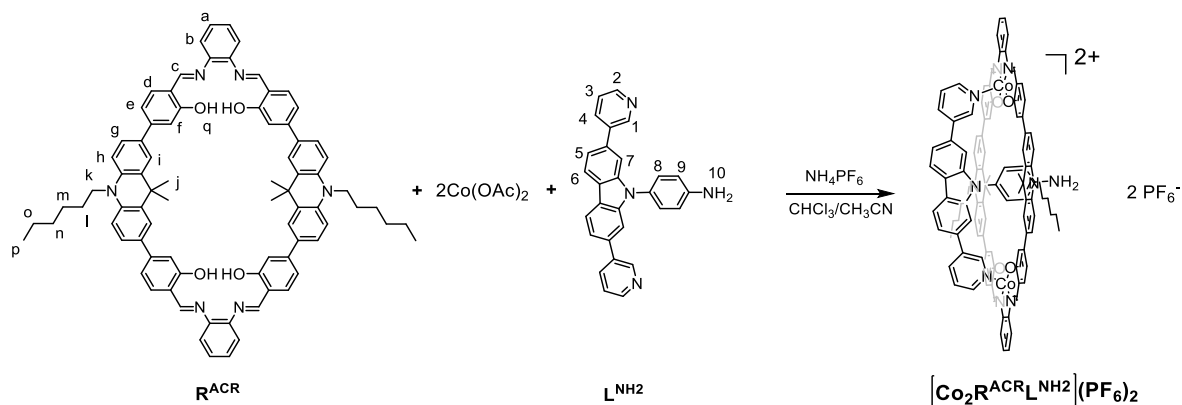


Figure 5.76:  $^1\text{H}$ - $^1\text{H}$  NOESY NMR spectrum of **Bowl-1** (500 MHz, 298 K,  $\text{CD}_3\text{CN}$ ).

## 5. Coordination-driven construction of [3]rotaxane based on hierarchical assembly



$\text{R}^{\text{ACR}}$  (2 mg, 1.65  $\mu\text{mol}$ , 1 equiv.), and  $\text{Co}_2(\text{OAc})_2$  (48.8  $\mu\text{L}$ , 20 mg/mL in DMSO solution, 2 equiv.) were dissolved in 2 mL  $\text{CH}_3\text{CN}/\text{CHCl}_3$  (v:v=1:1) and stirred at room temperature for 15 min.  $\text{L}^{\text{NO}_2}$  (0.73 mg, 1.65  $\mu\text{mol}$ , 1 equiv.) and  $\text{NH}_4\text{PF}_6$  (0.54 mg, 3.3  $\mu\text{mol}$ , 2 equiv.) was added. The reaction mixture was heated at 70  $^\circ\text{C}$  overnight. Afterwards, the solvent was removed under reduced pressure. The residue was dissolved in a minimal amount of DCM and precipitated with  $\text{Et}_2\text{O}$  to provide product.



$\text{R}^{\text{ACR}}$  (2 mg, 1.65  $\mu\text{mol}$ , 1 equiv.), and  $\text{Co}_2(\text{OAc})_2$  (48.8  $\mu\text{L}$ , 20 mg/mL in DMSO solution, 2 equiv.) were dissolved in 2 mL  $\text{CH}_3\text{CN}/\text{CHCl}_3$  (v:v=1:1) and stirred at room temperature for 15 min.  $\text{L}^{\text{NH}_2}$  (0.68 mg, 1.65  $\mu\text{mol}$ , 1 equiv.) and  $\text{NH}_4\text{PF}_6$  (0.54 mg, 3.3  $\mu\text{mol}$ , 2 equiv.) was added. The reaction mixture was heated at 70  $^\circ\text{C}$  overnight. Afterwards, the solvent was removed under reduced pressure. The residue was dissolved in a minimal amount of DCM and precipitated with  $\text{Et}_2\text{O}$  to provide product.

## 5. Coordination-driven construction of [3]rotaxane based on hierarchical assembly

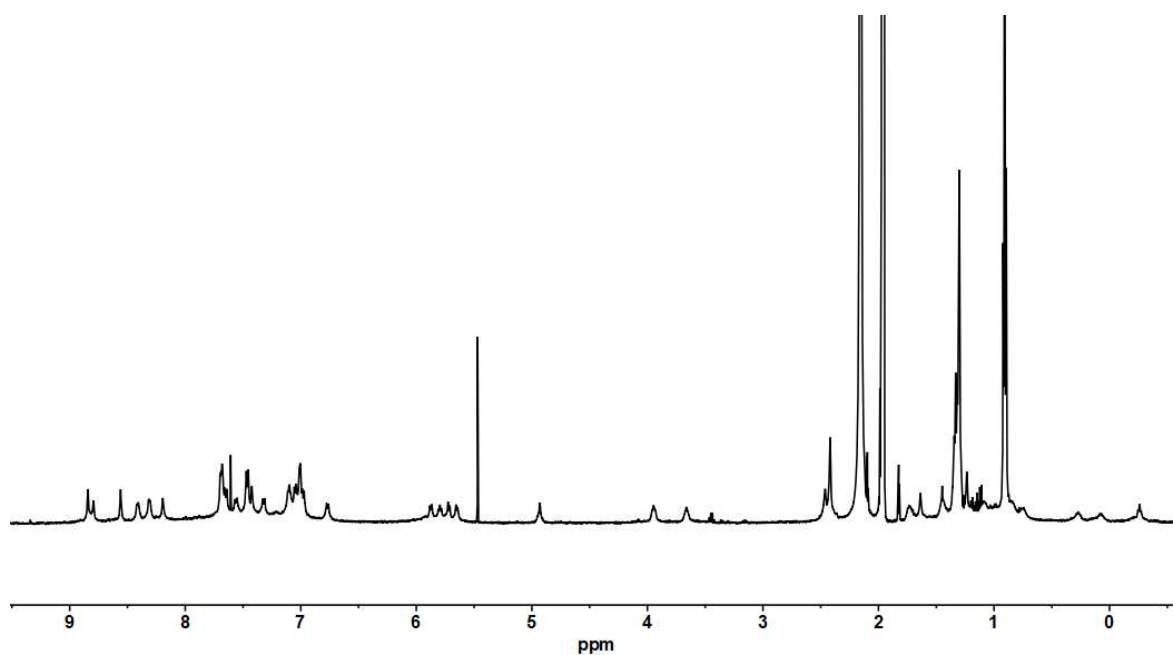


Figure 5.77:  $^1\text{H}$  NMR spectrum of **Bowl-3** (500 MHz, 298 K,  $\text{CD}_3\text{CN}$ ).

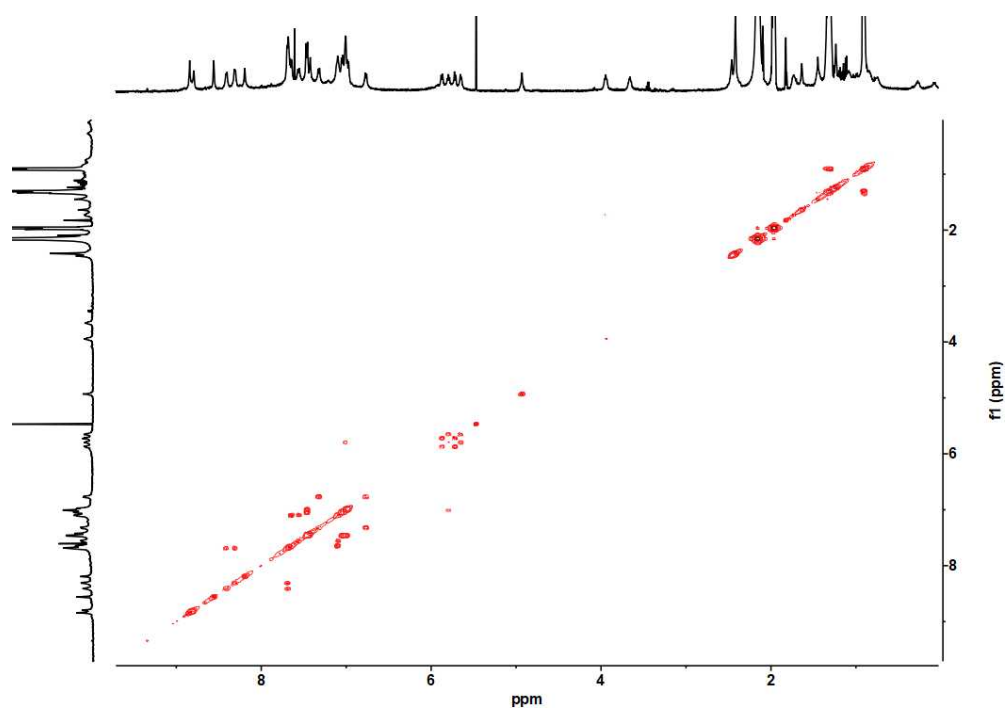


Figure 5.78:  $^1\text{H}$ - $^1\text{H}$  COSY spectrum of **Bowl-3** (500 MHz, 298 K,  $\text{CD}_3\text{CN}$ ).

## 5. Coordination-driven construction of [3]rotaxane based on hierarchical assembly

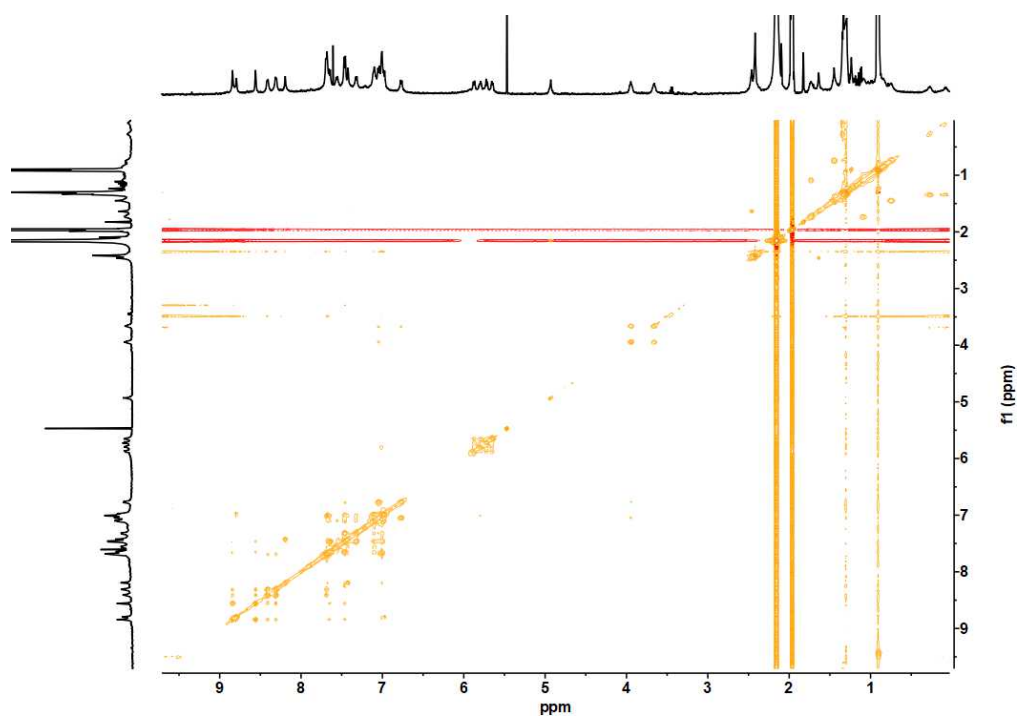


Figure 5.79: <sup>1</sup>H-<sup>1</sup>H NOESY spectrum of **Bowl-3** (500 MHz, 298 K, CD<sub>3</sub>CN).

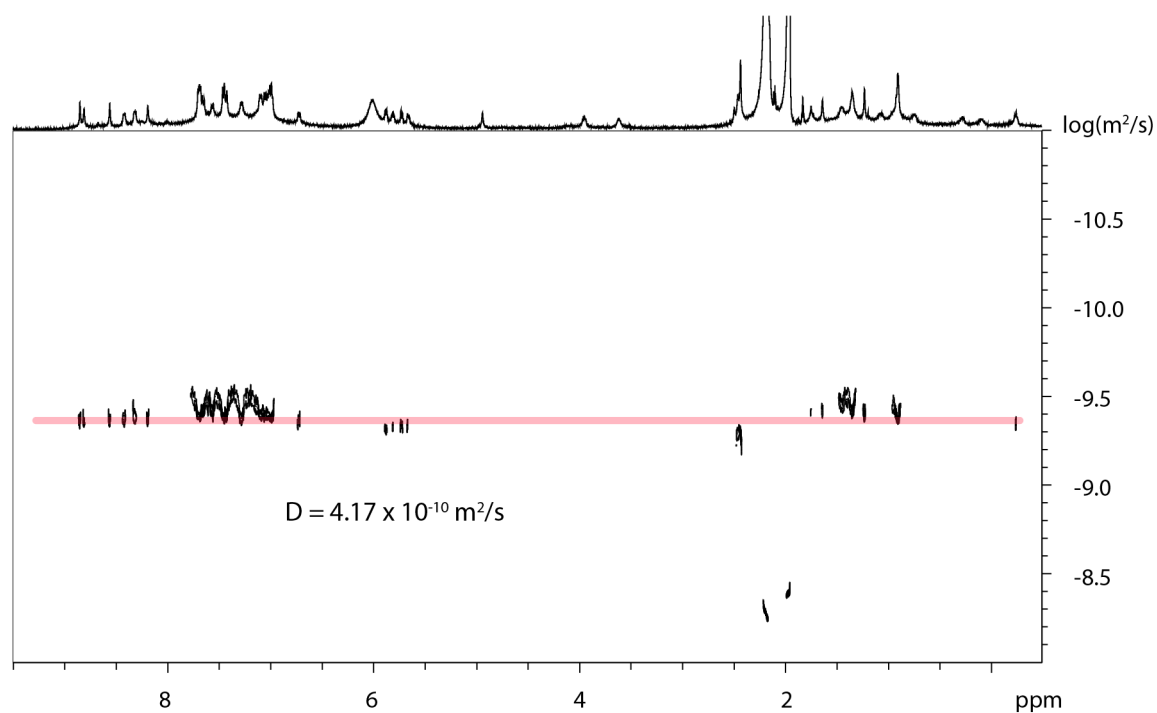


Figure 5.80: DOSY spectrum (500 MHz, 289 K, CD<sub>3</sub>CN) of **Co<sub>2</sub>R<sup>ACR</sup>L<sup>NH<sub>2</sub></sup>**, diffusion coefficient  $D = 4.17 \times 10^{-10} \text{ m}^2\text{s}^{-1}$ ,  $r_H = 1.52 \text{ \AA}$ .



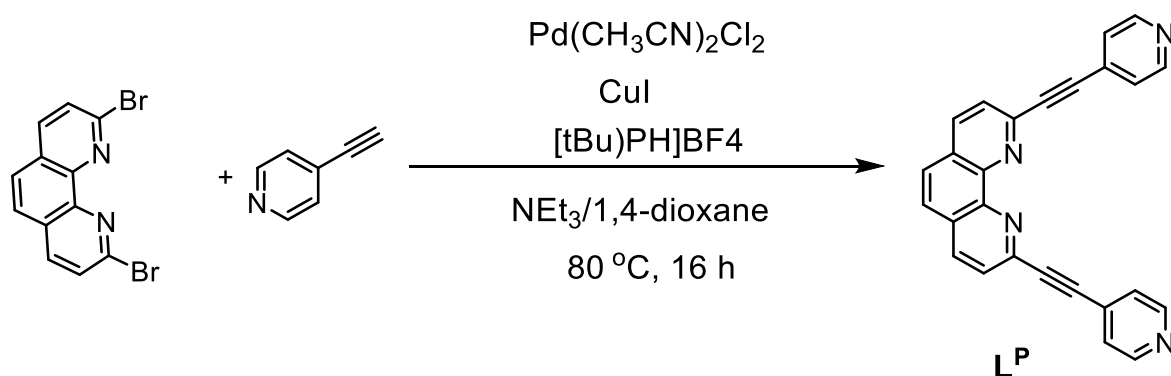
## 5. Coordination-driven construction of [3]rotaxane based on hierarchical assembly

## 5.8.11 Crystal information

	<b>R<sup>ACR</sup></b>	<b>Bowl 1</b>
Empirical formula	C <sub>42</sub> H <sub>39</sub> Cl <sub>2</sub> N <sub>3</sub> O <sub>2</sub>	C <sub>127</sub> H <sub>133</sub> Co <sub>2</sub> F <sub>12</sub> N <sub>9</sub> O <sub>16</sub> P <sub>2</sub>
Formula weight	688.66	2449.22
Temperature (K)	100(2)	100(2)
Crystal system	Triclinic	Triclinic
Space group	<i>P</i> -1	<i>P</i> $\bar{1}$ (2)
Unit cell dimensions, a (Å)	10.2128(3)	17.319(3)
b (Å)	10.3513(3)	18.156(3)
c (Å)	17.1384(5)	20.062(3)
$\alpha$ (°)	98.4660(10)	81.008(4)
$\beta$ (°)	100.1650(10)	74.778(7)
$\gamma$ (°)	103.2360(10)	70.752(3)
Volume (Å <sup>3</sup> )	1702.37(9)	5729.9(16)
Z	2	2
Density (calculated) (Mg/m <sup>3</sup> )	1.343	1.420
Absorption coefficient (mm <sup>-1</sup> )	2.045	0.373
F(000)	724.0	2556
Crystal size (mm <sup>3</sup> )	0.200 x 0.150 x 0.100	0.200 x 0.080 x 0.040
Theta range for data collection (°)	5.342 to 120.024	2.04 to 60.91 (0.68Å)
Radiation	MoK $\alpha$ ( $\lambda$ =0.71073 Å)	Synchrotron ( $\lambda$ =0.6888 Å)
Index ranges	-11 $\leq$ h $\leq$ 11, -11 $\leq$ k $\leq$ 11, -19 $\leq$ l $\leq$ 19	-25 $\leq$ h $\leq$ 25, -25 $\leq$ k $\leq$ 24, -29 $\leq$ l $\leq$ 29
Reflections collected	26248	374828
Independent reflections	5054 [R(int) = 0.0213]	34286 [R(int) = 0.1110] [R(sigma) = 0.0337]
Completeness to theta	97.80%	99.6%
Absorption correction	Semi-empirical from equivalents	Semi-empirical from equivalents
Refinement method	Full-matrix least-squares on F <sup>2</sup>	Full-matrix least-squares on F <sup>2</sup>
Data / restraints / parameters	5054/0/445	34286 / 3787 / 1732
Goodness-of-fit on F <sub>2</sub>	1.033	1.510
Final R indices [I > 2sigma(I)]	R1 = 0.0759, wR2 = 0.2259	R1 = 0.0875 wR2 = 0.2646
R indices (all data)	R1 = 0.0773, wR2 = 0.2259	R1 = 0.0974 wR2 = 0.2775
Largest diff. peak and hole (e.Å <sup>-3</sup> )	1.13 / -0.35	2.31/-1.22

## 5. Coordination-driven construction of [3]rotaxane based on hierarchical assembly

### 5.8.12 Synthesis of L<sup>P</sup>



2,9-dibromo-1,10-phenanthroline (400 mg, 1.18 mmol, 1 equiv.) and 4-ethynylpyridine (269 mg, 2.60 mmol, 2.2 equiv.) were combined in a 100 mL Schlenk flask and dissolved in a mixture of triethylamine and dioxane (1:3, 20 mL). The solution was degassed via freeze-thaw cycles, followed by addition of Pd(CH<sub>3</sub>CN)<sub>2</sub>Cl<sub>2</sub> (30.7 mg, 0.12 mmol, 10 mol%), CuI (22.5 mg, 0.12 mmol, 10 mol%) and [(<sup>t</sup>Bu)PH]BF<sub>4</sub>. (71 mg, 0.25 mmol, 0.2 equiv.). The reaction mixture was heated to 80 °C for 16 h until the starting material had been fully consumed. After cooling to room temperature, the mixture was diluted with 20 mL chloroform, filtered and the solvent was removed under reduced pressure. The crude product was purified by flash chromatography (on Isolera, chloroform:methanol 9:1) and GPC (chloroform) (183 mg, 40.4% yield.)

<sup>1</sup>H NMR (500 MHz, DMSO-*d*<sub>6</sub>): δ 8.78 – 8.67 (m, 4H), 8.62 (d, *J* = 8.3 Hz, 2H), 8.14 – 8.07 (m, 4H), 7.76 – 7.69 (m, 4H).

HR ESI-MS: calculated for [C<sub>26</sub>H<sub>14</sub>N<sub>4</sub>]<sup>+</sup> *m/z* 383.1291 [M + H]<sup>+</sup>  
found: 383.1286

## 5. Coordination-driven construction of [3]rotaxane based on hierarchical assembly

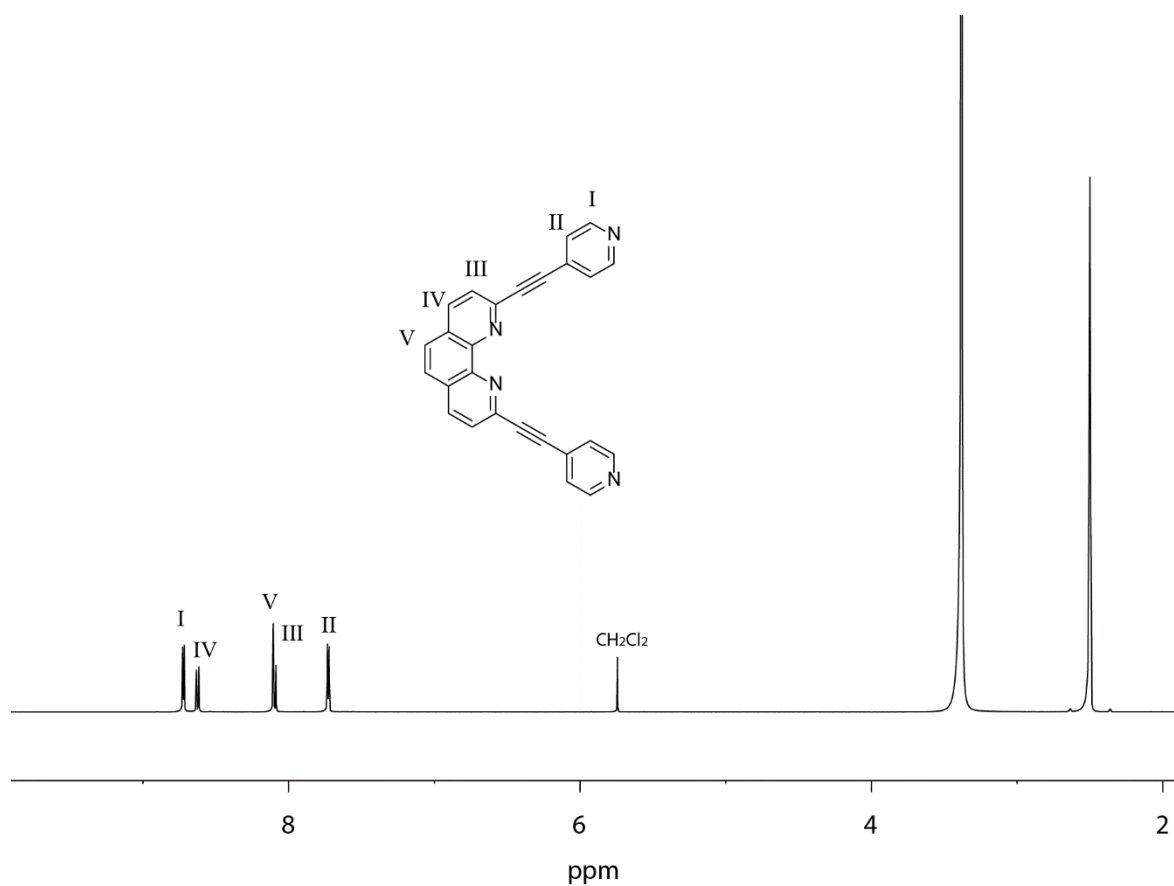
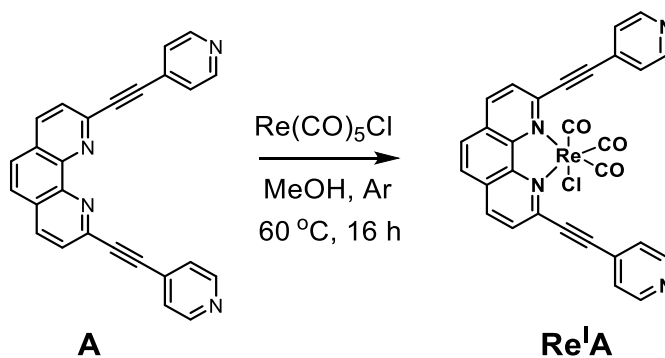


Figure 5.81: <sup>1</sup>H NMR spectrum of L<sup>P</sup> (500 MHz, 298 K, DMSO-*d*<sub>6</sub>).

### 5.8.13 Synthesis of Re(I)L<sup>P</sup>



<sup>1</sup>H NMR (500 MHz, DMSO-*d*<sub>6</sub>): δ 8.99 (d, *J* = 8.4 Hz, 2H), 8.83 – 8.74 (m, 4H), 8.47 (d, *J* = 8.4 Hz, 2H), 8.33 (s, 2H), 7.76 – 7.70 (m, 4H).

HR ESI-MS: calculated for [ReC<sub>26</sub>H<sub>14</sub>N<sub>4</sub>(CO)<sub>3</sub>Cl]<sup>+</sup> *m/z* 689.0377 [M]<sup>+</sup>  
found: 689.0322

## 5. Coordination-driven construction of [3]rotaxane based on hierarchical assembly

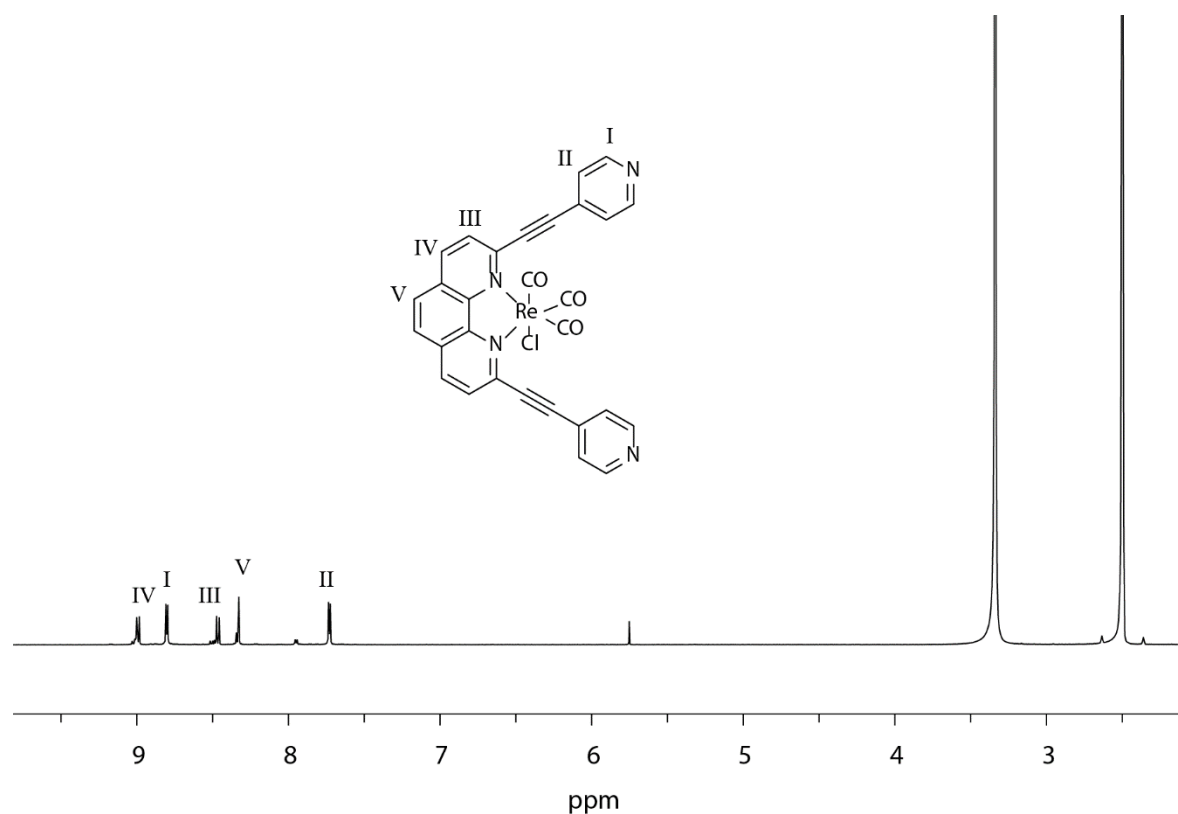
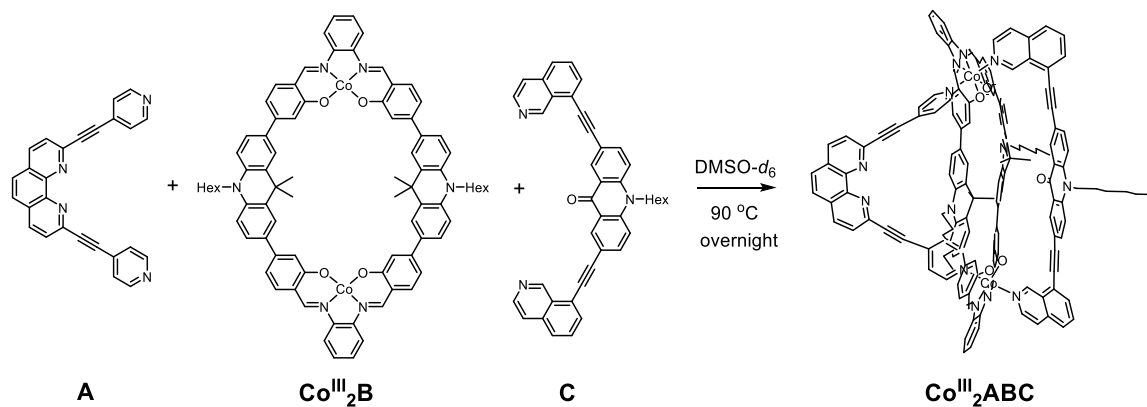


Figure 5.82:  $^1\text{H}$  NMR spectrum of  $\text{Re}^{\text{I}}\text{L}^{\text{P}}$  (500 MHz, 298 K,  $\text{DMSO-}d_6$ ).

### 5.8.14 Self-assembly of heteroleptic cages



**B** (2 mg, 1.65  $\mu\text{mol}$ ),  $\text{Co}(\text{OAc})_2$  (0.58 mg, 3.30  $\mu\text{mol}$ ) were dissolved  $\text{DMSO}$ .  $\text{NH}_4\text{PF}_6$  (0.54 mg, 3.30  $\mu\text{mol}$ ) was added and stirred at room temperature for 15 min under air condition. **A** (0.63 mg, 1.65  $\mu\text{mol}$ ) and **B** (0.98 mg, 1.65  $\mu\text{mol}$ ) were added into the solution. The reaction mixture stirred at 90  $^\circ\text{C}$  overnight to get the product.

HR ESI-MS: calculated for  $[\text{C}_{149}\text{H}_{119}\text{N}_{13}\text{O}_5]^{2+}$   $m/z$  1144.4071  $[\text{M}]^{2+}$   
 found: 1144.4027

## 5. Coordination-driven construction of [3]rotaxane based on hierarchical assembly

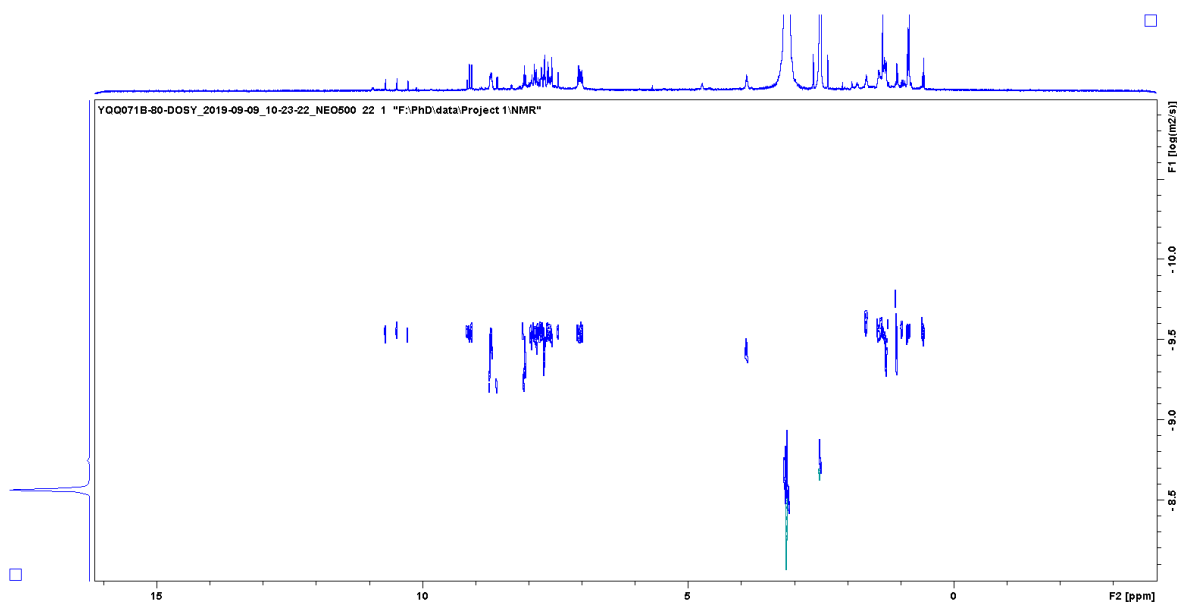
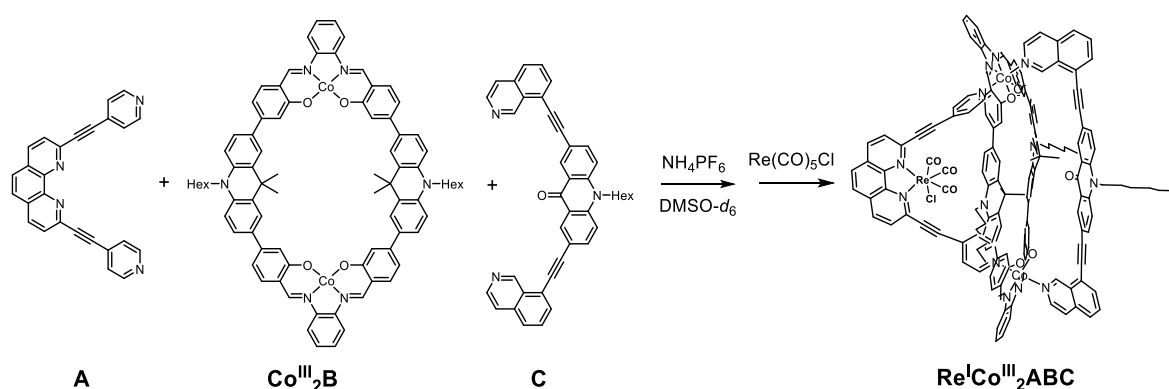
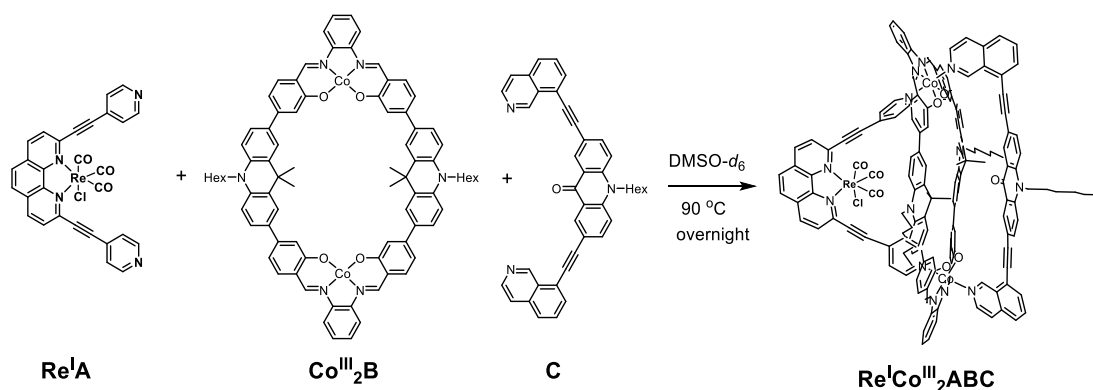


Figure 5.83: DOSY spectrum of **Co(III)<sub>2</sub>ABC** (500 MHz, 353 K, DMSO-*d*<sub>6</sub>).  $r_H=1.86$  nm.



**B** (2 mg, 1.65  $\mu\text{mol}$ ),  $\text{Co(OAc)}_2$  (0.58 mg, 3.30  $\mu\text{mol}$ ) were dissolved DMSO.  $\text{NH}_4\text{PF}_6$  (0.54 mg, 3.30  $\mu\text{mol}$ ) was added and stirred at room temperature for 15 min under air condition. **A** (0.63 mg, 1.65  $\mu\text{mol}$ ) and **B** (0.98 mg, 1.65  $\mu\text{mol}$ ) were added into the solution. The reaction mixture stirred at 90 °C overnight.  $\text{Re(CO)}_5\text{Cl}$  (0.60 mg, 1.65  $\mu\text{mol}$ ) was added and stirred for 3 h to afford the product.



## 5. Coordination-driven construction of [3]rotaxane based on hierarchical assembly

**B** (2 mg, 1.65  $\mu\text{mol}$ ),  $\text{Co}(\text{OAc})_2$  (0.58 mg, 3.30  $\mu\text{mol}$ ) were dissolved in DMSO.  $\text{NH}_4\text{PF}_6$  (0.54 mg, 3.30  $\mu\text{mol}$ ) was added and stirred at room temperature for 15 min under air condition. **Re(I)A** (1.14 mg, 1.65  $\mu\text{mol}$ ) and **B** (0.98 mg, 1.65  $\mu\text{mol}$ ) were added into the solution. The reaction mixture stirred at 90  $^\circ\text{C}$  overnight to get the product.

HR ESI-MS: calculated for  $[\text{ReCo}_2\text{C}_{152}\text{H}_{119}\text{N}_{13}\text{O}_8\text{Cl}]^+$   $m/z$  1297.3618  $[\text{M}]^+$   
found: 1297.3509

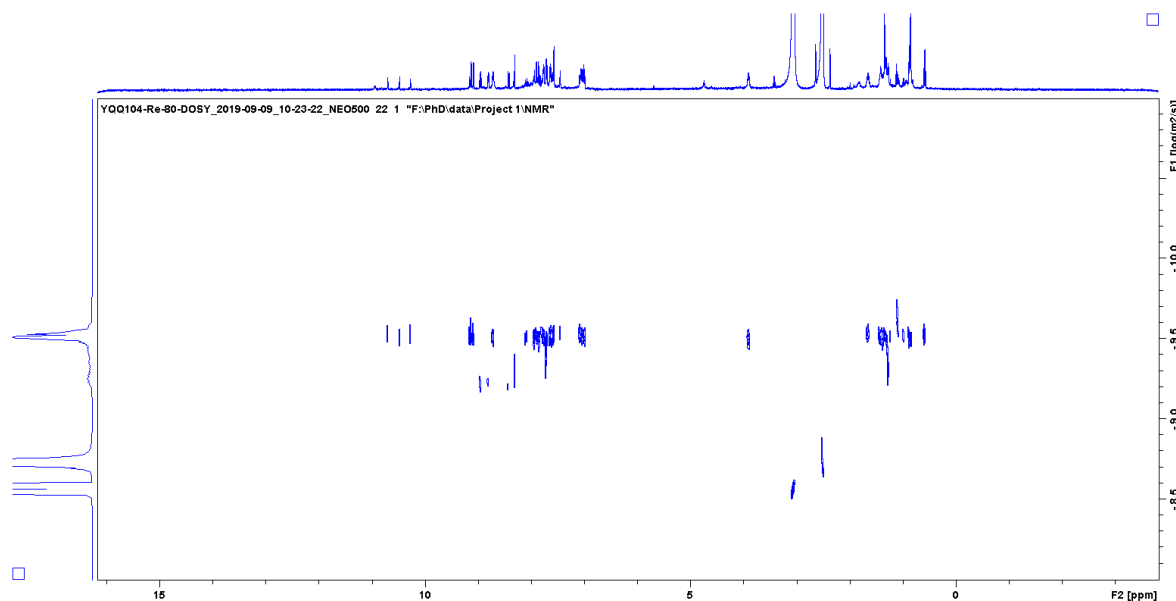


Figure 5.84: DOSY spectrum of **Re(I)Co(III)<sub>2</sub>ABC** (500 MHz, 353 K,  $\text{DMSO}-d_6$ ).  $r_H=1.80$  nm.

## 5.9 References

- [1] S. Mena-Hernando, E. M. Pérez, *Chem. Soc. Rev.* **2019**, *48*, 5016–5032.
- [2] J. D. Crowley, S. M. Goldup, A.-L. Lee, D. A. Leigh, R. T. McBurney, *Chem. Soc. Rev.* **2009**, *38*, 1530–1541.
- [3] S. Erbas-Cakmak, D. A. Leigh, C. T. McTernan, A. L. Nussbaumer, *Chem. Rev.* **2015**, *115*, 10081–10206.
- [4] J. F. Stoddart, *Angew. Chem. Int. Ed.* **2018**, *56*, 11094–11125.
- [5] H.-Y. Zhou, Q.-S. Zong, Y. Han, C.-F. Chen, *Chem. Commun.* **2020**, *56*, 9916–9936.
- [6] T. A. Barendt, A. Docker, I. Marques, V. Félix, P. D. Beer, *Angew. Chem. Int. Ed.* **2016**, *55*, 11069–11076.
- [7] J. Berná, J. D. Crowley, S. M. Goldup, K. D. Hänni, A. Lee, D. A. Leigh, *Angew. Chem. Int. Ed.* **2007**, *46*, 5709–5713.

## 5. Coordination-driven construction of [3]rotaxane based on hierarchical assembly

- [8] S. Kassem, T. van Leeuwen, A. S. Lubbe, M. R. Wilson, B. L. Feringa, D. A. Leigh, *Chem. Soc. Rev.* **2017**, *46*, 2592–2621.
- [9] E. A. Neal, S. M. Goldup, *Angew. Chem. Int. Ed.* **2016**, *55*, 12488–12493.
- [10] J. E. M. Lewis, R. J. Bordoli, M. Denis, C. J. Fletcher, M. Galli, E. A. Neal, E. M. Rochette, S. M. Goldup, *Chem. Sci.* **2016**, *7*, 3154–3161.
- [11] E. A. Neal, S. M. Goldup, *Chem. Sci.* **2015**, *6*, 2398–2404.
- [12] G. H. Clever, P. Punt, *Acc. Chem. Res.* **2017**, *50*, 2233–2243.
- [13] B. Zhang, Design and Synthesis of Novel Self Assembled Supramolecular Coordination Cages. Doctoral dissertation, TU Dortmund, **2020**.
- [14] J. Tessarolo, H. Lee, E. Sakuda, K. Umakoshi, G. H. Clever, *J. Am. Chem. Soc.* **2021**, *143*, 6339–6344.
- [15] M. D. Ward, P. R. Raithby, *Chem. Soc. Rev.* **2012**, *42*, 1619–1636.
- [16] J. L. Bolliger, T. K. Ronson, M. Ogawa, J. R. Nitschke, *J. Am. Chem. Soc.* **2014**, *136*, 14545–14553.
- [17] C. García-Simón, M. Garcia-Borràs, L. Gómez, T. Parella, S. Osuna, J. Juanhuix, I. Imaz, D. MasPOCH, M. Costas, X. Ribas, *Nat. Commun.* **2014**, *5*, 5557.
- [18] L.-X. Cai, S.-C. Li, D.-N. Yan, L.-P. Zhou, F. Guo, Q.-F. Sun, *J. Am. Chem. Soc.* **2018**, *140*, 4869–4876.
- [19] G. H. Clever, S. Tashiro, M. Shionoya, *J. Am. Chem. Soc.* **2010**, *132*, 9973–9975.
- [20] W. M. Bloch, Y. Abe, J. J. Holstein, C. M. Wandtke, B. Dittrich, G. H. Clever, *J. Am. Chem. Soc.* **2016**, *138*, 13750–13755.
- [21] N. P. Liyanage, W. Yang, S. Guertin, S. S. Roy, C. A. Carpenter, R. E. Adams, R. H. Schmehl, J. H. Delcamp, J. W. Jurss, *Chem. Commun.* **2018**, *55*, 993–996.
- [22] S. Pullen, S. Löffler, A. Platzek, J. J. Holstein, G. H. Clever, *Dalton. Trans.* **2020**, *49*, 9404–9410.
- [23] X. Qi, R. Zhong, M. Chen, C. Sun, S. You, J. Gu, G. Shan, D. Cui, X. Wang, Z. Su, *ACS. Catal.* **2021**, *11*, 7241–7248.
- [24] G. H. Clever, M. Shionoya, *Chem. Eur. J.* **2010**, *16*, 11792–11796.
- [25] H. Jian, J. M. Tour, *J. Org. Chem.* **2003**, *68*, 5091–5103.





## 6 Conclusion and perspectives

A series of salicylaldehyde ligands possessing functions owing to the introduced AIE-active TPE and photosensitizer phenoxazine units were successfully synthesized. The construction of the bis-salen or salphen macrocycles in a quantitative yield was achieved via a facile condensation reaction of the corresponding salicylaldehyde ligands and diamine derivatives.  $N_2O_2$  coordination-sites of the obtained salen/salphen complexes allowed the introduction of metals. Structure and photophysical properties of the synthesized (metal-organic) macrocycles were fully characterized by NMR spectroscopy, ESI-MS, X-ray diffraction, UV-Vis absorption, and other variety of spectroscopic techniques.

Emissive binuclear metallamacrocycle  $Zn_2R$  with AIE property was obtained by the self-assembly of TPE based salen-macrocycle with Zn(II) ions. Successful introduction of chirality was shown by changing ethylene diamine to enantiomerically pure 1,2-diphenylethane-1,2-diamine for the condensation reaction. Over increasing the portion of water in a THF solution of  $Zn_2R$ , emission properties were enhanced, probably owing to the AIE active TPE unit. Compared with  $Zn_2R$ , **R** shows weaker emission, which proves the molecular design of macrocycles having salen/salphen coordination-sites to manipulate optical properties by introduction of a metal center. In addition, specifically for  $Zn_2R$ , the chiral input from the salphen-moiety was translated into helical chirality in the aggregated state induced by addition of water. The aggregated metal-containing macrocycle showed a reversion of the CPL properties with a high  $|g_{lum}|$  value of  $1 \times 10^{-2}$ . On the other hand, **R** did not show such aggregation-induced CPL properties.

A new kind of salen macrocycle (metal free macrocycle  $R^{PZ}$ , metal-containing macrocycle  $Zn_2R^{PZ}$ ), comprised of phenoxazine cores and salen-moieties was designed and synthesized aiming for a use in photoredox catalysis. Comprehensive characterization and investigations of photophysical properties of the ligand,  $R^{PZ}$ , and  $Zn_2R^{PZ}$  were performed. Pinacol coupling reaction of several aldehydes using the synthesized photoredox catalysts were performed. All of the newly obtained photoredox catalysts showed a good catalytic ability in the homo-coupling reaction even with low catalyst loading. Investigation of electronic properties of the

## 6. Conclusion and perspectives

photoredox catalysts implied that the catalytic activity can be tuned through macrocyclization and coordination of the metal. Considering that a wide range of catalytic applications of metal salen complexes mostly originate from the metal center,  $Zn_2R^{PZ}$  should have a potential as a catalyst promotes tandem catalytic reactions.

Self-assembly of a salphen macrocycle possessing Co(III) having an octahedral coordination geometry provides an opportunity to introduce one or two extra bis-monodentate ligands to the metal-organic macrocycle to yield a bowl or cage topology. By taking an advantage of such a coordination geometry, the synthesis of rotaxanes has been investigated. A carbazole-based ligand with an introduced chain for a further click/condensation reaction was prepared. Consequently, the synthesis of a bowl-shaped coordination cage by combining the synthesized carbazole-based ligand and binuclear Co(III)-macrocycle has been demonstrated. The solid-state structure of the synthesized bowls was revealed by single crystal X-ray diffraction. In the X-ray structures, the chemical pendant on the carbazole-based ligands were found to be penetrating through the macrocycle. The following condensation reaction of two such coordination bowls seemed to work to facilitate a [3]rotaxane consisting of the two Co(III)-macrocycles and the axle supposedly threading the macrocycles. Further structural characterization shall be performed in due course to valid such a [3]rotaxane structure. Furthermore, based on the shape complementary approach, a heteroleptic cage designed for applications in catalysis was obtained by self-assembly of Co(III)-macrocycle and two bis-monodentate ligands having catalytically active sites. The purification of products needs to be improved and catalytic activity should be further investigated.

To conclude, in this thesis, several new salen-/salphen macrocycles have been synthesized and investigated for their ability as a versatile platform for the development of CPL-active materials, photoredox catalysis, establishment of coordination-assisted rotaxane synthesis, and heteroleptic cage synthesis. The efficient and facile synthetic method of such salen/salphen macrocycles is of great advantage for diversification.

## Abbreviations

Å	Ångström
°C	Celcius
BODIPY	Boron-dipyrromethene
CH <sub>3</sub> CN	Acetonitrile
CHCl <sub>3</sub>	Chloroform
COSY	Correlated spectroscopy
Cp	Cyclopentadienyl
DFT	Density Functional theory
DIPEA	N,N-Diisopropylethylamine
DMSO	Dimethylsulfoxide
DOSY	Diffusion ordered spectroscopy
dppf	1,1'-Bis(diphenylphosphino)ferrocene
equiv.	equivalent
Et <sub>2</sub> O	Diethyl ether
GPC	Gel permeation chromatography
h	Hour
HR ESI-MS	High resolution electrospray ionization mass spectroscopy
LED	Light-emitting diode
MeOH	Methanol
MHz	Megahertz
m/z	Mass-to-charge ratio
mM	mmol•L <sup>-1</sup>
nm	nanometer
NMR	Nuclear magnetic resonance
NOESY	Nuclear overhauser effect spectroscopy
Oac <sup>-</sup>	Acetate anion
PC	Photoredox catalyst
Pin <sub>2</sub> B <sub>2</sub>	Bis(pinacolato)diboron
PPh	triphenylphosphine
ppm	Parts per million
r.t.	Room temperature

SET	Single electron transfer
$\text{SOCl}_2$	Thionyl chloride
THF	Tetrahydrofuran
TLC	Thin layer chromatography

## Acknowledgements

First of all, biggest thanks go to my supervisor Prof. Dr. Guido H. Clever for giving me the opportunity to pursue my PhD in his group. I am grateful to him for supervising this Ph.D. work, especially for the valuable suggestions, the continuous encouragement, and his strong support for many things. His enthusiasm and passion towards research largely motivated me. I was often helped by this personality with full of kindness and humor. Thank you very much for these fruitful four years

Second of all, I would like to thank Prof. Dr. Sebastian Henke for being part of the examination committee. Thanks for his warm encouragement and supports for my thesis.

I am also thankful to my country and China Scholarship Council, which have provided me with this precious opportunity to study abroad and experience different cultures. All the experience in Germany, especially in the Clever Lab, where the people from many different countries are working, have greatly broadened my horizon, deepened understandings into other cultures and enriched my knowledge.

I would like to thank Dr. Jacopo Tessarolo for CPL measurement. I would like to thank Dr. Julian J. Holstein for single crystal X-ray structure analysis. I would like to thank Shota Hasegawa for the helps with DFT calculation, X-ray structure refinement and the CV measurements. I would like to thank Laura Schneider and Dr. Anaya Baksi for ESI-MS measurements. I would like to thank Dr. Sudhakar Ganta for DLS measurements. I would like to thank Dr. Yen-Ting Chen for SEM measurements. I appreciate André Platzek and Kristina Ebbert for teaching me how to use Topspin and Adobe Illustrator softwares. I would like to thanks Dr. Jacopo Tessarolo, Shota Hasegawa, Elie Benchimol and Laura Neukirch for proofreading this thesis. I thanks to my student Ziyi for her works done under my supervision. Special hanks to Birgit Thormann and Dr. Gabriele Trötscher-Kaus for their helps and supports.

Many thanks to the whole Clever Lab for group trips (Juist, hiking, boat trip), international movie nights, girls' night, Christmas party, BBQ in Guido's place every year, and the spontaneous trips in Göttingen, Granada, Münster, Düsseldorf, Leiden,

and many other places. I would like to thank Bin, Jacopo, Haeri for helping me adapt to a new environment as soon as possible when I first joined the Clever Lab. I would like to thank Sonja, Jacopo, Shota, Bo, Kai, Elie for scientific discussion. I would like to thank our G-force lab members (Sonja, Bo, Rujin, Pedro, Elie, Alexandre) for a relaxed working environment. I would like to thank André and Kristina for their sincere concern and help. I would like to thank Irene and Lukas for inviting me to their Schützenfest and wedding in Illingen. I would like to thank Ana for inviting me to her defense in Spain. I would like to thank Kristian, Maike, Laura for their efforts on organizing the lab. I would also like to thank Eri, Thorben, Philip, Robin, Christoph, Armin, Simon, Hannah, Shing, Ertugrul, David Ocklenburg, Malavika, Björn and Lars for their friendships. Thanks to all the members. I'm really thankful to the members for their help and supports. I'm really enjoyed the time with them in the Clever Lab. I would like to thank my lifetime friends Tingting Ruan and Jing Zhang who also studied in Germany. Thanks for their accompany and help in the last years.

Last but not least, I am really grateful for my family, especially my parents, for their unconditional support.